

Use of Low Enriched Uranium Fuel in Accelerator Driven Subcritical Systems

**IAEA**

International Atomic Energy Agency

USE OF LOW ENRICHED URANIUM
FUEL IN ACCELERATOR DRIVEN
SUBCRITICAL SYSTEMS

The following States are Members of the International Atomic Energy Agency:

AFGHANISTAN	GEORGIA	OMAN
ALBANIA	GERMANY	PAKISTAN
ALGERIA	GHANA	PALAU
ANGOLA	GREECE	PANAMA
ANTIGUA AND BARBUDA	GUATEMALA	PAPUA NEW GUINEA
ARGENTINA	GUYANA	PARAGUAY
ARMENIA	HAITI	PERU
AUSTRALIA	HOLY SEE	PHILIPPINES
AUSTRIA	HONDURAS	POLAND
AZERBAIJAN	HUNGARY	PORTUGAL
BAHAMAS	ICELAND	QATAR
BAHRAIN	INDIA	REPUBLIC OF MOLDOVA
BANGLADESH	INDONESIA	ROMANIA
BARBADOS	IRAN, ISLAMIC REPUBLIC OF	RUSSIAN FEDERATION
BELARUS	IRAQ	RWANDA
BELGIUM	IRELAND	SAN MARINO
BELIZE	ISRAEL	SAUDI ARABIA
BENIN	ITALY	SENEGAL
BOLIVIA, PLURINATIONAL STATE OF	JAMAICA	SERBIA
BOSNIA AND HERZEGOVINA	JAPAN	SEYCHELLES
BOTSWANA	JORDAN	SIERRA LEONE
BRAZIL	KAZAKHSTAN	SINGAPORE
BRUNEI DARUSSALAM	KENYA	SLOVAKIA
BULGARIA	KOREA, REPUBLIC OF	SLOVENIA
BURKINA FASO	KUWAIT	SOUTH AFRICA
BURUNDI	KYRGYZSTAN	SPAIN
CAMBODIA	LAO PEOPLE'S DEMOCRATIC REPUBLIC	SRI LANKA
CAMEROON	LATVIA	SUDAN
CANADA	LEBANON	SWAZILAND
CENTRAL AFRICAN REPUBLIC	LESOTHO	SWEDEN
CHAD	LIBERIA	SWITZERLAND
CHILE	LIBYA	SYRIAN ARAB REPUBLIC
CHINA	LIECHTENSTEIN	TAJIKISTAN
COLOMBIA	LITHUANIA	THAILAND
CONGO	LUXEMBOURG	THE FORMER YUGOSLAV REPUBLIC OF MACEDONIA
COSTA RICA	MADAGASCAR	TOGO
CÔTE D'IVOIRE	MALAWI	TRINIDAD AND TOBAGO
CROATIA	MALAYSIA	TUNISIA
CUBA	MALI	TURKEY
CYPRUS	MALTA	TURKMENISTAN
CZECH REPUBLIC	MARSHALL ISLANDS	UGANDA
DEMOCRATIC REPUBLIC OF THE CONGO	MAURITANIA	UKRAINE
DENMARK	MAURITIUS	UNITED ARAB EMIRATES
DJIBOUTI	MEXICO	UNITED KINGDOM OF GREAT BRITAIN AND NORTHERN IRELAND
DOMINICA	MONACO	UNITED REPUBLIC OF TANZANIA
DOMINICAN REPUBLIC	MONGOLIA	UNITED STATES OF AMERICA
ECUADOR	MONTENEGRO	URUGUAY
EGYPT	MOROCCO	UZBEKISTAN
EL SALVADOR	MOZAMBIQUE	VANUATU
ERITREA	MYANMAR	VENEZUELA, BOLIVARIAN REPUBLIC OF
ESTONIA	NAMIBIA	VIET NAM
ETHIOPIA	NEPAL	YEMEN
FIJI	NETHERLANDS	ZAMBIA
FINLAND	NEW ZEALAND	ZIMBABWE
FRANCE	NICARAGUA	
GABON	NIGER	
	NIGERIA	
	NORWAY	

The Agency's Statute was approved on 23 October 1956 by the Conference on the Statute of the IAEA held at United Nations Headquarters, New York; it entered into force on 29 July 1957. The Headquarters of the Agency are situated in Vienna. Its principal objective is "to accelerate and enlarge the contribution of atomic energy to peace, health and prosperity throughout the world".

IAEA-TECDOC-1821

USE OF LOW ENRICHED URANIUM
FUEL IN ACCELERATOR DRIVEN
SUBCRITICAL SYSTEMS

INTERNATIONAL ATOMIC ENERGY AGENCY
VIENNA, 2017

COPYRIGHT NOTICE

All IAEA scientific and technical publications are protected by the terms of the Universal Copyright Convention as adopted in 1952 (Berne) and as revised in 1972 (Paris). The copyright has since been extended by the World Intellectual Property Organization (Geneva) to include electronic and virtual intellectual property. Permission to use whole or parts of texts contained in IAEA publications in printed or electronic form must be obtained and is usually subject to royalty agreements. Proposals for non-commercial reproductions and translations are welcomed and considered on a case-by-case basis. Enquiries should be addressed to the IAEA Publishing Section at:

Marketing and Sales Unit, Publishing Section
International Atomic Energy Agency
Vienna International Centre
PO Box 100
1400 Vienna, Austria
fax: +43 1 2600 29302
tel.: +43 1 2600 22417
email: sales.publications@iaea.org
<http://www.iaea.org/books>

For further information on this publication, please contact:

Division of Nuclear Fuel Cycle and Waste Technology
International Atomic Energy Agency
Vienna International Centre
PO Box 100
1400 Vienna, Austria
Email: Official.Mail@iaea.org

© IAEA, 2017
Printed by the IAEA in Austria
August 2017

IAEA Library Cataloguing in Publication Data

Names: International Atomic Energy Agency.
Title: Use of low enriched uranium fuel in accelerator driven subcritical systems /
International Atomic Energy Agency.
Description: Vienna : International Atomic Energy Agency, 2017. | Series: IAEA TECDOC
series, ISSN 1011-4289 ; no. 1821 | Includes bibliographical references.
Identifiers: IAEAL 17-01106 | ISBN 978-92-0-106217-8 (paperback : alk. paper)
Subjects: LCSH: Accelerator-driven systems. | Uranium as fuel. | International cooperation.

FOREWORD

An accelerator driven subcritical system (ADS) consists of a subcritical assembly and an external source of neutrons that may be either generated by an accelerator or provided by a radionuclide source (e.g. americium–beryllium or californium). The subcritical assembly has an array of nuclear fuel elements without the possibility of sustaining a fission chain reaction.

This publication documents the results and conclusions of an international research collaboration devoted to gaining a better understanding of the physics of an ADS, with particular emphasis on the investigation of various technical options for carrying out ADS research using low enriched uranium fuel. This effort was conducted under the auspices of the IAEA over a period of five years at laboratories in several countries, and some of the material presented here originated from the IAEA coordinated research project entitled Analytical and Experimental Benchmark Analysis of Accelerator Driven Systems.

The purpose of this publication is to document the history of the research programme, explore the technical issues involved and offer interpretations of the results. The publication contains information on nine ADS facilities, including descriptions of the hardware deployed, experiments conducted, computational resources and procedures used in the analyses, principal results obtained, and conclusions drawn from the knowledge gained as a consequence of this work.

The IAEA is grateful to all the contributors for their assistance, in particular Y. Gohar (United States of America), who led the preparation of this publication. The IAEA officers responsible for this publication were D. Jinchuk, F. Marshall and M. Voronov of the Division of Nuclear Fuel Cycle and Waste Technology.

EDITORIAL NOTE

This publication has been prepared from the original material as submitted by the contributors and has not been edited by the editorial staff of the IAEA. The views expressed remain the responsibility of the contributors and do not necessarily represent the views of the IAEA or its Member States.

Neither the IAEA nor its Member States assume any responsibility for consequences which may arise from the use of this publication. This publication does not address questions of responsibility, legal or otherwise, for acts or omissions on the part of any person.

The use of particular designations of countries or territories does not imply any judgement by the publisher, the IAEA, as to the legal status of such countries or territories, of their authorities and institutions or of the delimitation of their boundaries.

The mention of names of specific companies or products (whether or not indicated as registered) does not imply any intention to infringe proprietary rights, nor should it be construed as an endorsement or recommendation on the part of the IAEA.

The IAEA has no responsibility for the persistence or accuracy of URLs for external or third party Internet web sites referred to in this publication and does not guarantee that any content on such web sites is, or will remain, accurate or appropriate.

CONTENTS

1.	INTRODUCTION AND BACKGROUND	1
1.1.	Background.....	1
1.1.1.	Concept of an ADS reactor	2
1.1.2.	Practical applications for ADS	5
1.1.3.	Physics considerations	7
1.1.4.	Research on zero-power ADS facilities	11
1.2.	Objectives of ADS research.....	11
1.3.	Scope of the present research programme	12
1.4.	Contents and structure of this publication	13
	References to Section 1	15
2.	YALINA-BOOSTER BENCHMARK ANALYSES.....	16
2.1.	Introduction.....	17
2.2.	Yalina-Booster configuration with 90% enriched uranium fuel.....	19
2.2.1.	Kinetic parameters of the YALINA-Booster configuration with 1141 fuel rods in the thermal zone.....	20
2.2.2.	Reaction rates of the YALINA-Booster configuration with 1141 fuel rods in the thermal zone.....	21
2.2.3.	Neutron Spectrum of the YALINA-Booster configuration with 1141 fuel rods in the thermal zone.....	25
2.2.4.	Reaction rates from D-D and D-T neutron pulses for the YALINA-Booster configuration with 1141 fuel rods in the thermal zone	28
2.2.5.	Kinetic parameters of the YALINA-Booster configuration with 902 fuel rods in the thermal zone.....	32
2.2.6.	Reaction rates of the YALINA-Booster configuration with 902 fuel rods in the thermal zone.....	33
2.2.7.	Neutron spectrum of the YALINA-Booster configuration with 902 fuel rods in the thermal zone.....	36
2.2.8.	Reaction rates from D-D and D-T neutron pulses of the YALINA-Booster configuration with 902 fuel rods in the thermal zone	38
2.3.	Yalina-Booster configuration with 36% enriched uranium fuel.....	41
2.3.1.	Kinetic parameters of the YALINA-Booster configuration with 1185 fuel rods in the thermal zone.....	41
2.3.2.	Reaction rates of the YALINA-Booster configuration with 1185 fuel rods in the thermal zone.....	42
2.3.3.	Neutron spectrum of the YALINA-Booster configuration with 1185 fuel rods in the thermal zone.....	45
2.3.4.	Reaction rates from D-D and D-T Neutron Pulses of the YALINA-Booster configuration with 1185 fuel rods in the thermal zone	47
2.4.	Yalina-Booster configuration with 21% enriched uranium fuel.....	50
2.4.1.	Kinetic parameters of the YALINA-Booster configuration with 1185 fuel rods in the thermal zone.....	51
2.4.2.	Reaction rates of the YALINA-Booster configuration with 1185 fuel rods in the thermal zone.....	51

2.4.3.	Reaction rates from D-D and D-T neutron pulses of the YALINA-Booster configuration with 1185 fuel rods in the thermal zone	52
2.5.	Comparison of computational and experimental results	55
2.5.1.	YALINA-Booster configuration with 90% enriched uranium fuel in the fast zone	55
2.5.2.	YALINA-Booster configuration with 36% enriched uranium fuel in the fast zone	57
2.5.3.	YALINA-Booster configuration with 21% enriched uranium fuel in the fast zone	61
2.5.4.	Conclusions	63
	References to Section 2	65
3.	YALINA-THERMAL FACILITY EXPERIMENTS	66
3.1.	Introduction.....	66
3.2.	Facility details	67
3.3.	Research activity	71
3.4.	Results	78
3.4.1.	Kinetic Parameters	78
3.4.2.	Reaction Rates	81
3.4.3.	Neutron Spectrum	101
3.4.4.	Reaction Rates from D-D and D-T Neutron Pulses and Corrected Effective Neutron Multiplication Factor.....	109
3.5.	Conclusions.....	117
	References to Section 3	117
4.	IPEN-MB-01 SUBCRITICAL CONFIGURATIONS BENCHMARK	119
4.1.	Introduction.....	119
4.2.	Facility description.....	119
4.3.	Research activity	121
4.3.1.	Phase I.....	121
4.3.2.	Phase II.....	123
4.4.	Results	125
4.4.1.	Phase I.....	125
4.4.2.	Phase II.....	134
4.5.	Conclusions.....	136
	References to Section 4	137
5.	TRADE EXPERIMENTAL BENCHMARK	138
5.1.	Introduction.....	138
5.2.	Facility details	139
5.2.1.	Description of the TRIGA Reactor	139
5.2.2.	Instrumentation	141
5.2.3.	Core Configurations.....	142
5.3.	Research activity and results.....	145

5.3.1.	Experimental Studies	145
5.3.2.	Benchmark Analyses.....	147
5.4.	Conclusions.....	160
	References to Section 5	161
6.	EXPERIMENTAL NEUTRON SOURCE FACILITY OF KHARKOV INSTITUTE OF PHYSICS AND TECHNOLOGY.....	162
6.1.	Introduction.....	162
6.1.1.	Target Assembly	163
6.1.2.	Subcritical Assembly	167
6.1.3.	Biological Shield	171
6.2.	Neutron source facility design	172
6.3.	Conclusions.....	174
	References to Section 6	175
7.	KUCA SUBCRITICAL EXPERIMENTS	178
7.1.	Introduction.....	178
7.2.	Benchmark specifications.....	179
7.2.1.	KUCA Core	179
7.2.2.	The 14-MeV Pulsed-neutron Generator Description.....	184
7.2.3.	The Neutron Shield and Beam Duct	184
7.2.4.	Acquisition of the Experimental Results.....	187
7.3.	Core configurations	189
7.4.	Static experimental results	193
7.4.1.	Excess Reactivity and Subcriticality.....	193
7.4.2.	Reaction-rate Distribution	194
7.4.3.	Reaction Rates of Activation Foils	195
7.5.	Core conditions	196
7.6.	Kinetic experimental results	197
7.6.1.	Neutron-Noise Method (Feynman- α and Rossi- α Methods).....	197
7.6.2.	Source Multiplication Method.....	199
7.6.3.	Pulsed-neutron Method.....	202
7.7.	Bechmark results.....	206
7.7.1.	Static Experiments	206
7.7.2.	Kinetic Experiments.....	215
7.8.	Conclusions.....	218
	References to Section 7	219
8.	ACCELERATOR DRIVEN SUBCRITICAL RESEARCH FACILITY H5B-C BENCHMARK	221
8.1.	Introduction.....	221
8.2.	Simulation of the charged particles interaction with the target materials	222
8.3.	Simulation of the neutron flux in the subcritical core.....	232

8.4.	Conclusions	240
	References to Section 8.....	241
9.	SUBCRITICAL FACILITY VENUS-1 OF THE CHINA INSTITUTE OF ATOMIC ENERGY	242
9.1.	Introduction	242
9.2.	Characteristics of the Venus-1 ADS facility	242
	9.2.1. Structural Description of Venus-1	242
	9.2.2. Venus-1 Zone Description.....	245
9.3.	Benchmark description.....	248
9.4.	Methodology and calculations.....	251
	9.4.1. Methodology.....	251
	9.4.2. Computational Procedures.....	251
9.5.	Calculated results	252
	9.5.1. Effective Multiplication Factor and Effective Prompt Multiplication Factor	252
	9.5.2. Effective Delayed Neutron Fraction β_{eff}	252
	9.5.3. Prompt Neutron Lifetime and Mean Neutron Generation Time	253
	9.5.4. Total Flux in the Experimental Channel.....	254
	9.5.5. Neutron Spectra	255
	9.5.6. Axial Distribution of the Total Neutron Flux.....	258
9.6.	Summary and conclusions.....	259
	References to Section 9.....	260
10.	THE MARIA EXPERIMENT FOR USE OF LOW ENRICHED URANIUM (LEU) IN AN ACCELERATOR DRIVEN SUBCRITICAL ASSEMBLY (ADS).....	261
10.1.	Introduction	261
10.2.	Experimental facilities and measurements	261
	10.2.1. Transmutation of minor actinides and fission products.....	261
	10.2.2. Pb-U-Blanket Target	275
10.3.	Numerical simulations.....	290
	10.3.1. Transmutation of minor actinides and fission products nuclei.....	290
10.4.	Conclusions	296
	References to Section 10.....	296
	Contributors to drafting and review.....	299

1. INTRODUCTION AND BACKGROUND

1.1. BACKGROUND

This publication documents the results and conclusions from international research collaboration devoted to gaining a better understanding of the physics of accelerator-driven subcritical nuclear systems (ADS). This effort has been carried out under the auspices of the IAEA over a period of five years at laboratories in several countries.

In principle High Enriched Uranium (HEU) or Low Enriched Uranium (LEU) can be used for sub-critical assembly fuel, however, proliferation concerns raised by the civil use of HEU have been addressed by several international undertakings supported by the IAEA, like the Reduced Enrichment for Research and Test Reactors (RERTR) programme. Accordingly, efforts have been undertaken to convert existing research reactors to LEU and to encourage the use of LEU in the design of new research reactors and other nuclear facilities like ADS.

At present, more than twenty IAEA Member States have technical activities for ADS, some Member States are already operating ADS facilities, and some have plans for constructing new ADS. In all cases it is recommended that these facilities utilize LEU fuel for the sub-critical assemblies.

An important component of this work has been the investigation of various technical options for carrying out ADS research using low enriched uranium fuel. Attention is given here to reporting on investigations aimed at attaining knowledge and understanding about existing or proposed ADS facilities that have been involved in this collaborative exercise. New knowledge and experience have been acquired through the conduct of various experiments, through the validation of codes and computational procedures used to model these facilities, through analyses of the acquired experimental data (where applicable), and through a variety of additional studies directed toward providing a broader understanding of the physics and operational characteristics of ADS. A feature of the present project has been that in most instances analytical studies corresponding to a particular facility have been carried out by several different investigating teams. The result of this approach is that in some cases several sets of comparable results have been generated that can be compared.

While extensive progress reports, conference contributions, theses, and journal publications have been generated to document various aspects of the work for this project during the past five years, there currently exists no single document that traces the history of this research programme, provides an overview discussion of the technical issues involved, and offers specific details and interpretations of the obtained results in a unified context. This deficiency was the motivation for undertaking the writing of the present publication. It aims to provide an overview of the research activities that were undertaken, to document the knowledge gained from this work, and to interpret these results in a comprehensive manner.

Seventeen (17) Member States have been involved in this work; they are indicated in Table 1.1 below. The grouping is by specific facility. In addition to gaining an understanding of both the static and dynamic properties of ADS, close collaborations between various research groups involved in this work have resulted in understanding and resolving a number of discrepancies initially observed for some of the results obtained during the course of these investigations. This has led to improved comprehension of the differences between various experimental methods used, between different employed nuclear data libraries, between the various nuclear system analysis codes used, and between the procedures employed in applying these resources in the context of ADS applications. In some cases observed C/E discrepancies stimulated additional measurements at certain facilities involved in this collaboration, followed by repeated analyses, often involving the use of more sophisticated tools and approaches. These outcomes largely serve to fulfil an important goal of this effort: comparable analytic results obtained by various means are expected to agree reasonably well

with each other as well as with reliable experimental information (where available), and the identified discrepancies should be understood and resolved wherever possible.

TABLE 1.1. MEMBER STATE PARTICIPATION IN THE RESEARCH ACTIVITIES DESCRIBED IN THIS PUBLICATION

Facility	Member States
YALINA-Booster	Argentina, Belarus, Brazil, China, India, Italy, Republic of Korea, Serbia, Spain, Ukraine, United States of America
YALINA-Thermal	Argentina, Belarus, Brazil, China, India, Republic of Korea, Poland, Serbia, United States of America
IPEN-MB-01	Argentina, Brazil,
TRADE	Italy, Japan, France
KIPT	Ukraine, United States of America
KUCA Subcritical Experiments	Japan, Pakistan
H5B-C	Brazil, Serbia
VENUS-1	China
MARIA	Poland

Some of the facilities involved in this collaboration received more attention than others, as is evident from Table 1.1. Details about the contributions from each Member State to the individual research projects are documented in considerable detail in the ensuing sections.

Research campaigns carried out at the nine considered ADS facilities covered in this publication, identified below by their abbreviated names, are as follows: YALINA-Booster with 90% , 36% , or 21% enriched fuel (Section 2); YALINA-Thermal (Section 3); IPEN-MB-01, Phase 1 and Phase 2 (Section 4); TRADE (Section 5); KIPT (Section 6); KUCA Subcritical Experiments (Section 7); H5B–C (Section 8); VENUS-1 (Section 9); and MARIA (Section 10). Brief descriptions of these facilities (existing or conceptual) are provided in the indicated sections, along with discussions of experiments (where applicable) and analytical studies conducted there, and with the corresponding analyses of the acquired results. As mentioned above, in some cases the work described pertains to conceptual design studies for facilities that have yet to be built or are in some stage of construction.

A collection of references is also provided in this TECDOC, section by section, to which the reader can refer to obtain not only further details about the present work, but also to learn about various aspects of ADS research in an even broader context than provided from the present investigations (see reference lists). Since there are so many possible references that could have been included, for practical purposes the listed references clearly represent just a modest subset. The choices as to what to include as references are somewhat arbitrary, but the intent here is to provide supplemental information that might be of use to readers rather than to give author credit to all possible sources of information mentioned in this TECDOC.

1.1.1. Concept of an ADS reactor

This Section outlines the basic physics characteristics of an ADS reactor and offers a comparison between ADS reactors and conventional fission nuclear reactors. The operation of conventional nuclear reactors, also known as critical reactors, relies on the presence within the system of an adequate supply of neutrons that can be generated on a continuing basis (steady

operation) by nuclear fission reactions induced by neutrons incident on uranium or plutonium nuclei (major actinides), and, to a much lesser extent, minor actinide (MA) materials, mainly neptunium, americium, and curium, in a fuel-bearing, multiplying medium (a reactor core) [1.1, 1.2]. This multiplying effect varies somewhat from nucleus to nucleus (and it is also modestly dependent on the energy of the incident neutron that induces the fission). However, on the average, this multiplication factor (called $\bar{\nu}$) is ≈ 2.5 neutrons per fission event. The great majority of these are prompt neutrons which are emitted at the time of fission (normally, on the order of 10^{-22} second after initiation of the fission reaction). A very small percentage of neutrons (typically, considerably less than 1%) are emitted in the fission process over a much longer time period (typically, ranging from a few milliseconds to approximately 60 seconds). These ‘delayed neutrons’ originate from the radioactive decay of neutron-rich fission products by beta decay. The time scales for the decays of these ‘precursor’ atoms ranges from milliseconds to several seconds. These decays can form daughter nuclei in highly excited states. Usually they decay by gamma emission, but in some cases the excitation energies of these daughter nuclei lie above the thresholds for neutron emission, in competition with gamma decay. Since the decays of these daughter nuclei, whether by gamma or neutron emission, is prompt, the ‘delay’ associated with delayed-neutron yield is governed by the lifetimes of the precursors. The existence of this small fraction of delayed neutrons is of crucial importance in assuring that critical reactors can be controlled safely.

The most important physics parameter associated with the design of any nuclear energy device based on nuclear fission, including ADS devices, is k_{eff} [1.1]. This parameter is a measure of the number of neutrons present in the system at each successive generation in the ‘chain’ of nuclear events within a reactor, when compared with the number of neutrons present in the preceding generation. Every produced neutron in a nuclear system is eventually lost in a quite short time period ($\ll 1$ millisecond) to the system neutron inventory, either through escape from the device or by initiating of a neutron-induced nuclear reaction. If it escapes, or it is lost within the system due to a reaction that does not produce a next-generation neutron, there is a reduction in the ability of that system to sustain a viable neutron inventory for continuous operation.

The only reason that fission reactors can be built in the first place happens because a multiplying medium can be constructed with sufficient fissionable material (nuclear fuel) to insure an adequate supply of neutrons to produce fission events, thereby generating energy (approximately 200 MeV per fission) as well as sustaining the neutron inventory within the core [1.1]. Thus, if k_{eff} , which is also a property of the reactor system itself as a whole, not solely of the fissionable material, is equal to one, then stable operation of the system is possible, and a steady-state condition of the neutron population in that system can be established. This is the condition of ‘criticality’, and it gives rise to the name ‘critical reactor’. If k_{eff} exceeds 1, then the neutron population after n generations grows according to the factor $(k_{eff})^n$. Since the effective time between generations is very short, this multiplication factor expands the neutron population very rapidly (non-linearly) and ultimately leads to a super-critical condition (i.e. an explosion or ‘criticality accident’). If k_{eff} is less than unity, the neutron population in the system will die out rather rapidly unless a new supply of neutrons is introduced. Then, the neutron population becomes exceedingly small (effectively vanishing) after n generations (excluding consideration of the small fraction of delayed neutrons). Actually, the presence of neutrons in a system that can be attributed to delayed neutrons also dies out eventually as well (on a time scale of no more than a few seconds, as mentioned above), but certainly this occurs on a much longer time scale than is the fate for prompt neutrons.

Critical reactors are designed to have an inherent capability of achieving k_{eff} greater than unity, but they are maintained at an operating level not exceeding k_{eff} equal to unity, i.e. at

‘criticality’, through the use of control (or safety) rods composed of elements with strong neutron absorption cross-sections [1.1]. These control rods remove excess neutrons and reduce the reactivity of the system to a level that is sufficient to insure safe operation. The ability of a reactor to safely maintain stable operation is afforded by the longer time scale of delayed neutron emission decay in the system when compared with prompt neutrons. This is sometimes referred to the condition of ‘prompt subcritical – delayed critical’. In other words, in order that they can be controlled safely on a reasonable time scale, ‘critical’ reactors are actually designed to be slightly subcritical for prompt neutrons and only achieve criticality as a consequence of the delayed neutrons. Nevertheless, concern for the possibility (although very small) of criticality accidents occurring in ordinary operating critical reactors has prompted interest for many years in devising, designing, constructing, and operating nuclear energy systems for which criticality accidents are physically impossible, thereby effectively side-stepping the issue of criticality hazards completely. Such devices are therefore considered to be ‘inherently safe’, at least safe to the possibility of unwanted criticality occurring in the reactor core [1.3]. Fission reactors utilize negative reactivity feedback to achieve the inherent safe operation.

There are two fundamentally different ways to generate nuclear energy in the absence of criticality. One is via the use of nuclear fusion, where the driving energy source in the reactor is the fusion of hydrogen atoms (e.g. deuterium + deuterium or deuterium + tritium), with the release of one or fewer neutrons per reaction event. The second approach involves nuclear fission of actinide materials as the driving fuel, but where inherent subcriticality ($k_{eff} < 1$ under all operating conditions) is assured by designing the core to entail, by geometric design or other means, effectively less than a critical mass of fissionable materials under all conditions. Such a device would, of course, be useless as an energy source unless a steady external source of neutrons is generated and introduced into the core to sustain its continuous operation, albeit in the inherently safe subcritical mode ($k_{eff} < 1$). The coupling of a continuous (or sometimes pulsed in time) source of external neutrons with a subcritical core constitutes an ADS. As conceived for eventual high-power systems, these external neutrons would be generated by the use of powerful accelerators [1.4]. The approach most commonly envisioned involves bombarding high atomic number (high-Z) materials such as lead, bismuth, mercury, or tungsten with energetic protons to generate copious spallation neutrons. An alternative concept, one that involves the use of energetic electrons bombarding high-Z targets to generate photons which, in turn, generate neutrons via photonuclear processes, is also discussed in this publication (Section 6).

A key to understanding the basic difference between conventional critical reactors and subcritical ADS can be acquired by considering the total number of neutrons produced within a multiplying medium, including n generations. This is given by the ‘amplification factor’:

$$A_n = \sum_{i=0,n} (k_{eff})_i = 1 + (k_{eff})^1 + (k_{eff})^2 + \dots + (k_{eff})^n \quad (1.1)$$

In other words, the conditions in the reactor core are such that neutrons from at least n generations are present in the core at a particular time. For ‘ n ’ very large, the amplification factor A_n approaches the value:

$$A_\infty \approx \frac{1}{1-k_{eff}} \quad (1.2)$$

This follows from the rule for calculating the sum of an infinite geometric series. As k_{eff} approaches unity, the factor A_∞ actually approaches infinity (criticality), and there would indeed be an ‘explosion’ in the neutron population if the system were not controlled as described earlier [1.1]. However, if $k_{eff} < 1$, but still very close to unity, then A_∞ can be a quite large number which, nevertheless, is constrained to never be exceeded by the inherent subcritical design of the core. Under these circumstances, the neutron population present in

the core as a consequence of the N_0 first-generation neutrons from the external source becomes:

$$N \approx \frac{N_0}{1-k_{eff}} \quad (1.3)$$

This level of neutron density in the core can be maintained effectively at a steady-state condition by maintaining N_0 at a stable level. Thus, a core containing fissionable material can act as a neutron (or power) ‘amplifier’ when operating at steady conditions in subcritical mode [1.4]. A facility with a modest value of N_0 will operate at low power, but it can exhibit many of the basic features of a high-power facility corresponding to large N_0 . The increase of the neutron inventory in the core, and therefore the power produced, will increase linearly with the external neutron driver source intensity, according to this scheme [1.1]. The sensitivity of the neutron and power densities in the core is even greater (nonlinearly) to k_{eff} for values of this parameter approaching unity, according to the factor $\frac{1}{1-k_{eff}}$ which is referred to as the amplification factor for a subcritical reactor. The consequences of this fundamental feature of externally driven subcritical cores can be put to very good practical use, as discussed in the following Sections.

Externally driven subcritical systems exhibit very different operating characteristics from critical reactors [1.1]. Also, the experimental determination of these operating characteristics (reactor kinetics) requires techniques (both experimental and analytical) that are often considerably more complicated (and difficult to implement) than is the usual experience for critical systems. This leads to interesting physics which, in part, is discussed in the details of the present publication. A thorough understanding of these physics issues is an essential prerequisite to designing practical and effective high-power ADS for energy production and transmutation applications. Important technical issues to be considered are related to design, construction, and utilization of the external neutron source along with those related to the behaviour of the driven core itself. These issues can be quite complicated, and to a large extent they are the basis for the research described in this publication.

1.1.2. Practical applications for ADS

As mentioned above, ADS nuclear-energy devices are being suggested as possible options to generate energy for both electric power production and the reduction of nuclear waste through nuclear transmutation reactions [1.3, 1.4]. The key to practical implementation of these opportunities lies in gaining a thorough understanding of the details of the neutron inventories in these systems. Nuclear power, and a potential surplus of neutrons in the multiplying medium, both can eventually be attributed to the fission process itself. The external neutrons introduced into the core either escape (since every core is finite) or produce nuclear reactions. Some of these reactions involve fission. As mentioned earlier, each fission event yields ≈ 2.5 neutrons for the succeeding generation on average. Reactions of the (n,2n) category generate just one net neutron per event. The cross-sections for (n,xn) reactions for $n \geq 3$ tend to be quite small. These reactions tend to have a very modest effect on the neutron inventory in a reactor, but they can shift the neutron-energy spectrum with consequences that must be considered in detailed studies of the dynamics of ADS. In addition to providing surplus neutrons, each fission event generates considerable energy (≈ 185 MeV from prompt fission + ≈ 15 MeV from decay of the fission fragment nuclei) [1.1]. The prompt fission neutrons exhibit a source (initial) energy spectrum that resembles a Maxwellian distribution with an average energy of ≈ 2 MeV, depending somewhat on the particular actinide target isotope (e.g. U, Pu, etc.). This spectrum is eventually modified by neutron scattering, and it becomes much softer than a pure fission spectrum throughout most of the reactor. Depending on the core design, many of the neutrons become thermalized. The balance of the prompt energy released is kinetic energy of the fragments which quickly converts to heat. This energy

is needed to provide the useful output (e.g. the generation of electricity for the grid as well as for powering the source of external neutrons). The delayed neutrons are emitted with discrete energies of a few-MeV or less, and therefore they are not Maxwellian-distributed at birth but tend to be lower in energy, on average. As mentioned before, they serve mainly to provide a means of controlling a reactor that is operating in the vicinity of criticality.

What productive use can be made of the excess neutrons that have neither been lost unproductively or have produced new fissions? There are two important ones, and it happens that a detailed understanding of them is fraught with many complications owing to the inherent complexity and rich variety of nuclear processes, both nuclear reactions and the decay of radioactive nuclei [1.5].

First, they can be used to produce valuable new isotopes through nuclear reactions, e.g. new actinide fuel-element isotopes that do not exist in nature (e.g. ^{233}U , ^{239}Pu) or certain medical isotopes (e.g. $^{99\text{m}}\text{Tc}$) [1.3]. These will generally involve the capture of neutrons in fertile materials, i.e. in actinides that don't fission easily in their normal state by collisions with low-energy neutrons (e.g. threshold fission reactions ^{238}U or ^{232}Th) or in parent materials that can be transmuted into useful daughter medical or industrial isotopes (e.g. ^{99}Mo , ^{60}Co , ^{137}Cs).

The second use is to transmute nuclear waste [1.3]. That is, to burnup useless long-lived minor actinides (MA) that build up during the operation of power reactors, mainly due to neutron-capture reactions in reactor fuel, or to transmute equally useless longer-lived fission-product (FP) nuclei to shorter-lived or stable isotopes. It happens that achieving the transmutation for these two categories of nuclear waste may require a variety of neutron environments (spectra), e.g. thermal, epithermal, and fast-neutrons, in order to be effective. Analyses of processes involved in the reduction of long-lived nuclear waste by neutron-induced reactions require accurate knowledge of half-lives, decay chains, and neutron-capture and fission cross-sections. These can vary significantly from one isotope to another. A further consideration is the available neutron fluence level in an operating nuclear reactor. For example, in very high neutron flux environments it may be possible for a sequence of neutron-capture reactions to take place, starting with the parent FP or MA isotopes, in such a manner that the possibility of radioactive decays to occur between the various steps in a sequence is minimized. This would not be the case in lower-flux environments.

Concerning toxicity, as a general rule, MA nuclei tend to be more radiotoxic than FP nuclei because they decay mainly by emitting alpha particles that are biologically more damaging than the electrons or positrons emitted by FP isotopes. One exception is the beta decay of radioactive iodine because of its propensity to be absorbed by the thyroid gland. In practice, it is important to consider both chemical and mechanical issues to predict the extent to which sequestered nuclear waste could inadvertently be released to the environment. These are also complex issues that have a major bearing on the potential hazards of the various waste materials.

Finally, an additional potential use for excess neutrons is to provide external neutron beams (usually moderated to thermal or subthermal, 'cold-neutron' energies) for research in materials science and other diagnostic applications. For present purposes, these particular applications will not be discussed further [1.5].

ADS nuclear systems have the capability of producing both sufficient energy and neutrons to achieve the goals mentioned in the preceding paragraph, through the possibility of operating them with k_{eff} less than but close to unity (but never at unity), and thereby achieving considerable neutron (and power) multiplication while still maintaining the inherent safety of subcritical operation [1.1]. Furthermore, it has been shown that considerable tailoring of the neutron spectra produced in various locations within the external neutron source driven subcritical core can lead to effective simultaneous transmutation of both MA and FP waste isotopes. The exploration of these possibilities, both experimentally and through analytical

studies, constituted the significant portion of the research programme discussed in this publication.

1.1.3. Physics considerations

The design and operation of ADS ultimately depends on several fundamental physics considerations. These affect such technical aspects as the production of the external source neutrons, the design of the core and ancillary components such as the reflector, the measurement of important static and dynamic parameters of the system, the extraction of energy, transmutation processes, etc. This Section touches upon these areas very briefly and in very general terms. In particular, the main emphasis in this discussion is on external source neutron production, the benefits that can be gained from experiments involving zero-energy ADS facilities, and the essential features of transmutation physics. Further details regarding these issues appear in discussions that can be found in the chapters dealing with individual ADS research projects.

1.1.3.1. External Neutron Sources for ADS

It was pointed out in an earlier subsection of this Section that the capabilities of any specific ADS device for the production of power, transmutation of waste, etc., ultimately depend primarily on the external source neutron intensity N_0 that drives the system, and to a lesser extent on the neutron spectra to be found within the ADS core. The larger the external driving source intensity N_0 is, the more powerful the facility. Concerning the neutron spectrum, an important consideration is that there are advantages to employing external neutron sources that resemble fission neutron spectra since these will correspond to the dominant spectral characteristic of neutrons born from fission events in the core. In addition, high energy neutrons have higher probabilities to escape from the core and cause shielding difficulties.

Various approaches are used to produce these external neutrons. Radionuclide sources can be used, e.g. ^{252}Cf spontaneous fission or Pu-Be, where Pu-atom decays produce α -particles and these induce (α, n) reactions on Be. While these are normally relatively compact sources, they are comparatively weak and can be used only as sources of constant neutron output. They are employed for limited applications in research conducted at zero-power ADS facilities. However, they generally do produce source spectra that are either equal to or are relatively similar to fission-neutron spectra. The second category involves the use of neutron sources that incorporate low-energy proton or deuteron accelerators and such reactions as $\text{D}(d, n)$, $\text{T}(d, n)$, $^7\text{Li}(p, n)$, or $^9\text{Be}(d, n)$ to produce the neutrons. These neutrons generally have energies below 14 MeV, and they can exhibit spectra that are either mono-energetic (or nearly so) or are much broader in energy (continuum sources), depending on the target thickness and other physical factors. The advantage here is that these sources can be pulsed, leading to pulsed-neutron bursts that are very useful for several types of kinetic measurements for ADS devices. The disadvantage is that once again the attainable neutron-source intensities tend to be rather limited. Nevertheless, these low-energy accelerator sources are shown to be useful in studying the properties of ADS in zero- (or low-) power facilities. Several of them have been employed in the research described in this publication.

The approach that is most likely to be employed to produce the intense external neutron sources for high-power ADS facilities is the spallation process initiated by high-energy proton beams [1.3, 1.4]. The physics is as follows: high energy protons (normally 1 GeV or higher) impinge on high-Z targets such as lead, bismuth, mercury, or tungsten. The emission of several neutrons (approximately 30 neutrons/GeV of proton energy at high energies) occurs due to several processes that can be modelled with reasonable reliability using contemporary theories of light particle interactions with heavy nuclei. Basically, neutrons are emitted first with relatively high, quasi-discrete energies due to direct proton interactions with the target

and, subsequently, through intra-nuclear cascades. Each step in the cascade chain leads to lower-mass, cooler (less-excited), and very short-lived nuclei until, ultimately, the last neutrons are emitted with spectra characteristic of thermal evaporation. These spectra are relatively similar to fission neutron spectra, i.e. they exhibit Maxwellian distributions.

Detailed analyses of the ‘neutron economics’ of ADS require complex calculations that take into account details of the geometries, locations, and quantities of the component materials, including fuels, structural elements, reflector/blanket elements, fundamental nuclear data such as cross-sections, and extensive neutron transport issues. For this reason, it is important for the future of ADS applications to be able to carry out these analytic studies in a reliable manner. The need for such investigations is the primary motivation for the research activities that are discussed in this TECDOC.

The potential for using photo-neutron sources in ADS has also been investigated, and one example of this appears in the work described in this publication (Section 6). The physics is as follows: High energy electrons impinge on a high-Z target. Energetic photon spectra are generated by the bremsstrahlung process. These photons in turn produce neutrons via (γ,n) reactions. The yield of neutrons will be lower than comparable yields per MeV of incident charged-particle (e.g. protons) energy owing to the two-step process and the often smaller cross-sections associated with photonuclear reactions. However, an advantage of this option is that electron accelerators with relatively high energies can be built much more cheaply than proton machines of the same energy. There are a couple of obvious reasons for this. One is that sources of electrons are relatively easy to design and construct. Electrons are emitted from metallic sources that are heated to high temperatures, and they can be extracted easily to form beams. The second is that electrons, although possessing the same magnitude of charge as protons, have a mass roughly 2000 times smaller than protons. Thus, the ion optics apparatus required to steer and focus electron beams tends to be much less massive and consume less power than counterparts used in proton-beam optics.

Finally, it is important to understand that the very highest energy neutrons produced either by spallation or photonuclear processes are usually moderated in energy to a considerable extent in ADS devices by interactions in the materials in the vicinity of the external driver sources, regardless of the initial energies of these neutrons. Such interactions of neutrons with the surrounding medium lead to a decrease in the average energy of the neutron inventory, along with some neutron multiplication potential.

1.1.3.2. Nuclear Waste Transmutation

The point has already been made that the burnup of certain MA elements by fission can often be accomplished effectively in fast-neutron spectra. This follows from the nature of the fundamental cross-sections involved in these processes [1.1, 1.3]. That is, the fission cross-sections of certain MA isotopes are fairly modest at energies below a few hundred keV. An example is ^{237}Np , a known MA waste product in spent nuclear fuel (e.g. see Fig. 1.1).

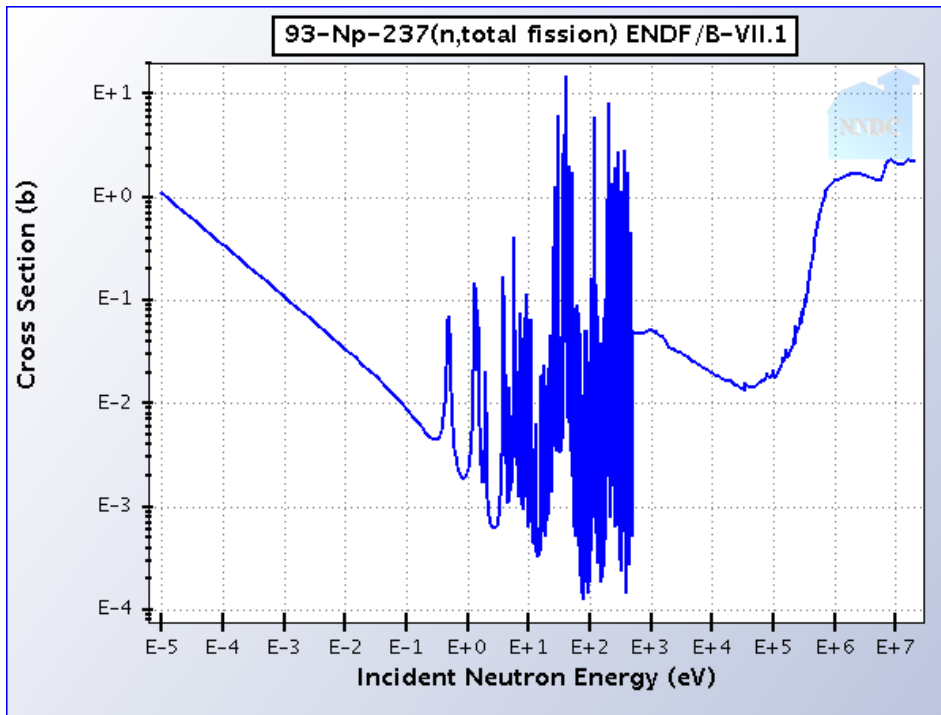


FIG. 1.1. Evaluated total fission cross-section for ^{237}Np [1.6].

If fast neutrons are used to burn MA elements, the probability of further production of MA elements (burn-in) by neutron capture reactions is much reduced when compared to what can take place in lower-energy neutron spectra. Neutron capture reactions in these MA materials therefore tend to be a nuisance rather than a benefit, unlike the situation for fertile materials such as ^{238}U and ^{232}Th where low-energy neutron capture can eventually lead to the production of useful fissionable fuels (^{239}Pu and ^{233}U). The additional MA isotopes generated by capture will add to the inventory of long-lived species in the nuclear waste that accumulates in the fuel materials of power reactors. Since the approach of using ADS to burn MA involves introducing chemically processed material extracted from spent fuel rods from light water reactors and burning them in the ADS reactor, any nuclear processes which simply add more MA isotopes to the waste system are counterproductive.

The beneficial transmutation of FP nuclear waste to isotopes with shorter lifetimes relies primarily on neutron capture, as mentioned earlier and neutron-capture cross-sections tend to be the largest in the resonance- and thermal-energy regions rather than in the fast-neutron regime, as mentioned earlier. This is exemplified in Fig. 1.2. It shows the neutron capture cross-section for ^{99}Tc (a known long lived FP waste isotope). Notice that the available experimental data are plotted along with the evaluated results. Evidently, transmutation by fast neutrons is far less effective in this case. However, not all FP nuclei transmute effectively in thermal neutron spectra, since their thermal-capture cross-sections may be modest. Therefore, transmutation of FP isotopes is often most effective when there are also adequate neutrons in the resonance regions corresponding to the target FP elements to be transmuted [1.4].

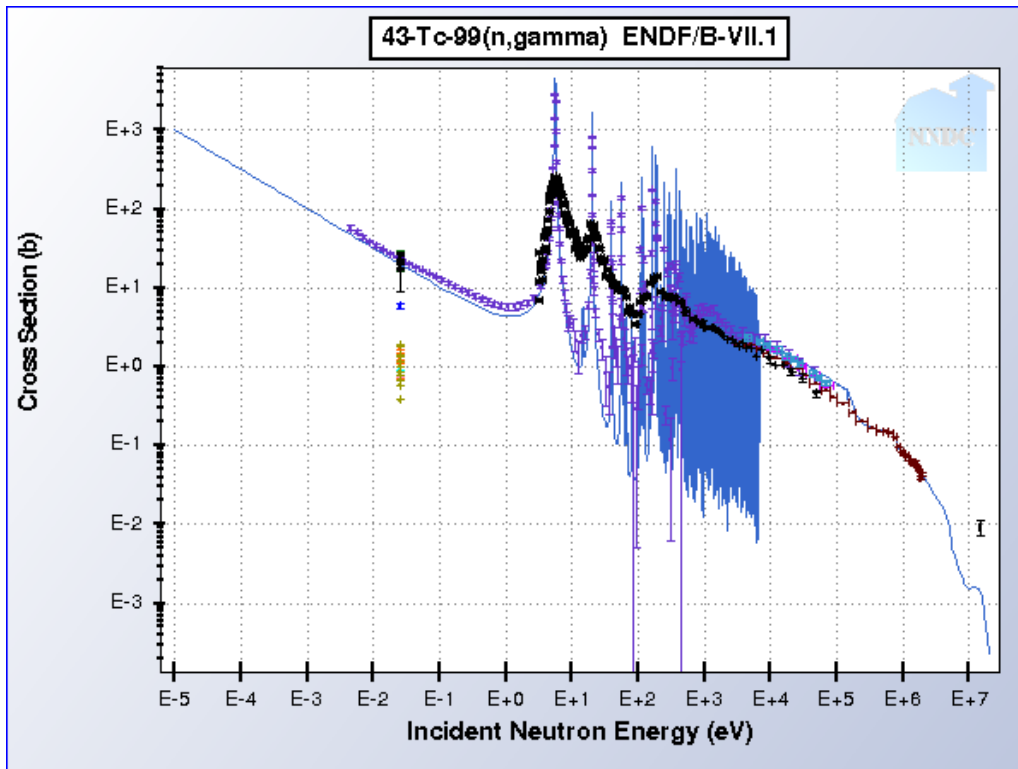


FIG. 1.2. Evaluated neutron radiative capture cross-section for ^{99}Tc . [1.6].

1.1.3.3. Tailoring Neutron Spectra in ADS Facilities

As discussed in the preceding subsection, most MA nuclei are normally most effectively transmuted by fast neutrons whereas FP nuclei transmutation may require a mixed spectrum of neutrons in the thermal, epithermal, and resonance regions. While some tailoring of neutron spectra is possible in critical reactors, the options for doing so are somewhat limited. For the most part, neutron spectra in critical reactors tend to be relatively homogeneous in nature, especially for thermal reactors that utilize low atomic number moderators (e.g. water). For fast reactors, the spectra in the core are harder (in the keV region), although lower-energy spectra can be found in regions peripheral to the central core where the neutrons produced by fission have been further moderated through the reflector. However, for much lower-energy spectra after the reflector region, the neutron intensities are much lower than in the central core itself. On the other hand, the options for tailoring spectra in ADS reactors are much more flexible, and potentially interesting for applications, than for thermal or even fast critical reactors. For example, quite energetic, and very intense neutron fields, can be found in the vicinity of the external neutron source, especially if the materials included in this region are predominantly higher-Z elements. Further away from the source, in the core itself, or near the blanket/reflector, the neutron spectra can be quite soft as a consequence of using light-element-moderator materials along with the fuel materials. Also, a neutron ‘valve’ approach can be applied to allow fast neutrons to propagate from the region near the external neutron source, pass into the core region, and be moderated there to much lower energies, as might be the case if a thermal field were needed. These lower-energy neutrons in the main part of the core can be prevented from migrating back into the fast region. This ‘valve’ effect is achieved by using thin layers of materials having very strong low-energy neutron absorption sections but much smaller cross-sections for fast neutrons. Natural uranium and compounds of boron have been employed effectively for this purpose. The reaction processes involved are (n,γ) and (n,α) , respectively. Careful design of such a ‘valve’ arrangement is required to insure that

the impact of the ‘valve’ on the reactivity of the system is as modest as possible, owing to the highly perturbing effect of the utilized neutron absorbent materials on the ADS neutronics.

1.1.4. Research on zero-power ADS facilities

Many of the essential neutronic characteristics of ADS can be rather conveniently investigated on a very small scale, at zero power, and for relatively low cost. Most of the facilities discussed in this TECDOC tend to fall into this category. These ‘zero-power’ ADS devices are proving to be useful surrogates for investigating many of the physical characteristics of and potential applications for counterpart high-power ADS that are under design consideration but are not yet built. Small scale facilities (e.g. KIPT facility of Section 6) can serve as test beds for exploring the properties of a large-scale facility in the following ways: testing instrumentation; validation of system modelling codes; prediction of transmutation yields; and investigation of various non-nuclear issues (cooling, materials properties, etc.). Such research is the essence of the collaborative work described in the present TECDOC. It cannot be overemphasized that this possibility to learn much about high-power ADS behaviour using small-scale test beds owes much to the fortunate fact that the neutron spectra to be anticipated at large-scale facilities with spallation neutron sources can be produced on a small scale by clever engineering design and exploitation of the physical properties of neutrons from spontaneous-fission production or nuclear reactions induced by radiations from low-energy accelerators (as mentioned above in the discussion on neutron sources). Repeating the earlier arguments, external source neutron spectra that resemble those that would be generated in systems of much higher power and more costly machines by spallation can be produced using either relatively low-energy neutrons (in the several-MeV region) from radionuclide sources, from low-energy, charged-particle induced nuclear reactions, or from photonuclear process where the photon sources are produced by electrons with relatively modest energies. The transport of neutrons in the vicinity of the target, the core, or the blanket/reflector in small-scale ADS facilities is also similar to what would occur in high-power facilities. Also, neutron production in the reactor fuel, neutron capture losses, etc., will be similar. The main difference between large-scale and small-scale facilities has to do with details of geometry and non-neutronic issues related to cooling, radiation damage of materials in high-power facilities, high power spallation target technologies, etc.

1.2. OBJECTIVES OF ADS RESEARCH

Public apprehension over the use of nuclear energy is well known, and has three fundamental aspects: the first relates to the safe operation of nuclear energy devices intended to generate power for public consumption. The second concerns minimizing the potential risks that fissionable and/or biologically hazardous nuclear materials might be diverted by rogue governments and/or terrorist groups for illicit use in the development of nuclear weapons, or with the intent of otherwise doing harm to the public for political or ideological purposes. The third is the need to safely convert nuclear waste generated from fission nuclear power reactors to smaller volumes, with lower chemical and radioactive toxicity (radiotoxicity). The latter might be accomplished by reprocessing spent reactor fuel and transmuting the long-lived fission products and the minor actinides so as to reduce the scope, cost, and environmental impact of the infrastructure required for long-term storage of unusable waste products. Finally, from an economics perspective, in order for nuclear energy to be competitive with alternative energy sources, nuclear systems need to be designed in such a way that they are cost effective through all stages of the fuel cycle, from mining of the raw materials (e.g. uranium or thorium) to eventually handling waste products generated by the operation of these facilities.

The possibility that use of ADS could provide a viable option for satisfying these requirements, as well as for producing usable power for the grid, has been well advertised

[1.3, 1.4]. Furthermore, it has stimulated research in several Member States on the properties of these systems. The rationale for this assumption is clarified to some extent in the ensuing discussion. To date, no high-power ADS has been constructed, but investigations have been carried out at several zero-power (or low-power) facilities (including those described in this TECDOC), and conceptual design studies for additional low-power as well as high-power facilities are in progress [1.7]. A discussion of conceptual high-power ADS designs is beyond the scope of this publication.

As a prelude to more detailed discussions in this publication of individual facilities, it is worthwhile mentioning some of the basic concepts associated with ADS. In particular, the emphasis of the present exposition relates mainly to physics considerations rather than to concerns associated with materials properties, thermal hydraulics, etc. The objective is to explain how an ADS works and why the concept itself is appealing.

1.3. SCOPE OF THE PRESENT RESEARCH PROGRAMME

The ADS research carried out by the participants in the present collaborative project can be grouped into two broad categories of physical properties: static and dynamic. Examination of these physical properties of ADS devices has involved, to varying degrees, both measurements and system modelling. It was mentioned earlier that investigations of subcritical systems pose many technical challenges not encountered in considering critical reactors. The research discussed in this TECDOC has resulted in the development and/or refinement of measurement and analytical techniques that will prove to be of great value for research and development work on future ADS. Details pertaining to the specific facilities considered in this project are described more fully in Sections 2–10.

The most important parameter to be investigated, as indicated in earlier discussions, is k_{eff} for a particular ADS viewed in its entirety. This parameter can be both measured and calculated [1.8]. Measurements of k_{eff} for subcritical systems are more complicated, and more indirect, to carry out than determining the criticality point for critical reactors. There are several methods which have been employed by participants in the present research collaboration. These include the Slope Fit Method, the Sjöstrand (Area) Method, the Source Jerk Method, the Feynman-Alpha Method, and the Rossi-Alpha method. Details of these techniques are described in the literature [1.8, 1.9]. In addition to determination of k_{eff} , knowledge of k_s ('s' stands for source neutrons) and k_{∞} (value of k for an infinite medium) is of considerable interest for acquiring a deeper understanding of the nature of ADS [1.10]. Additional versions of criticality parameters ' k ', corresponding to various component regions of particular ADS facilities or the external-driver neutron source, can also be calculated using modern analytical techniques, even though these parameters may be difficult to measure. Also of interest are the prompt neutron lifetime (l_p), the mean neutron generation time (Λ), the effective delayed-neutron fraction (β_{eff}), as well as various additional parameters of somewhat lesser significance, but that nevertheless provide interesting information about the kinetic properties of ADS and offer the means for comparing diverse computational techniques. These various kinetic parameters, for the most part, depend on the specific designs and materials composition of the facilities in question.

Calculations of these kinetic parameters require the use of extensive fundamental nuclear data that are essential input for the deterministic or Monte Carlo codes that are capable of modelling specific design details of an ADS device. It is important to gain an understanding of the sensitivity of ADS performance calculations to nuclear data so that an assessment can be made of the adequacy (scope and accuracy) of the existing databases of evaluated nuclear constants. The present TECDOC presents extensive tables and figures of measured and computed data related to these ADS parameters. Of significance here are the comparisons between results from diverse calculations of the same physical parameters for the same facilities, but obtained by different laboratories, using various codes and nuclear data

libraries as well as distinct analytical procedures. An underlying assumption of the present research collaboration is that a robust understanding of the operating characteristics of ADS facilities will have been achieved if various laboratories, using various codes, various computational procedures, and various nuclear data sets, can generate results that are in reasonably good agreement within anticipated uncertainties. Comparisons with experimental results are also clearly very valuable in validating these analytical studies, and results from such comparisons are provided in this TECDOC where applicable.

Somewhat more mundane, but nevertheless interesting and quite important, is that measurements and calculations have been made of relative values of physical quantities, under steady-state neutron flux conditions, corresponding to different physical positions situated within measurement channels in the studied ADS devices, both with or without regard for the neutron-energy spectrum. A number of these investigations are discussed in the present TECDOC. Some determinations of absolute flux levels have also been made, mostly for the lowest-power facilities. Positional scanning measurements have been made, mainly in fields that are relatively uniform in energy-spectrum characteristics across the ADS core, although varying in intensity depending on location, using simple neutron detectors such as proportional counters. Ratios of lower-energy to higher-energy neutrons at various positions within these ADS facilities have also been measured using the spectral-index approach. Detector pairs (or even multiple arrays) are introduced into accessible measurement locations in the ADS external source, core, and blanket/reflector regions. They consist of various active or passive detector types that respond differently to low- and high-energy neutrons. Rough estimates of neutron spectrum shapes can be made from these data, in conjunction with results obtained from neutron transport calculations. Even more elaborate and extensive spectrum determinations have been made using dosimetry foil sets that permit the estimation of spectral characteristics in greater detail by the technique of ‘spectrum unfolding’ (or ‘spectrum adjustment’). Calculations of spectra at various locations in the ADS have been made using Monte Carlo simulation codes. Further adjustments to these spectra, using the ‘spectrum adjustment’ technique, have then been carried out using analytical methods such as least-squares minimization. The key point is that while extensive calculations can be made, often of quantities that cannot be measured, ‘benchmark’ comparisons with experimental data are of great importance for validation purposes, and they have been made wherever possible for existing facilities. In cases where measurements could not be made, e.g. for conceptual facilities that have not yet been built, detailed comparisons of calculated results obtained by various investigators have been carried out, thereby providing some degree of validation based on computational consistency of the various approaches.

1.4. CONTENTS AND STRUCTURE OF THIS PUBLICATION

This publication contains ten sections (including this introductory Section). Each one corresponds to a particular facility, as indicated in the Background subsection 1.1 of this introductory Section. Each Section is essentially self-contained, consisting of its own introduction, descriptions of the relevant facility and the research carried out there, experimental and/or computational results, a discussion of the conclusions, and a list of pertinent references. The material included in the present publication has been drawn to a great extent from documents, presentations, plots, and numerical data sets provided at or following ADS research project coordination meetings held in 2005 (Vienna, Austria), 2006 (Vienna, Austria), 2007 (Rome, Italy), 2009 (Vienna, Austria), and 2010 (Mumbai, India), as well as from submitted final reports. This raw material has been archived by the IAEA and it is available from the before mentioned IAEA website.

REFERENCES TO SECTION 1

- [1.1] NIFENECKER, H., et al., Basics of accelerator driven subcritical reactors, Nuclear Instruments and Methods in Physics Research, **A463** (2001) 428-467.
- [1.2] DEGWEKER, S.B., et al., The physics of accelerator driven sub-critical reactors, PRAMANA – Journal of Physics, Indian Academy of Sciences, 68 (2007), No. 2., 161-171.
- [1.3] BOWMAN, C.D., et al., Nuclear energy generation and waste transmutation using an accelerator-driven intense thermal neutron source, Nuclear Instruments and Methods in Physics Research, A320 (1992) 336-367.
- [1.4] RUBBIA, C., et al., Conceptual design of a fast neutron operated high power energy amplifier, Report CERN/AT 95-44 (ET), 1995.
- [1.5] INTERNATIONAL ATOMIC ENERGY AGENCY, Applications of Research Reactors, IAEA Nuclear Energy Series No. NP-T-5.3, IAEA, Vienna (2014).
- [1.6] BROOKHAVEN NATIONAL LABORATORY, Nuclear Data Center. www.nndc.bnl.gov
- [1.7] MANSANI, L., et al., The Designs of an Experimental ADS facility (XT-ADS) and of a European Industrial Transmutation Demonstrator (EFIT), in Technology & Components of Accelerator-driven Systems, Karlsruhe, Germany, 15-17 March 2010, Paris, France, OECD - NEA, 321-334, 2011.
- [1.8] PERSSON, C.-M. et al., Analysis of reactivity determination methods in the subcritical experiment Yalina, Nuclear Instruments and Methods in Physics Research, A554 (2005) 374-383.
- [1.9] GOHAR, Y., SMITH, D.L., YALINA facility a sub-critical Accelerator- Driven System (ADS) for nuclear energy research facility description and an overview of the research program (1997-2008), Report ANL-10/05, Argonne National Laboratory, 2010.
- [1.10] TALAMO, A. et al., Pulse superimposition calculational methodology for estimating the subcriticality level of nuclear fuel assemblies, Nuclear Instruments and Methods in Physics Research, A606 (2009) 661-668.

2. YALINA-BOOSTER BENCHMARK ANALYSES

Contributed by

H. Kiyavitskaya, V. Bournos, Y. Fokov, C. Routkovskaya, S. Sadovich
*Joint Institute for Power and Nuclear Research – Sosny,
National Academy of Sciences of Belarus, Minsk,
Belarus*

A. Cintas, J.I. Márquez Damián, E.M. Lopasso
*División Física de Reactores Avanzados
Unidad de Energía Nuclear (CNEA) - Instituto Balseiro, Bariloche,
Argentina*

J.R. Maiorino, T. Carluccio, P.C.R. Rossi, A. Antunes, F.L. de Oliveira and S.M. Lee.
*Nuclear Technology Post Graduate School
Instituto de Pesquisas Energeticas e Nucleares- Universidade de Sao Paulo (IPEN-USP), Sao Paulo,
Brazil*

P. Xia, Y. Shi, H. Xia, Q. Zhu, T. Yu, X. Wu, W. Zhang, J. Cao, H. Luo, Y. Quan
*China Institute of Atomic Energy, Beijing,
China*

K. Kulkarni, R.D.S. Yadav, A. Bajpai, S.B. Degweker, R.S. Modak
*Bhabha Atomic Research Centre, Trombay, Mumbai,
India*

H.J. Park, H.J. Shim, C.H. Kim
*Nuclear Engineering Department, Seoul National University,
Republic of Korea*

A. Wojciechowski, M. Szuta
*Institute of Atomic Energy, Otwock-Swierk,
Poland*

M. Pešić, I. Avramović, P. Beličev
*Vinca Institute of Nuclear Sciences, Belgrade,
Serbia*

Y. Gohar, A. Talamo, G. Aliberti,
*Argonne National Laboratory,
USA*

2.1. INTRODUCTION

This section presents the YALINA-Booster subcritical assembly benchmark analyses of the International Atomic Energy Agency (IAEA) coordinated Research Project (CRP) entitled Analytical and Experimental Benchmark Analysis on Accelerator Driven Systems, and Low Enriched Uranium Fuel Utilization in Accelerator Driven Subcritical Assembly Systems using the results from the work performed by the different IAEA Member States. The overview of this research programme is represented in more details in Ref. [2.1]. Each Member State used different neutron-transport computer programs. Argentina, China, and Serbia used MCNP5 [2.2], Republic of Korea used McCARD [2.3], and the USA used MCNPX [2.4] and ERANOS [2.5]. These computer programs use the Monte Carlo method for solving the neutron transport equation except ERANOS, which uses deterministic algorithms. Republic of Korea-McCARD calculations used the ENDF/B-VII.0 library; the USA MCNPX simulations used the ENDF/B-VI.8 and ENDF/B-VII.0 libraries, and the other IAEA Member States used the ENDF/B-VI (different modes) library [2.6]. Detailed specifications of the benchmarks are documented in Ref. [2.1]. Table 2.1 represents the list of contributors to this work. Analyses of the YALINA-Booster facility by the USA are documented in Refs [2.7–2.10]. Figures 2.1 and 2.2 illustrate the USA computational models of the YALINA-Booster subcritical assembly using MCNPX.

TABLE 2.1. CONTRIBUTORS TO THE YALINA-Booster IAEA BENCHMARK

Country	Code	Library
Argentina	MCNP5	ENDF/B-VI
Serbia	MCNP5	ENDF/B-VI
Republic of Korea	McCARD	ENDF/B-VII
USA	PARTISN	ENDF/B-VI
USA	MCNPX	ENDF/B-VI
USA	ERANOS	ENDF/B-VI

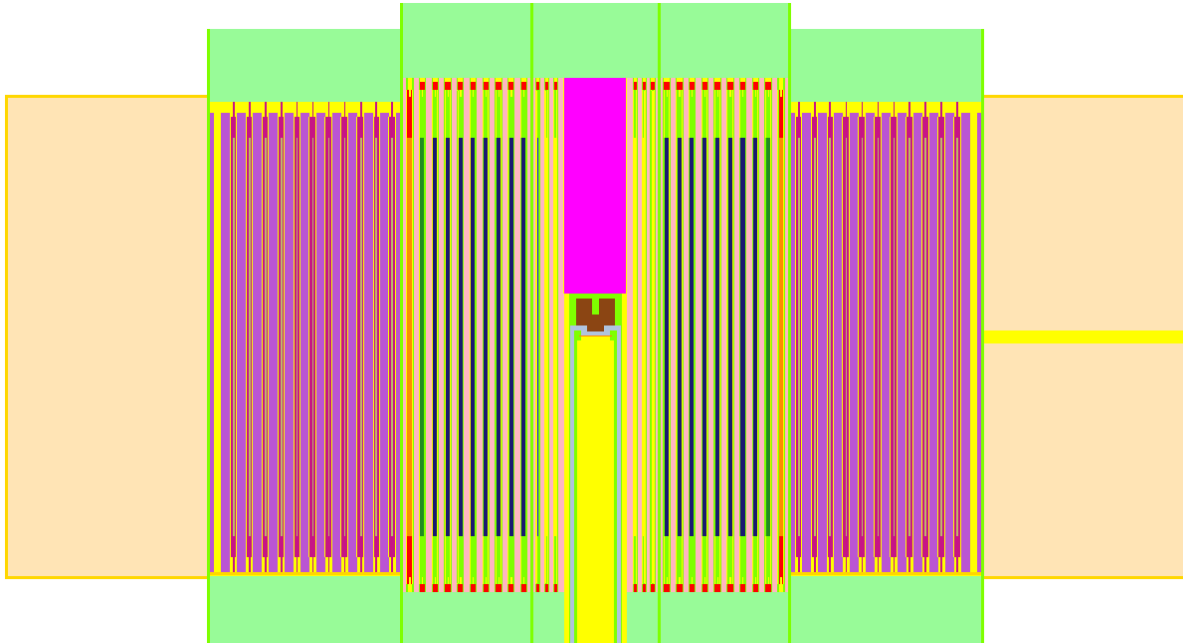


FIG. 2.1. Vertical cross-section of the USA MCNPX model of YALINA-Booster facility (reproduced from Ref. [2.10] with permission courtesy of the Argonne National Laboratory, USA).

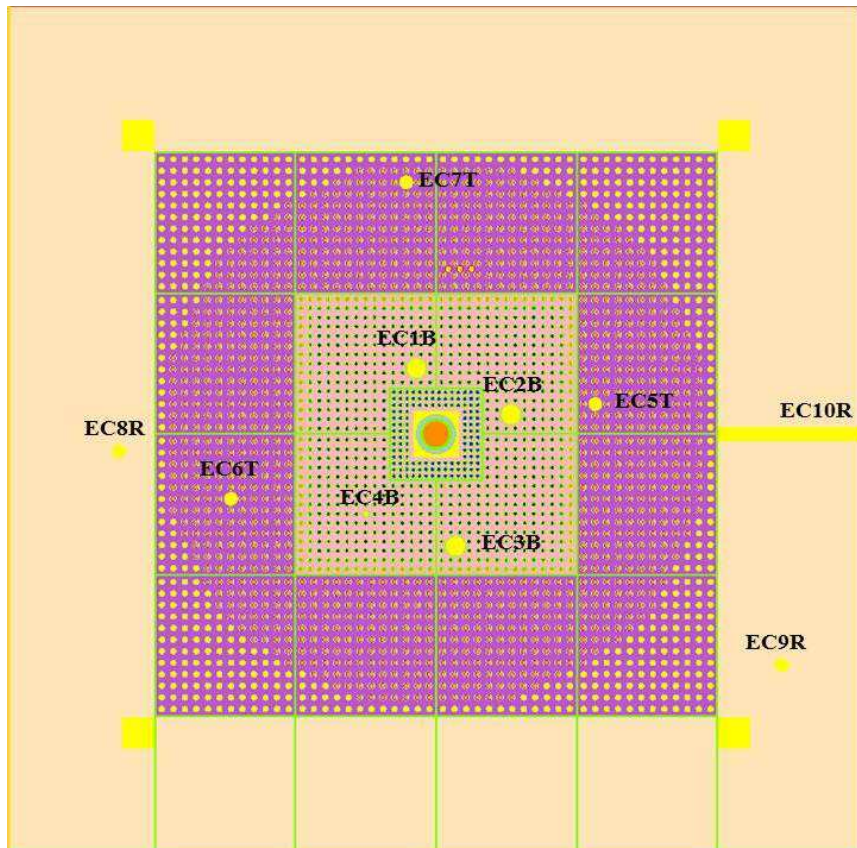


FIG. 2.2. Horizontal cross-section of the USA MCNPX model of YALINA-Booster facility (reproduced from Ref. [2.10] with permission courtesy of the Argonne National Laboratory, USA).

There are two ways for external neutron production in YALINA-Booster: use of either a ^{252}Cf spontaneous-fission point source or an accelerator source. The accelerator source is produced by low-energy deuterons incident on targets of deuterium via $\text{D}(\text{d},\text{n})^3\text{He}$ reactions or $\text{T}(\text{d},\text{n})^4\text{He}$ reactions on tritium targets.

The YALINA assembly consists of three regions: booster region, a ‘valve’ region that filters the low-energy neutrons, and thermal region. *The booster* is the closest region to the primary neutron source, where the fast neutron spectrum is maintained through fast-fission reactions in lead matrix material. The booster is divided into two different parts. The first one, which is closest to the axis, is a lead structure with holes drilled in it, arranged in a square lattice with a 1.14 cm pitch. These holes are filled with metallic uranium rods with 90% enrichment in ^{235}U . In the very centre of the assembly, there is a cavity, oriented along the axis, for the target and neutron beam insertion. Another part of the booster region envelops the first one on four sides and also consists of lead with drilled holes in it, arranged in a square lattice with a 1.6 cm pitch. This structure is filled with UO_2 fuel rods enriched to 36% ^{235}U [2.1].

The ‘valve’ region allows migration of neutrons from the booster to the thermal region due to the small effective capture cross-section for higher-energy neutrons, but prevents thermal neutrons from migrating back into the booster region from the core. This region is a 3 cm thick lead structure and it surrounds the booster region on four sides. There is a layer of holes drilled in it, with a 1.6 cm pitch, which are filled with rods that consist of either natural uranium (0.7% ^{235}U) or B_4C [2.1].

The thermal region is a polyethylene matrix material that envelops the inner regions. It is fuelled with UO_2 fuel rods with 10% enrichment, arranged in drilled holes in a square lattice with a 2 cm pitch. By having two distinct regions of the core with two very different neutron spectra, it is possible to perform a wide variety of transmutation measurements on samples of minor actinides and fission products [2.1].

The subcritical assembly is surrounded by two reflectors [2.1]. There is a radial graphite reflector and an axial borated polyethylene reflector. The radial reflector and the backside of the thermal zone are covered by organic glass sheet. There are four axial experimental channels (EC1B, EC2B, EC3B, and EC4B) in the fast zone, three axial experimental channels in the thermal zone (EC5T, EC6T, and EC7T), two axial experimental channels in the reflector (EC8R, and EC9R), and one radial experimental channel in the reflector zone (EC10R).

Similar models of YALINA-Booster were developed by the other Member States. The experimental channels of the facility are shown in Fig. 2.2. The present study is comprised of three parts based on the maximum uranium fuel enrichment in the inner fast zone. The three ^{235}U enrichments are 90%, 36%, and 21%. The configuration with high uranium fuel enrichment loads either 1141 or 902 EK10 fuel rods in the thermal region of the assembly. The configurations with 36% and 21% uranium fuel enrichments in the fast zone load 1185 EK10 fuel rods in the thermal zone [2.10]. China provided simulation results with Deuterium-Deuterium (D-D) and Deuterium-Tritium (D-T) neutron sources. Serbia provided simulation results for a californium (^{252}Cf) neutron source. Argentina, Republic of Korea, and Serbia examined the configurations with 1141 and 902 EK10 fuel rods in the thermal zone.

2.2. YALINA-BOOSTER CONFIGURATIONS WITH 90% ENRICHED URANIUM FUEL

Two YALINA-Booster configurations that utilize 90% uranium fuel were considered in this study. The difference between these two configurations is the number of EK10 fuel rods in the thermal zone, 1141 or 902.

2.2.1. Kinetic parameters of the YALINA-Booster configuration with 1141 fuel rods in the thermal zone

Figure 2.3 (a) shows the multiplication factors obtained by the Member States for the YALINA-Booster configuration with 1141 EK10 fuel rods in the thermal region. The statistical errors of the effective and prompt multiplication factors are lower than 9 pcm for all the results except for the Serbia result which has 13 pcm error. Excluding Serbia and the USA ERANOS results, the effective (k_{eff}) and prompt (k_{pro}) multiplication factors calculated by the different Member States agree within a margin of 150 pcm. The USA ERANOS result is 750–900 pcm lower than the other results, and it is excluded from the average value of all multiplication factors. In Figs 2.3 and 2.4, the average values are indicated by horizontal lines. The USA ERANOS deterministic results are different from the Monte Carlo results due to the space, energy, and angle approximations in ERANOS simulations. The Serbia results are 300–500 pcm lower because the MCNP Serbian geometrical model homogenizes the steel frame of the assembly with the other zones. This introduces an approximation in the computational model, which affects the results. The prompt multiplication factor is about 704 pcm lower than the effective multiplication factor; this difference is consistent with the effective delayed-neutron fraction value.

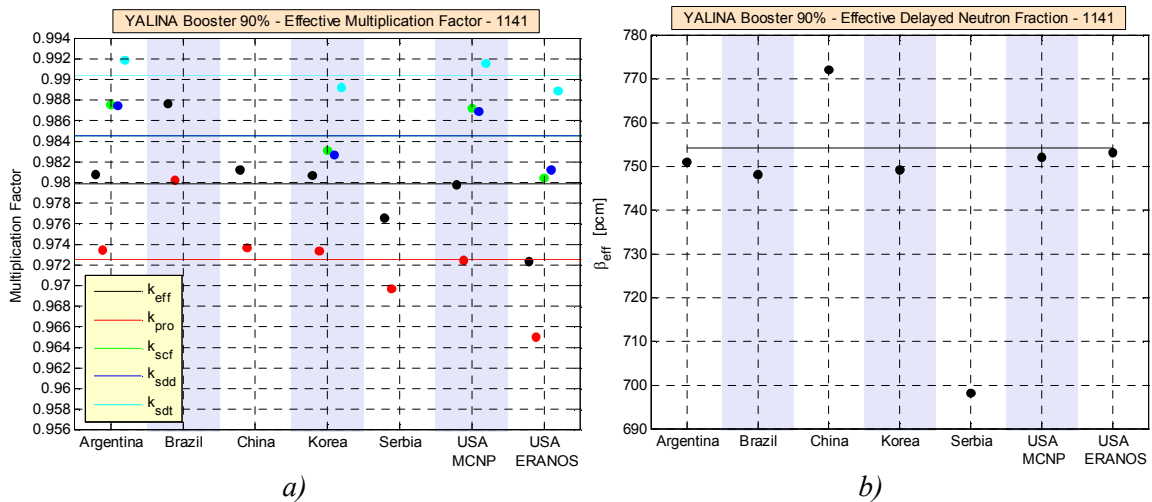


FIG. 2.3. Multiplication factors (a) and effective delayed-neutron fraction (b) of YALINA-Booster configuration with 90% enriched uranium fuel and 1141 EK10 fuel rods in the thermal zone (Courtesy of the Argonne National Laboratory, USA).

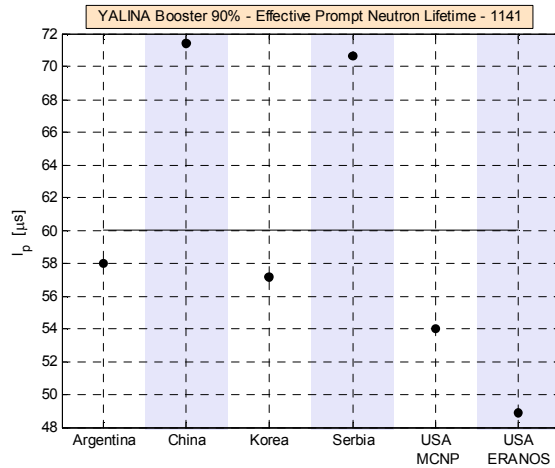


FIG. 2.4. Prompt neutron lifetime of YALINA-Booster configuration with 90% enriched uranium fuel and 1141 EK10 fuel rods in the thermal zone (Courtesy of the Argonne National Laboratory, USA).

The source multiplication factors calculated by Argentina and USA MCNP agree within a margin of 80 pcm; the difference increases up to 700 pcm if the Republic of Korea and USA ERANOS results are included. China and Serbia did not provide such results. The differences between the source multiplication factor results can be traced to three factors: the used method to include the contributions from (n,xn) reactions, the model of the space-energy-angle profile of the external neutron source, and the definition of the source multiplication factor. All the values of the neutron-source multiplication factors are higher than the effective multiplication factor value which is determined using only fission neutrons. The external neutron source is located in a high-importance zone of the assembly (at the centre), and the high energy of the external neutrons relative to the fission neutrons accounts for this difference. The californium (Cf) and D-D source multiplication factors (k_{scf} and k_{sdd} , respectively) have similar values because the two sources emit neutrons with similar average energy. The higher average energy of deuterium-tritium (D-T) source neutrons (~ 14.1 MeV), relative to D-D and Cf source neutrons, increases the contribution from the (n,xn) reactions, which enhances the D-T source multiplication factor k_{sdt} . The dimensions of the YALINA-Booster facility are large enough to reduce the D-T neutrons leakage.

The deterministic and the Monte Carlo computer analyses estimated an effective delayed-neutron fraction β_{eff} between 750 and 770 pcm, as shown in Fig. 2.3. The results obtained by Serbia have a higher statistical error of ~ 18 pcm and therefore they are not included in the average value of the delayed-neutron fraction. The prompt neutron lifetime l_p shown in Fig. 2.4 ranges from 50 to 70 μ s; the latter value has been obtained by China and Serbia.

2.2.2. Reaction rates of the YALINA-Booster configuration with 1141 fuel rods in the thermal zone

The $^3\text{He}(n,p)$ and $^{235}\text{U}(n,f)$ reaction rates, as a function of the axial position parallel to the fuel rods, have been calculated for the YALINA-Booster assembly driven by Cf, D-D, and D-T external neutron sources in the EC6T and EC2B experimental channels. These results are shown in Figs 2.5 and 2.6.

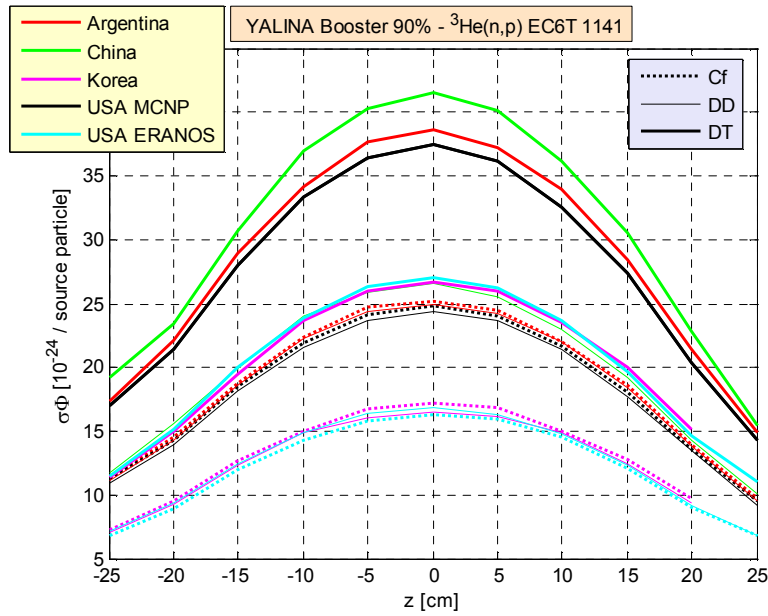


FIG 2.5. ${}^3\text{He}(n,p)$ reaction rate in EC6T experimental channel of YALINA-Booster configuration with 90% enriched uranium fuel and 1141 EK10 fuel rods in the thermal zone (Courtesy of the Argonne National Laboratory, USA).

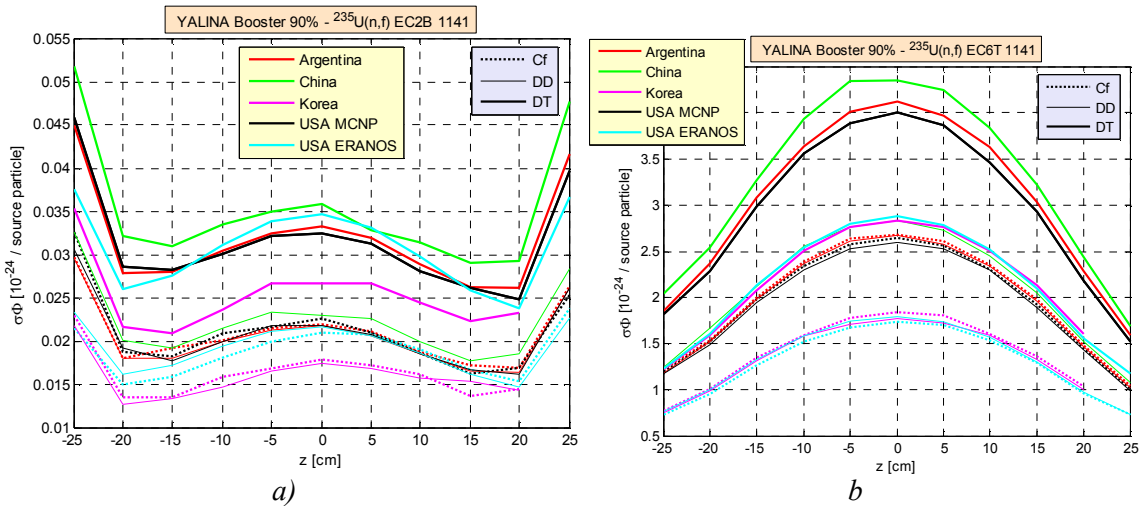


FIG 2.6. ${}^{235}\text{U}(n,f)$ reaction rate in EC2B (a) and in EC6T (b) experimental channels of YALINA-Booster configuration with 90% enriched uranium fuel and 1141 EK10 fuel rods in the thermal zone (Courtesy of the Argonne National Laboratory, USA).

In these figures, the ticks on the z -axis indicate the centre of the tally volume. The neutron detector was not modelled; consequently, the self-shielding effect is not considered. The unit of all the time-independent reaction rates of this Section is barn per source particle and square centimetre ($10^{-24}/\text{source particle}$). The Monte Carlo statistical error for one standard deviation for the EC6T reaction rates is lower than 0.9% for the Argentina and USA MCNP results. This value increases to 2.3 or 3.6% if the Chinese or Korean results are included, respectively. The Monte Carlo statistical error for the EC2B reaction rates is lower than 3% for the Argentina and USA MCNP results, and this value increases to 7 or 20% if the Chinese or Korean results are included, respectively. There is a relatively good agreement in the reaction rates calculated by Argentina, China, and the USA MCNP. The reaction rates of the USA ERANOS and Korea are lower than the other results because of the lower source

multiplication factor obtained from these calculations. The thermal neutron fraction in the fast zone of the assembly that was calculated by the ERANOS code is overestimated, as discussed in Section 2.2.3, consequently, the ERANOS $^{235}\text{U}(n,f)$ reaction rate values in the EC2B experimental channel are enhanced and are similar to those calculated by Monte Carlo codes. In general, examining the obtained reaction rate results reveals the following observations:

- In all the experimental channels, the reaction rates from the Cf neutron source are similar to those from the D-D neutron source, since the two neutron sources have similar source multiplication factors;
- The reaction rates from the D-T neutron source are always higher than that of the Cf and D-D neutron sources. This is due to the higher k_{sdt} value relative to k_{scf} and k_{sdd} ;
- The $^{235}\text{U}(n,f)$ reaction rate in the EC6T experimental channel is much higher than that in the EC2B experimental channel. This is the case since the EC6T experimental channel is located in the thermal zone where the ^{235}U thermal fission cross-section and the thermal neutron flux values are higher than the corresponding values in the fast EC2B experimental channel;
- The $^3\text{He}(n,p)$ reaction rate in the EC6T experimental channel is much higher than the $^{235}\text{U}(n,f)$ reaction rate because the $^3\text{He}(n,p)$ microscopic cross-section is much higher than the $^{235}\text{U}(n,f)$ microscopic cross-section;
- The axial neutron flux profile in the EC6T experimental channel has a cosine shape. In the EC2B experimental channel, the values of the reaction rate at the boundaries of the active fuel zone are larger due to the additional thermal neutron fraction from the polyethylene reflector.

The $^{155}\text{In}(n,\gamma)$, $^{197}\text{Au}(n,\gamma)$, and $^{55}\text{Mn}(n,\gamma)$ reaction rates in the EC5T, EC6T, EC7T, and EC10R experimental channels obtained with californium, D-D, and D-T neutron sources are plotted in Figs 2.7–2.9. In these calculations, the irradiation samples were modelled explicitly, and therefore the self-shielding effect is included. The statistical error for one standard deviation is less than 2% in the EC5T, EC6T, and EC7T thermal experimental channels, and is less than 6% in the EC10R experimental channel. The reaction rate values from McCARD and ERANOS calculations are lower than the other Monte Carlo results because of the lower source-multiplication factor values, as discussed above. However, the ERANOS reaction rates do not take into account the self-shielding effect, which overestimates their values. For this reason, the ERANOS $^{115}\text{In}(n,\gamma)$ and $^{197}\text{Au}(n,\gamma)$ reaction rates are much higher than those calculated by Monte Carlo codes, and the ERANOS $^{115}\text{In}(n,\gamma)$ reaction rates have not been included in Figs 2.7–2.8.

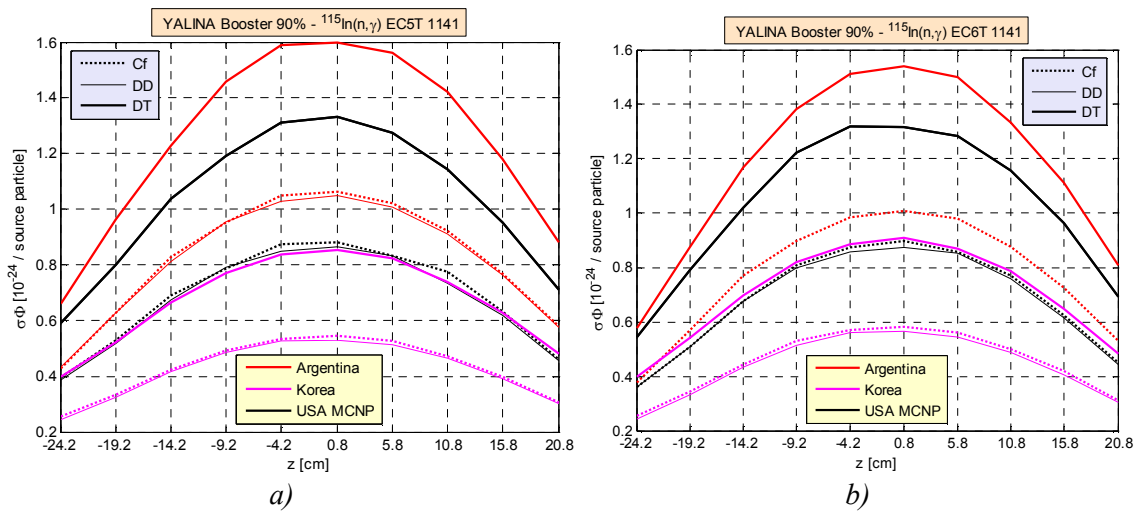


FIG. 2.7. $^{115}\text{In}(n,\gamma)$ reaction rate in EC5T (a) and in EC6T (b) experimental channels of YALINA-Booster configuration with 90% enriched uranium fuel and 1141 EK10 fuel rods in the thermal zone (Courtesy of the Argonne National Laboratory, USA).

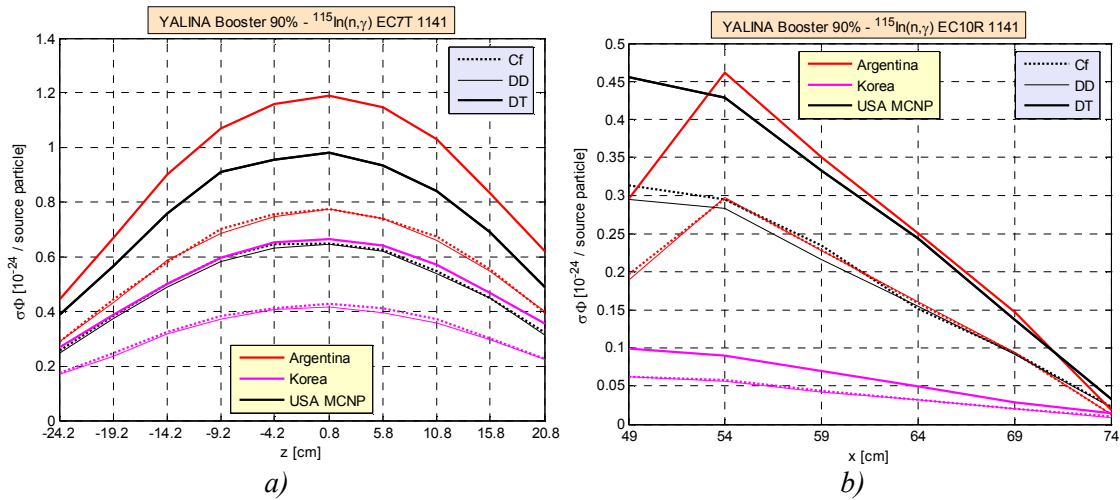


FIG. 2.8. $^{115}\text{In}(n,\gamma)$ reaction rate in EC7T (a) and in EC10R (b) experimental channels of YALINA-Booster configuration with 90% enriched uranium fuel and 1141 EK10 fuel rods in the thermal zone (Courtesy of the Argonne National Laboratory, USA).

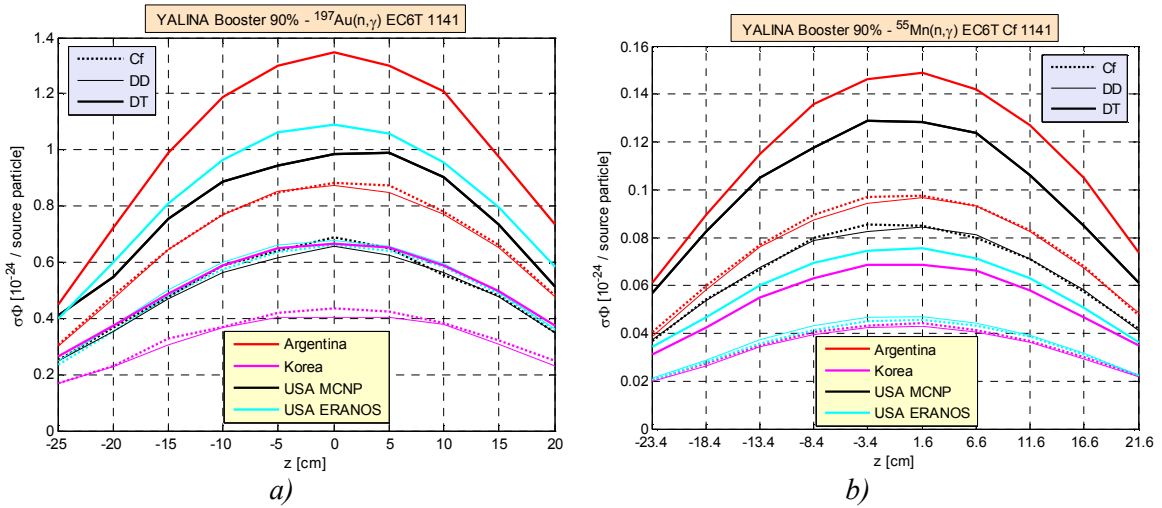


FIG. 2.9. $^{197}\text{Au}(n,\gamma)$ (a) and $^{55}\text{Mn}(n,\gamma)$ (b) reaction rates in EC6T experimental channel of YALINA-Booster configuration with 90%-enriched uranium fuel and 1141 EK10 fuel rods in the thermal zone (Courtesy of the Argonne National Laboratory, USA).

In addition, the Republic of Korea results used ENDF/B-VII.0 for $^3\text{He}(n,p)$, $^{235}\text{U}(n,f)$, $^{115}\text{In}(n,\gamma)$, $^{197}\text{Au}(n,\gamma)$, and $^{55}\text{Mn}(n,\gamma)$ cross-sections, which were evaluated in 1990, 2006, 2006, 2006, and 2000, respectively [2.6]. The results of Argentina and USA MCNP used ENDF/B-VI for the same cross-sections, which were evaluated earlier in 1965, 1990, 1997, 1984, and 1988, respectively [2.2, 2.6]. In addition, the ENDF/B-VI library only contains natural indium data but the ENDF/B-VII.0 library has only ^{115}In data. These factors contribute to the difference between the obtained reaction-rate results.

2.2.3. Neutron Spectrum of the YALINA-Booster configuration with 1141 fuel rods in the thermal zone

The neutron spectra in the EC2B, EC6T, and EC8R experimental channels from Cf, D-D, and D-T neutron sources are illustrated in Figs 2.10–2.14. In these figures, the neutron spectra have been sampled using 172 energy groups and the neutron flux has been first normalized to unity and then to the group lethargy. For the EC6T and EC8R experimental channels, where the neutron spectrum is well thermalized, there is a quite good agreement between the results obtained by the IAEA benchmark participants. The statistical error of the Serbian results is much larger relative to the other results. The ERANOS and McCARD codes underestimated and overestimated, respectively, the number of thermal neutrons in the EC2B experimental channel, where the neutron flux has a fast spectrum.

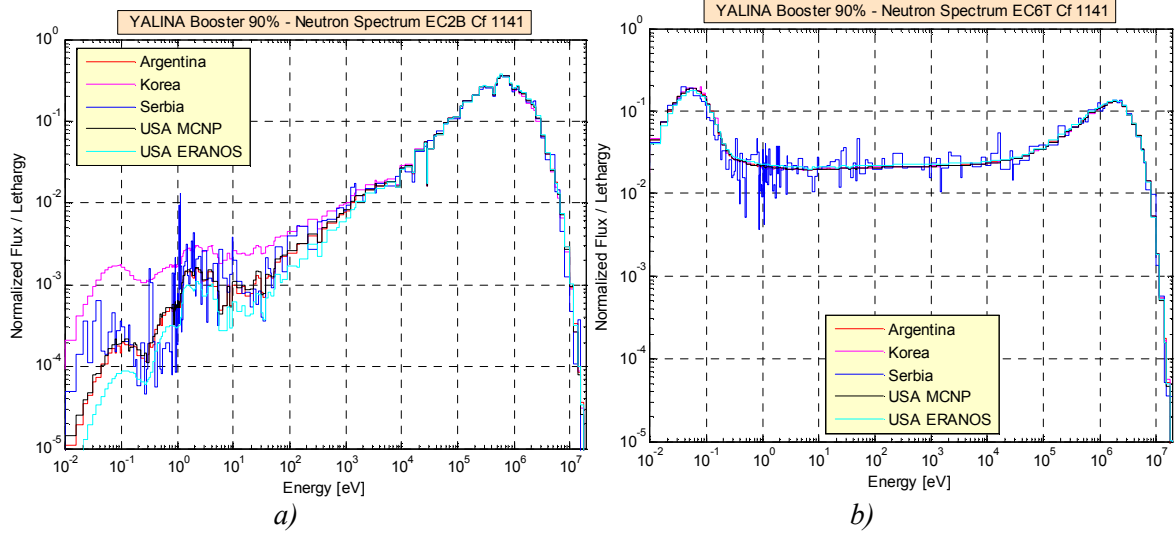


FIG. 2.10. Neutron spectrum in EC2B (a) and in EC6T (b) experimental channels using a californium neutron source in YALINA-Booster configuration with 90% enriched uranium fuel and 1141 EK10 fuel rods in the thermal zone (Courtesy of the Argonne National Laboratory, USA).

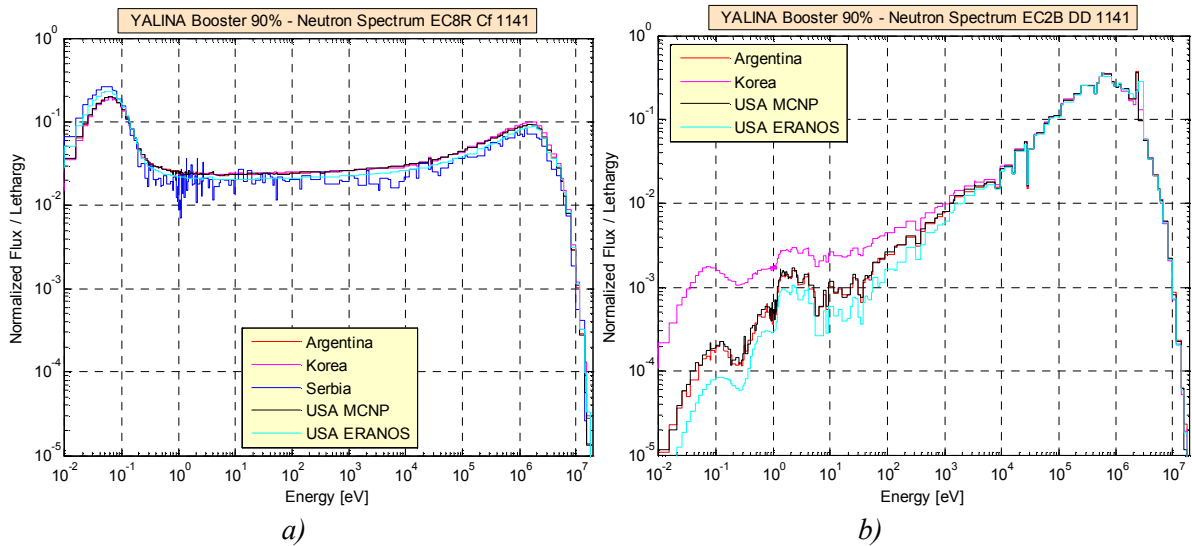


FIG. 2.11. Neutron spectrum in EC8R (left plot) using a californium neutron source and in EC2B (right plot) experimental channels using the D-D neutron source in YALINA-Booster configuration with 90% enriched uranium fuel and 1141 EK10 fuel rods in the thermal zone (Courtesy of the Argonne National Laboratory, USA).

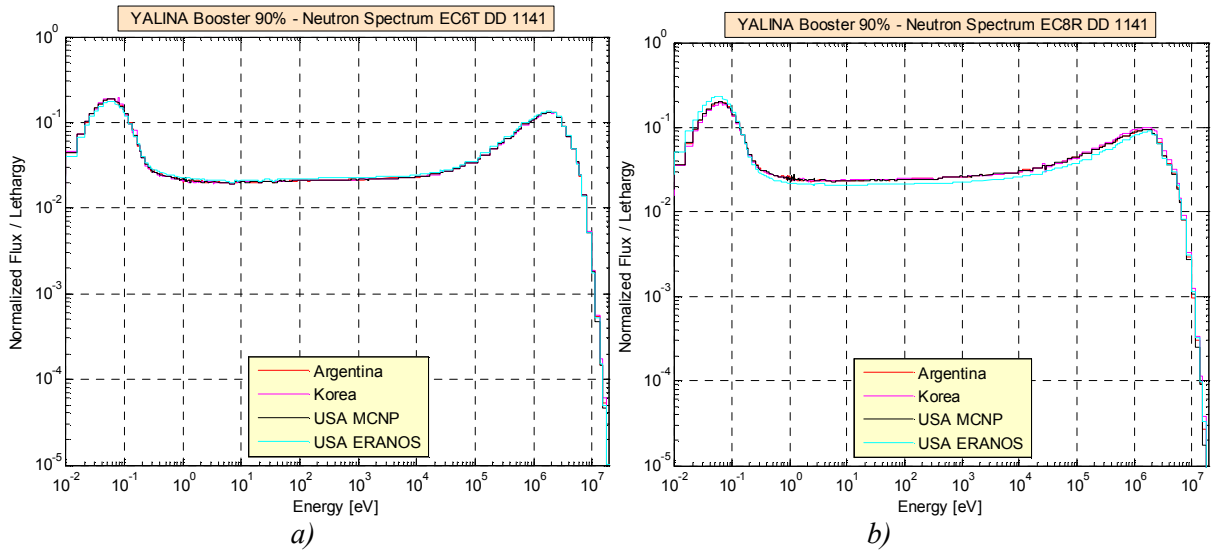


FIG. 2.12. Neutron spectrum in EC6T (a) and in EC8R (b) experimental channels using the D-D neutron source in YALINA-Booster configuration with 90% enriched uranium fuel and 1141 EK10 fuel rods in the thermal zone (Courtesy of the Argonne National Laboratory, USA).

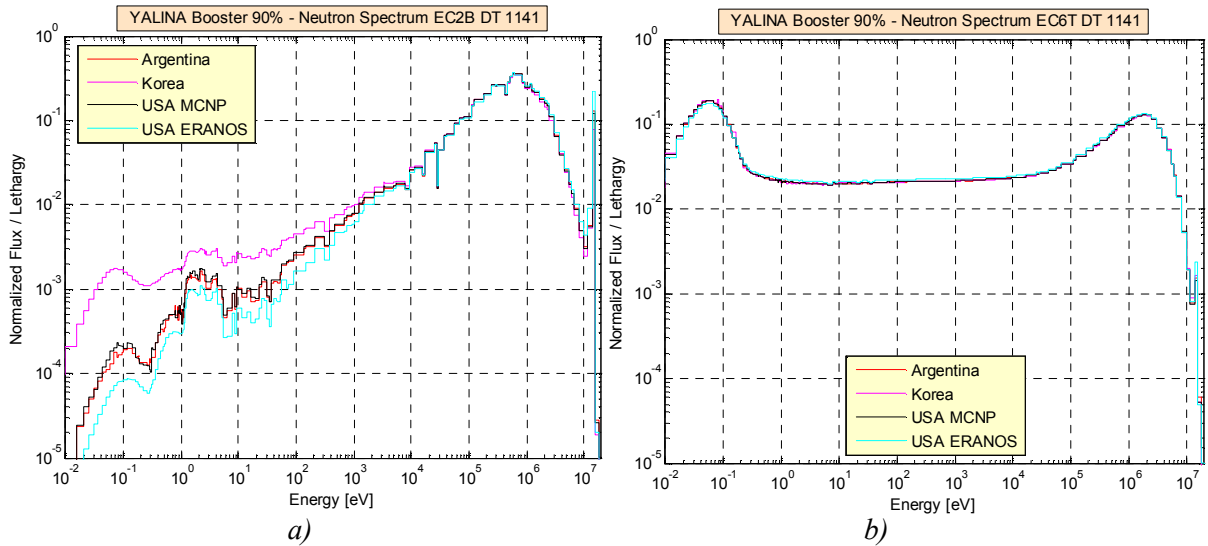


FIG 2.13. Neutron spectrum in EC2B (a) and in EC6T (b) experimental channels using the D-T neutron source in YALINA-Booster configuration with 90% enriched uranium fuel and 1141 EK10 fuel rods in the thermal zone (Courtesy of the Argonne National Laboratory, USA).

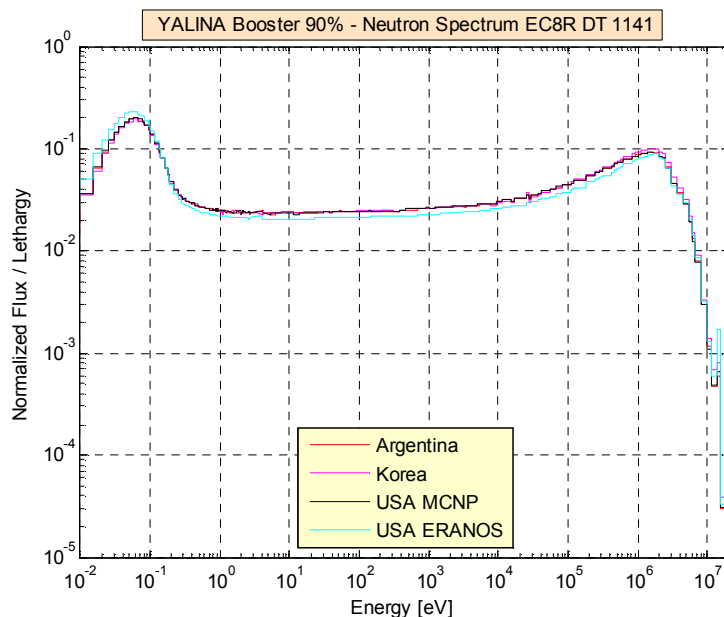


FIG. 2.14. Neutron spectrum in EC8R experimental channel using the D-T neutron source of YALINA-Booster configuration with 90% enriched uranium fuel and 1141 EK10 fuel rods in the thermal zone (Courtesy of the Argonne National Laboratory, USA).

In all the experimental channels, the neutron spectra due to the Cf, D-D or D-T neutron source are very similar, except for the peaks at 2.45 MeV for the D-D neutron source and at 14.1 MeV for the D-T neutron source. In the EC8R experimental channel, the D-T neutron source peak is negligible; this indicates that the leakage of the D-T neutrons is very small.

2.2.4. Reaction rates from D-D and D-T neutron pulses for the YALINA-Booster configuration with 1141 fuel rods in the thermal zone

Figures 2.15–2.20 plot the ${}^3\text{He}(n,p)$ and ${}^{235}\text{U}(n,f)$ reaction rates as a function of time in the EC6T, EC8R, EC1B, EC2B, and EC3B experimental channels from D-D and D-T neutron pulses. In these plots, the reaction rates have been normalized to their maximum values from a single neutron pulse with 5 μs duration. Generally, there is a good agreement between the results obtained by the different Member States.

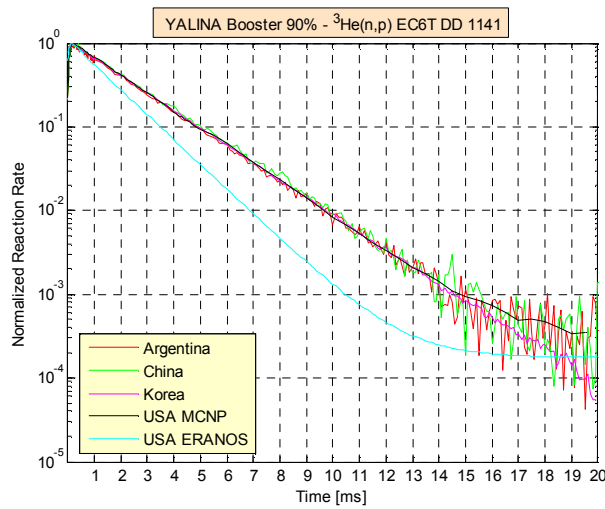


FIG. 2.15. $^3\text{He}(n,p)$ reaction rate in EC6T experimental channel using the D-D neutron source of YALINA-Booster configuration with 90% enriched uranium fuel and 1141 EK10 fuel rods in the thermal zone (Courtesy of the Argonne National Laboratory, USA).

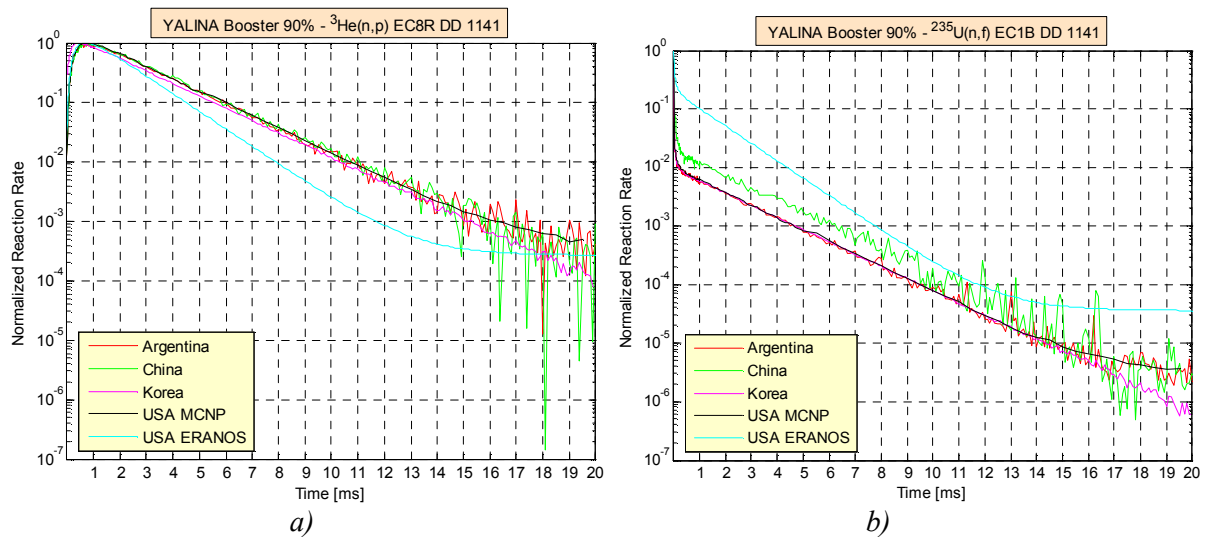


FIG. 2.16. $^3\text{He}(n,p)$ reaction rate in EC8R experimental channel (a) and $^{235}\text{U}(n,f)$ reaction rate in EC1B experimental channel (b) using the D-D neutron source in YALINA-Booster configuration with 90% enriched uranium fuel and 1141 EK10 fuel rods in the thermal zone (Courtesy of the Argonne National Laboratory, USA).

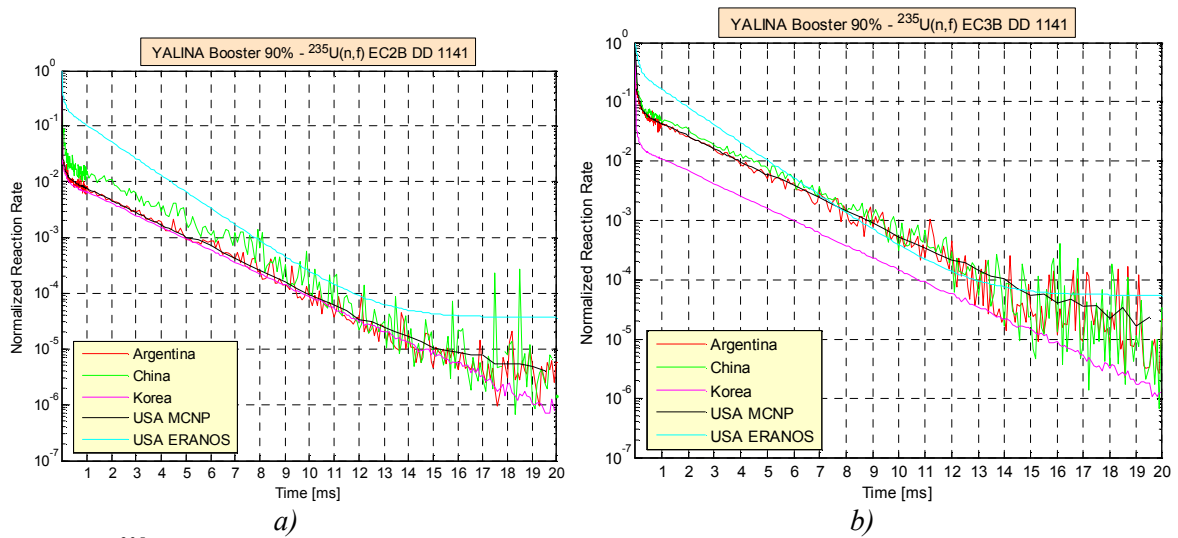


FIG. 2.17. $^{235}\text{U}(n,f)$ reaction rate in EC2B (a) and in EC3B (b) experimental channels using the D-D neutron source in YALINA-Booster configuration with 90% enriched uranium fuel and 1141 EK10 fuel rods in the thermal zone (Courtesy of the Argonne National Laboratory, USA).

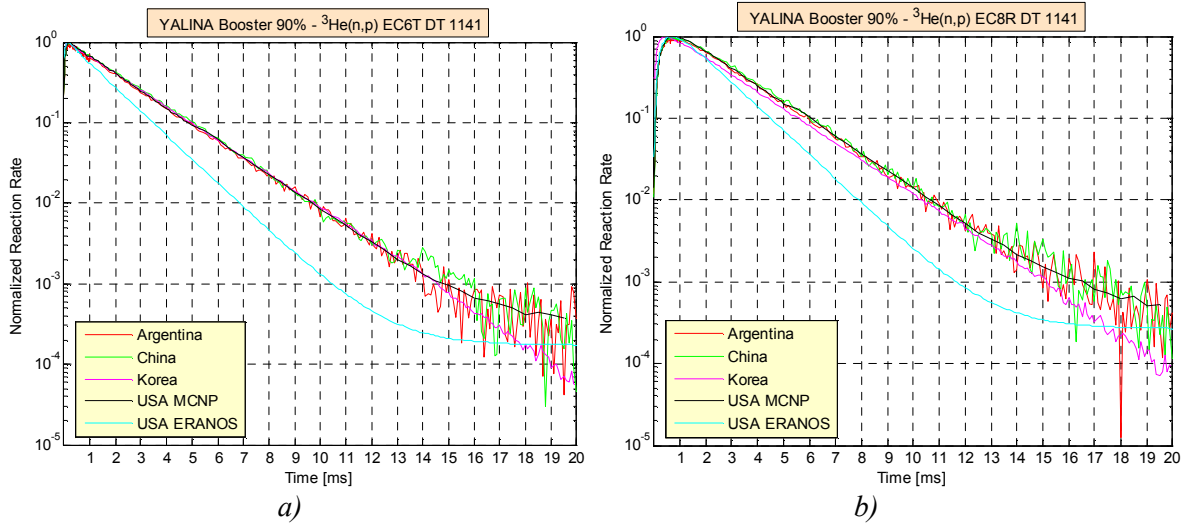


FIG. 2.18. $^3\text{He}(n,p)$ reaction rate in EC6T (a) and in EC8R (b) experimental channels using the D-T neutron source in YALINA-Booster configuration with 90% enriched uranium fuel and 1141 EK10 fuel rods in the thermal zone (Courtesy of the Argonne National Laboratory, USA).

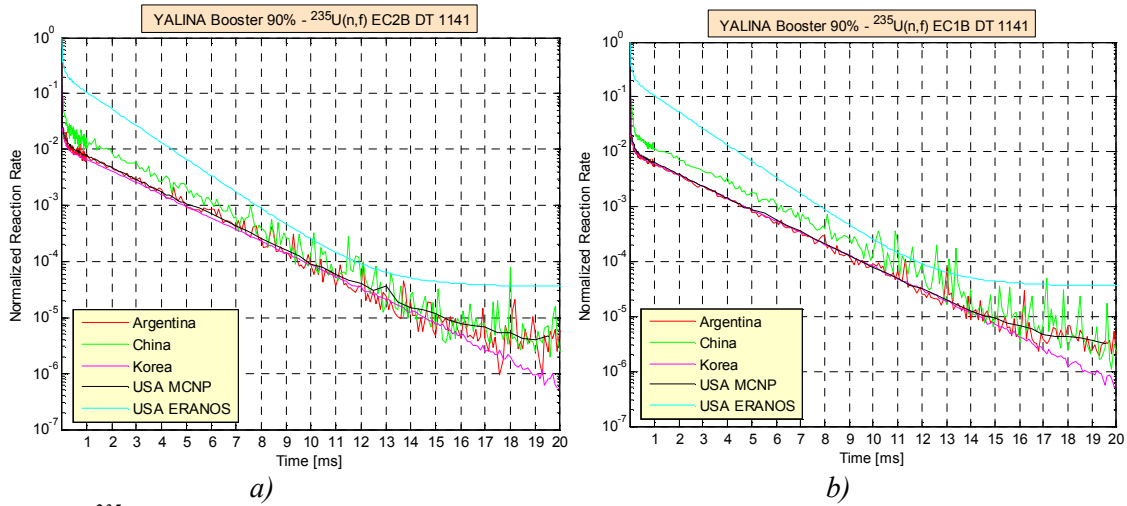


FIG. 2.19. $^{235}\text{U}(n,f)$ reaction rate in EC1B (a) and in EC2B (b) experimental channels using the D-T neutron source in YALINA-Booster configuration with 90% enriched uranium fuel and 1141 EK10 fuel rods in the thermal zone (Courtesy of the Argonne National Laboratory, USA).

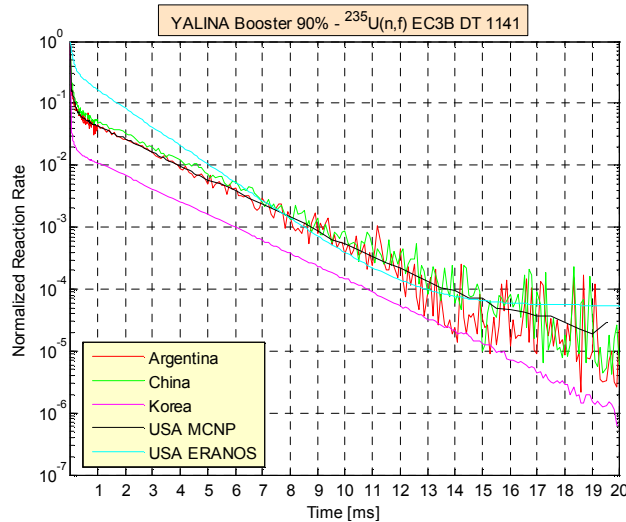


FIG. 2.20. $^{235}\text{U}(n,f)$ reaction rate in EC3B experimental channel using the D-T neutron source in YALINA-Booster configuration with 90% enriched uranium fuel and 1141 EK10 fuel rods in the thermal zone (Courtesy of the Argonne National Laboratory, USA).

The maximum value of the Korean reaction rates in the EC2B experimental channel is higher than the values calculated by other countries because the Korean calculations overestimate the thermal neutron flux in the fast zone, as shown in the Figs 2.11(b) and 2.13(a). This higher maximum value shifts the Korean curves below the others when the results are normalized to their maximum value.

The reaction rates calculated by ERANOS decay more rapidly than the others. This is a direct consequence of the lower multiplication factor computed by ERANOS. In the experimental channels of the fast zone, ERANOS yields a lower thermal-neutron flux relative to the other results. This results in a lower maximum value of the $^{235}\text{U}(n,f)$ reaction rate in the EC1B, EC2B, and EC3B experimental channels, and raises the ERANOS curves above the others.

The time dependent reaction rates show that, in the experimental channels of the thermal and reflector zones, the peak value of the reaction rate occurs after the neutron pulse.

This time delay is the required time to produce the thermal neutrons in these channels due to the external fast neutron pulse in the fast zone. There is a negligible difference between the results obtained for D-D and D-T neutron sources.

2.2.5. Kinetic parameters of the YALINA-Booster configuration with 902 fuel rods in the thermal zone

Figures 2.21–2.22 show the kinetic parameters for the YALINA-Booster configuration with 902 fuel rods in the thermal zone. Unless otherwise stated, the observations of Section 2.2.1 apply to these results. Excluding the Serbia and USA ERANOS results, as explained in Section 2.2.1, the effective (k_{eff}) and prompt (k_{pro}) multiplication factors calculated by the different Member States agree within a margin of 250 pcm. The results obtained by the Serbia for the effective (k_{eff}) and prompt (k_{pro}) multiplication factors are 500 and 750 pcm higher than those obtained by the other Member States, respectively. For the USA ERANOS results, the corresponding differences are 100 and 350 pcm, respectively. For this YALINA-Booster configuration, the ERANOS multiplication factors have been included in the average values. The prompt multiplication factor is about 730 pcm lower than the effective multiplication factor.

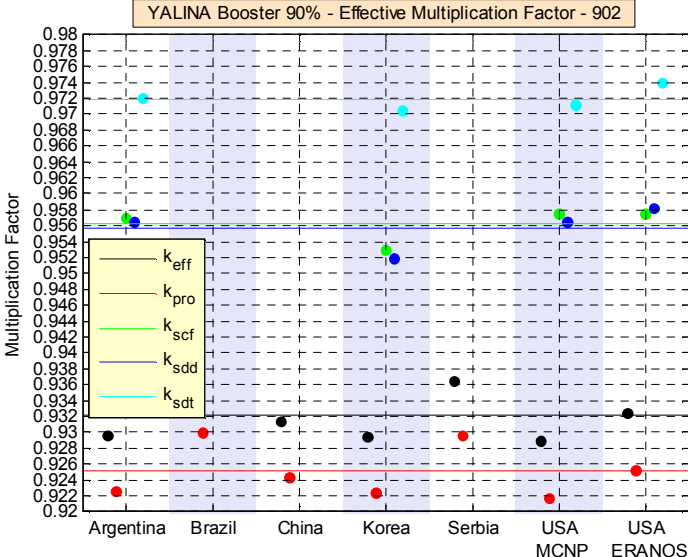


FIG. 2.21. Multiplication factors of YALINA-Booster configuration with 90% enriched uranium fuel and 902 EK10 fuel rods in the thermal zone (Courtesy of the Argonne National Laboratory, USA).

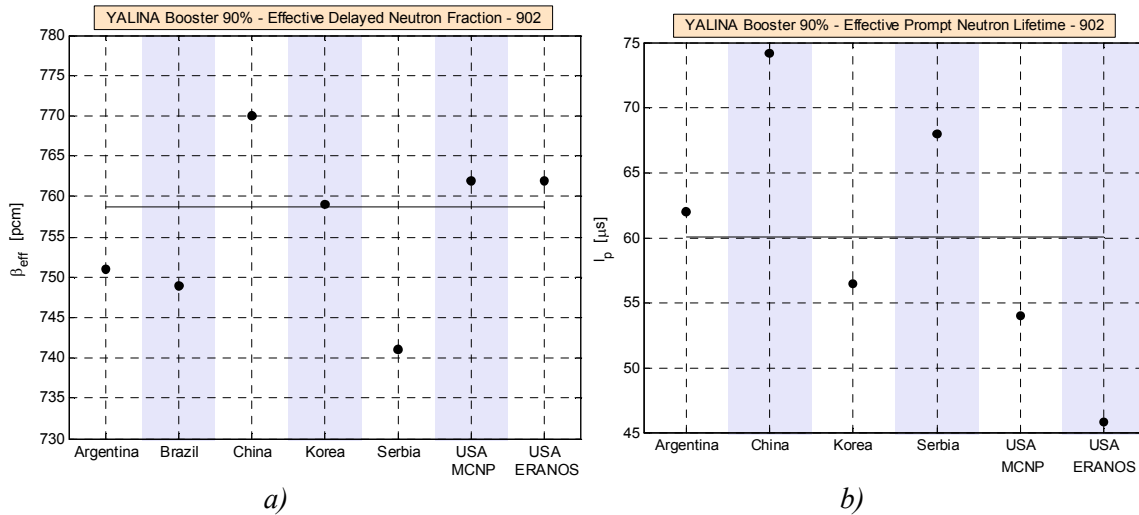


FIG. 2.22. Effective delayed-neutron fraction (a) and prompt neutron lifetime (b) of YALINA-Booster configuration with 90% enriched uranium fuel and 902 EK10 fuel rods in the thermal zone (Courtesy of the Argonne National Laboratory, USA).

The source multiplication factors calculated by Argentina and USA MCNP agree within a margin of 80 pcm; the difference increases up to 450 pcm if the data of Korea and USA ERANOS are included. The (effective) prompt neutron lifetime λ_p shown in the Fig. 22 (b) ranges from 45 to 75 μ s. The higher values shown in the plot have been obtained by China and Serbia.

2.2.6. Reaction rates of the YALINA-Booster configuration with 902 fuel rods in the thermal zone

The $^3\text{He}(n,p)$ and $^{235}\text{U}(n,f)$ reaction rates for the YALINA-Booster configuration with 902 fuel rods in the thermal zone are plotted in Figs 2.23–2.27. The observations of Section 2.2.2 are valid unless otherwise stated. The reaction-rate values of the YALINA-Booster 902 configuration are much lower than the 1141 configuration values because of the lower number of EK10 fuel rods in the thermal zone, 902 versus 1141. The Monte Carlo statistical error for one standard deviation in the reaction rate results for the EC6T experimental channel is less than 1.5% for the Argentina and USA MCNP results; this number increases up to 4 and 7% for the Chinese and the Korean results, respectively. The corresponding error for the EC2B experimental channel is less than 4.7% for the Argentina and USA MCNP results, and this error increases up to 10 and 30% for the Chinese and the Korean results, respectively. The USA ERANOS reaction rates in the EC6T experimental channel agree with the MCNP results. The statistical error in the $^{115}\text{In}(n,\gamma)$, $^{197}\text{Au}(n,\gamma)$, and $^{55}\text{Mn}(n,\gamma)$ reaction rates of the experimental channels of the thermal zone, calculated by Argentina, Korea, and USA MCNP, is less than 2.5%. For the reaction rates of the EC10R experimental channel, this error is up to 8% in the Argentina and the USA MCNP results, and the corresponding value for the Korean results is 50%.

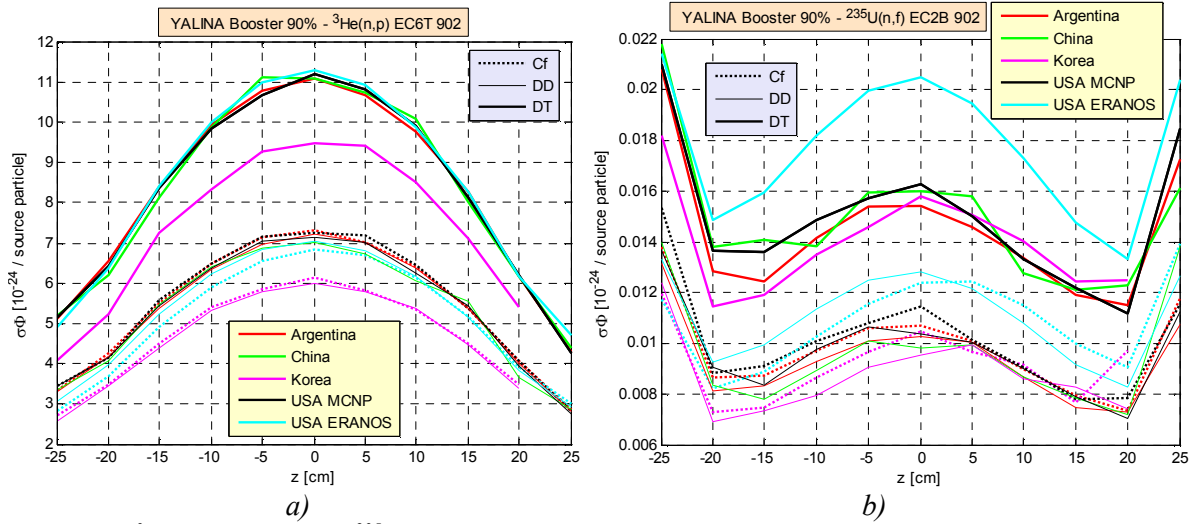


FIG. 2.23. $^3\text{He}(n,p)$ (a) and $^{235}\text{U}(n,f)$ (b) reaction rates in EC6T (a) and EC2B (b) experimental channels of YALINA-Booster configuration with 90% enriched uranium fuel and 902 EK10 fuel rods in the thermal zone (Courtesy of the Argonne National Laboratory, USA).

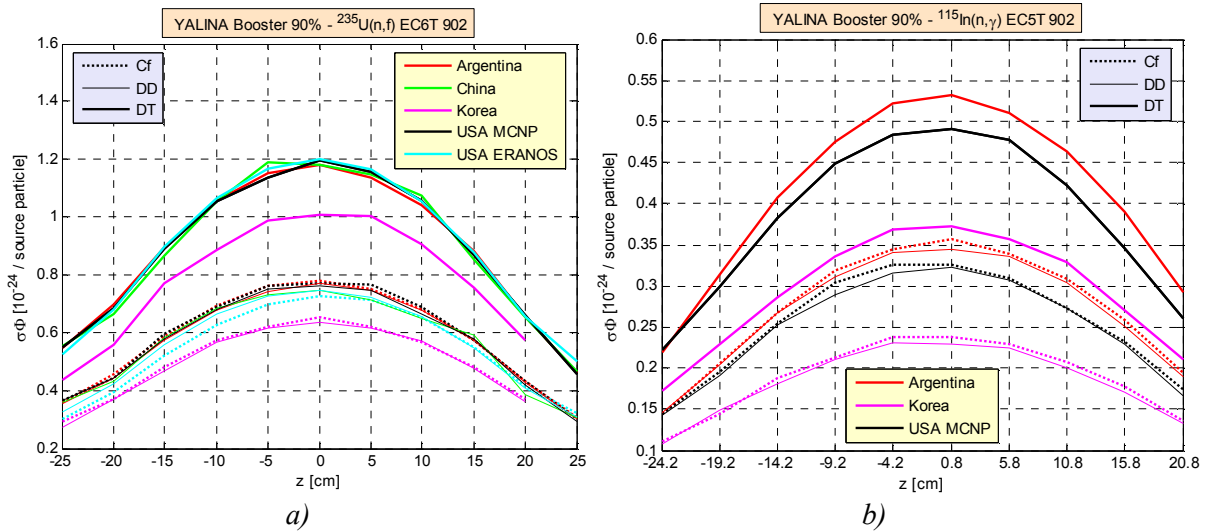


FIG. 2.24. $^{235}\text{U}(n,f)$ (a) and $^{115}\text{In}(n,\gamma)$ (b) reaction rates in EC6T (a) and EC5T (b) experimental channels of YALINA-Booster configuration with 90% enriched uranium fuel and 902 EK10 fuel rods in the thermal zone (Courtesy of the Argonne National Laboratory, USA).

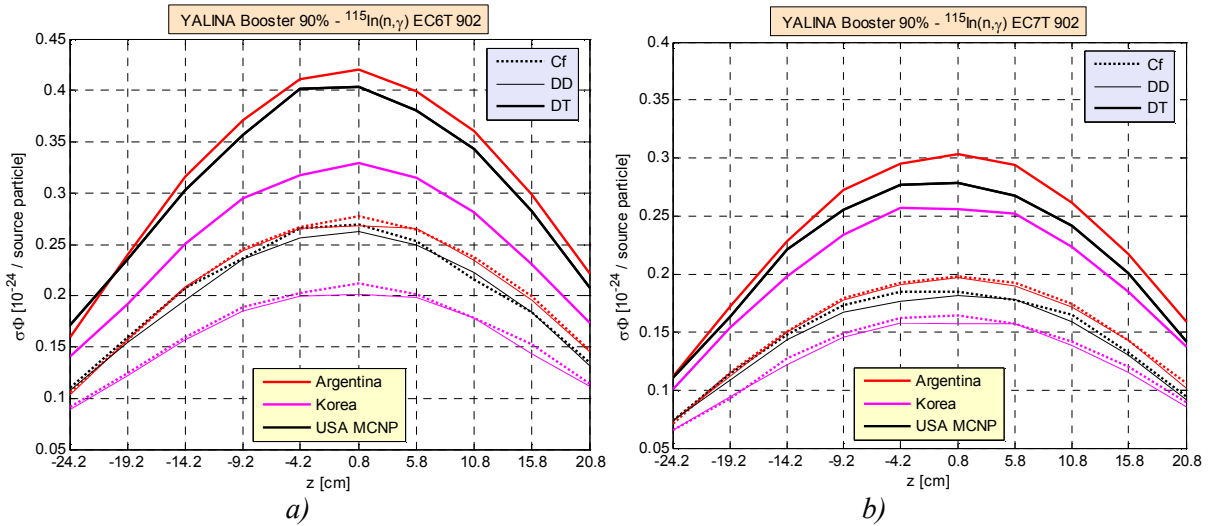


FIG. 2.25. $^{115}\text{In}(n,\gamma)$ reaction rates in EC6T (a) and EC7T (b) experimental channels in YALINA-Booster configuration with 90% enriched uranium fuel and 902 EK10 fuel rods in the thermal zone (Courtesy of the Argonne National Laboratory, USA).

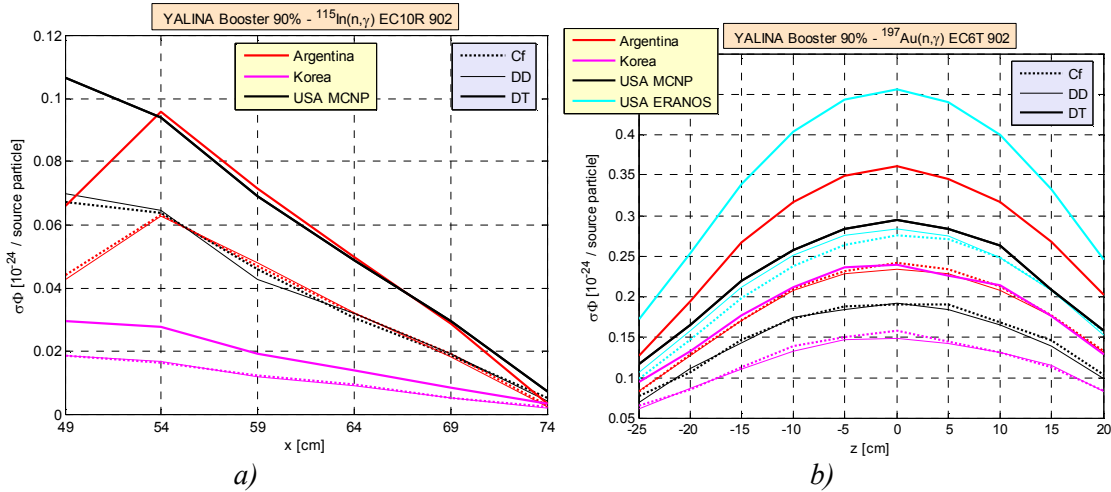


FIG. 2.26. $^{115}\text{In}(n,\gamma)$ (a) and $^{197}\text{Au}(n,\gamma)$ (b) reaction rates in EC10R (a) and EC6T (b) experimental channels of YALINA-Booster configuration with 90% enriched uranium fuel and 902 EK10 fuel rods in the thermal zone (Courtesy of the Argonne National Laboratory, USA).

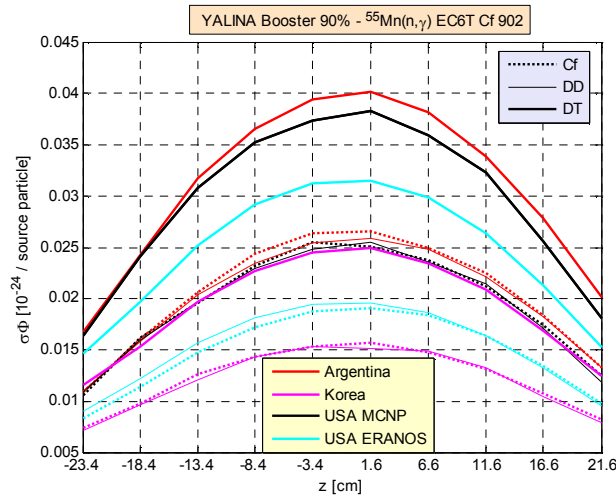


FIG. 2.27. $^{55}\text{Mn}(n,\gamma)$ reaction rates in EC6T experimental channel of YALINA-Booster configuration in YALINA-Booster configuration with 90% enriched uranium fuel and 902 EK10 fuel rods in the thermal zone (Courtesy of the Argonne National Laboratory, USA).

2.2.7. Neutron spectrum of the YALINA-Booster configuration with 902 fuel rods in the thermal zone

The neutron spectra in the EC2B, EC6T, and EC8R experimental channels, for the YALINA-Booster configuration with 902 fuel rods in the thermal zone, are plotted in Figs 2.28–2.32. The results are very similar to those obtained for the YALINA-Booster configuration with 1141 fuel rods in the thermal zone of Section 2.2.3.

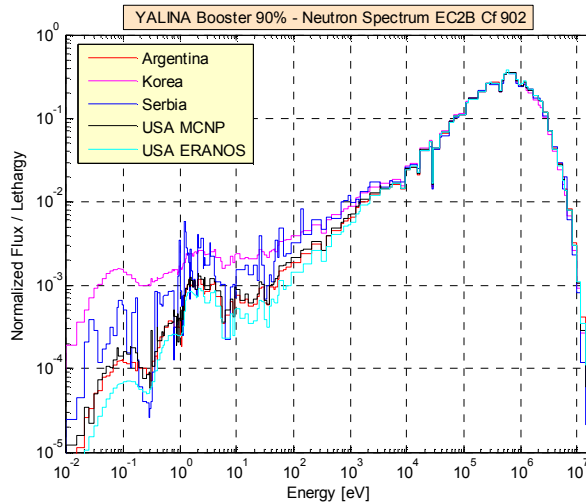


FIG. 2.28. Neutron spectrum in EC2B experimental channel using a Cf neutron source (b) of YALINA-Booster configuration in YALINA-Booster configuration with 90% enriched uranium fuel and 902 EK10 fuel rods in the thermal zone (Courtesy of the Argonne National Laboratory, USA).

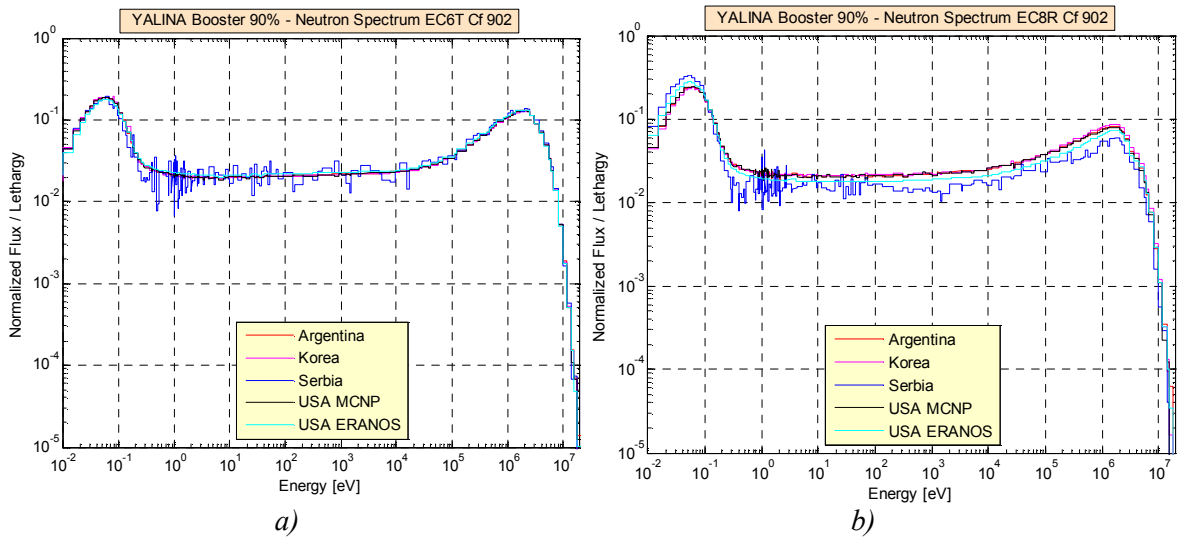


FIG. 2.29. Neutron spectrum in EC6T (a) and EC8R (b) experimental channels using a Cf neutron source in YALINA-Booster configuration with 90% enriched uranium fuel and 902 EK10 fuel rods in the thermal zone (Courtesy of the Argonne National Laboratory, USA).

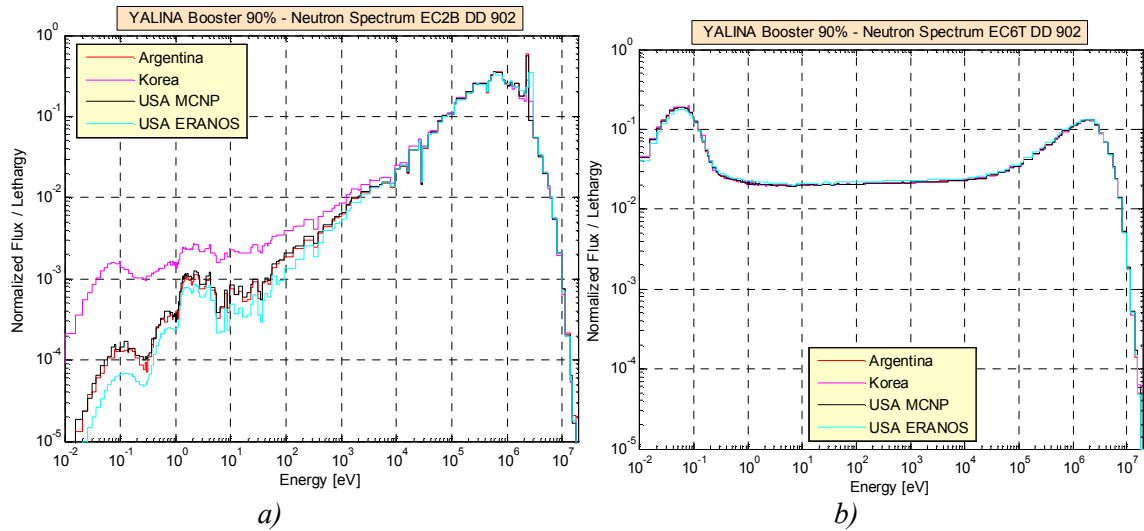


FIG. 2.30. Neutron spectrum in EC2B (a) and EC6T (b) experimental channels using the D-D neutron source in YALINA-Booster configuration with 90% enriched uranium fuel and 902 EK10 fuel rods in the thermal zone (Courtesy of the Argonne National Laboratory, USA).

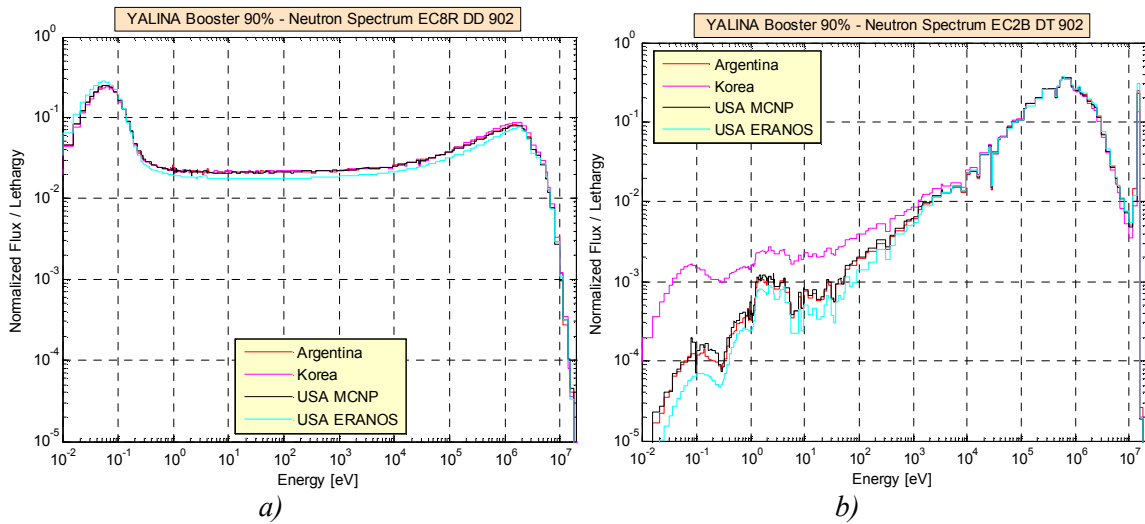


FIG. 2.31. Neutron spectrum in EC8R (a) and EC2B (b) experimental channels using D-T neutron sources in YALINA-Booster configuration with 90% enriched uranium fuel and 902 EK10 fuel rods in the thermal zone (Courtesy of the Argonne National Laboratory, USA).

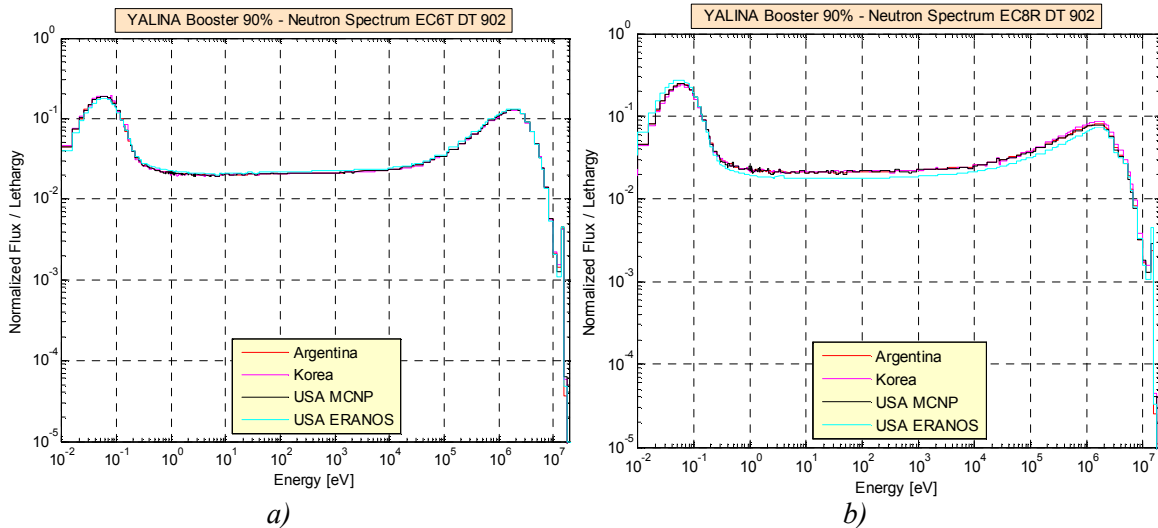


FIG. 2.32. Neutron spectrum in EC6T (a) and EC8R (b) experimental channels using the D-T neutron source in YALINA-Booster configuration with 90% enriched uranium fuel and 902 EK10 fuel rods in the thermal zone (Courtesy of the Argonne National Laboratory, USA).

2.2.8. Reaction rates from D-D and D-T neutron pulses of the YALINA-Booster configuration with 902 fuel rods in the thermal zone

Figures 2.33–2.37 show plots of the time dependent ${}^3\text{He}(n,p)$ and ${}^{235}\text{U}(n,f)$ reaction rates for the YALINA-Booster configuration with 902 fuel rods in the thermal zone. The results are similar to those obtained for the YALINA-Booster configuration with 1141 fuel rods in the thermal zone in Section 2.2.4. However, these reaction rates reach asymptotic levels, set by delayed neutrons, after ~ 8 ms. For the YALINA-Booster configuration with 1141 fuel rods in the thermal zone, the asymptotic level was not reached after 20 ms since this configuration is much closer to the critical state and the prompt fission chains take more time to vanish. The 902 configuration was not analysed by US ARANOS.

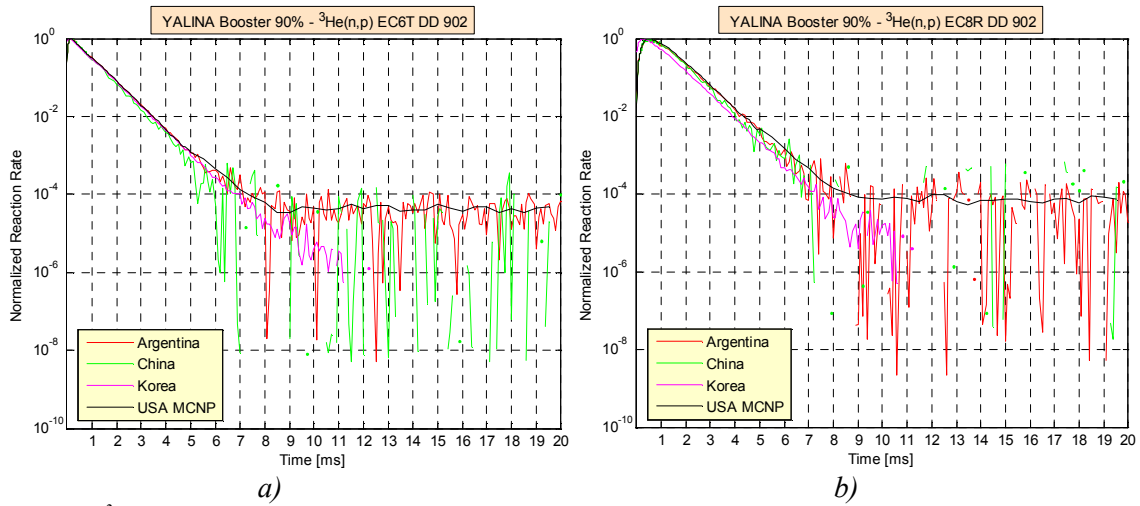


FIG. 2.33. ${}^3\text{He}(n,p)$ reaction rate in EC6T (a) and EC8R (b) experimental channels using the D-D neutron source in YALINA-Booster configuration with 90% enriched uranium fuel and 902 EK10 fuel rods in the thermal zone (Courtesy of the Argonne National Laboratory, USA).

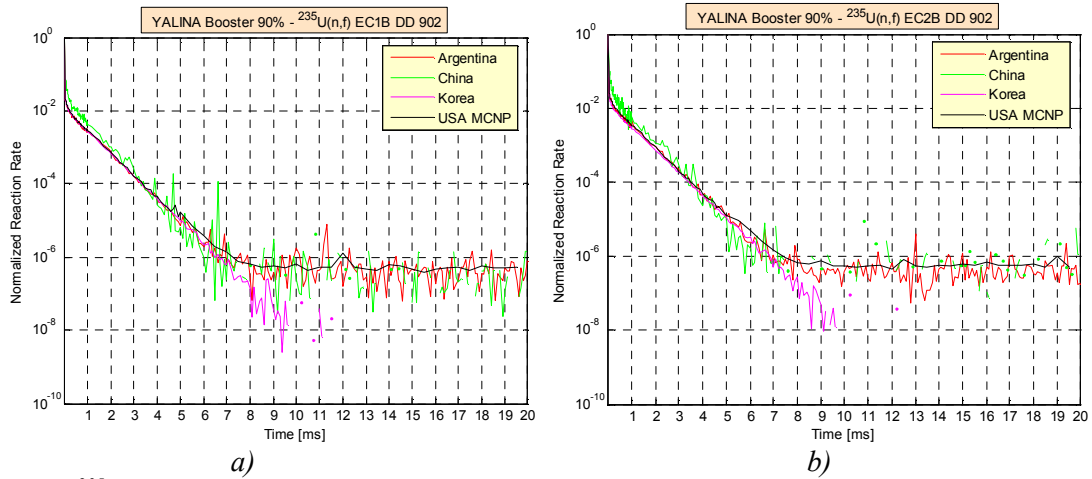


FIG. 2.34. ${}^{235}\text{U}(n,f)$ reaction rate in EC1B (a) and EC2B (b) experimental channels using the D-D neutron source in YALINA-Booster configuration with 90% enriched uranium fuel and 902 EK10 fuel rods in the thermal zone (Courtesy of the Argonne National Laboratory, USA).

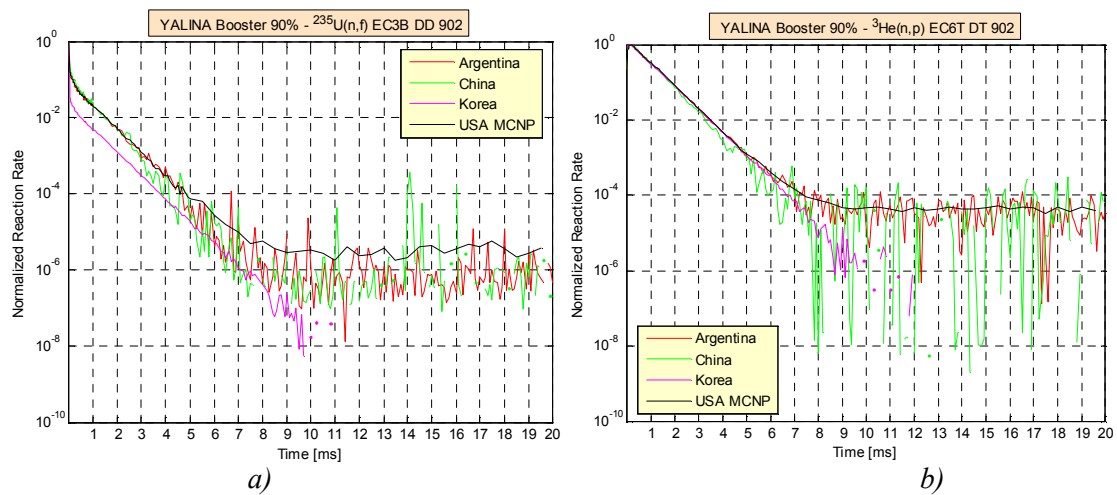


FIG. 2.35. $^{235}\text{U}(n,f)$ reaction rate in EC3B experimental channel using the D-D source (a) and $^3\text{He}(n,p)$ reaction rate in EC6T experimental channel using the D-T neutron source (b) in YALINA-Booster configuration with 90% enriched uranium fuel and 902 EK10 fuel rods in the thermal zone (Courtesy of the Argonne National Laboratory, USA).

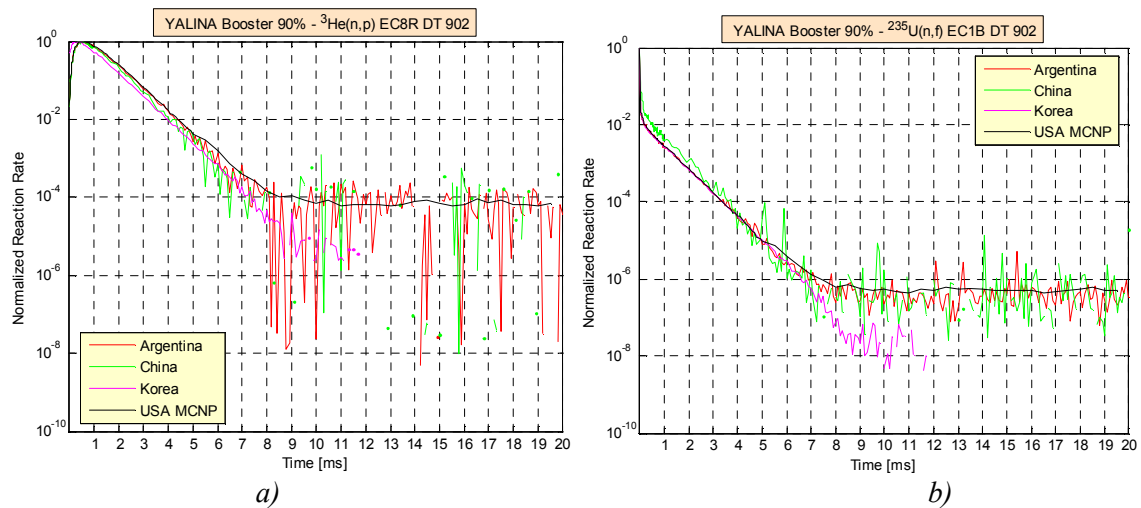


FIG. 2.36. $^3\text{He}(n,p)$ reaction rate in EC8R experimental channel (a) and $^{235}\text{U}(n,f)$ reaction rate in EC1B experimental channel (b) using the D-T neutron source in YALINA-Booster configuration with 90% enriched uranium fuel and 902 EK10 fuel rods in the thermal zone (Courtesy of the Argonne National Laboratory, USA).

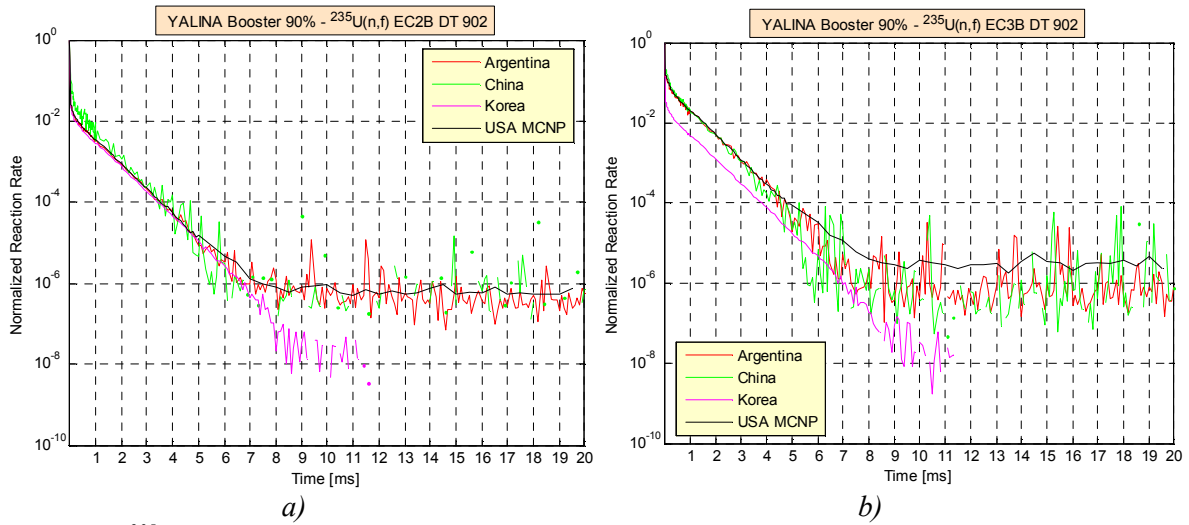


FIG. 2.37. $^{235}\text{U}(n,f)$ reaction rates in EC2B (a) and EC3B (b) experimental channels with the D-T neutron source in YALINA-Booster configuration with 90% enriched uranium fuel and 902 EK10 fuel rods in the thermal zone (Courtesy of the Argonne National Laboratory, USA).

2.3. YALINA-BOOSTER CONFIGURATION WITH 36% ENRICHED URANIUM FUEL

One YALINA-Booster configuration with 36% enriched uranium fuel was considered in this study. This configuration was the first step for converting the YALINA-Booster facility to use low enriched uranium fuel. The thermal zone of this configuration has 1185 EK10 fuel rods.

2.3.1. Kinetic parameters of the YALINA-Booster configuration with 1185 fuel rods in the thermal zone

The kinetic parameters of the YALINA-Booster configuration with 36% enriched uranium fuel in the fast zone and 1185 fuel rods in the thermal zone are plotted in Figs 2.38–2.39. Unless otherwise specified, the observations of Sections 2.2.1 through 2.2.4 are relevant for the subsections of Section 2.3. The effective (k_{eff}) and prompt (k_{pro}) multiplication factors calculated by the different Member States agree within 150 pcm margin, excluding the USA ERANOS results. This margin increases up to 900 pcm if the USA ERANOS results are considered. For the 36% enriched fuel configuration, the ERANOS multiplication factors have been excluded from the average values of the multiplication factors. The prompt multiplication factor is about 728 pcm lower than the effective multiplication factor. The source multiplication factors calculated by Argentina and USA MCNP agree within a margin of 180 pcm. This margin increases up to 950 pcm if the USA ERANOS results are included. Reducing the uranium fuel enrichment in the fast zone from 90% to 36% decreases the difference between the source and the effective multiplication factors. For the californium and D-D neutron sources, this difference becomes negligible. The USA MCNP calculations for this YALINA-Booster configuration used the ENDF/B-VII.0 nuclear data library, which results in a lower effective delayed neutron fraction relative to ENDF/B-VI.

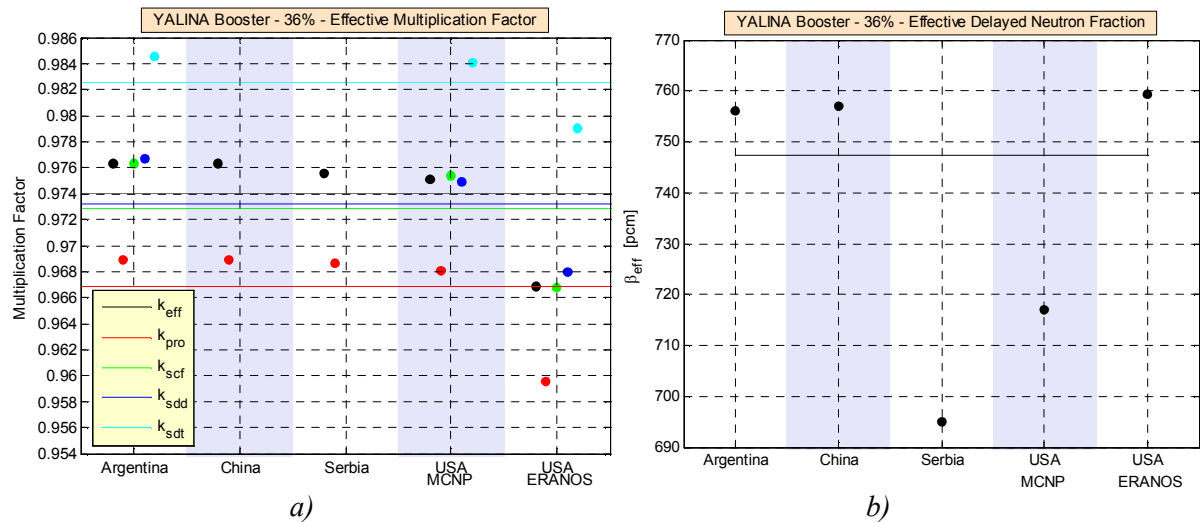


FIG. 2.38. Multiplication factors (a) and effective delayed-neutron fraction (b) of YALINA-Booster configuration with 36% enriched uranium fuel and 1185 EK10 fuel rods in the thermal zone (Courtesy of the Argonne National Laboratory, USA).

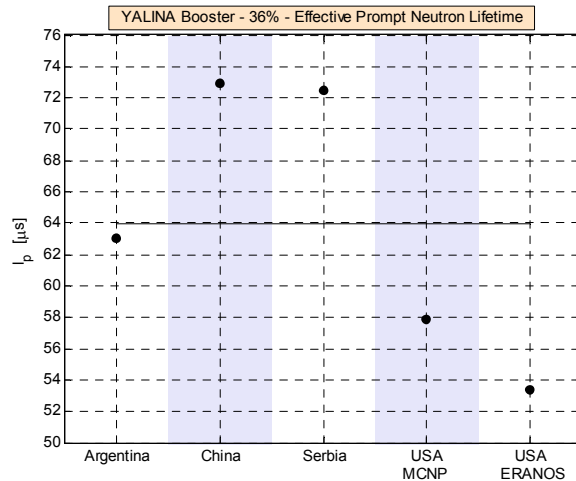


FIG. 2.39. Prompt neutron lifetime (a) of YALINA-Booster configuration with 36% enriched uranium fuel and 1185 EK10 fuel rods in the thermal zone (Courtesy of the Argonne National Laboratory, USA).

2.3.2. Reaction rates of the YALINA-Booster configuration with 1185 fuel rods in the thermal zone

The spatial distributions of the $^3\text{He}(n,p)$ and the $^{235}\text{U}(n,f)$ reaction rates in the different experimental channels of the YALINA-Booster configuration with 1185 fuel rods in the thermal zone are illustrated in Figs 2.40–2.44. There is quite a good match between the results obtained by the different Member States. The reaction rates of this configuration are lower than the results obtained for the configuration with the 90% enriched uranium fuel in the fast zone, since the effective neutron multiplication factor is lower.

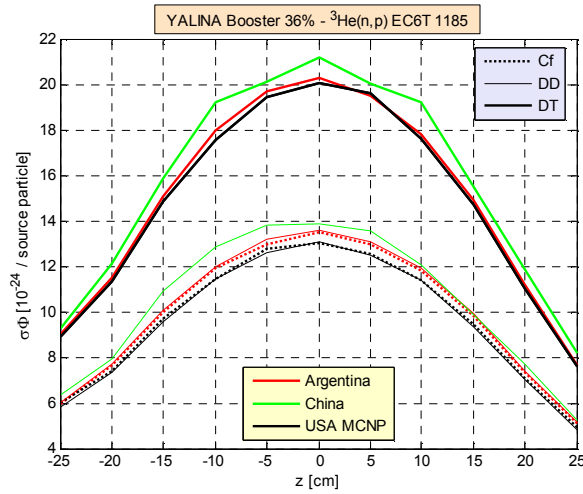


FIG. 2.40. ${}^3\text{He}(n,p)$ reaction rate in EC6T experimental channel of YALINA-Booster configuration with 36% enriched uranium fuel and 1185 EK10 fuel rods in the thermal zone (Courtesy of the Argonne National Laboratory, USA).

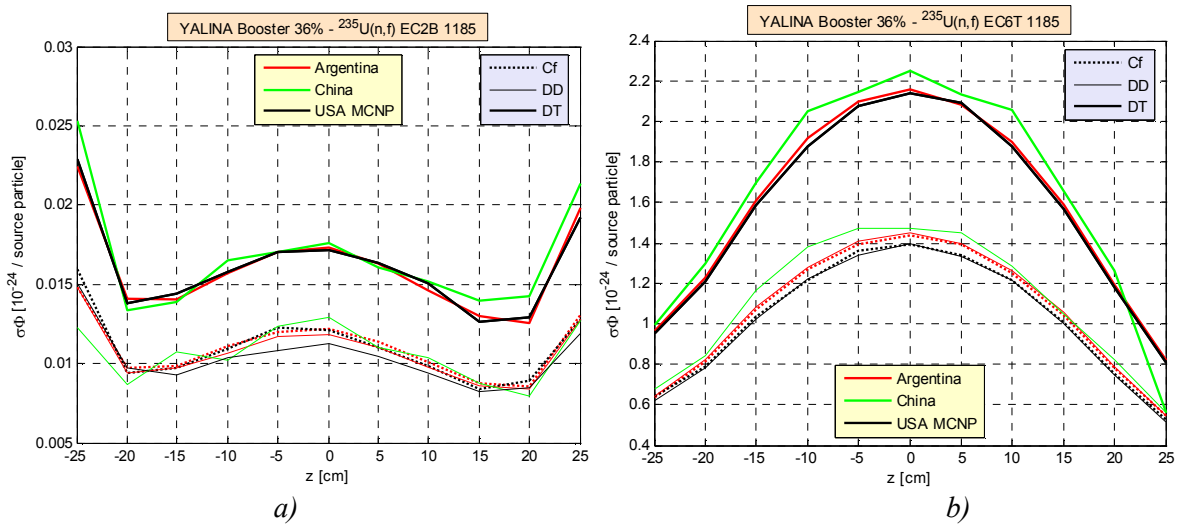


FIG. 2.41. ${}^{235}\text{U}(n,f)$ reaction rate in EC2B (a) and EC6T (b) experimental channels in YALINA-Booster configuration with 36% enriched uranium fuel and 1185 EK10 fuel rods in the thermal zone (Courtesy of the Argonne National Laboratory, USA).

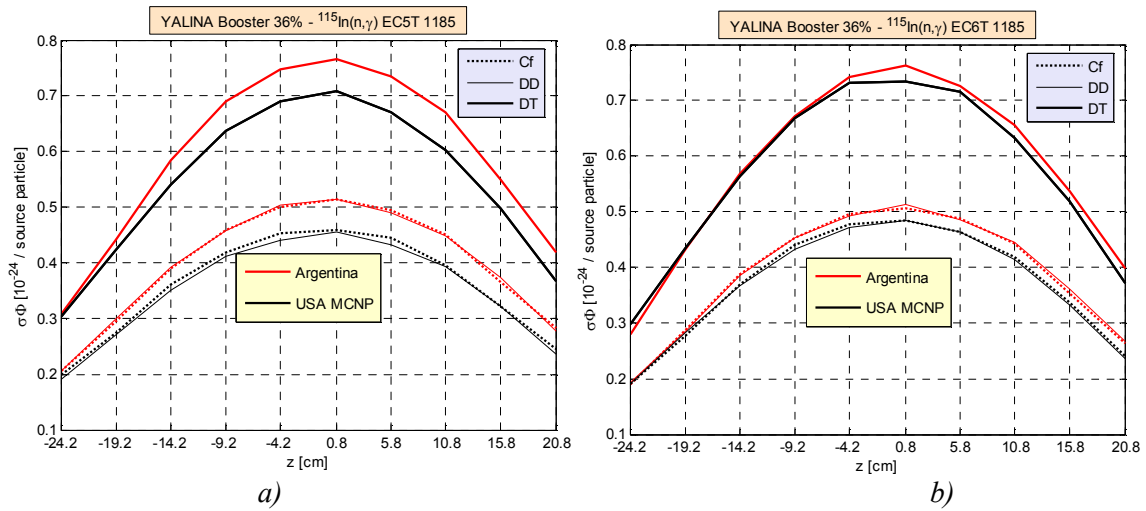


FIG. 2.42. $^{115}\text{In}(n,\gamma)$ reaction rate in EC5T (a) and EC6T (b) experimental channels in YALINA-Booster configuration with 36% enriched uranium fuel and 1185 EK10 fuel rods in the thermal zone (Courtesy of the Argonne National Laboratory, USA).

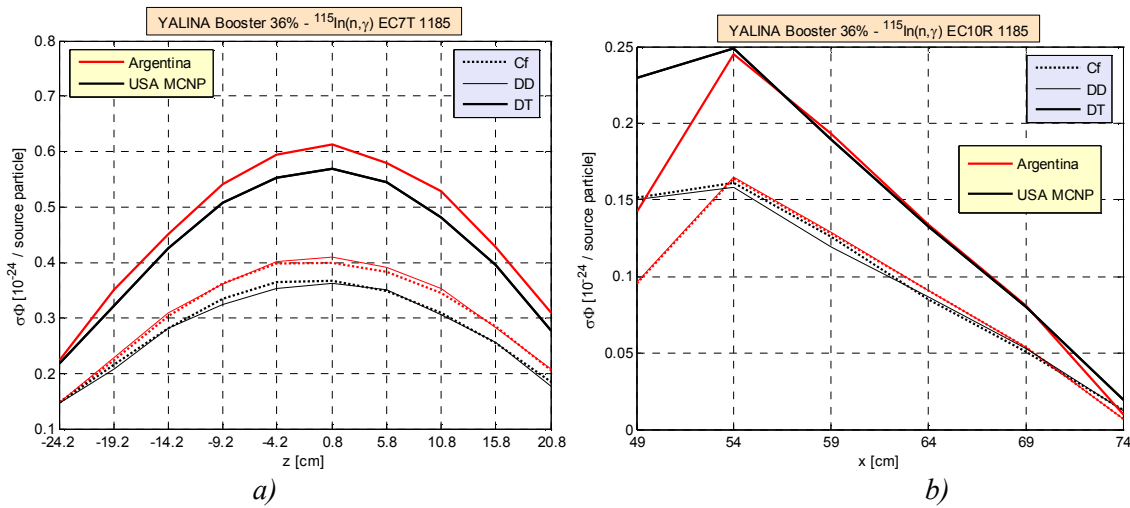


FIG. 2.43. $^{115}\text{In}(n,\gamma)$ reaction rate in EC7T (a) and EC10R (b) experimental channels in YALINA-Booster configuration with 36% enriched uranium fuel and 1185 EK10 fuel rods in the thermal zone (Courtesy of the Argonne National Laboratory, USA).

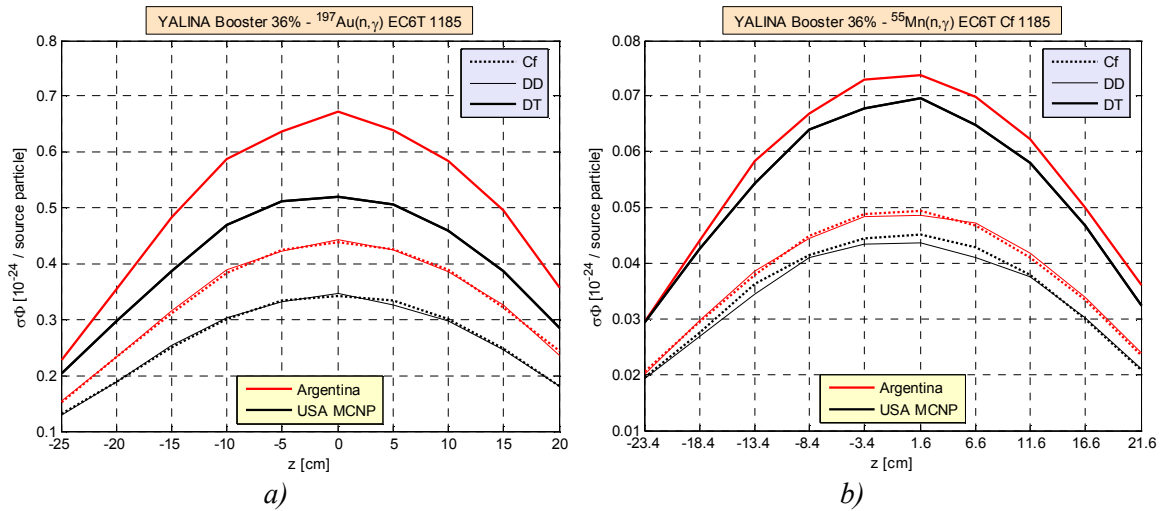


FIG. 2.44. $^{197}\text{Au}(n,\gamma)$ (a) and $^{55}\text{Mn}(n,\gamma)$ (b) reaction rates in EC6T experimental channel in YALINA-Booster configuration with 36% enriched uranium fuel and 1185 EK10 fuel rods in the thermal zone (Courtesy of the Argonne National Laboratory, USA).

2.3.3. Neutron spectrum of the YALINA-Booster configuration with 1185 fuel rods in the thermal zone

The neutron spectra in the EC2B, EC6T, and EC8R experimental channels of the YALINA-Booster configuration with 1185 fuel rods in the thermal zone are shown in Figs 2.45–2.49. The results are very similar to the Section 2.2.3 results for the configuration with the 90% enriched uranium fuel in the fast zone.

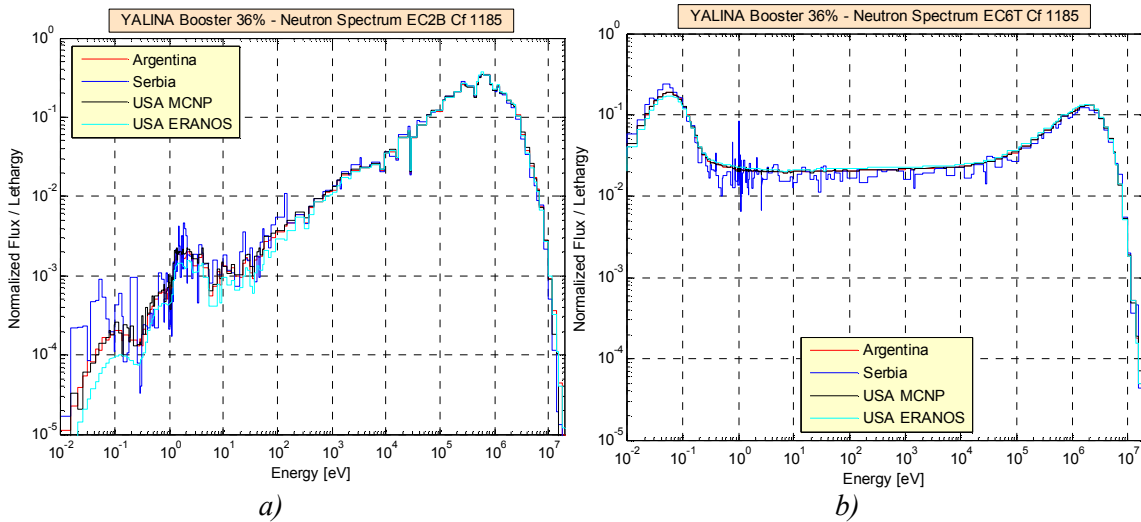


FIG. 2.45. Neutron spectrum in EC2B (a) and EC6T (b) experimental channels using a Cf neutron source in YALINA-Booster configuration with 36% enriched uranium fuel and 1185 EK10 fuel rods in the thermal zone (Courtesy of the Argonne National Laboratory, USA).

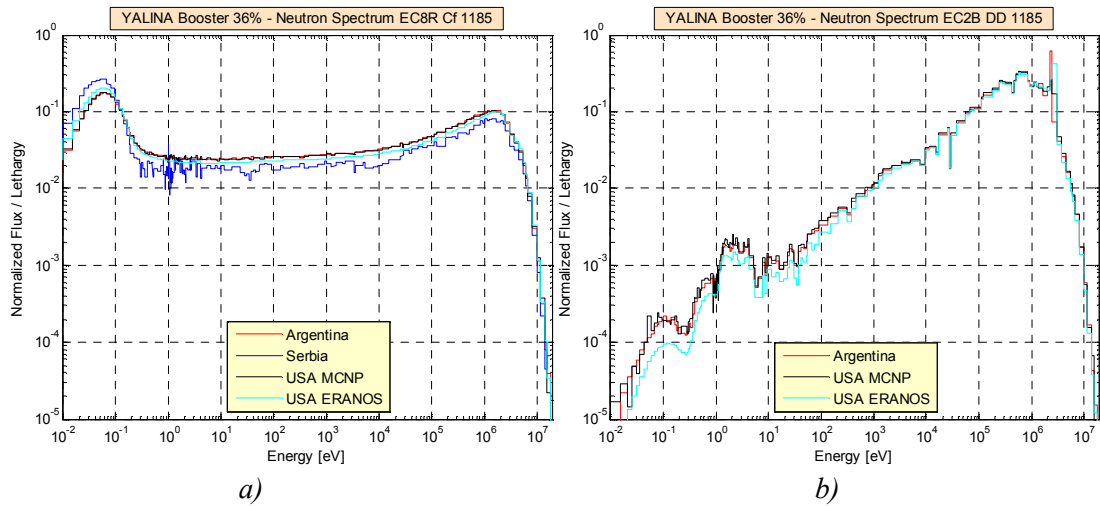


FIG. 2.46. Neutron spectrum in EC8R experimental channel using a californium neutron source (a) and EC2B experimental channel using the D-D neutron source (b) in YALINA-Booster configuration with 36% enriched uranium fuel and 1185 EK10 fuel rods in the thermal zone (Courtesy of the Argonne National Laboratory, USA).

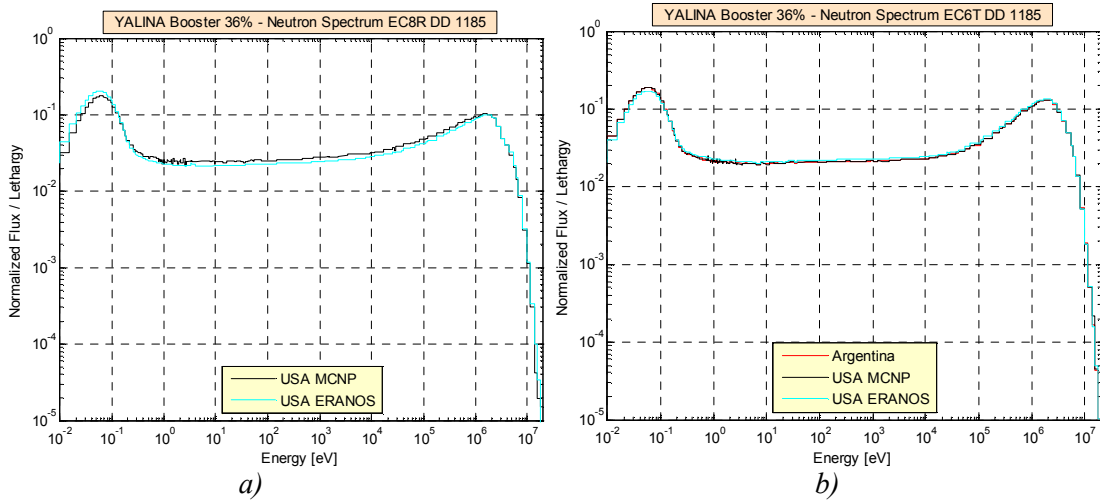


FIG. 2.47. Neutron spectrum in EC6T (left plot) and EC8R (right plot) experimental channels using the D-D neutron source in YALINA-Booster configuration with 36% enriched uranium fuel and 1185 EK10 fuel rods in the thermal zone (Courtesy of the Argonne National Laboratory, USA).

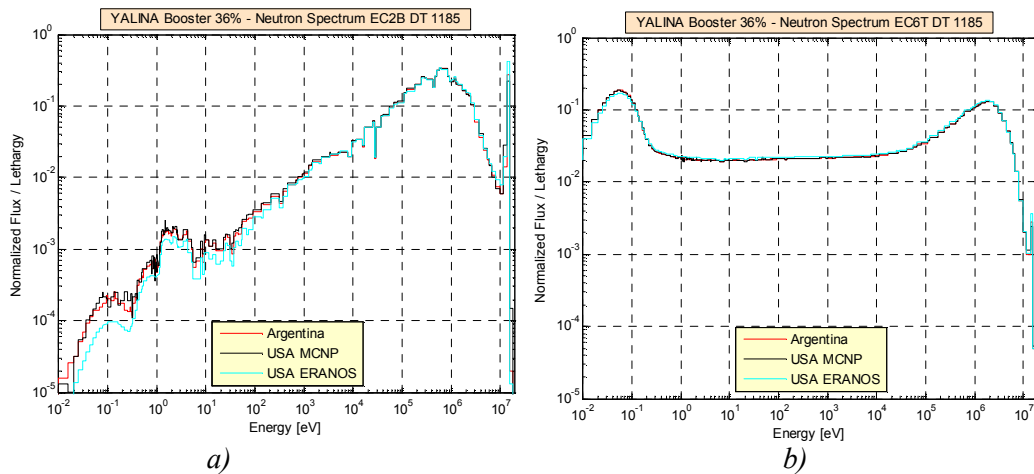


FIG. 2.48. Neutron spectrum in EC2B (a) and EC6T (b) experimental channels using the D-T neutron source in YALINA-Booster configuration with 36% enriched uranium fuel and 1185 EK10 fuel rods in the thermal zone (Courtesy of the Argonne National Laboratory, USA).

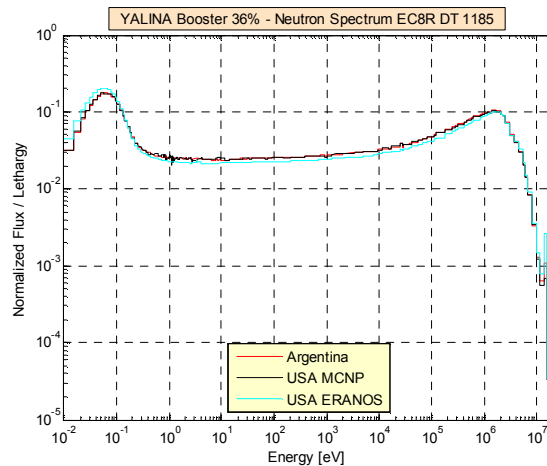


FIG. 2.49. Neutron spectrum in EC8R experimental channel using the D-T neutron source in YALINA-Booster configuration with 36% enriched uranium fuel and 1185 EK10 fuel rods in the thermal zone (Courtesy of the Argonne National Laboratory, USA).

2.3.4. Reaction rates from D-D and D-T Neutron Pulses of the YALINA-Booster configuration with 1185 fuel rods in the thermal zone

The time-dependent ${}^3\text{He}(n,p)$ and ${}^{235}\text{U}(n,f)$ reaction rates of the YALINA-Booster configuration with 1185 fuel rods in the thermal zone are shown in Figs 2.50–2.55. The results are very similar to the Section 2.2.4 results for the configuration with the 90% enriched uranium fuel in the fast zone. However, the reaction rates decay faster because of the lower effective neutron multiplication factor. The results from the different Member States show good agreement if the statistical fluctuations are ignored.

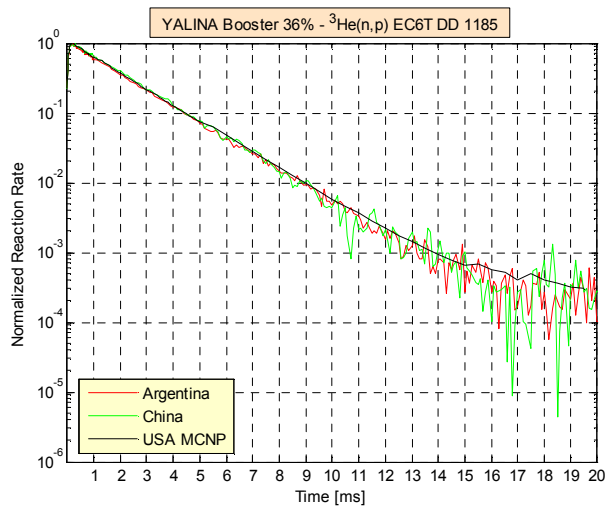


FIG. 2.50. ${}^3\text{He}(n,p)$ reaction rate in EC6T experimental channel using the D-D neutron source pulse (right plot) in YALINA-Booster configuration with 36% enriched uranium fuel and 1185 EK10 fuel rods in the thermal zone (Courtesy of the Argonne National Laboratory, USA).

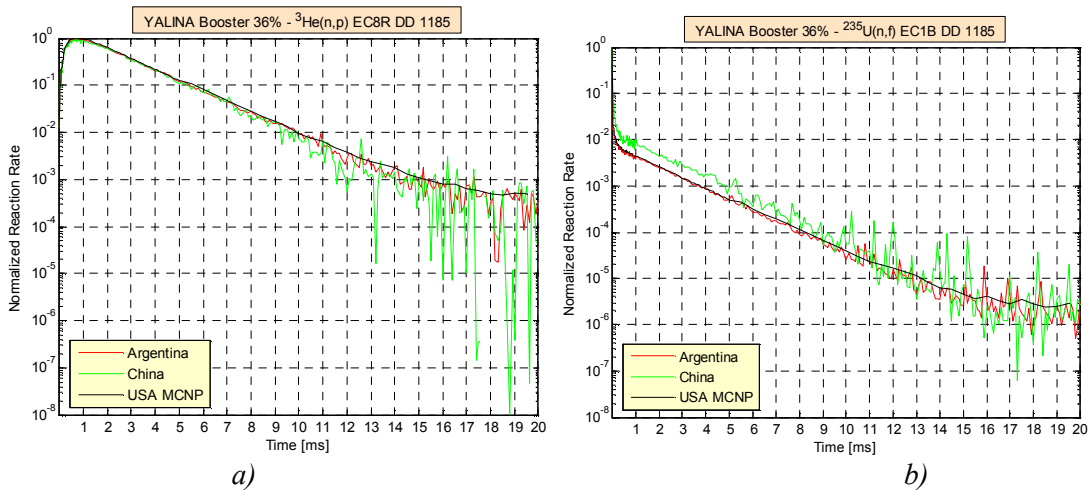


FIG. 2.51. ${}^3\text{He}(n,p)$ reaction rate in EC8R experimental channel (a) and ${}^{235}\text{U}(n,f)$ reaction rate in EC1B experimental channel (b) using the D-D neutron source pulse in YALINA-Booster configuration with 36% enriched uranium fuel and 1185 EK10 fuel rods in the thermal zone (Courtesy of the Argonne National Laboratory, USA).

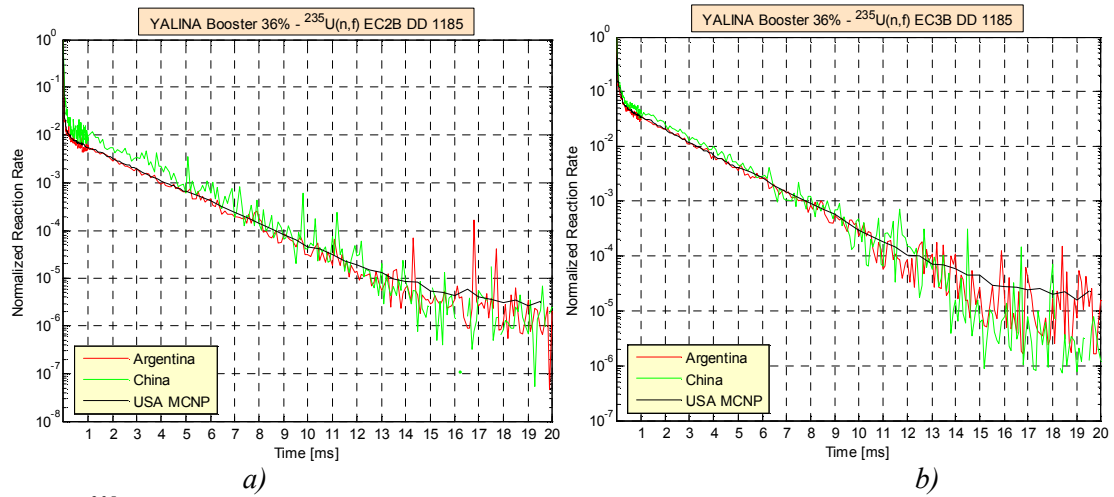


FIG. 2.52. $^{235}\text{U}(n,f)$ reaction rate in EC2B (a) and EC3B (b) experimental channels using the D-D neutron source pulse in YALINA-Booster configuration with 36% enriched uranium fuel and 1185 EK10 fuel rods in the thermal zone (Courtesy of the Argonne National Laboratory, USA).

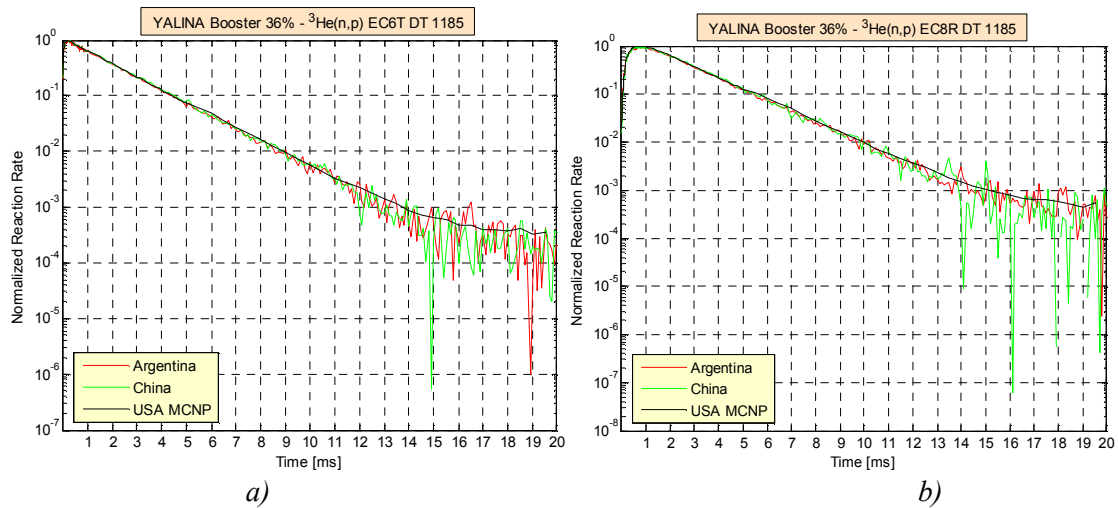


FIG. 2.53. $^3\text{He}(n,p)$ reaction rate in EC6T (a) and EC8R (b) experimental channels using the D-T neutron source pulse in YALINA-Booster configuration with 36% enriched uranium fuel and 1185 EK10 fuel rods in the thermal zone (Courtesy of the Argonne National Laboratory, USA).

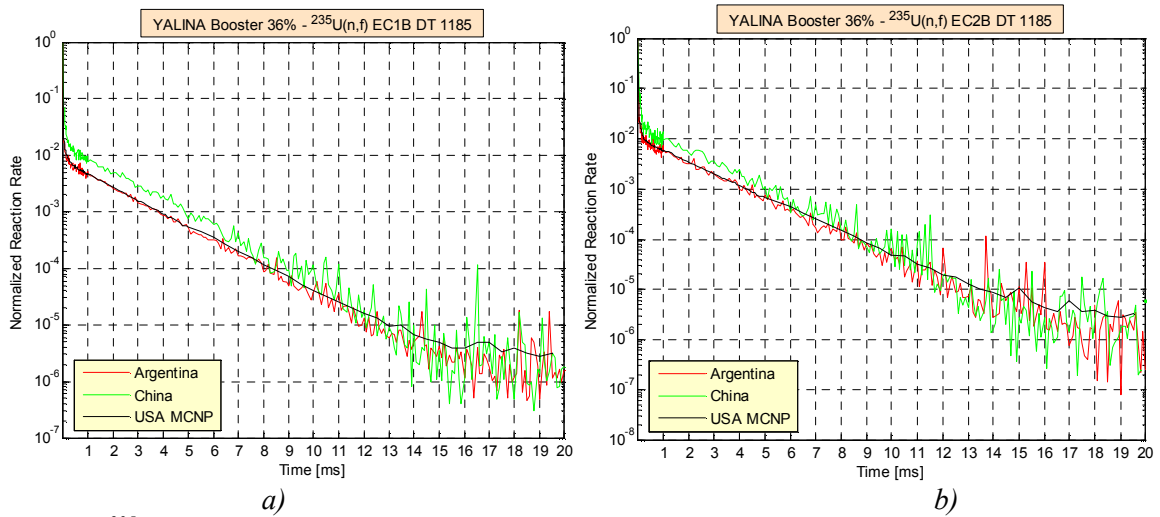


FIG. 2.54. $^{235}\text{U}(n,f)$ reaction rate in EC1B (a) and EC2B (b) experimental channels using the D-T neutron source pulse in YALINA-Booster configuration with 36% enriched uranium fuel and 1185 EK10 fuel rods in the thermal zone (Courtesy of the Argonne National Laboratory, USA).

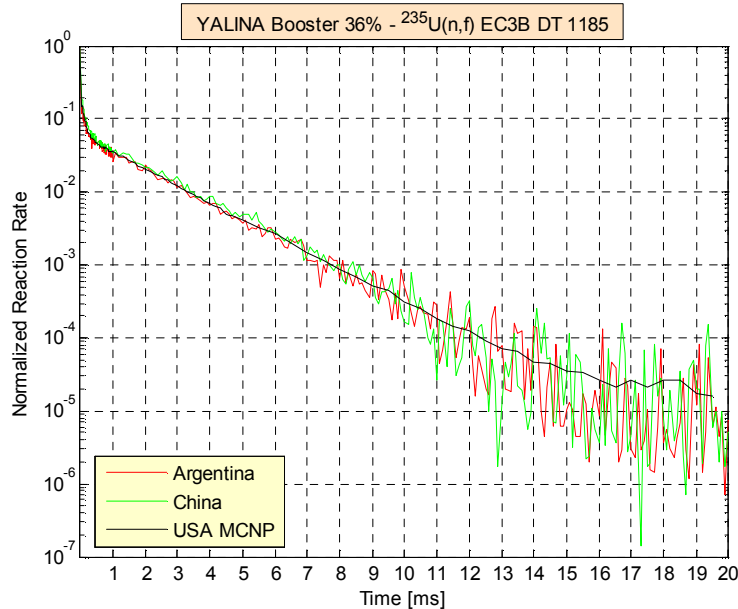


FIG. 2.55. $^{235}\text{U}(n,f)$ reaction rate in EC3B experimental channel using the D-T neutron source pulse in YALINA-Booster configuration with 36% enriched uranium fuel and 1185 EK10 fuel rods in the thermal zone (Courtesy of the Argonne National Laboratory, USA).

2.4. YALINA-BOOSTER CONFIGURATIONS WITH 21%-ENRICHED URANIUM FUEL

In this YALINA-Booster configuration, the fast zone has 21% enriched uranium and the thermal zone has 1185 EK10 fuel rods. This configuration was the second step for converting YALINA-Booster facility to use 21% enriched uranium fuel instead of 90% enriched uranium fuel. The number of EK10 fuel rods in the thermal zone did not change when the uranium enrichment of the fast zone changed from 36% to 21%.

2.4.1. Kinetic parameters of the YALINA-Booster configuration with 1185 fuel rods in the thermal zone

Only China and the USA examined the YALINA-Booster Configurations with 21% enriched uranium fuel using Monte Carlo simulations. The kinetic parameters are listed in Table 2.2. The results obtained by China and the USA for the effective and the prompt multiplication factors are in good agreement. Reducing the fuel enrichment in the fast zone from 36% to 21% reduces the neutron multiplication. The delayed neutron fraction calculated by the USA is lower than the one calculated by China because it is based on the ENDF/B-VII.0 nuclear data files instead of ENDF/B-VI, as used by the Chinese. The 14 μ s difference in the prompt neutron lifetime is due to the different methodologies for calculating the effective prompt neutron lifetime.

TABLE 2.2. KINETIC PARAMETERS FOR THE YALINA-BOOSTER ASSEMBLY LOADED WITH 21% ENRICHED FUEL

Member State	k_{eff}	k_{pro}	β_{eff} [pcm]	l_p [μ s]
China	0.96466 ± 4	0.95725 ± 4	768	74
USA MCNP	0.96404 ± 4	0.95709	721 ± 1.4	60 ± 0.7

2.4.2. Reaction rates of the YALINA-Booster configuration with 1185 fuel rods in the thermal zone

The spatial distributions of the $^3\text{He}(n,p)$ and the $^{235}\text{U}(n,f)$ reaction rates in the EC2B and EC6T experimental channels are illustrated in Figs 2.56–2.57. There is quite a good match between the results obtained by China and the USA. These reaction-rate values are lower than the values obtained in the YALINA-Booster configuration with the 36% enriched fuel in the fast zone. It is due to the lower neutron multiplication of the YALINA-Booster configuration with 21% enriched uranium fuel.

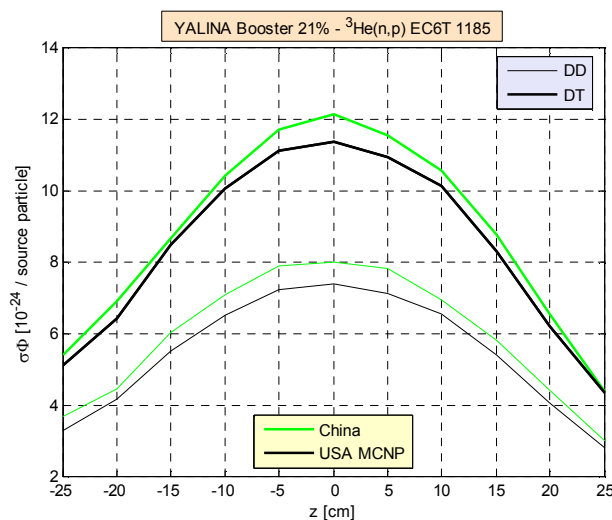


FIG. 2.56. $^3\text{He}(n,p)$ reaction rate in EC6T experimental channel in YALINA-Booster configuration with 21% enriched uranium fuel (Courtesy of the Argonne National Laboratory, USA).

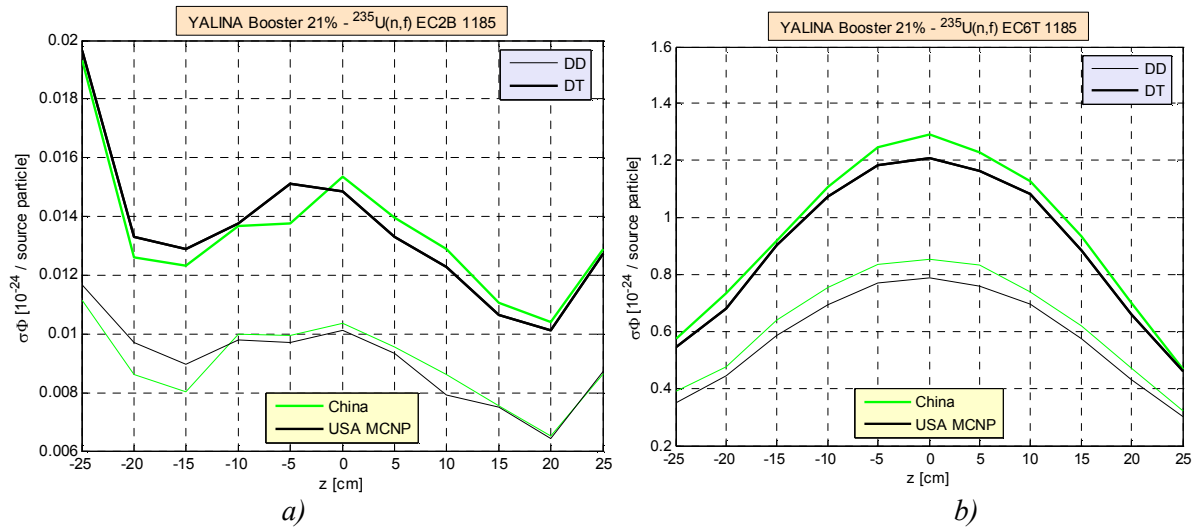


FIG. 2.57. $^{235}\text{U}(n,f)$ reaction rate in EC2B (a) and EC6T (b) experimental channels in YALINA-Booster configuration with 21% enriched uranium fuel (Courtesy of the Argonne National Laboratory, USA).

2.4.3. Reaction rates from D-D and D-T neutron pulses of the YALINA-Booster configuration with 1185 fuel rods in the thermal zone

The time dependent $^3\text{He}(n,p)$ and $^{235}\text{U}(n,f)$ reaction rates for the YALINA-Booster configuration, with 21% enriched fuel in the fast zone and 1185 EK10 fuel rods in the thermal zone, are shown in Figs 2.58–2.62. The results are very similar to those obtained for the 1141 configuration of Section 2.2.4. However, the 21% enriched fuel results reach the asymptotic level, set by delayed neutrons, after 13 ms. The latter value is higher than the 8 ms value obtained for the YALINA-Booster configuration with 90% enriched uranium in the fast zone and 902 EK10 fuel rods in the thermal zone discussed in Section 2.2.8. The higher effective multiplication factor of the YALINA-Booster with 21% enriched uranium fuel is the main reason for the extra time for the reaction rates to reach the asymptotic level.

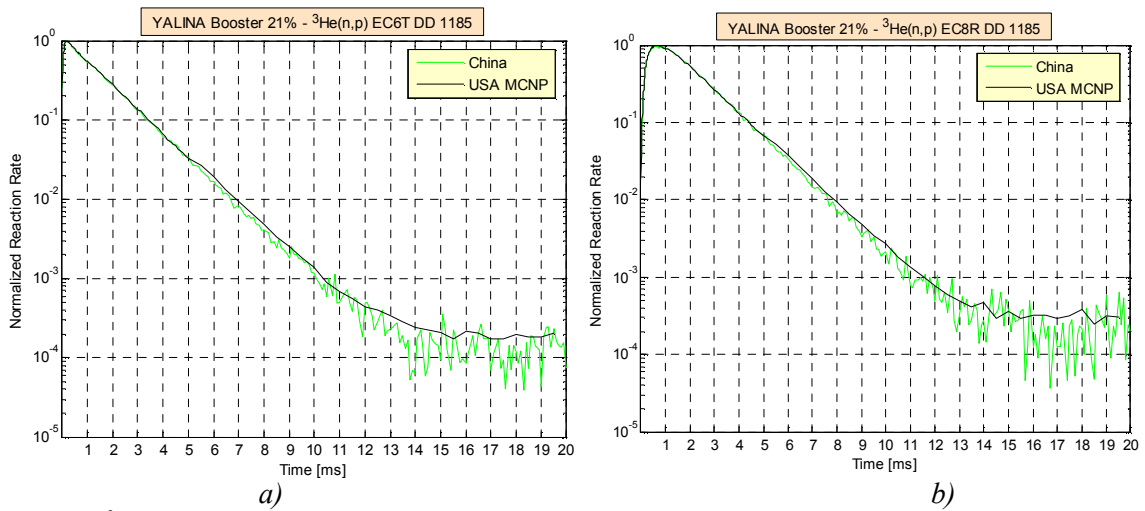


FIG. 2.58. ${}^3\text{He}(n,p)$ reaction rate in EC6T (a) and EC8R (b) experimental channels using the D-D neutron source pulse in YALINA-Booster configuration with 21% enriched uranium fuel (Courtesy of the Argonne National Laboratory, USA).

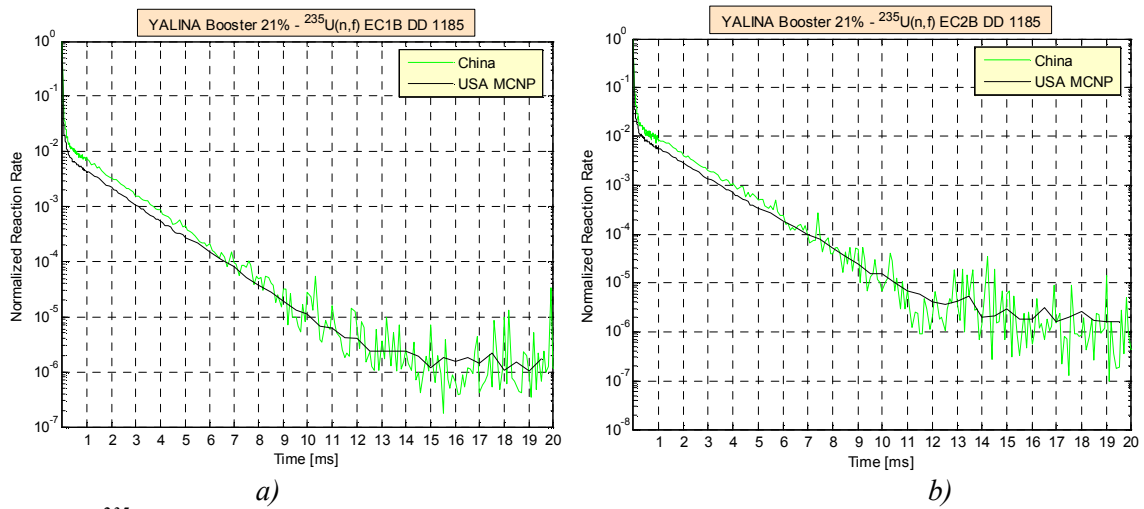
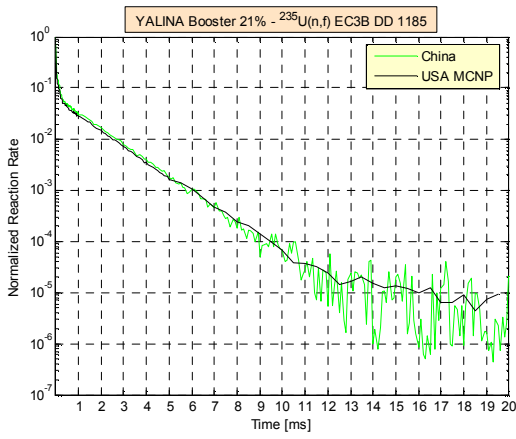
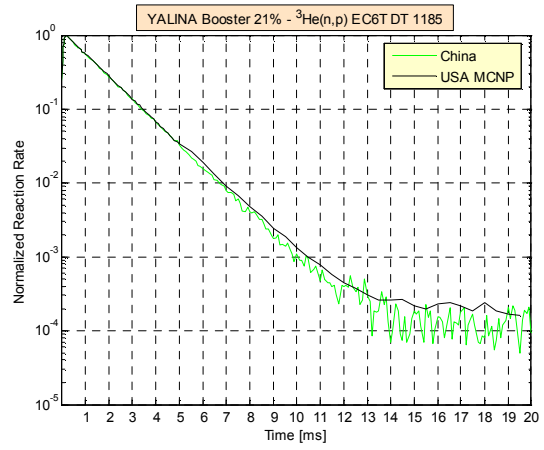


FIG. 2.59. ${}^{235}\text{U}(n,f)$ reaction rate in EC1B (a) and EC2B (b) experimental channels using the D-D neutron source pulse in YALINA-Booster configuration with 21% enriched uranium fuel (Courtesy of the Argonne National Laboratory, USA).

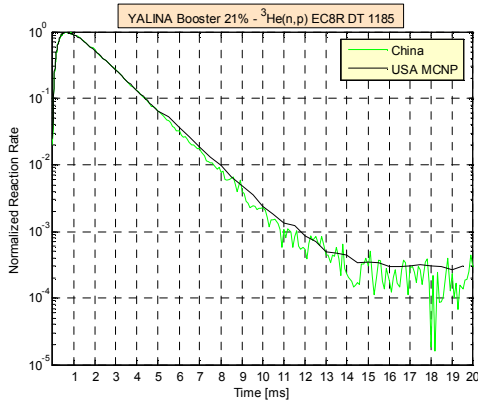


a)

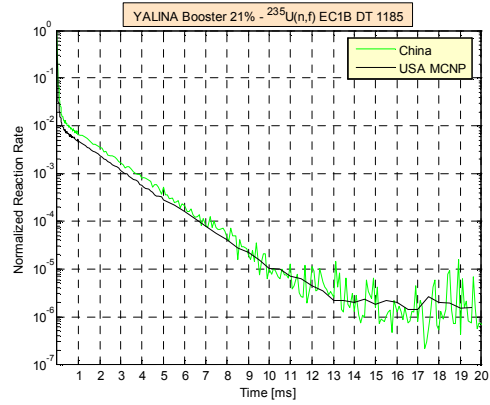


b)

FIG. 2.60. $^{235}\text{U}(n,f)$ reaction rate in EC3B experimental channel using the D-D neutron source pulse (a) and $^3\text{He}(n,p)$ reaction rate in EC6T experimental channels using the D-T neutron source pulse (b) in YALINA-Booster configuration with 21% enriched uranium fuel (Courtesy of the Argonne National Laboratory, USA).



a)



b)

FIG. 2.61. $^3\text{He}(n,p)$ reaction rate in EC8R experimental channel (a) and $^{235}\text{U}(n,f)$ reaction rate in EC1B (b) experimental channel using the D-T neutron source pulse in YALINA-Booster configuration with 21% enriched uranium fuel (Courtesy of the Argonne National Laboratory, USA).

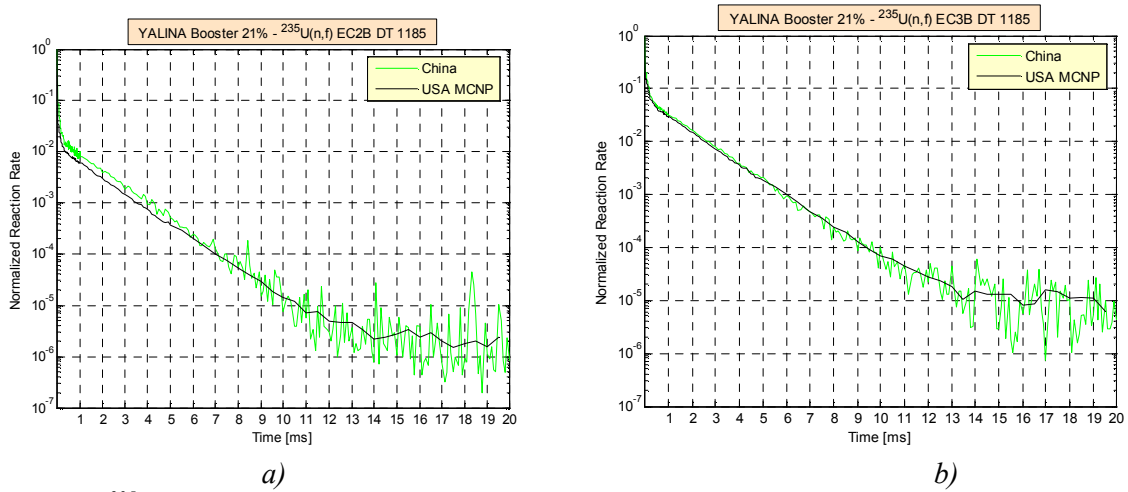


FIG. 2.62. $^{235}\text{U}(n,f)$ reaction rate in EC2B (a) and EC3B (b) experimental channels using the D-T neutron source pulse in YALINA-Booster configuration with 21% enriched uranium fuel (Courtesy of the Argonne National Laboratory, USA).

2.5. COMPARISON OF COMPUTATIONAL AND EXPERIMENTAL RESULTS

2.5.1. YALINA-Booster configuration with 90% enriched uranium fuel in the fast zone

The dynamic and static correction factors calculated by MCNPX for the experimental channels in the YALINA Booster assembly are shown in Fig. 2.63 for the 90% enriched fuel configuration with D-D and D-T neutron sources [2.10–2.11]. The term ‘correction factor’ is normally introduced to account for the detector’s position. The correction factor is referred to as the *dynamic* correction factor when a time dependant neutron source simulation is required. Otherwise, when the calculations are done with the time independent source, the correction factor is referred to as *static*.

For this TECDOC the static correction factors were calculated using the MCNPX code. No detector geometry modelling was performed. The reaction rates were tallied without the variance reduction techniques for a cylindrical volume with 25 cm length and the experimental channel radius. The dynamic correction factors of the D-T source for the EC1B, EC2B, and EC3B experimental channels were calculated using techniques such as the space-energy weight window and the delayed-neutrons bias variance reduction. Furthermore, ^3He detectors of 1 cm length and 0.45 cm radius were inserted simultaneously into each of the three experimental channels. The dynamic correction factors calculations of the D-D source for the experimental channels of the thermal zone were performed with the delayed-neutron bias variance reduction technique. No detector geometry modelling was performed. The mean reaction rate was calculated over a model of a cylindrical volume with 20 cm length and 1.2 cm radius for the experimental channels of the thermal zone. The dynamic correction factors calculations of the D-D source for the EC8R experimental channel were performed with the space weight window and delayed-neutrons bias variance reduction techniques. Furthermore, ^3He detectors of 25 cm length and 0.45 cm radius were inserted simultaneously into each of the two experimental channels EC6T and EC8R [2.10].

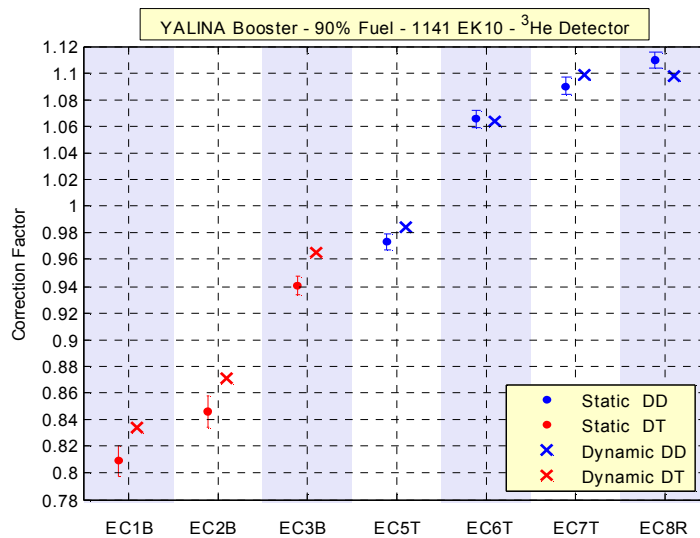


FIG. 2.63. The dynamic and the static spatial correction factors calculated by MCNPX using the D-D and D-T neutron sources and ^3He detector in the different experimental channels of YALINA-Booster configuration with 90% enriched uranium and 1141 EK10 fuel rods in the thermal zone, the vertical ticks for the static correction factors indicate the statistical error for one standard deviation (Reproduced from Ref. [2.10] with permission courtesy of the Argonne National Laboratory, USA).

The results are in a good correspondence between the static and the dynamic correction factors. The difference between the two factors occurs when the $^3\text{He}(n,p)$ reaction rate has a large statistical error. This occurs in the fast zone where the reaction-rate values are small. Figure 2.64 shows the results of uncorrected and the corrected effective neutron multiplication factors obtained from the experimental measurements. The technical part of experimental measurements is described in Table II of Ref. [2.11]. The average multiplication factor of the corrected experimental values is 450 pcm lower than the k_{eff} calculated by MCNPX [2.10]. But in the MCNPX model, neither ^{234}U nor the impurities in the fuel were considered, while these impurities are very important the EK10 fuel of the assembly's thermal zone because of large cross-section for thermal neutrons. The experimental and numerical multiplication factors appear to be in a good correspondence after including the fuel compositions in numerical parameters, as shown in Table III of Ref. [2.11]. The dead-time correction lowers the experimental multiplication factor values. The MCNPX results obtained in criticality mode slightly overestimates the experimental results because graphite and polyethylene impurities have not been taken into account in the numerical model. Graphite and polyethylene are the only materials of the YALINA Booster subcritical assembly which have not been examined for impurities content. All the MCNPX simulations of this section have been performed using the ENDF/B-VI.6 nuclear data library.

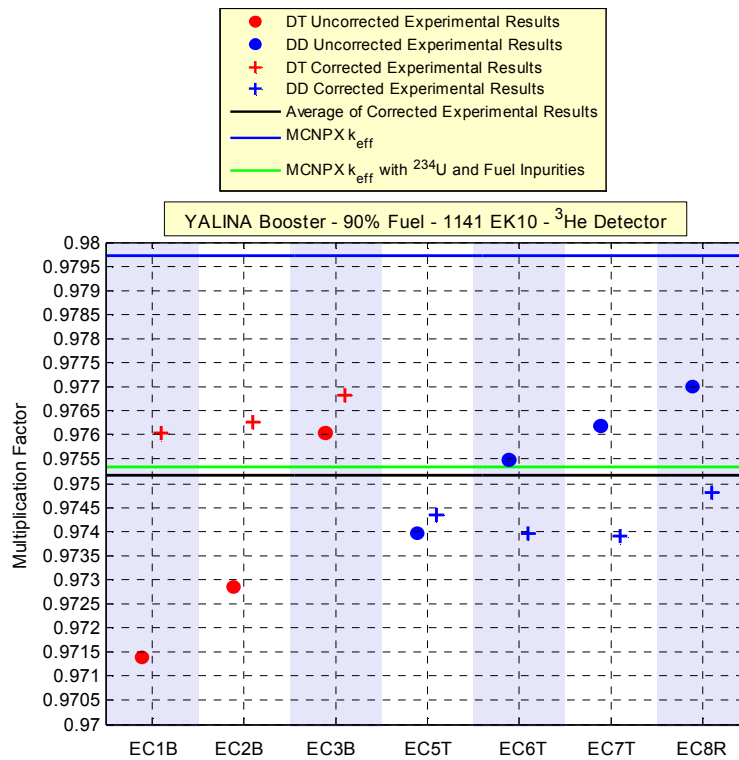


FIG. 2.64. The uncorrected and the corrected experimental effective neutron multiplication factors using the dynamic correction factor, and the calculated MCNPX neutron multiplication factor for YALINA-Booster configuration with 90% enriched uranium and 1141 EK10 fuel rods in the thermal zone (Reproduced from Ref. [2.10] with permission courtesy of the Argonne National Laboratory, USA).

2.5.2. YALINA-Booster configuration with 36% enriched uranium fuel in the fast zone

Figures 2.65 and 2.66 show the static correction factors for D-D and D-T neutron sources for the case, when the fast zone of the assembly is loaded with 36% enriched fuel [2.10–2.11]. The dynamic correction factor has been calculated for the D-D neutron source in the EC5T and EC6T experimental channels using the space weight window and delayed-neutrons bias variance reduction techniques. In these calculations, two long detectors were inserted into EC5T and EC6T experimental channels at the same time, and five detector reactions were examined: $^{238}\text{U}(n,f)$, $^{237}\text{Np}(n,f)$, $^{235}\text{U}(n,f)$, $^3\text{He}(n,p)$, and $^{10}\text{B}(n,\alpha)$. The correction factor based on the neutron flux implies the detector scores the neutron flux instead of the reaction rate, which is impossible to do experimentally. $^{238}\text{U}(n,f)$ and $^{237}\text{Np}(n,f)$ score fast neutron reactions above 2 MeV and 0.5 MeV, respectively. $^3\text{He}(n,p)$, and $^{10}\text{B}(n,\alpha)$, $^{235}\text{U}(n,f)$, scores neutrons mainly in the thermal energy range. Consequently, the correction factor increases with the decrease of the average scoring energy of the detector reaction. The effect of the detector material is amplified in the fast experimental channels near the external source because more source neutron reactions are scored. The results show, that ‘the correction factors for the D-T neutrons are similar to those for the D-D neutrons’ [2.10], and the dynamic correction factors are in good agreement with the static ones.

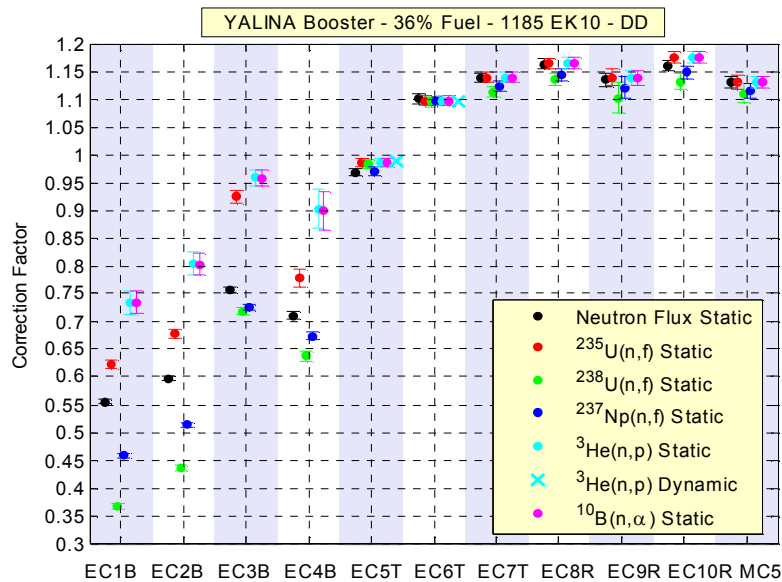


FIG. 2.65. The dynamic and the static spatial correction factors calculated by MCNPX using the D-D neutron source for the different experimental channels of YALINA-Booster configuration with 36% enriched uranium and 1141 EK10 fuel rods in the thermal zone, the vertical ticks for the static correction factors indicate the statistical error for one standard deviation (Reproduced from Ref. [2.10] with permission courtesy of the Argonne National Laboratory, USA).

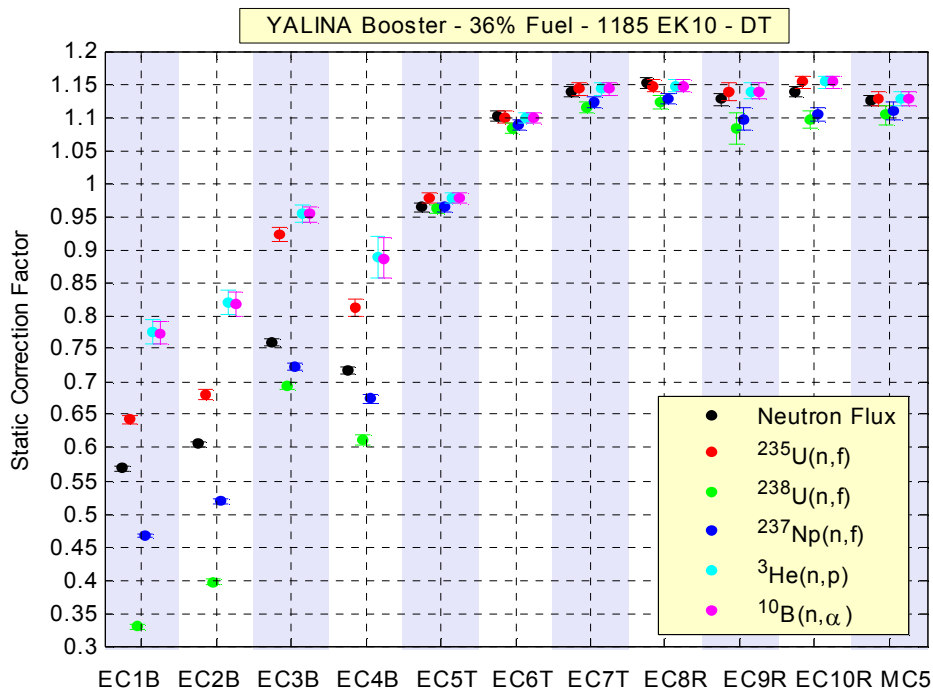


FIG. 2.66. The static spatial correction factors calculated by MCNPX using the D-T neutron source for the different experimental channels of YALINA-Booster configuration with 36% enriched uranium and 1141 EK10 fuel rods in the thermal zone, the vertical ticks for the static correction factors indicate the statistical error for one standard deviation (Reproduced from Ref. [2.10] with permission courtesy of the Argonne National Laboratory, USA).

The experimental measurements have been performed with two long ^3He detectors inserted at the same time in the subcritical assembly. Table II of Ref. [2.11] represents the

technical part of experiments that were performed using the D-D neutron source with 5 μ s duration and 20 ms period.

The average experimental multiplication factor using the static correction factor is 725 pcm lower than the value obtained from the MCNPX simulation, as shown in Fig. 2.70. The experimental measurements used three detectors at the same time, as listed in Table II of Ref. [2.11]. By including in the simulation the impurities (i.e. ^{234}U) in the EK10 fuel rod composition according to the Table III of Ref. [2.11], the differences between MCNPX multiplication factors and average experimental multiplication factors decrease to 250 pcm, and detector dead-time correction decreases k_{eff} by 100 pcm [2.10, 2.12, 2.13]. The dead-time correction is important for long detectors placed in the thermal region, as shown in Fig. 2.67. Again, the MCNPX multiplication factor calculation does not account for the graphite and the polyethylene impurities, which results in a slight increase in the obtained value. The MCNPX simulations for k_{eff} and static correction factors have been performed using the ENDF/B-VII.0 nuclear data library. The MCNPX simulations for k_{eff} , with the ^{234}U isotope and EK10 fuel impurities and the dynamic correction factors, have been performed with the ENDF/B-VI.6 nuclear data library.

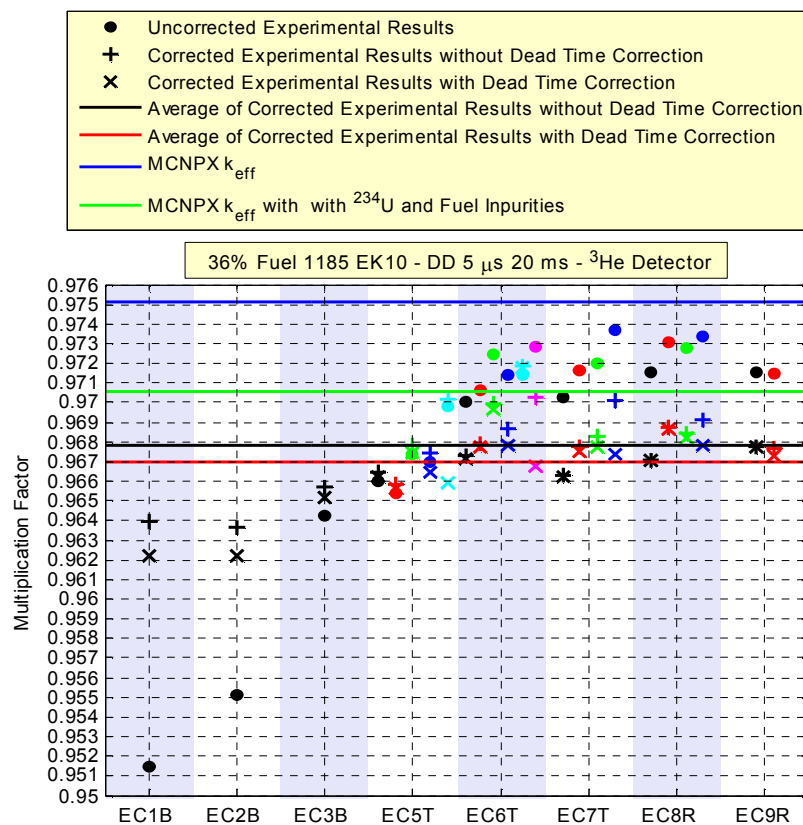


FIG. 2.67. The uncorrected and the corrected experimental effective neutron multiplication factors using the static correction factor, and the calculated MCNPX neutron multiplication factor for YALINA-Booster configuration with 36% enriched uranium and 1141 EK10 fuel rods in the thermal zone, the colours of the experimental data in each channel match the colours listed in Table II of Ref. [2.11] (Reproduced from Ref. [2.10] with permission courtesy of the Argonne National Laboratory, USA).

The MCNPX calculations results and the experimental measurements of the reaction rates in EC5T and EC6T experimental channels with long ^3He detectors are in a good correspondence, as shown in Fig 2.68 and 2.69. Two detectors have been inserted in the channels simultaneously, as demonstrated in the first row of Table II of Ref. [2.11] for the 36% enriched fuel. For these simulations the following methods were used [2.9–2.10]:

- the ENDF/B-VI.6 nuclear data library;
- space weight window and delayed neutron bias variance reduction techniques;
- long ^3He detector model; and
- a C program to superimpose the pulses.

For the detector material simulation in MCNP, a mixture with 80% (atomic fraction) ^3He and 20% natural Kr of 8.143 mg/cm^3 density was modelled. The results have been normalized to their maximum values. Two long detectors inserted in experimental channels EC5T and EC6T result in a decrease of the multiplication factor from $0.975\ 10 \pm 8$ down to $0.973\ 44 \pm 8$ [2.10].

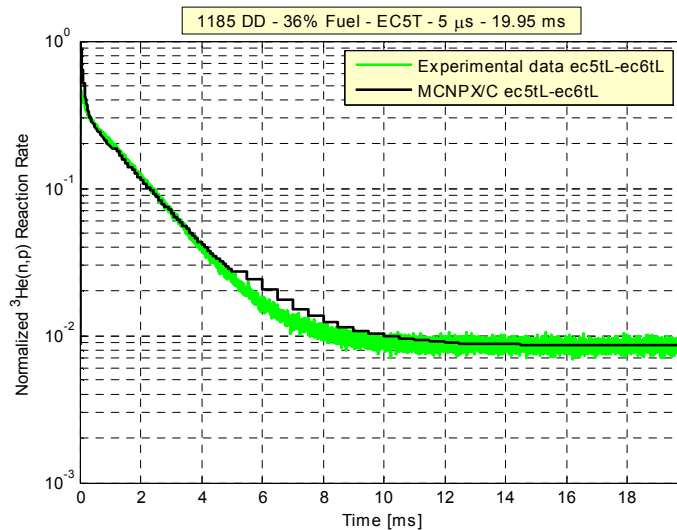


FIG. 2.68. Normalized $^3\text{He}(n,p)$ reaction rate in EC5T experimental channels using the D-D neutron source pulse and long ^3He detector ($L=25\text{ cm}$) in YALINA-Booster configuration with 36% enriched uranium fuel (Courtesy of the Argonne National Laboratory, USA).

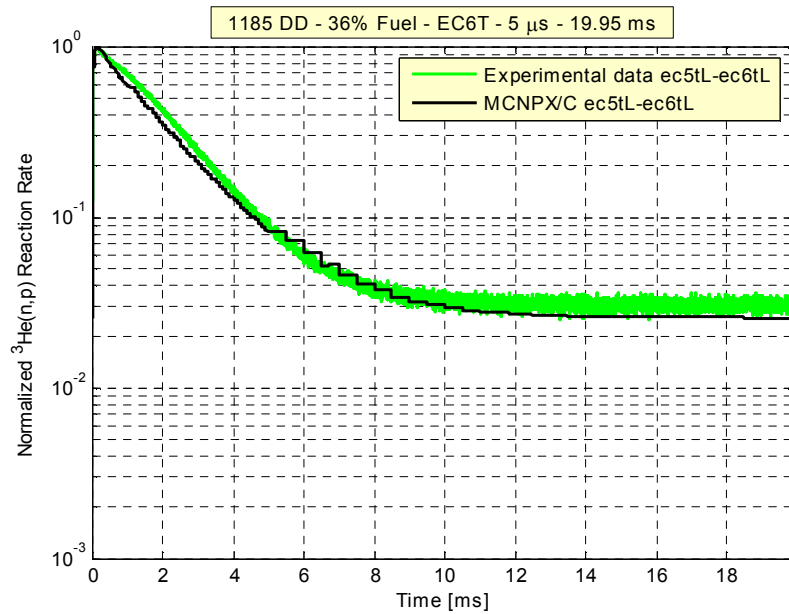


FIG. 2.69. Normalized ^3He (n,p) reaction rate in EC6T experimental channels using the D-D neutron source pulse and long ^3He detector ($L=25$ cm) in YALINA-Booster configuration with 36% enriched uranium fuel (Courtesy of the Argonne National Laboratory, USA).

2.5.3. YALINA-Booster configuration with 21% enriched uranium fuel in the fast zone

The static and dynamic correction factors for the D-D neutron sources are shown in Fig. 2.70, when the assembly is loaded with 21% enriched uranium fuel in the fast zone [2.11]. The static correction factor computational methodology followed the one described for the 90% and 36% enriched fuel configurations. The dynamic correction factor has been calculated with delayed-neutron bias variance reduction technique without modelling the detectors. The tallying volume is a cylindrical volume with 20 cm length and the experimental channel radius. The correction factors are similar to the ones calculated for the other fuel configurations.

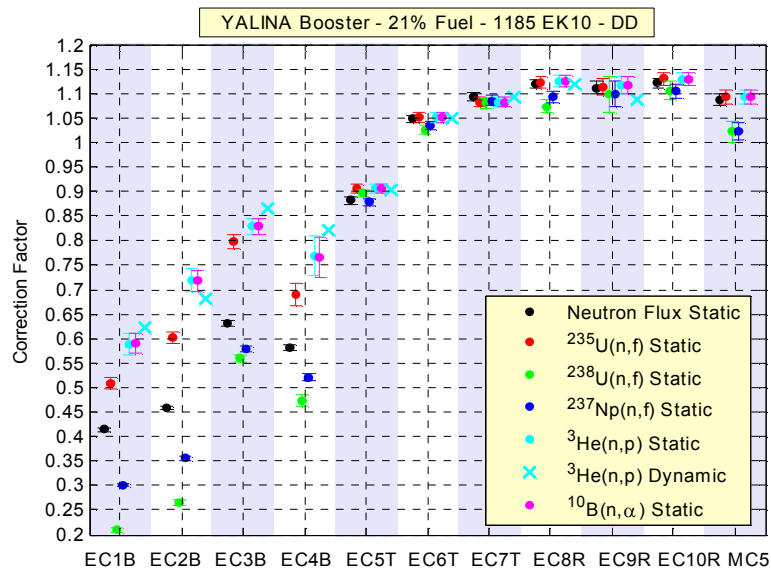


FIG. 2.70. The static spatial correction factors calculated by MCNPX using the D-D neutron source for the different experimental channels of YALINA-Booster configuration with 21% enriched uranium and 1141 EK10 fuel rods in the thermal zone, the vertical ticks for the static correction factors indicate the statistical error for one standard deviation (Reproduced from Ref. [2.10] with permission courtesy of the Argonne National Laboratory, USA).

Figure 2.71 shows that the use of the static correction for average experimental multiplication factor results in a 675 pcm value lower than the value obtained from the MCNPX simulation [2.10]. In these experiments two detectors were inserted in the assembly channels at the same time and a D-D pulsed neutron source with 5 μ s duration and 20 ms period was used. The technical part of the experiment is described in Table II of Ref. [2.11]. If the EK10 fuel composition includes the ^{234}U isotope and impurities, then the difference between the average experimental multiplication factor and the MCNPX criticality multiplication factor decreases to 260 pcm. The dead-time correction for the experimental results diminishes the experimental k_{eff} by 200 pcm [2.12–2.13]. Similar to the other configurations, the graphite and polyethylene impurities are not included in the calculations, which results in a slight over estimate for the MCNPX-calculated neutron multiplication factor.

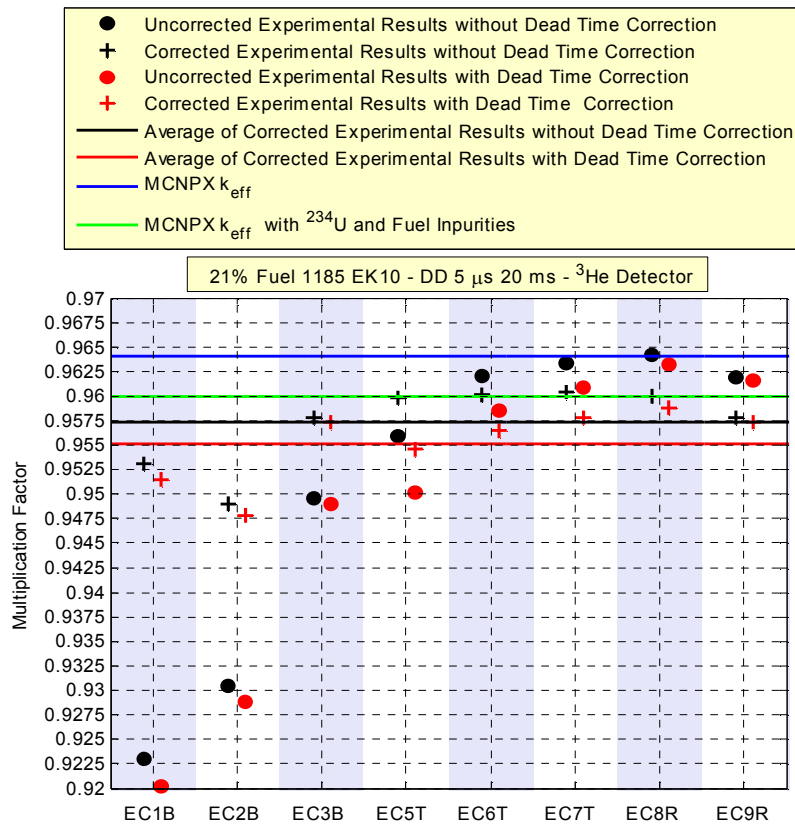


FIG. 2.71. The uncorrected and the corrected experimental effective neutron multiplication factors using the static correction factor, and the calculated MCNPX neutron multiplication factor for YALINA-Booster configuration with 21% enriched uranium and 1185 EK10 fuel rods in the thermal zone; the experimental reactivity has been corrected by the static correction factor (Reproduced from Ref. [2.10] with permission courtesy of the Argonne National Laboratory, USA).

2.5.4. Conclusions

The IAEA coordinated research project on the YALINA Booster facility was carried out successfully, and this project enhanced the physics understanding of the accelerator driven systems. In particular, the analyses of such systems, to define their performance, were greatly improved. The participating Member States used both Monte Carlo and deterministic computational tools for their analyses, including MCNP5, MCNPX, McCARD, and ERANOS computer programs. All the calculations utilized ENDF/B-VI (different modes) nuclear data library, except for the Korean simulations, and some of the USA analyses used the ENDF/B-VII.0 nuclear data libraries. Generally, there is good agreement between the results obtained by all the Member States. The USA deterministic analyses required space, energy, and angle discretization, and materials homogenizations, which introduced major approximations because of the severe heterogeneity of the YALINA-Booster geometry. Another challenge for the deterministic model is the presentation of thin absorber layers between the different zones. Such issues affected the accuracy of the USA ERANOS results.

The 90% enriched uranium fuel in the fast zone of YALINA-Booster facility was replaced with 21% enriched uranium fuel without affecting the facility performance. Additional EK10 fuel rods were added in the facility thermal zone to maintain the facility subcriticality level. In the YALINA-Booster facility, decreasing the fuel enrichment reduces the difference between the effective and the source multiplication factors. This difference becomes negligible when the 21% enriched uranium fuel is used for the californium and D-D

neutron sources. The neutron leakage from the YALINA Booster facility did not change when the uranium fuel enrichment was reduced in the fast zone around the external neutron source. The large assembly size, and locating the external neutron source at the assembly centre, reduces the neutron leakage.

In YALINA-Booster configurations with low effective multiplication factor, i.e. YALINA-Booster configuration with 902 EK10 fuel rods in the thermal zone, the time dependent reaction rates from a single D-D or D-T neutron pulse reach an asymptotic value produced by the delayed neutrons.

For the YALINA Booster assembly, the comparison between analytical and experimental neutron multiplication factor values exhibits differences of 450, 700, and 650 pcm for the 90%-, 36%-, and 21%-enriched uranium fuel configurations, respectively. However, when the ^{234}U isotope concentration, EK10 fuel impurities, and the detector dead time are taken into account, the previous differences diminish to less than 50, 350, and 350 pcm, respectively.

REFERENCES TO SECTION 2

- [2.1] GOHAR, Y. and SMITH, D.L., YALINA, Facility, A Sub-Critical Accelerator-Driven System (ADS) for Nuclear Energy Research. Facility Description and Overview of the Research Program, Argonne National Laboratory, ANL-10/05, 2010.
- [2.2] MCNP Team, MCNP5.1.40, Los Alamos National Laboratory, LA-UR-05-8617, 2005.
- [2.3] SHIM, H.J. and KIM, C.H., Error Propagation Module Implemented in the MC-CARD Monte Carlo Code, Trans. Am. Nucl. Soc. 86, 2002.
- [2.4] PELOWITZ, D.B. et al., MCNPX 2.7a Extensions, Los Alamos National Laboratory, LA-UR-08-7182, 2008.
- [2.5] RIMPAULT, G. et al., The ERANOS Code and Data System for Fast Reactor Neutronic Analyses, Proc. Int. Conf. PHYSOR 2002, Seoul, Korea, 2002.
- [2.6] LOS-ALAMOS NATIONAL LABORATORY, T-2 Nuclear Information Service, US ENDF/B Libraries, <http://t2.lanl.gov/data/data.html>.
- [2.7] ALIBERTI, G., and GOHAR, Y., YALINA Analytical Benchmark Analyses Using the Deterministic ERANOS Code System, Argonne National Laboratory, ANL-09/23, 2009. (www.osti.gov/bridge).
- [2.8] TALAMO, A. and GOHAR, Y., Monte Carlo Modeling and Analyses of the YALINA-Booster – Part I: Analytical Models and Main Neutronics Parameters, Argonne National Laboratory, ANL-NE-08/13, 2008.
- [2.9] TALAMO, A. and GOHAR, Y., Monte Carlo Modeling and Analyses of the YALINA-Booster – Part II: Pulsed Neutron Source, Argonne National Laboratory, ANL-08/33, 2008.
- [2.10] TALAMO, A. and GOHAR, Y., Monte Carlo Modeling and Analyses of the YALINA-Booster – Part III: Low Enriched Uranium Conversion Analyses, Argonne National Laboratory, ANL-11/03, 2011.
- [2.11] TALAMO, A. Y. Gohar, Y. Cao, et al., Impact of the Neutron Detector Choice on Bell and Glasstone Spatial Correction Factor for Subcriticality Measurement, Nuclear Instruments and Methods in Physics Research **668** (2012) 71-82.
- [2.12] ARGONNE NATIONAL LABORATORY, YALINA-Booster Subcritical Assembly Pulsed-Neutron Experiments: Data Processing and Spatial Corrections, Rep. ANL-10/22, Argonne Natl Lab., IL (2010).
- [2.13] ARGONNE NATIONAL LABORATORY, YALINA-Booster Subcritical Assembly Pulsed-Neutron Experiments: Detector Dead Time and Spatial Corrections, Rep. ANL-10/31, Argonne Natl Lab., IL (2010).

3. YALINA-THERMAL FACILITY EXPERIMENTS¹

Contributed by

H. Kiyavitskaya, V. Bournos, Y. Fokov, C. Routkovskaya, S. Sadovich
*Joint Institute for Power and Nuclear Research – Sosny,
National Academy of Sciences of Belarus, Minsk,
Belarus*

A. Cintas, J.I. Márquez Damián, E.M. Lopasso
*División Física de Reactores Avanzados
Unidad de Energía Nuclear (CNEA) - Instituto Balseiro, Bariloche,
Argentina*

J.R. Maiorino, T. Carluccio, P.C.R. Rossi, A. Antunes, F.L. de Oliveira and S.M. Lee.
*Nuclear Technology Post Graduate School
Instituto de Pesquisas Energeticas e Nucleares – Universidade de Sao Paulo(IPEN-USP), Sao Paulo,
Brazil*

P. Xia, Y. Shi, H. Xia, Q. Zhu, T. Yu, X. Wu, W. Zhang, J. Cao, H. Luo, Y. Quan
China Institute of Atomic Energy, Beijing, China

K. Kulkarni, R.D.S. Yadav, A. Bajpai, S.B. Degweker, R.S. Modak
*Bhabha Atomic Research Centre, Trombay, Mumbai,
India*

H.J. Park, H.J. Shim, C.H. Kim
*Nuclear Engineering Department, Seoul National University,
Republic of Korea*

A. Wojciechowski, M. Zuta
*Institute of Atomic Energy, Otwock-Swierk,
Poland*

M. Pešić, I. Avramović, P. Beličev
*Vinca Institute of Nuclear Sciences, Belgrade,
Serbia*

Y. Gohar, A. Talamo, G. Aliberti,
*Argonne National Laboratory,
USA*

3.1. INTRODUCTION

YALINA-Thermal is a zero-power subcritical assembly driven by a high-intensity neutron generator [3.1]. It has a single fuel zone using a polyethylene matrix with graphite reflector. This configuration produces a thermal neutron spectrum in the assembly. The overall layout of YALINA, the external neutron sources and other general characteristics of the facility have already been described in Ref. [3.1]. The present Section focuses on details

¹ This section is based on Ref. [3.1]

of the YALINA-Thermal assembly design that correspond exclusively to the presentation of results of the experiments and corresponding modelling conducted, as well as to the conclusions drawn from this research.

3.2. FACILITY DETAILS

The shape and geometrical dimensions of the YALINA critical assembly are described in Ref. [3.1]:

“The core is a rectangular parallelepiped 40.0-cm wide, 40.0-cm long, and 57.0-cm high. It is assembled from polyethylene blocks with channels to place the fuel pins. The core has a square lattice with 2.0-cm pitch. The central part of the sub-critical assembly is a neutron producing lead target with dimensions 7.8 cm by 7.8 cm and total length of 57.6 cm formed from 12 blocks that can be slipped into a square cross-section cavity, with 8.0 cm by 8.0 cm dimensions, centered on the axis.”

If neutrons are generated by deuteron beam, the cavity is partly occupied by the beam tube. There are four channels, 55 mm diameter each, located at the assembly's boundaries, and three channels, 25 mm diameter each, at radii of 5, 10, and 16 cm from the central axis of the assembly, in which can be placed different types of samples or neutron flux monitoring detectors. The reflector surrounds the fuel zone and consists of two layers: 40.0 cm of high-purity graphite and 1.5 mm of cadmium [3.1]. Two axial and one radial experimental channels of 25.0 cm diameter are located in the graphite reflector. The assembly core is fuelled with UO₂ fuel rods mixture with a small amount of MgO. The EK10 fuel rods are enriched to 10% of ²³⁵U [3.1]. A three-dimensional cutaway diagram of the YALINA-Thermal with main components is represented in Fig. 3.1. A detailed diagram of the polyethylene matrix with locations for measurement equipment and channels for fuel pins is represented in Fig. 3.2.

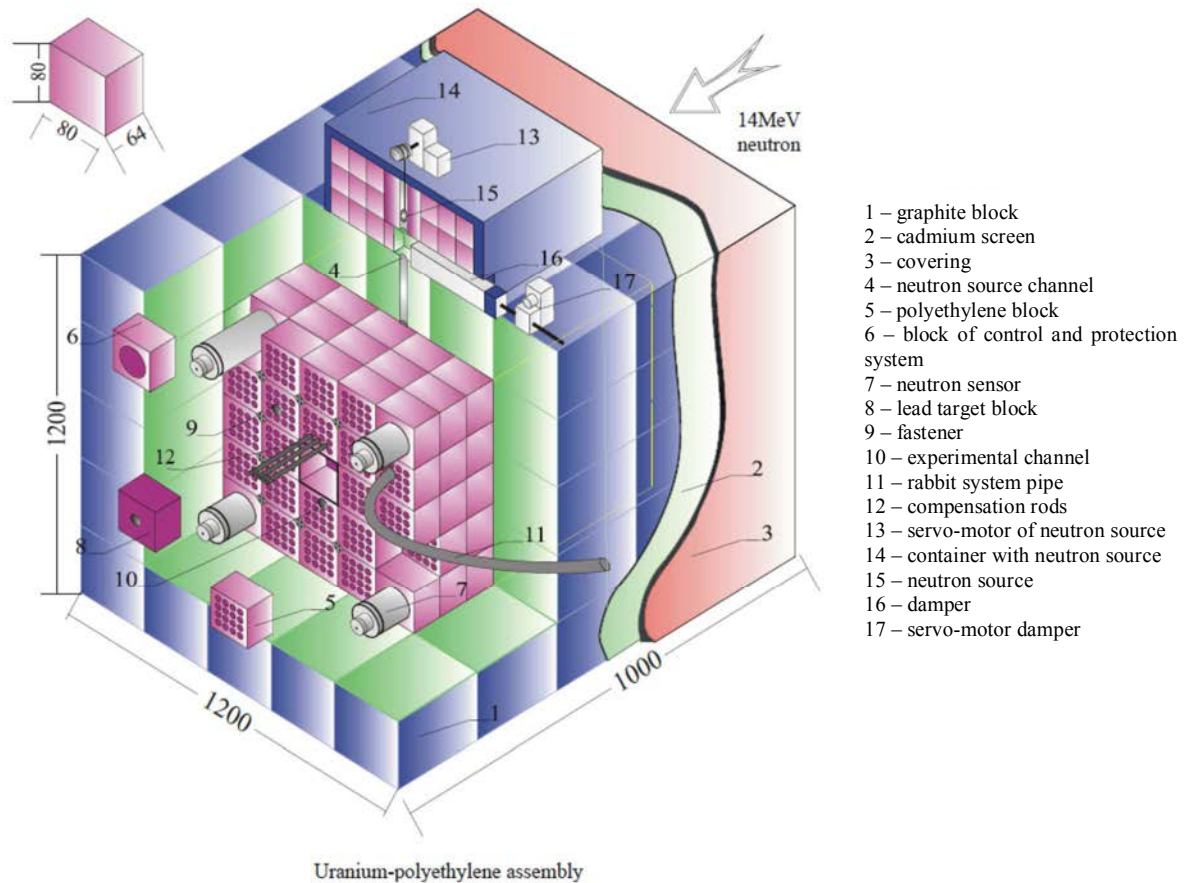
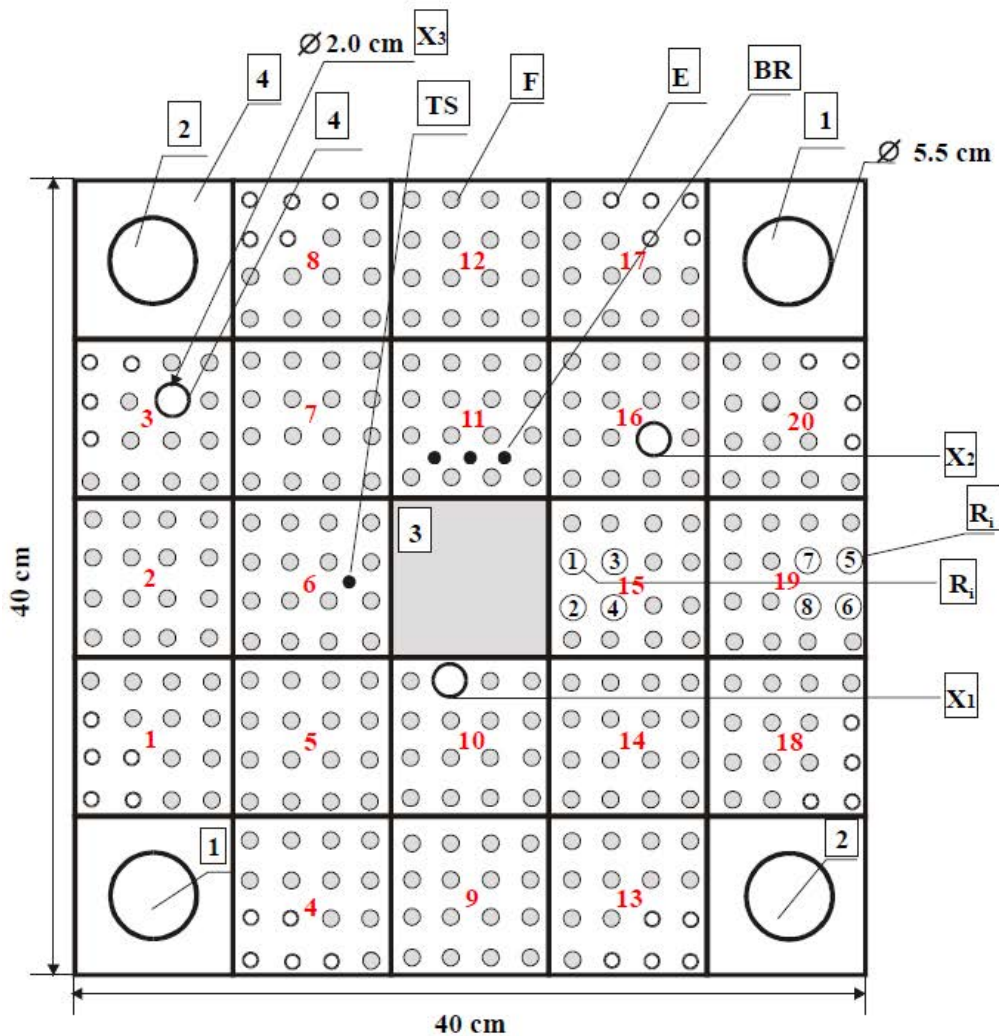


FIG. 3.1. Three-dimensional cutaway view of the YALINA-Thermal subcritical assembly. Dimensions are given in mm (Reproduced from [3.1] with permission courtesy of the Argonne National Laboratory, USA).



1	Detector SNM-11	X_i	Experimental channel
2	Detector KNK-56	R_i	Central and peripheral fuel rods removed for reactivity change calculations
3	Lead	TS	Temperature sensor
4	Polyethylene	BR	B₄C rods
F	Channel with a fuel rod		
E	Empty channel (filled with air)		

FIG. 3.2. Cross-section view of the YALINA-Thermal subcritical assembly (Reproduced from [3.1] with permission courtesy of the Argonne National Laboratory, USA).

The design of the facility provides capacity to maintain $k_{eff} < 0.98$ with different fuel loading configurations. This is still the case even for the worst accident scenario, either internal or external, e.g. structural failure of the fuel matrix or flooding of the assembly and its surroundings with water [3.1]. In YALINA-Thermal research collaboration participants performed a benchmark activity for the core configurations with 216, 245, and 280 EK10 fuel rods to compare the calculation and experimental results. The total loads of ^{235}U are equal to

1.67, 1.89, and 2.16 kg for each of the configurations. A full description of the benchmark technical data needed for system modelling is in Ref. [3.1]

In Fig. 3.2 the central region is a lead block with dimensions 8×8×60 cm, which has common axes with the core and the accelerator beam. A side view of this arrangement is shown in Fig. 3.3.

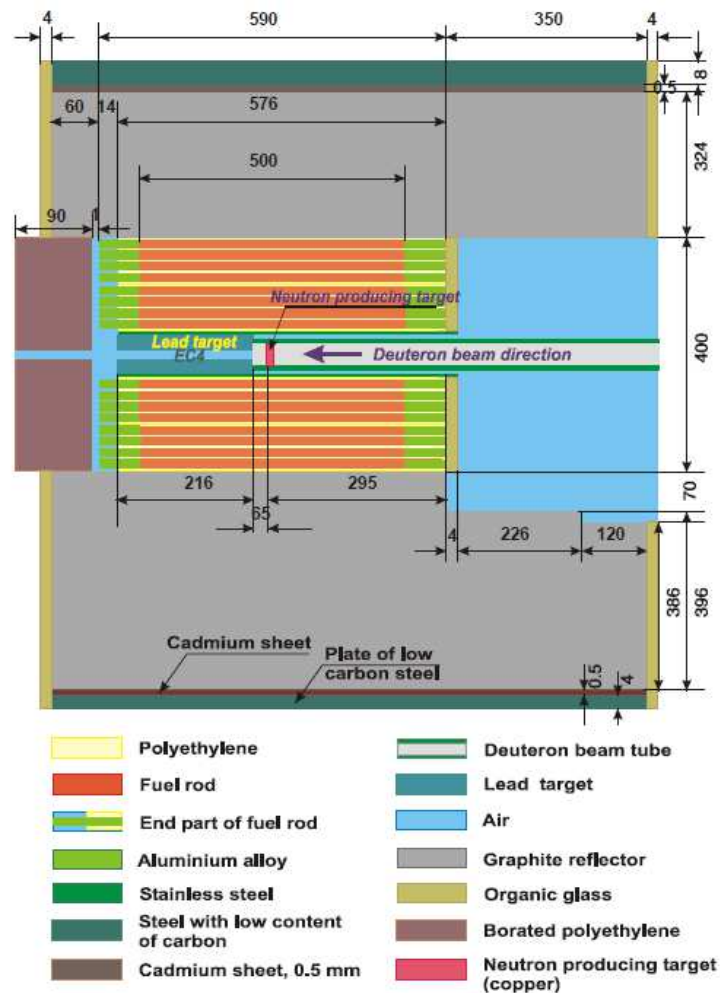


FIG. 3.3. YALINA-Thermal subcritical assembly dimensions (mm) (Courtesy of the Joint Institute for Power and Nuclear Research – Sosny, National Academy of Sciences of Belarus).

The lead blocks are intended to help maintain a constant neutron spectrum without absorbing the neutrons from the source. Even though the assembly was designed to produce neutrons in thermal spectrum, the actual spectrum includes some fast neutrons in addition to the predominant thermal neutrons. This is due to the fact that the spectrum from external sources, e.g. $D(d,n)^3\text{He}$, or $T(d,n)^4\text{He}$ reactions, or ^{252}Cf spontaneous-fission, is primarily fast [3.1]. Therefore, neutron energies of a several-MeV range (up to 14 MeV for tritium source) as well as scattered neutrons can be found in different locations of the assembly, where they are being continually moderated to thermal energies. Depending on the location in the assembly, the relative intensities of these neutrons of different spectra will be different. For instance, the density of fast neutrons will be highest in the vicinity closest to the neutron source, but the thermal neutrons still dominate in this region. These neutron energy

distribution variations that are dependent on the location in the assembly, instead of a uniform spectrum, make it possible to obtain better understanding of subcritical assembly behaviour.

Another feature that makes the subcritical assembly a diverse research facility is a possibility to use different fuel loading configurations and number of fuel rods for measurements. A maximum of 280 fuel rods can be located in 317 channels. The variation of the number of fuel rods in loading allows the YALINA-Thermal performance studies with different subcriticality levels [3.1].

3.3. RESEARCH ACTIVITY²

Table 3.1 represents a list of Member States that contributed to the YALINA-Thermal benchmarking effort and computational tools they used in their work.

TABLE 3.1. CONTRIBUTORS TO THE YALINA-THERMAL IAEA BENCHMARK

Country	Code	Library
Argentina	MCNP5	ENDF/B-VI
Serbia	MCNP5	ENDF/B-VI
Republic of Korea	McCARD	ENDF/B-VII
USA	PARTISN	ENDF/B-VI
USA	MCNPX	ENDF/B-VI
USA	ERANOS	ENDF/B-VI

The main objective of this research activity is to compare the results from different computational methods, performed by different research institutes, and with experimental data. The benchmark is based on the current YALINA facility configuration, which provides the opportunity to verify the prediction capability of the different methods. The YALINA Thermal configuration and its operating conditions define the benchmark specifications. The benchmark is carried out with ²⁵²Cf, D-D, and D-T neutron sources.

For the YALINA-Thermal benchmark three core configurations were used: with 216, 245, and 280 EK10 fuel rods. Each of the configurations contains 1.67, 1.89, and 2.16 kg ²³⁵U mass respectively. The fuel loading configurations are represented in [3.1]. For each configuration the following results are considered³:

- a) Axial distribution of the following reaction rates:
 - i. ³He(n,p) reaction rate in EC1, EC2, and EC3 experimental channels, normalized to one external source neutron and one ³He atom. The average neutron flux $\phi(E)$ was used for reaction values calculations in the cylindrical cells at z from -250 mm to 250 mm at a pitch of 50 mm (as in Fig. D.11 of Ref. [3.1]). There was no detector modelling performed for this calculation.

² This section is based on Ref. [3.1].

³ The following is based on the recommended benchmark calculations from Ref. [3.1].

- ii. $^{235}\text{U}(n,f)$ reaction rate in EC1, EC2, and EC3 experimental channels, normalized to one external source neutron and one ^{235}U atom. The average neutron flux $\varphi(E)$ was used for all calculations in all channels in the cylindrical cells at z from -250 mm to 250 mm at a pitch of 50 mm (as in Fig. D.11 of Ref. [3.1]). There was no detector modelling performed for this calculation.
 - iii. $^{115}\text{In}(n,\gamma)$ reaction rate in EC2 experimental channel, normalized to one external source neutron and one ^{115}In atom. The calculations were performed for the ^{115}In samples located at z from -242 mm to 208 mm at a pitch of 50 mm. The ^{115}In samples are modelled together with their polyethylene holder (as in Fig. D.12 of Ref. [3.1]). No other isotopes were loaded in the holder.
- b) Radial distribution of the $^{115}\text{In}(n,\gamma)$ reaction rate in the EC7 radial experimental channel for the radial distances from 200 to 600 mm at a pitch of 50 mm. All reaction-rate values are normalized to one source neutron and one ^{115}In atom. The samples are modelled together with their polyethylene holder (as in Fig. D.13 of Ref. [3.1]).
- c) $^{197}\text{Au}(n,\gamma)$ and $^{55}\text{Mn}(n,\gamma)$ reaction rates in EC2 experimental channel, normalized to one external source neutron and one isotope atom. The modelling of samples was performed together with their sample holder, as done in the task (a)-iii of this Section. The isotope loading distribution is shown in Fig. D12 of Ref. [3.1]. The calculation has to be performed with the holder containing only ^{197}Au or ^{55}Mn .
- d) For the 172 energy groups structure in Table D.2 of Ref. [3.1] the neutron energy spectra in the EC1, EC2, EC3, EC5, and EC6 experimental channels are calculated at $z = 0$. Each spectrum is averaged over a cylindrical volume of length 100 mm and cross-section area the same the channel. The spectrum is normalized by the lethargy and the integral of the normalized neutron spectrum is expected to equal unity, as per Eq. (2.1):

$$\int \varphi(E)dE = 1.0 \quad (2.1)$$

- e) The neutron flux calculations are performed after a 5 μs D-D or D-T neutrons pulse insertion at $z=0$ as a function of time for a period of 20 ms with two different detectors:
- i. $^3\text{He}(n,p)$ detector in the EC2 and EC5 experimental channels, without modelling the detector in the calculation. The results are normalized to the EC2 experimental channel maximum value.
 - ii. $^{235}\text{U}(n,f)$ detector in the EC1 experimental channel, without modelling the detector in the calculation. The results are normalized to the maximum value in the experimental channel. The ^3He gas detector is included in the transport calculations to allow for comparison with the experimental results. 10 and 250 mm detector lengths were used. The gas atom densities are as follows per cm^3 :
 - $^3\text{He} = 0.8 \times 10^{-24}$,
 - $^{78}\text{Kr} = 7 \times 10^{-28}$,
 - $^{80}\text{Kr} = 4.5 \times 10^{-27}$,
 - $^{82}\text{Kr} = 2.32 \times 10^{-26}$,
 - $^{83}\text{Kr} = 2.3 \times 10^{-26}$,
 - $^{84}\text{Kr} = 1.14 \times 10^{-25}$,
 - $^{86}\text{Kr} = 3.46 \times 10^{-26}$.
 - iii. The calculations are to be done with 5 μs time bins from 0 to 1 ms, and with 100 μs time bins from 1 ms to 20 ms.
- f) Kinetic parameters for the three configurations are:
- i. Effective multiplication factor, k_{eff} .

- ii. Source multiplication factor, k_s .
- iii. Mean neutron generation time, Λ .
- iv. Prompt neutron lifetime, l_p , and mean-neutron lifetime,
- v. Effective delayed-neutron fraction, β_{eff} .

In the YALINA Thermal subcritical assembly benchmark, the participating Member States of the IAEA sponsored project on Analytical and Experimental Benchmark Analysis on Accelerator Driven Systems, and Low Enriched Uranium Fuel Utilization in Accelerator Driven Subcritical Assembly Systems [3.1] used different computational tools and nuclear data libraries. Argentina and Serbia used MCNP5 [3.2], Republic of Korea used McCARD code [3.3], and the U.S.A. used MCNPX [3.4], PARTISN [3.5, 3.6], and ERANOS [3.7]; the latter two tools use deterministic algorithms to solve the neutron transport equation. All the participating Member States used the ENDF/B-VI (different modes) nuclear data library with the exception of Republic of Korea, which used the ENDF/B-VII.0 library [3.8]. The USA analyses of the YALINA thermal facility are documented in Refs [3.9] and [3.10]. Figs 3.4–3.11 illustrate the computational models of the YALINA Thermal subcritical assembly developed by the participating Member States. The experimental channels of the facility are shown in Fig. 3.7.

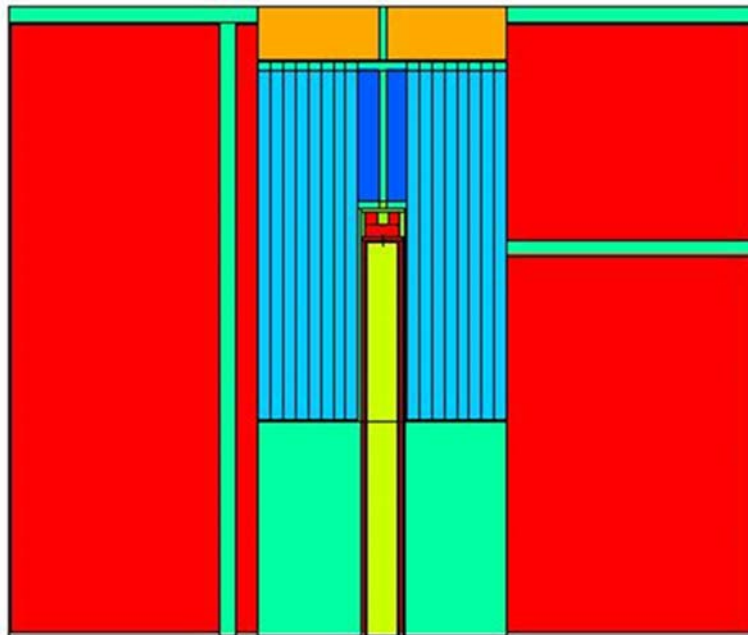


FIG. 3.4. Vertical section of Argentina's model of YALINA-Thermal facility (Courtesy of the Argonne National Laboratory, USA).

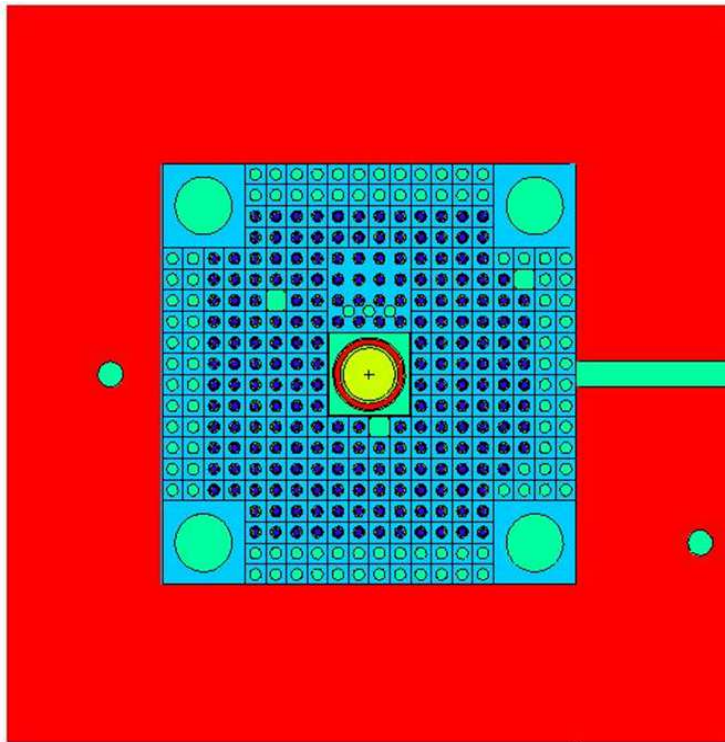


FIG. 3.5. Horizontal section of Argentina's model of YALINA-Thermal facility (Courtesy of the Argonne National Laboratory, USA).

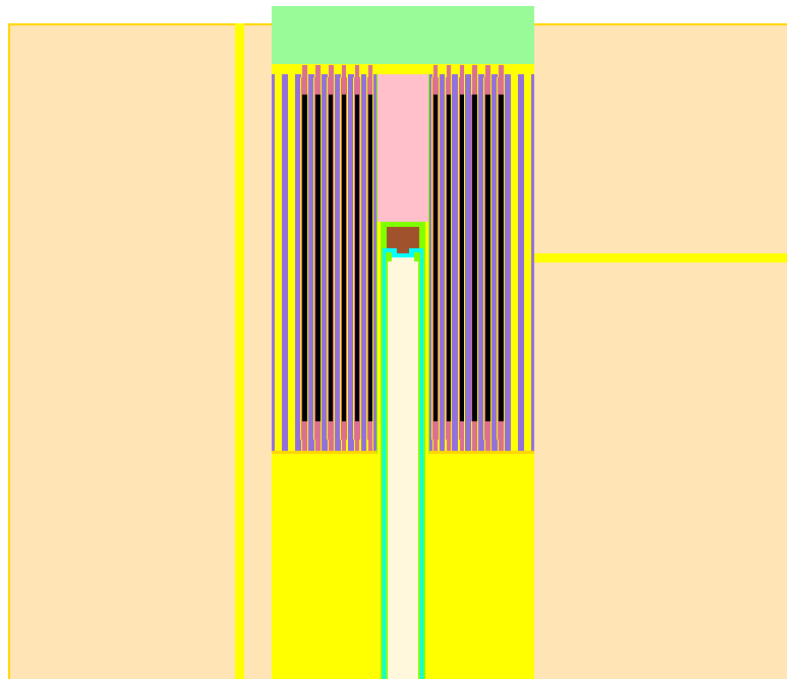


FIG. 3.6. Vertical section of the USA MCNP model of YALINA-Thermal facility (Courtesy of the Argonne National Laboratory, USA).

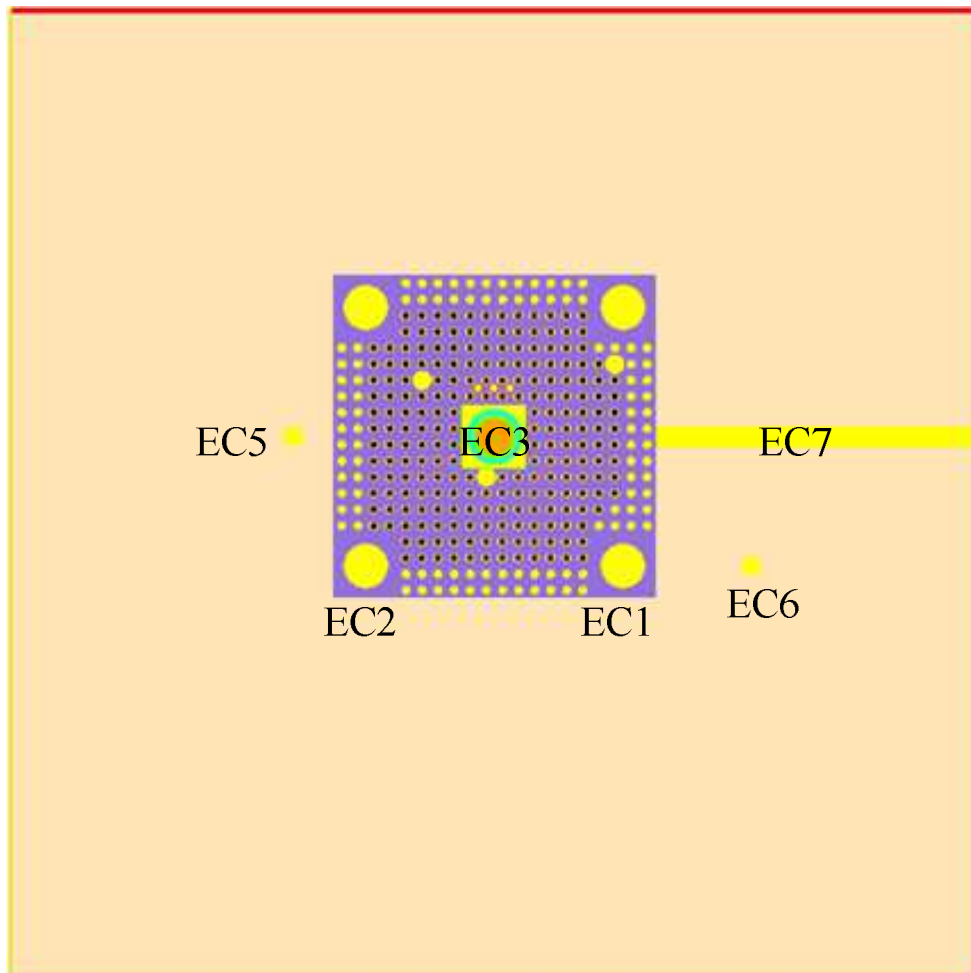


FIG. 3.7. Horizontal section of the USA MCNP model of YALINA-Thermal facility (Courtesy of the Argonne National Laboratory, USA).

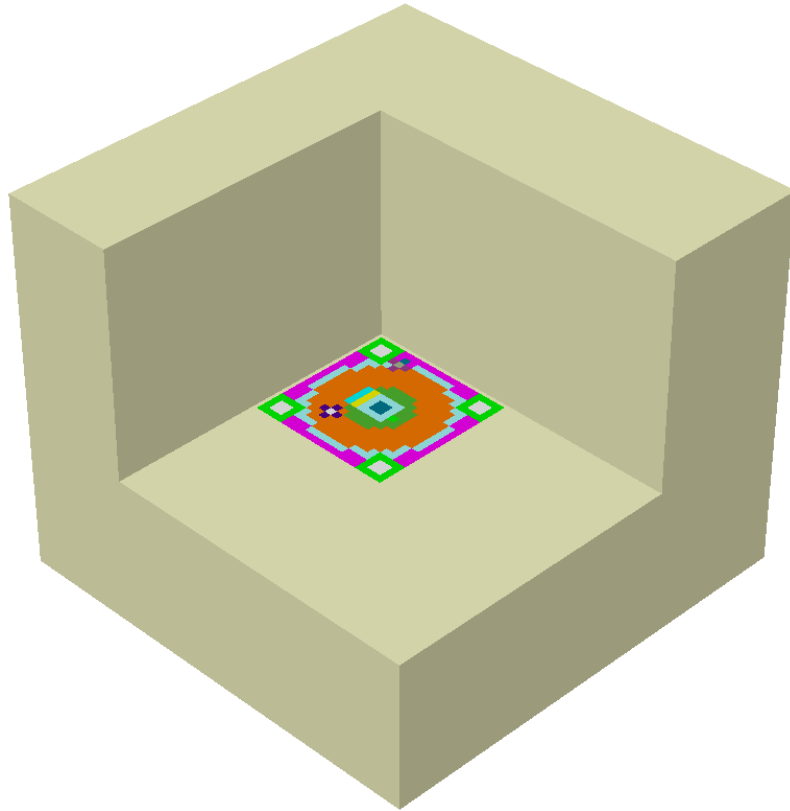


FIG. 3.8. Overview of the USA PARTISN model of YALINA-Thermal facility with corner cut showing the horizontal section (Courtesy of the Argonne National Laboratory, USA).

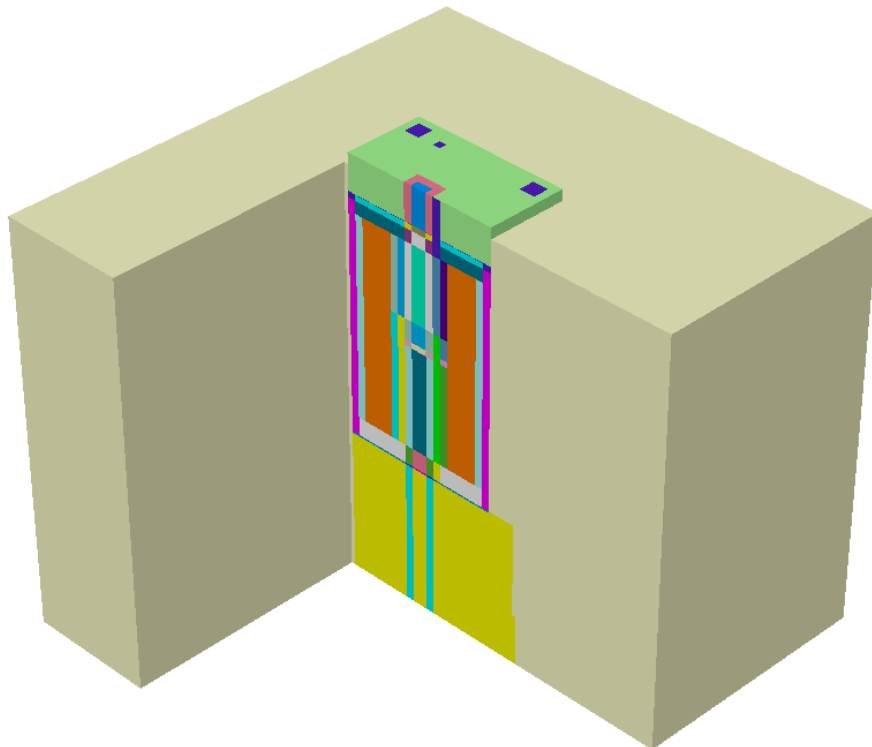


FIG. 3.9. Overview of the USA PARTISN model of YALINA-Thermal facility with side cut showing the vertical section (Courtesy of the Argonne National Laboratory, USA).

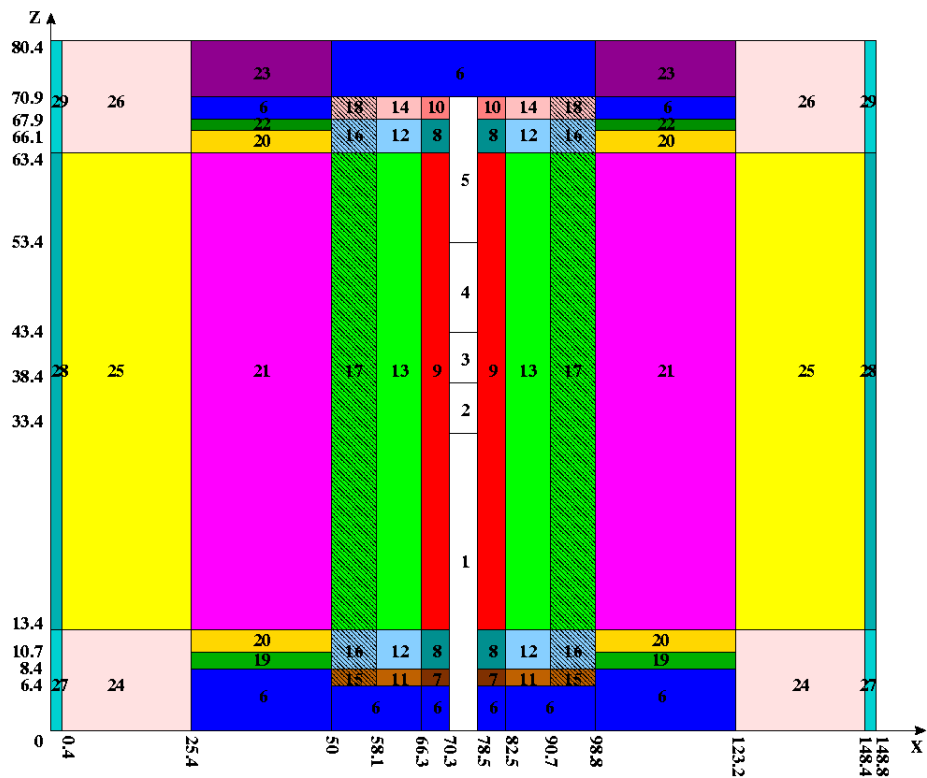


FIG. 3.10. Vertical section of the USA ERANOS model of YALINA-Thermal facility. Dimensions are in cm (Courtesy of the Argonne National Laboratory, USA).

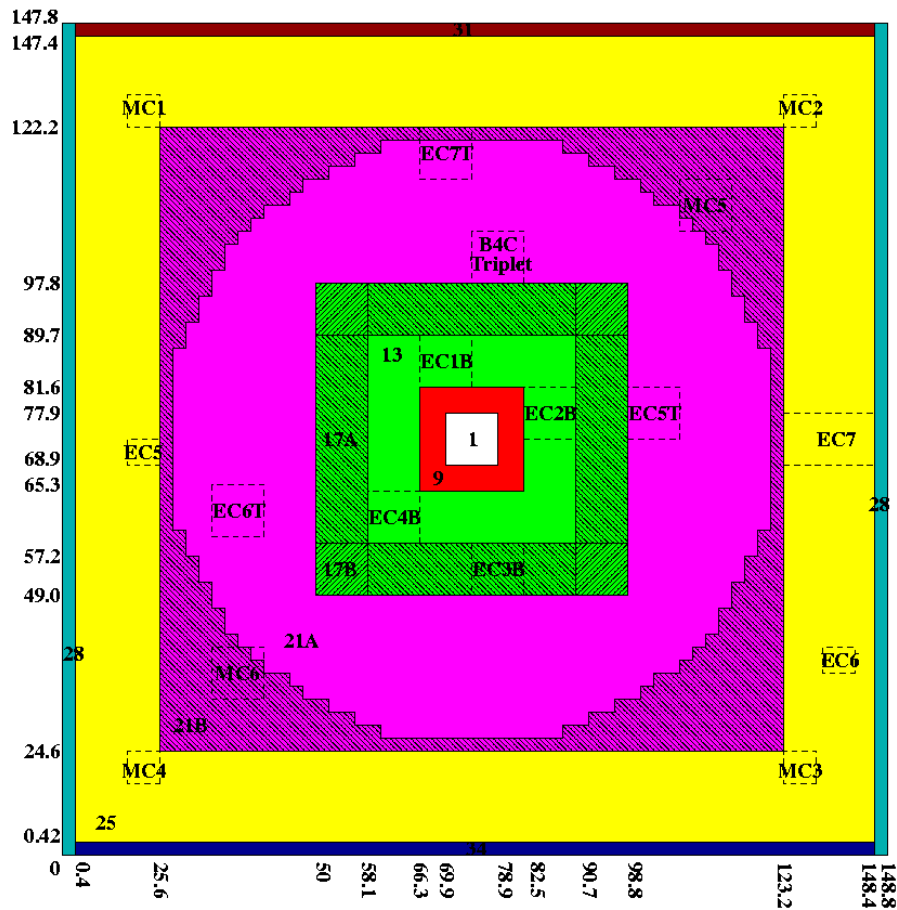


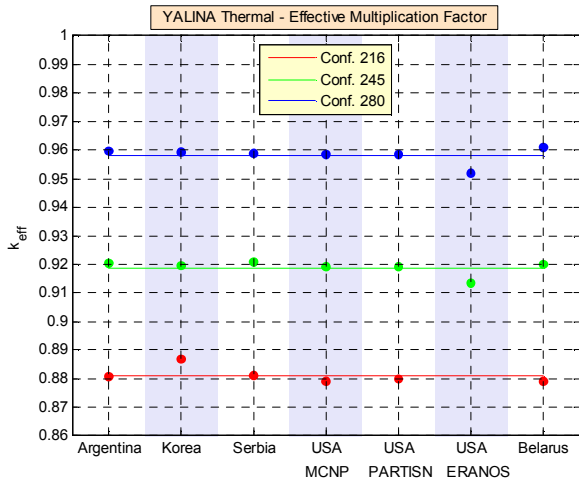
FIG. 3.11. Horizontal section of the USA ERANOS model of YALINA-Thermal facility. Dimensions are in cm (Courtesy of the Argonne National Laboratory, USA).

3.4. RESULTS

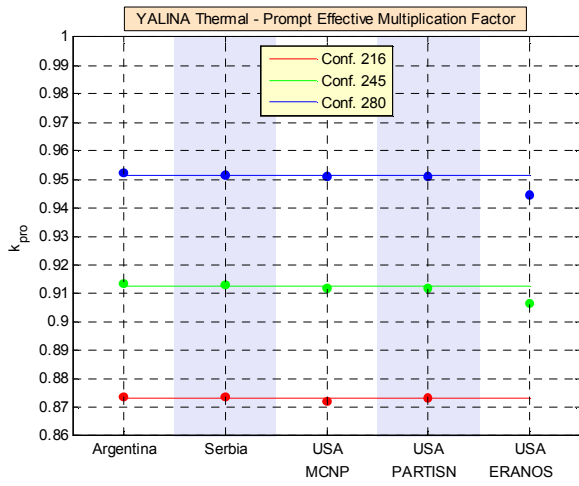
The obtained results are compared graphically to the extent possible. The next three sections report the results for the kinetic parameters, the reactions rates, and the neutron spectra.

3.4.1. Kinetic Parameters

The multiplication factors for the configurations using 216, 245, and 280 fuel rods are plotted in Figs 3.12–3.14. The standard deviations of the effective multiplication factors obtained by Serbia, Argentina, Korea, and USA MCNP are 16, 12, 7, and 2 pcm, respectively. Figure 3.12 (a) includes the Belarus results obtained from MCNP4 simulations with ENDF/B-VI nuclear data library [3.8]. The effective (k_{eff}) and prompt (k_{pro}) multiplication factors calculated by the different participants generally agree within ± 150 pcm. The results obtained by USA using the ERANOS code are little lower than others, and they were excluded from the average values which are shown in Figs 3.12–3.15 by horizontal lines. The effective multiplication factor of Republic of Korea for the configuration with 216 fuel rods is above the average. The Argentina, USA MCNP, and USA PARTISN results for the source multiplication factors agree within a margin of 300 pcm; the latter value increases up to 700 pcm with the inclusion of Republic of Korean results. Multiple factors may contribute to the differences between the source-multiplication factors, including: the contribution from (n,xn) reactions, the modelling of the space-energy-angle distribution of the external neutron source, and the definition of the source-multiplication factor [3.11].

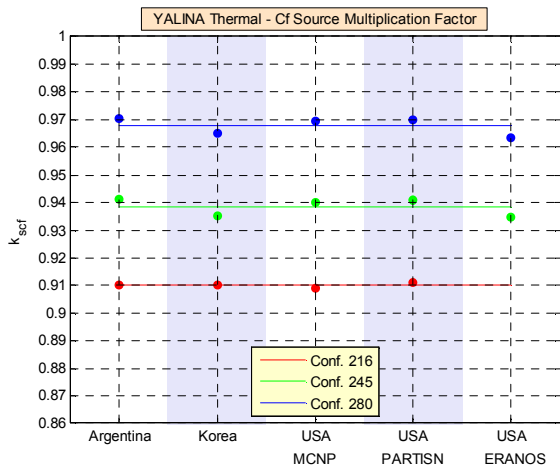


a)

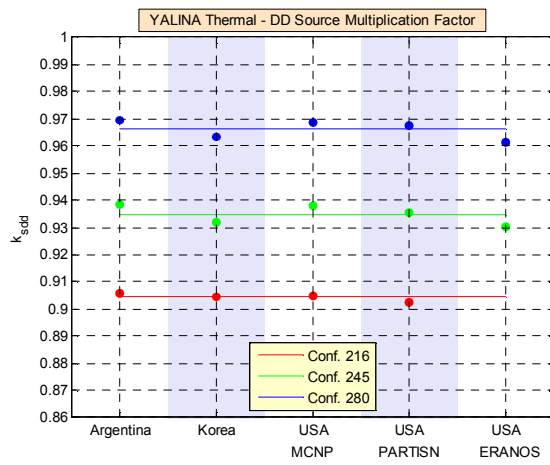


b)

FIG. 3.12. Effective (a) and prompt (b) multiplication factors (Courtesy of the Argonne National Laboratory, USA).



a)



b)

FIG. 3.13. Cf (a) and D-D (b) source-multiplication factors (Courtesy of the Argonne National Laboratory, USA).

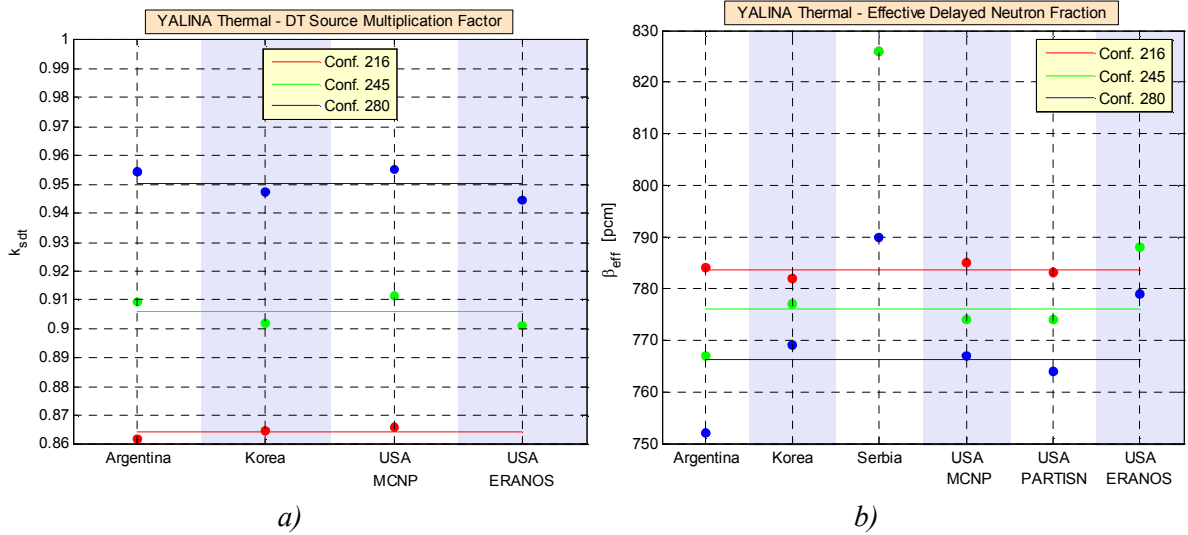


FIG. 3.14. D-T source-multiplication factor (a) and effective delayed-neutron fraction (b) (Courtesy of the Argonne National Laboratory, USA).

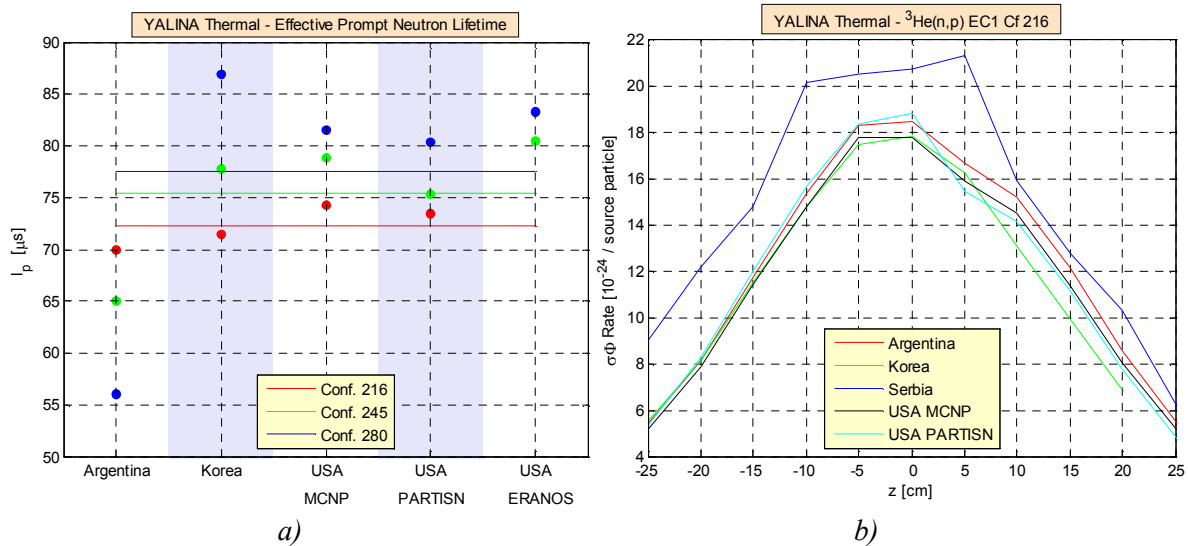


FIG. 3.15. Effective prompt-neutron lifetime (a) and $^3\text{He}(n,p)$ reaction rate in EC1 experimental channel for the Cf neutron source and 216 configuration (b) (Courtesy of the Argonne National Laboratory, USA).

As expected, the multiplication factor increase as the number of fuel rods increases. The prompt multiplication factor is about 750 pcm lower than the effective multiplication factor; this difference matches the effective delayed-neutron fraction value. The californium source multiplication factor k_{scf} is higher than the effective multiplication factor because ^{252}Cf source neutrons are emitted in a high importance zone of the assembly, the assembly centre. For the 280 configuration, the californium k_{scf} is closer to k_{eff} because source neutrons contribute less to the fission chain; the 280 configuration has the highest neutron multiplication factor among the three configurations.

The deuterium-deuterium (D-D) source multiplication factor k_{sdd} is smaller than the californium source multiplication factor because D-D neutrons have higher average energy (~ 2.45 MeV) relative to the californium neutrons (~ 2 MeV), which increases neutron leakage. Consistently, the higher average energy of deuterium-tritium (D-T) source neutrons (~ 14.1 MeV), relative to D-D source neutrons (~ 2.45 MeV), increases neutron leakage; this

decreases the value of k_{sdt} (D-T source) relative to k_{sdd} and k_{eff} . Close to criticality (if the external neutron source is placed in the fuel region and away from strong neutron absorbers), the source multiplication factor converges to the effective multiplication factor since source neutrons are outnumbered by fission neutrons.

All the deterministic and the Monte Carlo computer programs estimated an effective delayed-neutron fraction β_{eff} between 750 and 790 pcm, as shown in Fig. 3.14 (a). The results obtained by Serbia have a very high standard deviation of ~ 22 pcm, and therefore it is excluded from the average value. The effective delayed neutron fraction increases as the number of fuel rods decreases, because of the increase of the thermal neutrons fraction. More precisely, when the number of fuel rods decreases, and the polyethylene mass remains the same in the assembly, the thermal neutron fraction increases causing more fission reaction, which increases β_{eff} .

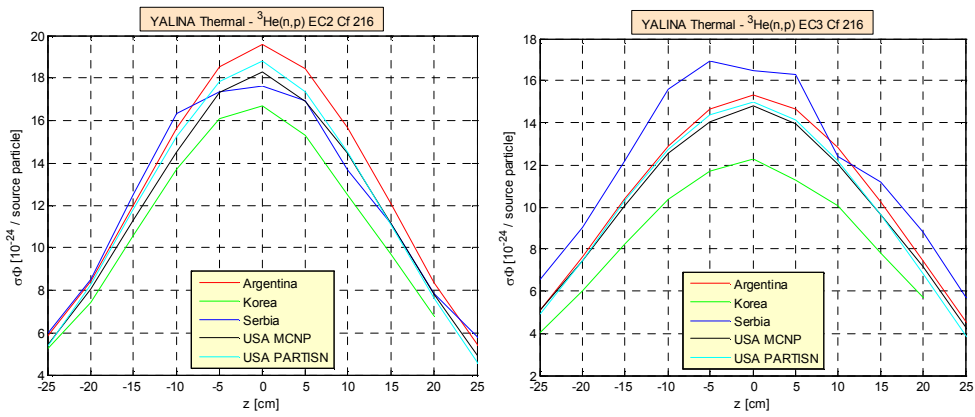
The (effective) prompt neutron lifetime l_p ranges from 55 to 87 μ s, as illustrated in Fig. 3.15 (a). The prompt neutron lifetime increases with the increase of the number of fuel rods. As the number of fuel rods increases, the neutron multiplication and the number of neutrons scattered back from the reflector zone into the fuel zone increases. The back-scattered neutrons have a longer prompt neutron lifetime, which increases the effective prompt neutron lifetime. However, the results obtained by Argentina do not follow this trend.

The maximum energy value of the nuclear data library used by the PARTISN code is 10 MeV; therefore, this code was not used for D-T neutron source calculations. The fuel configuration with 216 fuel rods was not analysed by the ERANOS code. Serbia provided only results from criticality analyses and Cf neutron source calculations.

3.4.2. Reaction Rates

The ${}^3\text{He}(n,p)$ and ${}^{235}\text{U}(n,f)$ reaction rates, as a function of the axial position parallel to the fuel rods, have been calculated for the assembly driven by Cf, D-D, and D-T external neutron sources in the EC1, EC2, and EC3 experimental channels, as shown in Figs 3.15–3.42. In these Figs, the ticks on the y axis indicate the centre of the tally volume. The unit of all the reaction rates of this section is barn-per-source-particle-per-square-centimetre ($10^{-24}/\text{source particle} \times \text{cm}^2$). The Monte Carlo statistical errors of the reaction rates are less than 1.5% for Argentina and USA MCNP results, and less than 7% for the Republic of Korea and Serbia results. The ERANOS reaction rates are lower than the Monte Carlo results because of the lower source multiplication factor calculated by this code. The following observations can be seen from the obtained results:

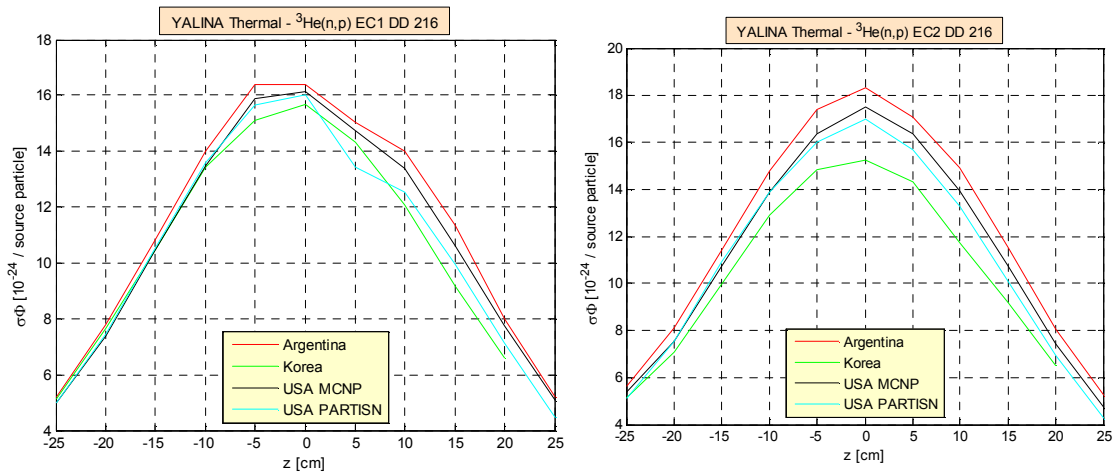
- In all the experimental channels, the reaction rate from the Cf neutron source is always higher than the reaction rate from the D-D neutron source, and the reaction rate from the D-D neutron source is always higher than the reaction rate from the D-T neutron source per source neutron. This is due to the higher leakage of D-D source neutrons relative to Cf source neutrons and the higher leakage of D-T source neutrons relative to D-D source neutrons. The average energy of source neutrons increases in the following order: Cf < D-D < D-T. Neutron leakage increases as the average energy of source neutrons increases, since the assembly has a small volume and a thin reflector;
- In all the experimental channels, the reaction rate increases as the number of the fuel rods increases due to the higher neutron multiplication;
- The reaction rate in the experimental channels decreases as the distance between the experimental channel and the neutron source increases;
- The axial neutron flux distributions have cosine shapes in all the experimental channels parallel to the fuel rods.



a)

b)

FIG. 3.16. ${}^3\text{He}(n,p)$ reaction rate in EC2 (a) and EC3 (b) experimental channels for the Cf neutron source and 216 configuration (Courtesy of the Argonne National Laboratory, USA).



a)

b)

FIG. 3.17. ${}^3\text{He}(n,p)$ reaction rate in EC1 (a) and EC2 (b) experimental channels for the D-D neutron source and 216 configuration (Courtesy of the Argonne National Laboratory, USA).

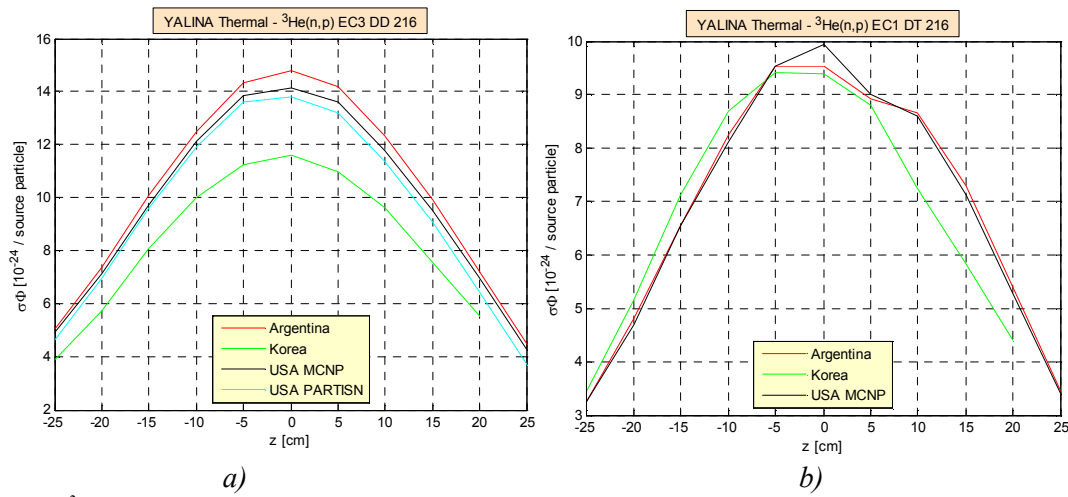


FIG. 3.18. ${}^3\text{He}(n,p)$ reaction rate in EC3 (a) and EC1 (b) experimental channels for the D-D (a) and D-T (b) neutron sources and 216 configuration (Courtesy of the Argonne National Laboratory, USA).

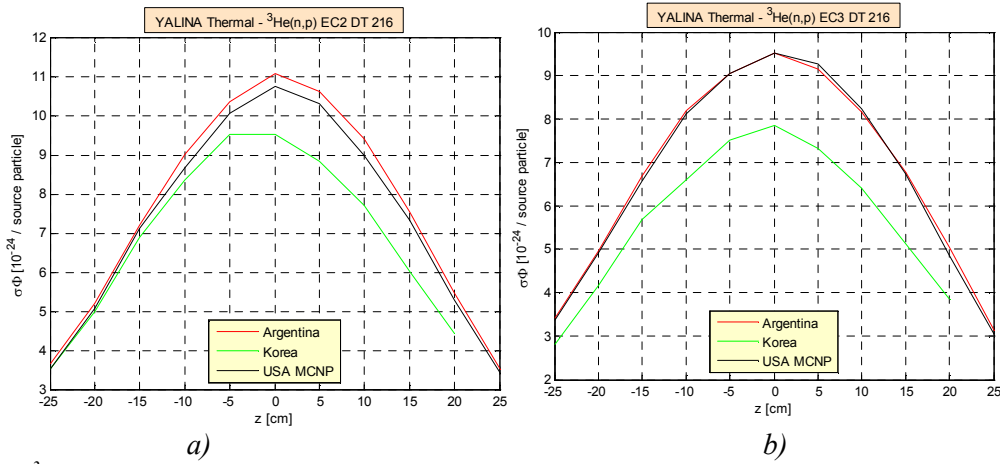


FIG. 3.19. ${}^3\text{He}(n,p)$ reaction rate in EC2 (a) and EC3 (b) experimental channels for the D-T neutron source and 216 configuration (Courtesy of the Argonne National Laboratory, USA).

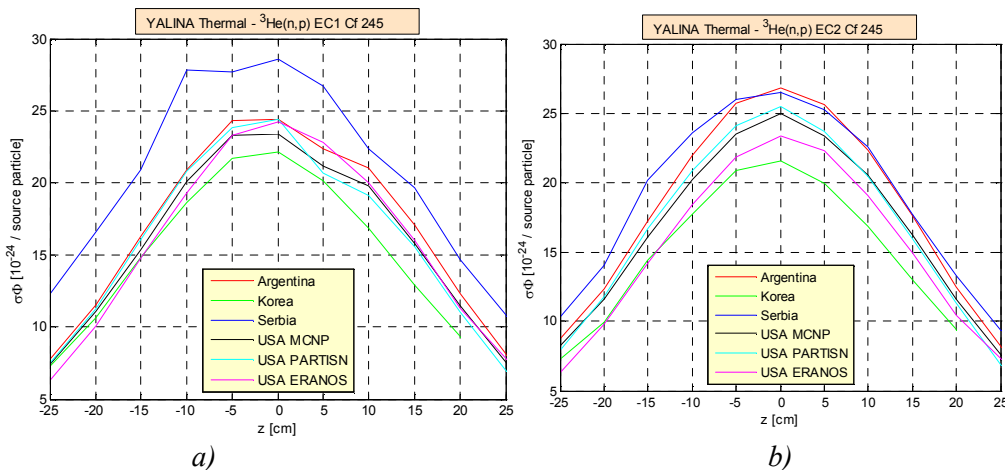


FIG. 3.20. ${}^3\text{He}(n,p)$ reaction rate in EC1 (a) and EC2 (b) experimental channels for the Cf neutron source and 245 configuration (Courtesy of the Argonne National Laboratory, USA).

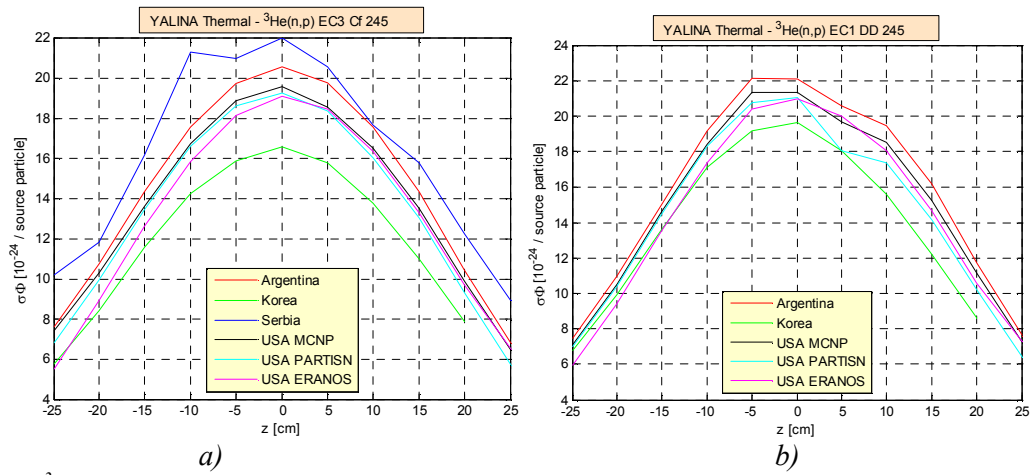


FIG. 3.21. ${}^3\text{He}(n,p)$ reaction rate in EC3 (a) and EC1 (b) experimental channels for Cf (a) and D-D (b) neutron sources and 245 configuration (Courtesy of the Argonne National Laboratory, USA).

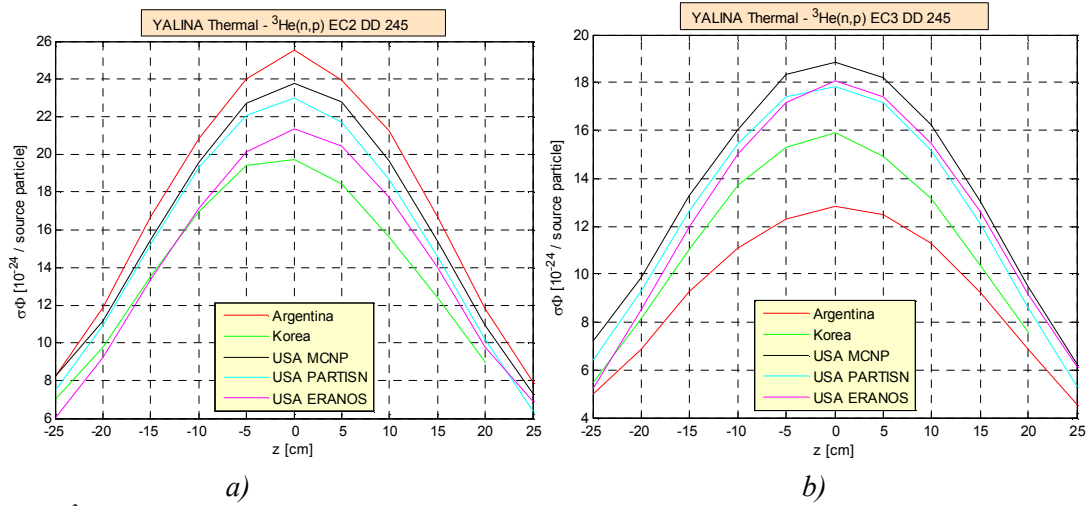


FIG. 3.22. ${}^3\text{He}(n,p)$ reaction rate in EC2 (a) and EC3 (b) experimental channels for the D-D neutron source and 245 configuration (Courtesy of the Argonne National Laboratory, USA).

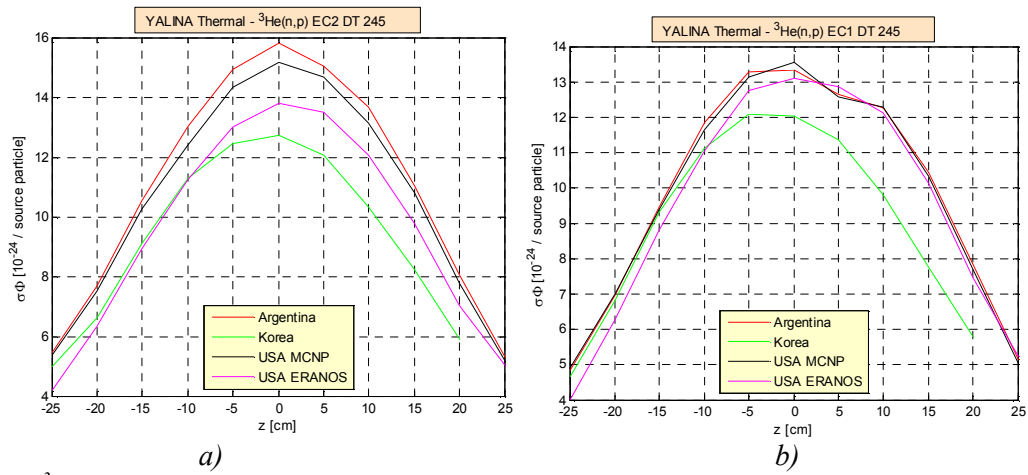


FIG. 3.23. ${}^3\text{He}(n,p)$ reaction rate in EC1 (left plot) and EC2 (right plot) experimental channels for the D-T neutron source and 245 configuration (Courtesy of the Argonne National Laboratory, USA).

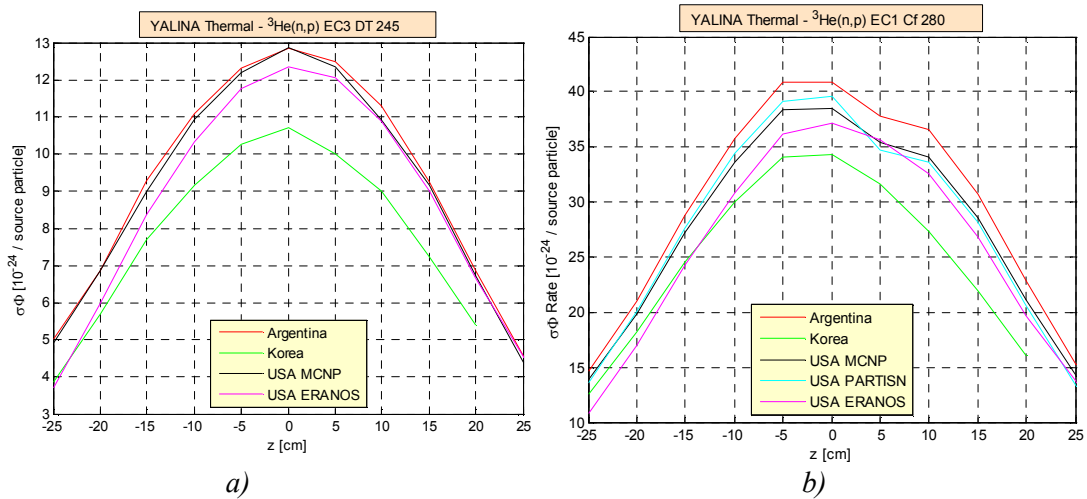


FIG. 3.24. ${}^3\text{He}(n,p)$ reaction rate in EC3 (a) and EC1 (b) experimental channels for D-T (a) and Cf (b) neutron sources and 245 (a) and 280 (b) configurations (Courtesy of the Argonne National Laboratory, USA).

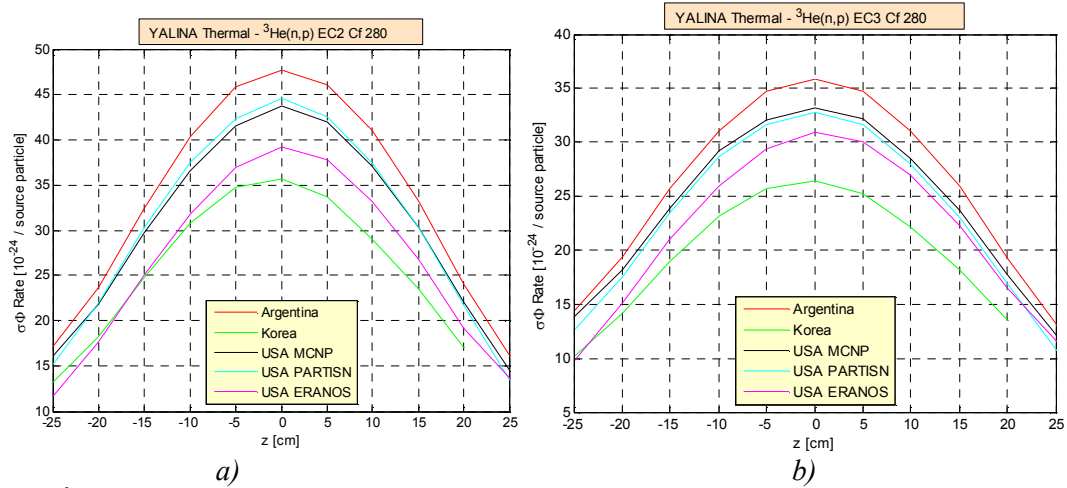


FIG. 3.25. ${}^3\text{He}(n,p)$ reaction rate in EC2 (a) and EC3 (b) experimental channels for the Cf neutron source and 280 configuration (Courtesy of the Argonne National Laboratory, USA).

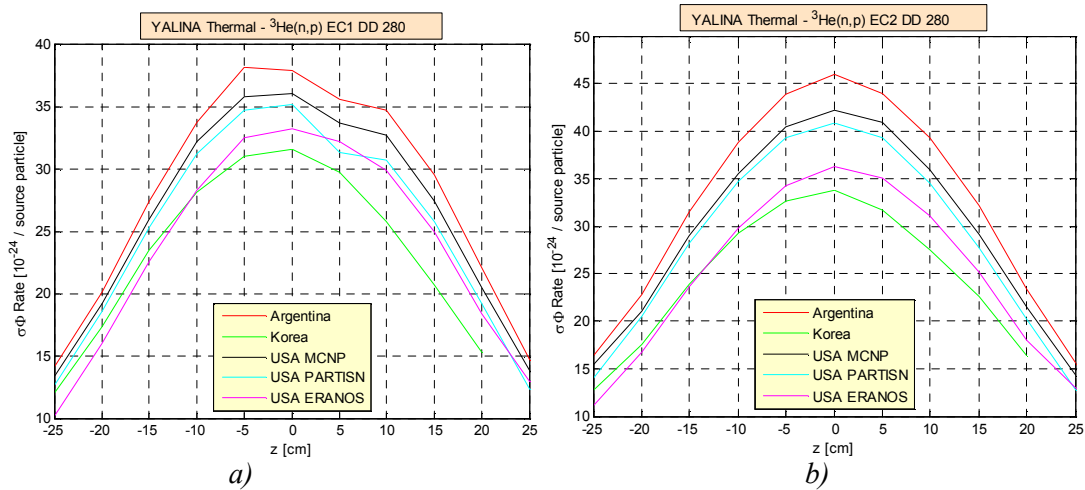
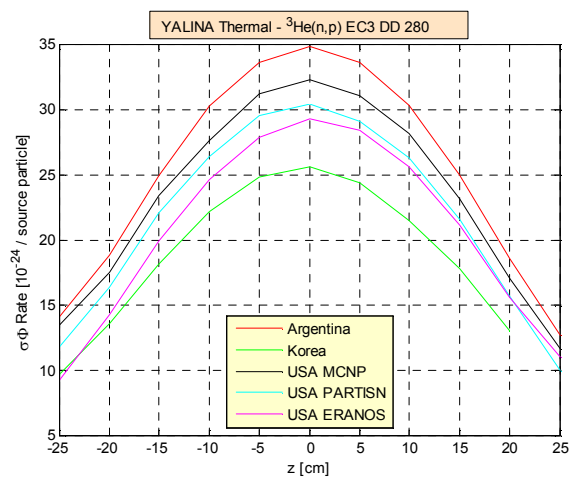
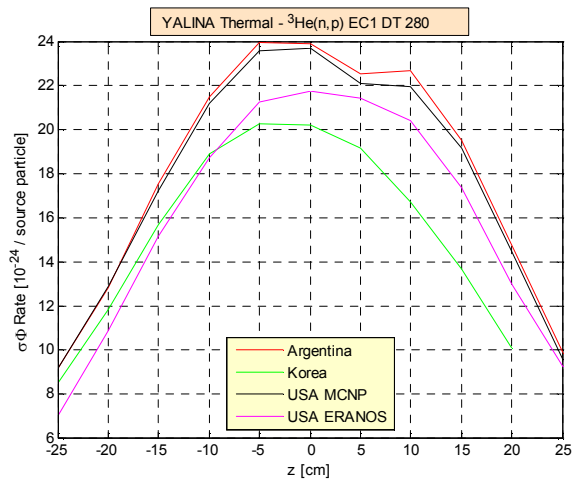


FIG. 3.26. ${}^3\text{He}(n,p)$ reaction rate in EC1 (a) and EC2 (b) experimental channels for the D-D neutron source and 280 configuration (Courtesy of the Argonne National Laboratory, USA).

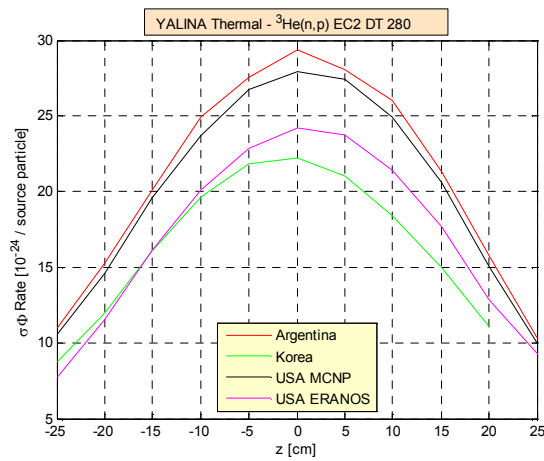


a)

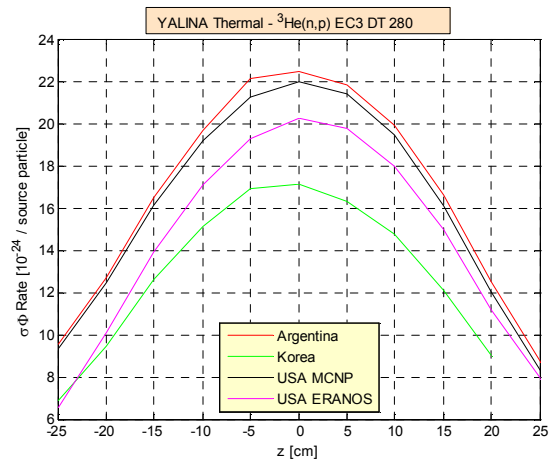


b)

FIG. 3.27. ${}^3\text{He}(n,p)$ reaction rate in EC3 (a) and EC1 (b) experimental channels for D-D (a) and D-T (b) neutron sources and 280 configuration (Courtesy of the Argonne National Laboratory, USA).



a)



b)

FIG. 3.28. ${}^3\text{He}(n,p)$ reaction rate in EC2 (a) and EC3 (b) experimental channels for the D-T neutron source and 280 configuration (Courtesy of the Argonne National Laboratory, USA).

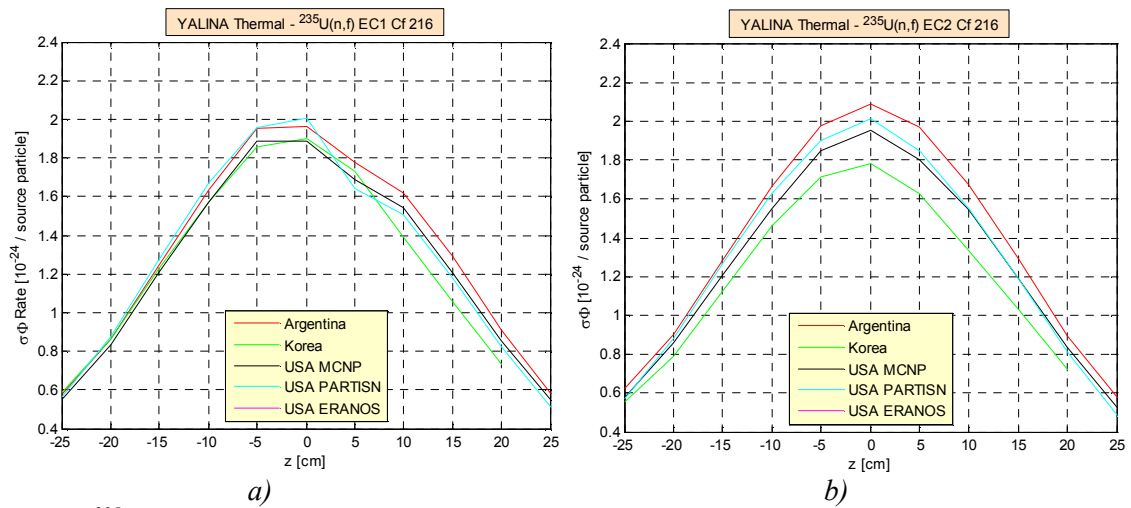


FIG. 3.29. $^{235}\text{U}(n,f)$ reaction rate in EC1 (a) and EC2 (b) experimental channels for the Cf neutron source and 216 configuration (Courtesy of the Argonne National Laboratory, USA).

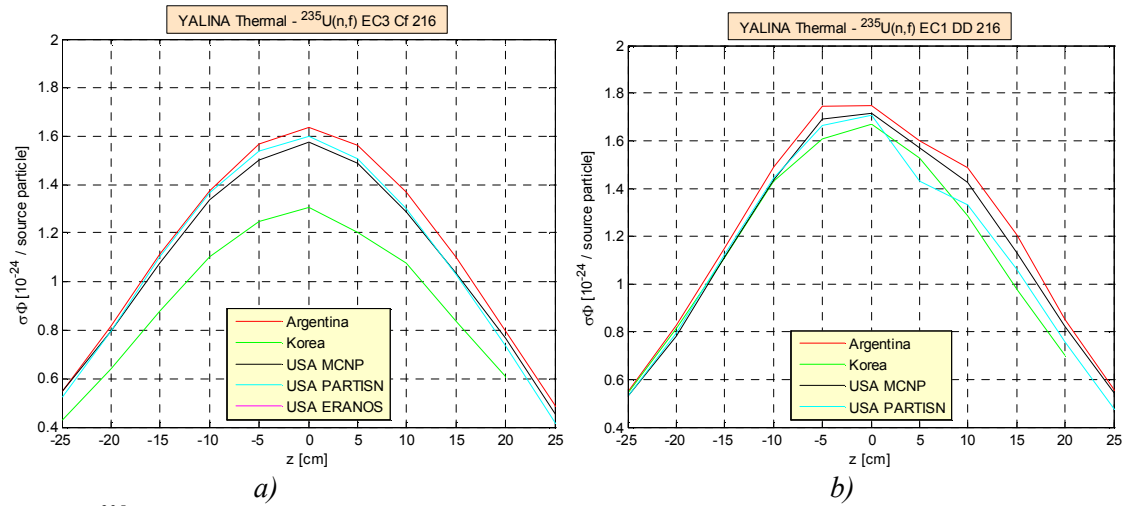


FIG. 3.30. $^{235}\text{U}(n,f)$ reaction rate in EC3 (a) and EC1 (b) experimental channels for Cf (a) and D-D (b) neutron sources and 216 configuration (Courtesy of the Argonne National Laboratory, USA).

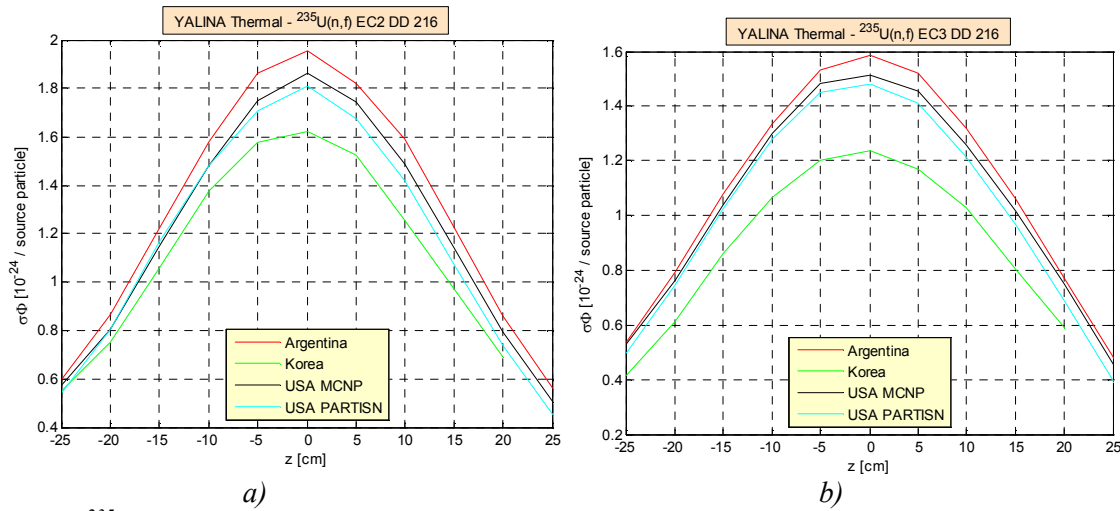


FIG. 3.31. $^{235}\text{U}(n,f)$ reaction rate in EC2 (a) and EC3 (b) experimental channels for the D-D neutron source and 216 configuration (Courtesy of the Argonne National Laboratory, USA).

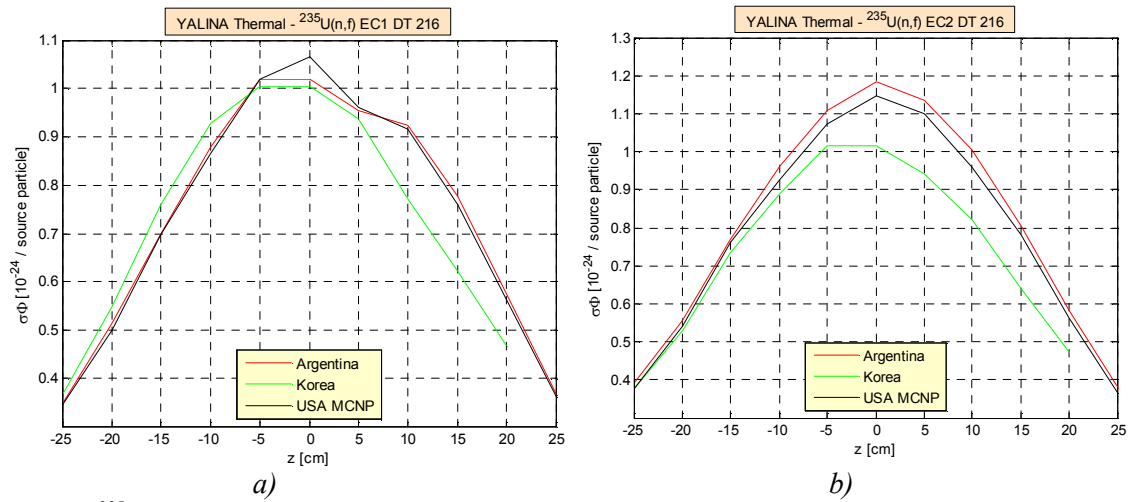


FIG. 3.32. $^{235}\text{U}(n,f)$ reaction rate in EC1 (a) and EC2 (b) experimental channels for the D-T neutron source and 216 configuration (Courtesy of the Argonne National Laboratory, USA).

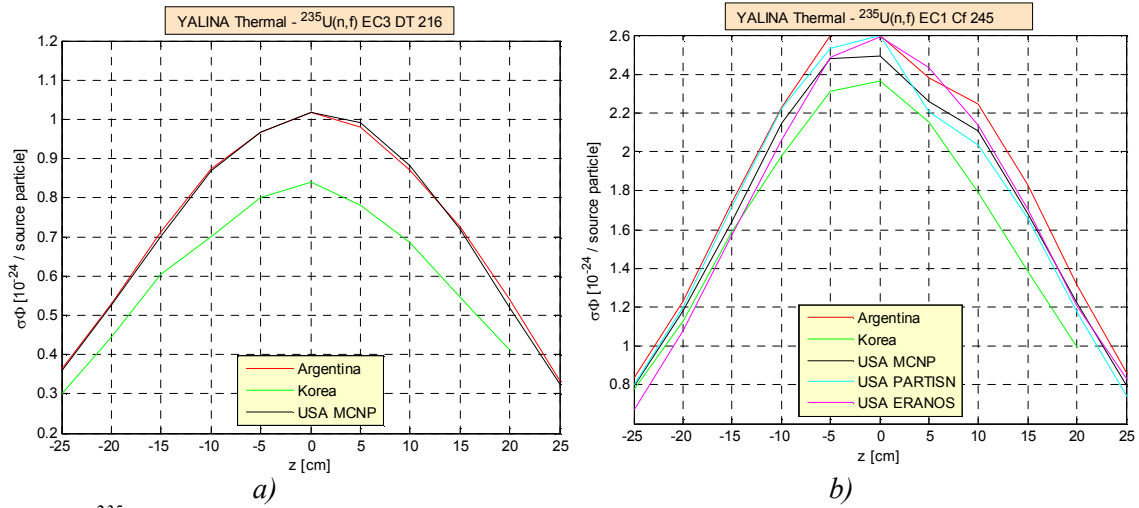


FIG. 3.33. $^{235}\text{U}(n,f)$ reaction rate in EC3 (a) and EC1 (b) experimental channels for D-T (a) and Cf (b) neutron sources and 216 (a) and 245 (b) configurations (Courtesy of the Argonne National Laboratory, USA).

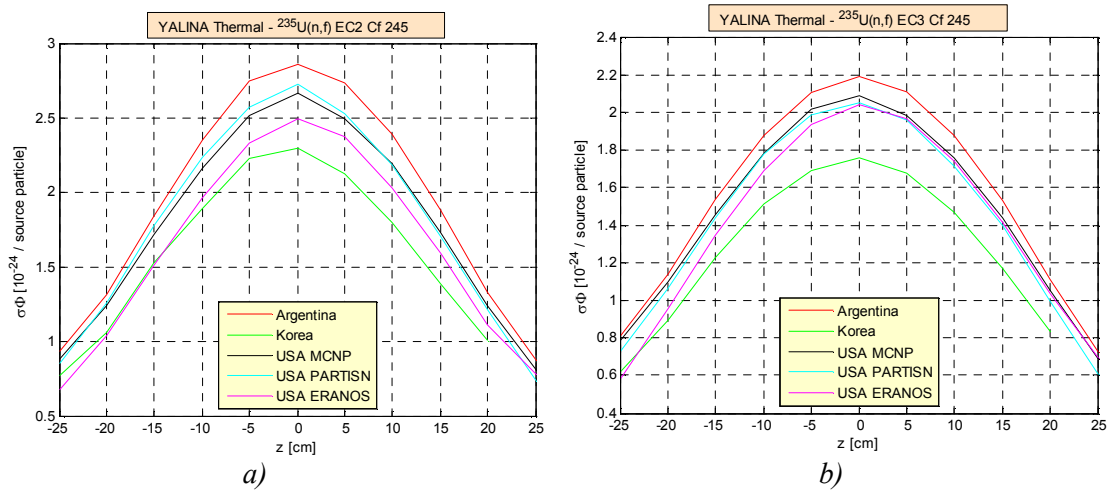


FIG. 3.34. $^{235}\text{U}(n,f)$ reaction rate in EC2 (a) and EC3 (b) experimental channels for the Cf neutron source and 245 configuration (Courtesy of the Argonne National Laboratory, USA).

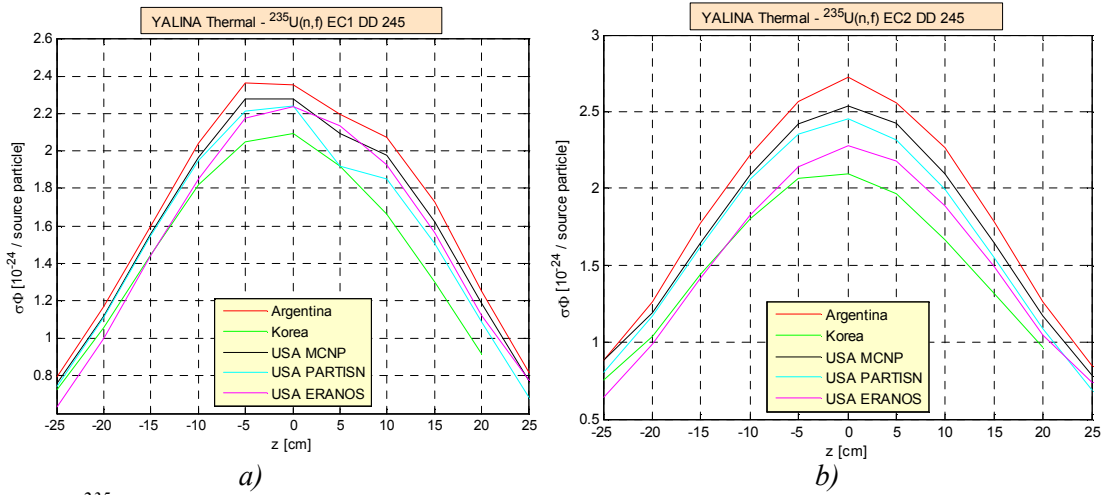


FIG. 3.35. $^{235}\text{U}(n,f)$ reaction rate in EC1 (a) and EC2 (b) experimental channels for the D-D neutron source and 245 configuration (Courtesy of the Argonne National Laboratory, USA).

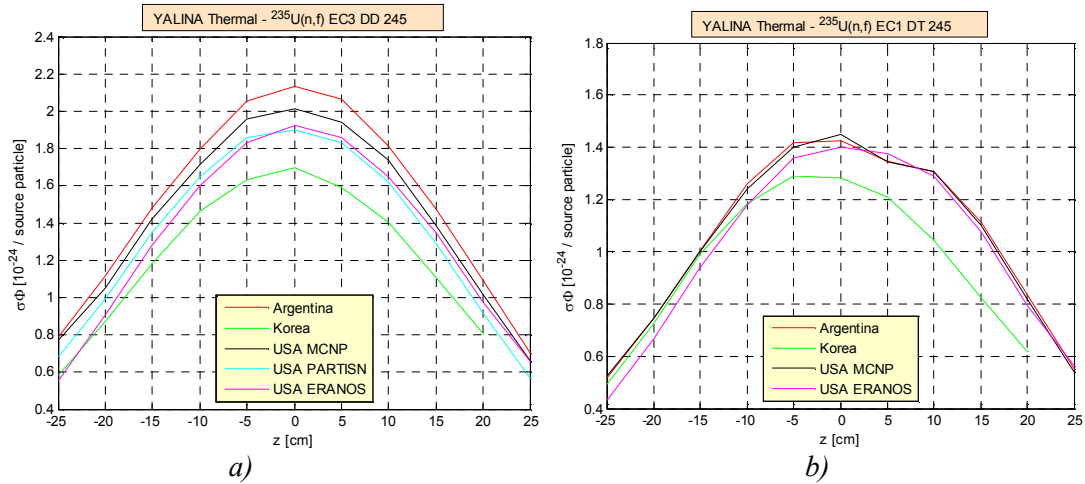


FIG. 3.36. $^{235}\text{U}(n,f)$ reaction rate in EC3 (a) and EC1 (b) experimental channels for D-D (a) and D-T (b) neutron sources and 245 configuration (Courtesy of the Argonne National Laboratory, USA).

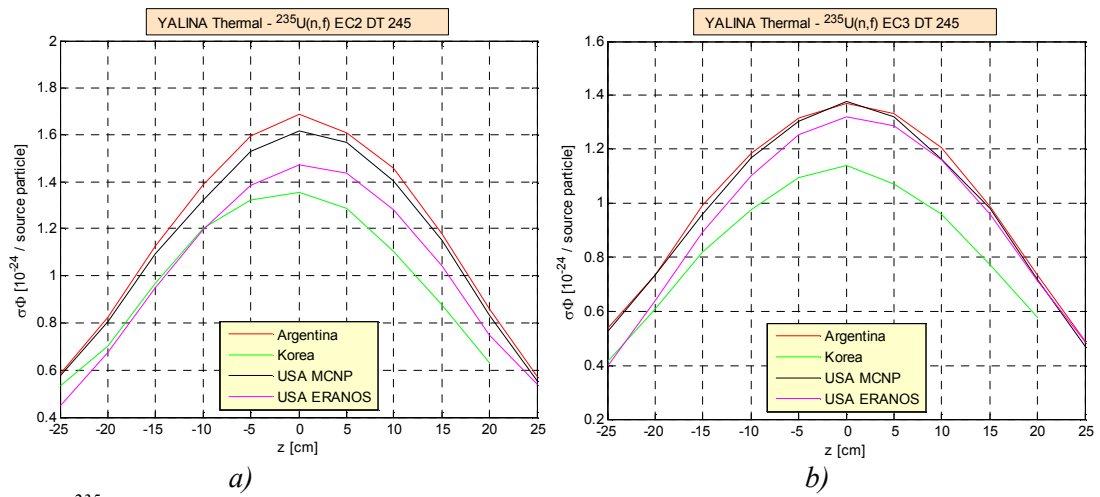


FIG. 3.37. $^{235}\text{U}(n,f)$ reaction rate in EC2 (a) and EC3 (b) experimental channels for the D-T neutron source and 245 configuration (Courtesy of the Argonne National Laboratory, USA).

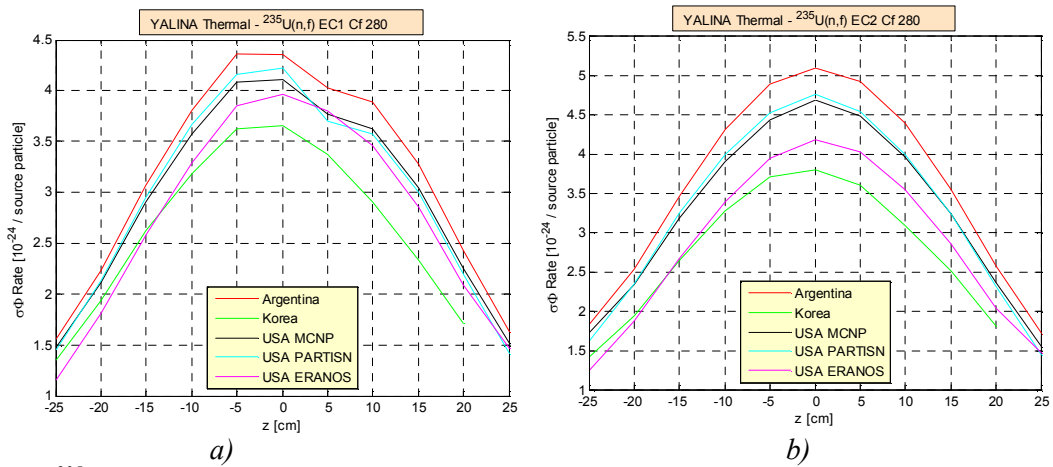


FIG. 3.38. $^{235}\text{U}(n,f)$ reaction rate in EC1 (a) and EC2 (b) experimental channels for the Cf neutron source and 280 configuration (Courtesy of the Argonne National Laboratory, USA).

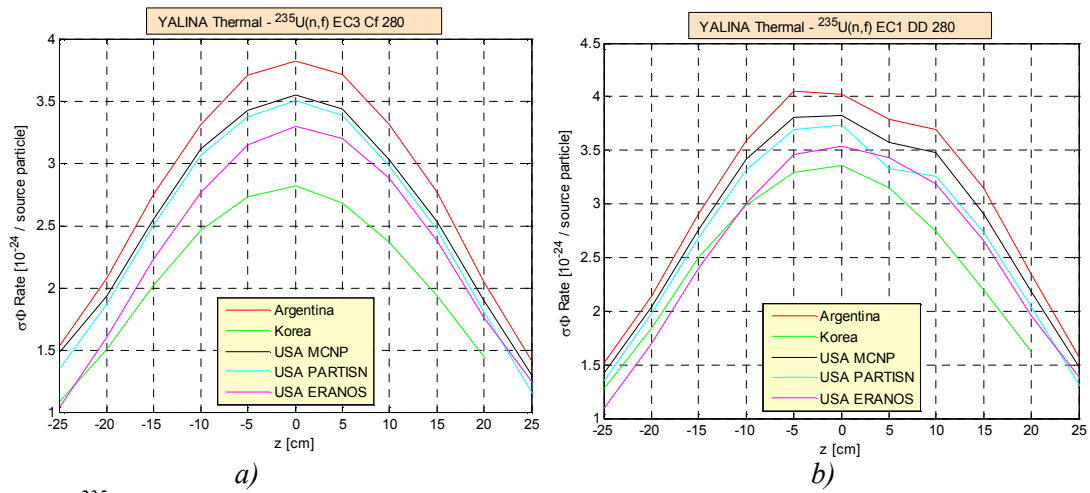


FIG. 3.39. $^{235}\text{U}(n,f)$ reaction rate in EC3 (a) and EC1 (b) experimental channels for Cf (a) and D-D (b) neutron sources and 280 configuration (Courtesy of the Argonne National Laboratory, USA).

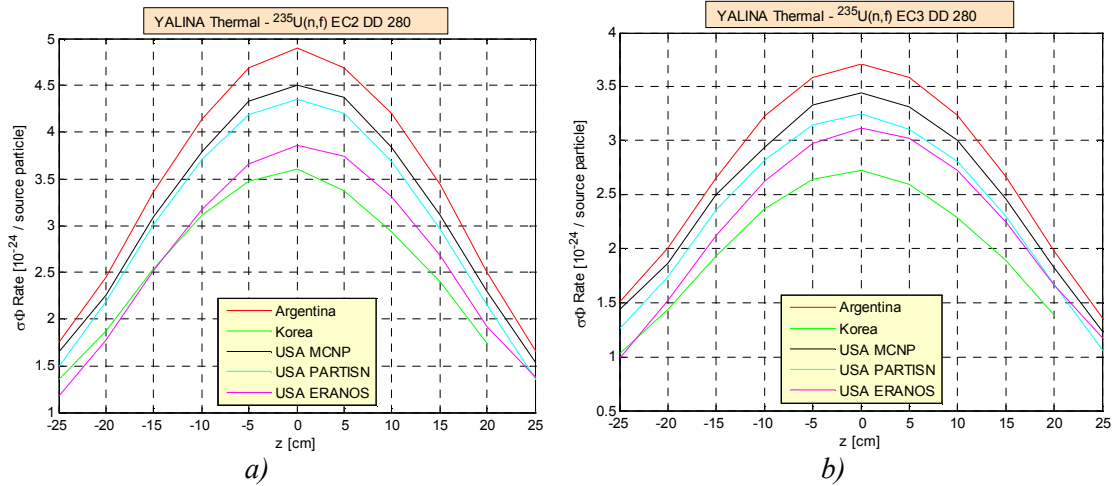


FIG. 3.40. $^{235}\text{U}(n,f)$ reaction rate in EC2 (a) and EC3 (b) experimental channels for the D-D neutron source and 280 configuration (Courtesy of the Argonne National Laboratory, USA).

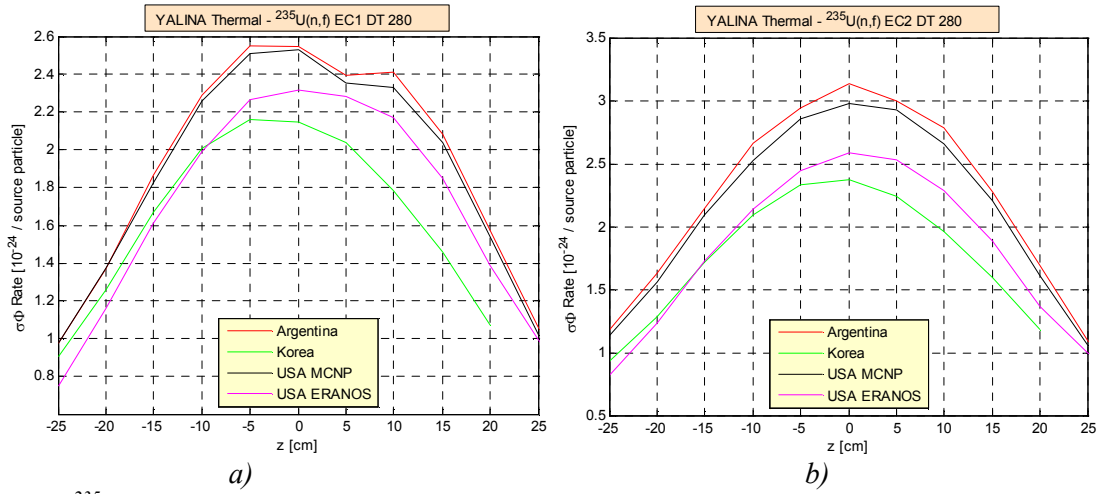


FIG. 3.41. $^{235}\text{U}(n,f)$ reaction rate in EC1 (a) and EC2 (b) experimental channels for the D-T neutron source and 280 configuration (Courtesy of the Argonne National Laboratory, USA).

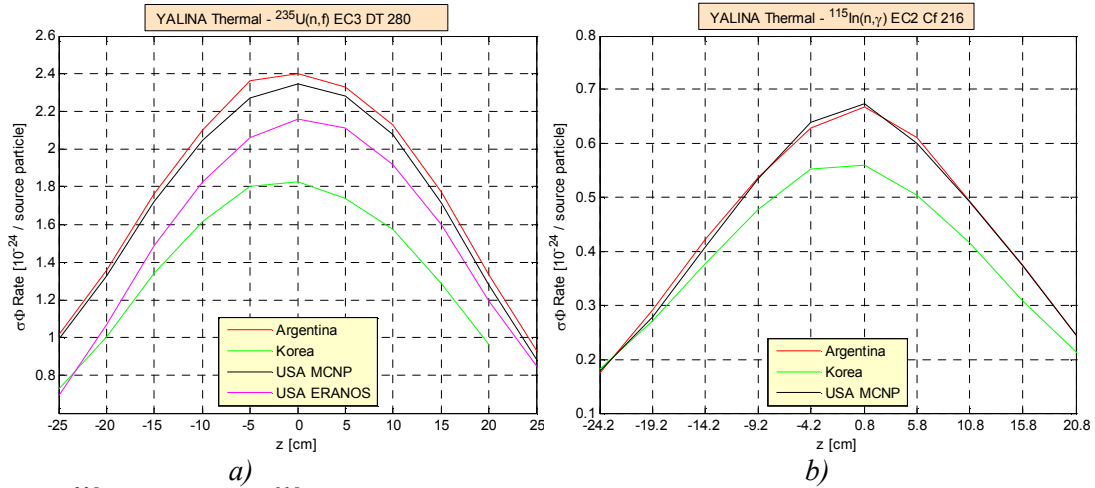


FIG. 3.42. $^{235}\text{U}(n,f)$ (a) and $^{115}\text{In}(n,\gamma)$ (b) reaction rates in EC3 (a) and EC2 (b) experimental channels for D-T (a) and Cf (b) neutron sources and 280 (a) and 216 (b) configurations (Courtesy of the Argonne National Laboratory, USA).

The $^{155}\text{In}(n,\gamma)$, $^{197}\text{Au}(n,\gamma)$, and $^{55}\text{Mn}(n,\gamma)$ reaction rates in the experimental channels EC2 and EC7, obtained with Cf, D-D, and D-T neutron sources, are plotted in Figs 3.42 (b)–3.60. In these calculations the irradiation samples have been modelled explicitly, and therefore the self-shielding effect is included. The values of the reaction rates are proportional to the magnitude of the microscopic cross-sections in the thermal energy region, corresponding to the following order:

$${}^3\text{He}(n,p) > {}^{235}\text{U}(n,f) > {}^{155}\text{In}(n,\gamma) > {}^{197}\text{Au}(n,\gamma) > {}^{55}\text{Mn}(n,\gamma)$$

The source multiplication factors calculated by ERANOS are lower than those obtained by other computer programs; consequently, the ERANOS reaction rates are lower than those obtained by other computer programs. In addition, the reaction rates calculated by deterministic codes do not take into account the self-shielding effect and therefore they overestimate the reaction rates. This explains why in Figs 3.53–3.55 the reactions rates calculated by the ERANOS code are higher than those obtained by the MCNP code. A better match between Monte Carlo and deterministic results has been found when MCNP does not

model the irradiation sample (and the self-shielding effect is not taken into account) [3.11]. The reaction rate profiles in the radial experimental channel EC7 (perpendicular to the fuel rods) show an exponential attenuation rather than a cosine shape.

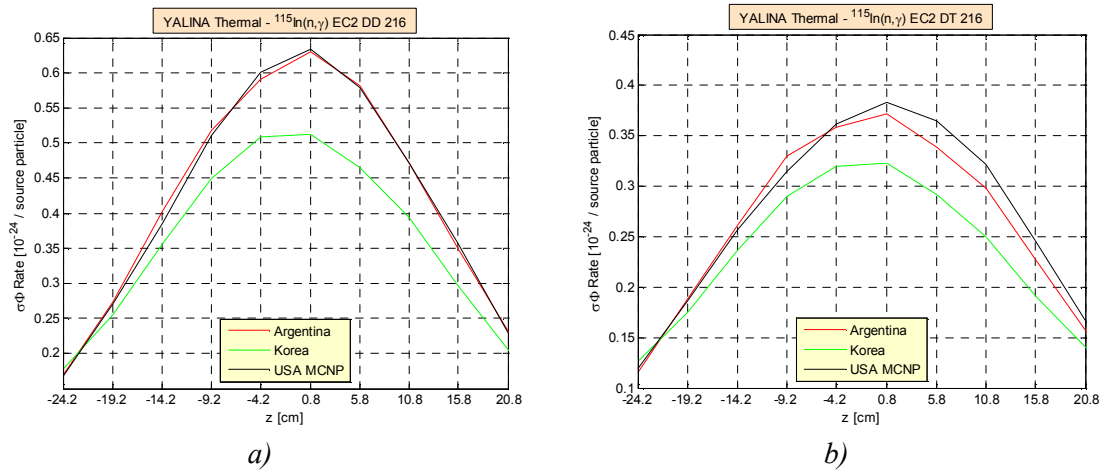


FIG. 3.43. $^{115}\text{In}(n,\gamma)$ reaction rate in EC2 experimental channel for D-D (a) and D-T (b) neutron sources and 216 configuration (Courtesy of the Argonne National Laboratory, USA).

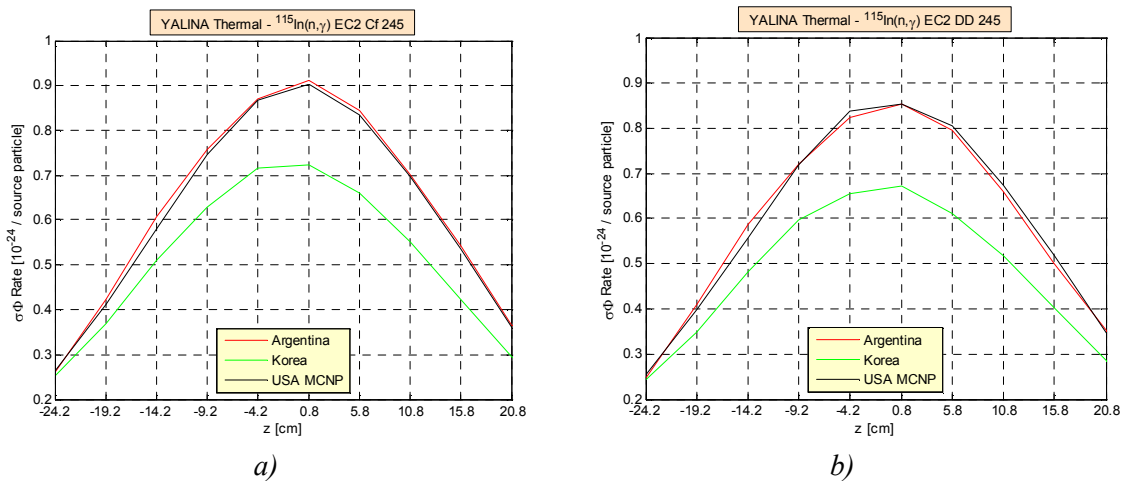
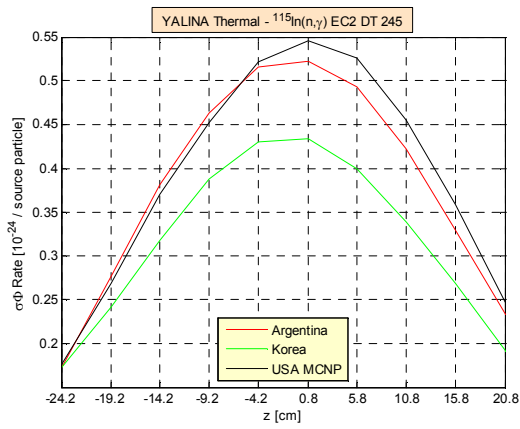
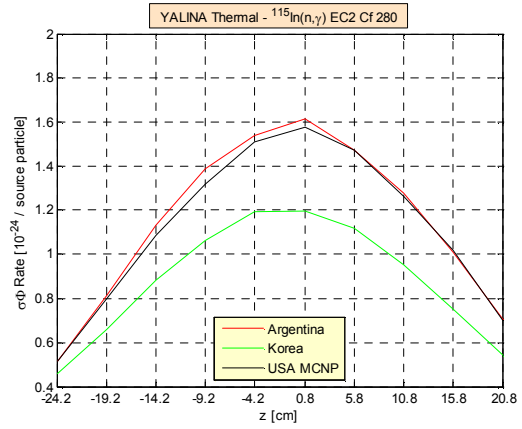


FIG. 3.44. $^{115}\text{In}(n,\gamma)$ reaction rate in EC2 experimental channel for Cf (left plot) and D-D (right plot) neutron sources and 245 configuration (Courtesy of the Argonne National Laboratory, USA).

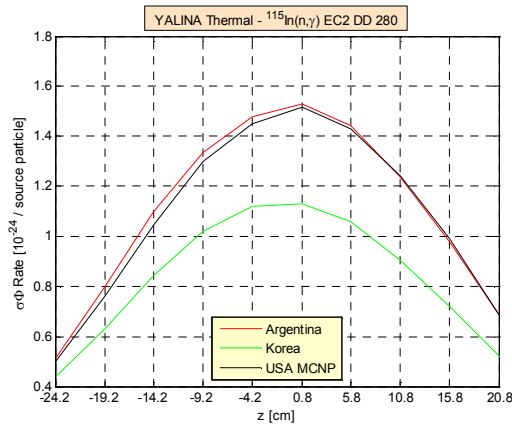


a)

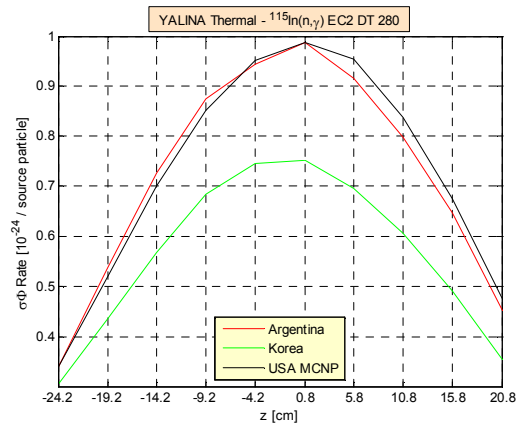


b)

FIG. 3.45. $^{115}\text{In}(n,\gamma)$ reaction rate in EC2 experimental channel for D-T (a) and Cf (b) neutron sources and 245 (a) and 280 (b) configurations (Courtesy of the Argonne National Laboratory, USA).

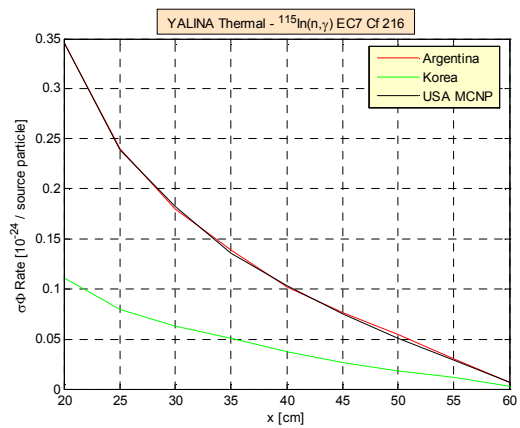


a)

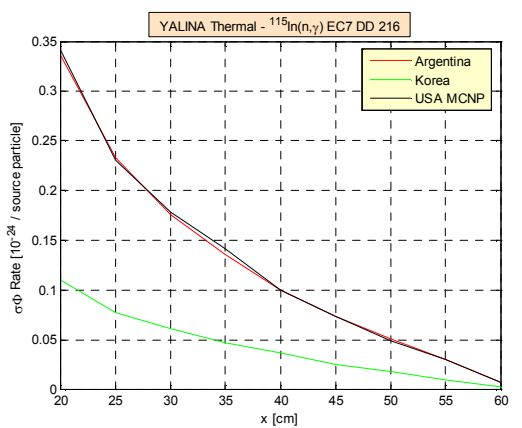


b)

FIG. 3.46. $^{115}\text{In}(n,\gamma)$ reaction rate in EC2 experimental channel for D-D (a) and D-T (b) neutron sources and 280 configuration (Courtesy of the Argonne National Laboratory, USA).

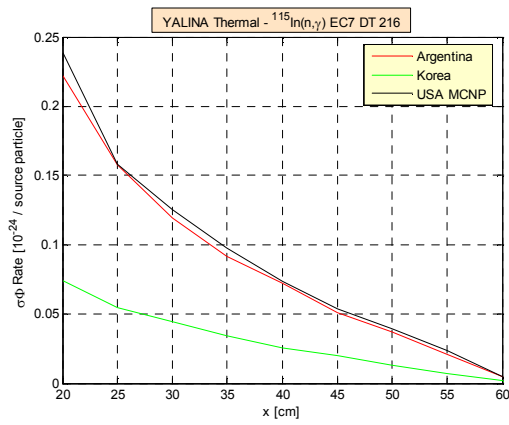


a)

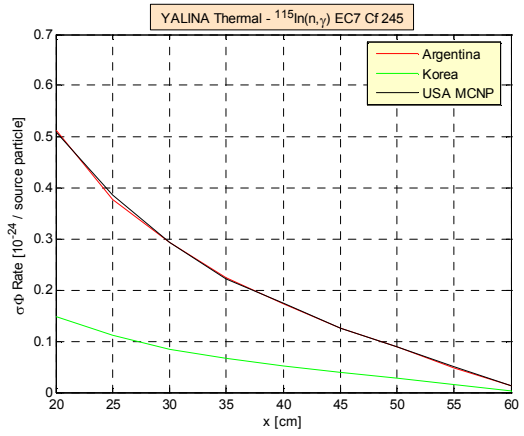


b)

FIG. 3.47. $^{115}\text{In}(n,\gamma)$ reaction rate in EC7 experimental channel for Cf (a) and D-D (b) neutron sources and 216 configuration (Courtesy of the Joint Institute for Power and Nuclear Research – Sosny, National Academy of Sciences of Belarus).

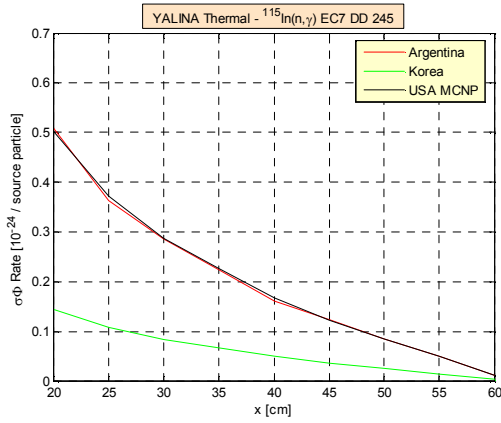


a)

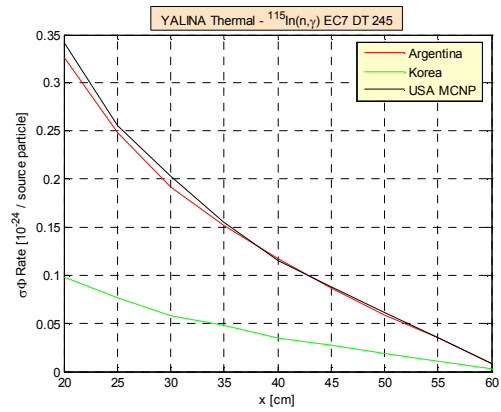


b)

FIG. 3.48. $^{115}\text{In}(n,\gamma)$ reaction rate in EC7 experimental channel for D-T (a) and Cf (b) neutron sources and 216 (a) and 245 (b) configurations (Courtesy of the Argonne National Laboratory, USA).

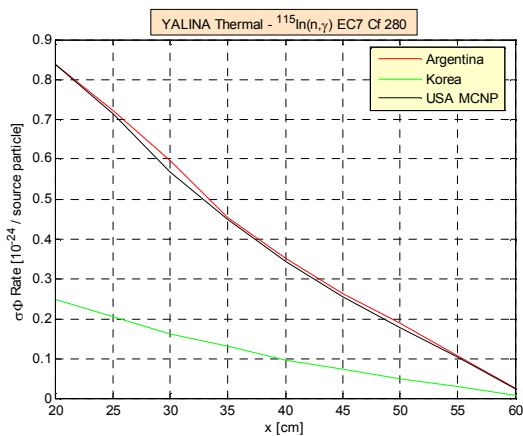


a)

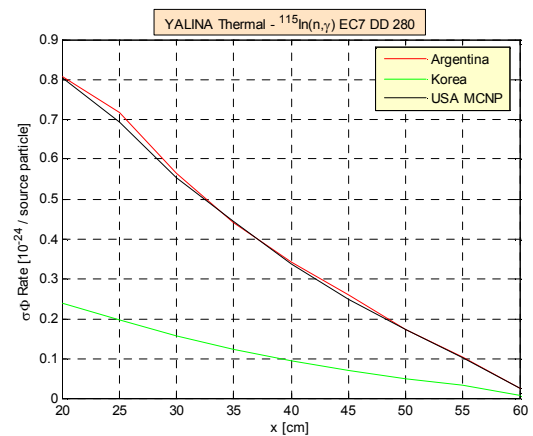


b)

FIG. 3.49. $^{115}\text{In}(n,\gamma)$ reaction rate in EC7 experimental channel for D-D (a) and D-T (b) neutron sources and 245 configuration (Courtesy of the Argonne National Laboratory, USA).

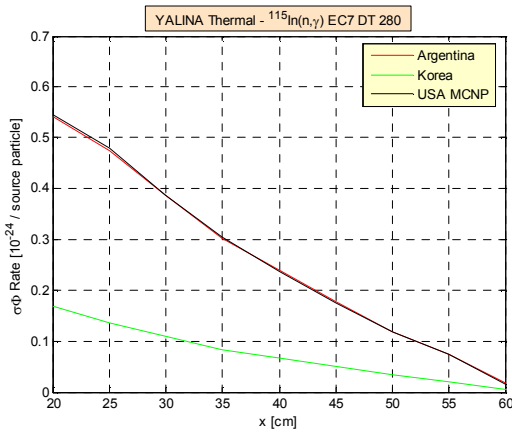


a)

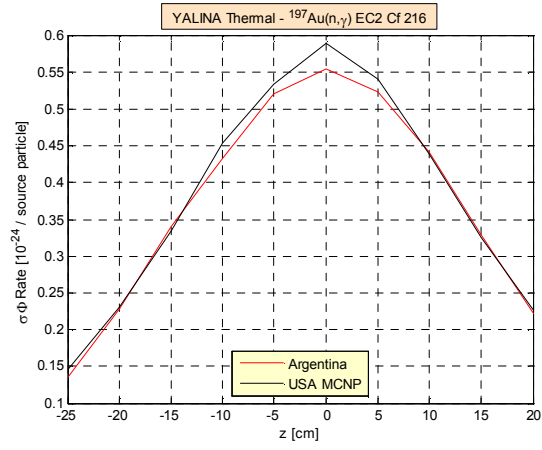


b)

FIG. 3.50. $^{115}\text{In}(n,\gamma)$ reaction rate in EC7 experimental channel for Cf (a) and D-D (b) neutron sources and 280 configuration (Courtesy of the Argonne National Laboratory, USA).

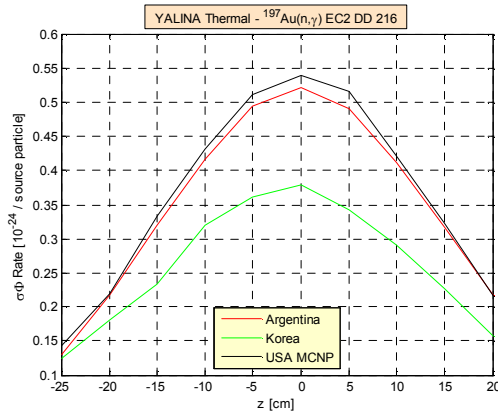


a)

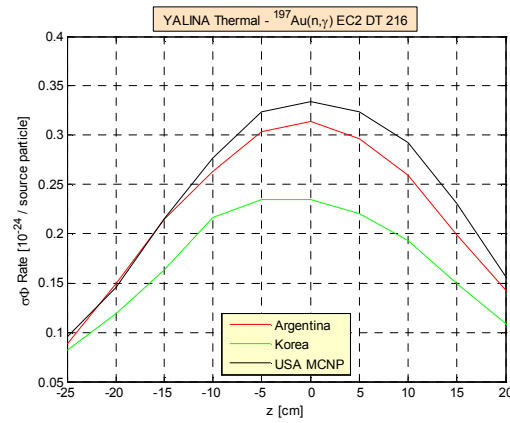


b)

FIG. 3.51. $^{115}\text{In}(n,\gamma)$ (a) and $^{197}\text{Au}(n,\gamma)$ (b) reaction rates in EC7 (a) and EC2 (b) experimental channels for D-T (a) and Cf (b) neutron sources and 280 (a) and 216 (b) configurations (Courtesy of the Argonne National Laboratory, USA).

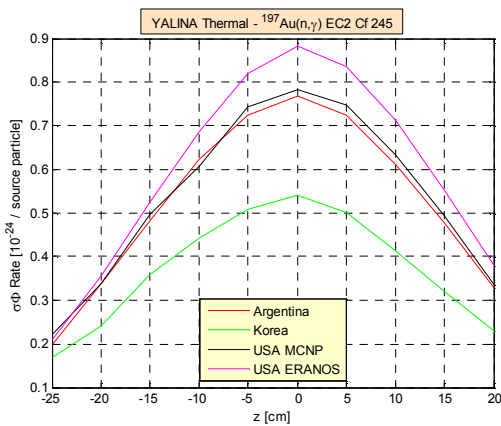


a)

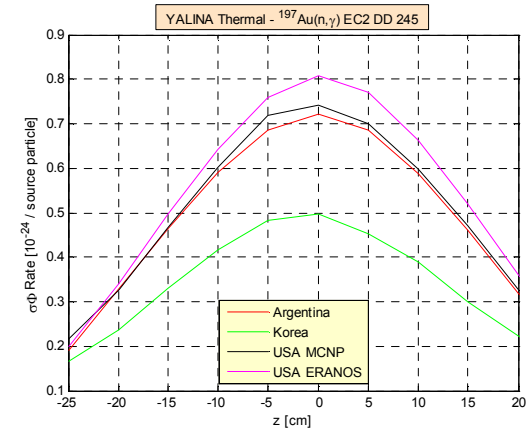


b)

FIG. 3.52. $^{197}\text{Au}(n,\gamma)$ reaction rate in EC2 experimental channel for D-D (a) and D-T (b) neutron sources and 216 configuration (Courtesy of the Argonne National Laboratory, USA).

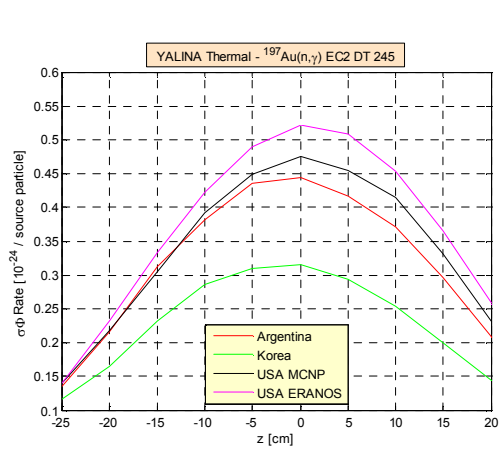


a)

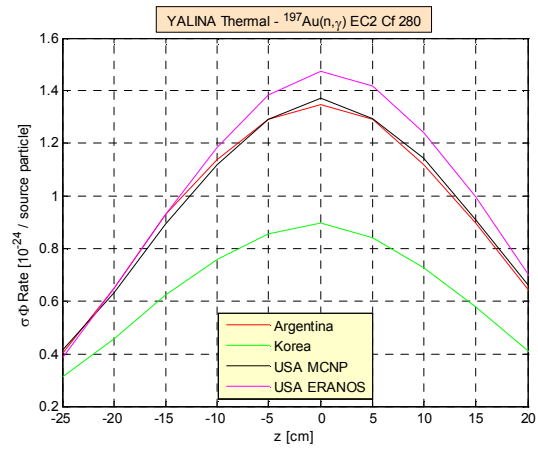


b)

FIG. 3.53. $^{197}\text{Au}(n,\gamma)$ reaction rate in EC2 experimental channel for Cf (a) and D-D (b) neutron sources and 245 configuration (Courtesy of the Argonne National Laboratory, USA).

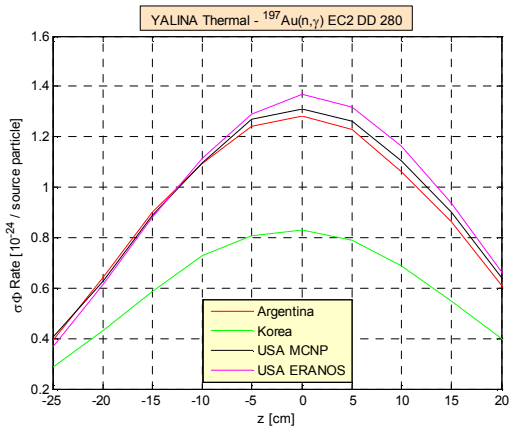


a)

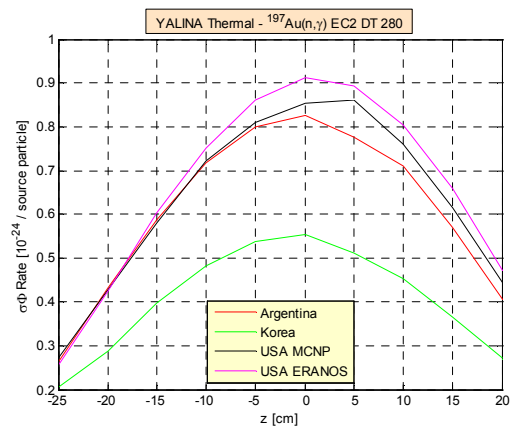


b)

FIG. 3.54. $^{197}\text{Au}(n,\gamma)$ reaction rate in EC2 experimental channel for D-T (a) and Cf (b) neutron sources and 245 (a) and 280 (b) configurations (Courtesy of the Argonne National Laboratory, USA).

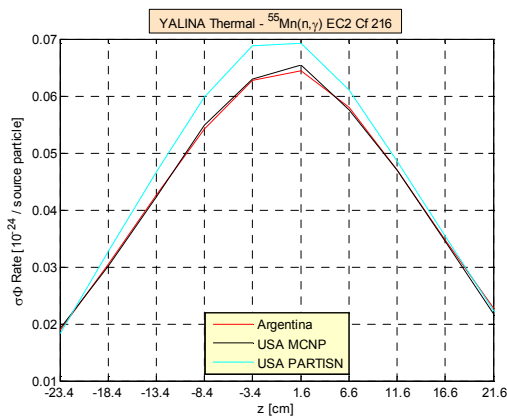


a)

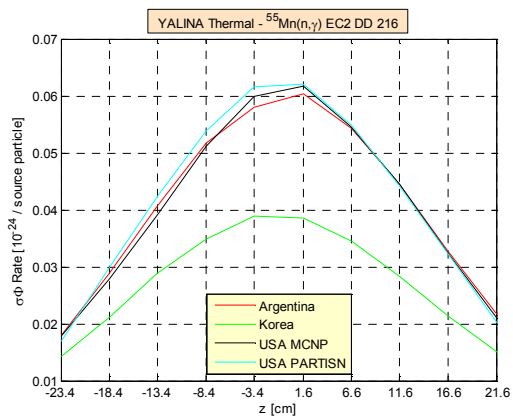


b)

FIG. 3.55. $^{197}\text{Au}(n,\gamma)$ reaction rate in EC2 experimental channel for D-D (a) and D-T (b) neutron sources and 280 configuration (Courtesy of the Argonne National Laboratory, USA).

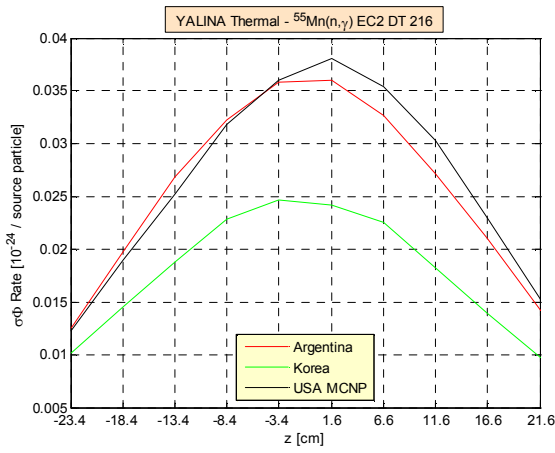


a)

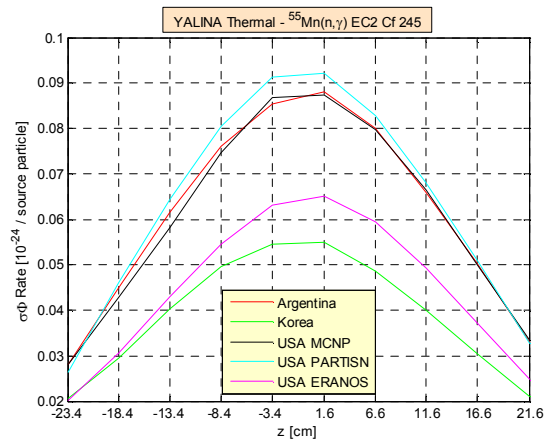


b)

FIG. 3.56. $^{55}\text{Mn}(n,\gamma)$ reaction rate in EC2 experimental channel for Cf (a) and D-D (b) neutron sources and 216 configuration (Courtesy of the Argonne National Laboratory, USA).

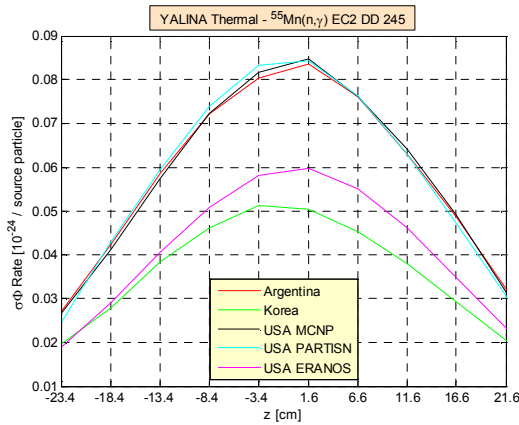


a)

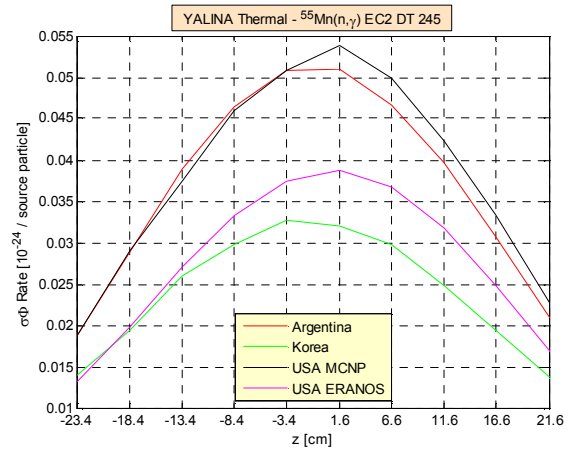


b)

FIG. 3.57. $^{55}\text{Mn}(n,\gamma)$ reaction rate in EC2 experimental channel for D-T (a) and Cf (b) neutron sources and 216 (a) and 245 (b) configurations (Courtesy of the Argonne National Laboratory, USA).

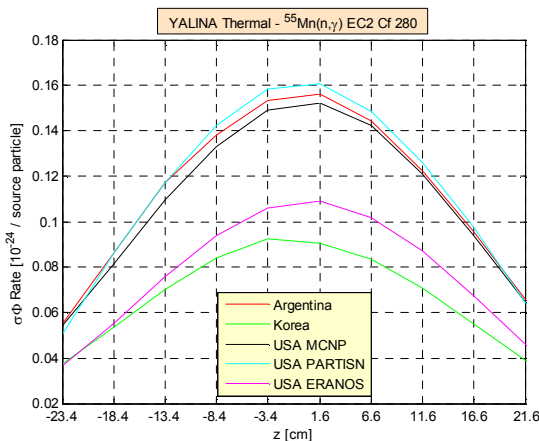


a)

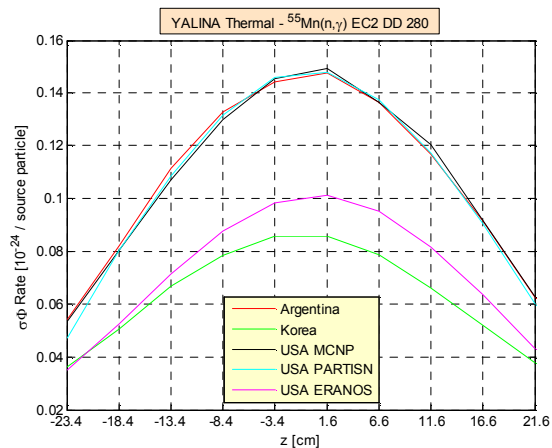


b)

FIG. 3.58. $^{55}\text{Mn}(n,\gamma)$ reaction rate in EC2 experimental channel for D-D (a) and D-T (b) neutron sources and 245 configuration (Courtesy of the Argonne National Laboratory, USA).



a)



b)

FIG. 3.59. $^{55}\text{Mn}(n,\gamma)$ reaction rate in EC2 experimental channel for Cf (a) and D-D (b) neutron sources and 280 configuration (Courtesy of the Argonne National Laboratory, USA).

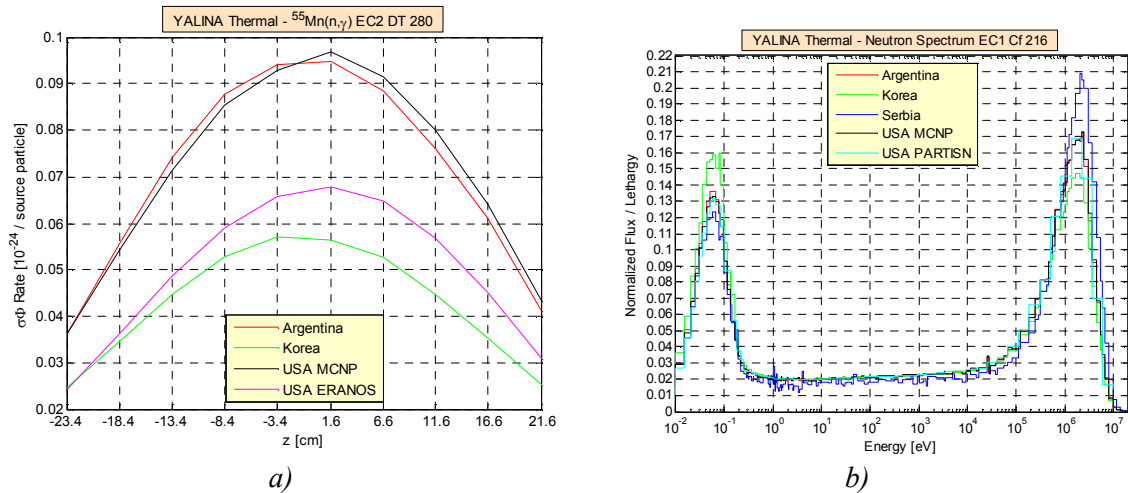


FIG. 3.60. $^{55}\text{Mn}(n,\gamma)$ reaction rate in EC2 experimental channel for D-T neutron source (a); neutron spectrum in EC1 experimental channel for the Cf neutron source and 216 configuration (b) (Courtesy of the Argonne National Laboratory, USA).

The results obtained by Republic of Korea used the ENDF/B-VII.0 nuclear data library; in this library the data of $^3\text{He}(n,p)$, $^{235}\text{U}(n,f)$, $^{115}\text{In}(n,\gamma)$, $^{197}\text{Au}(n,\gamma)$, and $^{55}\text{Mn}(n,\gamma)$ cross-sections were evaluated in the following years: 1990, 2006, 2006, 2006, and 2000, respectively [3.9]. The results of Argentina and USA MCNP used the ENDF/B-VI (different modes) nuclear data library; in this library, the data of $^3\text{He}(n,p)$, $^{235}\text{U}(n,f)$, $\text{In}(n,\gamma)$, $^{197}\text{Au}(n,\gamma)$, and $^{55}\text{Mn}(n,\gamma)$ cross-sections were evaluated in the following years: 1965, 1990, 1997, 1984, and 1988, respectively [3.3, 3.9]. In addition, the ENDF/B-VI library contains only data for natural indium whereas the ENDF/B-VII.0 library contains data for ^{115}In . These differences account for the difference in the obtained results between the Republic of Korean results and the others.

3.4.3. Neutron Spectrum

The neutron spectra in the EC1, EC2, EC3, EC5, and EC6 experimental channels of the YALINA Thermal facility from Cf, D-D, and D-T neutron sources are illustrated in Figs 3.60 (b) – 3.82. In these figures, the neutron spectra have been sampled using 172 energy groups and the neutron flux has been first normalized to unity and then to lethargy. Generally, there is quite a good agreement between the neutron spectra obtained by the various Member States. In the Republic of Korean calculations, Figs 3.63 and 3.66 show that the D-D and the D-T neutron sources are not mono-energetic. The following observations can be seen from the obtained results:

- The neutron spectrum in the experimental channel is further thermalized as the distance between the neutron source and the experimental channel increases;
- The thermal neutron flux in the EC3, EC5, and EC6 experimental channels increases as the number of the fuel rods in the assembly decreases. The fuel mass decreases but the polyethylene and graphite mass do not change, which increases the mass ratio of the reflector/the moderator relative to the fuel in the assembly;
- The neutron spectrum in the EC2 experimental channel is insensitive to the variation in the number of the fuel rods since this channel is in the middle of the active fuel zone;
- The fast component of the neutron spectrum in the EC1 experimental channel increases as the number of the fuel rods decreases. This channel is very close to the neutron source. The decrease of the fuel mass in the assembly enhances the contribution from

the external neutron source, which emits fast neutrons. In addition, the neutron multiplication is decreased, which enhances the external neutron contribution in this channel;

- In all experimental channels, the neutron spectra due to the Cf, D-D or D-T neutron source are very similar except for the peaks at 2.45 MeV for the D-D neutron source and at 14.1 MeV for the D-T neutron source. The relative contribution of the peak to the neutron spectrum increases as the number of fuel rods decreases and/or the channel distance from the source decreases;
- The D-T neutron source peak is visible in all the experimental channels, including the ones in the reflector. This indicates that a fraction of the D-T source neutrons reaches all the experimental channels.

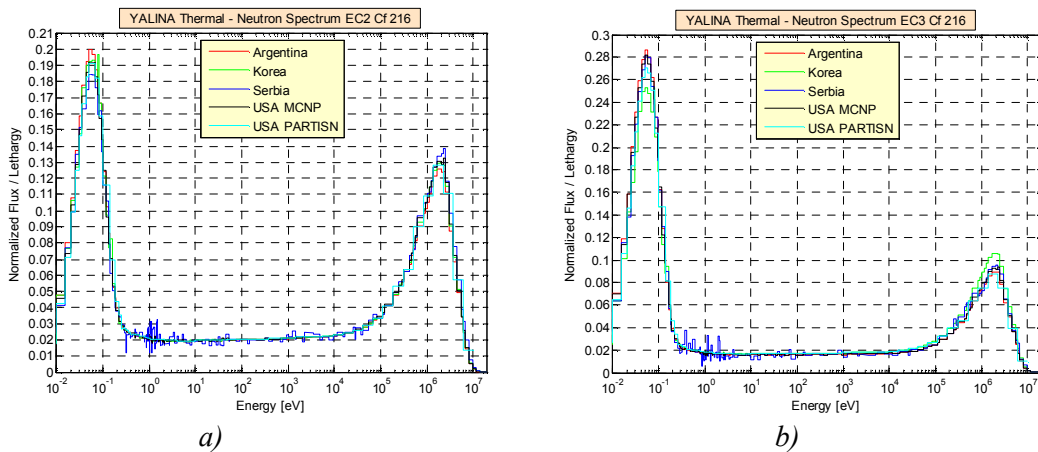


FIG. 3.61. Neutron spectrum in EC2 (a) and EC3 (b) experimental channels for the Cf neutron source and 216 configuration (Courtesy of the Argonne National Laboratory, USA).

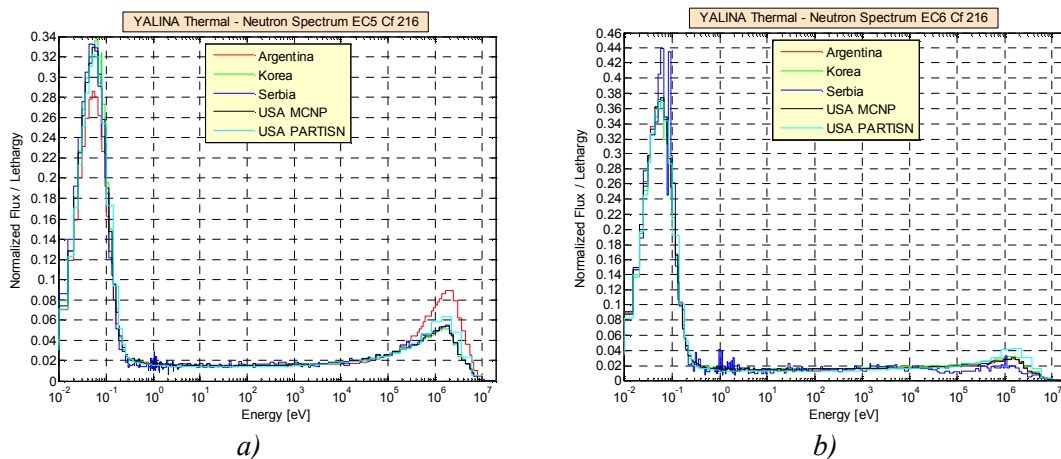
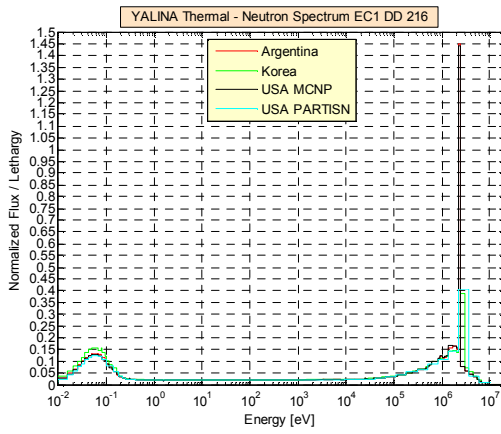
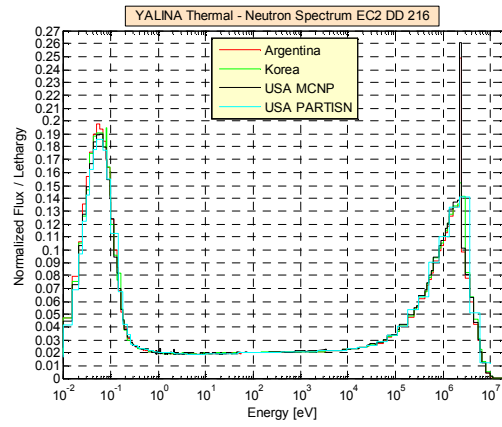


FIG. 3.62. Neutron spectrum in EC5 (a) and EC6 (b) experimental channels for the Cf neutron source and 216 configuration (Courtesy of the Argonne National Laboratory, USA).

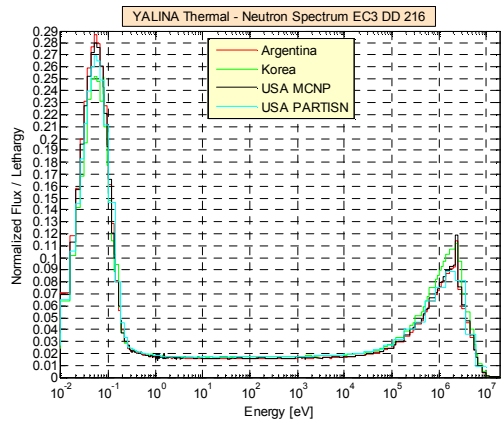


a)

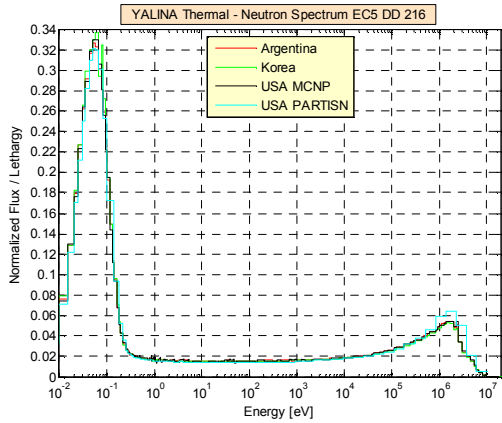


b)

FIG. 3.63. Neutron spectrum in EC1 (a) and EC2 (b) experimental channels for the D-D neutron source and 216 configuration Courtesy of the Argonne National Laboratory, USA).

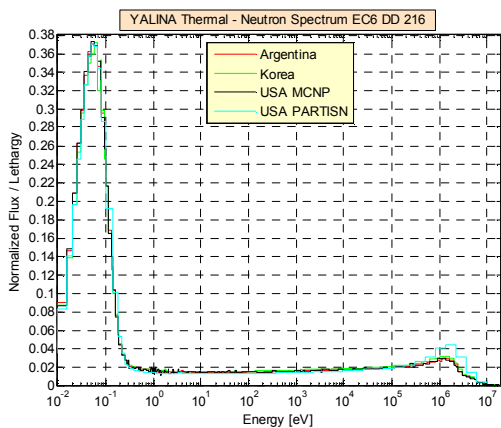


a)

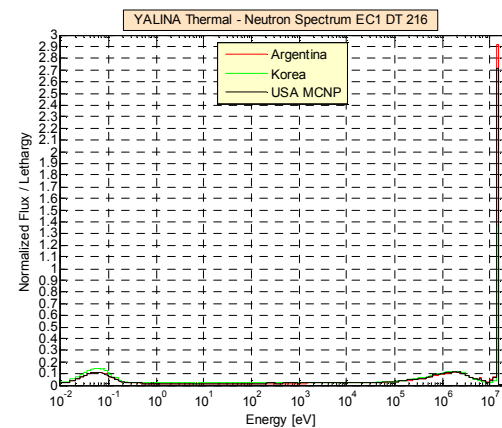


b)

FIG. 3.64. Neutron spectrum in EC3 (a) and EC5 (b) experimental channels for the D-D neutron source and 216 configuration (Courtesy of the Argonne National Laboratory, USA).

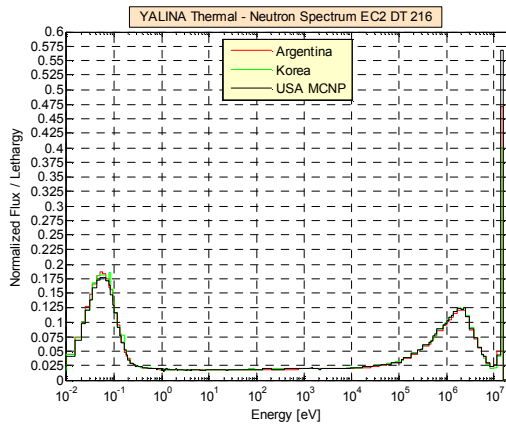


a)

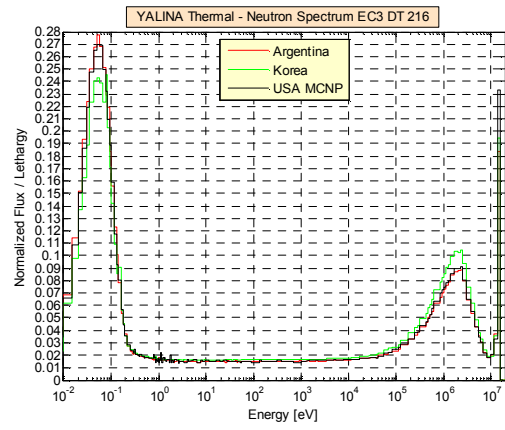


b)

FIG. 3.65. Neutron spectrum in EC6 (a) and EC1 (b) experimental channels for D-D (a) and D-T (b) neutron sources and 216 configuration (Courtesy of the Argonne National Laboratory, USA).

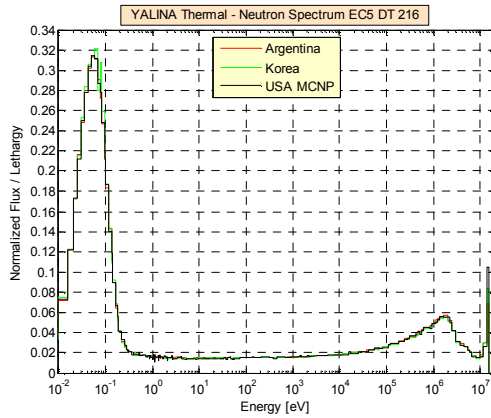


a)

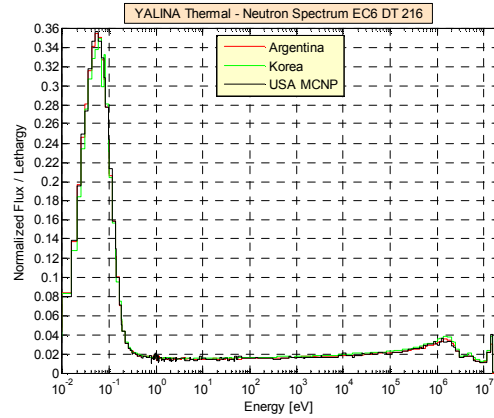


b)

FIG. 3.66. Neutron spectrum in EC2 (a) and EC3 (b) experimental channels for the D-T neutron source and 216 configuration (Courtesy of the Argonne National Laboratory, USA).

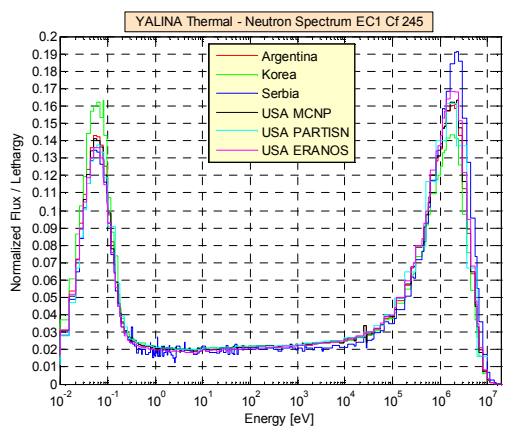


a)

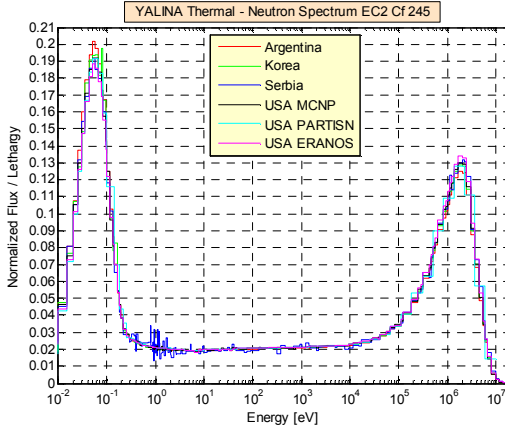


b)

FIG. 3.67. Neutron spectrum in EC5 (a) and EC6 (b) experimental channels for the D-T neutron source and 216 configuration (Courtesy of the Argonne National Laboratory, USA).

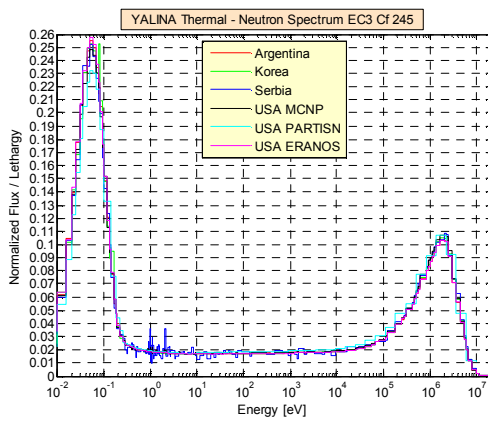


a)

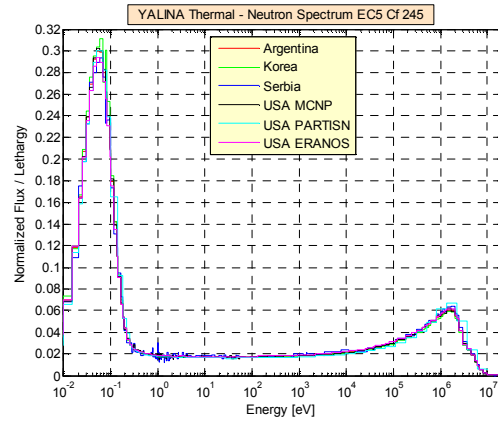


b)

FIG. 3.68. Neutron spectrum in EC1 (a) and EC2 (b) experimental channels for the Cf neutron source and 245 configuration (Courtesy of the Argonne National Laboratory, USA).

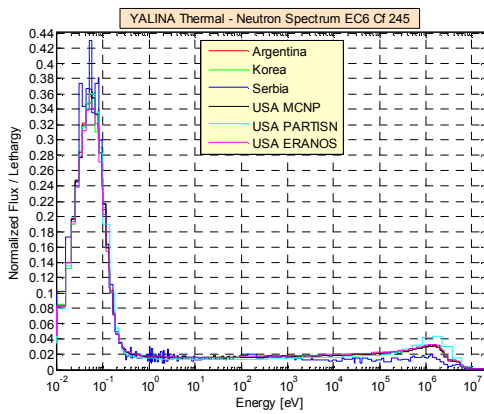


a)

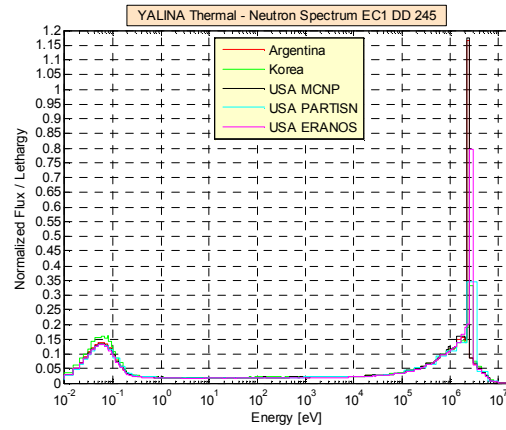


b)

FIG. 3.69. Neutron spectrum in EC3 (a) and EC5 (b) experimental channels for the Cf neutron source and 245 configuration (Courtesy of the Argonne National Laboratory, USA).

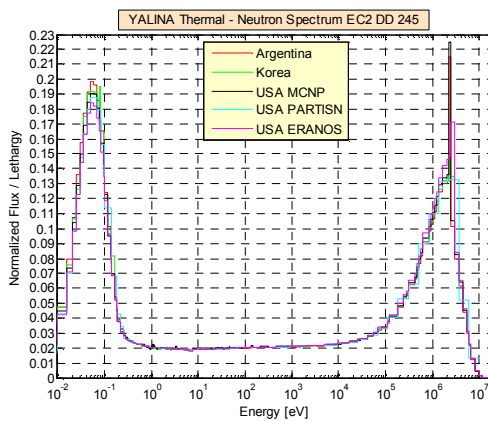


a)

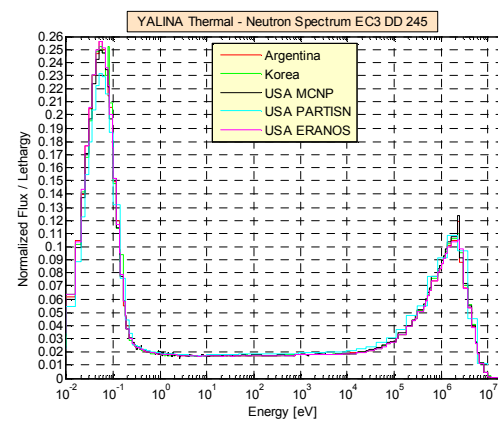


b)

FIG. 3.70. Neutron spectrum in EC6 (a) and EC1 (b) experimental channels for Cf (a) and D-D (b) neutron sources and 245 configuration (Courtesy of the Argonne National Laboratory, USA).

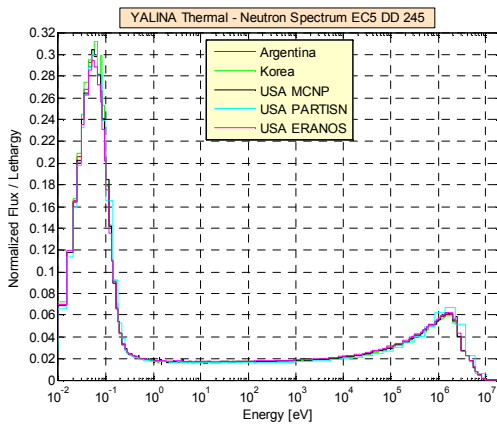


a)

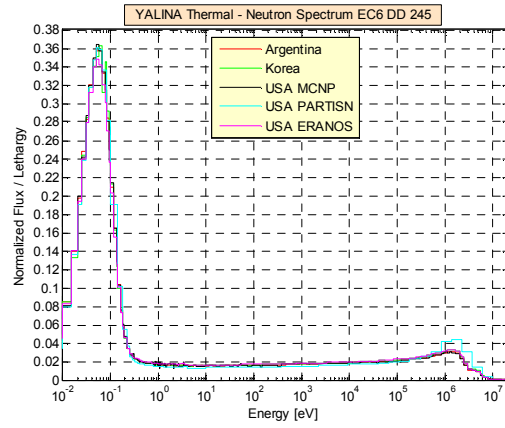


b)

FIG. 3.71. Neutron spectrum in EC2 (a) and EC3 (b) experimental channels for the D-D neutron source and 245 configuration (Courtesy of the Argonne National Laboratory, USA).

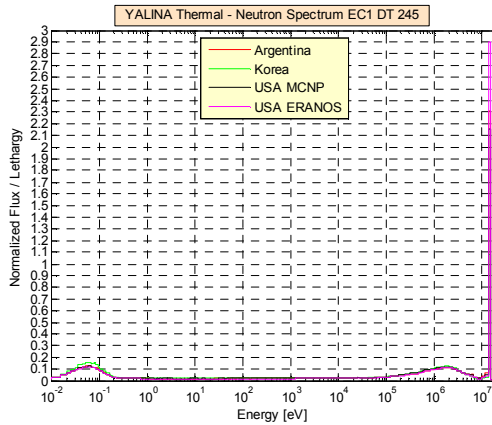


a)

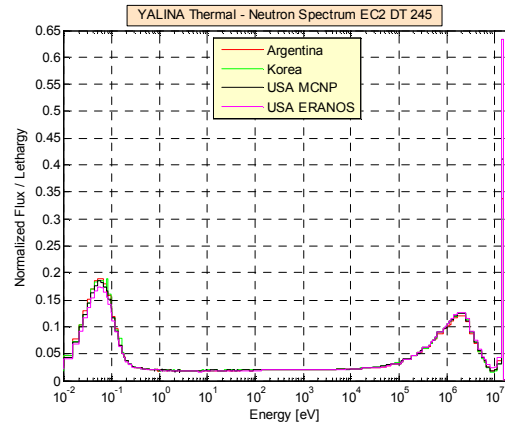


b)

FIG. 3.72. Neutron spectrum in EC5 (a) and EC6 (b) experimental channels for the D-D neutron source and 245 configuration (Courtesy of the Argonne National Laboratory, USA).

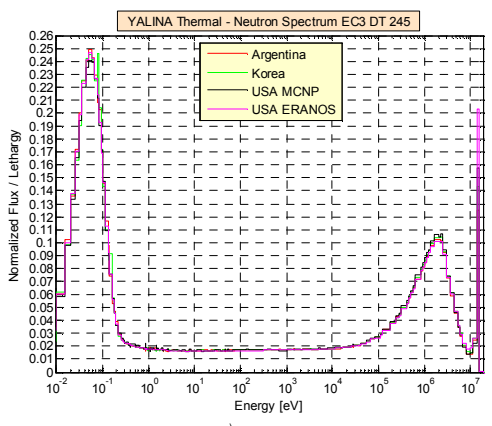


a)

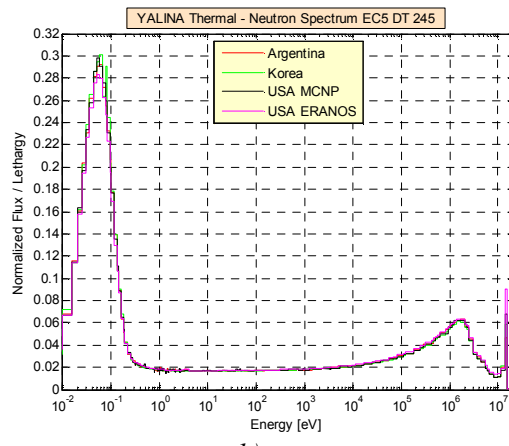


b)

FIG. 3.73. Neutron spectrum in EC1 (a) and EC2 (b) experimental channels for the D-T neutron source and 245 configuration (Courtesy of the Argonne National Laboratory, USA).

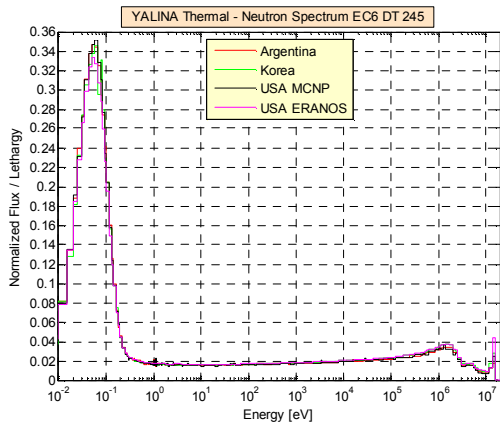


a)

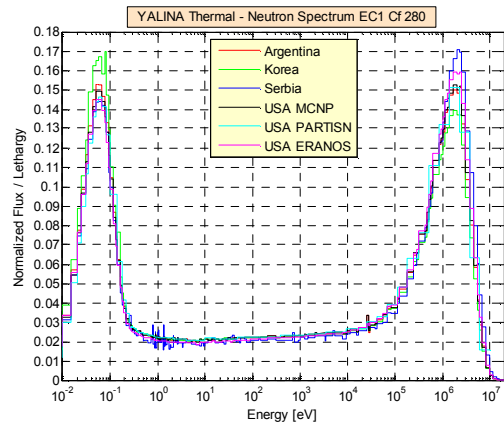


b)

FIG. 3.74. Neutron spectrum in EC3 (a) and EC5 (b) experimental channels for the D-T neutron source and 245 configuration (Courtesy of the Argonne National Laboratory, USA).

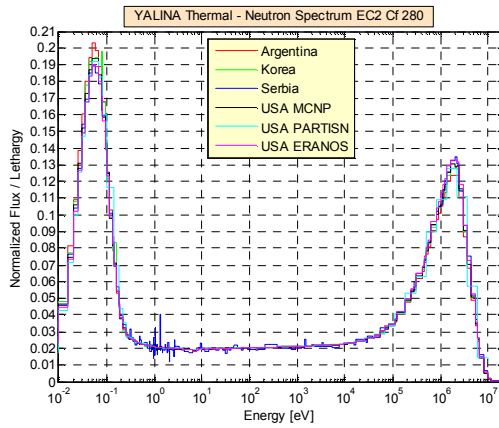


a)

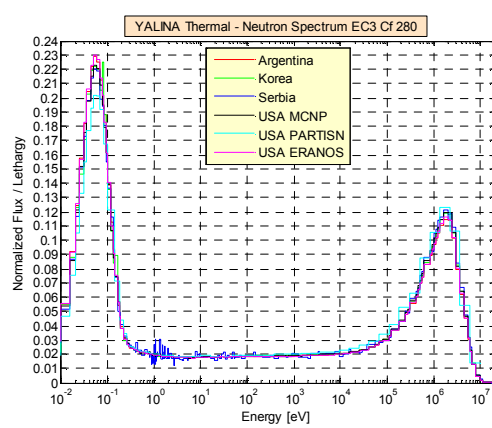


b)

FIG. 3.75. Neutron spectrum in EC6 (a) and EC1 (b) experimental channels for D-T (a) and Cf (b) neutron sources and 245 (a) and 280 (b) configurations (Courtesy of the Argonne National Laboratory, USA).

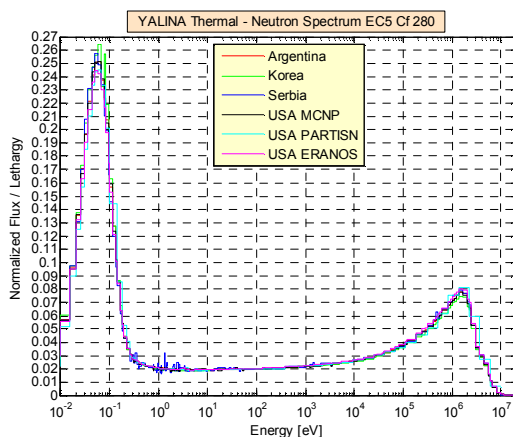


a)

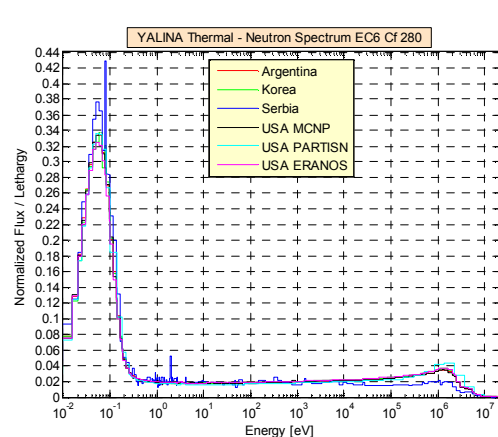


b)

FIG. 3.76. Neutron spectrum in EC2 (a) and EC3 (b) experimental channels for the Cf neutron source and 280 configuration (Courtesy of the Argonne National Laboratory, USA).



a)



b)

FIG. 3.77. Neutron spectrum in EC5 (a) and EC6 (b) experimental channels for the Cf neutron source and 280 configuration (Courtesy of the Argonne National Laboratory, USA).

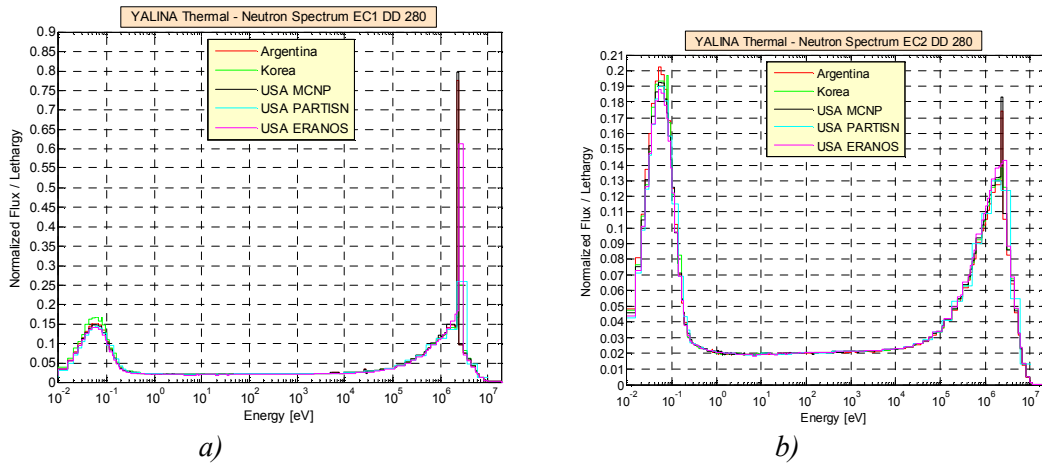


FIG. 3.78. Neutron spectrum in EC1 (a) and EC2 (b) experimental channels for the D-D neutron source and 280 configuration (Courtesy of the Argonne National Laboratory, USA).

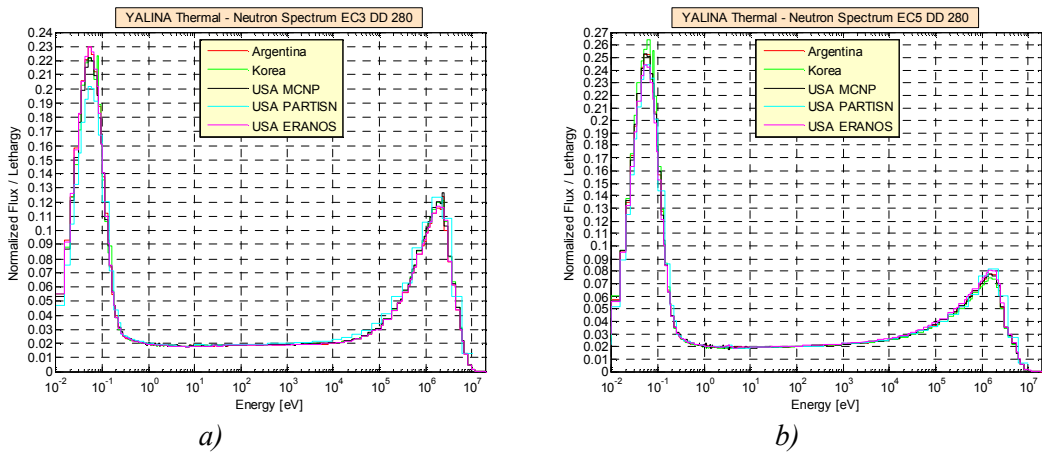


FIG. 3.79. Neutron spectrum in EC3 (a) and EC5 (b) experimental channels for the D-D neutron source and 280 configuration (Courtesy of the Argonne National Laboratory, USA).

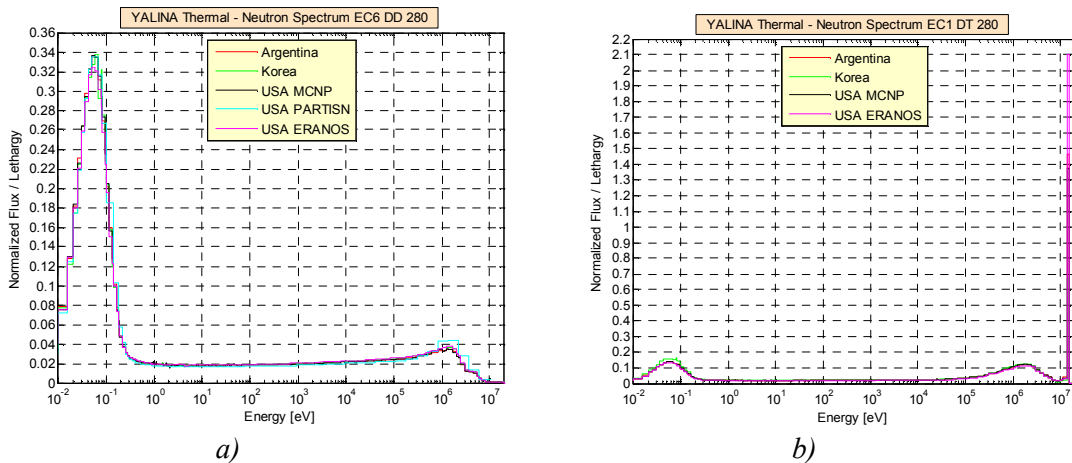


FIG. 3.80. Neutron spectrum in EC6 (a) and EC1 (b) experimental channels for D-D (a) and D-T (b) neutron sources and 280 configuration (Courtesy of the Argonne National Laboratory, USA).

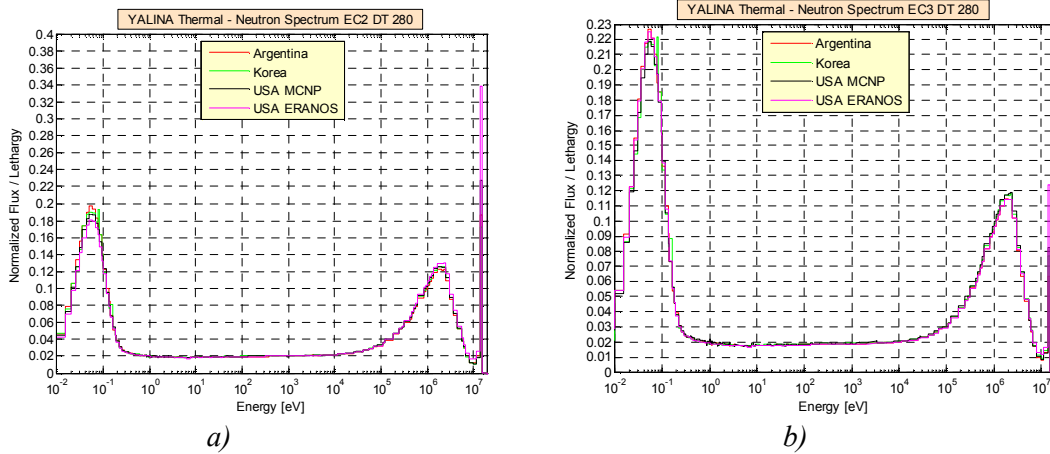


FIG. 3.81. Neutron spectrum in EC2 (a) and EC3 (b) experimental channels for the D-T neutron source and 280 configuration (Courtesy of the Argonne National Laboratory, USA).

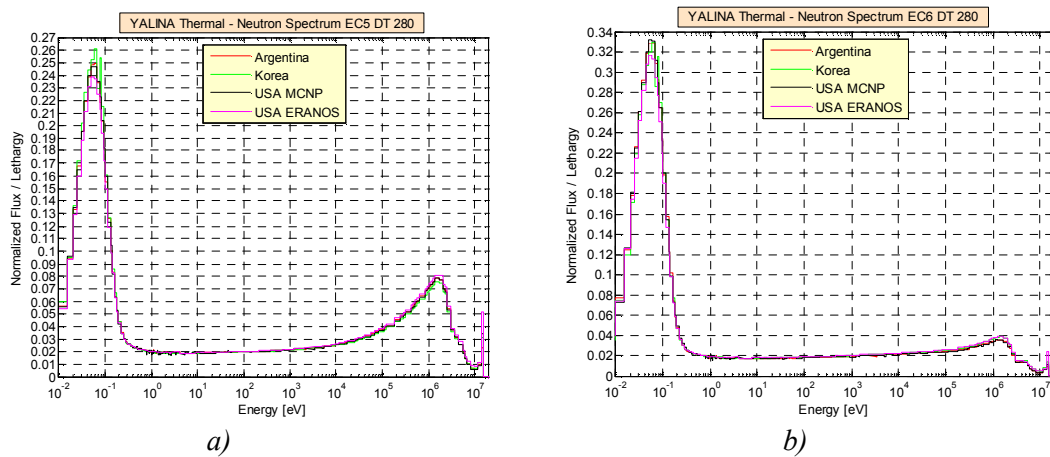
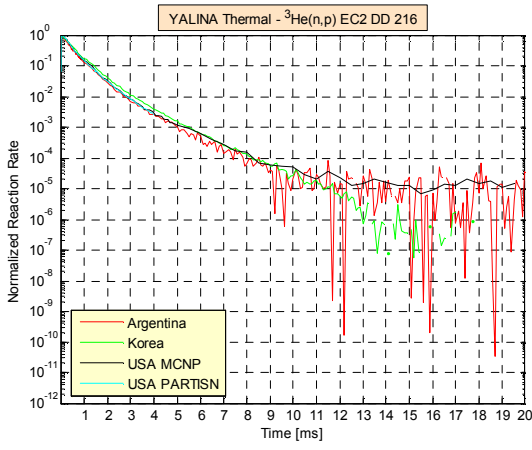


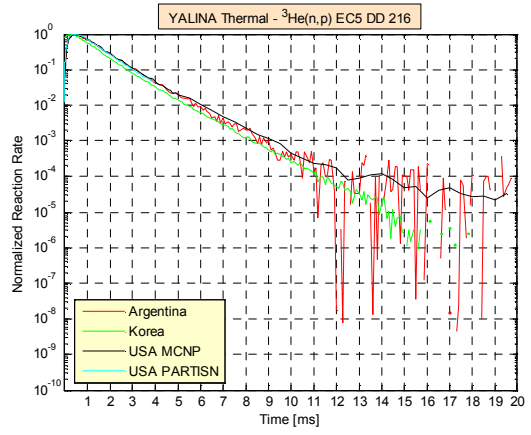
FIG. 3.82. Neutron spectrum in EC5 (a) and EC6 (b) experimental channels for the D-T neutron source and 280 configuration (Courtesy of the Argonne National Laboratory, USA).

3.4.4. Reaction Rates from D-D and D-T Neutron Pulses and Corrected Effective Neutron Multiplication Factor

${}^3\text{He}(n,p)$ and ${}^{235}\text{U}(n,f)$ reaction rates in the EC1, EC2, and EC5 experimental channels for the D-D and D-T neutron pulses for all the three fuel configurations are shown in Figs 3.83–3.91. In these plots, the reaction rates have been normalized to their maximum values from a single $5\ \mu\text{s}$ neutron pulse within 20 ms time period. In some of the plots, the first value of the Korean data has been neglected. The reaction rates calculated by the ERANOS code decay more rapidly than others; this is a direct consequence of the lower multiplication factor computed by ERANOS. The PARTISN curves end at 4 ms since the PARTISN code does not model the delayed neutrons.

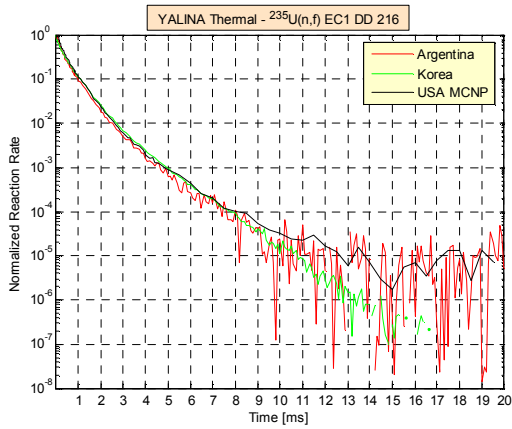


a)

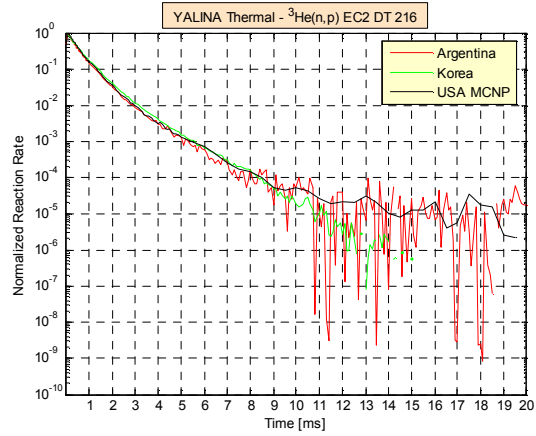


b)

FIG. 3.83. ${}^3\text{He}(n,p)$ reaction rate in EC2 (a) and EC5 (b) experimental channels for the D-D neutron source and 216 configuration (Courtesy of the Argonne National Laboratory, USA).

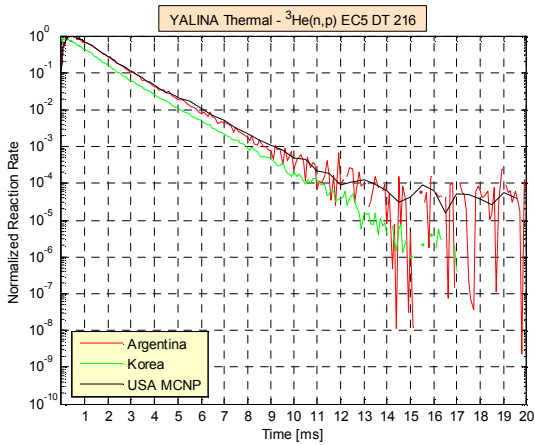


a)

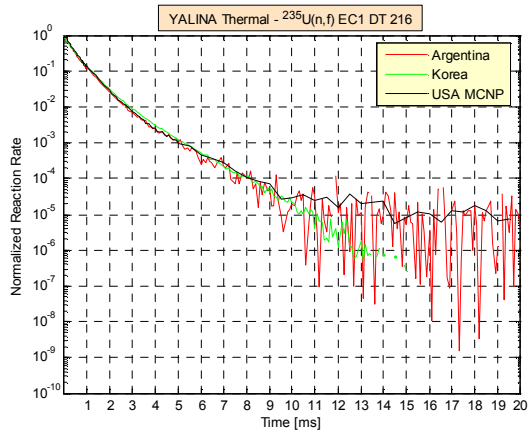


b)

FIG. 3.84. ${}^{235}\text{U}(n,f)$ (a) and ${}^3\text{He}(n,p)$ (b) reaction rates in EC1 (a) and EC2 (b) experimental channels for D-D (a) and D-T (b) neutron sources and 216 configuration (Courtesy of the Argonne National Laboratory, USA).

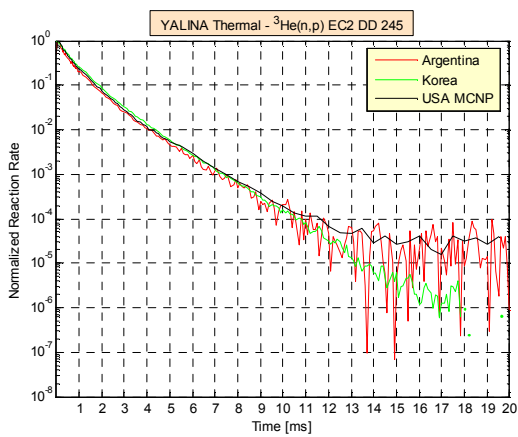


a)

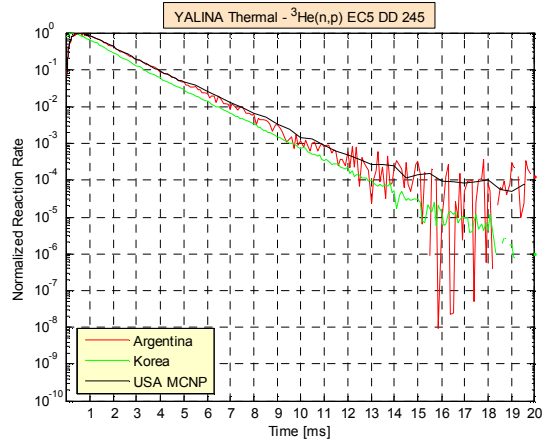


b)

FIG. 3.85. ${}^3\text{He}(n,p)$ (a) and ${}^{235}\text{U}(n,f)$ (b) reaction rates in EC5 (a) and EC1 (b) experimental channels for the D-T neutron source and 216 configuration (Courtesy of the Argonne National Laboratory, USA).

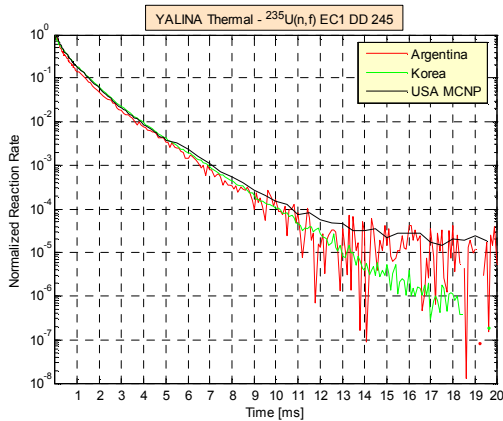


a)

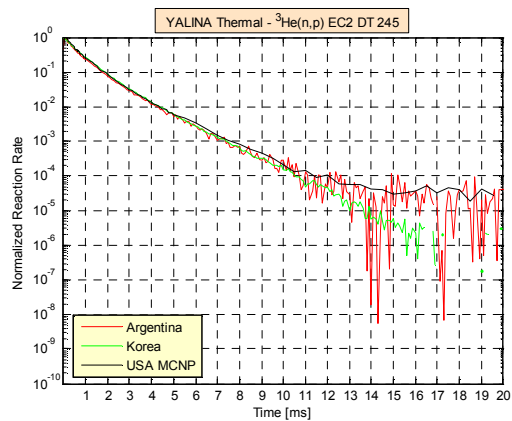


b)

FIG. 3.86. ${}^3\text{He}(n,p)$ reaction rate in EC2 (a) and EC5 (b) experimental channels for the D-D neutron source and 245 configuration (Courtesy of the Argonne National Laboratory, USA).

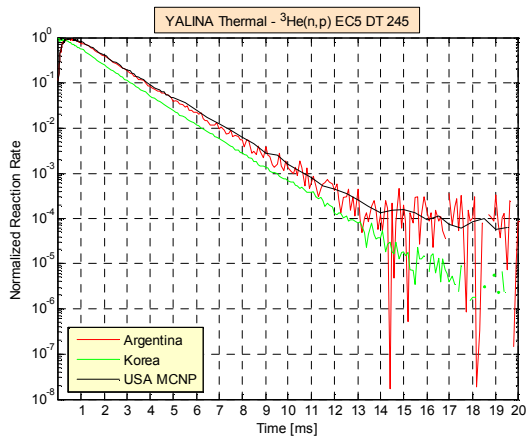


a)

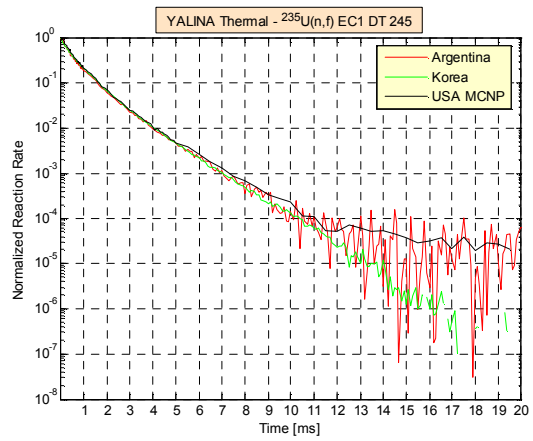


b)

FIG. 3.87. ${}^{235}\text{U}(n,f)$ (a) and ${}^3\text{He}(n,p)$ (b) reaction rates in EC1 (a) and EC2 (b) experimental channels for D-D (a) and D-T (b) neutron sources and 245 configuration (Courtesy of the Argonne National Laboratory, USA).

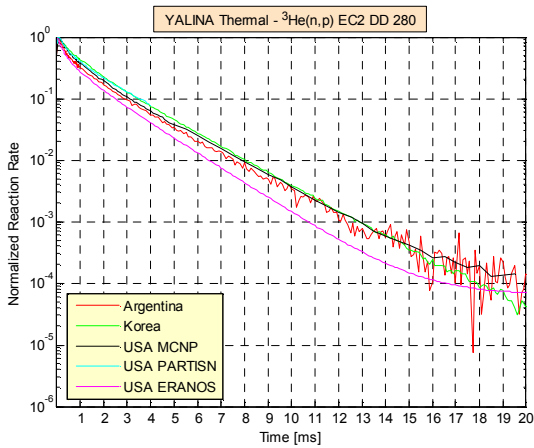


a)

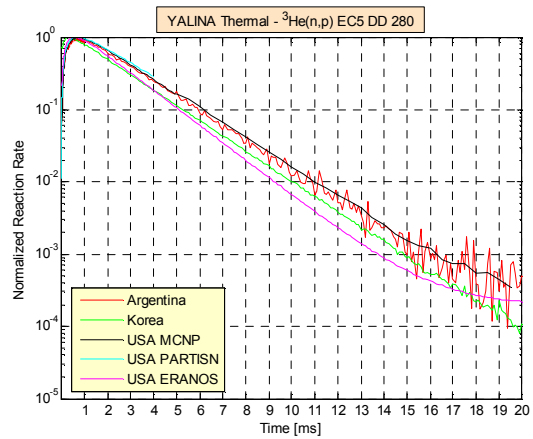


b)

FIG. 3.88. ${}^3\text{He}(n,p)$ (a) and ${}^{235}\text{U}(n,f)$ (b) reaction rates in EC5 (a) and EC1 (b) experimental channels for the D-T neutron source and 245 configuration (Courtesy of the Argonne National Laboratory, USA).

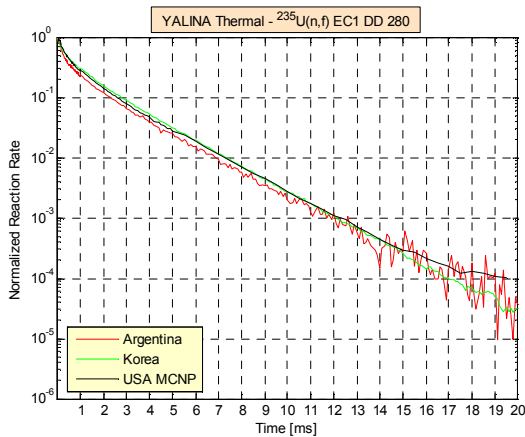


a)

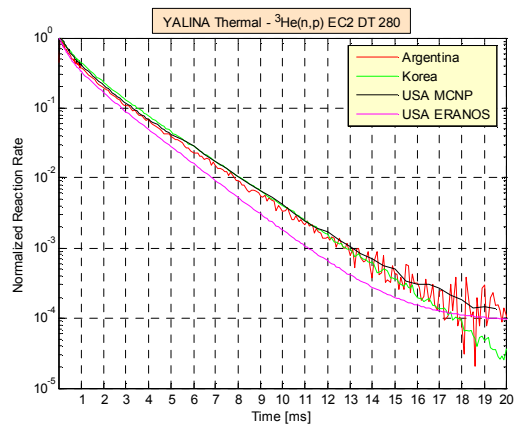


b)

FIG. 3.89. ${}^3\text{He}(n,p)$ reaction rate in EC2 (a) and EC5 (b) experimental channels for the D-D neutron source and 280 configuration (Courtesy of the Argonne National Laboratory, USA).



a)



b)

FIG. 3.90. ${}^{235}\text{U}(n,f)$ (a) and ${}^3\text{He}(n,p)$ (b) reaction rates in EC1 (a) and EC2 (b) experimental channels for D-D (a) and D-T (b) neutron sources and 280 configuration (Courtesy of the Argonne National Laboratory, USA).

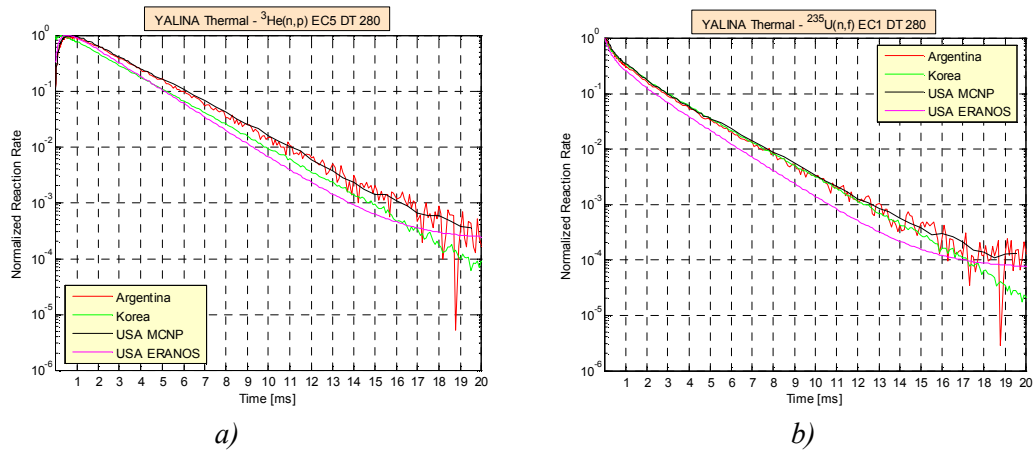


FIG. 3.91. $^3\text{He}(n,p)$ (a) and $^{235}\text{U}(n,f)$ (b) reaction rates in EC5 (a) and EC1 (b) experimental channels for the D-T neutron source and 280 configuration (Courtesy of the Argonne National Laboratory, USA).

The comparison between MCNPX, PARTISN, and experimental results for the $^3\text{He}(n,p)$ dependent reaction rate are shown in Fig. 3.92 for the 245 and 280 configurations. In the reaction rate plots, the maximum of the experimental values has been normalized to the maximum of the MCNPX values since the external neutron source strength has not been measured in the experiments. In these calculations and experiments, the beam tube has been removed from the assembly and replaced by air. Generally, the comparison between the deterministic, the Monte Carlo, and the experimental results shows a good agreement. At the centre of the EC1 experimental channel, which is close to the neutron source, the small difference between MCNPX and PARTISN is due to the difference in the neutron source modelling and the material homogenizations.

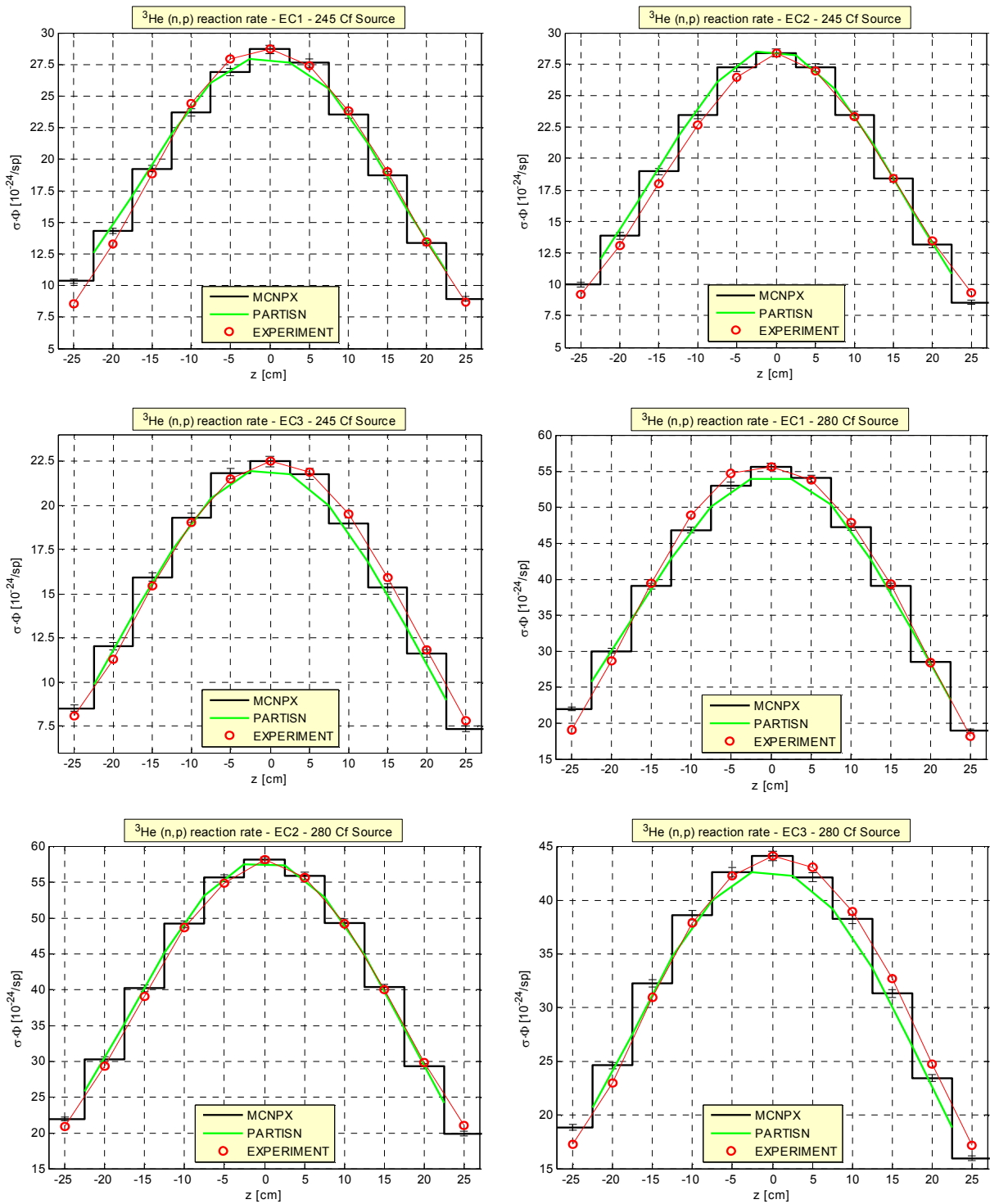


FIG. 3.92. Comparison of MCNPX, PARTISN and experimental results for the ^3He reaction rate in the EC1 and EC2 experimental channels of YALINA thermal with 245 and 280 fuel rods for the Cf neutron source (Courtesy of the Argonne National Laboratory, USA).

The time-dependent reaction rates show that the delay of the peak value increases as the distance between the external neutron source and the experimental channel increases as shown in Fig. 3.93. This delay arises from the time required for the neutrons to reach the detector position from the external neutron source location. The contribution of delayed neutrons to the reaction rate increases with the increase of the number of the fuel rods. Source

neutrons contribute only to the prompt reaction rate; therefore, when the number of fuel rods increases, the delayed-neutron contribution to the reaction rate increases and the prompt neutron contribution decreases.

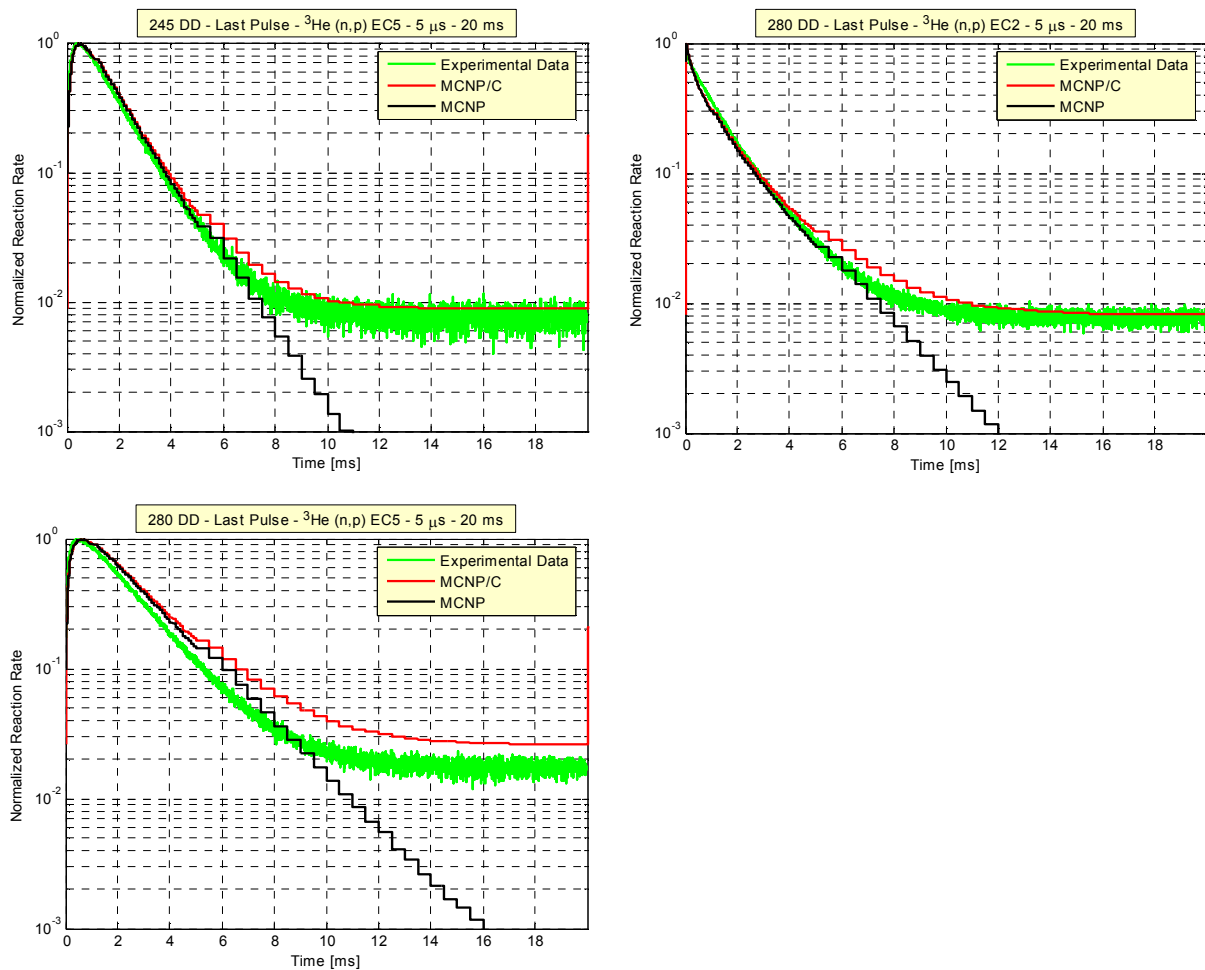


FIG. 3.93. ³He(n,p) reaction rate in the EC2 and EC5 experimental channels of YALINA thermal with 245 and 280 fuel rods from the D-D pulsed-neutron source. MCNP legend refers to a single pulse calculation and MCNP/C legend refers to a single pulse calculation including the delayed neutron contribution from a large number of previous pulses (Courtesy of the Argonne National Laboratory, USA).

Table 3.2 summarizes the multiplication factors calculated in criticality mode by the Monte Carlo code MCNPX. The computer simulations have been performed with different detector modelling: a) without any detector; b) with one detector inserted in EC2 or EC5 experimental channel; and c) with two detectors in two different channels: EC2 and EC3 or EC5 and EC6. All the detector models have 0.45 cm radius and 25 cm length. When the detector is placed in the fuel zone (EC2), the multiplication factor diminishes by 300 pcm relative to the values obtained without the detector. The addition of the second detector in the fuel zone (EC2 and EC3) lowers the multiplication factor by 150–180 pcm relative to the values obtained with one detector. The insertion of the detectors in the reflector zone does not change the neutron multiplication factor by much.

TABLE 3.2. NEUTRON MULTIPLICATION FACTOR (k_{eff}) OBTAINED BY MCNP/MCNPX WITH THE ENDF/B-VI.6 LIBRARY FOR YALINA-THERMAL AND WITH 245 AND 280 FUEL RODS, THE STATISTICAL ERROR FOR ONE STANDARD DEVIATION IN PCM

Number of Modelled Detectors	Configuration			
	245		280	
	EC2	EC5	EC2	EC5
No Detector	0.91911 ± 4	0.91911 ± 4	0.95833 ± 7	0.95833 ± 7
1 Detector	0.91578 ± 7	0.91881 ± 8	0.95524 ± 8	0.95801 ± 8
2 Detectors	0.91435 ± 8	0.91874 ± 9	0.95341 ± 7	0.95767 ± 8

Table 3.3 reports the uncorrected experimental k_{eff} and the corrected experimental k_{eff} for the 245 and the 280 configurations. The experimental reactivity has been measured by the area method using the $^3\text{He}(n,p)$ detector with D-D neutron pulses having 5 μs pulse duration and 20 ms period. The experimental measurements have been carried out using two detectors. For EC2 experimental channel, the other detector is located in EC3. For EC5 experimental channel, the other detector is located in EC6. The detector acquiring the reaction rate signal has 0.45 cm radius and 25 cm length. The correction factor has been applied using both the kinetic and the static methods [3.10]. The first case has been investigated with and without modelling of the detector. The results of Table 3.3 show that the difference between the corrected experimental k_{eff} and the MCNP/MCNPX k_{eff} , with the one detector model (second row of Table 3.2), is between 390 and 1170 pcm. The present numerical results have been obtained by MCNPX using the fuel composition of the IAEA benchmark specifications. This composition neglects the presence of ^{234}U and the fuel impurities, which contribute to this difference [3.1]. If the fuel composition is taken into account: ^{234}U mass, impurities, and the average uranium mass per rod from gamma spectroscopy, then the criticality multiplication factor for the configuration with 280 fuel rods decreases from 0.95833 ± 7 to 0.95487 ± 4 [3.10], which matches the experimental results.

TABLE 3.3. NEUTRON MULTIPLICATION FACTOR (k_{eff}) OBTAINED BY PULSED-NEUTRON-SOURCE EXPERIMENTS USING THE AREA METHOD, THE STATISTICAL ERROR FOR ONE STANDARD DEVIATION IN PCM

Correction Type and Number of Modelled Detectors	Configuration			
	245		280	
	EC2	EC5	EC2	EC5
No Correction No Detector	0.92402 ± 410	0.91647 ± 340	0.95072 ± 180	0.94857 ± 230
Kinetic Correction No Detector	0.92464	0.91257	0.95112	0.94596
Kinetic Correction 1 Detector	0.92449	0.91152	0.95136	0.94635
Static Correction 2 Detectors	0.92593 ± 404	0.91198 ± 363	0.95228 ± 176	0.94667 ± 239

3.5. CONCLUSIONS

This Section discussed the results obtained by the Member States participating in the IAEA coordinated research project on Analytical and Experimental Benchmark Analysis on Accelerator Driven Systems, and Low Enriched Uranium Fuel Utilization in Accelerator Driven Subcritical Assembly Systems for the YALINA Thermal facility. Member States used both Monte Carlo and deterministic computational tools to analyse the YALINA Thermal subcritical assembly, including: MCNP5, MCNPX, McCARD, PARTISN, and ERANOS computer programs. All calculations have been performed using the ENDF/B-VI (different modes) nuclear data libraries with the exception of Republic of Korea which used the ENDF/B-VII.0 nuclear data library. Generally, there is a good agreement between the results obtained by all the Member States. Deterministic codes perform space, energy, and angle discretization and materials homogenizations, which introduce approximations affecting the obtained results.

In subcritical assemblies, the neutron multiplication and the detector counting rate depend strongly on the external neutron source. Cf and D-D sources provide similar results since they emit neutrons with similar average energy. D-T neutrons trigger (n,xn) reactions and have a longer mean free path, which increases the neutron leakage if the geometry dimensions of the assembly are small, as in the case of the YALINA-Thermal subcritical assembly. Close to criticality, the effect of the external neutron source diminishes since fission neutrons dominate the neutron population.

REFERENCES TO SECTION 3

- [3.1] GOHAR, Y., SMITH, D.L., YALINA Facility, A Sub-Critical Accelerator-Driven System (ADS) for Nuclear Energy Research. Facility Description and an Overview of the Research Program, Argonne National Laboratory, ANL-10/05, 2010.
- [3.2] MCNP Team, MCNP5.1.40, Los Alamos National Laboratory, LA-UR-05-8617, 2005.
- [3.3] SHIM, H.J., KIM, C.H., Error Propagation Module Implemented in the MC-CARD Monte Carlo Code, *Trans. Am. Nucl. Soc.* **86**, 2002.
- [3.4] PELOWITZ, D.B. et al., MCNPX 2.7a Extensions, Los Alamos National Laboratory, LA-UR-08-7182, 2008.
- [3.5] ALCOUFFE, R.E., BAKER, R.S., DAHL, J.A., TURNER, S.A. and R.C. WARD, PARTISN: A Time Dependent, Parallel Neutral Particle Transport Code System, Los Alamos National Laboratory, LA-UR-08-07258, 2008.
- [3.6] FAVORITE, J., A Brief User's Guide for PARTISN, Los Alamos National Laboratory, LA-UR-08-6339, 2008.
- [3.7] RIMPAULT, G. et al., The ERANOS Code and Data System for Fast Reactor Neutronic Analyses, *Proc. Int. Conf. PHYSOR 2002*, Seoul, Korea, 2002.

- [3.8] LOS-ALAMOS NATIONAL LABORATORY, T-2 Nuclear Information Service, US ENDF/B Libraries, <http://t2.lanl.gov/data/data.html>.
- [3.9] ALIBERTI, G., GOHAR, Y., YALINA Analytical Benchmark Analyses Using the Deterministic ERANOS Code System, Argonne National Laboratory, ANL-09/23, 2009.
- [3.10] TALAMO, A., GOHAR, Y., Deterministic and Monte Carlo Modeling and Analyses of YALINA-Thermal Subcritical Assembly, Argonne National Laboratory, ANL-NE-10/17, 2010.
- [3.11] BRIESMEISTER, J. F., A General Monte Carlo N-Particle Transport Code, Version 4c, Los Alamos National Laboratory, LA-13709-M, 2002.

4. IPEN-MB-01 SUBCRITICAL CONFIGURATIONS BENCHMARK

Contributed by

J.R. Maiorino, T. Carluccio, P.C.R. Rossi, A. Antunes, F.L. de Oliveira and S.M. Lee.
Nuclear Technology Post Graduate School
Instituto de Pesquisas Energeticas e Nucleares – Universidade de Sao Paulo (IPEN-USP),
Sao Paulo,
Brazil

A. Cintas, J.I. Márquez Damián, E.M. Lopasso
División Física de Reactores Avanzados
Unidad de Energía Nuclear (CNEA) – Instituto Balseiro
San Carlos de Bariloche,
Argentina

4.1. INTRODUCTION

Since the Brazilian IPEN-MB-01 reactor [4.1] achieved criticality in 1988, it has been used for several basic reactor physics measurements, such as determinations of spectral indices, reactivity coefficients, critical kinetics parameters, spectrum characterizations, flux measurements, etc. Currently, this facility is involved in the Nuclear Energy Agency (NEA) International Reactor Physics Experiment Evaluation Project (IRPhEP) [4.2].

The IPEN-MB-01 reactor was initially designed to operate in a critical mode with the criticality managed by the control rods. However, by changing the control rods position and/or the amount of fuel pins in the core it is possible to create a subcritical core. Additionally, there is a capability to insert a pulsed, compact neutron generator (D-D, D-T) can into a subcritical loading configuration of the IPEN-MB-01 reactor core. The generator was developed by the Plasma and Ion Source Technology Group at the Lawrence Berkeley National Laboratory. Using this combination of the compact pulsed neutron generator and subcritical core extends the application capacities of the IPEN-MB-01 facility. In this context, a computational benchmark has been established, and analyses performed, that focus on this facility when it is operated in subcritical mode and coupled to a D-D or D-T accelerator external neutron source.

The research carried out for the IPEN-MB-01 subcritical experiments benefited from contributions provided by Argentina, Brazil, China, India, Republic of Korea, Spain Member States for IPEN-MB-01 (Phase I) and Argentina, Belarus, China, Germany, Serbia, Spain, United States of America for IPEN-MB-01 (Phase II).

The present Section summarizes the results obtained from this collaborative research programme. Further details can be found in Refs [4.3] and [4.4].

4.2. FACILITY DESCRIPTION

The Brazilian IPEN-MB-01 facility (Fig. 4.1) is a zero-power reactor (100 Watts) of the light water tank type, consisting of a 28×26 rectangular array of UO_2 fuel pins (4.3 w% ^{235}U enrichment) with stainless steel (SS-304) cladding. As mentioned in the introduction, the IPEN/MB-01 reactor achieved criticality on 9 November, 1988. Since then it has been utilized for basic reactor-physics research.

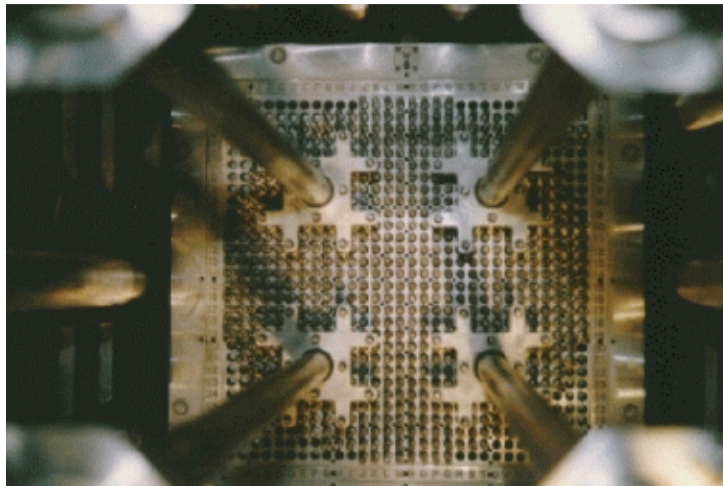


FIG. 4.1. IPEN-MB_01 zero-power reactor (Courtesy of the Energetic and Nuclear Research Institute (IPEN), Brazil).

The moderator tank dimensions (see Fig. 4.2) are 1830 mm diameter and 2750 mm height in the form of an open-top cylinder. The material thickness of the cylinder is 8.5 mm of SS-304. This tank incorporates two valves for rapid water removal in ~5 sec. Demineralized light water (H_2O) serves as the moderator material in the IPEN/MB-01 reactor. During normal operations, the water level is 450 mm above the active part of the reactor core. Laterally, the water layer thickness is larger than 600 mm. The water is at least 530 mm deep beneath the active core.

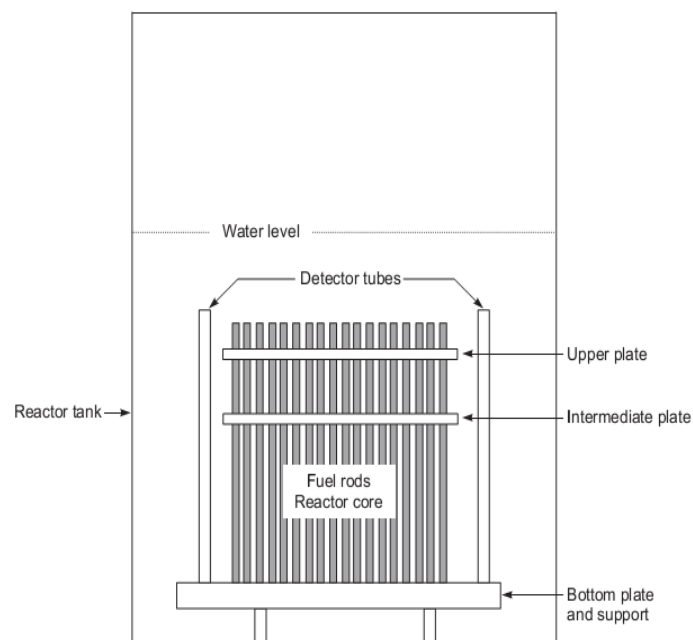


FIG. 4.2. Schematic diagram of the moderator tank (Courtesy of the Energetic and Nuclear Research Institute (IPEN), Brazil).

The lattice configuration for the critical reactor consists of a nearly square, uniform arrangement of stainless-steel-clad cylindrical fuel rods immersed in light water (Fig. 4.3). The pitch of these rods is 15.0 mm, close to the optimal pitch for maximum k_{∞} . The facility is controlled by two control rod banks (labelled A and B in Fig. 4.3) that consist of 12 Ag-In-Cd pins. Also, there are two Safety Rods banks (labelled S in Fig. 4.3). Each of them is comprised of 12 B₄C pins. These are normally withdrawn from the core during operation.

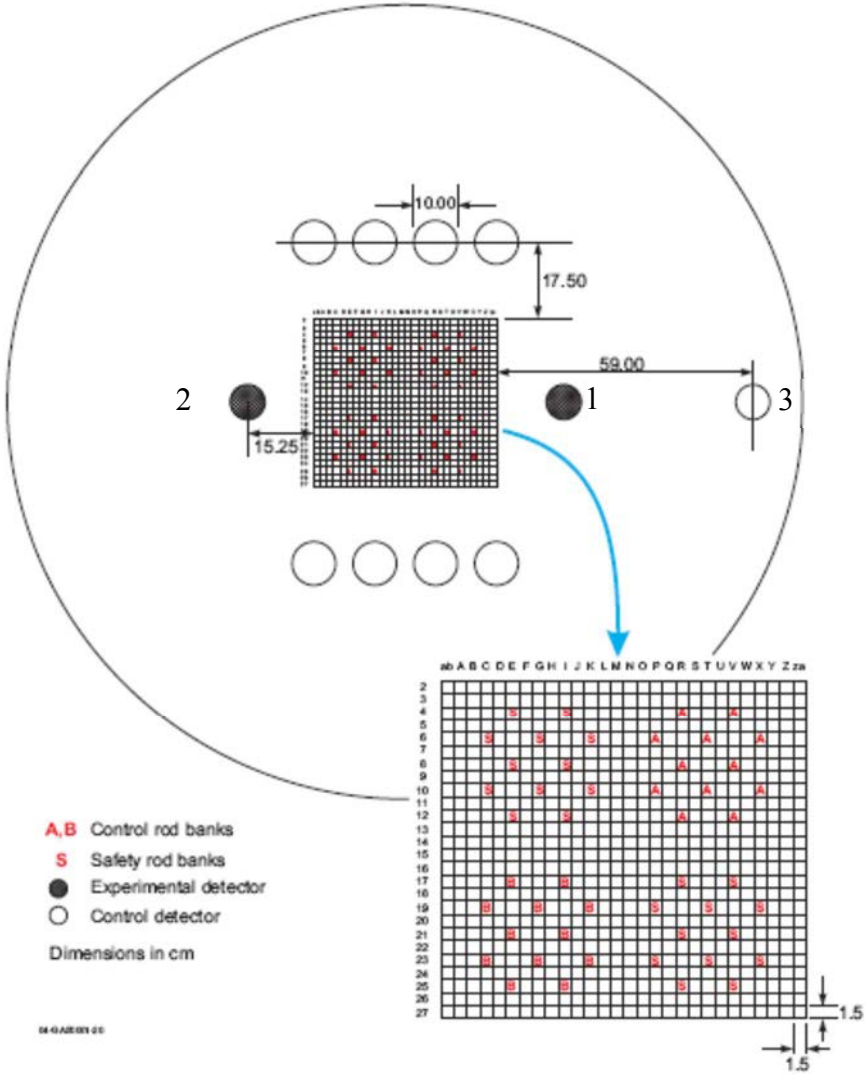


FIG. 4.3. Schematic diagram of the detector distribution around the core (Courtesy of the Energetic and Nuclear Research Institute (IPEN), Brazil).

4.3. RESEARCH ACTIVITY

The research activity associated with this project has focused on a benchmark study that is subdivided into two phases which are defined below.

4.3.1. Phase I

This phase entailed the analysis of a subcritical configuration of the IPEN-MB-01 reactor that is obtained by removing all the control rods and two rows and columns of fuel elements relative to the critical configuration. This core configuration is shown in Fig. 4.3. A

point neutron source is assumed to be located in the centre of the active core in the mid-plane at the position (M,14), as shown in Fig. 4.4.

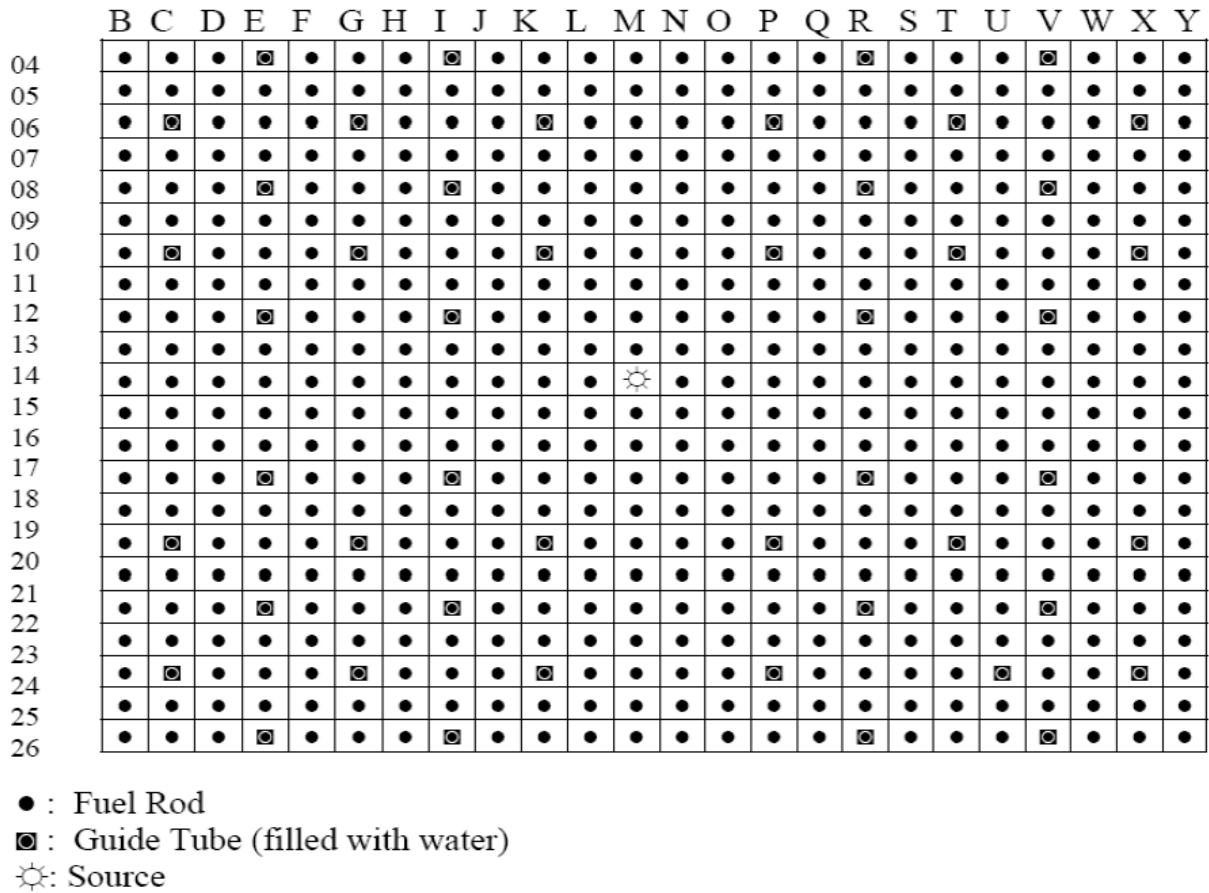


FIG. 4.4. Benchmark Phase I subcritical core configuration (Reproduced from [4.5] with permission courtesy of ABEN, Brazil).

The point source is assumed to emit mono-energetic neutrons (isotropically) from the D-D reaction ($E = 2.45$ MeV) or D-T reaction ($E = 14.1$ MeV). The following parameters were investigated for this phase of the benchmark:

4.3.1.1. Static Parameters

- k_{eff} , k_s (source multiplication factor).
- Total neutron flux distribution averaged axially for each cell over the entire active fuel length of the subcritical configuration.
- Total power and total neutron flux at the experimental detector positions 1, 2, 3 (Fig. 4.3).
- Neutron spectra (averaged axially) at cells (N,14) (R,14) (P,10) (O,11) (R,8), as shown in Fig. 4.4.
- Axial distribution of the total neutron flux for the same cells described in (b) along the entire rod length (both active and non-active portions).

4.3.1.2. Dynamic and Kinetic Parameters

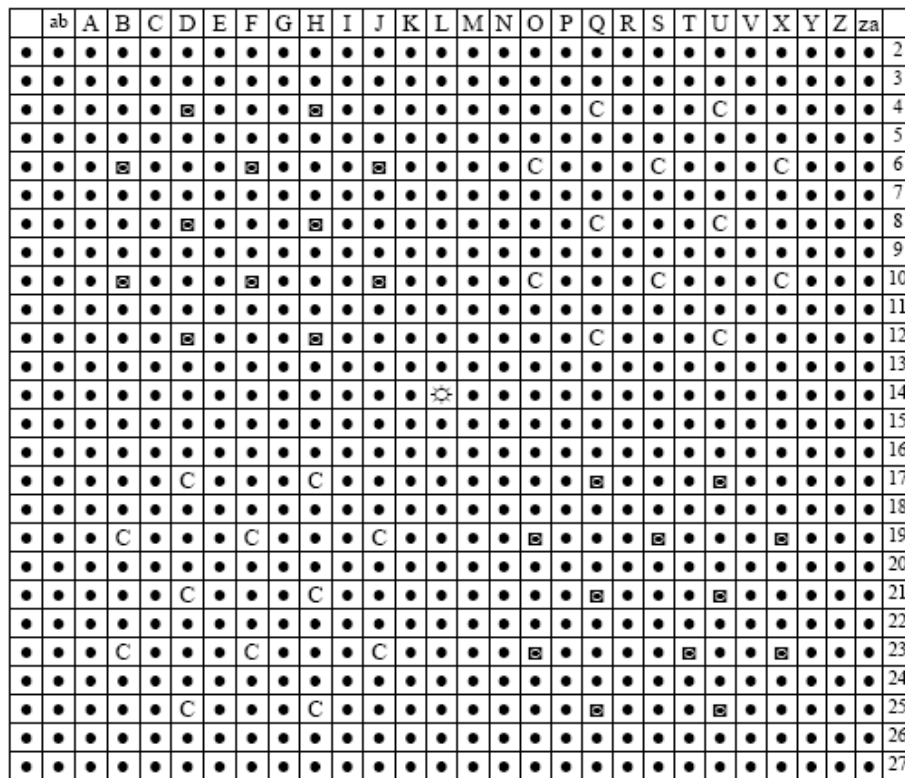
A rectangular pulse that is 10 μs wide with amplitude 10 times the average beam current (CW) is assumed for the pulsed deuteron beam.

The following experimental procedure was followed in this part of the investigation:

- Calculate the time evolution of the total neutron flux for $t = 50, 102, 103, 104, 105,$ and $106 \mu\text{s}$, corresponding to $x = 14$ traverses (Fig. 4.4), starting from the source position up to the experimental detectors.
- Plot the total neutron flux versus time at the detector positions 1, 2, 3 (Fig. 4.3).
- Use these data to estimate the reactivity in dollar units $\rho(\$)$ by the Area Method.

4.3.2. Phase II

An analysis of the reactor performance was undertaken with the nominal fuel loading configuration (unlike the Phase I benchmark phase) and several degrees of subcriticality that were achieved by moving one bank of control rods while keeping the other bank of rods fixed at an insertion level of 50%. A point neutron source (emitting, as in the previous case, mono-energetic neutrons isotropically from the D-D or D-T reactions) was assumed to be situated at the position (L,14) for each degree of subcriticality (Fig. 4.5).



- : Fuel Rod
- ◩ : Guide Tube (filled with water)
- ☼ : Source
- C: Control pin

FIG. 4.5. Benchmark Phase II subcritical configuration (Courtesy of the Energetic and Nuclear Research Institute (IPEN), Brazil).

The following parameters were investigated for this phase of the benchmark:

- Without source: k_{eff} versus the position of BC1, keeping the BC2 insertion level at 50%;
- With the source: k_s (source multiplication factor) for $k_{eff} = 0.999, 0.990, \text{ and } 0.980$;
- Total power for $k_{eff} = 0.999, 0.990, \text{ and } 0.980$;
- The kinetics parameters (ρ , β_{eff} , and Λ – Mean neutron generation time) for $k_{eff} = 0.999, 0.990, \text{ and } 0.980$.

The participants in this collaboration were at liberty to choose to use Monte Carlo and/or deterministic approaches for their calculations. All the participants (except India) chose to use Monte Carlo calculations for this exercise, however with various codes and nuclear data libraries. An example of a Monte Carlo model used for these calculations (from the Brazil contribution) is shown in Fig. 4.6. The following definitions have been adopted for the neutronic parameters associated with these Monte Carlo analyses.

- The source multiplication factor, k_s is computed by using the Monte Carlo code in the source mode, accounting for the neutron production by fission and (n,xn) reactions according to Eq. (3.1):

$$k_s = \frac{\langle P \rangle}{\langle P \rangle + \langle S \rangle} \quad (3.1)$$

Where

- $\langle P \rangle$ is the fission and (n,xn) neutron production;
- $\langle S \rangle$ is the amount of neutrons from the external source.

- Effective delayed neutron fraction β_{eff} is obtained from Eq. (3.2):

$$\beta_{eff} = \left(1 - \frac{k_{prompt}}{k_{eff}} \right) \quad (3.2)$$

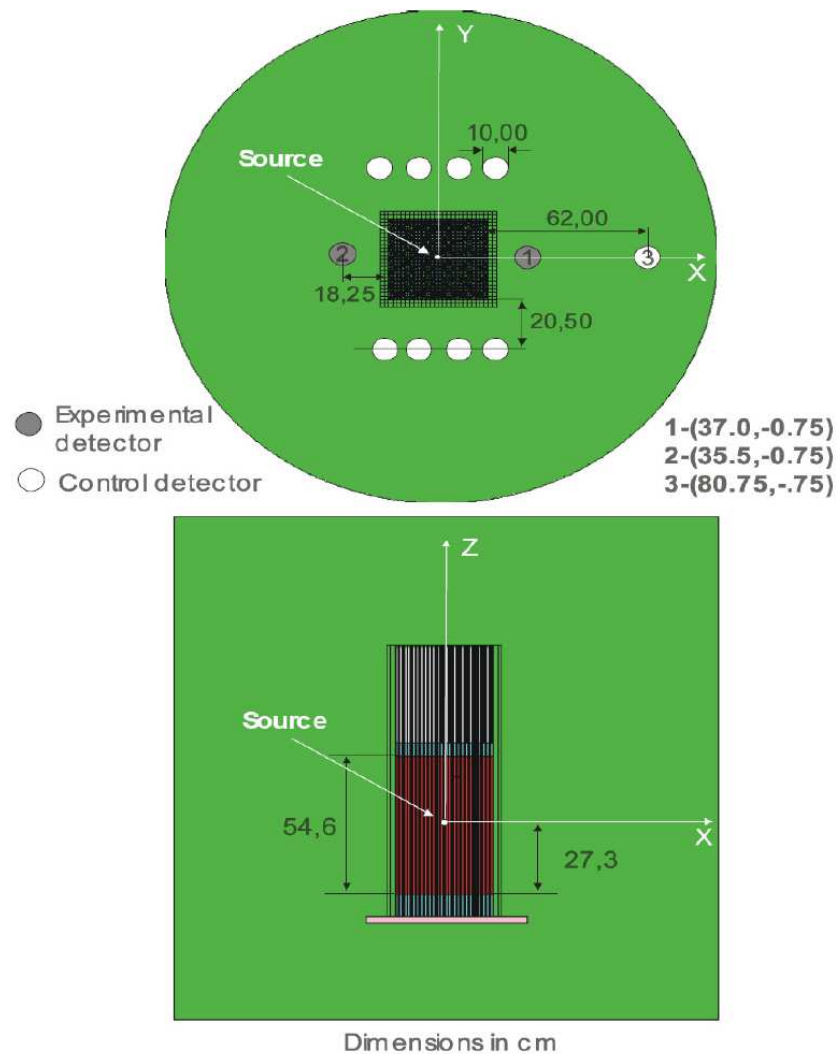


FIG. 4.6. IPEN-MB-01 reactor Monte Carlo model (from the Brazil contribution) (Reproduced from [4.5] with permission courtesy of ABEN, Brazil).

4.4. RESULTS

The results obtained by the participants from their Monte Carlo calculations were generated using the following specific nuclear data libraries and Monte Carlo codes:

- Argentina: ENDF/B-VI & -V, MCNP5;
- Brazil: ENDF/B-VII, MCNP5 1.4;
- China: ENDF/B-VI, MCNP/4C;
- Republic of Korea: ENDF/B-VII, McCARD;
- Spain: ENDF/B-VI, MCNPX.

4.4.1. Phase I

Selected integral results from the Phase I investigation are summarized in Table 4.1. The k_{eff} values that were generated from the Monte Carlo calculations that were performed by the collaborators in this research project exhibit a relatively modest spread (~ 200 pcm). On the other hand, the spread is considerably greater (~ 1200 pcm) for the obtained values of k_s in the in presence of either D-D or D-T neutron sources.

A close examination of the data in Table 4.1 suggests that the significant spread in the case of k_s can be traced mainly to the results provided by China. This group produced results for k_s , corresponding to the D-D and D-T sources, which were definitely higher for k_{eff} ($\sim +2300$ pcm) than the results provided by the other collaborators. However, even if these results from China are excluded, the results from the remaining reporting groups still scatter by about 700 pcm.

Good agreement between the reported results from the various groups in this collaboration is observed for the β_{eff} and Λ values. A standard deviation in the various comparable results of no higher than about 20% is observed for the calculated total fission power. However, a different conclusion can be drawn from the corresponding flux values reported for the various detectors, where deviations between them of up to a factor of two can be observed, provided that the results from China for Flux Detector 3 are neglected. The values reported by China for Flux Detector 3, in the presence of the D-D source, show an unexpected apparent discrepancy of an order of magnitude, especially when compared with the D-T source results.

Furthermore, concerning the results from Argentina, it is interesting to notice the very good agreement observed, far from criticality, of the measured reactivity obtained by the Area Method relative to the reference k_{eff} value. Some 3D neutron flux distribution maps are shown in Fig. 4.7.

TABLE 4.1. SELECTED INTEGRAL RESULTS FOR IPEN-MB-01

Argentina	value		σ	
	k_{eff}	0.96908		0.00011
β_{eff} (pcm)	788		15	
Λ (μ s)	33		1	
Source	DD		DT	
	value	σ	value	σ
k_s	0.96953	0.0001	0.96581	0.00033
Total power (fissions)	21.3	0.1	18.7	0.1
Flux detector 1 (cm^{-2})	2.90×10^{-4}	2.64×10^{-6}	2.60×10^{-4}	6.01×10^{-6}
Flux detector 2 (cm^{-2})	5.44×10^{-4}	4.46×10^{-6}	4.98×10^{-4}	1.04×10^{-5}
Flux detector 3 (cm^{-2})	1.87×10^{-7}	3.72×10^{-8}	5.55×10^{-7}	1.62×10^{-7}
Area reactivity (pcm)	-3063	60	-2905	79
Brazil	value		σ	
k_{eff}	0.97233		0.00025	
β_{eff} (pcm)	756		29	
Λ (μ s)	36		26	
Source	DD		DT	
	value	σ	value	σ
k_s	0.96441	0.00038	0.96173	0.00045
Total power (fissions)	18.569	0.004	16.505	0.063
Flux detector 1 (cm^{-2})	5.78×10^{-4}	3.41×10^{-6}	5.74×10^{-4}	3.72×10^{-6}
Flux detector 2 (cm^{-2})	1.12×10^{-3}	5.47×10^{-6}	1.03×10^{-3}	5.86×10^{-5}
Flux detector 3 (cm^{-2})	6.84×10^{-7}	8.79×10^{-8}	1.18×10^{-6}	1.50×10^{-7}

TABLE 4.1. SELECTED INTEGRAL RESULTS FOR IPEN-MB-01 (Cont.)

China		value		σ	
k_{eff}		0.97			
β_{eff} (pcm)					
Λ (μ s)					
Source	DD		DT		
	value	σ	value	σ	
k_s	0.99280		0.99200		
Total power (fissions)					
Flux detector 1 (cm^{-2})	2.43×10^{-4}	3.04×10^{-6}	2.25×10^{-4}	1.01×10^{-6}	
Flux detector 2 (cm^{-2})	1.97×10^{-4}	2.50×10^{-6}	1.71×10^{-4}	7.86×10^{-7}	
Flux detector 3 (cm^{-2})	2.38×10^{-5}	3.83×10^{-7}	4.03×10^{-7}	2.23×10^{-8}	

Spain		value		σ	
k_{eff}		0.9738		0.0017	
β_{eff} (pcm)		759			
Λ (μ s)					
Source	DD		DT		
	Value	σ	value	σ	
k_s	0.9797	0.01362	0.9768	0.01358	
Total power (fissions)	28.499		24.668		
Flux detector 1 (cm^{-2})	2.44×10^{-3}	4.68×10^{-5}	2.15×10^{-3}	1.40×10^{-5}	
Flux detector 2 (cm^{-2})	2.00×10^{-3}	3.97×10^{-5}	1.72×10^{-3}	1.15×10^{-5}	
Flux detector 3 (cm^{-2})	2.59×10^{-6}	9.04×10^{-7}	2.20×10^{-6}	3.00×10^{-7}	

Republic of Korea		value		σ	
k_{eff}		0.97			
β_{eff} (pcm)		757		3	
Λ (μ s)		36.9		0.6	
Source	DD		DT		
	value	σ	value	σ	
k_s	0.97492	0.00402	0.97572		
Total power (fissions)	18.436	0.076	16.562		
Flux detector 1 (cm^{-2})	4.64×10^{-4}	1.98×10^{-6}	4.43×10^{-4}	1.84×10^{-6}	
Flux detector 2 (cm^{-2})	6.18×10^{-4}	2.57×10^{-6}	5.78×10^{-4}	2.30×10^{-6}	
Flux detector 3 (cm^{-2})	5.29×10^{-7}	3.83×10^{-8}	9.83×10^{-7}	6.13×10^{-8}	

TABLE 4.1. SELECTED INTEGRAL RESULTS FOR IPEN-MB-01 (Cont.)

Average values	value		St. Dev.	
	k_{eff}	0.97104		0.00195
β_{eff} (pcm)	765		15	
Λ (μ s)	35		6%	
Source	DD		DT	
	value	St. Dev.	value	St. Dev.
k_s	0.97627	0.01087	0.97441	0.01174
Total power (fissions)	21.701	22%	19.1088	20%
Flux detector 1 (cm^{-2})	8.03×10^{-4}	115%	8.57×10^{-4}	94%
Flux detector 2 (cm^{-2})	8.96×10^{-4}	78%	9.57×10^{-4}	63%
Flux detector 3 (cm^{-2})	5.56×10^{-6}	184%	1.06×10^{-6}	67%

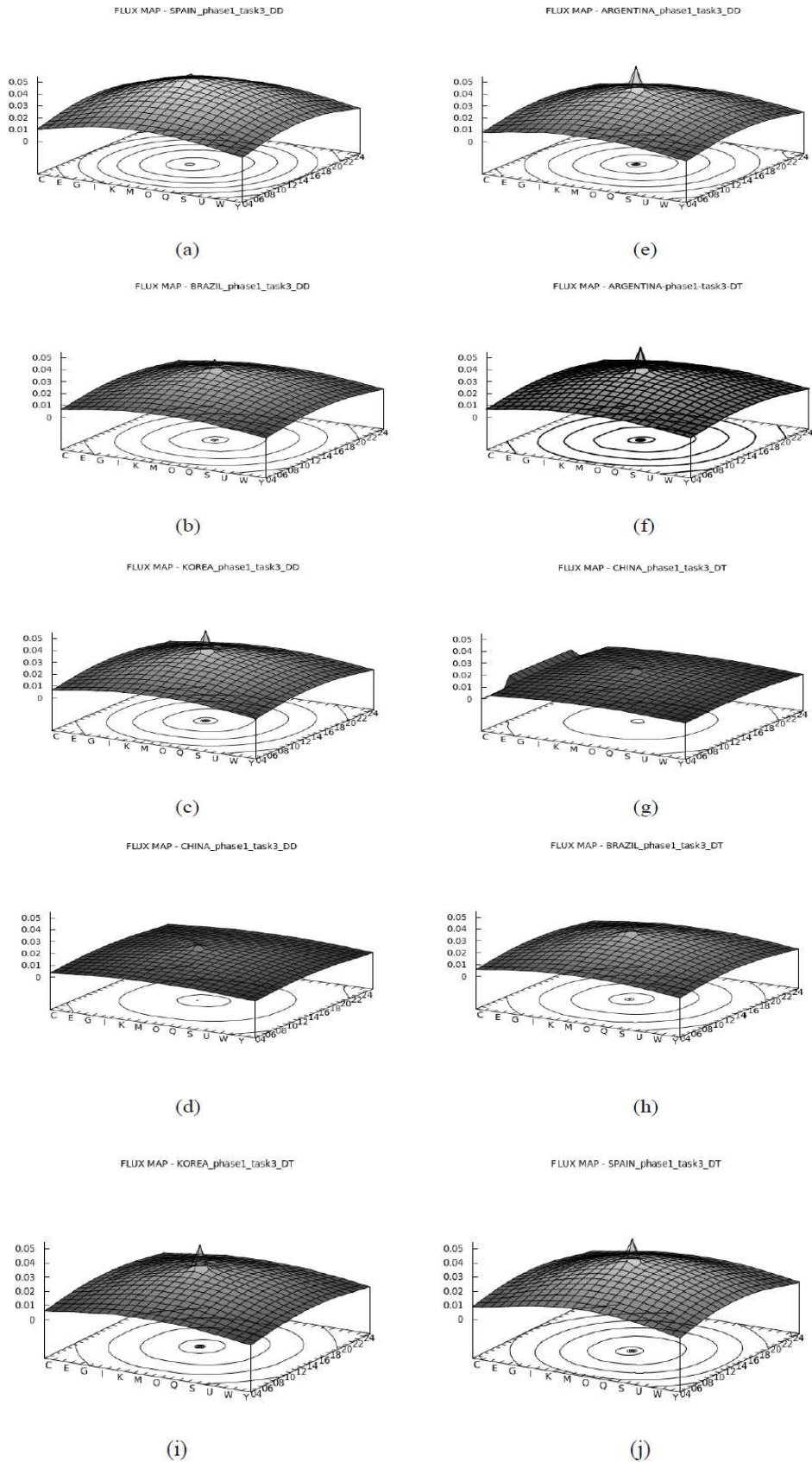


FIG. 4.7. Flux map distributions for the D-D (a, b, c, d, e) and D-T (f, g, h) sources (Courtesy of the Energetic and Nuclear Research Institute (IPEN), Brazil).

Normalized neutron spectra at some selected positions in the reactor are shown in Fig. 4.8 (a) (D-D neutron source) and Fig. 4.8 (b) (D-T neutron source).

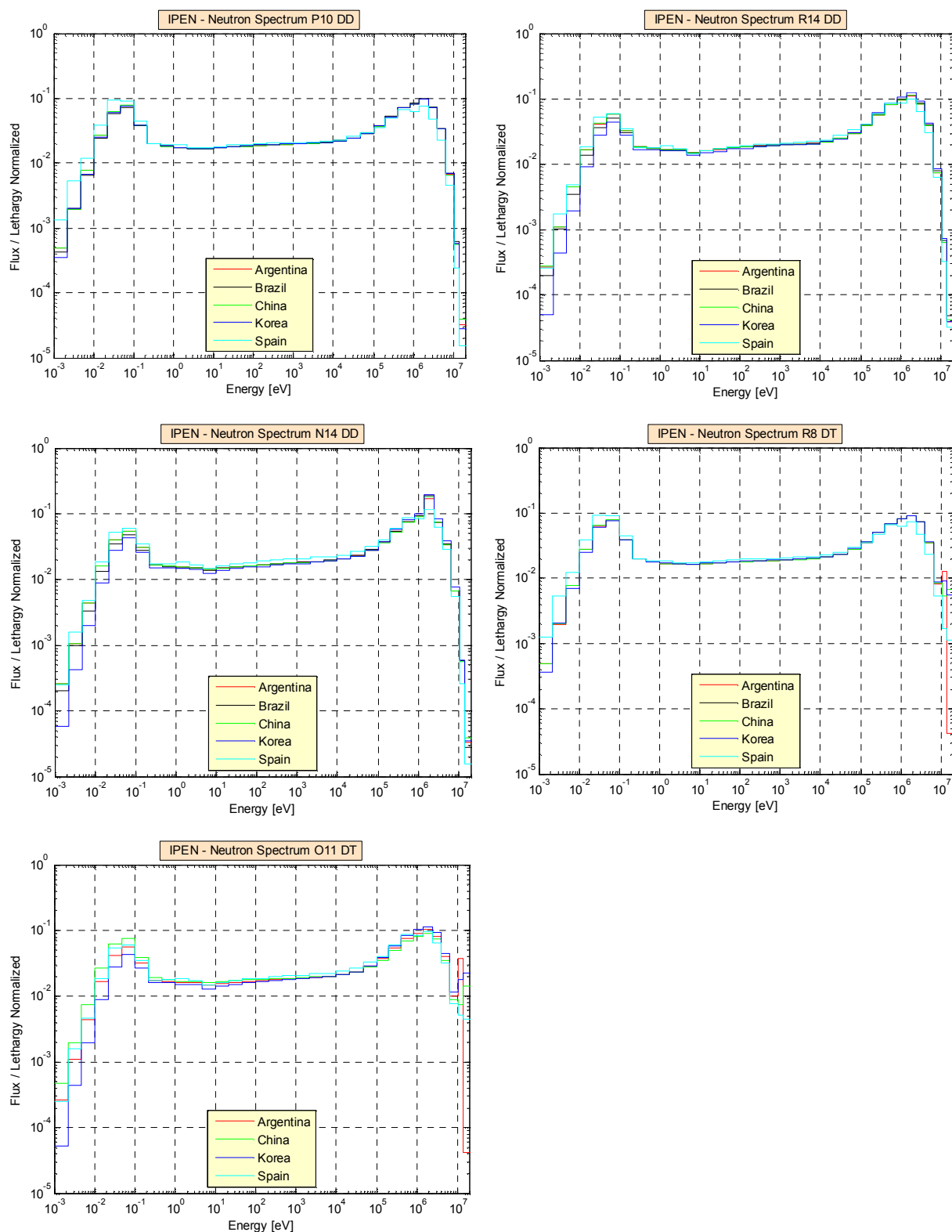


FIG. 4.8. (a) Neutron Spectra for the D-D neutron source (Courtesy of the Energetic and Nuclear Research Institute (IPEN), Brazil).

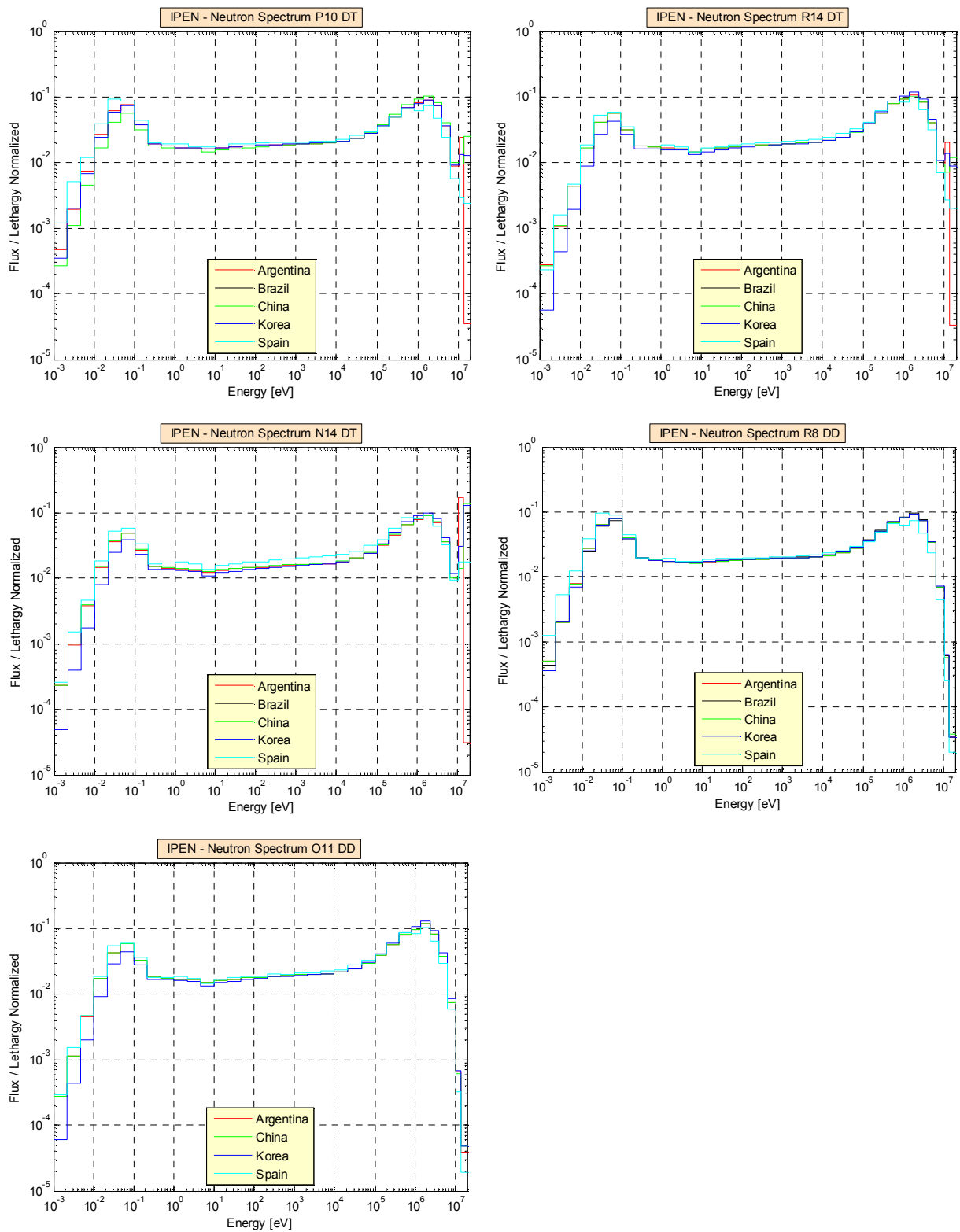


FIG. 4.8. (b) Neutron Spectra for the D-T neutron source (Courtesy of the Energetic and Nuclear Research Institute (IPEN), Brazil).

Axial neutron-flux profiles at selected positions in the system are shown in Fig. 4.9 (a) (D-D neutron source) and Fig. 4.9 (b) (D-T neutron source).

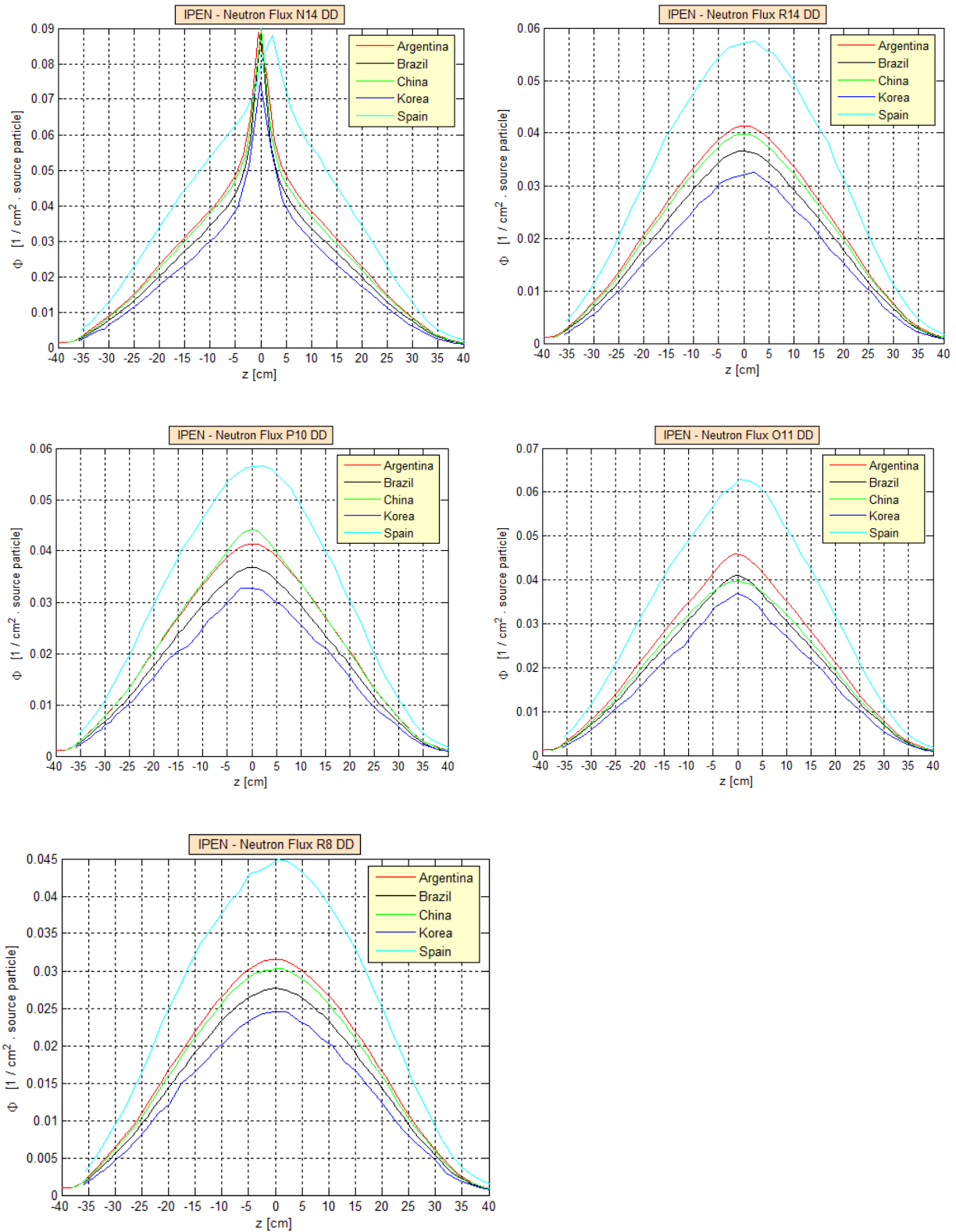


FIG. 4.9. (a) Axial neutron-flux profiles for the D-D neutron source (Courtesy of the Energetic and Nuclear Research Institute (IPEN), Brazil).

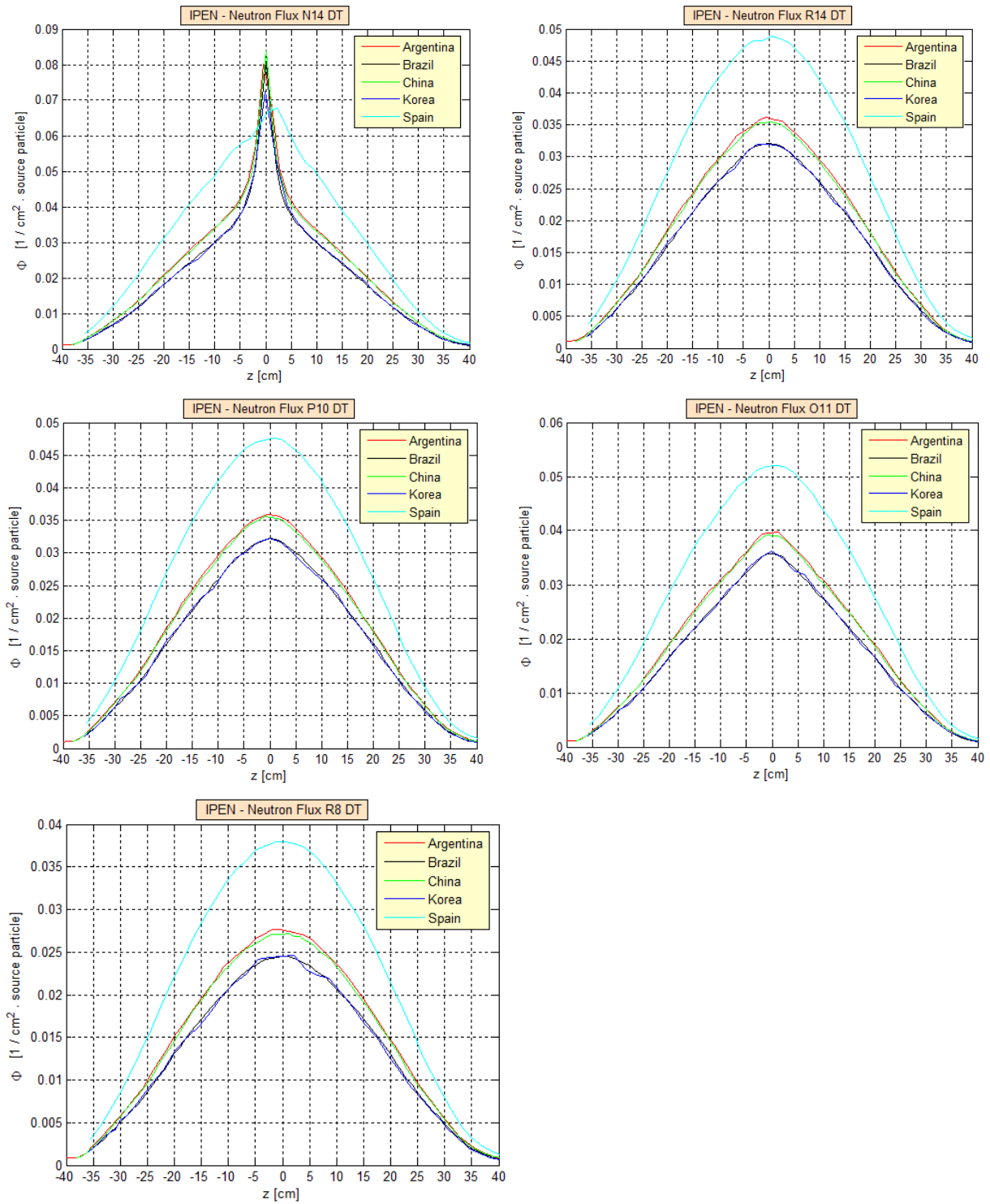


FIG. 4.9. (b) Axial neutron-flux profiles for the D-T neutron source (Courtesy of the Energetic and Nuclear Research Institute (IPEN), Brazil).

It is evident from Figs 4.8 and 4.9 that, except in the case of Spain results, the obtained results cluster together fairly closely, showing that good agreement among the various participants was achieved for the calculated spectra and axial flux profiles. The Spain model has some approximations, which affected the calculated results. For example, Figs 4.9 (a) and

(b) show the neutron source is not located at $z = 0$ similar to the other calculations, which results in unsymmetrical neutron flux distributions around $z = 0$.

4.4.2. Phase II

Selected integral results obtained by Argentina and Brazil are summarized in Table 4.2. It can be seen that the discrepancies regarding the k_s values can approach ~ 500 pcm for the deepest subcritical level (with $k_{eff} = 0.98$). Noteworthy as well are the discrepancies that are observed regarding the total power up to $\sim 80\%$. As in the Phase I situation, it is interesting to notice the very good agreement, far from criticality, of the measured reactivity values provided by Argentina that were obtained by the Area Method, relative to the reference k_{eff} values.

TABLE 4.2. SELECTED PHASE II INTEGRAL RESULTS

$k_{eff}=0.99900$

	Argentina				Brazil			
	DD		DT		DD		DT	
	value	σ	value	σ	value	σ	value	σ
k_s	0.99914	0.00004	0.99901	0.00005	0.99560	0.00005	0.99520	0.00006
Total power (fissions)	487	16	426	13	222	5	205	4
Area reactivity (pcm)	-152	6	-105	5				
β_{eff} (pcm)	809	14	809	14	757 ^(*)	8	757 ^(*)	8
Λ (μ s)								

$k_{eff}=0.99000$

	Argentina				Brazil			
	DD		DT		DD		DT	
	value	σ	value	σ	value	σ	value	σ
k_s	0.99380	0.00090	0.99371		0.98950	0.00015	0.98880	0.00010
Total power (fissions)	67.10	0.60	60.50		94.24	0.70	87.74	0.55
Area reactivity (pcm)	-991	25	-922					
β_{eff} (pcm)	779	14	779		757 ^(*)	8	757 ^(*)	8
Λ (μ s)	31	1	31					

$k_{eff}=0.98000$

	Argentina				Brazil			
	DD		DT		DD		DT	
	value	σ	value	σ	value	σ	value	σ
k_s	0.98750	0.00090	0.98693	0.00090	0.98310	0.00020	0.98200	0.00010
Total power (fissions)	32.9	0.2	30.7	0.1	57.9	0.3	54.4	0.3
Area reactivity (pcm)	-2086	56	-2016	73				
β_{eff} (pcm)	791	14	791	14	757 ^(*)	8	757 ^(*)	8
Λ (μ s)	33	1	33	1				

* At criticality

A comparison between the Argentina and Brazil results concerning the k_{eff} behaviour as a function of control-rod withdrawal is shown in Fig. 4.10.

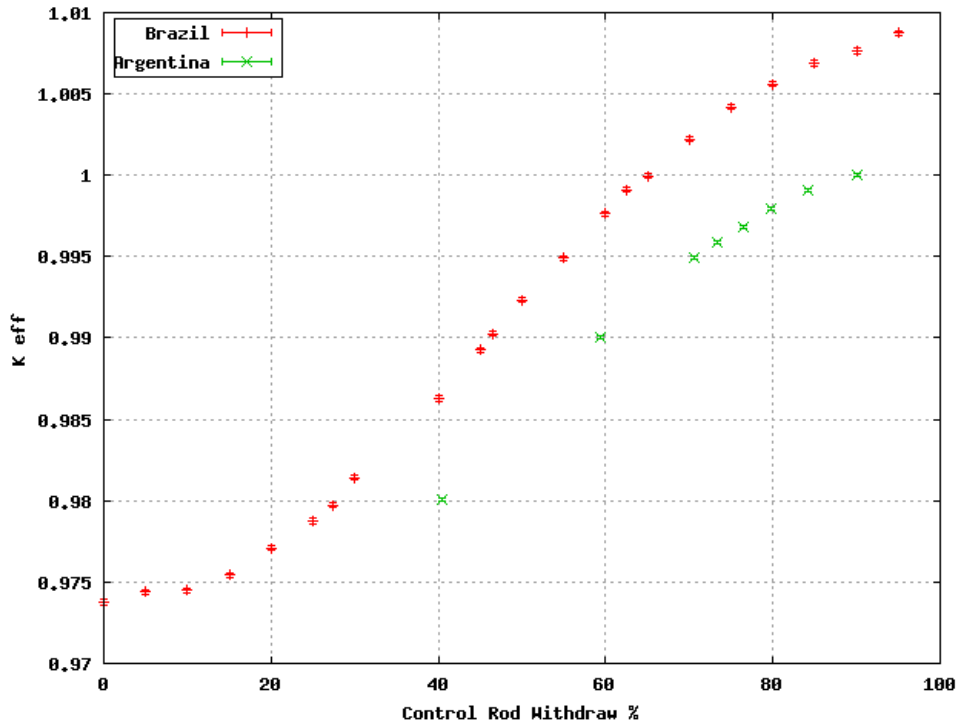


FIG. 4.10. k_{eff} as a function of control rod withdrawal (Reproduced from [4.6] with permission courtesy of the ANS, USA).

4.5. CONCLUSIONS

The Brazilian reactor facility IPEN-MB-01 can be made subcritical quite easily by changing the control-rod positions or the numbers of fuel pins in the core. A computational benchmark, that focused on having the facility operated in a subcritical mode, and coupled to a D-D or D-T accelerator neutron source, has been defined and investigated in view of the possibility of establishing a subcritical experimental effort at the Brazilian IPEN-MB-01 reactor in support of ADS technology development. This benchmark effort was divided into two phases: where the subcritical configurations were obtained by removing fuel elements (Phase I) or by control rod insertion (Phase II). Several integral parameters and flux characteristics were investigated for both phases of this benchmark.

The principal results from the benchmark investigations that were performed using Monte Carlo calculations and ENDF/B nuclear data by the participating Member States (except for India) can be summarized for both of these benchmark phases as follows:

- The spread between the various results obtained by the participants for k_{eff} is relatively narrow (less than ~ 200 pcm), and their results were also found to be in good agreement for the integral kinetic parameters β_{eff} and Λ ;
- The calculations performed by the various participants of the source multiplication factors k_s , irrespective of the energy characteristics of the external neutron source (D-D or D-T), appear to be accompanied by considerable uncertainty (a spread of up to ~ 1000 pcm);
- Comparisons of energy-integrated neutron fluxes at different positions in the system, in presence of an external neutron source, exhibit significant spreads in the reported values of up to a factor of two, even close to the external source. Several factors contributed to these differences in the calculated results. First, the used neutron source spectra are not exactly the same. Second, different versions of ENDF/B data libraries were used in the

calculations. Third, different neutron transport programs including different version of the same program were employed in the neutron transport calculations. Nevertheless, relatively good agreement is observed concerning calculations of the neutron flux profiles at various positions in the system;

- Very good agreement is observed far from criticality between the reactivity values obtained by the Area Method, with respect to the reference k_{eff} values (from results provided by Argentina).

REFERENCES TO SECTION 4

- [4.1] INSTITUTE OF NUCLEAR AND ENERGY RESEARCH, Research Reactor IPEN-MB/01 Description, Fact Sheet, https://www.ipen.br/portal_por/portal/interna.php?secao_id=723 (2016)
- [4.2] THE NUCLEAR ENERGY AGENCY (NEA), International Reactor Physics Experiment Evaluation (IRPhE) Project <http://www.oecd-nea.org/science/wprs/irphe/>
- [4.3] MAIORINO, J.R., SANTOS, A., BITELLI, U.D., Specification of the Subcritical Core of the IPEN/MB-01 Driven by a Neutron Generator within the IAEA sub-CRP on Low Enrichment Uranium (LEU) Fuel Utilization in Accelerator Driven Sub Critical Assembly System (ADS), Phase I-Rev.0., November 2006.
- [4.4] MAIORINO, J.R., BITELLI, U.D., Specification of the sub critical core of the IPEN/MB-01 driven by a neutron generator within the IAEA sub CRP on Low Enrichment Uranium (LEU) Fuel Utilization in Accelerator Driven Sub Critical Assembly System (ADS), Phase II: Sub Critical Core with control rods, one source point Rev 0," IAEA Collaborative Work on utilization of LEU in ADS, IAEA (2007).
- [4.5] ANTUNES, A., CARLUCCIO, T., MENDONCA, A.G., et al., "Reactor Physics Calculations for a Sub critical Core of the IPEN-MB-01 driven by an external neutron source", Proc. Int. Nucl. Atlantic Conf. – INAC 2007, Santos, SP, 2007.
- [4.6] MAIORINO, J.R., A., CARLUCCIO, The sub critical core of ipen-mb-01 driven by a neutron source in the IAEA collaborative work on LEU fuel utilization in accelerator driven system – final results, Proc. Int. Conf. on Mathematics and Computational Methods Applied to Nuclear Science and Engineering – M&C 2011, Rio de Janeiro, RJ, Brazil, (2011), CD-ROM.

5. TRADE EXPERIMENTAL BENCHMARK

Contributed by

M. Carta, N. Burgio, V. Peluso, R. Rosa, A. Santagata
*Italian National agency for new technologies, Energy and
sustainable economic development (ENEA),
Italy*

C. Jammes
*The French Alternative Energies and Atomic Energy Commission (CEA),
France*

M. Martina
*Politecnico di Torino,
Italy*

T. Sasa, T. Sugawara
*Japan Atomic Energy Agency (JAEA),
Japan*

5.1. INTRODUCTION

The TRADE (TRiga Accelerator Driven Experiment) programme was conceived to investigate the static and dynamic behaviour of accelerator driven systems (ADS) at low power and with thermal-neutron spectra [5.1]. It was intended to be implemented in the RC-1 TRIGA reactor facility located at ENEA-Casaccia Research Centre near Rome, Italy. However, because of problems in obtaining financial support, this programme was interrupted at the end of 2004. In spite of these circumstances, a large experimental data bank had been accumulated during the time period prior to the programme's discontinuation.

In June 2007, TRADE experimental activities were endorsed by the IAEA for continued investigation under the auspices of a research project entitled 'pre-TRADE Experimental Benchmark'. Furthermore, a computational benchmark activity was also launched within the framework of a Coordinated Research Project (CRP) entitled 'Analytical and Experimental Benchmark Analyses of Accelerator Driven Systems'. In particular, this work was intended to be carried out under the auspices of the sub-CRP entitled 'Collaborative Work on Utilization of Low enriched Uranium (LEU) in ADS'. This activity has involved the evaluation of nuclear parameters for reactors driven by external sources [5.1]. The particular benchmark activity, designated as the 'pre-TRADE Experimental Benchmark', has focused since its initiation on the evaluation, via computation, of the spatial-energy correction factors to be applied to raw experimental data corresponding to certain reactivity parameters that have been measured for subcritical conditions in the RC-1 TRIGA reactor. These measurements, carried out for the TRADE programme [5.2], were based on the Pulsed Neutron Source (PNS) Area-ratio [5.3, 5.4] and Source Multiplication [5.6] methods. They were performed at various core locations relative to three distinct 'clean' (without control rods) subcritical core configurations, designated respectively as SC0 (~ -500 pcm), SC2 (~ -2500 pcm), and SC3 (~ -5000 pcm). This Section describes this research activity and presents the most significant results that were generated from the work.

The research carried out for the TRADE subcritical experiment, within the framework of the IAEA sponsored programme, benefited from contributions provided by Italy, Japan, and Germany Member States.

5.2. FACILITY DETAILS

This section discusses the basic characteristics of the TRIGA reactor facility, the external-driver neutron source for the ADS concept implementation, and the various core configurations that were investigated in the TRADE experiments.

5.2.1. Description of the TRIGA Reactor⁴

The RC-1 TRIGA reactor, which is located at the ENEA Casaccia Research Centre near Rome, Italy, is a 1 MW Mark II category reactor that was constructed in 1960. It is a light water reactor that is cooled by water that circulates via natural convection. This means that the reactor has no pumps to actively circulate the water. The reactor core consists of an annular-shaped structure (Fig. 5.1) that is comprised of a honeycomb-like array of six coaxial cylindrical rings of fuel elements [5.7]. The reactor and its supporting experimental components are enclosed within a concrete shield structure. The core and the reflector assemblies are located at the bottom of an aluminium tank (190.5 cm in diameter). The overall height of this tank is about 7 m. The core, which is <1 m high (see Fig. 5.1 and the following paragraph), is therefore effectively shielded by about 6 m of water located above it.

The reactor core, which is surrounded by a graphite reflector, consists of a lattice of fuel elements, graphite dummy elements, control rods, and a regulation rod (REG). There are 127 included channels that are divided into seven concentric rings, with 1 to 36 channels per ring, as shown in Fig. 5.2. These channels are loaded with fuel rods, graphite dummies, and regulation and control rods, in configurations that depend specifically on the required power level. One of these channels (normally) houses an Am-Be neutron source, while two other fixed channels (the central one and a peripheral one) are available for sample irradiations or other experimental applications. The pitch of the core elements is 4.05 cm and the mean ratio of fuel to water is 0.635 to 0.365. The diameter of the core is about 56.5 cm while its height is 72 cm. Neutron reflection is provided by graphite that is enclosed in an aluminium container. This container is surrounded by 5 cm of lead which acts as a thermal shield. An empty aluminium tube (15 cm diameter and 0.6 cm thick) that traverses the graphite reflector tangentially to the reactor core can be used for thermal-neutron flux irradiations. The core components are contained between two aluminium grid plates that are located at the top and bottom of the core, respectively. The top grid plate has 126 holes for fuel elements and control rods as well as a central thimble for use in high-flux sample irradiations. The fuel elements incorporate stainless steel cladding (AISI-304, 0.05 cm thick, and 7.5 g/cm³ density) that is characterized by an external diameter of 3.73 cm and a total height of 72 cm, including the end cap (see Fig. 5.2). Each fuel element is comprised of a cylinder (38.11 cm high by 3.63 cm external diameter, and 5.9 g/cm³ theoretical density) of a ternary alloy consisting of uranium-zirconium-hydrogen with a H-to-Zr atom ratio of 1.7 to 1. The uranium, enriched to 20% in ²³⁵U, makes up 8.5% of this mixture by weight. The uranium mass of an individual fuel rod is, on the average, 197 g. Of this total uranium mass, 39 g is fissile material. As is evident from Fig. 5.2, there is also an inner metallic zirconium rod (38.11 cm high by 0.5 cm in diameter, and 6.49 g/cm³ density). Furthermore, there are two graphite cylinders (8.7 cm high by 3.63 cm in diameter, and 2.25 g/cm³ density) situated at the top and bottom of each fuel rod, respectively. Two end fittings are present externally in order to enable remote movement of the rods and as well as adequate locking to the grid plate. The regulation rod has the same structure as a fuel rod. The only difference is that instead of a mixture of the ternary alloy of uranium-zirconium-hydrogen there is an absorber consisting of graphite mixed with powdered boron carbide. Furthermore, the inner Zr cylinder found in fuel rods is not present in the regulation rod. The control rods are 'fuel followed'. By that it is meant that the

⁴ This section is based on Ref. [5.5]

geometry is similar to that of the regulation rod, with the bottom graphite cylinder replaced with fuel. The graphite dummies there are similar to the regulation rod, but without boron inside the central volume.

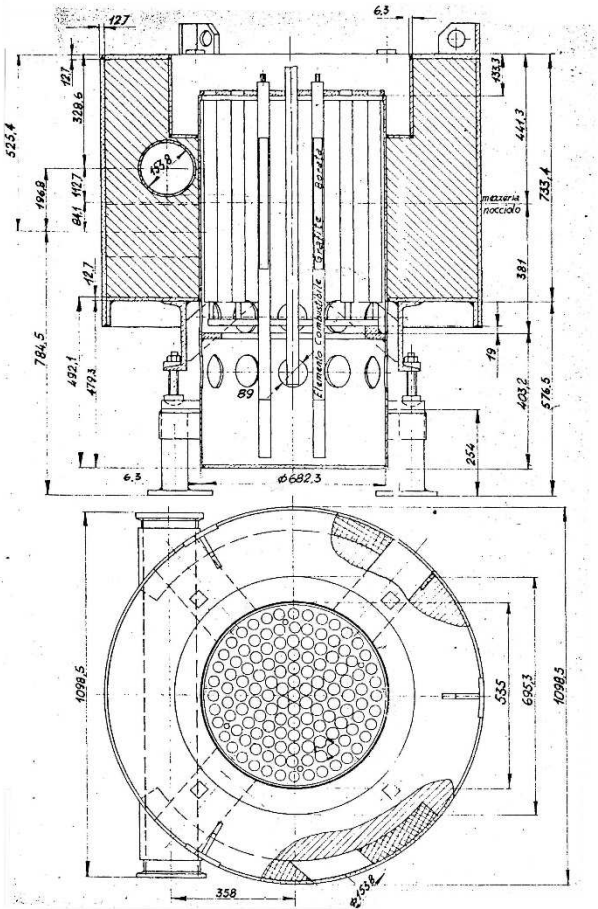


FIG. 5.1 Schematic representation of the reactor assembly: side view (upper drawing) and top view (lower drawing) [5.7]. All dimensions are in mm (Courtesy of the Italian National Agency for New Technologies, Energy and Sustainable Economic Development (ENEA), Italy).

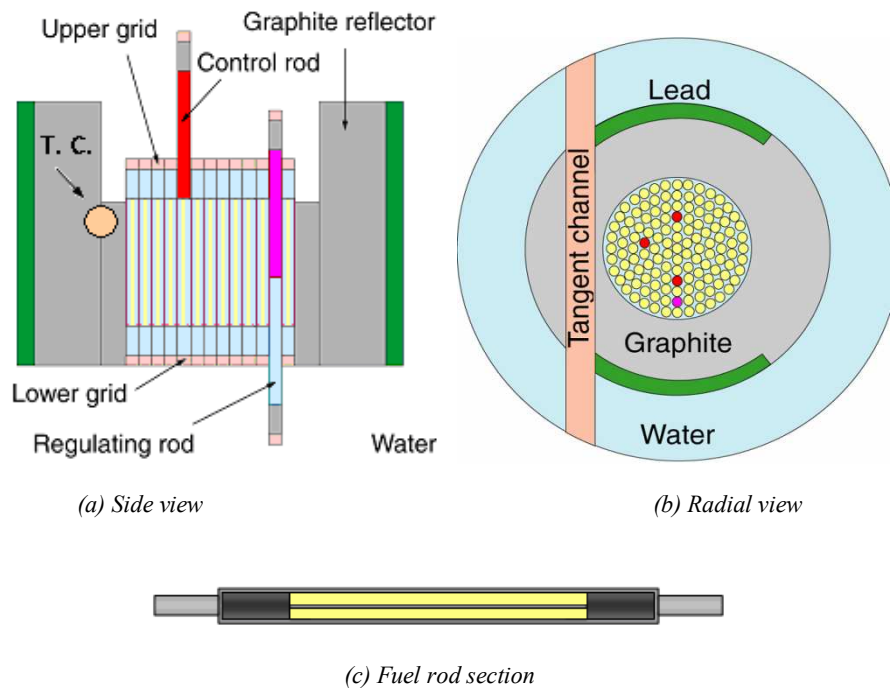


FIG. 5.2. Drawing of the TRIGA reactor with the three control rods shown in red while the single regulation rod (REG) is shown in violet (Courtesy of the Italian National Agency for New Technologies, Energy and Sustainable Economic Development (ENEA), Italy).

The principal physical characteristics of the TRIGA RC-1 reactor components are specified in Table 5.1.

TABLE 5.1. PRINCIPAL PHYSICAL CHARACTERISTICS OF THE TRIGA RC-1 REACTOR ELEMENTS

Nominal fuel density (g/cm^3)	5.8
U weight	8.5%
Enrichment in ^{235}U	20.0%
Atomic ratio H/Zr	1.70
Internal Zr rod diameter (cm)	0.5
Fuel diameter (cm)	3.63
Clad thickness (cm)	0.05
Element active length (cm)	38.11
Elements pitch (cm)	4.054
Water volume associated with each element (cm^2) ^(*)	6.28

^(*) For the central element the associated water volume is 1.98 cm^3 .

5.2.2. Instrumentation

5.2.2.1. Neutron Generator

The pulsed neutron generator used to provide an external neutron source for PNS measurements is of the type All-Russian Research Institute of Automatics Model No. ING-

101-150 [5.6, 5.8]. The neutrons are produced by accelerating deuterium ions onto a tritium target. This facility generates 14.1 MeV pulsed neutron bursts with an intensity 10^8 neutrons/s when operated at the maximum pulsing frequency. The range of attainable pulsing frequencies for this neutron generator is 1 to 150 Hz, and the pulse duration is less than 1 μ s. The source of neutrons from this generator was situated at the centre of the core A01 (which is labelled DT in Fig. 5.3).

5.2.2.2. *Fast Rabbit and External Sources*

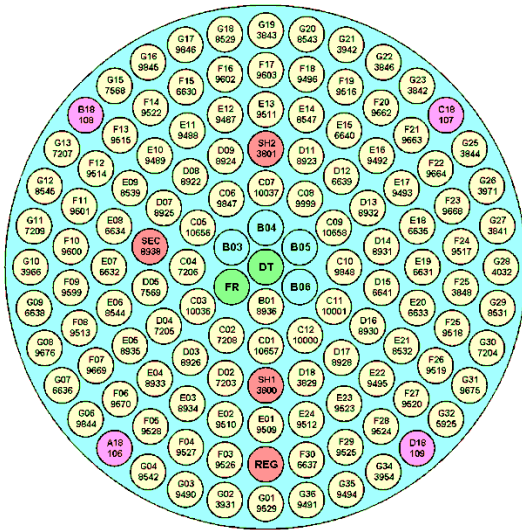
The Source-Multiplication type measurements were performed using the Fast Rabbit (FR) facility that is installed in the core at cell B02 (which is labelled FR in Fig. 5.3). This instrumentation was designed by the LPC-Caen CNRS laboratory [5.9]. The external neutrons used in these measurements were provided by a ^{252}Cf source with strength 0.4 Ci.

5.2.2.3. *Fission Chambers*

The fission chambers employed in the present measurements were of the type PHOTONIS CFUM18. The sensitivities of these neutron detectors were about 10^{-1} cps/n (thermal neutrons). All of the fission chamber locations are identified in Fig. 5.3 by cells that are shown in the drawing with pink colouring.

5.2.3. **Core Configurations**

The four core configurations (cores) investigated in this research project were as follows: one reference (REF) critical configuration (Fig. 5.3) and three subcritical configurations, denoted by SC0, SC2, and SC3, as indicated in the introduction. These subcritical configurations are illustrated in Figs 5.4 to 5.6. The three configurations, namely SC0, SC2 and SC3 have different experimental multiplication factors, 0.997, 0.977 and 0.959, respectively. In order to change from a configuration to another, some fuel elements were removed. The fission chambers, the Fast Rabbit (FR) pipe, and the neutron generator itself were situated in-core throughout the experimental campaign. The reference core configuration (REF) was designed so that the reactor would become critical with the regulation rod (REG) inserted to the 51% level.



TITLE: REF - DATE: November 2005

- Fuel
- Water hole
- Graphite
- Control rod
- Fission chamber
- Source

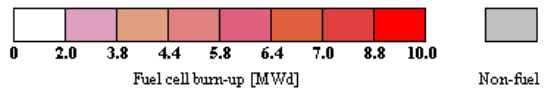
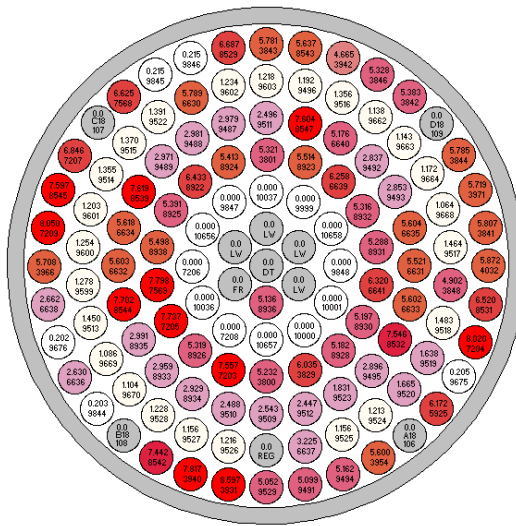
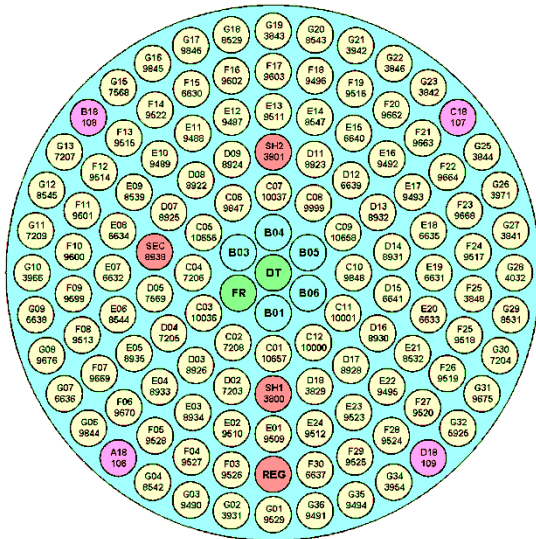


FIG. 5.3. Reference (REF) core (Courtesy of the Italian National Agency for New Technologies, Energy and Sustainable Economic Development (ENEA), Italy).



TITLE: SC0 - DATE: November 2005

- Fuel
- Water hole
- Graphite
- Control rod
- Fission chamber
- Source

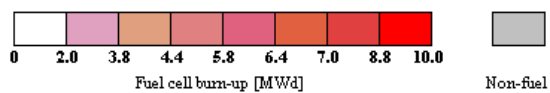
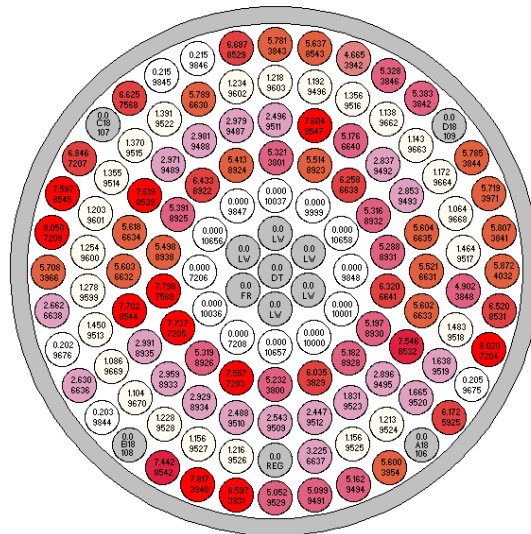
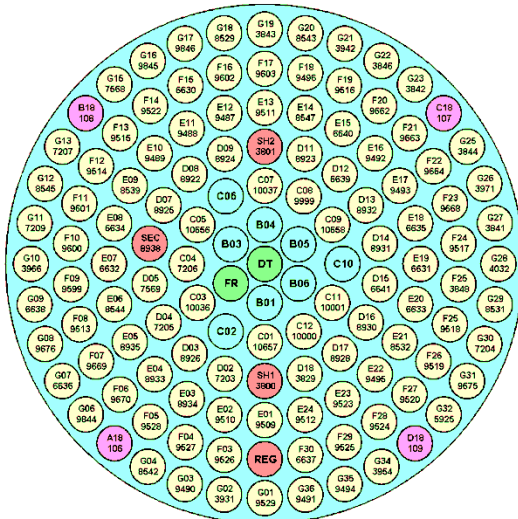


FIG. 5.4. SC0 configuration for the TRADE core (Courtesy of the Italian National Agency for New Technologies, Energy and Sustainable Economic Development (ENEA), Italy).



TITLE: SC2 - DATE: November 2005

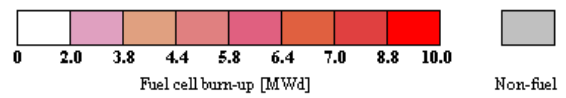
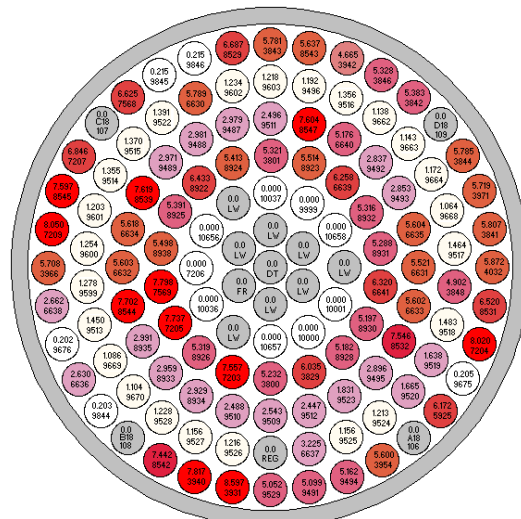
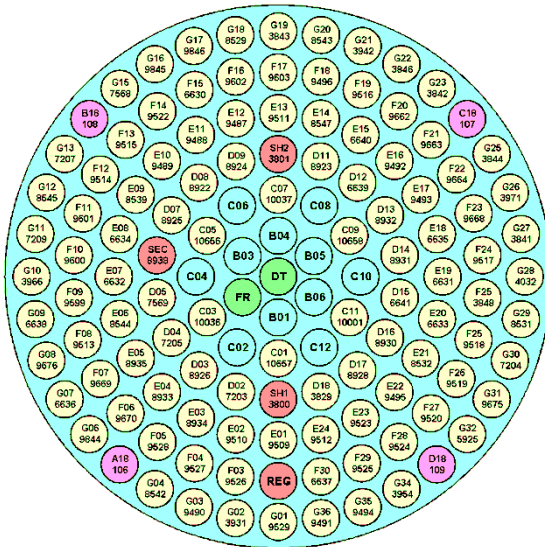


FIG. 5.5. SC2 configuration for the TRADE core (Courtesy of the Italian National Agency for New Technologies, Energy and Sustainable Economic Development (ENEA), Italy).



TITLE: SC3 - DATE: November 2005

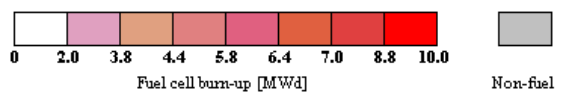
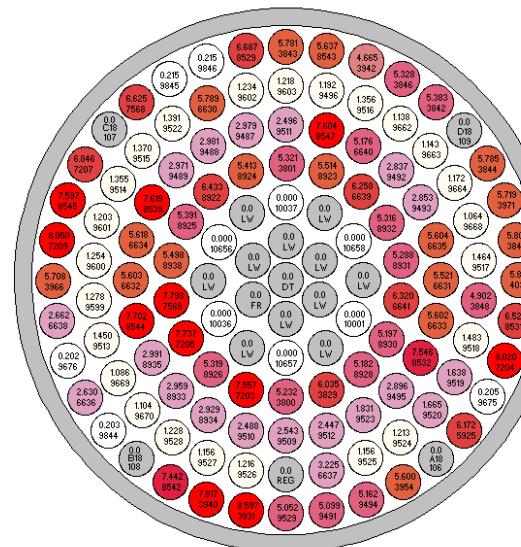


FIG. 5.6. SC3 configuration for the TRADE core (Courtesy of the Italian National Agency for New Technologies, Energy and Sustainable Economic Development (ENEA), Italy).

5.3. RESEARCH ACTIVITY AND RESULTS

The two major portions in this section describe and provide results for the experimental studies and the computational benchmark analyses, respectively, corresponding to the pre-TRADE research programme.

5.3.1. Experimental Studies

The experimental results presented here were selected from those documented in an earlier publication [5.10]. The experimental reactivity estimates were obtained by applying the following two experimental techniques:

- PNS Area-ratio method (PNS-Area) [5.3];
- MSA (Modified Source Approximated) method [5.6].

The experimental results obtained by those two techniques were proposed for use in studying this benchmark since the spatial and energy correction factors required for analysing the obtained data can be computed by both deterministic and Monte Carlo codes. The reactivity estimates for the reference configuration are shown in Table 5.2. Those estimates correspond to a confidence level of 95%. The results illustrated in Fig. 5.7 are given in detail in Tables 5.3–5.5. The MSA technique is clearly the one most dependent on detector location [5.6]. The discrepancies from the PNS-Area estimates are about 1% to 5% for SC0, 5% to 19% for SC2 and 16% to 40% for SC3. The PNS-Area technique is the least detector-location dependent, with a spread of 1.22% at most.

TABLE 5.2. REACTIVITY ESTIMATES FOR THE REF CONFIGURATION OBTAINED WITH THE REG ROD DOWN

Detector	Reactivity (\$)		
	ρ	σ_ρ	σ_ρ/ρ
A	-0.4278	0.0133	-3.11%
B	-0.4011	0.0125	-3.11%
C	-0.4002	0.0125	-3.12%
D	-0.4257	0.0133	-3.11%
Spread		-3.65%	

TABLE 5.3. REACTIVITY ESTIMATES OBTAINED USING THE PNS AND MSA TECHNIQUES FOR THE SC0 CORE WITH ALL THE RODS UP

(a) PNS-Area reactivity estimates				(b) MSA reactivity estimates			
Detector	Reactivity (\$)			Detector	Reactivity (\$)		
	ρ	σ_ρ	σ_ρ/ρ		ρ	σ_ρ	σ_ρ/ρ
A	-0.6644	0.0086	1.29%	A	-0.6730	-0.0210	3.12%
B	-0.6593	0.0068	1.03%	B	-0.7067	-0.0220	3.12%
C	-0.6527	0.0074	1.13%	C	-0.7149	-0.0223	3.12%
D	-0.6550	0.0063	0.96%	D	-0.6859	-0.0214	3.12%
Spread		0.78%		Spread		2.75%	

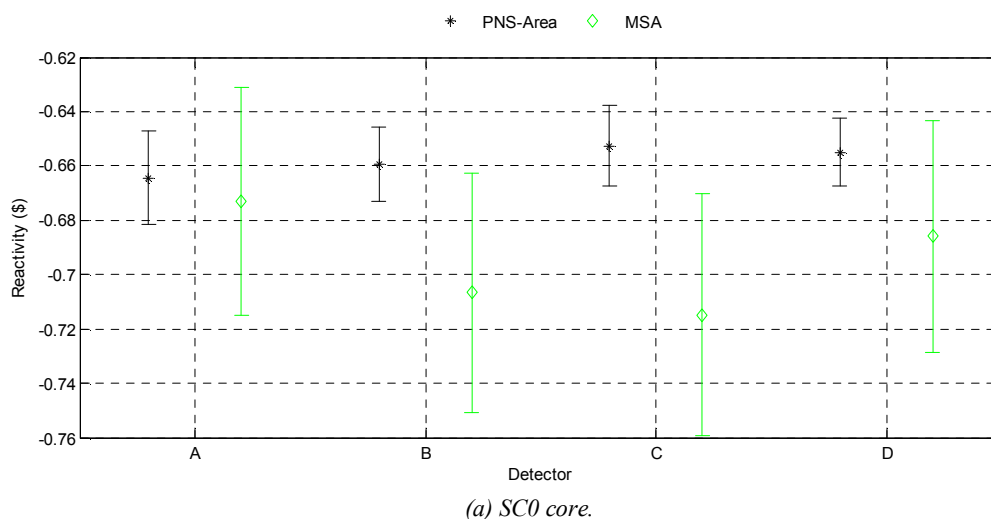
TABLE 5.4. REACTIVITY ESTIMATES OBTAINED USING THE PNS AND MSA TECHNIQUES FOR THE SC2 CORE WITH ALL THE RODS UP

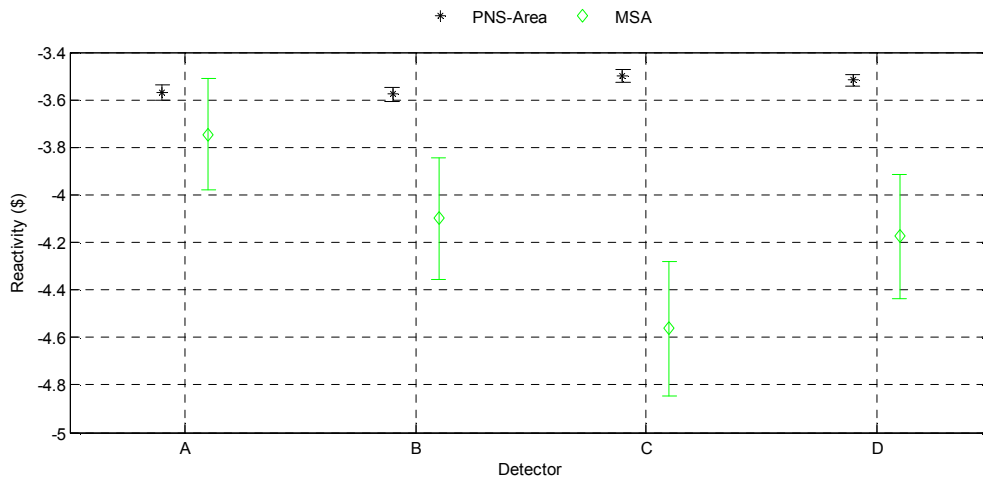
(a) PNS-Area reactivity estimates				(b) MSA reactivity estimates			
Detector	Reactivity (\$)			Detector	Reactivity (\$)		
	ρ	σ_ρ	σ_ρ/ρ		ρ	σ_ρ	σ_ρ/ρ
A	-3.5718	0.0162	0.45%	A	-3.7452	-0.1169	3.12%
B	-3.5766	0.0155	0.43%	B	-4.1002	-0.1280	3.12%
C	-3.4976	0.0137	0.39%	C	-4.5633	-0.1425	3.12%
D	-3.5173	0.0128	0.36%	D	-4.1756	-0.1302	3.12%
Spread	11%			Spread	8.09%		

TABLE 5.5. REACTIVITY ESTIMATES OBTAINED USING THE PNS AND MSA TECHNIQUES FOR THE SC3 CORE WITH ALL THE RODS UP

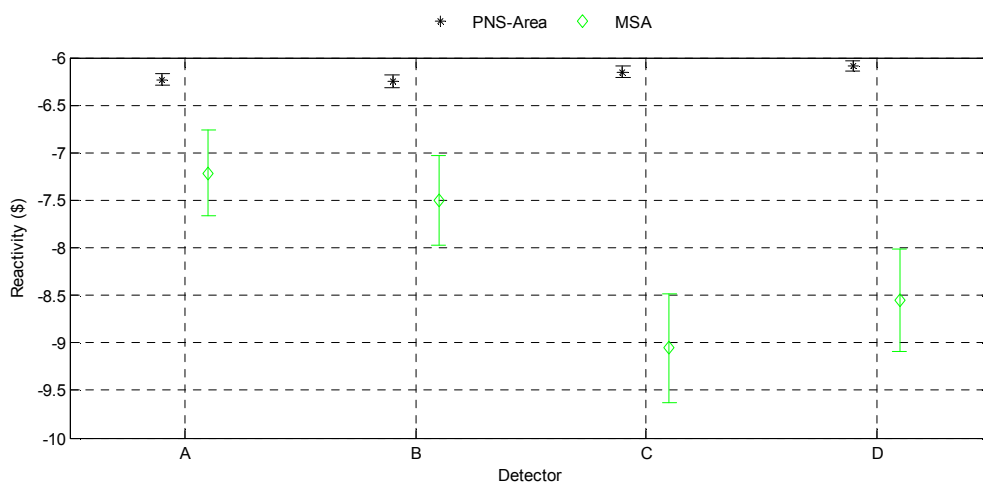
(a) PNS-Area reactivity estimates				(b) MSA reactivity estimates			
Detector	Reactivity (\$)			Detector	Reactivity (\$)		
	ρ	σ_ρ	σ_ρ/ρ		ρ	σ_ρ	σ_ρ/ρ
A	-6.2296	0.0324	0.52%	A	-7.2184	0.2256	3.12%
B	-6.2511	0.0322	0.52%	B	-7.4979	-0.2342	3.12%
C	-6.1497	0.0286	0.47%	C	-9.0570	-0.2832	3.13%
D	-6.0876	0.0265	0.44%	D	-8.5528	-0.2674	3.13%
Spread	1.22%			Spread	10.74%		

Note: The following three plots that collectively comprise Fig. 5.7 show results obtained for the SC0, SC2, and SC3 subcritical cores. The main caption located immediately below the third plot at the bottom is applicable to all three plots.





(b) SC2 core.



(c) SC3 core.

FIG. 5.7. Comparison of results obtained using the PNS and MSA techniques with all rods up. The error bars correspond to a confidence level of 95% (Courtesy of the Italian National Agency for New Technologies, Energy and Sustainable Economic Development (ENEA), Italy).

5.3.2. Benchmark Analyses

Two separate sets of analyses of the TRADE data, corresponding to work by the ENEA and the JAEA laboratories, respectively, are discussed in this section.

5.3.2.1. ENEA Analyses

A time-dependent analysis approach was followed in evaluating the correction factors required for an application of the PNS Area-ratio method. The calculations needed to determine the required correction factors for applying this method were performed using the MCNPX code [5.11] and the JEFF 3.1 nuclear data library. In carrying out this analysis, the neutrons generated from the source were ultimately distributed in time by first assuming that every neutron starts at time $t = 0$ (a delta function source time spectrum). The estimators were defined, with their appropriate time binning, in order to evaluate the fission-rate time evolution. The final results from these calculations provided an estimation of the system transfer functions, as seen by the fission chambers, when the origination time of each emitted neutron is distributed as a delta function. A convolution of the evaluated transfer function,

with a suitable source time distribution, provides the simulated response of the fission chambers for the desired simulation period (see Fig. 5.8). This procedure allows reliable results to be obtained quickly that are very difficult to achieve using direct time-resolved Monte Carlo simulations.

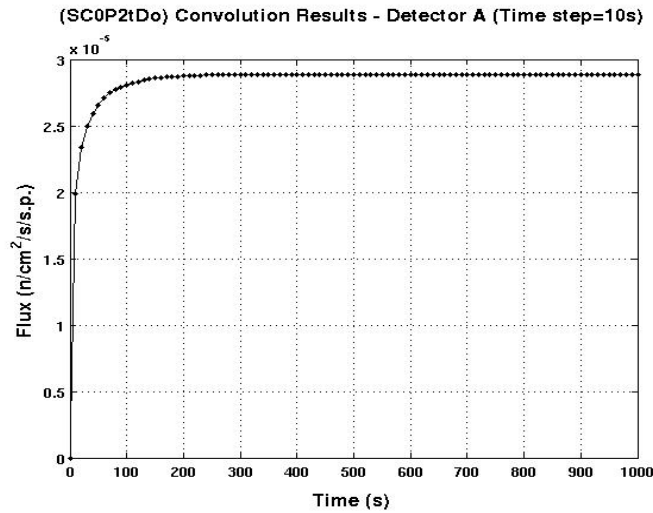


FIG. 5.8. Simulated response (shown with 10-second time steps) of a detector to a train of pulses from the neutron source (at 50 Hz frequency). Notice that the flux saturates after 300 s (Courtesy of the Italian National Agency for New Technologies, Energy and Sustainable Economic Development (ENEA), Italy).

The reactivity of the system was estimated by considering the ratio of the prompt neutron flux component to the delayed-neutron flux component, integrated over a time period defined by the source (see Fig. 5.9). This determination was made with the assumption that the delayed-neutron production is in the saturation regime (see Fig. 5.8). Time-resolved measurements are needed in order to distinguish between the relative numbers of delayed-neutron-induced fissions and prompt-neutron-induced fissions.

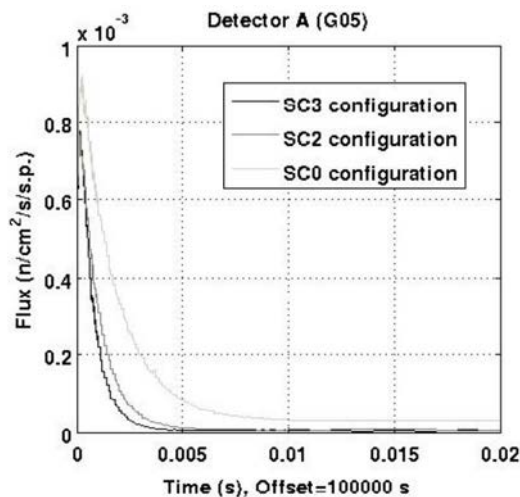


FIG. 5.9. Simulated system response exhibited on a time scale corresponding to a one neutron source pulse after saturation (20 ms) (Courtesy of the Italian National Agency for New Technologies, Energy and Sustainable Economic Development (ENEA), Italy).

The correction factors required for applying the PNS Area-ratio method, by implementing equivalent steady-state methods, were evaluated following the procedure described in Ref. [5.4]. An example of the application of this approach to the MUSE-4 case can be found in Ref. [5.12]. Modified Source Approximated (MSM) factors have also been calculated following the procedure described in Ref. [5.6].

The REF core configuration (Fig. 5.3) was found experimentally to achieve criticality with an absorber insertion level of 51% for the regulation rod. The estimation of k_{eff} by MCNPX (using the KCODE module) for this configuration yielded 0.98349 (± 0.00022), corresponding to a reactivity $\rho = -1679$ pcm, or equivalently, $\rho = -2.40$ \$, assuming that for the RC-1 TRIGA 1 \$ = 700 pcm. This underestimation of the reactivity level, which amounts to -3.89 \$ for the SC3 configuration, as described below, can be attributed to difficulty in estimating the actual burnup distribution of the reactor, in spite of considerable effort lavished on reconstructing the burnup history. Tables 5.6–5.8, as well as Fig 5.10–5.12, show the results for the configurations SC0, SC2, and SC3, respectively.

TABLE 5.6. RESULTS FOR THE SC0 CORE

SC0 (\$)					
Detector position	Experimental results				
	G05	G14	G24	G33	Mean $\pm \sigma$
ρ Area (\$)	-0.66	-0.66	-0.65	-0.66	-0.66 ± 0.01
ρ MSA (\$)	-0.67	-0.71	-0.71	-0.69	-0.70 ± 0.02
ρ Mean (\$)					-0.68 ± 0.02
Calculated results					
ρ (\$)	-3.10				
ρ Area TD (\$)	-2.76	-2.74	-2.70	-2.75	-2.74 ± 0.03
CF Area TD	1.12	1.13	1.15	1.13	1.13 ± 0.01
ρ Area ESS (\$)	-2.76	-2.66	-2.62	-2.70	-2.66 ± 0.03
CF Area ESS	1.16	1.16	1.18	1.15	1.16 ± 0.01
T_d	3.9	4.0	3.9	4.0	3.95 ± 0.05
F MSM	0.98	1.00	0.99	1.00	0.99 ± 0.01
Corrected experimental results					
ρ Area TD (\$)	-0.75	-0.74	-0.75	-0.74	-0.74 ± 0.01
ρ Area ESS (\$)	-0.77	-0.77	-0.77	-0.75	-0.77 ± 0.01
ρ Area Mean (\$)	-0.76	-0.76	-0.76	-0.74	-0.75 ± 0.01
ρ MSM (\$)	-0.66	-0.71	-0.70	-0.69	-0.69 ± 0.02
SC0 (pcm)					
Detector position	Experimental results				
	G05	G14	G24	G33	Mean $\pm \sigma$
ρ Area (\$)	-465	-462	-457	-459	-460 ± 4
ρ MSA (\$)	-471	-495	-500	-480	-487 ± 13
ρ Mean (\$)					-474 ± 17
Calculated results					
ρ (\$)	-2169				
ρ Area TD (\$)	-1933	-1920	-1890	-1928	-1918 ± 19
CF Area TD	1.12	1.13	1.15	1.13	1.13 ± 0.01
ρ Area ESS (\$)	-1868	-1863	-1835	-1892	-1865 ± 23
CF Area ESS	1.16	1.16	1.18	1.15	1.16 ± 0.01
T_d	3.9	4.0	3.9	4.0	3.95 ± 0.05
F MSM	0.98	1.00	0.99	1.00	0.99 ± 0.01
Corrected experimental results					
ρ Area TD (pcm)	-522	-521	-524	-516	-521 ± 4
ρ Area ESS (pcm)	-540	-537	-540	-526	-536 ± 7
ρ Area Mean (pcm)	-531	-529	-532	-521	-528 ± 9
ρ MSM (pcm)	-460	-494	-493	-481	-482 ± 16

In particular, each of these three tables provides the following numerical results (given in both dollar units and pcm):

- Experimental results: Measured reactivity values obtained by the PNS Area and MSA methods for each detector position;
- Calculated results: Reactivity values calculated using the MCNPX (KCODE module). Reactivity values obtained by the Area Time Dependent (TD) calculations, as well as the relative correction factor for each detector position. Reactivity values obtained from

Area Equivalent Steady State (ESS) calculations, as well as the relative correction factor for each detector position. Counting rate and MSM factor values for each detector position;

- Corrected experimental results: Corrected measured reactivity values based on applying the Area Time Dependent correction factor for each detector position. Corrected measured reactivity values based on applying the Area Equivalent Steady State correction factor for each detector position. Mean values obtained from these two corrected Area results are provided. Corrected measured reactivity values obtained by applying MSM factors for each detector position are also given.

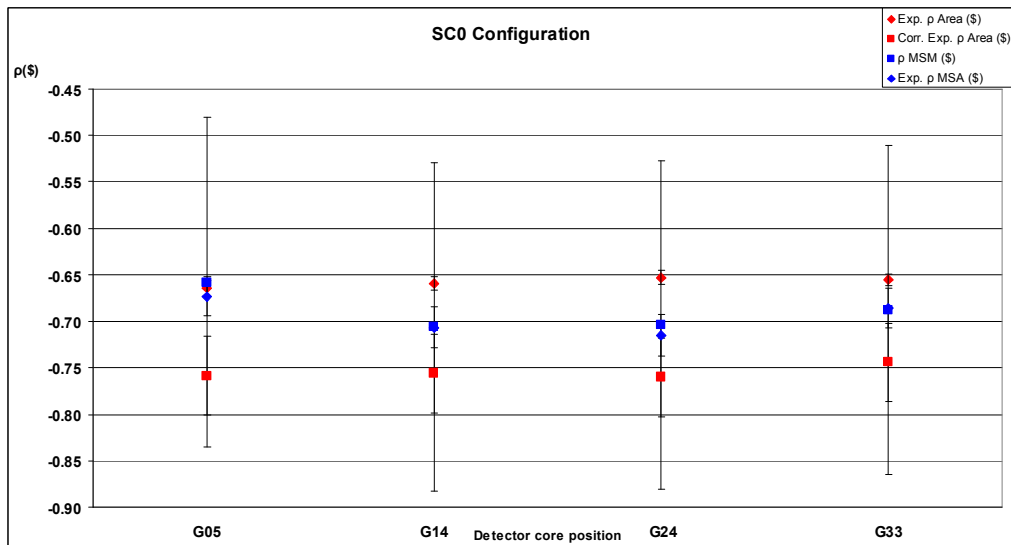


FIG. 5.10. Results for the SC0 core (Courtesy of the Italian National Agency for New Technologies, Energy and Sustainable Economic Development (ENEA), Italy).

TABLE 5.7. RESULTS FOR THE SC2 CORE

SC2 (\$)					
Experimental results					
Detector position	G05	G14	G24	G33	Mean \pm σ
ρ Area (\$)	-3.57	-3.58	-3.50	-3.52	-3.54 ± 0.04
ρ MSA (\$)	-3.75	-4.10	-4.56	-4.18	-4.15 ± 0.34
ρ Mean (\$)					-3.84 ± 0.39
Calculated results					
ρ (\$)			-7.17		
ρ Area TD (\$)	-6.36	-6.29	-6.13	-6.53	-6.33 ± 0.17
CF Area TD	1.13	1.14	1.17	1.10	1.13 ± 0.03
ρ Area ESS (\$)	-6.30	-6.13	-6.24	-6.69	-6.34 ± 0.24
CF Area ESS	1.14	1.17	1.15	1.07	1.13 ± 0.04
T_d	1.6	1.5	1.4	1.5	1.51 ± 0.10
F MSM	0.94	0.90	0.80	0.88	0.88 ± 0.06
Corrected experimental results					
ρ Area TD (\$)	-4.03	-4.08	-4.09	-3.86	-4.02 ± 0.11
ρ Area ESS (\$)	-4.06	-4.18	-4.02	-3.77	-4.01 ± 0.17
ρ Area Mean (\$)	-4.05	-4.13	-4.05	-3.82	-4.01 ± 0.13
ρ MSM (\$)	-3.52	-3.69	-3.67	-3.66	-3.63 ± 0.08
SC2 (pcm)					
Experimental results					
Detector position	G05	G14	G24	G33	Mean \pm σ
ρ Area (\$)	-2500	-2504	-2448	-2462	-2479 ± 28
ρ MSA (\$)	-2622	-2870	-3194	-2923	-2902 ± 235
ρ Mean (\$)					-2690 ± 274
Calculated results					
ρ (\$)			-5020		
ρ Area TD (\$)	-4451	-4401	-4291	-4571	-4429 ± 116
CF Area TD	1.13	1.14	1.17	1.10	1.13 ± 0.03
ρ Area ESS (\$)	-4411	-4291	-4371	-4681	-4439 ± 169
CF Area ESS	1.14	1.17	1.15	1.07	1.13 ± 0.04
T_d	1.6	1.5	1.4	1.5	1.51 ± 0.10
F MSM	0.94	0.90	0.80	0.88	0.88 ± 0.06
Corrected experimental results					
ρ Area TD (pcm)	-2820	-2856	-2864	-2704	-2811 ± 74
ρ Area ESS (pcm)	-2845	-2929	-2812	-2640	-2807 ± 121
ρ Area Mean (pcm)	-2833	-2892	-2838	-2672	-2809 ± 93
ρ MSM (pcm)	-2465	-2585	-2566	-2561	-2544 ± 54

TABLE 5.8. RESULTS FOR THE SC3 CORE

SC3 (\$)					
Detector position	Experimental results				
	G05	G14	G24	G33	Mean $\pm \sigma$
ρ Area (\$)	-6.23	-6.25	-6.15	-6.09	-6.18 \pm 0.08
ρ MSA (\$)	-7.22	-7.50	-9.06	-8.55	-8.08 \pm 0.87
ρ Mean (\$)					-7.13 \pm 1.17
Calculated results					
ρ (\$)			-11.02		
ρ Area TD (\$)	-9.90	-9.63	-9.00	-9.00	-9.38 \pm 0.45
CF Area TD	1.11	1.14	1.22	1.22	1.18 \pm 0.06
ρ Area ESS (\$)	-9.20	-8.33	-8.67	-8.80	-8.75 \pm 0.36
CF Area ESS	1.20	1.32	1.27	1.25	1.26 \pm 0.05
T_d	1.2	1.1	0.9	1.0	1.04 \pm 0.14
F MSM	1.07	0.97	0.78	0.89	0.93 \pm 0.12
Corrected experimental results					
ρ Area TD (\$)	-6.94	-7.16	-7.53	-7.46	-7.27 \pm 0.28
ρ Area ESS (\$)	-7.46	-8.27	-7.82	-7.63	-7.79 \pm 0.35
ρ Area Mean (\$)	-7.20	-7.71	-7.67	-7.54	-7.53 \pm 0.40
ρ MSM (\$)	-7.69	-7.25	-7.03	-7.62	-7.40 \pm 0.31
SC3 (pcm)					
Detector position	Experimental results				
	G05	G14	G24	G33	Mean $\pm \sigma$
ρ Area (\$)	-4361	-4376	-4305	-4261	-4326 \pm 53
ρ MSA (\$)	-5053	-5249	-6340	-5987	-5657 \pm 607
ρ Mean (\$)					-4991 \pm 816
Calculated results					
ρ (\$)			-7717		
ρ Area TD (\$)	-6931	-6741	-6301	-6301	-6569 \pm 318
CF Area TD	1.11	1.14	1.22	1.22	1.18 \pm 0.06
ρ Area ESS (\$)	-6441	-5831	-6071	-6161	-6126 \pm 252
CF Area ESS	1.20	1.32	1.27	1.25	1.26 \pm 0.05
T_d	1.4	1.1	0.9	1.0	1.04 \pm 0.14
F MSM	1.07	0.97	0.78	0.89	0.93 \pm 0.12
Corrected experimental results					
ρ Area TD (pcm)	-4855	-5009	-5272	-5219	-5089 \pm 193
ρ Area ESS (pcm)	-5225	-5791	-5472	-5338	-5456 \pm 245
ρ Area Mean (pcm)	-5040	-5400	-5372	-5278	-5273 \pm 283
ρ MSM (pcm)	-5386	-5077	-4924	-5334	-5180 \pm 218

Comments on results obtained for the SC0 configuration are as follows: the calculated value (-3.10 \$) significantly underestimates the rough experimental one (-0.68 \$) by an amount -2.42 \$. As mentioned earlier, this can be attributed to the difficulty in estimating the burnup distribution of the reactor, in spite of the effort lavished on reconstructing the burnup history. However, even in such a case it is possible in general to see how the calculated correction factors behave with respect to the effect of clustering or scattering relative to the rough experimental results. In principle, even if the calculation overestimates or underestimates the reactivity level, the principal requirement for these correction factors is that they correctly represent the flux shape for the generic configuration. In fact, if the flux

shape is well established, it is possible to express the MSA relationship between the actual situation and the calculated one by the formula $\rho_{cal} \times T_{cal} = \rho_{actual} \times T_{actual}$. For the SC0 configuration it can be seen that the rough experimental data exhibit a standard deviation of $\pm 2 \text{ } \phi$, whereas the corresponding Area corrected values (-0.75 \$) exhibit a standard deviation of $\pm 1 \text{ } \phi$. Figure 5.10 shows graphically the experimental results for the SC0 configuration. In this plot, as well as those for the configurations SC2 and SC3, all the exhibited experimental corrected reactivity values obtained by the Area method (indicated as Corr. Exp. ρ Area (\$)) are mean values obtained by considering both the corrected results produced by the Time Dependent (TD) and the Equivalent Steady State (ESS) calculations. Finally, the MSM correction results exhibits a standard deviation of $\pm 2 \text{ } \phi$.

Comments on the results obtained for the SC2 configuration are as follows: In this case the calculated value (-7.17 \$) significantly underestimates the rough experimental one (-3.84 \$) by an amount -3.33 \$. For the SC2 configuration, it can be seen that the rough experimental data exhibit a standard deviation $\pm 39 \text{ } \phi$, whereas the Area method corrected ones (-4.01 \$) exhibit a standard deviation of $\pm 13 \text{ } \phi$ and the MSM method corrected ones (-3.63 \$) exhibit a standard deviation $\pm 8 \text{ } \phi$. The mean of both Area method and MSM corrected results provides -3.89 \$, with a standard deviation of $\pm 22 \text{ } \phi$. Therefore, the correction factors scatter relative to the original experimental results by $\pm 39 \text{ } \phi$ around -3.84 \$ to $\pm 22 \text{ } \phi$ around -3.89 \$. Figure 5.11 shows the experimental results graphically for the SC2 configuration.

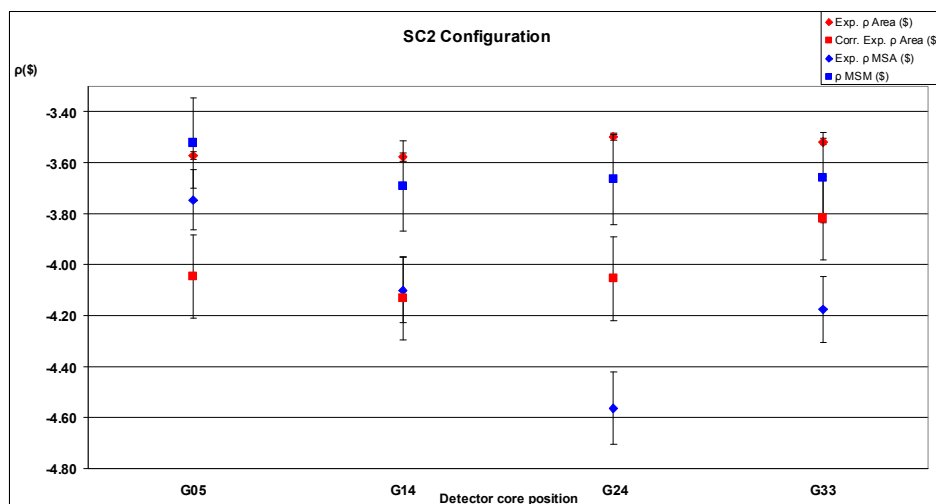


FIG. 5.11. Results for SC2 core (Courtesy of the Italian National Agency for New Technologies, Energy and Sustainable Economic Development (ENEA), Italy).

Comments on the results for the SC3 configuration are as follows: In this case the calculated value (-11.02 \$) underestimates the rough experimental one (-7.13 \$) by an amount -3.89 \$. For the SC3 configuration, the rough experimental data exhibit a standard deviation of $\pm 1.17 \text{ } \phi$ whereas the Area method corrected ones (-7.53 \$) have a standard deviation of $\pm 40 \text{ } \phi$ and the MSM method corrected ones (-7.40 \$) have a standard deviation of $\pm 31 \text{ } \phi$. The mean of both Area method and MSM corrected results is -7.49 \$ with a standard deviation of $\pm 37 \text{ } \phi$. Therefore the correction factors scatter relative to the original experimental results by $\pm 1.17 \text{ } \phi$ around -7.13 \$ to $\pm 37 \text{ } \phi$ around -7.49 \$. Figure 5.12 shows the experimental results graphically for the SC3 configuration.

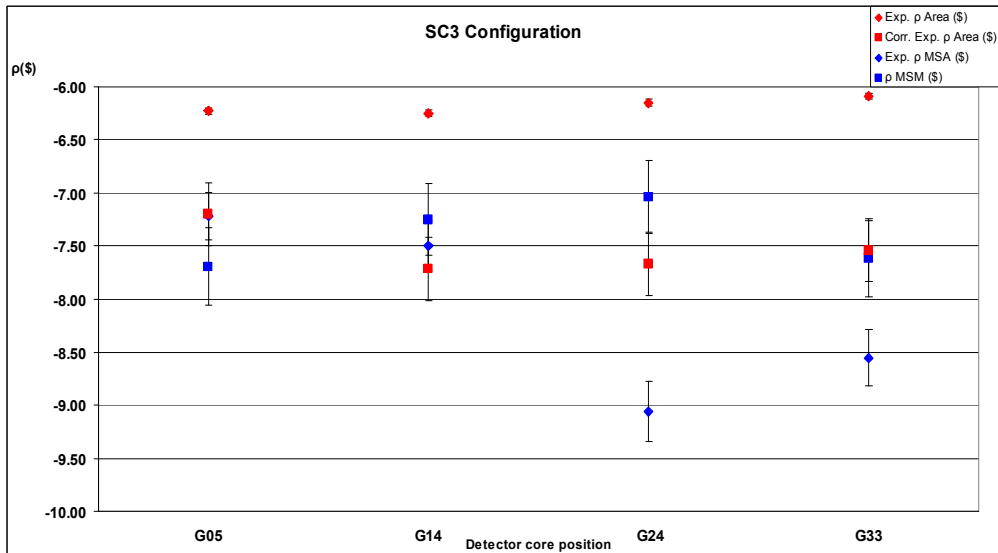


FIG. 5.12. Results for SC3 core (Courtesy of the Italian National Agency for New Technologies, Energy and Sustainable Economic Development (ENEA), Italy).

5.3.2.2. JAEA Analyses

The JAEA laboratory performed the calculations for k_{eff} and the level of subcriticality by means of the PNS α fitting method, using the input numerical data file prepared by the ENEA laboratory in conjunction with the JENDL-3.3 nuclear data library. The computational code employed for this purpose was MCNPX (ver. 2.7a). The k_{eff} calculations were performed using the MCNP (KCODE module).

The following assumptions were made for the PNS calculations:

- A 14 MeV neutron source was situated at the centre of the core;
- A volume tally (F4) was employed. Detectors with diameter $\phi = 3.74$ cm and length $L = 5.0$ cm were situated at each detector position and ^{235}U fission rates were determined.

Table 5.9 presents the calculated reactivity levels for each reactor core configuration together with the ENEA results for comparison. The same data are shown in a graphical way in Fig. 5.13 together with the mean experimental values (uncorrected) that were obtained by the Area Ratio and MSA techniques.

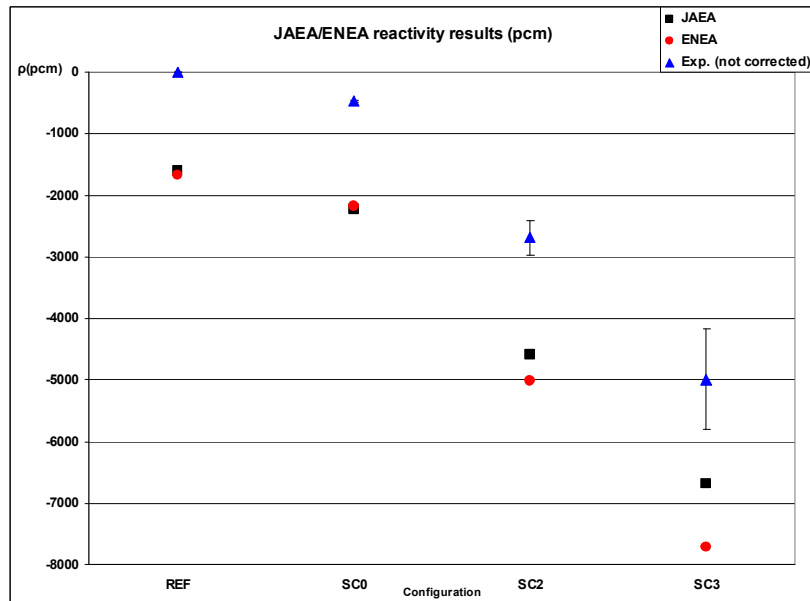


FIG. 5.13. JAEA/ENEA reactivity results (in pcm) (Courtesy of the Italian National Agency for New Technologies, Energy and Sustainable Economic Development (ENEA), Italy).

TABLE 5.9. COMPARISON OF THE JAEA AND ENEA REACTIVITY RESULTS (IN PCM)

	JAEA	ENEA	Exp. (not corrected)
REF	-1598	-1679	0
SC0	-2226	-2169	-474
SC2	-4586	-5020	-2690
SC3	-6687	-7717	-4991

The same general trend in the obtained results (significant underestimation of the rough experimental reactivity levels), already observed for ENEA results, is clearly noticeable in the JAEA results. In any case, the JAEA results appear to be closer to the experimental values when compared with the ENEA values, especially for the deeper subcriticality levels such as those encountered for the SC2 and SC3 core configurations.

The subcriticality level was calculated by means of the Eq. (5.1):

$$\rho = 1 - \frac{\alpha}{\alpha_c} \quad (5.1)$$

when the PNS α fitting method was applied. The parameter $\alpha = (\rho - \beta_{eff})/\Lambda$ was deduced from the experimental curves (see Fig. 5.14), and parameters $\alpha_c = -\beta_{eff}/\Lambda = 132 \text{ s}^{-1}$ and $\beta_{eff} = 678 \text{ pcm}$ were taken from Ref. [5.13].

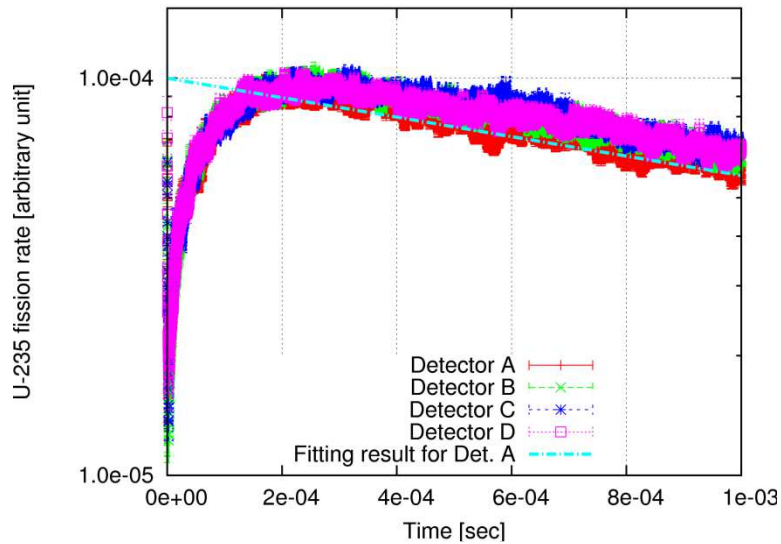


FIG. 5.14. Typical transient response for the ^{235}U fission-rate corresponding to the SC0 core (Courtesy of the Italian National Agency for New Technologies, Energy and Sustainable Economic Development (ENEA), Italy).

The calculated reactivity values for the SC0 core are shown together with ENEA results in Fig. 5.15 for each detector position, compared to results from the Area method.

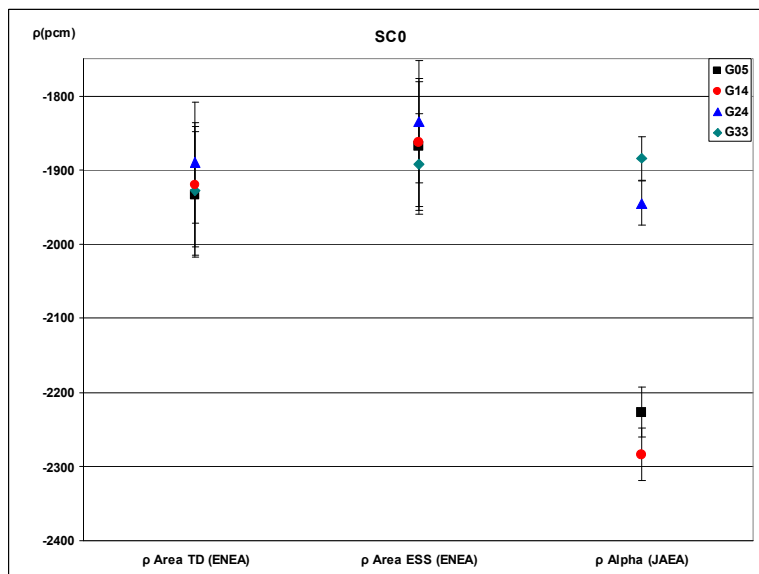


FIG. 5.15. Calculated results for the SC0 core (Courtesy of the Italian National Agency for New Technologies, Energy and Sustainable Economic Development (ENEA), Italy).

Except for two values obtained from PNS- α fitting, corresponding to the detectors at G05 and G14, the consistency of the plotted values is observed to be reasonable. In fact, the spatial dependence of the PNS- α fitting method has been observed already in MUSE-4 [5.14].

A typical transient response profile for the SC2 configuration is shown in Fig. 5.16.

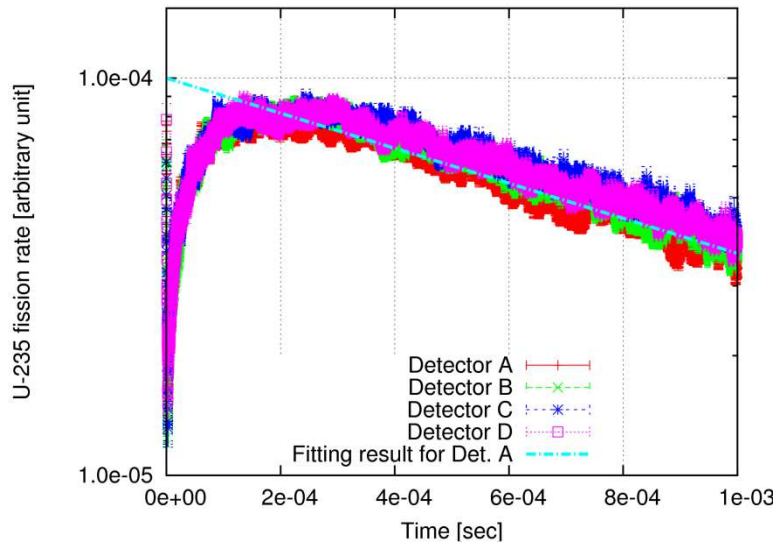


FIG. 5.16. Typical transient response for the ^{235}U fission rate corresponding to the SC2 core (Courtesy of the Italian National Agency for New Technologies, Energy and Sustainable Economic Development (ENEA), Italy).

The calculated reactivity values for the SC2 core are shown together with ENEA results in Fig. 5.17 for each detector position, compared to results from Area method.

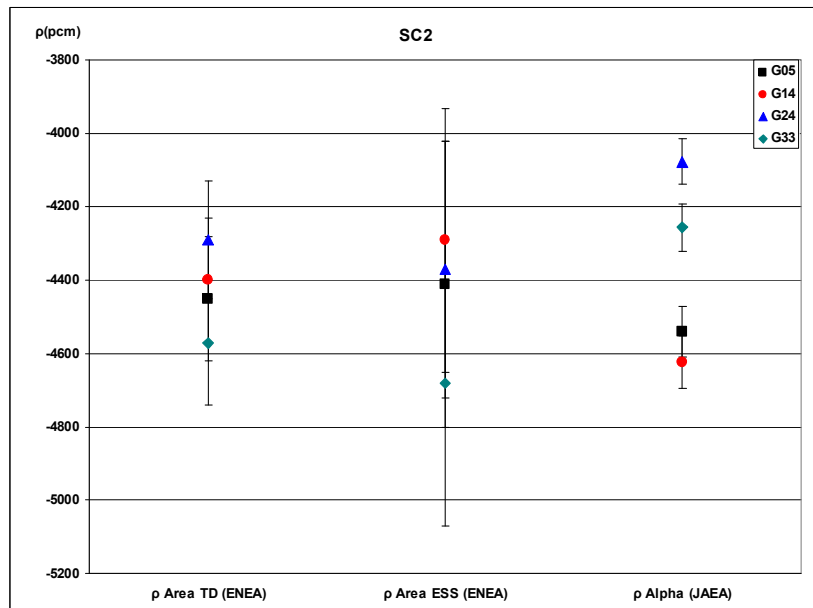


FIG. 5.17. Calculated results for SC2 (Courtesy of the Italian National Agency for New Technologies, Energy and Sustainable Economic Development (ENEA), Italy).

A typical transient response profile for the SC3 configuration is shown in Fig. 5.18.

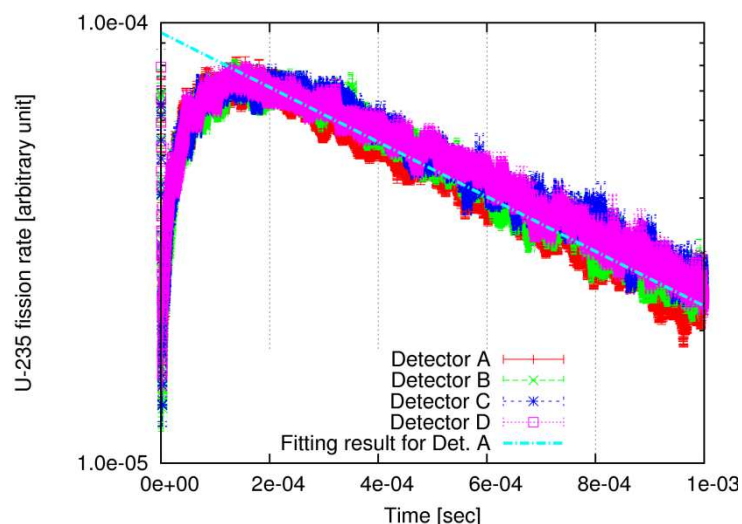


FIG. 5.18. Typical transient response for the ^{235}U fission-rate corresponding to the SC3 core (Courtesy of the Italian National Agency for New Technologies, Energy and Sustainable Economic Development (ENEA), Italy).

The calculated reactivity values for the SC3 core are shown together with ENEA results in Fig. 5.19 for each detector position, compared to results from Area method.

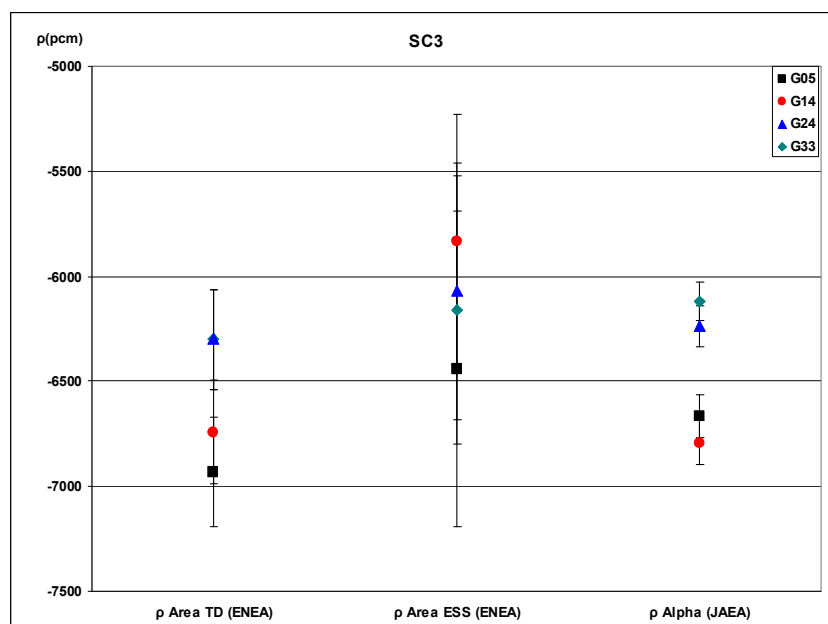


FIG. 5.19. Calculated results for SC3 (Courtesy of the Italian National Agency for New Technologies, Energy and Sustainable Economic Development (ENEA), Italy).

All the calculated results for the SC0, SC2 and SC3 core configurations exhibit a noticeable spatial dependence with respect to the detector position, including the Area results. It is noteworthy that this effect was not observed in the MUSE-4 experiments [5.14]. In addition, because of the large statistical uncertainty in the calculations that affect the ENEA

results (especially the Area ESS results), it is difficult to establish with any confidence whether the JAEA and ENEA reactivity evaluations are really in agreement or not. The TRADE experiment was conceived for fresh fuel. However, the actual fuel complement of the Casaccia TRIGA RC-1 reactor has been in use since 1960. As a consequence, it is impossible to evaluate the altered burnup distribution relative to fresh fuel with great precision because of the inherent difficulty in reconstructing the actual fuel history starting from the year 1960. Therefore, the approach taken in the present investigation probably represents an unfair bench test for the analytic procedures pursued in this work.

5.4. CONCLUSIONS

The TRADE experiment was formally endorsed at the international level on 7 June, 2002 (in Rome). The objective of this project was to couple an external proton accelerator to a neutron-producing target to be installed in the central channel of the RC-1 TRIGA reactor located at the ENEA-Casaccia Research Centre near Rome. The reactor facility would be operated under subcritical conditions for the TRADE experiments. A huge body of experimental data was acquired during the period 2002—2004 in the framework of the pre-analysis activities of the TRADE experiment. Unfortunately, due to problems associated with securing financial backing, the TRADE programme was interrupted at the end of 2004.

During the ‘pre-TRADE’ experimental phase, reactivity determinations were carried out using the Area-ratio and Source Multiplication methods. These were performed at various core locations and for distinct ‘clean’ (without control rods) core subcritical configurations.

A benchmark was established in June 2007 within the framework of the Coordinated Research Project (CRP) entitled ‘Analytical and Experimental Benchmark Analyses of Accelerator Driven Systems’. In particular, a coordinated research project was initiated under the auspices of the CRP entitled ‘Collaborative Work on Utilization of LEU in ADS’. This activity involves the evaluation of nuclear parameters for subcritical reactors driven by external neutron sources.

In addition to the ENEA, Japan Atomic Energy Agency (JAEA) participated in this benchmark programme by carrying out k_{eff} calculations and subcriticality determinations by the PNS- α fitting method. Use was made of an input file prepared by ENEA and the JENDL-3.3 nuclear data library. By comparison, the ENEA used JEFF 3.1 as the nuclear data library for its work. Both the ENEA and JAEA employed the Monte Carlo code MCNPX.

The main results can be summarized as follows:

- A significant underestimation of the experimental reactivity level from the calculations was observed, with the underestimation reaching values of around -4 \$ for the deepest subcritical level configuration (the SC3 core). This underestimation effect can be attributed to the difficulty in estimating the actual burnup distribution of the reactor in spite of effort lavished on reconstructing the burnup history;
- Rough experimental reactivity results (without corrections) obtained by PNS Area-ratio and MSA methods showed large deviations, depending on the method and on the detector position, with the differences amounting to more than 1 \$ standard deviation for the SC3 configuration;
- This spatial dependence of the reactivity estimate based on the method and detector position was confirmed by both the ENEA and JAEA calculations.
- In spite of the discrepancy in the calculated reactivity levels, the calculated correction factors clustered around the experimental results for both PNS Area-ratio and MSA methods.

In conclusion, the ‘pre-TRADE Experimental Benchmark’ can be considered as a ‘limited’ test benchmark to use in validating ADS experimental techniques. It is clearly necessary to take into account all the inherent difficulties associated with characterizing the

neutronic behaviour of the system for subcritical core configurations. Furthermore, the actual composition of the fuel itself is an important issue that needs to be addressed. Nevertheless, the observed clustering of the experimental results obtained from calculating the spatial correction factors for both the PNS Area-ratio and MSA methods suggests that there is room for optimism concerning the application of such techniques to on-going or future experimental campaigns designed to gain a satisfactory understanding of ADS neutronic characterization.

REFERENCES TO SECTION 5

- [5.1] INTERNATIONAL ATOMIC ENERGY AGENCY, Nuclear Power Technology Development, IAEA Coordinated Research Projects (CRP), <https://www.iaea.org/NuclearPower/Technology/CRP/>.
- [5.2] MONTI, S. et al., TRADE: A full experimental validation of the ADS concept in a European perspective, Int. Conf. AccApp'03: Accelerator Applications in a Nuclear Renaissance, June 1-5, San Diego, California, (2003).
- [5.3] SJÖSTRAND, N.J., Arkiv. Fis. 11, 233, 1956. See also in G.I. Bell and S. Glasstone, Nuclear Reactor Theory, Van Nostrand Reinhold Company, 546-549, (1970).
- [5.4] BELL, G.I. and GLASSTONE, S., Nuclear Reactor Theory, Van Nostrand Reinhold Company, 550-551, (1970).
- [5.5] PANCIN, J., ANDRIAMONJE, S., AUNE, S. et al., Piccolo Micromegas: First in-core measurements in a nuclear reactor, Nuclear Instruments and Methods in Physics Research, **A592**, Issues 1-2, (2008) 104-113.
- [5.6] MERCATALI, L., CARTA, M., PELUSO, V., "Interpretation of the TRADE in-pile source multiplication experiments (Seventh Intl Topical Meeting on Nuclear Applications of Accelerator Technology, Venice, Italy, 2005), Nuclear Instruments and Methods in Physics Research **562(2)** (2006) 875-878.
- [5.7] DI PALO, L., FOCACCIA, G., LO PRATO, E., MARSILI, F., PERNI, M., VERRI, A., RC-1 REATTORE 1 MW – Progetto Definitivo e Rapporto di Sicurezza", CNEN Centro Studi Nucleari Casaccia, (1966).
- [5.8] VNIIA. Neutron Generator IHG-101-150 - Operating Manual. All-Russian Research Institute of Automatics - The Russian Federation Ministry on Atomic Energy, (2003).
- [5.9] BAN, G. et al., Neutron flux measurements in the TRADE experiment: Critical configuration, Nuclear Energy Systems for Future Generation and Global Sustainability, GLOBAL 2005, Tsukuba, Japan, (2005).
- [5.10] JAMMES, C. et al., Experimental reactivity estimates of the three sub-critical configurations of the zero-power RACE-T program, CEA Technical Note, NT-DEN/CAD/DER/SPEX/LDCI/06/14, (2006).
- [5.11] WATERS, L.S., Ed., MCNPX User's Manual, Version 2.4.0, LA-CP-02-408 (2002).
- [5.12] CARTA, M. et al., "Reactivity assessment and spatial time-effects from the MUSE kinetics experiment", Proc. PHYSOR 2004 – The Physics of Fuel Cycles and Advanced Nuclear Systems: Global Developments, Chicago, Illinois, April 25-29, 2004, American Nuclear Society, Lagrange Park, IL. (2004).
- [5.13] BURGIO, N., Scoping Calculations for the Pre-TRADE Benchmark, presented at the IAEA Technical meeting, Rome, Italy, Nov. 2007.
- [5.14] GONZÁLEZ-ROMERO, E. et al., "The MUSE4 pulsed neutron source experiments", Proc. PHYSOR 2004 – The Physics of Fuel Cycles and Advanced Nuclear Systems: Global Developments, Chicago, Illinois, April 25-29, 2004, American Nuclear Society, Lagrange Park, IL. (2004).

6. EXPERIMENTAL NEUTRON SOURCE FACILITY OF KHARKOV INSTITUTE OF PHYSICS AND TECHNOLOGY⁵

Contributed by

I. Neklyudov, I. Karnaukhov, A. Zelinsky, I. Ushakov
*National Science Centre Kharkov Institute of Science and Technology, Kharkov,
Ukraine*

Y. Gohar, G. Aliberti, Y. Cao, A. Talamo, Z. Zhong
*Argonne National Laboratory, Argonne,
USA*

I. Bolshinsky
*National Nuclear Security Administration – Department of Energy, Washington, DC,
USA*

6.1. INTRODUCTION

In this section the collaboration of the Kharkov Institute of Physics and Technology (KIPT), Ukraine, and Argonne National Laboratory (ANL) USA, on development and construction of an experimental neutron source facility is described [6.1–6.28]. The facility is an LEU-fuelled subcritical assembly driven by electron accelerator that generates neutrons from photonuclear reactions on high-Z material (e.g. natural uranium or tungsten). It is designed for medical radioisotope production, nuclear staff training, and conducting experiments in material researches, reactor physics, and fundamental sciences.

In order to meet the abovementioned objectives, research on facility design development and main design parameters testing has been conducted [6.22]:

“The electron beam target assembly design; the spatial energy deposition in the target materials; and the intensity, spectrum, and spatial distribution of the neutron source have been studied as a function of the electron beam parameters, target materials, and target configurations”.

The main focus of the research is to maximize the neutron production from an electron beam of 100 kW power and to satisfy the engineering design requirements. These studies resulted in new target designs. Engineering analyses were conducted for these designs, including thermal stresses, heat transfer, material requirements, and thermal hydraulics. The developed target geometrical configuration allows maximization of the neutron utilization and fits the geometry of fuel assemblies. The neutron flux distribution study was carried out for k_{eff} approximately 0.98, depending on different enrichments, uranium densities, reflector materials and thickness, and target materials.

With the developed design, taking into account safety, reliability, and environmental considerations, the facility utilization is maximized, such that time for replacing the target, fuel, and irradiation cassettes is reduced due to the use of simple and efficient procedures. The dose map of the facility area during its operation was studied depending on the heavy concrete shield thicknesses. The facility provides good opportunity for future design upgrades and setting new missions in various fields of applications. For example, it has an excellent

⁵ This section is based on Ref. [6.13]

capability for medical radioisotopes production. The irradiation locations and sample sizes were defined for production of 50 different medical radioisotopes. For fundamental research, there are several horizontal channels and a cold neutron source. This Section highlights the facility design, key results from the design analyses, and the current facility status.

The steady state operation of the experimental neutron source facility is provided by the incorporation of main components, such as the electron accelerator, the target assembly, the subcritical assembly, the biological shielding, and the radial neutron ports, and auxiliary components, such as cooling loops, fuel loading machine, removable biological shield for accessing the subcritical assembly and the target assembly, and a cold neutron source. The key performance characteristics are provided for the components are described in this section.

6.1.1. Target Assembly

The target design choices and the accelerator beam parameters were studied with the focus on maximizing the neutron production from 100 kW beam power with 100 MeV electrons and satisfactory operation of chosen target design. The following software was used in this research:

- the MCNPX computer program [6.29] – to “determine the neutron source intensity, the neutron spectrum, the spatial neutron distribution, and the spatial energy deposition in the target assembly as a function of the beam parameters, the target materials, and the target design details” [6.22];
- the CFD – Computational Fluid Dynamics software packages STAR-CD [6.30] and STAR-CCM+ [6.31] – thermal-hydraulic analyses. The coolant velocity profiles and the spatial temperature distributions in the target assembly have been studied using the spatial energy deposition distributions obtained from the MCNPX analyses;
- the NASTRAN [6.32] structure analysis computer code – to calculate the thermal stresses in the target materials using the spatial temperature distributions from the CFD analyses.

These analyses have been iterated to satisfy both temperature and thermal stress limits for satisfactory operation. These analyses have resulted in target designs development based on the engineering practices, including nuclear physics, heat transfer, thermal hydraulics, structure, fabrication, and material requirements. This section summarizes the results of the target studies.

The physics of the process is as follows [6.22]:

“The electron beam generates x-rays with a continuous energy spectrum (Bremsstrahlung radiation) from the interactions with the target materials. These x-rays are absorbed in a variety of photonuclear reactions in the target materials and neutrons are produced from these reactions. Target materials with high atomic number are required to maximize the neutron yield. In addition, high melting point, high thermal conductivity, chemical inertness, high radiation damage resistance, and low neutron absorption cross-sections are the desirable properties for the target materials”.

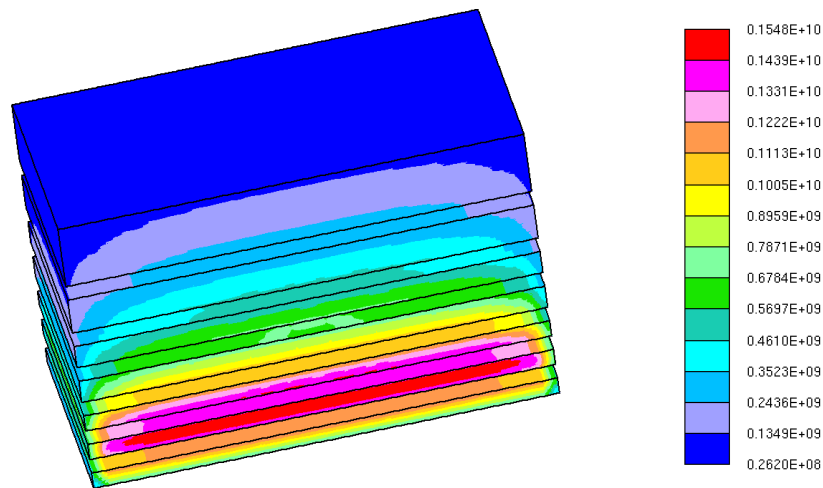
Several materials were analysed as target materials; lead, tantalum, tungsten and uranium showed the highest number of generated neutrons per electron. Uranium and tungsten were selected as target materials in this research due to their physical properties, neutron yields, and global experience of using these materials in accelerators. The tungsten melting point is the highest among all metals (~3422°C), but uranium as target material generates the highest neutron yield per electron because of its photo- and neutron fission reactions. However, uranium is subject to extensive swelling caused by fission gasses and the target operating lifetime becomes shorter.

Each target material was characterized by performing analysis of several parameters: the total neutron yield, total energy deposition, neutron spectrum, neutron and energy deposition spatial distributions, and required target length. Each of these parameters contributes to the target performance and design as follows: the neutron source intensity, enhanced by the neutron yield, defines the neutron flux level and contributes to the subcritical assembly total power; the neutron yield and the design of the target coolant system depend on the target energy deposition; the neutron spectrum affects the system's effectiveness for performing material characterizations and producing medical radioisotopes; the target location inside the subcritical assembly and the neutron source utilization fraction are determined by the spatial neutron distribution from the target. Based on the parametric and optimization studies of these parameters the target performance characteristics and the design configuration were defined.

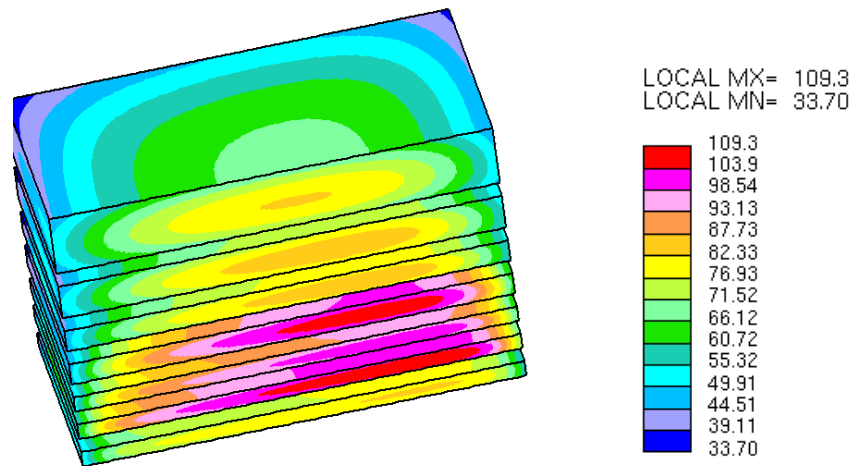
Table 6.1 represents the main geometrical parameters of the target designs. The calculated neutron yields are 1.88×10^{14} n/s for tungsten and 3.06×10^{14} n/s for uranium target designs operating 100 kW electron beam power. Figure 6.1 represents the resulting temperature distribution in the tungsten target disk and the spatial energy deposition from 2 kW/cm^2 power density on the beam window.

TABLE 6.1. TARGET DESIGN PARAMETERS

Channel Number	Tungsten Target			Uranium Target		
	Water channel thickness, mm	Target plate thickness, mm	Clad thickness, mm	Water channel thickness, mm	Target plate thickness, mm	Clad thickness, mm
0	1.0			1.0		
1	1.75	3.0	0.25×2	1.75	3.0	0.7×2
2	1.75	3.0	0.25×2	1.75	2.5	0.95×2
3	1.75	3.0	0.25×2	1.75	2.5	0.95×2
4	1.75	4.0	0.25×2	1.75	2.5	0.95×2
5	1.75	4.0	0.25×2	1.75	3.0	0.7×2
6	1.75	6.0	0.25×2	1.75	3.0	0.7×2
7	1.0	10.0	0.25×2	1.75	4.0	0.7×2
8				1.75	5.0	0.7×2
9				1.75	7.0	0.7×2
10				1.75	10.0	0.7×2
11				1.0	14.0	0.7×2
Total	12.5	33.0	3.5	19.5	56.5	16.9×2
Beam power:	100 kW					
Distribution:	Uniform					
Electron energy:	100 MeV					
Beam size:	64 × 64 mm					
Target plate:	66 × 66 mm					
Coolant:	Water					
Pressure:	5 atm					
Inlet temperature:	20.0 °C					
Outlet temperature:	24.1 °C					



a) Power density profile in the tungsten target plates [W/m^3]



b) Temperature distribution in the tungsten target plates [$^{\circ}C$], the arrow represents the flow direction.

FIG. 6.1. Power density profile and temperature distribution in tungsten target plates. (Courtesy of the Argonne National Laboratory, USA)

The target mechanical configuration, the water coolant channels size, and the temperature distribution in the target materials were defined based on heat transfer and thermal-hydraulic parametric studies. The following parameters were used: water coolant velocity inside the target manifold – 7.5 m/s; coolant pressure – 4 atmospheres; 100 kW electron beam power with approximately 2 kW/cm^2 uniform beam power density. The analyses also considered target performance enhancement via increased coolant velocity. The target is square with the axis parallel to the electron beam axis and perpendicular to the coolant flow direction. The target design is therefore formed by a stack of disks with water coolant channels of 1.75 mm thick between them. With the current coolant conditions the average temperature increase is less than $5^{\circ}C$. In order to minimize thermal deformation, each target disk is cooled from both sides. The target water coolant channels are connected in parallel to the input and the output manifolds. The analyses defined the thickness of the different target disks for a sub-cooled boiling margin of 30 to $40^{\circ}C$. The uranium disks are clad with 0.7 mm thick aluminium preventing water coolant contamination with fission

products, and the tungsten disks are coated/cladded with tantalum to improve the corrosion resistance.

The CFD thermal-hydraulic analyses were carried out with the use of the results from the MCNPX three-dimensional geometrical model studies. These models consider the target design details. The thickness of each target disk was defined by the means of the CFD calculations. In these analyses: “the water velocity distribution was calculated for each coolant channel and the spatial temperature profile was calculated for each target disk and each coolant channel using a single geometrical model for the target assembly and the three-dimensional MCNPX energy deposition results” [6.22]. The power density profiles and the temperature profiles in the tungsten and the uranium target materials are shown in Fig 6.1 and 6.2, respectively, for the 100 kW beam power using 100 MeV electrons with uniform power density on the target window. These temperature profiles meet the requirements of the adopted temperature design criteria.

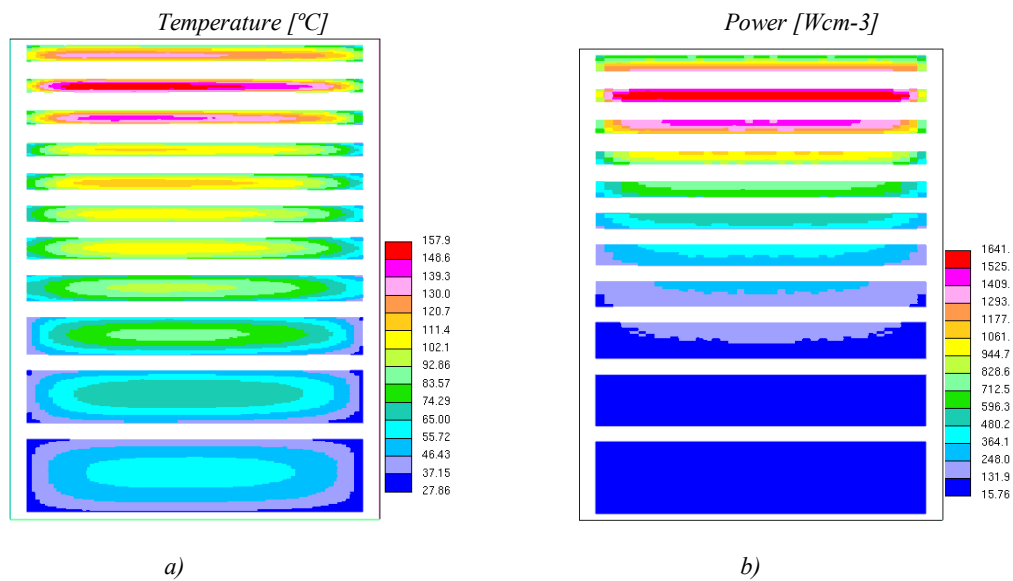


FIG. 6.2. Temperature distribution (a) and Power density distribution (b) in the uranium tungsten target plates. (Courtesy of the Argonne National Laboratory, USA)

The thermal stress analyses for the three-dimensional model and its temperature profiles of the uranium and tungsten targets were performed using the NASTRAN computer code. The intensity and distribution of the thermal stresses were evaluated for the normal operating conditions. The target design allows expansion of the disks in the radial and axial directions in order to reduce the operating stresses. The thermal stress intensity distribution during normal operation was evaluated. The maximum allowable value of the thermal stresses is limited to a fraction of the material yield stress, which is a very conventional approach to keep a large design margin that allows for radiation damage and thermal cycling effects. The results from tungsten target analysis demonstrate that the thermal stress peak is less than 100 MPa. The target design configurations for both target materials are shown in Fig. 6.3.

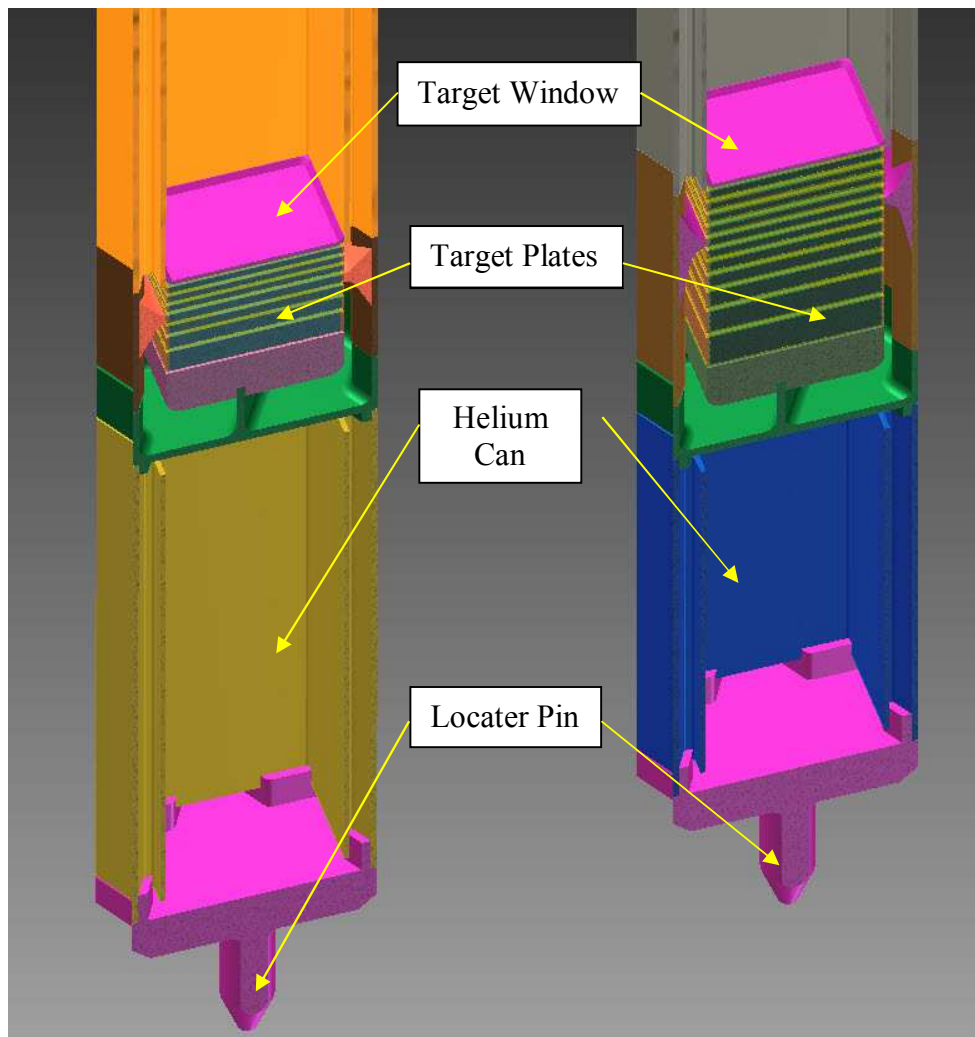


FIG. 6.3. Tungsten target assembly (left) and uranium target assembly (right) are shown side by side. Bottom locator pin, helium chamber, lower manifold, target plates, and electron beam windows are visible. (Courtesy of the Argonne National Laboratory, USA)

6.1.2. Subcritical Assembly

To maximize the neutron flux of the subcritical assembly with an effective neutron multiplication factor <0.98 parametric studies were performed, where different fuel designs, enrichments, and reflector materials were evaluated. The target assembly is located in the centre of the subcritical assembly. Fuels with densities of 1.0 and 2.7 g/cm³ of uranium for both LEU ($<20\%$) and HEU (90%) were analysed. The main focus of the analysis is to determine the effect on neutron source facility performance characteristics of LEU fuel use instead of HEU fuel. The neutron flux distribution and the subcriticality level were defined by developing the three-dimensional models of the subcritical assembly, including the detailed target and fuel assembly. Precise models were developed for the target and the fuel assemblies “without any geometrical approximation or material homogenization, to get an accurate performance characterization” [6.22]. Analysis was performed using the MCNPX computer code with continuous energy data libraries and $S(\alpha,\beta)$ thermal data from ENDF/B-VI.8. Beryllium, water, and carbon were modelled as reflector material. Parametric analyses were performed to assess the required amount of fuel assemblies to achieve k_{eff} of ~ 0.98 for

different combinations of the reflector and target materials, fuel densities, and fuel enrichments. The corresponding neutron fluxes were also calculated.

The analyses results show that [6.22]:

“the use of a uranium target requires the smallest number of fuel assemblies to achieve the desirable k_{eff} value. This small number of assemblies is due to the extra neutron multiplication produced from the natural uranium target material. The subcritical configurations with water reflector require a larger number of fuel assemblies compared to the configurations with beryllium and carbon reflectors, because of the neutron absorption in the water. The very small number of fuel assemblies limits the subcritical assembly flexibility to study different geometrical configurations. This is the case if HEU fuel is used. In addition, the HEU fuel assembly arrangements, with beryllium reflector and uranium target, are significantly asymmetric. The fuel design of the Kiev research reactor with LEU produced higher neutron flux relative to other fuel designs”.

The subcritical assembly capacity for irradiation experiments was analysed for both HEU and LEU fuels, and the average neutron flux was calculated in different locations. The results show that fuel enrichment doesn't substantially influence the irradiation capacity, but the HEU core consists of a very small number of fuel assemblies. This causes certain constraints in the core utilization for reactor physics, reactivity measurements, and calibration activities.

The calculated neutron spectra in the fuel region show the neutron energy distribution as follows: approximately half of the neutrons are below 100 keV, while the other half is in the range of 100 keV to 20 MeV. The fraction of high-energy neutrons (above 20 MeV) is very small, however, this influences biological shielding design. According to the results of target analyses the uranium target neutron flux intensity is twice as that of tungsten target. Carbon or beryllium as reflector material also increases the neutron flux relative to a water reflector. A beryllium-carbon hybrid reflector design is utilized to provide flexibility for changing the subcritical assembly configuration since a beryllium assembly can replace a fuel assembly. In addition, the fabrication of high-density carbon blocks is difficult and expensive relative to beryllium blocks. A carbon reflector ring is used around the beryllium reflector.

Figure 6.4 shows the MCNPX geometrical model of the subcritical assembly with uranium target, LEU fuel, and beryllium-carbon reflector, and Fig. 6.5 shows the subcritical assembly configurations with tungsten and uranium targets. The main parameters of the two subcritical configurations are listed in Table 6.2, including the effective neutron multiplication factors, the average neutron flux in the target coolant channel and the first fuel ring, and the energy deposition. The energy deposition distribution in the different materials is shown in Fig. 6.6 for the subcritical assembly with a uranium target and 100 kW electron beam. The corresponding total neutron flux distributions are shown in Fig. 6.7.

TABLE 6.2. EFFECTIVE NEUTRON MULTIPLICATION FACTOR, AVERAGE NEUTRON FLUX, AND ENERGY DEPOSITION VALUES USING BERYLLIUM-GRAPHITE REFLECTOR AND 100 kW/100 MeV ELECTRON BEAM

Target	# of FAs	k_{eff}	Average neutron flux ($n/cm^2 \cdot s$)		Target energy deposition (kW)	Subcritical energy deposition (kW)	Reflector energy deposition (kW)	Total energy deposition (kW)
			First fuel ring	Target coolant channel				
W	38	0.95686 ± 0.00013	6.281×10^{12} $\pm 0.26\%$	7.873×10^{12} $\pm 0.23\%$	85.70 $\pm 0.01\%$	69.19 $\pm 0.24\%$	5.84 $\pm 0.13\%$	160.73
U	37	0.97547 ± 0.00012	1.965×10^{13} $\pm 0.26\%$	2.470×10^{13} $\pm 0.25\%$	90.57 $\pm 0.01\%$	196.89 $\pm 0.35\%$	11.57 $\pm 0.19\%$	299.04

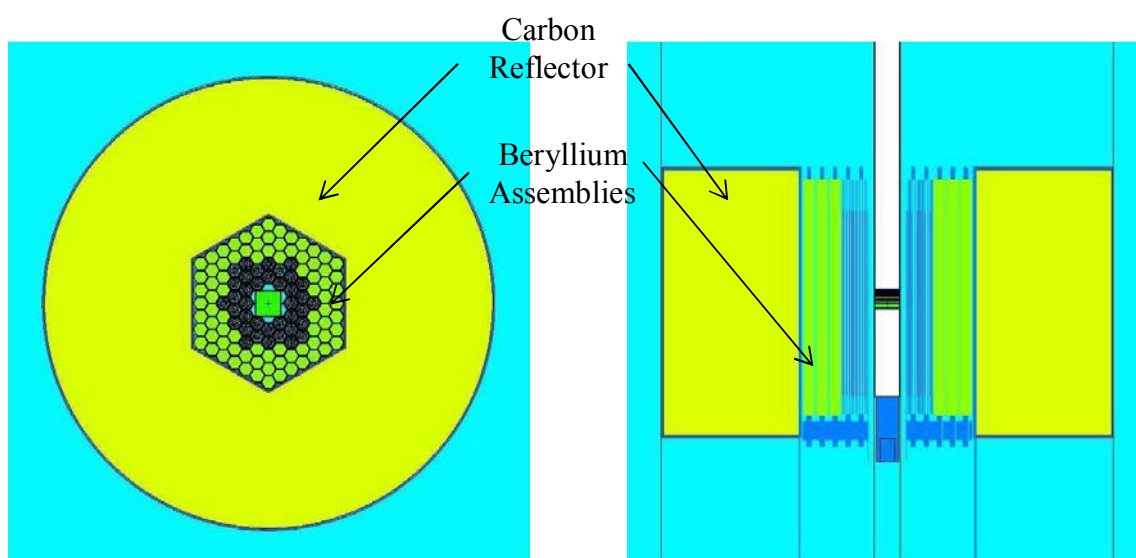


FIG. 6.4. MCNPX geometrical model of the subcritical assembly, X-Y cross-section on the left and X-Z cross-section on the right. (Courtesy of the Argonne National Laboratory, USA)

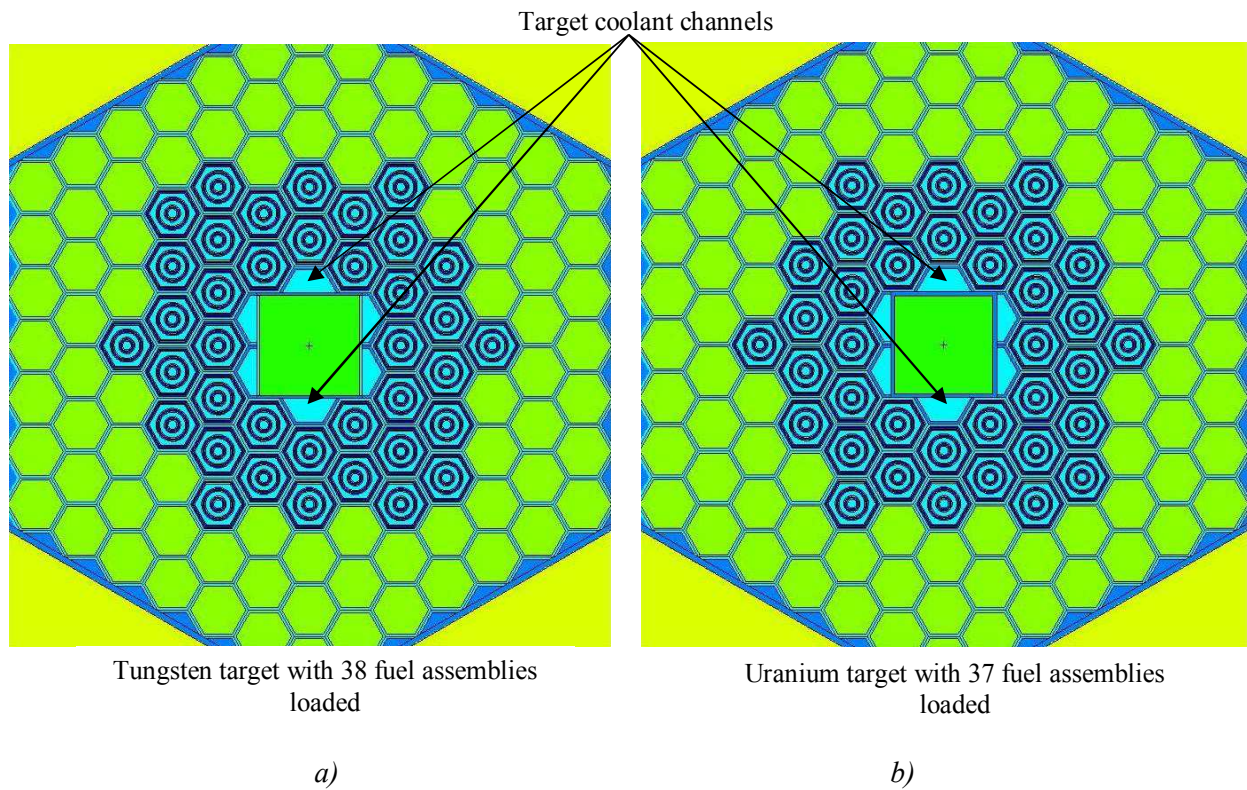


FIG. 6.5. Subcritical assembly configurations with tungsten target (a) and uranium target (b), with a beryllium-graphite reflector. (Courtesy of the Argonne National Laboratory, USA)

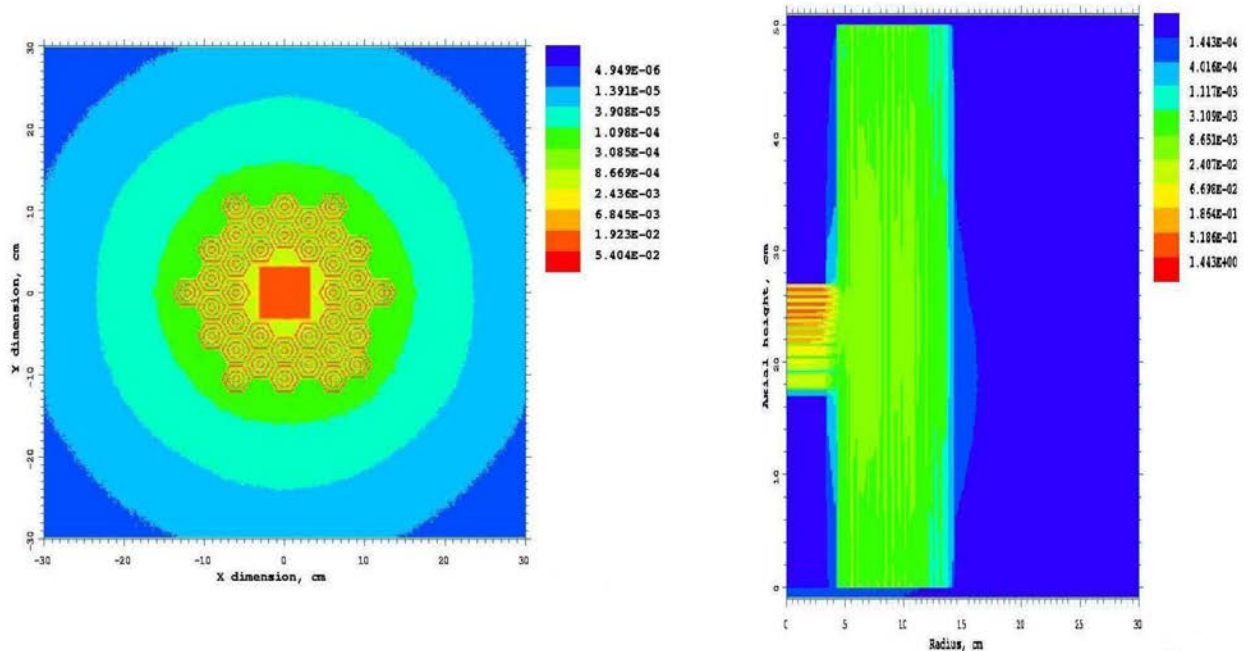


FIG. 6.6. Subcritical assembly energy deposition (KW/cm³) X-Y map on the left and X-Z map on the right for the configuration with a uranium target. (Courtesy of the Argonne National Laboratory, USA).

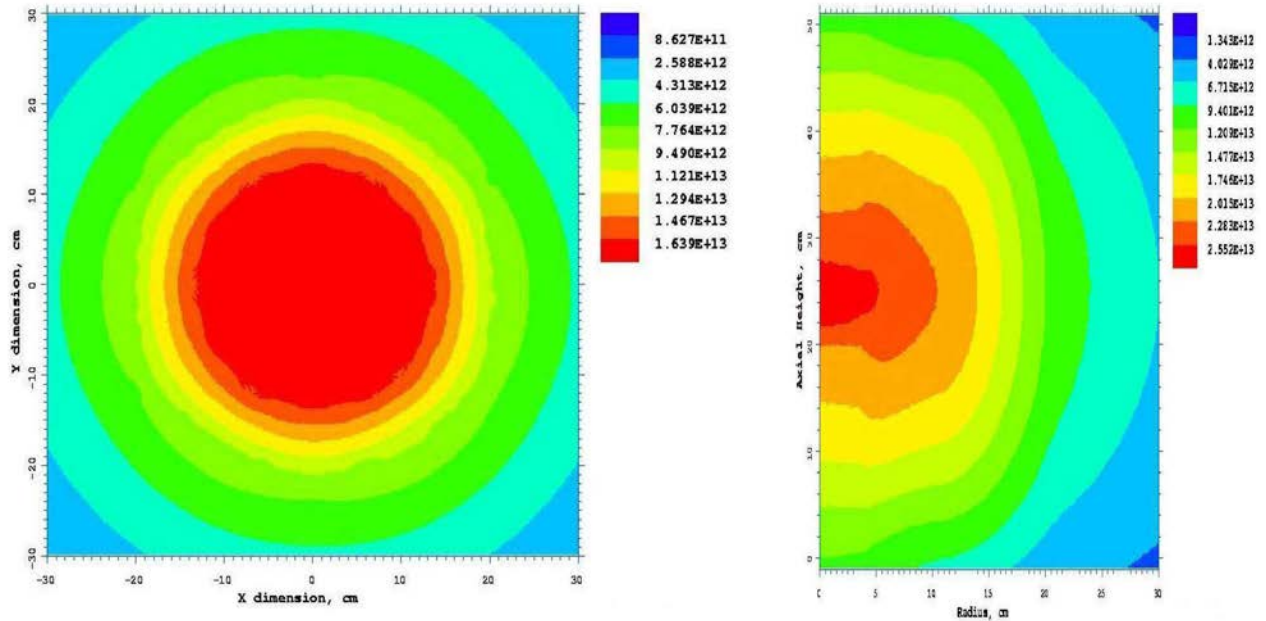


FIG. 6.7. Total neutron flux distributions, X-Y map on the left, and X-Z map on the right for the subcritical assembly configuration with a uranium target and 100-KW electron beam power. (Courtesy of the Argonne National Laboratory, USA).

6.1.3. Biological Shield

The shield thickness that allows personnel to access the subcritical assembly area during operation was determined by the biological shielding analysis. The biological dose is limited by the shielding design criterion with the value less than 2.5 mrem/h. This allows “a worker to have a 40-hour working week without exceeding the allowable international exposure limit” [6.22]. In the design analyses the biological dose criteria was reduced by a factor of five to take into account possible nuclear data uncertainties, computational method errors, and modelling details. For the purpose of the shielding analysis, precise three-dimensional models have been developed with MCNPX, starting with the electron beam. The biological shielding has two main sections: the top section, which comprises the subcritical assembly top cover and electron beam shielding, and the radial section.

According to the shielding analysis results, using a steel shielded zone followed by heavy concrete has a small influence on the biological dose and the shield thickness. Heavy concrete with the density 4.8 g/cm^3 was selected as shielding material which reduces fabrication and construction costs. The radial biological shield thickness must be 140 cm to meet the requirements of the total biological dose criteria 0.5 mrem/h, as shown in Table 6.3. The pool water, where the critical assembly is located, acts as a shielding material from the top of the assembly and reduces the required heavy concrete shielding thickness. However, the shielding design in this area is complicated by the radiation streaming from the beam tube and the electron beam losses at the bending beam magnet. The electron beam losses define the required shield thickness of the top section. Figure 6.8 shows the calculated dose map and the required shield dimensions at the top section due to 80 W electron beam losses at the first bending magnet.

TABLE 6.3. CALCULATED BIOLOGICAL DOSE VALUES AROUND THE SUBCRITICAL ASSEMBLY WITH A URANIUM TARGET DURING OPERATION WITH 100-kW BEAM POWER AND 140 cm OF HEAVY CONCRETE RADIAL SHIELD THICKNESS

Radiation source	Radiation biological dose (mrem/hr)
Neutron	$0.206 \pm 7.24\%$
Photon	$0.056 \pm 4.63\%$
Total	0.262

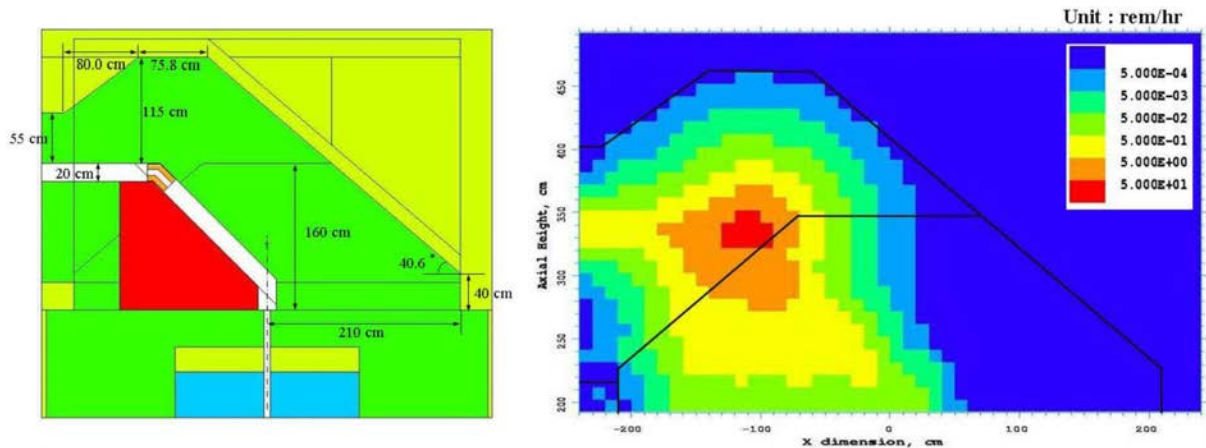


FIG. 6.8. Main dimensions of the biological shield top section on the left and the corresponding total biological dose map on the right. (Courtesy of the Argonne National Laboratory, USA)

6.2. NEUTRON SOURCE FACILITY DESIGN

Subcritical assembly facility design utilizes developed techniques and standard practices to facilitate optimum operation and maintenance to increase facility utilization. The facility consists of the target assembly, the subcritical assembly, the biological shield, and the auxiliary supporting systems. Figure 6.9 shows a quarter cut isometric view of the subcritical assembly design where the main components are viewed, including the target assembly, the fuel assemblies, the beryllium reflector assemblies, the carbon ring reflector, the fuel machine arm, the storage racks, and the support grid. The loading and unloading of the fuel assemblies, beryllium reflector assemblies, and irradiation cassettes are performed without opening the biological shield. Replacing the target assembly requires opening the top shield sections without removing the top cover of the subcritical assembly.

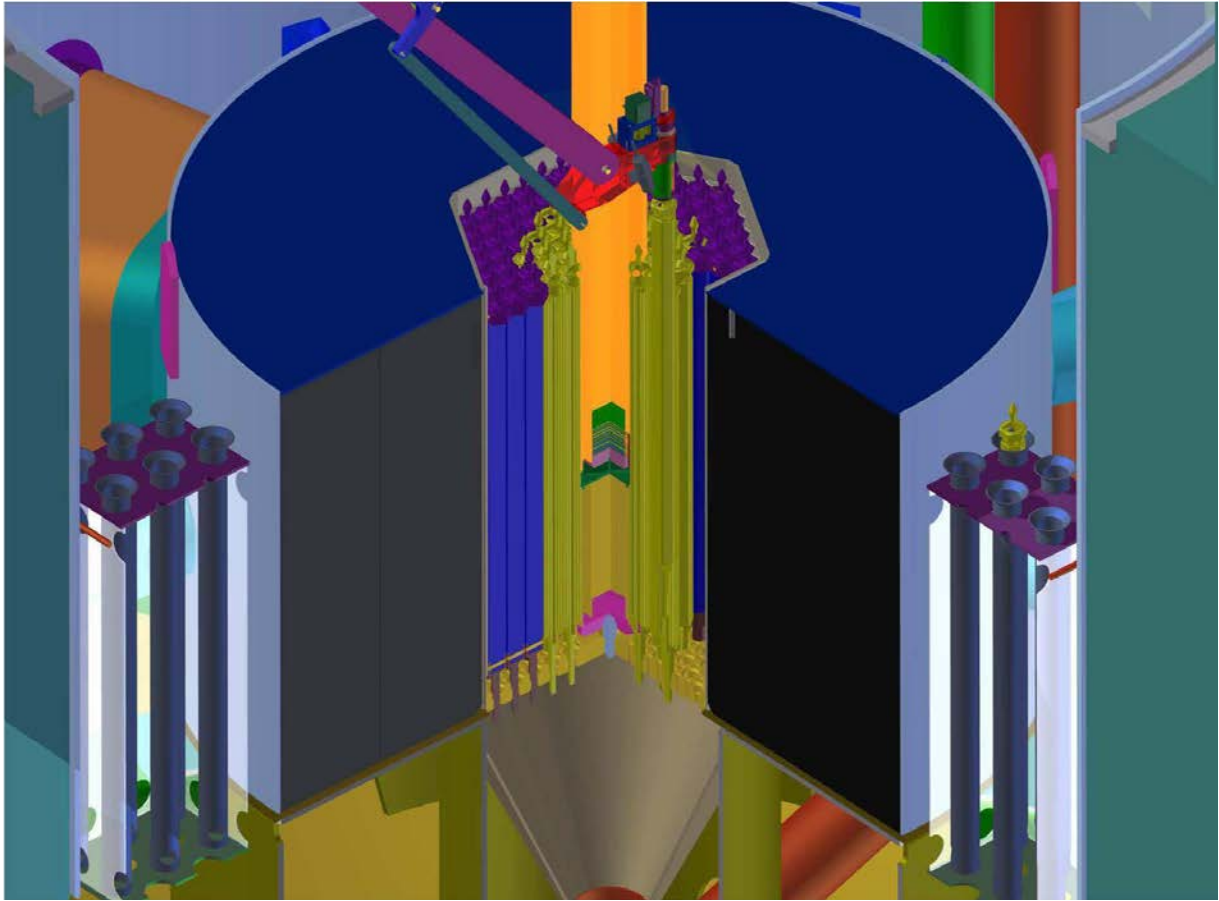


FIG. 6.9. Quarter cut isometric view of the subcritical assembly design. (Courtesy of the Argonne National Laboratory, USA)

The overview of the neutron source facility is shown in Fig. 6.10. It includes the accelerator building, the subcritical assembly hall, the attached laboratory building, the secondary coolant towers, and the electrical power station for operating the facility. Medical isotopes and material testing glove boxes, water distillation facility, backup diesel generator units, temporary spent fuel and used target storage pool, and temporary liquid radioactive waste storage are included in the design. The facility is currently under construction.



FIG. 6.10. Isometric view of KIPT accelerator driven system facility. (Courtesy of the National Science Centre Kharkov Institute of Science and Technology, Ukraine)

6.3. CONCLUSIONS

The design of the KIPT accelerator-driven subcritical assembly facility has been successfully developed, using a 100 kW–100 MeV electron accelerator, through a collaborative activity between ANL and KIPT [6.22]:

“The facility is designed based on the low enriched uranium fuel design of the Kiev research reactor. The developed design satisfies the facility objectives, and it has flexibility for future upgrades and new functions. It has excellent capabilities for producing medical isotopes, performing basic research using its radial neutron beams, performing physics studies, and training young nuclear scientists.”

Acknowledgments

Argonne National Laboratory's work was supported by the U.S. Department of Energy, Office of Global Nuclear Material Threat Reduction (NA213), and National Nuclear Security Administration of U. S. Department of Energy.

REFERENCES TO SECTION 6

- [6.1] GOHAR, Y., BAILEY, J., BELCH, H., NABEREZHNEV, D., STRONS, P., and BOLSHINSKY, I., “Accelerator-Driven Sub-critical Assembly: Concept Development And Analyses”, Proc. RERTR-2004 International Meeting on Reduced Enrichment for Research and Test Reactors, Vienna, Austria, November 7-12, (2004).
- [6.2] GOHAR, Y., BOLSHINSKY, I., NABEREZHNEV, D., DUO, J., BELCH, H., BAILEY, J., “Accelerator Driven Sub-Critical Facility: Conceptual Design Development”, paper presented and submitted to AccApp05, Venice, Italy, August 29 – September 1, (2005).
- [6.3] NABEREZHNEV, D.G., GOHAR, Y., BAILEY, J., BELCH, H., “Physics Analyses of Accelerator Driven Sub-Critical Assembly”, paper presented and submitted to AccApp05, Venice, Italy, August 29 – September 1, (2005).
- [6.4] GOHAR, Y., BOLSHINSKY, I., NABEREZHNEV, D., DUO J., BELCH H., BAILEY J., “Accelerator Driven Sub-Critical Facility: Conceptual Design Development”, Nuclear Instruments and Methods in Physics Research, **A562**, June (2006) 870-874.
- [6.5] NABEREZHNEV, D.G., GOHAR, Y., BAILEY, J., BELCH, H., “Physics Analyses of Accelerator Driven Sub-Critical Assembly”, Nuclear Instruments and Methods in Physics Research, **A562**, (2006) 841-844.
- [6.6] GOHAR, Y., BOLSHINSKY, I., BELCH, H., NABEREZHNEV, D.G., SOFU, T., TALAMO, A., ZHONG, Z., “Accelerator Driven Subcritical Facility Design Concept”, the 8th International Topical Meeting on Nuclear Applications and Utilization of Accelerators (AccApp07), Pocatello, Idaho, 30 to August 2, (2007).
- [6.7] TALAMO, A., GOHAR, Y., NABEREZHNEV, D.G., “MCNPX Analysis of the Medical Isotope Production in the Kharkov Electron Driven Subcritical Facility”, the 8th International Topical Meeting on Nuclear Applications and Utilization of Accelerators (AccApp07), Pocatello, Idaho, 30 to August 2, (2007).
- [6.8] SOFU, T., GOHAR, Y., BELCH, H., ZHONG, Z., NABEREZHNEV, D.G., “Neutronic, Thermal-Hydraulic, And Structural Analyses Of The Electron Target For An Accelerator-Driven Subcritical System”, the 8th International Topical Meeting on Nuclear Applications and Utilization of Accelerators (AccApp07), Pocatello, Idaho, 30 to August 2, (2007).
- [6.9] GOHAR, Y., BOLSHINSKY, I., BELCH, H., SOFU, T., TALAMO, A., ZHONG, Z., “Design and Analyses of KIPT Electron Accelerator Driven Subcritical Assembly Facility Concept”, the International Workshop on Charged Particle Accelerators, the Accelerator Driven Subcritical Assemblies Workshop, Alushta, Ukraine, September 9-15, (2007).
- [6.10] BELCH, H., GOHAR, Y., SOFU, T., ZHONG, Z., “Conceptual Design Configuration for Electron Accelerator Driven Subcritical Assembly”, the 20th International Workshop on Charged Particle Accelerators, the Accelerator Driven Subcritical Assemblies Workshop, Alushta, Ukraine, September 9-15, (2007).
- [6.11] SOFU, T., GOHAR, Y., BELCH, H., NABEREZHNEV, D.G., “Multi-Physics Analysis of an Electron Target for the KIPT Subcritical Assembly”, 20th International Workshop on Charged Particle Accelerators, the Accelerator Driven Subcritical Assemblies Workshop, Alushta, Ukraine, September 9-15, (2007).
- [6.12] TALAMO, A., GOHAR, Y., “Production of Medical Radioactive Isotopes Using KIPT Electron Driven Subcritical Facility”, Applied Radiation and Isotopes, **66** (2008) 577–586.

- [6.13] GOHAR, Y., BOLSHINSKY, I., NEKLUDOV, I.M., KARNAUKHOV, I.M., “Ukraine Experimental Neutron Source Facility”, The Second International Conference on Current Problems in Nuclear Physics and Atomic Energy (NPAE-2008) Kiev, UKRAINE, June 9 - 15, (2008).
- [6.14] TALAMO, A., GOHAR, Y., “Medical Isotopes Production Analyses of the Kharkov Electron Driven Subcritical Assembly”, American Nuclear Society Annual Meeting, (2008).
- [6.15] ZHONG, Z., GOHAR, Y., “KIPT Accelerator Driven Subcritical Facility Shield Design”, American Nuclear Society Annual Meeting, (2008).
- [6.16] ZHONG, Z., GOHAR, Y., NABEREZHNEV, D.G., DUO J., Shielding Analysis and Design of the KIPT Experimental Neutron Source Facility of Ukraine, Argonne National Laboratory Report, ANL-08/23, (2008).
- [6.17] SOFU, T., GOHAR, Y., ZHONG, Z., BELCH, H., NABEREZHNEV, D.G., Target Design Optimization for an Electron Accelerator Driven Subcritical Facility with Circular and Square Beam Profiles, Argonne National Laboratory Report, ANL-NE-08/25, (2008).
- [6.18] ZHONG, Z., GOHAR, Y., KELLOGG, R., Physics Design of a Cold Neutron Source for KIPT Neutron Source Facility, Argonne National Laboratory Report, ANL-08/36, (2008).
- [6.19] ZHONG, Z., GOHAR, Y., TALAMO, A., Burnup Calculations for KIPT Accelerator Driven Subcritical Facility Using Monte Carlo Computer Codes - MCB and MCNPX, Argonne National Laboratory Report, ANL-09/07, (2009).
- [6.20] ZHONG, Z., GOHAR, Y., TALAMO, A., “MCNPX and MCB Coupled Methodology for the Burnup Calculation of the KIPT Accelerator Driven Subcritical System”, International Conference on Mathematics, Computational Methods & Reactor Physics (M&C 2009), Saratoga Springs, New York, May 3-7, (2009).
- [6.21] ZHONG, Z., GOHAR, Y., KELLOGG, R., “KIPT Cold Neutron Source Physics Analyses”, American Nuclear Society Annual Meeting June, (2009).
- [6.22] GOHAR, Y., “Experimental Neutron Source Facility Based on Accelerator Driven System”, Proc. Workshop on Applications of High Intensity Proton Accelerators, Fermilab, Chicago 19-21 October 2009, ISBN-13 978-981-4317-28-3.
- [6.23] ZHONG, Z., GOHAR, “Fuel Cycle Analyses of the KIPT Neutron Source Facility With Low Enriched Uranium Fuel”, RERTR 2009 — 31st International Meeting on Reduced Enrichment for Research and Test Reactors, Beijing, China, November 1-5, (2009).
- [6.24] ZHONG, Z., GOHAR, BELCH, H., SOFU, T., “Biological Shield Design and Analysis of KIPT Accelerator Driven Subcritical Facility”, Nuclear Technology, (2009).
- [6.25] ZHONG, Z., GOHAR, Y., TALAMO, A., “Analysis of Fuel Management in the KIPT Neutron Source Facility”, Annals of Nuclear Energy, Vol. 38, No. 5, 1014 (2011).
- [6.26] ZHONG, Z., GOHAR, Y., “Shielding design and analyses of KIPT neutron source facility”, Progress in Nuclear Energy, Vol. 53, Issue 1, (2011).
- [6.27] ZHONG, Z., GOHAR, Y., “Use of a Neutron Source File in MCNPX Shielding Calculation for an Electron Accelerator Driven Facility”, PHYSOR 2012 – Advances in Reactor Physics, Knoxville, Tennessee, USA, April 15-20, (2012).
- [6.28] ZHONG, Z., GOHAR, Y., “Accelerator Shield Design of KIPT Neutron Source Facility”, International Conference on Mathematics and Computational Methods Applied to Nuclear Science & Engineering (M&C 2013), Sun Valley, Idaho, USA, May 5-9, (2013).
- [6.29] MCNPX Version 2.5.0 User's Manual (LA-CP-05-0369) Los Alamos National Laboratory, (<http://mcnpx.lanl.gov/>), (2005).

- [6.30] II.3.2 “User Guide, STAR-CD 4.08”, CD-ADAPCO, 2009, Mellville, NY, USA.
- [6.31] II.3.3 “User Guide, STAR-CCM+ 5.06”, CD-ADAPCO, 2010, Mellville, NY, USA.
- [6.32] MSC NASTRAN and MARC User’s Manual, (<http://www.mscsoftware.com/>), MSC Software Corporation, Santa Ana, CA.

7. KUCA SUBCRITICAL EXPERIMENTS

Contributed by

C.H. Pyeon

*Nuclear Engineering Science Division, Research Reactor Institute, Kyoto University
Asashiro-nishi, Kumatori-cho, Sennan-gun, Osaka 590-0494,
Japan*

I. Masood

*Nuclear Engineering Division, Pakistan Institute of Nuclear Science and Technology
(PINSTECH), Islamabad,
Pakistan*

7.1. INTRODUCTION

A series of experiments has been carried out at the Kyoto University Critical Assembly (KUCA) that simulate an accelerator-driven system (ADS) driven with a 14 MeV neutron source. This research has been conducted with the goal of ultimately developing an actual accelerator driven system (ADS). A critical assembly consisting of a solid-moderated and -reflected core was coupled with a Cockcroft-Walton type accelerator. A neutron shield and specially designed beam handling configuration were installed in the reflector region in order to introduce as many 14 MeV neutrons generated from deuterium-tritium (D-T) reactions into the fuel region as possible. This approach was necessitated by the fact that the tritium target is located outside the core. The 14 MeV neutrons were guided into a subcritical system through a polyethylene reflector.

The reaction-rate distributions and the neutron spectra were measured using the foil activation method in order to investigate the neutronic properties of this 14 MeV neutron-driven ADS. Eigenvalue and fixed-source calculations were performed using the continuous-energy Monte Carlo calculation code MCNP-4C3, with the ENDF/B-VI.2 nuclear data library, to determine the effective multiplication factor. The MCNP5 code, with the ENDF/B-VII.0 library, was employed to determine the reaction-rate distributions. The SAND-II code, with the JENDL Activation Cross-section File (Version 96), was used to calculate the neutron spectra. The subcriticality of an actual ADS is $\sim 3\%$ ($\Delta k/k$), which is within the validated reactivity range of the KUCA reactor facility. Measurements and calculations of the KUCA reactor facility had been demonstrated previously up to 6% for the utilized KUCA cores. The prompt neutron decay constant was obtained by the pulsed-neutron method, and the reactivity was measured with the area-ratio method. These measurements were carried out using an optical-fibre detection system developed at KUCA. This optical-fibre detector technique is a promising, novel approach for measuring the reactivity and the prompt neutron decay constant for ADS. This technique had been assessed earlier for ADS kinetic experiments that involve 14 MeV neutrons.

The main objectives of the KUCA ADS experiments are: a) to examine the neutronic characteristics of the reaction-rate distribution and the neutron spectrum; b) to develop measurement techniques for determining neutronic parameters of the system; and c) to investigate the accuracy of the neutronic design parameters of the present configuration. Furthermore, these experiments would be useful for the conversion process of the KUCA facility to the use of low enriched uranium fuel.

Research on the KUCA experimental benchmarks was conducted under the auspices of the IAEA Coordinated Research Projects (CRP) entitled 'Analytical and Experimental

Benchmark Analyses of Accelerator Driven Systems (ADS) and Low Enriched Uranium Fuel Utilization in Accelerator Driven Subcritical Assembly Systems'. This particular project is identified under the label 'Experimental Benchmarks for Accelerator-Driven System (ADS) at the Kyoto University Critical Assembly (KUCA)'. This Section of the TECDOC summarizes the work of this project. Extensive use is made of drawings and graphs (Figs 7.1—7.45) as well as tabular data (Tables 7.1—7.34). Further details concerning this activity can be found in Refs [7.1—7.15].

The research carried out in the KUCA subcritical ADS facility has also benefited from contributions from the Member State Pakistan.

7.2. BENCHMARK SPECIFICATIONS

This section describes the various components of the KUCA subcritical experimental facility.

7.2.1. KUCA Core

KUCA configuration consists of solid-moderated and solid-reflected type-A and type-B cores, and a water-moderated and water-reflected type-C core. In the present series of experiments, the solid-moderated and solid-reflected type-A core was coupled with a Cockcroft-Walton type pulsed-neutron generator. The A-core configuration (A3/8"P36EU(3)) that was used for measuring the reaction-rate distribution and the neutron spectrum is shown in Fig. 7.1.

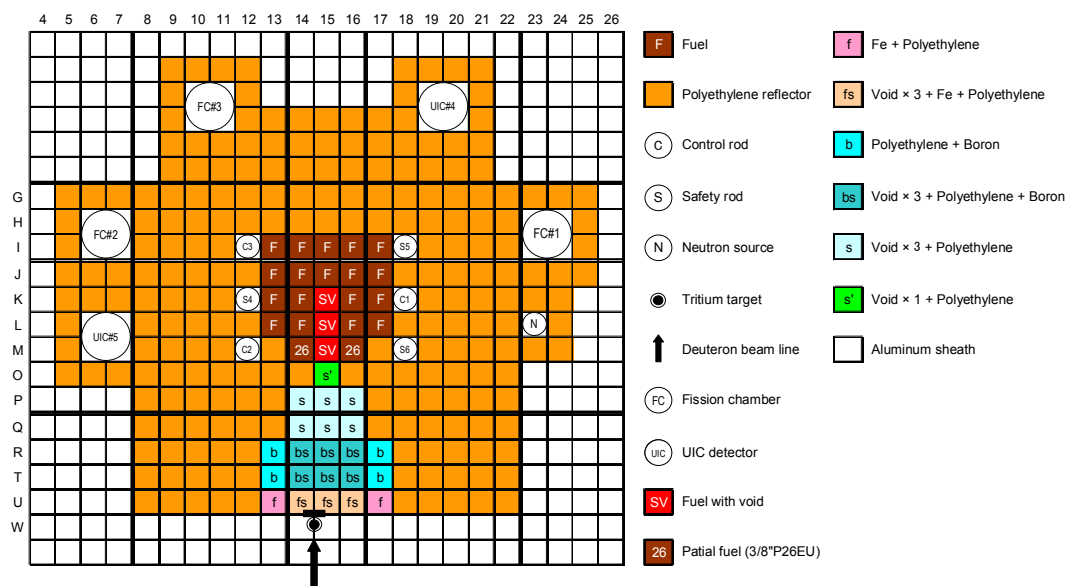


FIG. 7.1. Overall view of the KUCA A-core configuration (Courtesy of the Nuclear Engineering Science Division, Research Reactor Institute, Kyoto University, Japan).

The fuel assemblies consisted of 23 individual elements that were loaded onto the grid plate. The materials used in these critical assemblies were configured in the shape of rectangular parallelepipeds that were normally 2" square with thicknesses ranging from 1/16" to 2". The upper and lower parts of the fuel region have polyethylene reflector layers that are more than 50 cm long. The fuel rods are composed of 93% enriched uranium-aluminium (U-Al) alloy consist of 36 individual cells formed from 2 polyethylene plates 1/8" and 1/4" thick, and a U-Al plate 1/16" thick. The effective height of the core is approximately 40 cm.

Figures 7.2–7.11 illustrate various components of the KUCA facility used in the present experiments. Tables 7.1—7.6 provide relevant numerical data.

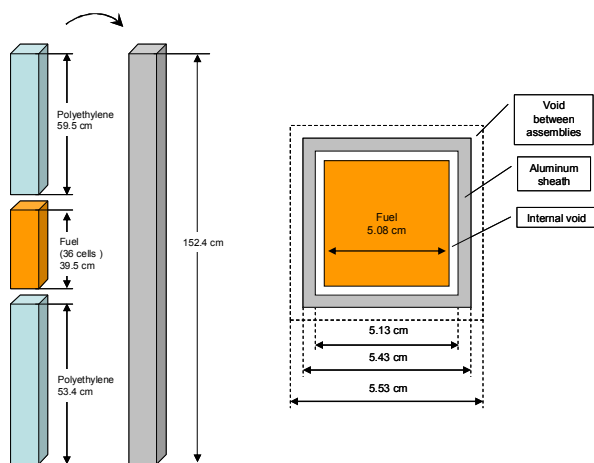


FIG. 7.2. Description of the fuel assembly (Courtesy of the Nuclear Engineering Science Division, Research Reactor Institute, Kyoto University, Japan).

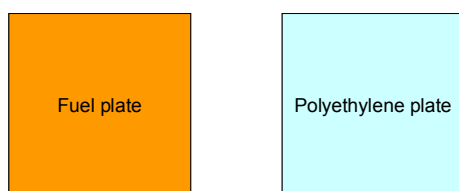


FIG. 7.3. Description of the fuel and polyethylene plates (Courtesy of the Nuclear Engineering Science Division, Research Reactor Institute, Kyoto University, Japan).

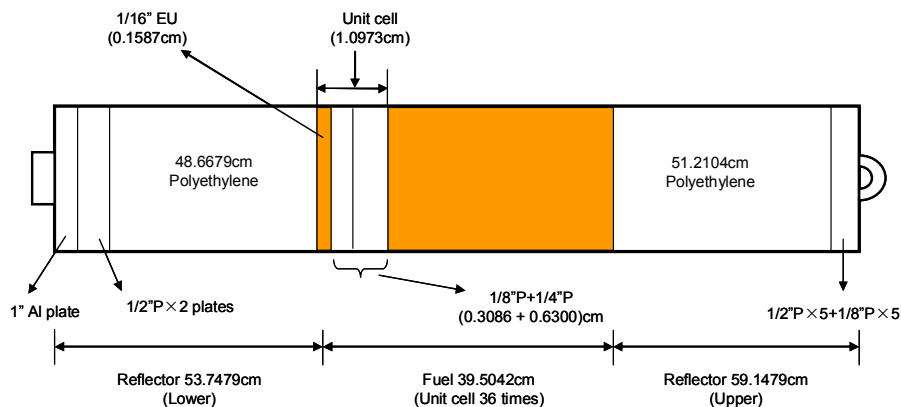


FIG. 7.4. Full side view of the fuel assembly 'F', as shown in Fig. 7.1 (Courtesy of the Nuclear Engineering Science Division, Research Reactor Institute, Kyoto University, Japan).

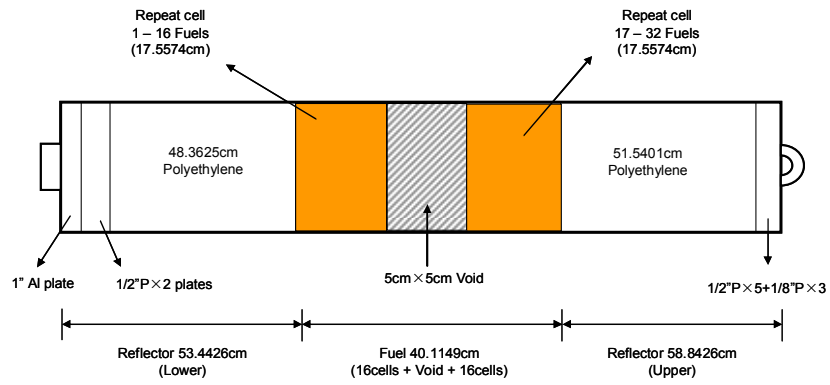


FIG. 7.5. Full side view of the fuel assembly 'SV' with the void, as shown in Fig. 7.1 (Courtesy of the Nuclear Engineering Science Division, Research Reactor Institute, Kyoto University, Japan).

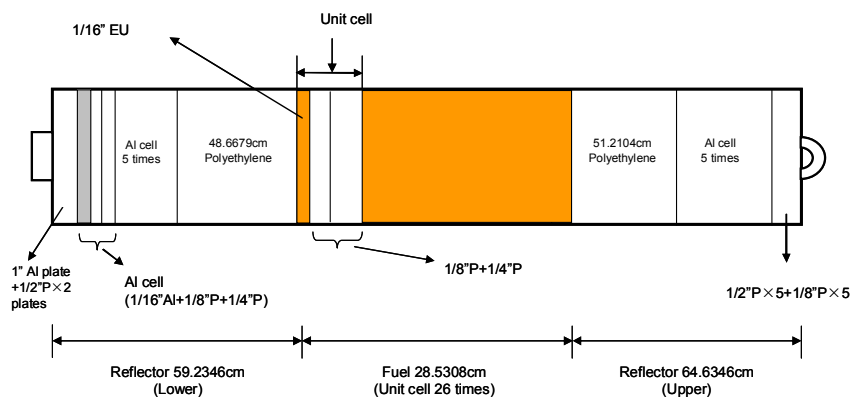


FIG. 7.6. Full side view of the partial fuel assembly '26', as shown in Fig. 7.1 (Courtesy of the Nuclear Engineering Science Division, Research Reactor Institute, Kyoto University, Japan).

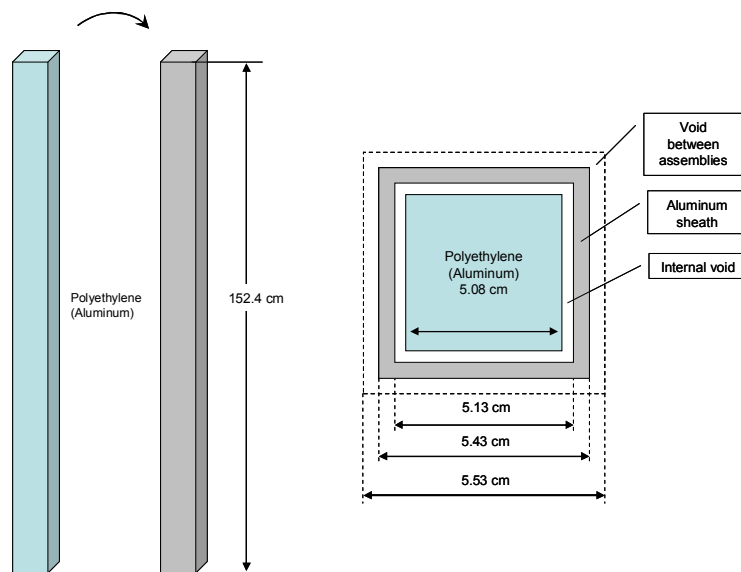


FIG. 7.7. Description of the polyethylene (aluminium) reflector (Courtesy of the Nuclear Engineering Science Division, Research Reactor Institute, Kyoto University, Japan).

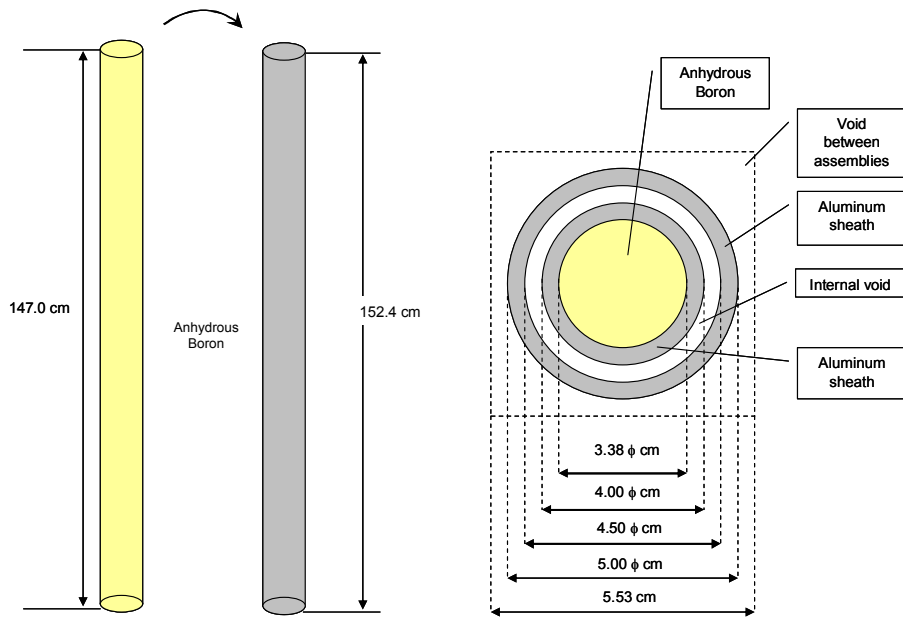


FIG. 7.8. Description of a control (safety) rod (Courtesy of the Nuclear Engineering Science Division, Research Reactor Institute, Kyoto University, Japan).

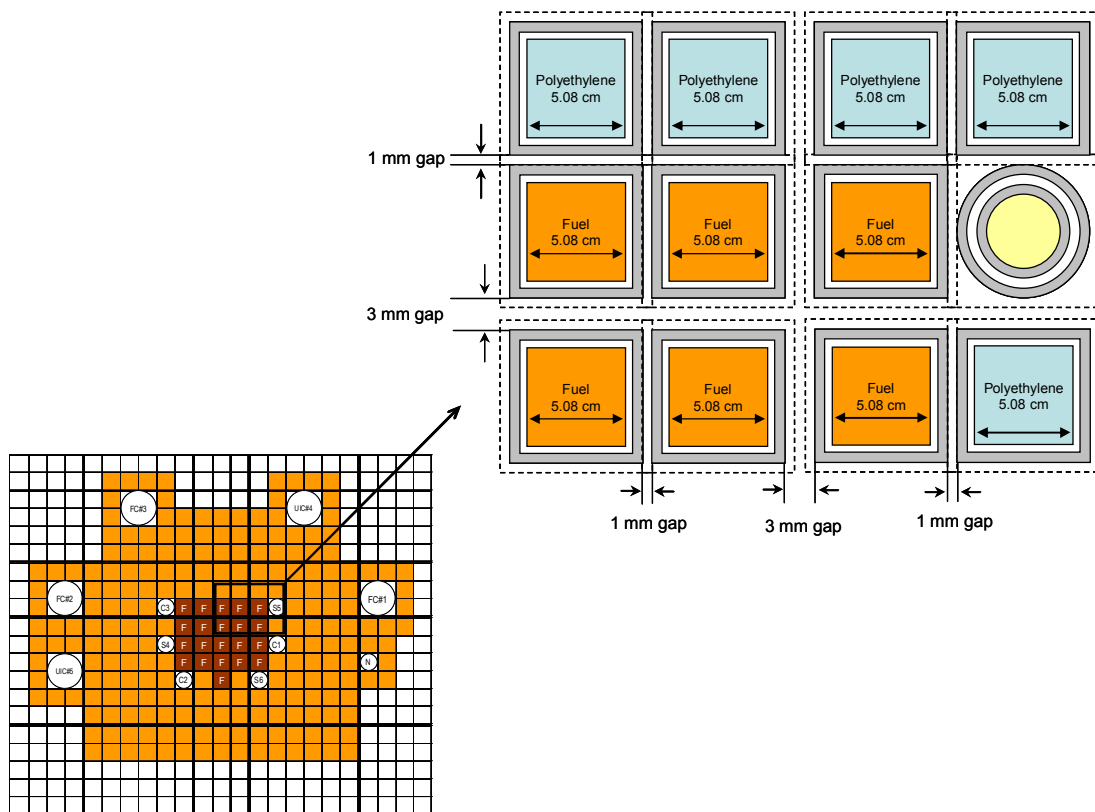


FIG. 7.9. Description of the fuel assembly, polyethylene reflector, and control rod (Courtesy of the Nuclear Engineering Science Division, Research Reactor Institute, Kyoto University, Japan).

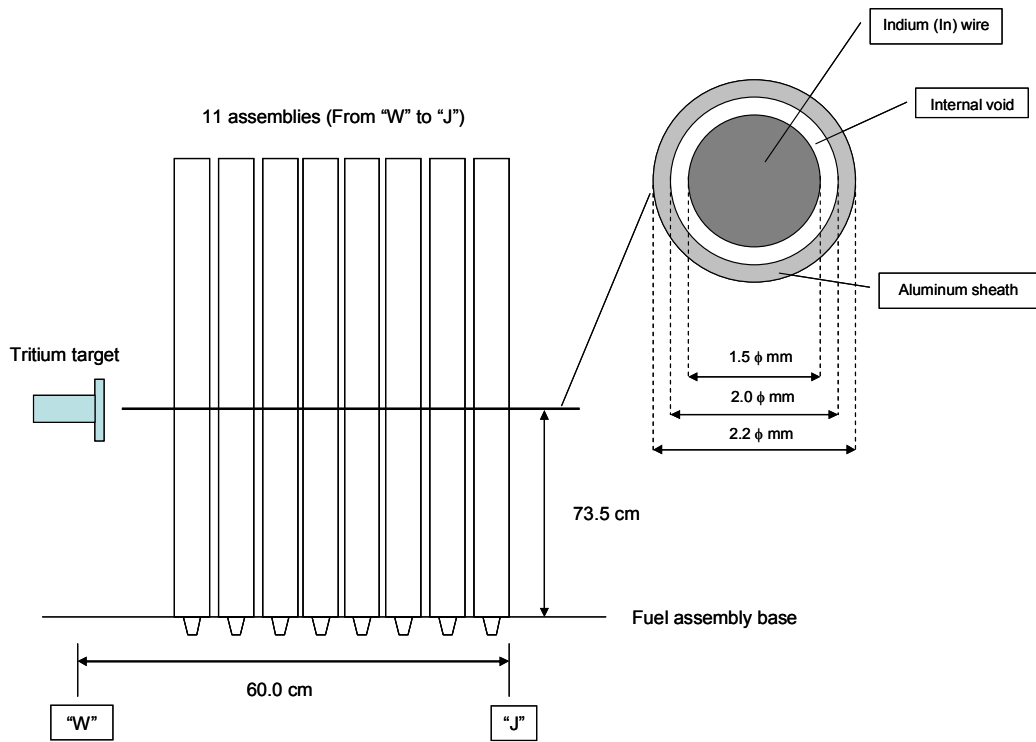


FIG. 7.10. Location of the Indium (In) wire (Courtesy of the Nuclear Engineering Science Division, Research Reactor Institute, Kyoto University, Japan).

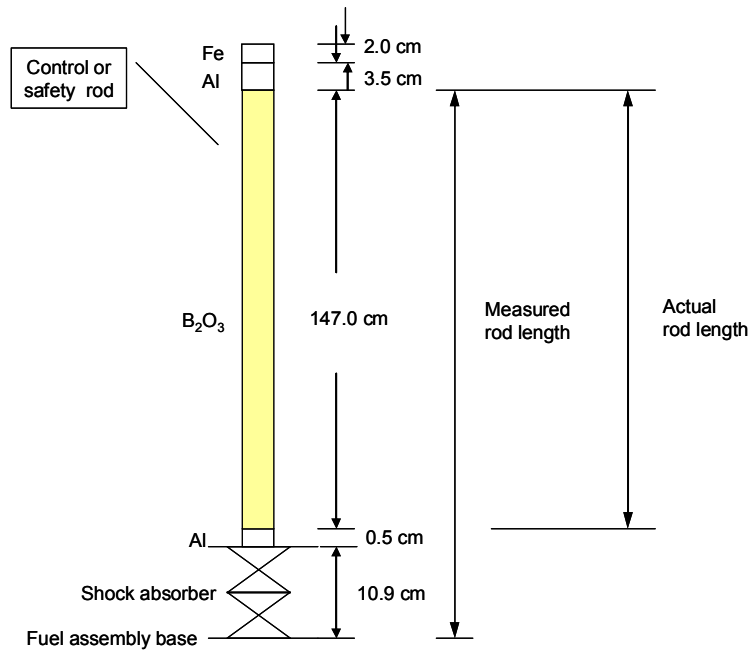


FIG. 7.11. Actual position of a control (safety) rod. The actual position = measured position - 11.4 cm (Courtesy of the Nuclear Engineering Science Division, Research Reactor Institute, Kyoto University, Japan).

7.2.2. The 14-MeV Pulsed-neutron Generator Description

The pulsed-neutron generator is connected with the KUCA A-core configuration to deliver pulsed 14 MeV neutrons into the subcritical system through the polyethylene reflector. In the experiments, the deuteron beam (with 160 keV in beam energy, 4.5 mA of beam current, a 10 μ s pulse width, and a 500 Hz pulse repetition rate) bombarded the tritium target that was located outside the polyethylene reflector. A peak beam intensity of about 0.5 mA for pulse widths up to 100 μ s, and repetition rates ranging from a few Hz to 30 kHz produced by the pulsed-neutron generator, results in the maximum neutron yield of 1×10^8 n/s.

7.2.3. The Neutron Shield and Beam Duct

The tritium target is located outside the core centre. Figure 7.1 shows the location of the beam duct and neutron shield in the polyethylene reflector for this series of experiments. This configuration enables the maximum possible number of high-energy neutrons, generated in the target region, to be directed towards the core centre. The neutron shield provides radiation protection from the thermal and high-energy neutrons, which consists of layers of different materials arranged in the core as shown in Figs 7.12, 7.13, and 7.14. The iron layer (Fe) provides shielding from the high-energy neutrons generated by inelastic scattering reactions in the target region. The borated polyethylene layer provides shielding from the thermal neutrons, which have been moderated in the reflector by absorption reactions. The beam duct serves to provide effectively collimated high-energy 14 MeV neutrons that can then enter the core region.

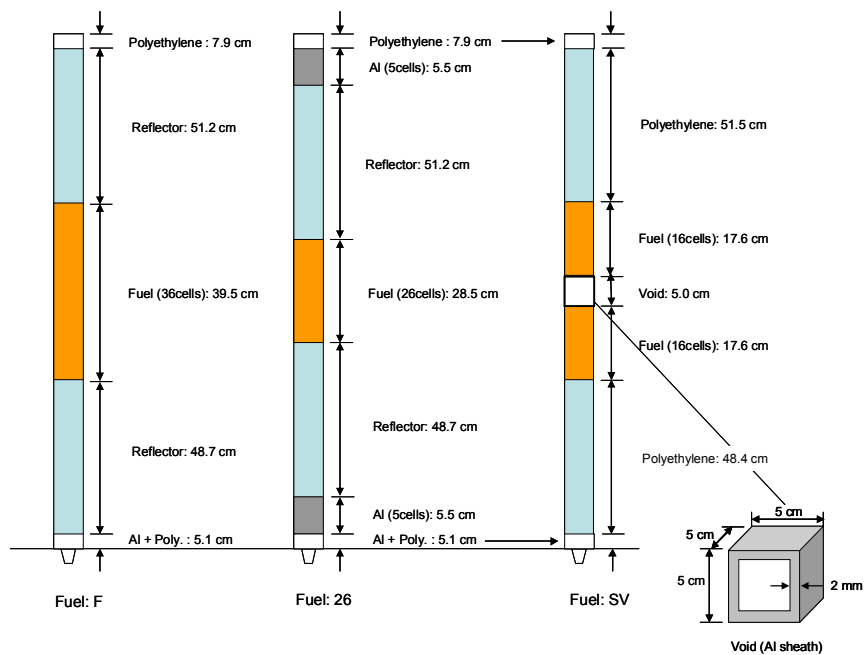


FIG. 7.12. Description of the fuel 'F', partial fuel '26', and fuel 'SV' assemblies, seen in Fig. 7.1 (Courtesy of the Nuclear Engineering Science Division, Research Reactor Institute, Kyoto University, Japan).

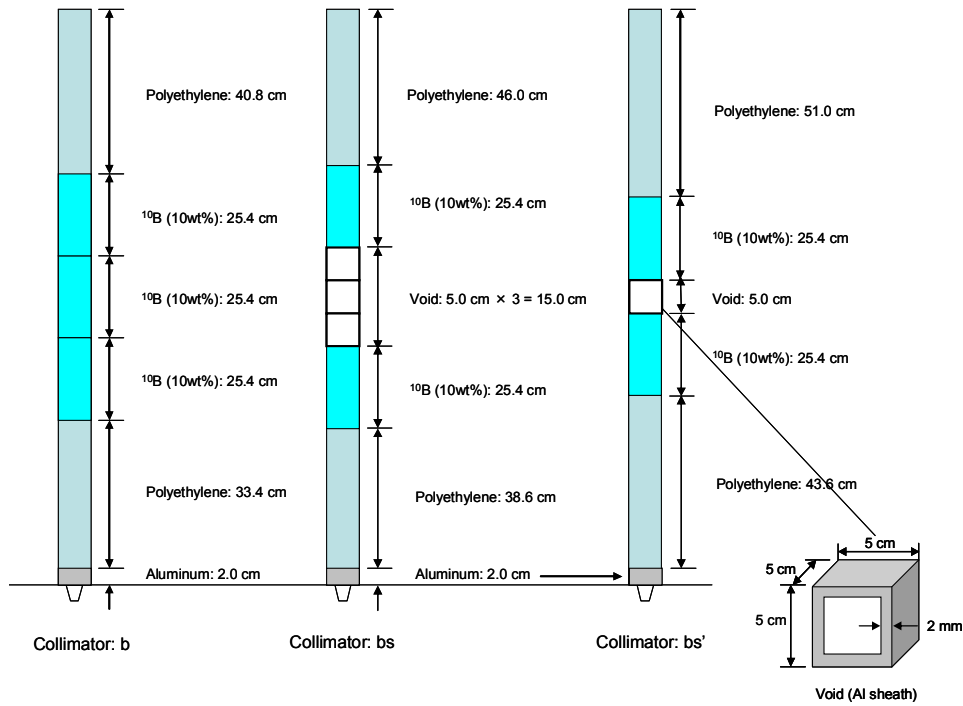


FIG. 7.13. Description of the neutron shield and beam ducts 'b', 'bs', and 'bs'', seen in Fig. 7.1 (Courtesy of the Nuclear Engineering Science Division, Research Reactor Institute, Kyoto University, Japan).

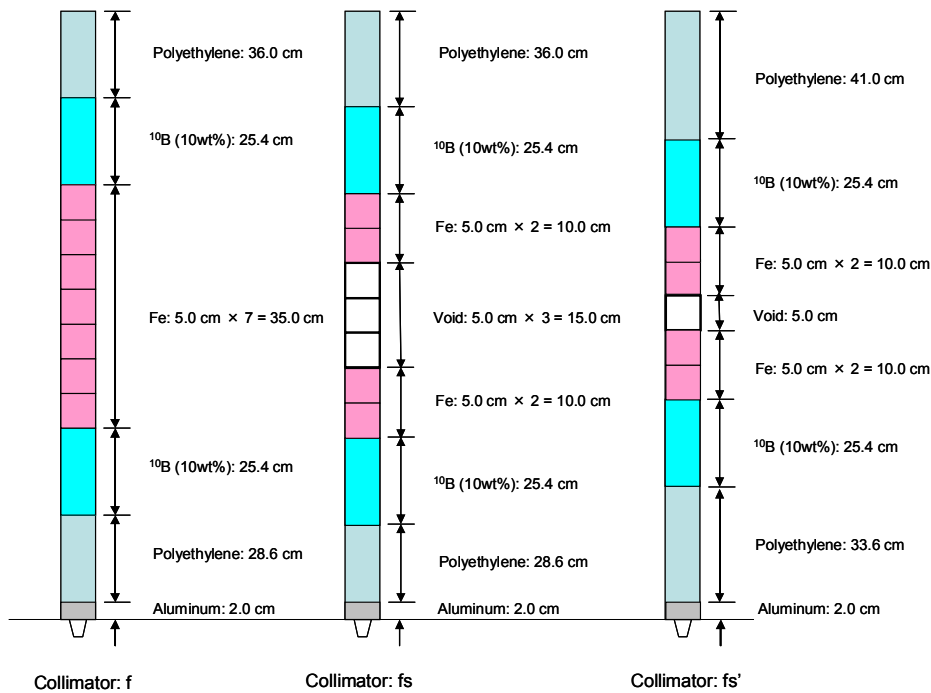


FIG. 7.14. Description of the neutron shield and beam ducts 'f', 'fs', and 'fs'', seen in Fig. 7.1 (Courtesy of the Nuclear Engineering Science Division, Research Reactor Institute, Kyoto University, Japan).

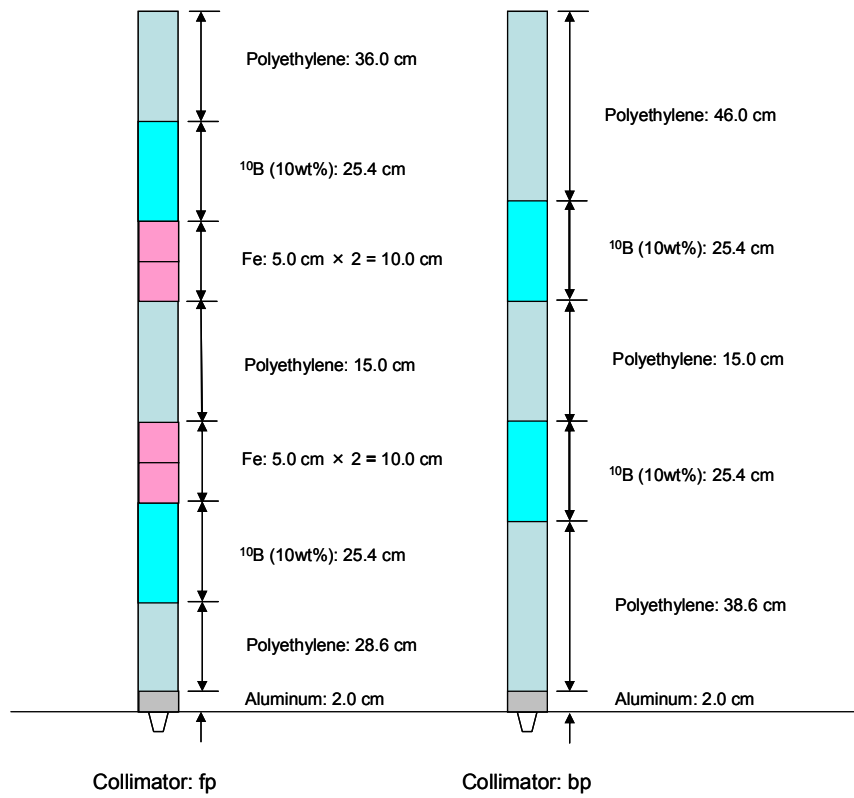


FIG. 7.15. Description of the neutron shields 'fp' and 'bp' (Courtesy of the Nuclear Engineering Science Division, Research Reactor Institute, Kyoto University, Japan).

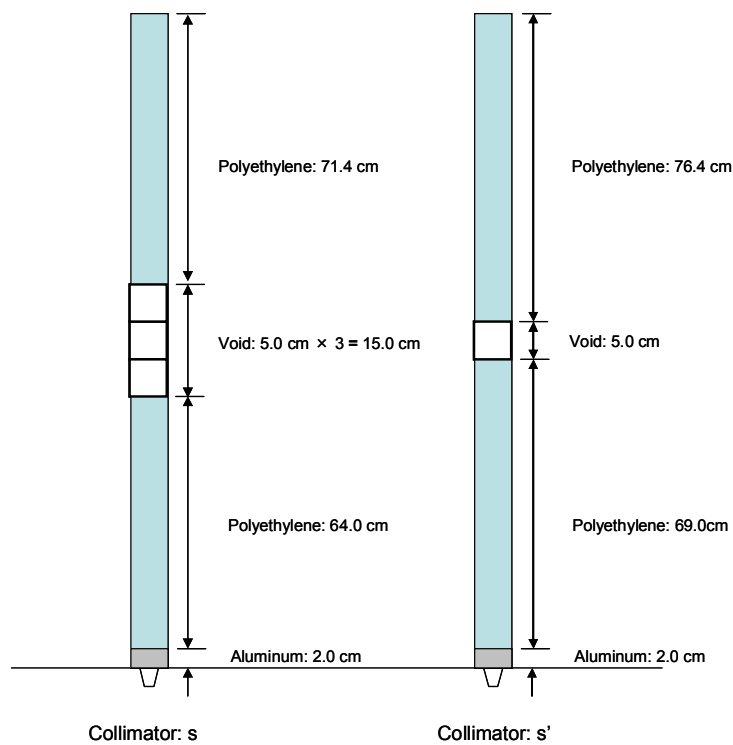


FIG. 7.16. Description of beam ducts 's' and 's'', seen in Fig. 7.1 (Courtesy of the Nuclear Engineering Science Division, Research Reactor Institute, Kyoto University, Japan).

7.2.4. Acquisition of the Experimental Results

7.2.4.1. Excess Reactivity and Subcriticality

When operating the KUCA facility, the critical state was adjusted by maintaining the control rods in certain positions. The subcritical state was then attained by inserting either the control or safety rods, or both. The level of subcriticality was established from the combination of both the reactivity worth of each control rod, evaluated by the rod drop method, and the excess reactivity determined on the basis of its integral calibration curve, as obtained by the positive-period method.

For eigenvalue and source calculations, it is necessary to consider the activated foils inserted in the matrix position (15,K) shown in Fig. 7.1. Note that the atomic densities, as well as the variations in the sizes of the foils, are given in Tables 7.7, 7.14 and 7.15, respectively.

7.2.4.2. Indium (In) Reaction-rate Distribution

Indium (In) wire (1.5 mm diameter in diameter and 60 cm long) was placed in the axial centre position of the core for measuring the reaction-rate distribution along the matrix positions (16,17–J,W), as shown in Fig. 7.1. Refer to Fig. 7.10 for a corresponding side view.

The experimental results from the In wire measurements were obtained by measuring detector total counts in the spectrum full-energy peaks for the emitted γ -rays from the $^{115}\text{In}(n, n')^{115\text{m}}\text{In}$ reaction. These measurements were performed using a high purity germanium (HPGe) detector. They were normalized to the comparable peak counts for an irradiated In foil ($20 \times 20 \times 1 \text{ mm}^3$) situated at the location of the tritium target.

7.2.4.3. Reaction Rates of Activated Foils

Activation foils of various materials were placed at chosen positions for measuring the neutron spectrum, including the matrix location (15,K) and near the tritium target as shown in Fig. 7.1. The rectangular dimensions of these foils were $45 \text{ mm} \times 45 \text{ mm}$, with thickness varying from 3 to 5 mm.

These foils were selected with the intent to cover a wide a range of neutron energy up to 14 MeV. The experimental results for the reaction rates of all the irradiated activation foils were obtained by measuring spectrum total counts of the γ -rays emitted from the induced reactions. They were normalized to the γ -rays counts of an irradiated Nb foil ($50 \times 50 \times 1 \text{ mm}^3$) emitted from the $^{93}\text{Nb}(n,2n)^{92\text{m}}\text{Nb}$ reactions.

This Nb foil was set in the location of the tritium target. In order to obtain information on the neutron spectrum, the activation foils consisted of a collection of several materials. Two sets of the activation foils were irradiated simultaneously at the positions of interest, matrix position (15,K) and the target.

TABLE 7.1. ATOMIC DENSITIES OF THE 1/16"-THICK HIGHLY ENRICHED URANIUM FUEL PLATES FABRICATED OF U-AL ALLOY

Isotope	Atomic density ($\times 10^{24}/\text{cm}^3$)
^{235}U	1.50694×10^{-3}
^{238}U	1.08560×10^{-4}
^{27}Al	5.56436×10^{-2}

TABLE 7.2. ATOMIC DENSITIES OF THE POLYETHYLENE REFLECTOR

Isotope	Atomic density ($\times 10^{24}/\text{cm}^3$)			
	1/2" t plate	1/4" t plate	1/8" t plate	Polyethylene square rod
^1H	8.06560×10^{-2}	8.08711×10^{-2}	8.02167×10^{-2}	8.00083×10^{-2}
^{12}C	4.03280×10^{-2}	4.04356×10^{-2}	4.01084×10^{-2}	4.00042×10^{-2}

TABLE 7.3. ATOMIC DENSITIES OF THE CONTROL AND SAFETY RODS

Isotope	Atomic density ($\times 10^{24}/\text{cm}^3$)
^{10}B	3.87448×10^{-3}
^{11}B	1.68447×10^{-2}
^{16}O	3.10787×10^{-2}

TABLE 7.4. ATOMIC DENSITY OF THE ALUMINUM SHEATH FOR THE CORE ELEMENT AND 1/16" AL PLATE

Isotope	Atomic density ($\times 10^{24}/\text{cm}^3$)
^{27}Al	6.00385×10^{-2}

TABLE 7.5. ATOMIC DENSITY OF ^{10}B (10 WEIGHT PERCENT), AS SHOWN IN FIG 7.13, 7.14, AND 7.15*

Isotope	Atomic density ($\times 10^{24}/\text{cm}^3$)
^1H	7.02275×10^{-2}
^{12}C	3.60038×10^{-2}
^{10}B	8.97693×10^{-4}
^{11}B	3.90281×10^{-3}
^{16}O	7.20074×10^{-3}

*Note: Atomic densities of other H, C, O and B isotopes in this material are indicated.

TABLE 7.6. ATOMIC DENSITIES OF ^{56}Fe AND ^{115}In , AS SHOWN IN FIG 7.13, 7.14, AND 7.15

Foil	Isotope	Abundance (%)	Purity (%)	Atomic density ($\times 10^{24}/\text{cm}^3$)
^{115}In	^{113}In	4.29	99.99	1.64406×10^{-3}
	^{115}In	95.71	99.99	3.66790×10^{-2}
	^{54}Fe	5.845	99.5	4.93395×10^{-3}
^{56}Fe	^{56}Fe	91.754	99.5	7.74524×10^{-2}
	^{57}Fe	2.119	99.5	1.78871×10^{-3}
	^{58}Fe	0.282	99.5	2.38045×10^{-4}

7.3. CORE CONFIGURATIONS

Figures 7.17–7.24 are diagrams of various KUCA core configurations utilized in the present investigation. The figure captions identify these particular configurations.

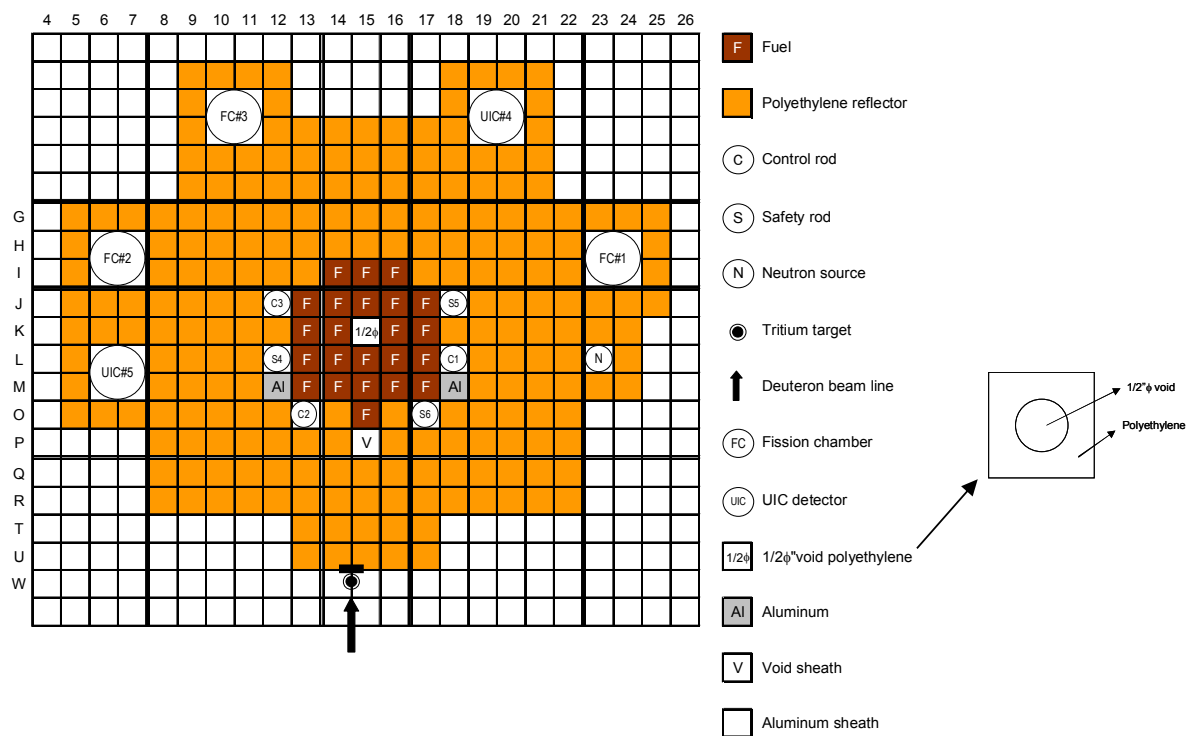


FIG. 7.17. No neutron shield and no beam duct core (Series-I: Case I-1) (Courtesy of the Nuclear Engineering Science Division, Research Reactor Institute, Kyoto University, Japan).

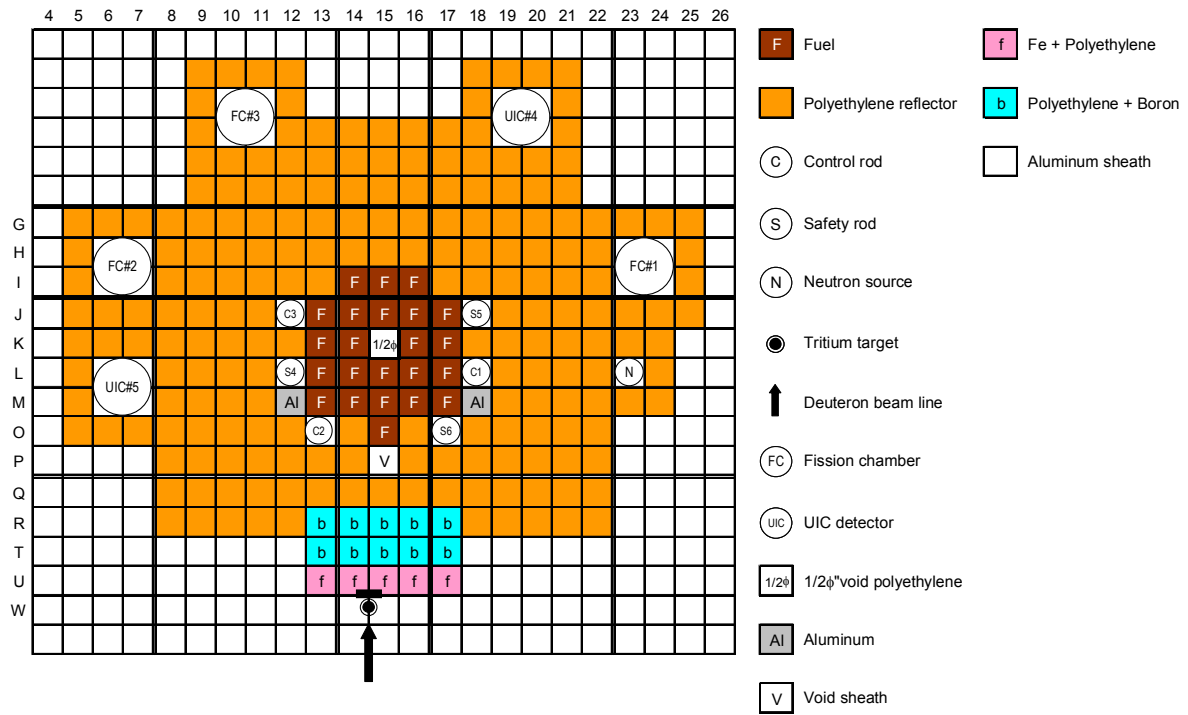


FIG. 7.20. Neutron shield and no beam duct core (Series-I: Case I-4) (Courtesy of the Nuclear Engineering Science Division, Research Reactor Institute, Kyoto University, Japan).

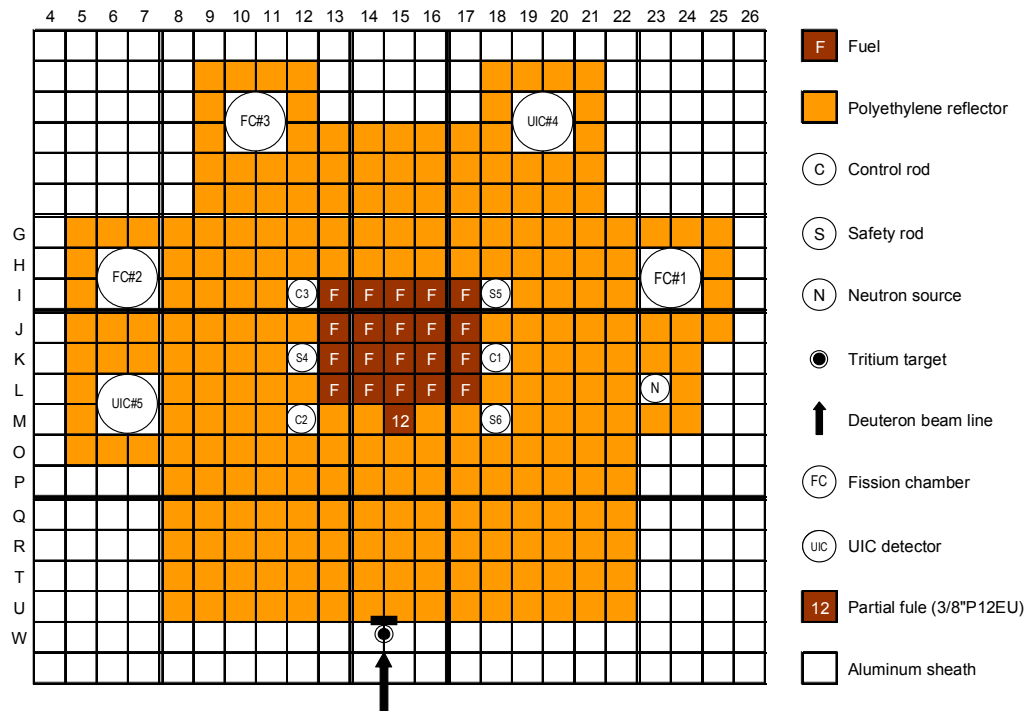


FIG. 7.21. No neutron shield, no beam duct, and no SV core (Series-II: Case II-1) (Courtesy of the Nuclear Engineering Science Division, Research Reactor Institute, Kyoto University, Japan).

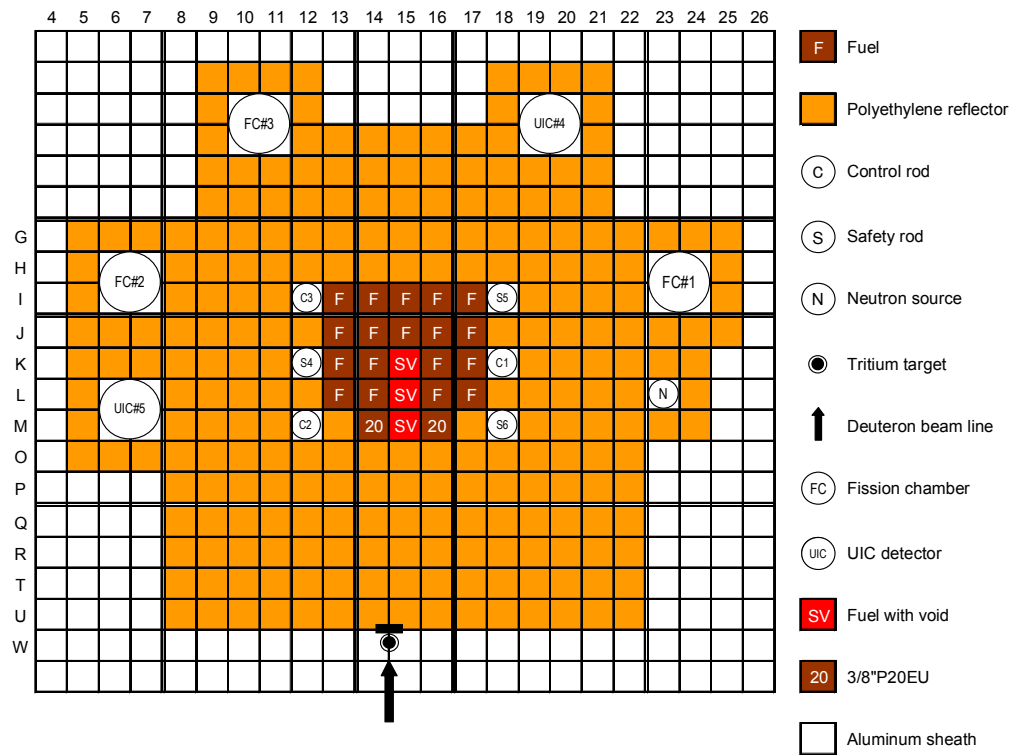


FIG. 7.22. No neutron shield, no beam duct, and SV core (Series-II: Case II-2) (Courtesy of the Nuclear Engineering Science Division, Research Reactor Institute, Kyoto University, Japan).

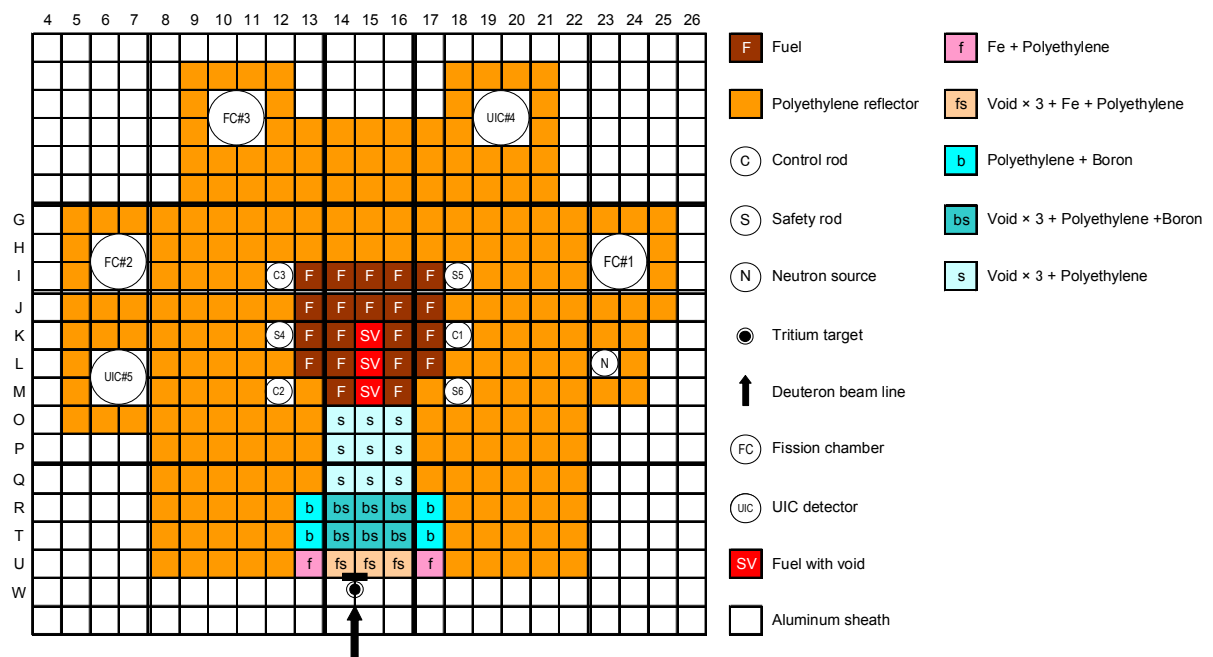


FIG. 7.23. Neutron shield, large beam duct (s) and SV core (Series-II: Case II-3) (Courtesy of the Nuclear Engineering Science Division, Research Reactor Institute, Kyoto University, Japan).

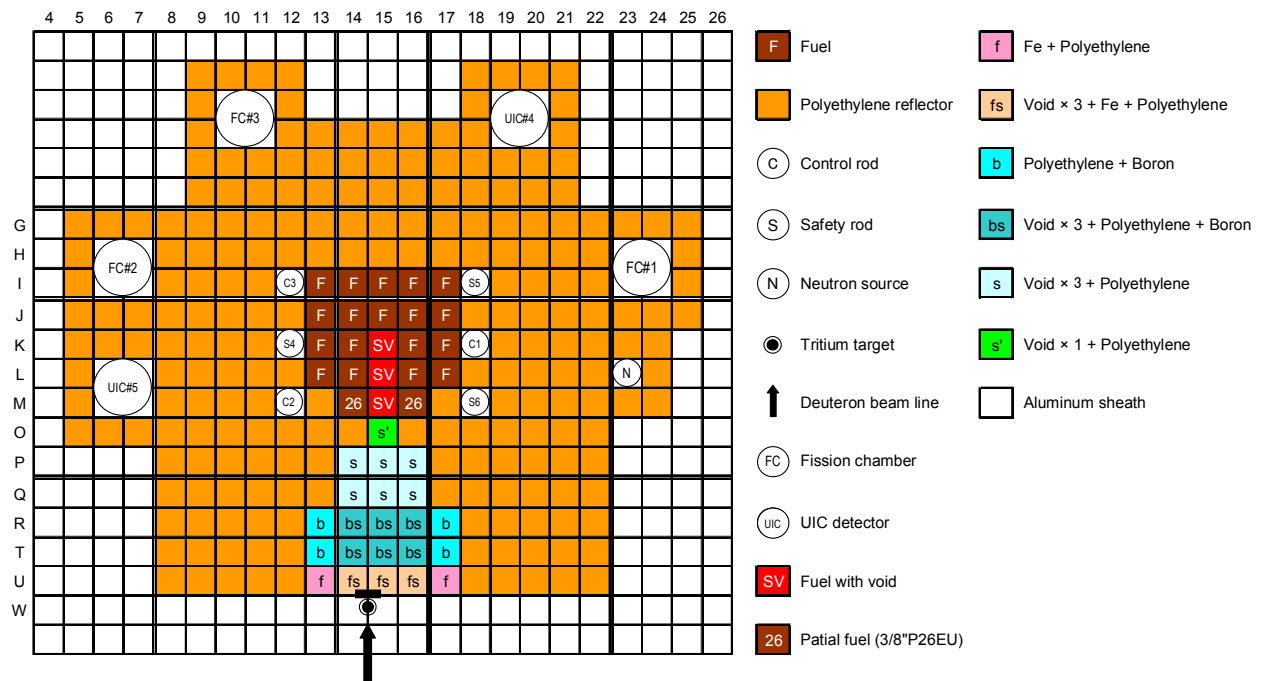


FIG. 7.24. Neutron shield, small beam duct (*s*) and SV core (Series-II: Case II-4) (Courtesy of the Nuclear Engineering Science Division, Research Reactor Institute, Kyoto University, Japan).

7.4. STATIC EXPERIMENTAL RESULTS

7.4.1. Excess Reactivity and Subcriticality

TABLE 7.7. MEASURED EXCESS REACTIVITY AND SUBCRITICALITY OBTAINED FROM THE CONTROL ROD CALIBRATION CURVE AND THE CONTROL ROD WORTH AND ITS CALIBRATION CURVE, RESPECTIVELY

Case name	Insertion rods pattern	Excess ($\% \Delta k/k$)	Subcriticality ($\% \Delta k/k$)
I-1	C1, C2, C3	0.295 ± 0.021	0.904 ± 0.063
I-2	C1, C2, C3	0.293 ± 0.021	0.925 ± 0.065
I-3	C1, C2, C3	0.020 ± 0.001	1.171 ± 0.082
I-4	C1, C2, C3	0.296 ± 0.021	0.907 ± 0.063
II-1	C1, C2, C3	0.143 ± 0.010	0.793 ± 0.056
II-2	C1, C2, C3	0.246 ± 0.017	0.677 ± 0.047
II-3	C1, C2, C3	0.037 ± 0.003	0.893 ± 0.063
II-4	C1, C2, C3	0.232 ± 0.016	0.702 ± 0.049
III-1	C1, C2, C3	0.050 ± 0.004	0.850 ± 0.060
III-2	C1, C2, C3, S4, S5, S6	0.049 ± 0.003	1.751 ± 0.123
III-3	C1, C2, C3, S5, S6	0.077 ± 0.005	1.223 ± 0.086

7.4.2. Reaction-rate Distribution

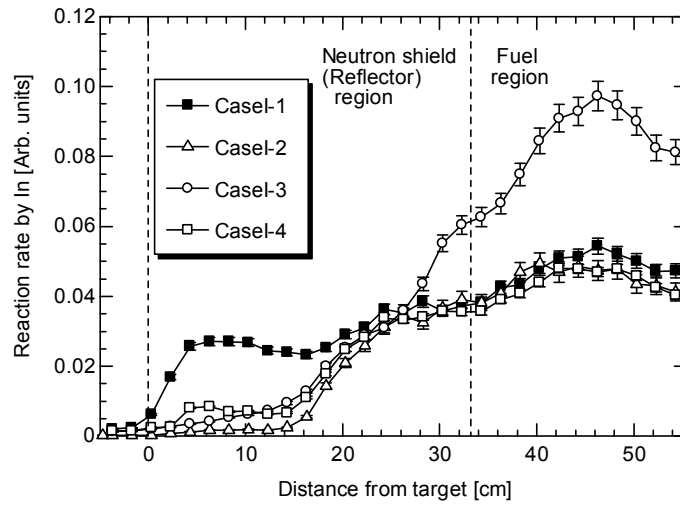


FIG. 7.25. Measured reaction-rate distributions obtained from the Indium wire measurements along the vertical direction, as shown in Fig 7.17–7.20 (Case I-1 to Case I-4) (Courtesy of the Nuclear Engineering Science Division, Research Reactor Institute, Kyoto University, Japan).

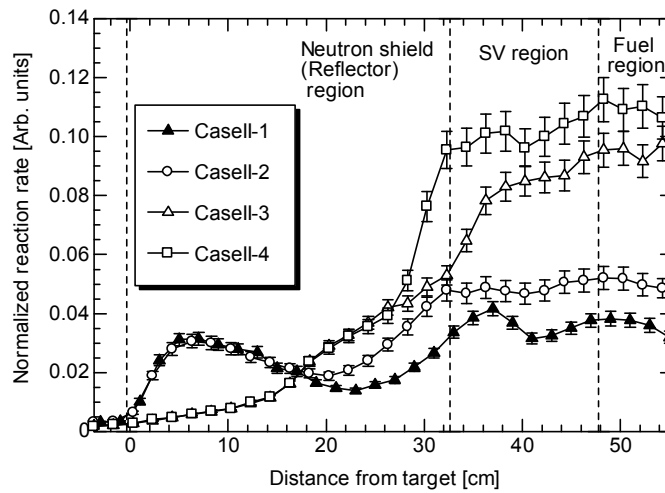


FIG. 7.26. Measured reaction-rate distributions obtained from the Indium wire measurements along the vertical direction, as shown in Fig 7.21–7.24 (Case II-1 to Case II-4) (Courtesy of the Nuclear Engineering Science Division, Research Reactor Institute, Kyoto University, Japan).

7.4.3. Reaction Rates of Activation Foils

TABLE 7.8. MEASURED REACTION RATES OF ACTIVATION FOILS CORRESPONDING TO SUBCRITICALITY LEVEL 0.85% $\Delta K/K$ (CASE III-1) AT MATRIX POSITION (15,K), AS SHOWN IN FIG. 7.24

Foil	Reaction	Saturation radioactivity (1/s/cm ³)
¹¹⁵ In	(<i>n, n'</i>)	$(3.160 \pm 0.036) \times 10^3$
⁵⁶ Fe	(<i>n, p</i>)	$(3.749 \pm 0.037) \times 10^2$
²⁷ Al	(<i>n, α</i>)	$(4.139 \pm 0.072) \times 10^1$
¹⁹⁷ Au	(<i>n, γ</i>)	$(3.516 \pm 0.034) \times 10^5$

TABLE 7.9. MEASURED REACTION RATES OF ACTIVATION FOILS CORRESPONDING TO SUBCRITICALITY 1.75% $\Delta K/K$ (CASE III-2) AT MATRIX POSITION (15,K), AS SHOWN IN FIG. 7.24

Foil	Reaction	Saturation radioactivity (1/s/cm ³)
¹¹⁵ In	(<i>n, n'</i>)	$(1.238 \pm 0.015) \times 10^3$
⁵⁶ Fe	(<i>n, p</i>)	$(1.750 \pm 0.018) \times 10^2$
²⁷ Al	(<i>n, α</i>)	$(3.573 \pm 0.042) \times 10^1$
¹⁹⁷ Au	(<i>n, γ</i>)	$(1.582 \pm 0.014) \times 10^5$

TABLE 7.10. MEASURED REACTION RATES OF ACTIVATION FOILS CORRESPONDING TO SUBCRITICALITY 1.22% $\Delta K/K$ (CASE III-3) AT MATRIX POSITION (15,K), AS SHOWN IN FIG. 7.24

Foil	Reaction	Saturation radioactivity (1/s/cm ³)
¹¹⁵ In	(<i>n, n'</i>)	$(2.085 \pm 0.023) \times 10^3$
⁵⁶ Fe	(<i>n, p</i>)	$(3.139 \pm 0.030) \times 10^2$
²⁷ Al	(<i>n, α</i>)	$(4.513 \pm 0.092) \times 10^1$
⁹³ Nb	(<i>n, 2n</i>)	$(3.389 \pm 0.172) \times 10^2$
¹⁹⁷ Au	(<i>n, γ</i>)	$(5.532 \pm 0.051) \times 10^5$

TABLE 7.11. MEASURED REACTION RATES OF THE ACTIVATION FOILS PLACED AT THE TARGET POSITION, AS SHOWN IN FIG. 7.24

Foil	Reaction	Saturation radioactivity (1/s/cm ³)
¹¹⁵ In	(<i>n, n'</i>)	$(5.164 \pm 0.051) \times 10^3$
⁵⁶ Fe	(<i>n, p</i>)	$(3.661 \pm 0.032) \times 10^3$
²⁷ Al	(<i>n, α</i>)	$(6.125 \pm 0.044) \times 10^3$
⁹³ Nb	(<i>n, 2n</i>)	$(2.487 \pm 0.028) \times 10^4$
⁹³ Nb*	(<i>n, γ</i>)	$(2.081 \pm 0.028) \times 10^4$

* Normalization foil

TABLE 7.12. ATOMIC DENSITY OF THE ACTIVATION FOILS UTILIZED IN THE REACTION-RATE MEASUREMENTS

Foil	Isotope	Abundance (%)	Purity (%)	Atomic density ($\times 10^{24}/\text{cm}^3$)
^{115}In	^{113}In	4.29	99.99	1.64406×10^{-3}
	^{115}In	95.71	99.99	3.66790×10^{-2}
	^{54}Fe	5.845	99.5	4.93395×10^{-3}
^{56}Fe	^{56}Fe	91.754	99.5	7.74524×10^{-2}
	^{57}Fe	2.119	99.5	1.78871×10^{-3}
	^{58}Fe	0.282	99.5	2.38045×10^{-4}
^{27}Al	^{27}Al	100	99.5	5.99156×10^{-2}
^{93}Nb	^{93}Nb	100	99.9	5.54750×10^{-2}
^{197}Au	^{197}Au	100	99.95	5.90193×10^{-2}

7.5. CORE CONDITIONS

The core configuration was described in section 7.2 and the control rod positions for the neutron spectrum characterization experiments are given in Table 7.13. The description of the foils is given in Table 7.14 and their dimensions are given in Table 7.15.

TABLE 7.13. CORE CONDITIONS FOR ALL THE CASES, INCLUDING FOILS, NEUTRONS SHIELD, SV, IN WIRE, PARTIAL FUEL, AND CONTROL ROD POSITIONS

Case	Foils No.	Neutron shield	SV fuel	In wire	Partial fuel	C1 (mm)	C2 (mm)	C3 (mm)	S4-S6 (mm)
Case I-1	×	×	×	○	×	U.L.	U.L.	524.34	U.L.
Case I-2	×	○ (s)	×	○	×	U.L.	U.L.	548.21	U.L.
Case I-3	×	○ (s')	×	○	×	U.L.	U.L.	745.54	U.L.
Case I-4	×	○ (s_NV)*	×	○	×	U.L.	U.L.	525.52	U.L.
Case II-1	×	×	×	○	12	U.L.	U.L.	635.94	U.L.
Case II-2	1	×	○	○	20	637.48	U.L.	U.L.	U.L.
Case II-3	1	○ (s)	○	○	36	U.L.	U.L.	742.48	U.L.
Case II-4	1	○ (s')	○	○	26	U.L.	U.L.	553.24	U.L.
Case III-1	2	○ (s')	○	○	20	U.L.	U.L.	725.35	U.L.
Target	3								
Case III-2	2	○ (s')	○	○	20	U.L.	U.L.	727.36	U.L.
Target	3								
Case III-3	2	○ (s')	○	○	20	U.L.	U.L.	694.11	U.L.
Target	3								

* No void (NV)

Foils No.: Refer to Table IV of Ref. [7.2]

U.L.: Upper Limit (1 200 mm)

TABLE 7.14. FOIL SELECTIONS UTILIZED IN THE NEUTRON-SPECTRUM CHARACTERIZATION EXPERIMENTS

Case	Foils No.								
Case II	1	Ni	Al	Fe	In	/	/	/	/
	Normalization foil (at target)	/	/	/	/	In*	/	/	/
Case III	2	/	Al	Fe	In	/	Nb	/	Au
	Normalization foil (at target)	/	/	/	/	/	/	Nb*	/
Target	3	/	Al	Fe	In	/	Nb	Nb*	/

TABLE 7.15. DIMENSIONS OF THE ACTIVATION FOILS

Foil	Dimensions
Ni	45 mm × 45 mm × 5 mm
Al	45 mm × 45 mm × 5 mm
Fe	45 mm × 45 mm × 5 mm
In	45 mm × 45 mm × 3 mm
In*	20 mm × 20 mm × 1 mm
Nb	45 mm × 45 mm × 2 mm
Nb*	50 mm × 50 mm × 1 mm
Au	20 mm × 20 mm × 1 mm

7.6. KINETIC EXPERIMENTAL RESULTS

7.6.1. Neutron-Noise Method (Feynman- α and Rossi- α Methods)

The control rod positions for the Feynman- α and Rossi- α experiments are given in Table 7.16. The obtained α values are given in Table 7.17 through 7.18 as well as the corresponding subcriticality values from using different pulse periods. The obtained subcriticality values using different pulse periods are identical. The core configuration for these experiments is shown in Fig. 7.27.

TABLE 7.16. CONTROL AND SAFETY ROD POSITIONS FOR THE SUBCRITICALITY MEASUREMENTS

Case	C1	C2	C3	S4	S5	S6
IV-1	0.0	0.0	1200.0	1200.0	1200.0	1200.0
IV-2	0.0	0.0	1200.0	0.0	1200.0	1200.0
IV-3	0.0	0.0	0.0	1200.0	0.0	0.0
IV-4	0.0	0.0	0.0	0.0	0.0	0.0

TABLE 7.17. MEASURED SUBCRITICALITY (% $\Delta K/K$) USING THE NEUTRON-NOISE METHOD, AS SHOWN IN FIG. 7.27 (20 MS PULSE PERIOD)

Case	Subcriticality (% $\Delta k/k$)	Reference* α (1/s)	Feynman** α (1/s)	Feynman*** α (1/s)	Rossi (1/s)
IV-1	0.50 ± 0.01	266 ± 2	253 ± 1	285 ± 1	263 ± 1
IV-2	0.99 ± 0.01	369 ± 3	373 ± 2	383 ± 1	368 ± 2
IV-3	1.58 ± 0.02	494 ± 3	495 ± 3	508 ± 1	500 ± 5
IV-4	2.07 ± 0.02	598 ± 4	601 ± 4	631 ± 2	599 ± 7

*: Reference α was obtained using the pulsed-neutron method.

** : Stochastic Feynman – α

***: Deterministic Feynman – α

Note that the calculated values of β_{eff} and l are 7.627×10^{-3} and 4.304×10^{-5} s, respectively, in this core.

TABLE 7.18. MEASURED SUBCRITICALITY (% $\Delta K/K$) USING THE NEUTRON NOISE METHOD, AS SHOWN IN FIG. 7.27 (THE PULSE PERIOD IS 10 MS)

Case	Subcriticality (% $\Delta k/k$)	Reference* α (1/s)	Feynman** α (1/s)	Feynman*** α (1/s)	Rossi (1/s)
IV-1	0.50 ± 0.01	266 ± 2	262 ± 1	310 ± 1	259 ± 1
IV-2	0.99 ± 0.01	369 ± 3	360 ± 2	397 ± 1	363 ± 2
IV-3	1.58 ± 0.02	494 ± 3	463 ± 3	530 ± 1	485 ± 5
IV-4	2.07 ± 0.02	598 ± 4	585 ± 6	641 ± 2	600 ± 14

TABLE 7.19. MEASURED SUBCRITICALITY (% $\Delta K/K$) USING THE NEUTRON NOISE METHOD, SHOWN IN FIG. 7.27 (THE PULSE PERIOD IS 1 MS).

Case	Subcriticality (% $\Delta k/k$)	Reference* α (1/s)	Feynman** α (1/s)	Feynman*** α (1/s)	Rossi (1/s)
IV-1	0.50 ± 0.01	266 ± 2	258 ± 1	None	260 ± 1
IV-2	0.99 ± 0.01	369 ± 3	367 ± 1	None	370 ± 2
IV-3	1.58 ± 0.02	494 ± 3	507 ± 2	None	502 ± 3
IV-4	2.07 ± 0.02	598 ± 4	604 ± 3	None	601 ± 6

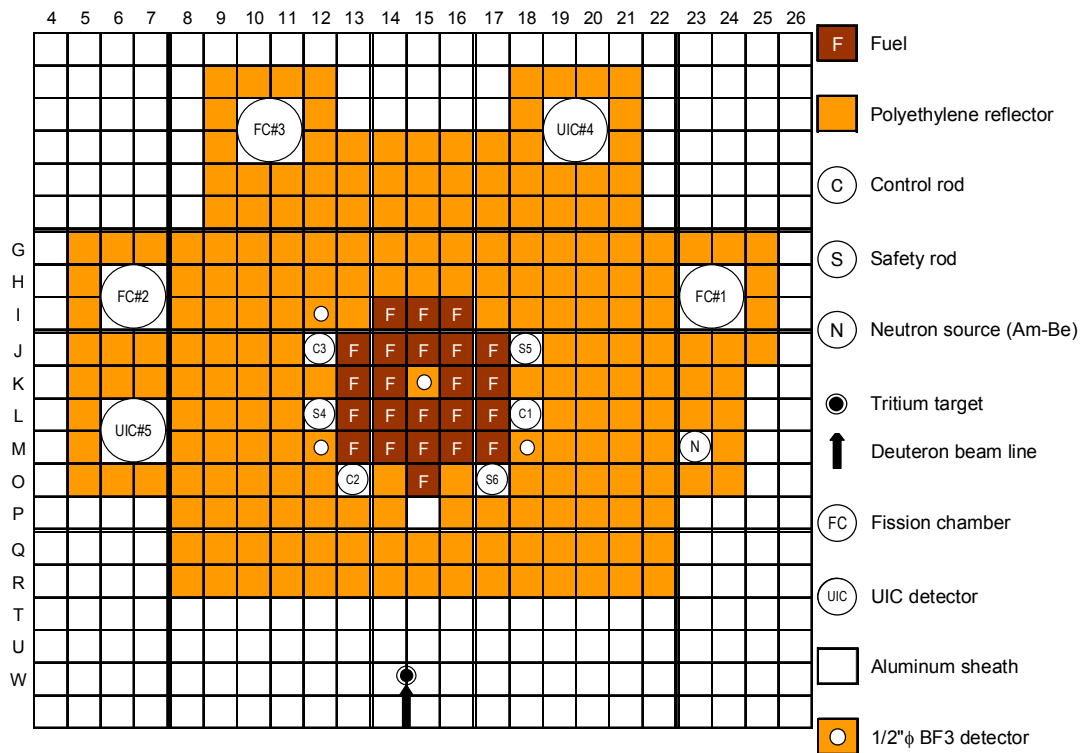


FIG. 7.27. Core configuration for the subcriticality measurements using the neutron-noise method (Cases VI-1 – VI-4) (Courtesy of the Nuclear Engineering Science Division, Research Reactor Institute, Kyoto University, Japan).

7.6.2. Source Multiplication Method

Four source multiplication experiments were performed for four different subcriticality values obtained with ^{252}Cf neutron source located at (15, Q) position and different control rod positions. These positions and the corresponding subcriticality levels are given in Table 7.20. The core configuration for these experiments is shown in Fig. 7.28. The measured subcriticality values using the source multiplication method are shown in Table 7.21. These values are in reasonable agreement with the reference values shown in Table 7.20.

Another six experiments (V-5 through V-10) were performed with the ^{252}Cf source located at different positions as shown in Tables 7.22 and 7.24. The control rod positions were the same except for experiment V-8 as shown in Tables 7.22 and 7.24. The core configuration is shown in Fig. 7.28 for experiment V-5 to V-7 and in Fig. 7.29 for experiment V-8 to V-10. The obtained subcriticality values using the source multiplication method with neutron detector located at different positions are given in Tables 7.23 and 7.25.

TABLE 7.20. CONTROL-ROD AND SAFETY-ROD POSITIONS IN THE SUBCRITICALITY SYSTEM AND THE REFERENCE SUBCRITICALITY MEASUREMENTS (LISTED BY CASE).

Case	Rod pattern	Subcriticality (% $\Delta k/k$)
V-1	C1, C2, C3, S4, S5, S6 (All rod positions: 650 mm)	1.00 ± 0.01
V-2	C1, C2, C3, S4, S5, S6 (All rod positions: 580 mm)	1.50 ± 0.02
V-3	C1, C2, C3, S4, S5, S6 (All rod positions: 510 mm)	2.00 ± 0.02
V-4	C1, C2, C3, S4, S5, S6 (All rod positions: Lower limit)	2.28 ± 0.02

TABLE 7.21. MEASURED SUBCRITICALITY (% $\Delta K/K$) USING THE SOURCE-MULTIPLICATION METHOD WITH THE DETECTOR LOCATED AT DIFFERENT POSITIONS, AS SHOWN IN FIG. 7.28.

Case	(15, K)	(20, I)	(20, K)	(20, L)	(20, O)
V-1	0.89 ± 0.01	0.95 ± 0.01	0.99 ± 0.01	0.96 ± 0.01	0.94 ± 0.01
V-2	1.54 ± 0.02	1.77 ± 0.02	1.99 ± 0.02	1.89 ± 0.02	1.79 ± 0.02
V-3	2.06 ± 0.02	2.47 ± 0.02	2.84 ± 0.03	2.74 ± 0.02	2.56 ± 0.02
V-4	2.38 ± 0.02	2.91 ± 0.02	3.39 ± 0.03	3.26 ± 0.02	3.03 ± 0.03

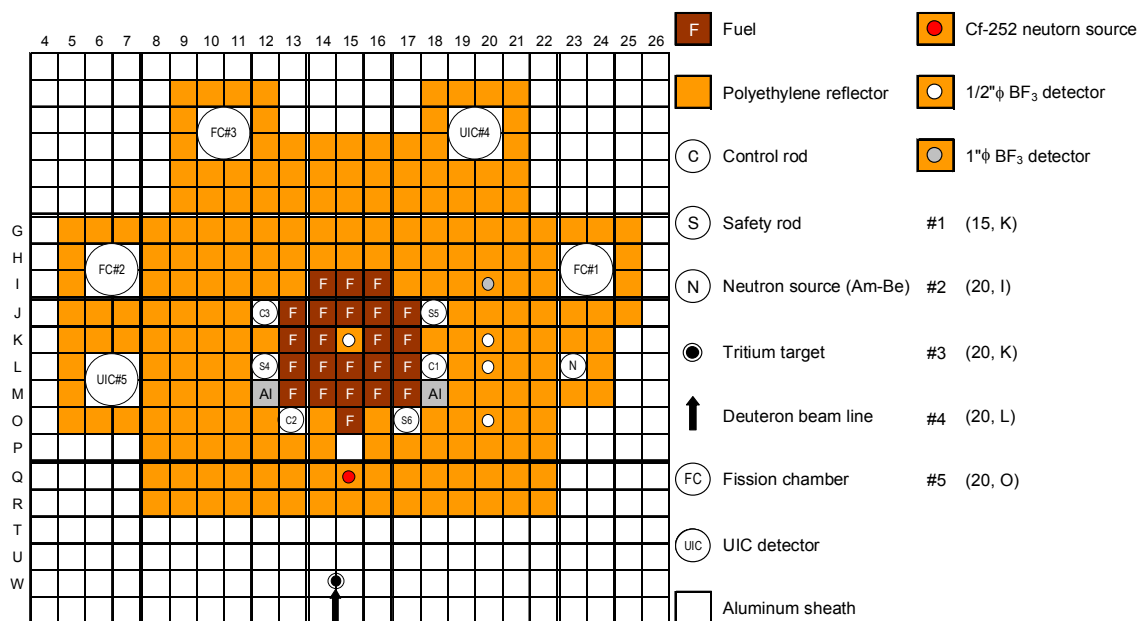


FIG. 7.28. Core configuration for the subcriticality measurements performed using the source-multiplication method (Cases V-1–V-4) (Courtesy of the Nuclear Engineering Science Division, Research Reactor Institute, Kyoto University, Japan).

TABLE 7.22. CONTROL-ROD, SAFETY-ROD, AND ^{252}Cf -SOURCE POSITIONS FOR THE SUBCRITICALITY MEASUREMENTS.

Case	C1	C2	C3	S4, S5, S6	^{252}Cf source
V-5	0.0	0.0	0.0	0.0	(15, K)
V-6	0.0	0.0	0.0	0.0	(16, J)
V-7	0.0	0.0	0.0	0.0	(16, L)

TABLE 7.23. MEASURED SUBCRITICALITY VALUES OBTAINED USING THE SOURCE-MULTIPLICATION METHOD FOR EACH DETECTOR POSITION SHOWN IN FIG. 7.29.

Case	Reference (% $\Delta k/k$)	(10, L)	(10, J)	(10, H)	(15, E)	FC#1	FC#2	FC#3
V-5		1.75 (0.02)	1.50 (0.02)	1.59 (0.02)	1.30 (0.01)	1.76 (0.02)	1.67 (0.02)	1.58 (0.02)
V-6	1.64 (0.02)	1.96 (0.02)	1.83 (0.02)	1.59 (0.02)	1.49 (0.01)	1.71 (0.02)	1.68 (0.02)	1.57 (0.02)
V-7		1.93 (0.02)	1.85 (0.02)	1.61 (0.02)	1.54 (0.01)	1.76 (0.02)	1.70 (0.02)	1.59 (0.02)

(): Error of the subcriticality values (% $\Delta k/k$).

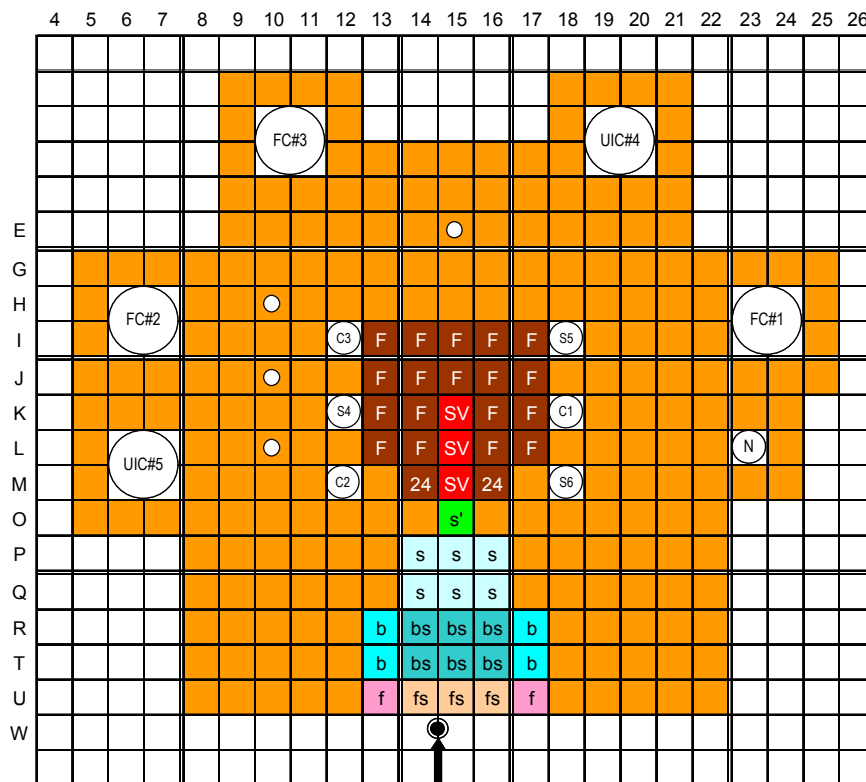


FIG. 7.29. Core configuration for the subcriticality measurements performed using the source-multiplication method (Cases II-5–II.7) (Courtesy of the Nuclear Engineering Science Division, Research Reactor Institute, Kyoto University, Japan).

TABLE 7.24. CONTROL-ROD, SAFETY-ROD, AND ²⁵²Cf-SOURCE POSITIONS FOR THE SUBCRITICALITY MEASUREMENTS.

Case	C1	C2	C3	S4, S5, S6	²⁵² Cf source
V-8	0.0	0.0	0.0	1200.0	(15, K)
V-9	0.0	0.0	0.0	0.0	(16, J)
V-10	0.0	0.0	0.0	0.0	(16, L)

TABLE 7.25. MEASURED SUBCRITICALITY USING THE SOURCE-MULTIPLICATION METHOD FOR EACH DETECTOR POSITION SHOWN IN FIG. 7.30.

Case	Reference (% $\Delta k/k$)	(10, L)	(10, J)	(10, H)	(15, E)	FC#1	FC#2	FC#3
V-8	7.64 (0.08)	10.2 (0.10)	11.3 (0.11)	13.5 (0.14)	2.98 (0.03)	—	—	—
V-9	8.57 (0.09)	23.3 (0.23)	22.0 (0.22)	20.8 (0.21)	3.12 (0.03)	—	—	—
V-10		12.9 (0.13)	8.67 (0.09)	15.5 (0.16)	3.10 (0.03)	—	—	—

(): Error of subcriticality (% $\Delta k/k$).

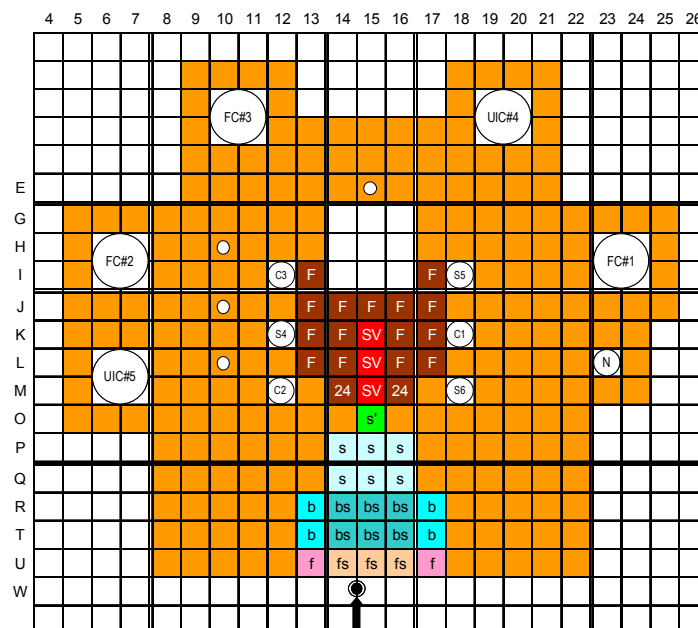


FIG. 7.30. Core configuration for the subcriticality measurements using the source-multiplication method (Cases II-8 through II-10) (Courtesy of the Nuclear Engineering Science Division, Research Reactor Institute, Kyoto University, Japan).

7.6.3. Pulsed-neutron Method

The subcriticality was measured using the pulsed neutron method with different pulse widths and pulse periods as listed in Table 7.26. The control rod positions for these

measurements are listed also in Table 7.26. Fig. 7.31 represents the core configuration for these measurements using the pulsed neutron methods (Cases VI-1–VI-2) and four supplements (a)–(d) for the other cases. Fig. 7.32 shows the schematic diagram of the optical-fibre detector system used for the measurements. The obtained subcriticality values and neutron decay constants are listed in Tables 7.27 and 7.28.

TABLE 7.26. CONTROL-ROD AND SAFETY-ROD POSITIONS IN THE SUBCRITICAL SYSTEM

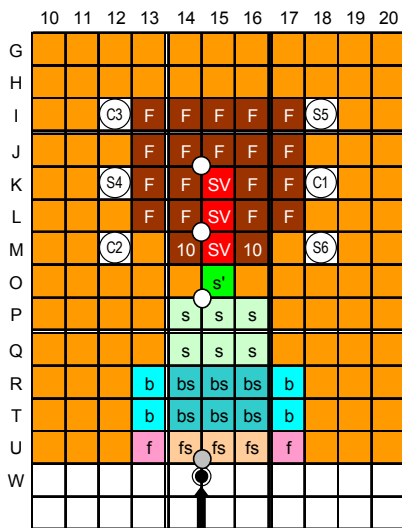
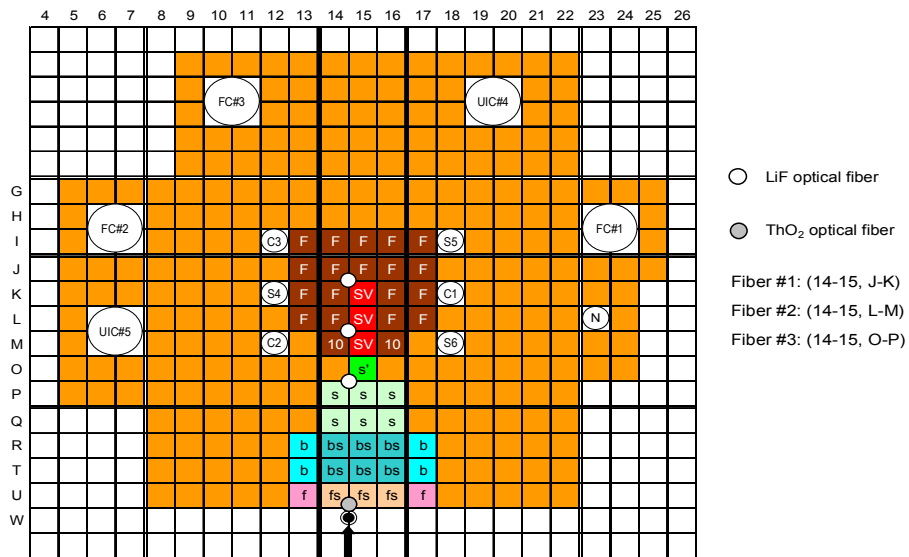
Case name	C1	C2	C3	S4	S5	S6	Pulse width (μs)	Pulse period (ms)
VI-1	0.0	0.0	0.0	1200.0	1200.0	1200.0	60	12
VI-2	0.0	0.0	0.0	0.0	0.0	0.0	80	32
VI-3	1200.0	1200.0	1200.0	1200.0	1200.0	1200.0	55	32
VI-4	0.0	0.0	0.0	1200.0	1200.0	1200.0	20	16
VI-5	0.0	0.0	0.0	0.0	0.0	0.0	30	12
VI-6	1200.0	1200.0	1200.0	1200.0	1200.0	1200.0	30	12
VI-7	0.0	0.0	0.0	1200.0	1200.0	1200.0	30	12
VI-8	0.0	0.0	0.0	0.0	0.0	0.0	30	12
VI-9	1200.0	1200.0	1200.0	1200.0	1200.0	1200.0	50	10

TABLE 7.27. MEASURED SUBCRITICALITY USING THE PULSED NEUTRON METHOD FOR EACH OPTICAL-FIBER DETECTOR POSITION, AS SHOWN IN FIG. 7.31

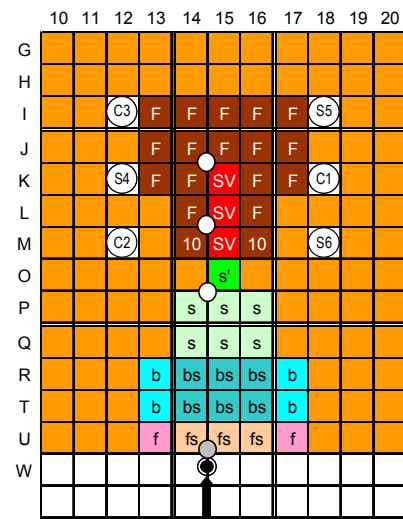
Case name	Fibre #1 (% $\Delta k/k$)	Fibre #2 (% $\Delta k/k$)	Fibre #3 (% $\Delta k/k$)
VI-1	0.99 ± 0.01	0.96 ± 0.01	0.99 ± 0.01
VI-2	1.88 ± 0.02	2.15 ± 0.02	1.78 ± 0.02
VI-3	2.55 ± 0.03	3.12 ± 0.03	2.42 ± 0.02
VI-4	3.40 ± 0.03	3.25 ± 0.03	3.63 ± 0.04
VI-5	4.49 ± 0.04	4.00 ± 0.04	4.60 ± 0.05
VI-6	5.89 ± 0.06	6.54 ± 0.07	6.87 ± 0.07
VI-7	6.59 ± 0.07	10.01 ± 0.10	7.56 ± 0.08
VI-8	7.55 ± 0.08	8.18 ± 0.08	8.64 ± 0.09
VI-9	10.24 ± 0.10	12.28 ± 0.12	11.93 ± 0.12

TABLE 7.28. MEASURED NEUTRON DECAY CONSTANT MEASURED USING THE PULSED-NEUTRON METHOD FOR EACH OPTICAL FIBER DETECTOR POSITION, AS SHOWN IN FIG. 7.31

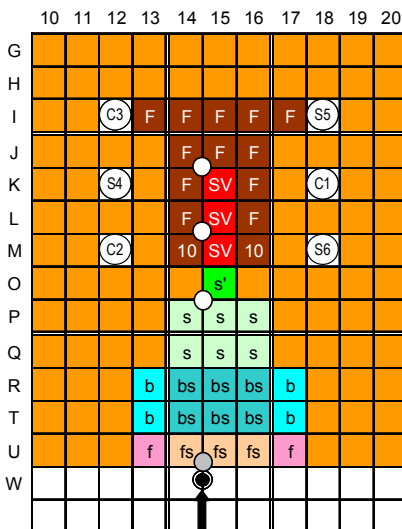
Case name	Fibre #1 (1/s)	Fibre #2 (1/s)	Fibre #3 (1/s)
VI-1	369 ± 4	372 ± 6	360 ± 5
VI-2	570 ± 6	586 ± 10	607 ± 7
VI-3	640 ± 5	640 ± 9	604 ± 7
VI-4	817 ± 14	820 ± 24	788 ± 17
VI-5	994 ± 19	1034 ± 34	922 ± 23
VI-6	1204 ± 21	1202 ± 37	1130 ± 23
VI-7	1419 ± 30	1364 ± 51	1510 ± 41
VI-8	1418 ± 33	1560 ± 64	1468 ± 44
VI-9	1640 ± 21	1797 ± 40	1701 ± 24



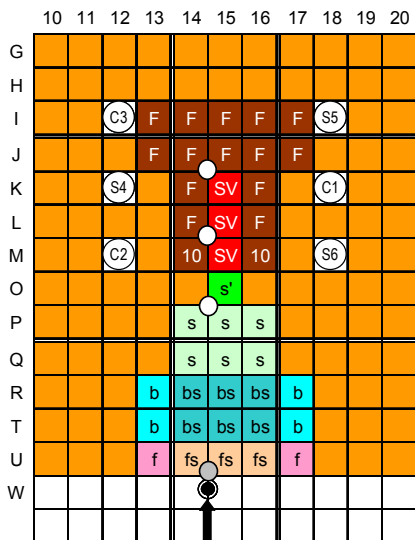
a) Cases VI-1 and VI-2



b) Cases VI-3 through VI-5



c) Cases VI-6 and VI-8



d) Case VI-9

FIG. 7.31. Core configuration for the subcriticality measurement using the pulsed-neutron method (Cases VI-1–VI-9) (Courtesy of the Nuclear Engineering Science Division, Research Reactor Institute, Kyoto University, Japan).

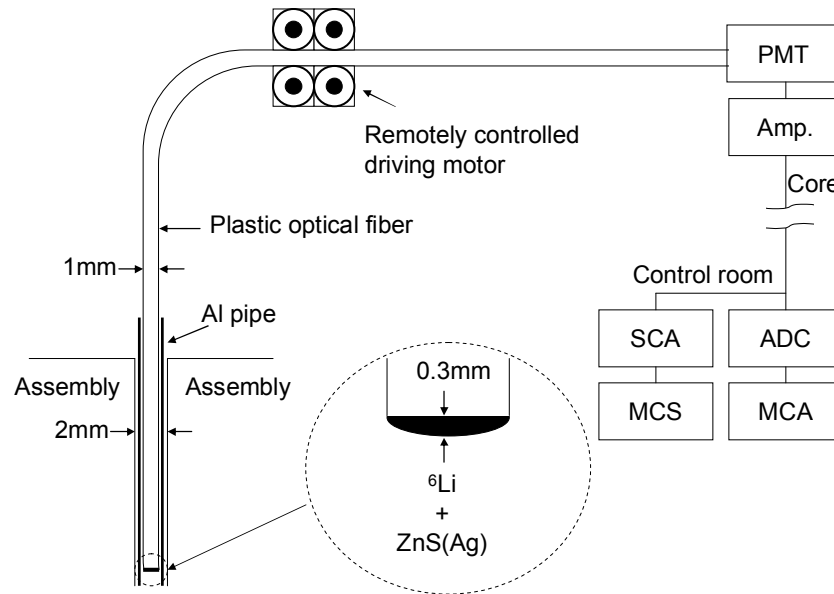


FIG. 7.32. Schematic diagram of the optical-fibre detector system (Courtesy of the Nuclear Engineering Science Division, Research Reactor Institute, Kyoto University, Japan).

7.7. BENCHMARK RESULTS

7.7.1. Static Experiments

The numerical analyses of the experimental data were carried using two Monte Carlo calculation codes (Japan used MCNP-4C3 with ENDF/B-VI.2 with and Pakistan used MCNP5 with ENDF/B-VII.0). The eigenvalue calculations were used to obtain the subcriticality level for the system operated in the subcritical state, and the excess reactivity when operated in the critical state. The fixed-source calculations were performed to determine values of the reaction rates by means of In wire activation and activation foils located in the core driven by the 14 MeV neutrons. Neutron spectral analyses were carried out using the SAND-II code. The Monte Carlo code MCNP-4C3, with JENDL Activation Cross-section File-96, was employed to generate the initial estimate values for the threshold reaction rates. The MCNP Monte Carlo statistical error that corresponded to one standard deviation was 0.03% $\Delta k/k$ for calculating the multiplication factor k_{eff} . The number of Monte Carlo neutron histories tracked was 2×10^7 .

7.7.1.1. Reactivity

Measured and calculated reactivity values are shown in Tables 7.29 to 7.31. A comparison between the measured and the calculated subcriticality levels showed that for each core the calculated subcriticality value $\rho_{cal-sub}$ is in good agreement with the measured $\rho_{exp-sub}$ within a relative difference of 5%, as shown in Table 7.29. An analysis of the excess reactivity revealed a discrepancy of 10% between the measured $\rho_{exp-sub}$ and the calculated $\rho_{cal-sub}$ values, as shown in Table 7.30. This discrepancy in the excess reactivity values exceeds what is expected considering the experimental error and the MCNP computational statistical error. Nevertheless, these results demonstrate that eigenvalue studies that compare computational and experimental values corresponding to reactivity analyses of an ADS core

loaded with highly enriched uranium fuel, and driven by 14 MeV neutrons, can produce reasonable results.

TABLE 7.29. COMPARISON BETWEEN MEASURED AND CALCULATED SUBCRITICALITY VALUES FOR ADS CONFIGURATIONS OBTAINED FROM EXPERIMENTS AND CALCULATIONS

Case	Measurement	Calculation (Japan)	Calculation (Pakistan)
	$\rho_{exp-sub}$ (% $\Delta k/k$)	$\rho_{cal-sub}$ (% $\Delta k/k$) MCNP-4C3 - ENDF/B-VI.2	$\rho_{cal-sub}$ (% $\Delta k/k$) MCNP-5 - ENDF/B-VII
I-1	0.90 ± 0.05	0.91 ± 0.03	0.94 ± 0.04
I-2	0.93 ± 0.05	0.89 ± 0.03	0.98 ± 0.04
I-3	1.17 ± 0.06	1.12 ± 0.03	1.16 ± 0.03
I-4	0.91 ± 0.05	0.89 ± 0.03	0.93 ± 0.03

TABLE 7.30. COMPARISON BETWEEN MEASURED AND CALCULATED EXCESS REACTIVITY VALUES OBTAINED FROM EXPERIMENTS AND CALCULATIONS

Case	Measurement	Calculation (Japan)	Calculation (Pakistan)
	$\rho_{exp-sub}$ (% $\Delta k/k$)	$\rho_{cal-sub}$ (% $\Delta k/k$) MCNP-4C3 - ENDF/B-VI.2	$\rho_{cal-sub}$ (% $\Delta k/k$) MCNP-5 - ENDF/B-VII
I-1	0.30 ± 0.02	0.33 ± 0.03	0.27 ± 0.03
I-2	0.29 ± 0.02	0.33 ± 0.03	0.36 ± 0.03
I-3	0.02 ± 0.01	0.06 ± 0.03	0.05 ± 0.03
I-4	0.30 ± 0.02	0.32 ± 0.03	0.30 ± 0.03

TABLE 7.31. COMPARISON BETWEEN MEASURED AND CALCULATED SUBCRITICALITY VALUES OBTAINED FROM ADS EXPERIMENTS AND MCNP-4C3 CALCULATIONS WITH ENDF/B-VI.2

Case	Measurement	Calculation (Japan)	Calculation (Pakistan)
	$\rho_{exp-sub}$ (% $\Delta k/k$)	$\rho_{cal-sub}$ (% $\Delta k/k$) MCNP-4C3 - ENDF/B-VI.2	$\rho_{cal-sub}$ (% $\Delta k/k$) MCNP-5 - ENDF/B-VII
II-1	0.79 ± 0.06	0.75 ± 0.02	0.78 ± 0.04
II-2	0.68 ± 0.05	0.68 ± 0.02	0.71 ± 0.03
II-3	0.89 ± 0.06	0.91 ± 0.02	1.14 ± 0.04
II-4	0.70 ± 0.05	0.76 ± 0.02	0.72 ± 0.03

7.7.1.2. Reaction Rate Distribution

Figure 7.32 shows the results of measurements from $^{115}\text{In}(n,\gamma)^{116\text{m}}\text{In}$ reaction rate distribution for ADS configurations with subcriticality values in the range of ~ 0.9 to 1.2 % $\Delta k/k$. For the Case I-3 the reaction rates appeared to be lower than the results obtained in the neutron shield (reflector) region for the Case I-1. On the other hand, the reaction rates approximately doubled in the fuel region. These results show that the neutron shield and beam duct have a combined influence on both the neutron shield and the fuel regions. That is to say, the high-energy neutrons were shielded by Fe located around the target region, the moderated thermal neutrons were absorbed by borated polyethylene (with 10 wt% boron) in front of the

fuel region, and the high-energy neutrons were guided through the beam duct. Furthermore, the results of the reaction rate calculations show that the window size of the beam duct in Case I-3 is more effective in front of the fuel region than in Case I-2. The effects of the beam duct itself can be observed from the results of Cases I-3 and I-4, as the difference between the beam duct and the polyethylene in the neutron shield region can be compared. In order to guide the high-energy neutrons into the fuel region efficiently, the optimal combination of the sizes for the beam duct and neutron shield was established. Thus, it was demonstrated that by having the beam duct and neutron shield installed it is possible to guide the high-energy neutrons flux into the fuel region more efficiently. The reaction-rate distribution results comparison shows that the specific layout of the neutron shield and the beam duct for the Case I-3 is the most beneficial to effectively deliver the high-energy flux into the fuel region.

In general, comparisons between the measured and the calculated reaction-rate distributions for the cores used in Cases I-1 through I-4, as shown in Fig 7.33–7.36, show that the computed reaction-rate distributions that were obtained using fixed-source calculations, involving the combined use of MCNP-4C3 and ENDF/B-VI.2, agree quite well with the corresponding experimental results.

Figures 7.33–7.36 demonstrate the analyses results for core configurations used in Cases 1–4. The comparisons between measured and calculated reaction-rate distributions show that the computed reaction-rate distributions, which were obtained using fixed-source calculations, involving the combined use of MCNP-4C3 and ENDF/B-VI.2, agree quite well with the corresponding experimental results.

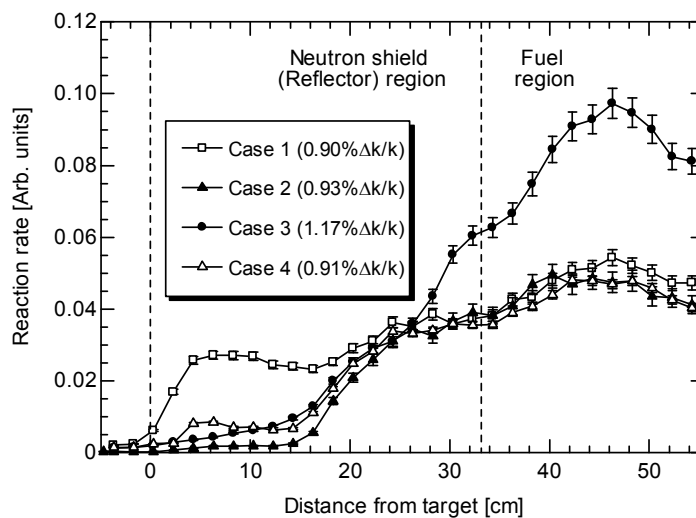


FIG. 7.33. Measured reaction-rate distributions for Cases I-1 through I-4 as obtained using an In wire positioned vertically along matrix positions (16,17-J,W) (Courtesy of the Nuclear Engineering Science Division, Research Reactor Institute, Kyoto University, Japan).

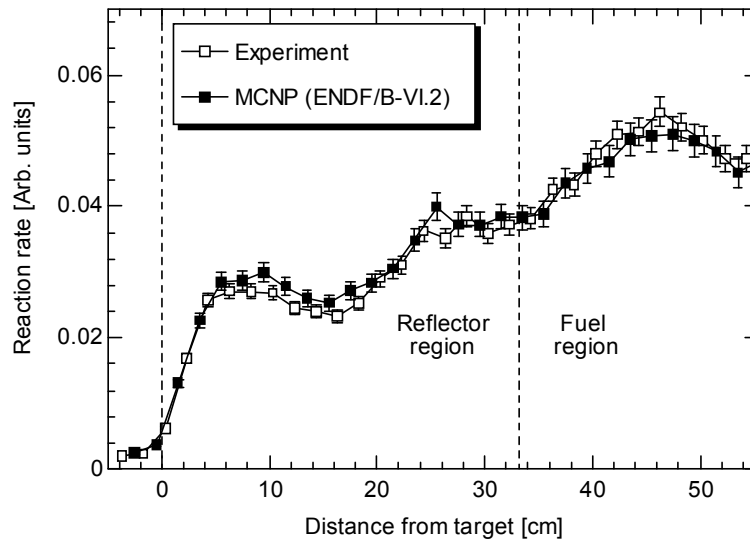


FIG. 7.34. Comparison between measured and calculated reaction-rate distributions in Case I-1 as obtained using an In wire positioned vertically along matrix positions (16,17-J,W) (Courtesy of the Nuclear Engineering Science Division, Research Reactor Institute, Kyoto University, Japan).

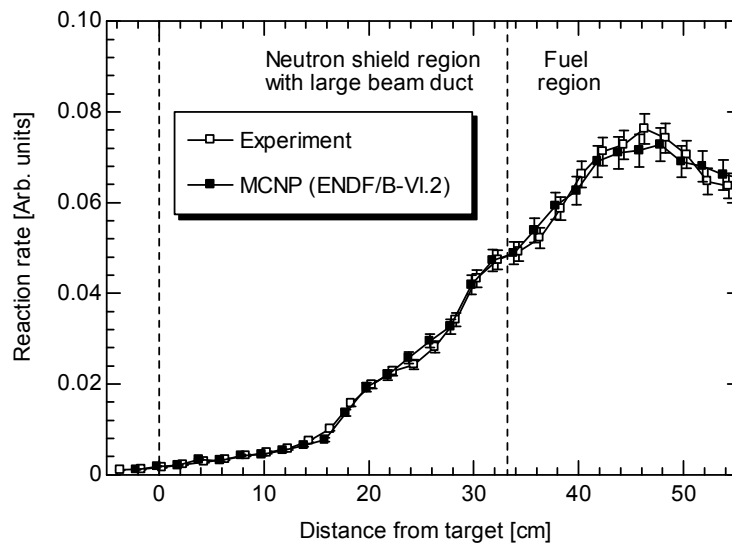


FIG. 7.35. Comparison between measured and calculated reaction-rate distributions in Case I-3 as obtained using an In wire positioned vertically along matrix positions (16,17-J,W) [Japan Calculations] (Courtesy of the Nuclear Engineering Science Division, Research Reactor Institute, Kyoto University, Japan).

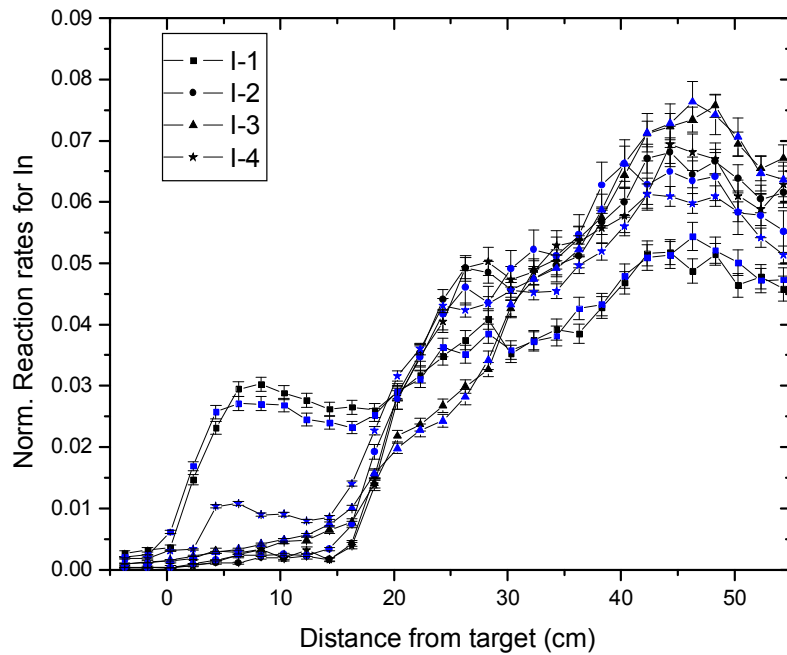


FIG. 7.36. Comparison between measured and calculated reaction-rate distributions in Cases I-1 through I-4 as obtained using an In wire positioned vertically along matrix positions (16,17-J,W) [Pakistan Calculations] (Courtesy of the Nuclear Engineering Science Division, Research Reactor Institute, Kyoto University, Japan).

The measured reaction-rate distribution (expressed in arbitrary units) for Cases II-1 through II-4 (Fig. 7.33) shows a 35% increase in neutron yield between Cases II-1 and II-2 in the fuel region. These two core configurations differ with respect to the SV assemblies, partial fuel rods, and irradiation samples. The SV assemblies have two opposing effects: an absorption effect and a streaming effect that favours the external neutrons reaching the centre of the fuel region where the neutron importance is greater. Consequently, the increase seen in the neutron yield between the reaction-rate distributions in Cases II-1 and II-2 demonstrates that partial assemblies and streaming effects can be employed to compensate for the absorption effect of the SV assemblies and the irradiation samples.

An approximate doubling of the neutron yield was observed between Case II-2 and Case II-3 or Case II-4, despite the lower subcritically values. This increase is attributed to the geometrical modifications alone, since the irradiation samples were identical in these two cases. This comparison proves that the introduction of the neutron guide is effective as a means of improving the neutron yield in the core region.

The difference in the results of Cases II-3 and II-4, corresponding to these two neutron guides, resides in the interface with the fuel region. First, to enhance irradiation of the core from the neutron source, the neutron guide with a large window (Case II-3) had the void in the reflector connected directly to the fuel region. On the other hand, the neutron guide in Case II-4 included a small window of the same size as the SV void in front of the fuel region. The increase in the neutron yield between the neutron guided cores of Cases II-3 and II-4 is about 15% in the core centre but it approached 80% in front of the fuel region, demonstrating that the optimum neutron yield was obtained with the neutron guide having the small window seen in Case II-4. Consequently, this neutron guide (a small window in Case II-4) has been adopted as the optimal choice for further experiments.

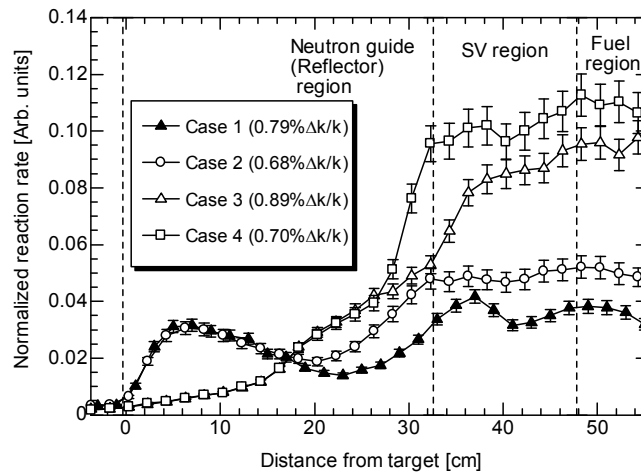


FIG. 7.37. Measured results for the $^{115}\text{In}(n,\gamma)^{116m}\text{In}$ reaction-rate distribution corresponding to Cases II-1 through II- 4, recorded vertically along matrix positions (16,17-J,W) (Courtesy of the Nuclear Engineering Science Division, Research Reactor Institute, Kyoto University, Japan).

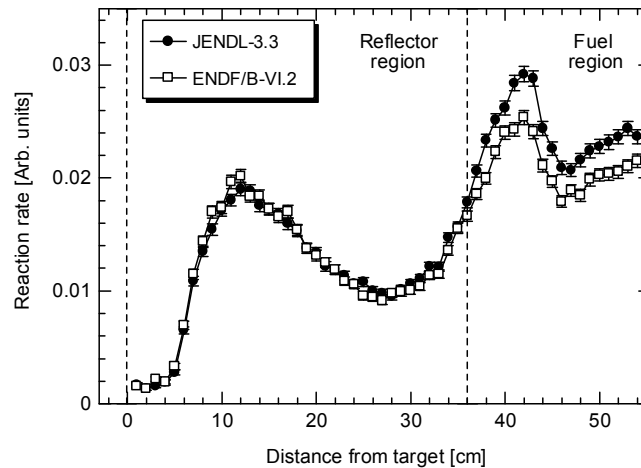


FIG. 7.38. Comparison of MCNP reaction-rate distribution in Case II-1 calculated using JENDL-3.3 and ENDF/B-VI.2, recorded vertically along matrix positions (16,17-J,W) [Japan Calculations] (Courtesy of the Nuclear Engineering Science Division, Research Reactor Institute, Kyoto University, Japan).

The computational results shown in Fig. 7.38 for Case II-1 provide a comparison between results obtained with different nuclear data libraries. The two libraries used were JENDL-3.3 and ENDF/B-VI.2. The differences between reaction rates calculated using different dosimetry files were negligible. The results shown in Fig. 7.38 are obtained with the same evaluated nuclear data library for both tally and transport: the ENDF/B-V dosimetry file for ENDF/B-VI.2 and JENDL-3.1 dosimetry file for JENDL-3.3. An increase of about 15% in the reaction rate in the fuel region was observed from the results obtained with JENDL-3.3 compared with those from ENDF/B-VI.2; however, the reaction-rate distribution within the reflector was little affected. This is consistent with the systematic underestimation of k_{eff} by ENDF/B-VI.2 when compared with the JENDL-3.3 results. Since the JENDL-3.3 library was considered more accurate for calculating the reaction-rate distribution, it has been adopted in obtaining the following calculated results to compare with the experimental results.

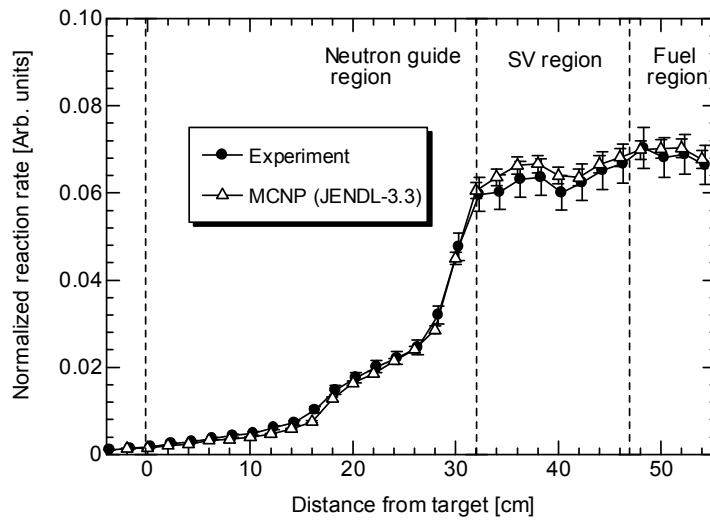


FIG. 7.39. Comparison of measured and calculated reaction-rate distribution of Case II-2 measured vertically along matrix positions (16,17-J,W) [Japan Calculations] (Courtesy of the Nuclear Engineering Science Division, Research Reactor Institute, Kyoto University, Japan).

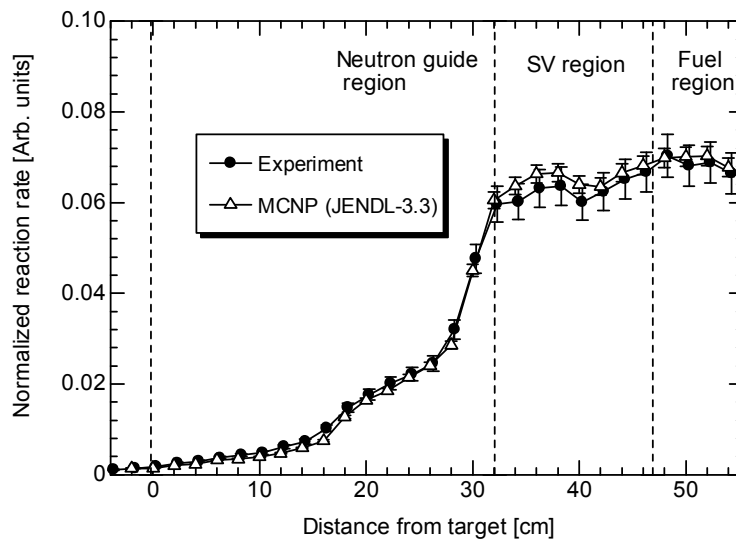


FIG. 7.40. Comparison of measured and calculated reaction-rate distribution in Case II-4 measured vertically along matrix positions (16,17-J,W) [Japan Calculations] (Courtesy of the Nuclear Engineering Science Division, Research Reactor Institute, Kyoto University, Japan).

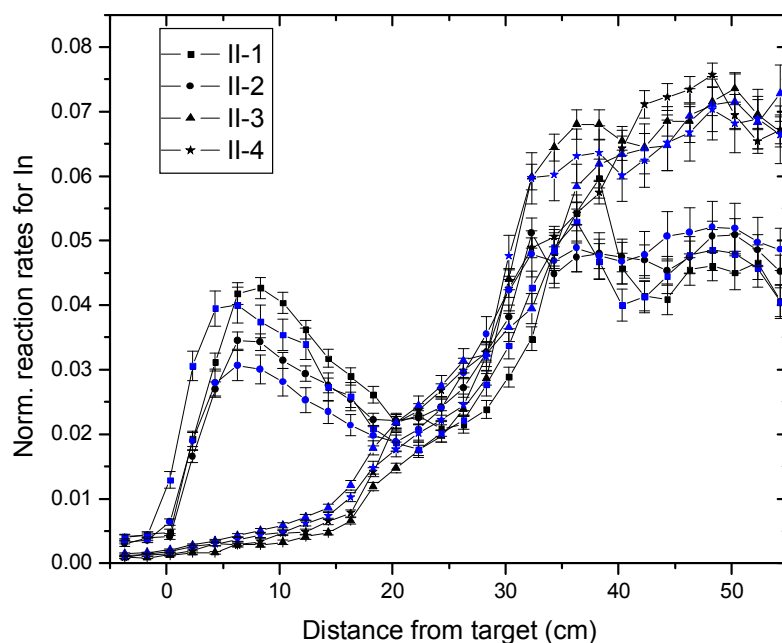


FIG. 7.41. Comparison of measured and calculated reaction-rate distributions in Cases II-1 through II-4 recorded vertically along matrix positions (16,17-J,W) [Pakistan Calculations] (Courtesy of the Nuclear Engineering Science Division, Research Reactor Institute, Kyoto University, Japan).

Figures 7.39–7.41 show the reaction-rate distributions obtained from calculations for the cores with and without the neutron guide in Cases II-2 and II-4, respectively. These analytical results are compared with the experimental results. The reaction rate distribution between the target and the fuel region were accurately predicted in these calculations. The relative increase in the neutron yield was estimated correctly. For the core without the neutron guide (neutron shield and beam duct; Fig. 7.39), the reaction rate is accurately predicted and the observed differences are within the Monte Carlo statistical errors. For the core with the neutron guide (Fig. 7.40), the relative increase in the neutron yield was reproduced well. Results for the various zones (near the target, the neutron guide, the active zone edge with or without the moderation peak, and the fuel region) were reproduced well.

7.7.1.3. Neutron Spectrum

For measuring the neutron spectrum, the activation foils (comprised of a collection of several samples) were positioned in the region of interest in front of the fuel region. The purpose of obtaining neutron-spectral information was to ascertain that the high-energy neutrons generated in the target are directed toward the fuel region. The measuring technique used at KUCA involves irradiating all the foils simultaneously. It is therefore denoted as a multi-foil activation method. The specific activation foils were selected to provide coverage of a wide range of reaction threshold energy values. Geometrically, they are 50 mm × 50 mm square and 3 to 5 mm thick. The ^{24}Mg and ^{127}I samples were made of MgO and NaI, respectively, both in powder form. The values obtained for the reaction rates were normalized to that of the In foil result from $^{115}\text{In}(n,n')^{115\text{m}}\text{In}$ reaction measurements at the attached target position. These reaction rates were obtained from the recorded counts of decay γ -rays emitted from the saturated radioactivity of the In samples. These measurements were performed using a high purity germanium (HPGe) detector. The experimental errors in the activation foil measurements were estimated to be 10 to 15%, including detection efficiency and statistical errors of γ -ray counts.

The experimental results at matrix position (15,P) with the neutron shield and the beam duct suggest an increase in the neutron flux by a factor of two to four, as shown in Table 7.31. An insufficient number of reactions resulted in a noticeable error of γ -ray emission results in the experimental measurements for ^{58}Ni and ^{60}Ni . Apparently, the effects of the neutron shield and the beam duct were also observed in the reaction rates obtained at matrix position (15,P) by other irradiated activation foils included in the multi-foil activation dosimetry procedure. This is evident from comparing the results of Case 3 with those of Case 1.

The neutron spectrum at matrix position (15,P) obtained from the SAND-II analysis demonstrates that the high-energy 14 MeV neutron flux at this position is about two times larger in Case 3 than in Case 1, as shown in Fig. 7.42. Therefore, the enhancement of the 14-MeV neutron flux is about a factor of two because of the neutron shield and the beam duct. This difference in the neutron flux for the cores with and without the neutron shield could also be observed from the unfolding analyses. However, a comparison of the experimental results from SAND-II and the calculated results from MCNP-4C3 demonstrates that the reliability of the unfolding analyses method is insufficient to enable a reliable determination of the spectrum to be made, as it is evident from Fig. 7.43. Therefore, this approach is not a viable technique to experimentally determine the neutron spectrum.

TABLE 7.32. MEASURED REACTION RATES IN CASES I-1 AND I-3, AS OBTAINED FROM IRRADIATED FOILS NORMALIZED TO IN FOIL REACTION THAT IS ATTACHED TO THE TARGET

Reaction	Threshold (MeV)	Target (Case I-1)	Irradiation position		
			Target (Case I-3)	(15, P) (Case I-1)	(15, P) (Case I-3)
$^{115}\text{In} (n,n') ^{115m}\text{In}$	0.32	1.00 ± 0.15	1.00 ± 0.19	0.96 ± 0.14	1.68 ± 0.29
$^{60}\text{Ni} (n,p) ^{60}\text{Co}$	2.08	5.31 ± 1.23	5.05 ± 0.35	0.73 ± 0.40	4.21 ± 2.51
$^{56}\text{Fe} (n,p) ^{56}\text{Mn}$	2.97	3.40 ± 0.28	3.66 ± 0.38	1.27 ± 0.11	2.51 ± 0.41
$^{27}\text{Al} (n,\alpha) ^{24}\text{Na}$	3.25	2.26 ± 0.36	2.58 ± 0.11	0.29 ± 0.02	0.69 ± 0.10
$^{24}\text{Mg} (n,p) ^{24}\text{Na}$	4.93	0.51 ± 0.07	0.51 ± 0.08	0.14 ± 0.01	0.25 ± 0.03
$^{127}\text{I} (n,2n) ^{126}\text{I}$	9.22	4.37 ± 0.18	5.25 ± 0.68	0.43 ± 0.08	1.59 ± 0.21
$^{58}\text{Ni} (n,2n) ^{57}\text{Ni}$	12.43	0.30 ± 0.31	0.31 ± 0.38	—	—

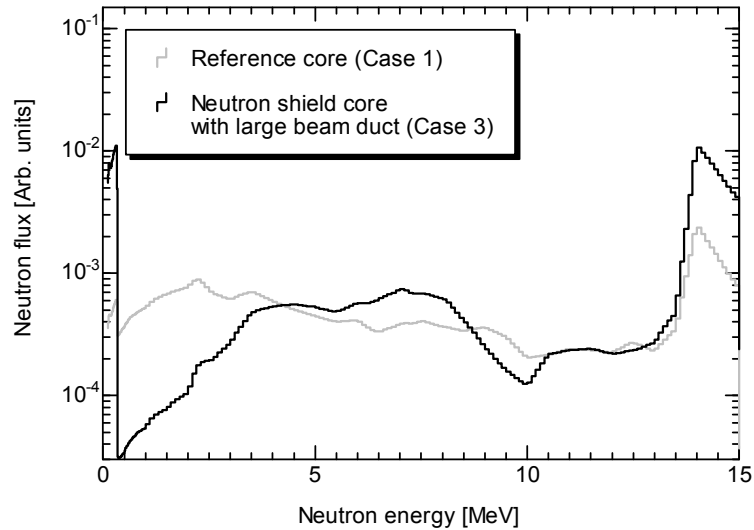


FIG. 7.42. Comparison of measured neutron spectra at matrix position (15,P) for Cases I-1 and I-3, as obtained from the SAND-II analyses [Japan Calculations] (Courtesy of the Nuclear Engineering Science Division, Research Reactor Institute, Kyoto University, Japan).

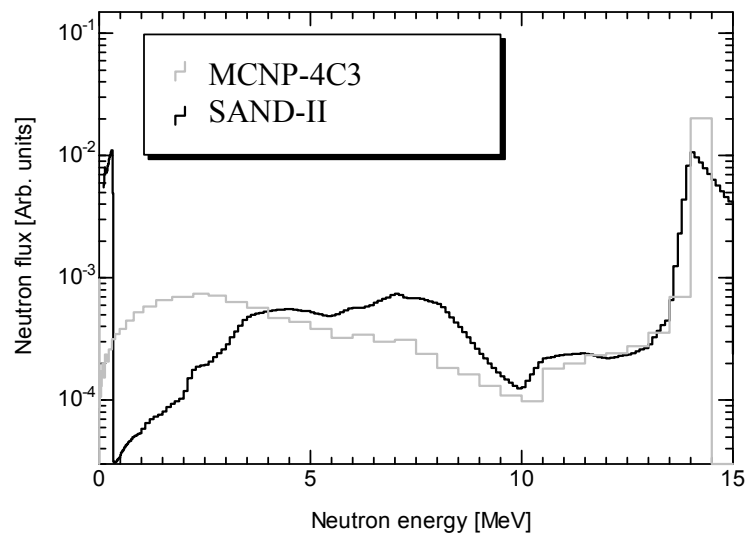


FIG. 7.43. Comparison of measured and calculated neutron spectra for Case I-3 at matrix position (15,P) [Japan Calculations] (Courtesy of the Nuclear Engineering Science Division, Research Reactor Institute, Kyoto University, Japan).

7.7.2. Kinetic Experiments

First, an adjustment of the fuel density was used for the calculations, which resulted in a correction factor of 5%. For cases with very small reactivity, the difference in the results appears to be within the computational precision. For consistency, the following results are obtained by applying this correction.

7.7.2.1. Subcriticality by the Pulsed-Neutron Method

A representative selection of the calculated subcriticality results is shown in Table 7.33 where the C/E values are given for each detector. An overall 10% relative error was observed from the comparison of the subcriticality values, although the agreement is better than that for

small subcriticality levels. In intercomparing the detectors, it is remarkable that Fibre #1 appeared to be little affected by the increase in the subcriticality level. The discrepancies in the obtained results were found to be within 7%, even for the largest subcriticality level. In contrast, the discrepancies for Fibres #2 and #3 amounted to up to about 30%. This tendency can be seen clearly in Fig. 7.44.

7.7.2.2. Prompt neutron Decay Constant

The results obtained in this investigation enabled some estimates to be obtained of the relative effects of the various parameters suspected to influence the subcriticality measurements by the pulsed-neutron technique, as well as enabling the prompt neutron decay constant to be determined. Data from Fibre #2 permitted an evaluation of the variation in the delayed-neutron fraction to be carried out as a function of the subcriticality level with the smallest level of uncertainty. The measurements from Fibre #2 (Fig. 7.44), although underestimating the subcriticality value (Fig. 7.45), tended to provide a relatively good determination of the prompt neutron decay constant compared with the results obtained from Fibre #3. However, Fibre #1 yielded an underestimation of the prompt neutron decay constant by less than 7%. Finally, Fibre #2 provided a good determination of the prompt neutron decay constant, taking into consideration the detector-position dependency of prompt neutron decay constant measurements.

TABLE 7.33. COMPARISONS OF MEASURED SUBCRITICALITY VALUES OBTAINED BY THE AREA-RATIO METHOD AND THE CALCULATED SUBCRITICALITY FROM MCNP CALCULATIONS USING JENDL-3.3 [JAPAN CALCULATIONS]

Case	Calculation (% $\Delta k/k$)	Fibre #1 (% $\Delta k/k$)	C/E	Fibre #2 (% $\Delta k/k$)	C/E	Fibre #3 (% $\Delta k/k$)	C/E
VI-1	0.97 ± 0.03	0.99 ± 0.01	0.98	0.96 ± 0.01	1.01	0.99 ± 0.01	1.03
VI-2	1.83 ± 0.03	1.88 ± 0.02	0.97	2.15 ± 0.02	0.85	1.78 ± 0.02	1.03
VI-3	2.55 ± 0.03	2.55 ± 0.03	1.00	3.12 ± 0.03	0.82	2.42 ± 0.02	1.05
VI-4	3.45 ± 0.03	3.40 ± 0.03	1.02	3.25 ± 0.03	1.06	3.63 ± 0.04	0.95
VI-5	4.15 ± 0.03	4.49 ± 0.04	0.93	4.00 ± 0.04	1.04	4.60 ± 0.05	0.90
VI-6	6.24 ± 0.03	5.89 ± 0.06	1.06	6.54 ± 0.07	0.95	6.87 ± 0.07	0.91
VI-7	6.76 ± 0.03	6.59 ± 0.07	1.03	10.01 ± 0.10	0.67	7.56 ± 0.08	0.89
VI-8	7.41 ± 0.03	7.55 ± 0.08	0.98	8.18 ± 0.08	0.91	8.64 ± 0.09	0.86
VI-9	10.38 ± 0.03	10.24 ± 0.10	1.01	12.28 ± 0.12	0.85	11.93 ± 0.12	0.87

TABLE 7.34. COMPARISONS OF C/E VALUES FOR THE MEASURED AND CALCULATED NEUTRON-DECAY CONSTANTS [JAPAN CALCULATIONS]

Case	Fibre #1	Fibre #2	Fibre #3
VI-1	1.02 ± 0.02	1.12 ± 0.03	1.07 ± 0.02
VI-2	1.16 ± 0.02	1.11 ± 0.03	1.18 ± 0.03
VI-3	1.05 ± 0.02	1.07 ± 0.03	1.09 ± 0.02
VI-4	1.04 ± 0.03	1.07 ± 0.04	1.12 ± 0.04
VI-5	1.07 ± 0.03	1.04 ± 0.04	1.14 ± 0.04
VI-6	1.16 ± 0.03	1.18 ± 0.05	1.21 ± 0.04
VI-7	1.11 ± 0.04	1.03 ± 0.05	1.06 ± 0.04
VI-8	0.88 ± 0.03	0.96 ± 0.05	0.83 ± 0.03
VI-9	1.13 ± 0.03	1.06 ± 0.03	1.12 ± 0.03

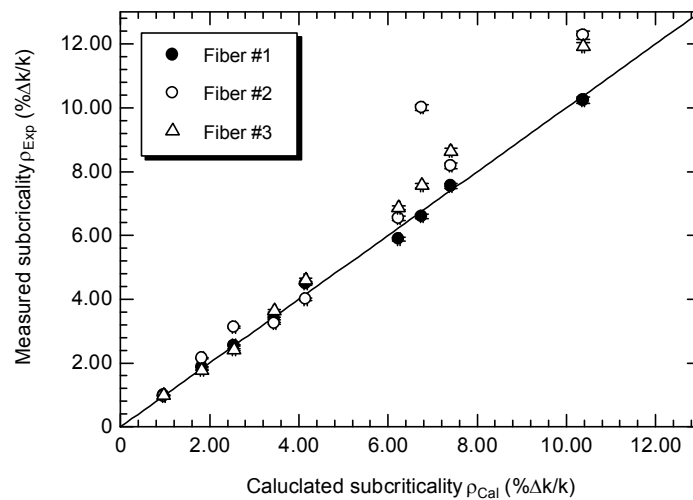


FIG. 7.44. Measured and calculated subcriticality results in the KUCA kinetic experiments [Japan Analyses] (Courtesy of the Nuclear Engineering Science Division, Research Reactor Institute, Kyoto University, Japan).

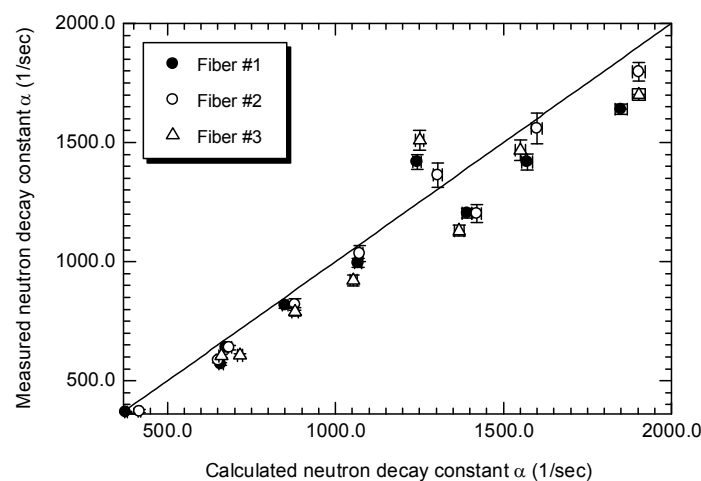


FIG. 7.45. Measured and calculated results for the neutron-decay constants in the KUCA kinetic experiments [Japan Analyses] (Courtesy of the Nuclear Engineering Science Division, Research Reactor Institute, Kyoto University, Japan).

7.8. CONCLUSIONS

A series of experiments of the performance of an ADS at the KUCA facility that is driven by 14 MeV neutrons was carried out using the foil activation method. The performed analyses that were carried out using Monte Carlo calculation codes led to the following conclusions:

- Eigenvalue calculations can be carried out to determine the reactivity of an ADS facility driven by 14-MeV neutrons. The use of MCNP-4C3 with ENDF/B-VI.2 and MCNP-5 with ENDF/V-II achieve similar results, with a differences observed of about 5%, including in the determination of the subcriticality values. The only exception has to do with small reactivity analyses. The measured reaction-rate distributions for a subcritical system can be predicted quite well using fixed-source calculations with the same combinations of the Monte Carlo code versions and nuclear data libraries;
- The effects of the neutron shield and the beam duct on the high-energy neutron flux can be confirmed reliably through measurements of reaction-rate distributions. The measured data were obtained from neutron irradiations of an In wire and activation foils. These effects can then be examined through spectrum unfolding procedures using the SAND-II code, with the JENDL Activation Cross-section File 96 and by results obtained from MCNP-4C3 Monte Carlo calculations;
- The foil activation method was demonstrated to be a useful measuring technique for examining the neutronic properties of an ADS facility driven by 14-MeV neutrons.
- SV assemblies that include a neutron guide proved experimentally to be effective in improving external-neutron-source multiplication in the core. The effect of the neutron guide (neutron shield and beam duct) on the thermal-neutron flux distribution in the KUCA core emphasized the importance of the window size and the reflector assemblies near the fuel rod positions;
- Measurement and calculation methods have proven to be reliable for the evaluation of subcriticality effects down to 6% $\Delta k/k$. Since it is anticipated that an ADS subcriticality level around 3% $\Delta k/k$ would normally be employed, the present measurement methodology and the calculation precision were considered acceptable for the ADS studies at KUCA;
- When the JENDL-3.3 nuclear library is used, the calculated reaction rates agree with experimental results within the experimental errors. However, the reaction rate results obtained from the use of ENDF/B-VI.2 differ significantly from the JENDL-3.3 results.
- Optical-fibre detectors are promising tools for investigating the subcriticality level and the prompt neutron decay constant at KUCA. A detector-position dependency was observed in kinetic measurements when the optical-fibre detection system was employed.

It should be noted that the research described in this Section was undertaken in part as an initial step toward embarking on a longer-term effort in the ADS field at KURRI. This long-term programme has been designated as the Kumatori Accelerator Driven Reactor Test Facility & Innovation Research Laboratory Project (Kart & Lab). It would entail using a new accelerator for generating high-energy neutrons by the bombardment of a heavy-metal (tungsten) target with 150 MeV protons. This neutron source would form the driver of an ADS facility that also includes KUCA. The new accelerator would be of the synchrotron type and would be called the Fixed Field Alternating Gradient (FFAG) accelerator. It is being developed by the High Energy Accelerator Research Organization (KEK) in Japan. Details of recent ADS studies at the KURRI laboratory under the auspices of this programme, and the

progress reports associated with the present research collaboration under the auspices of the IAEA, can be found in Refs [7.1–7.15].

REFERENCES TO SECTION 7

- [7.1] SHIROYA, S., UNESAKI, H., KAWASE, Y., MORIYAMA, H., INOUE, M., “Accelerator Driven Sub-critical System as A Future Neutron Source in Kyoto University Research Reactor Institute (KURRI) – Basic Study on Neutron Multiplication in the Accelerator Driven Sub-critical Reactor”, *Prog. Nucl. Energy* **37**, (2000) 357.
- [7.2] SHIROYA, S., UNESAKI, H., MISAWA, T., “Accelerator-Driven Sub-critical Reactors in Japanese Universities: Experimental Study Using the Kyoto University Critical Assembly”, *Trans. Am. Nucl. Soc., American Nuclear Society, Annual Mtg., Milwaukee, Wisconsin, June 17-21, (2000)* 78-79.
- [7.3] SHIROYA, S., et al., “Experimental Study on Accelerator Driven Sub-critical Reactor Using the Kyoto University Critical Assembly (KUCA)”, *Proc. Int. Conf. on New Frontiers of Nucl. Technol.: Reactor Physics, Safety and High-Performance Computing (PHYSOR 2002)*, American Nuclear Society, Seoul, Korea, Oct. 7-10, **7C-01**, (2002).
- [7.4] SHIROYA, S., YAMAMOTO, A., SHIN, K., IKEDA, T., NAKANO, S., UNESAKI, H., “Basic Study on Accelerator Driven Sub-critical Reactor in Kyoto University Research Reactor Institute (KURRI)”, *Prog. Nucl. Energy* **40**, (2002) 489.
- [7.5] PYEON, C.H., HIRANO, Y., MISAWA, T., UNESAKI, H., SHIROYA, S., “Preliminary Study on ADSR by using FFAG Accelerator in KUCA,” *Proc. Embedded Topical Mtg. Global 2003*, New Orleans, Louisiana, Nov. 16-20, American Nuclear Society, 2193-2200, (2003) CD-ROM.
- [7.6] TAGEI, H., IWASAKI, T., MISAWA, T., PYEON, C.H., “Activation Experiment at KUCA for Establishing an Experimental Facility of Accelerator Driven Sub-critical Reactor”, *Proc. Int. Conf. on Nucl. Data for Sci. & Technol. – ND2004*, Santa Fe, New Mexico, Sep. 26-Oct. 1, American Nuclear Society, (2004) CD-ROM.
- [7.7] PYEON, C.H., MISAWA, T., UNESAKI, H., SHIROYA, S., TAGEI, H., WADA, K., IWASAKI, T., “Experimental Analyses for Accelerator Driven Sub-critical Reactor in Kyoto University Critical Assembly by using Foil Activation Method”, *Proc. Int. Topical Mtg. on Mathematics and Computation, Supercomputing, Reactor Physics and Nucl. Biological Applications (M&C2005)*, Avignon, France, Sep. 12-15, American Nuclear Society, (2005) CD-ROM.
- [7.8] HERVAULT, M., PYEON, C.H., MISAWA, T., UNESAKI, H., SHIROYA, S., “Monte Carlo Analysis of Sub-criticality for Accelerator Driven Sub-critical Reactor Mock Up in Kyoto University Critical Assembly”, *Proc. Int. Topl. Mtg. on Mathematics and Computation, Supercomputing, Reactor Physics and Nucl. Biological Applications (M&C2005)*, Avignon, France, Sep. 12-15, American Nuclear Society, (2005) CD-ROM.
- [7.9] PYEON, C.H., PYEON, C.H., MISAWA, T., UNESAKI, H., SHIROYA, S., “Present Status of Accelerator Driven Sub-critical Reactor in Kyoto University Critical Assembly”, *Proc. Int. Topl. Mtg. on Advances in Nucl. Analysis and Simulation (PHYSOR2006)*, Vancouver, Canada, Sep. 10-14, American Nuclear Society, (2006) CD-ROM.
- [7.10] SHIGA, H., HERVAULT, M., PYEON, C.H., MISAWA, T., SHIROYA, S., “Neutron Spectrum Analyses by using Foil Activation Method at Accelerator Driven Sub-critical Reactor in Kyoto University Critical Assembly”, *Proc. 2nd COE-INES Int. Sympo. (INES-2)*, Yokohama, Japan, Nov. 28-30, (2006) CD-ROM.

- [7.11] HERVAULT, M., KITADA, T., UNESAKI, H., PYEON, C.H., MISAWA, T., SHIROYA, S., “Experiments for Accelerator Driven Sub-critical Reactor with Optical Fiber Detectors and Pulsed Neutron Generator in Kyoto University Critical Assembly”, Proc. First Int. Conf. Physics & Technol. of Reactors & Applications (PHYTRA-1), Caracas, Saidia, Morocco, Mar. 14-16, (2007) CD-ROM.
- [7.12] PYEON, C.H., MISAWA, T., UNESAKI, H., SHIROYA, S., “Benchmark Experiments of Accelerator Driven Systems (ADS) in Kyoto University Critical Assembly (KUCA)”, Proc. Fifth Int. Workshop on the Utilization and Reliability of High Power Proton Accelerators (HPPA5), May 6-9, Mol, Belgium, OECD/NEA, (2007) CD-ROM.
- [7.13] PYEON, C.H., MISAWA, T., UNESAKI, H., ICHIHARA, C., MISHIMA, K., “Research on Accelerator Driven Sub-critical Reactor at Kyoto University Critical Assembly (KUCA)”, Proc. Eighth Int. Topl. Mtg. on Nucl. Applications and Utilization of Accelerators (AccApp’07), Jul. 30 - Aug. 2, Pocatello, Idaho, USA. American Nuclear Society, (2007) CD-ROM.
- [7.14] PYEON, C.H., HIRANO, Y., MISAWA, T., UNESAKI, H., ICHIHARA, C., IWASAKI, T., SHIROYA, S., “Preliminary Experiments on Accelerator Driven Sub-critical Reactor with Pulsed Neutron Generator in Kyoto University Critical Assembly”, J. Nucl. Sci. Technol. **44**, (2007) 1368.
- [7.15] PYEON, C.H., HERVAULT, M., MISAWA, T., UNESAKI, H., IWASAKI, T., SHIROYA, S., “Static and Kinetic Experiments on Accelerator Driven Sub-critical Reactor with 14 MeV Neutrons in Kyoto University Critical Assembly”, J. Nucl. Sci. Technol. **45**, (2008) 1171.

8. ACCELERATOR DRIVEN SUBCRITICAL RESEARCH FACILITY H5B-C BENCHMARK⁶

Contributed by

M. Pesic, P. Belicev, I. Avramovic
*Vinca Institute of Nuclear Sciences (Vinca), Belgrade,
Serbia*

J.R. Maiorino, C.R. Rossi
*Instituto de Pesquisas Energeticas e Nucleares (IPEN), Sao Paulo,
Brazil*

8.1. INTRODUCTION

The H5B benchmark is a concept for an accelerator driven subcritical research facility (ADSRF) that has been developed at the Vinča Institute of Nuclear Sciences, Belgrade, Republic of Serbia. The objective has been to gain an understanding of the physics and technologies necessary to design and construct an ADS reactor that could be used for the development of nuclear techniques and technologies, and for basic and applied research in neutron physics, metrology, radiation protection, and radiobiology using low enriched uranium fuel.

The approach taken has been to consider extracting a beam of medium-energy protons or deuterons from the TESLA Accelerator Installation (TAI), and to transport and inject this beam into a target situated inside a subcritical core. The neutron source is comprised of a lead target bombarded by proton or deuteron beams extracted from TAI. The proton or deuteron beams are introduced into the core through a stainless steel vacuum assembly that penetrates the tank top and extends down into its centre. Neutron yields and neutron energy spectra from several target materials, using proton or deuteron beams, have been investigated. For the purpose of neutron source simulations, a simplified beam model has been proposed in which cylindrical symmetry and a continuous time structure of the beam have been assumed.

The total neutron flux emerging from the target and the neutron yields from various target materials were calculated. Neutron group spectra were used to specify the neutrons leaving the target volume for performing numerical simulations of the neutron flux in the subcritical core which is comprised of LEU fuel elements of type TVR-S. The neutron effective multiplication factor k_{eff} and the prompt neutron generation time l_p were calculated using Monte Carlo simulations. Neutron spectra are calculated for the H5B ADSRF for proton and deuteron beams, with a uranium target for the selected subcritical core.

The conceptual design of the accelerator driven subcritical research facility, the H5B ADSRF system, is intended to use low enriched uranium (LEU) fuel of Russian origin. This fuel consists of uranium dioxide (enriched to 19.7% in ²³⁵U) dispersed in aluminium and placed in a lead matrix. The neutron source is generated by the interaction of proton or deuteron beams that are extracted from the TAI at the high energy channel that is denoted by H5B [8.1]. The neutron-producing target is placed inside the subcritical core. The main parameters and specifications of the benchmark calculations of the H5B system are documented in Ref. [8.2]. This study compares the computational results obtained by the Vinča Institute (Vinča), Serbia and IPEN, Brazil. Simulations of proton and deuteron beam

⁶ This section is based on Ref. [8.1]

transport through the target were carried out using the MCNPX Monte Carlo code (versions 2.4.0 and 2.5.0) [8.3], with cross-section data either from the LA150 nuclear data library or analytical representations. Neutrons emerging from the target are obtained. These numerical neutron source data were used for the numerical simulations of neutron flux of the subcritical core. The MCNP5 code [8.4], combined with the LA150 nuclear data library, was used for the criticality calculations of the H5B ADSRF subcritical core.

8.2. SIMULATION OF THE CHARGED PARTICLES INTERACTION WITH THE TARGET MATERIALS

Simulations of proton and deuteron transport through the target materials were carried out for calculating the yield and the spectra of the generated neutrons. The calculations used the MCNPX code (versions 2.4.0 or 2.5.0) and LA150 or ENDL92 data libraries for most of the cases. MCNPX with the Bertini/Dresner or Isabel model was used for the interactions of the charged particles with the target materials when the nuclear data libraries were insufficient.

A simplified beam model was used for the neutron source simulations of this benchmark. Cylindrical symmetry and a continuous time structure of the beam were assumed [8.2]. The beam impact at the target base is assumed to occur along the central axis of the cylindrical target assembly, as shown in Fig. 8.1. The impact area around the axis at the cylinder base is assumed to be equal to the beam profile area (defined by a beam diameter). For this model, no beam window is included at the impact surface between the beam and the target. The charged particles within the beam are uniformly distributed over the beam cross-section area, and these charged particles move parallel to the beam direction. The assumed beam parameters are given in Table 8.1. Variations of the basic beam energy E_0 are assumed to be randomly distributed around E_0 within $\pm 1\%$ in the Vinča calculations. These beam parameters were used for studying the neutron production (yields and spectra) from the beam interaction with the target material. The neutron yield results were normalized per incident charged particle. An idealized cylindrical target of different materials in a vacuum, without neutron reflection from the surrounding materials, is assumed to model the interaction with the charged particle beam.

TABLE 8.1. CHARGED PARTICLES BEAM PARAMETERS

Particle beam	E_0 [MeV]	I_{max} [μ A]	No. of Particles [s^{-1}]
proton (p)	73	5	3.12×10^{13}
deuteron (d)	67	50	3.12×10^{14}

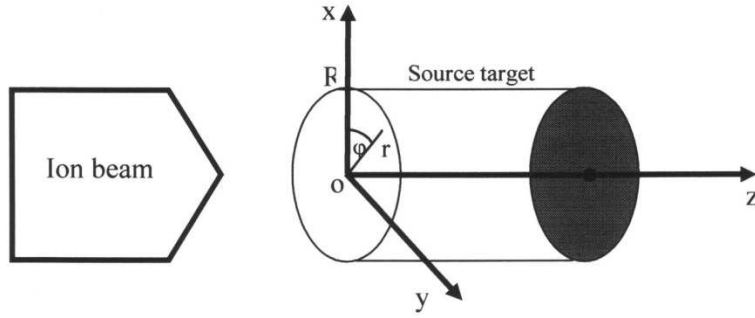


FIG. 8.1. Simplified geometry of the neutron source for the simulation analyses (Reproduced from Ref. [8.1] with permission courtesy of the Vinca Institute of Nuclear Sciences, Belgrade, Serbia).

Target material densities and specifications are given in Ref. [8.2]. The Vinča MCNPX results sampled 10^6 or 10^7 source particles with charged particle energy in the range of $0.99 E_0$ to $1.01 E_0$. The IPEN MCNPX results were obtained with E_0 charged particle energy, and sampled 10^6 source particles. Neutron flux densities escaping the target surfaces are presented in 63 energy groups. Energy group boundaries are given in Ref. [8.2].

The reported neutron yields are the total numbers of neutrons produced per incident source particle obtained from the MCNPX summary table. The neutron yield results of Table 8.2 were obtained from simulating 10^6 source particles, while the results of Table 8.3 were obtained from sampling 10^7 source particles. The reported neutron production results are the numbers of neutrons leaving the target, per incident charged particle, obtained with the F2 tally. The highest neutron yield values were obtained from the uranium target for the proton beam and from the beryllium target with the deuteron beam. Table 8.2 compares the neutron yields from different materials for proton and deuteron beams. The use of different nuclear libraries has a small impact on the neutron yield, as shown in Table 8.3. The statistical errors in the calculated results shown in Tables 8.2 and 8.3 correspond to one standard deviation. The difference between the yield results shown in Tables 8.2 and 8.3 are attributed to the use of different MCNPX models, cross-section libraries, and numbers of the simulated charged particles.

The neutron spectra Ψ_g , escaping the uranium target surfaces are shown in Fig 8.2 and 8.3 for deuteron and proton beams, respectively. The plotted neutron spectra are normalized to unity according to Equation (8.1):

$$\int_{E_{min}}^{E_{max}} \Psi_g(E) dE = \sum_{g=1}^{g=G_{max}} \Psi_g(E) \times \Delta E_g = 1 \quad (8.1)$$

The peak yield values for the neutron spectra $\Psi_g(E)$ were obtained for the uranium target for both beams. Energy boundaries of deuterons and protons escaping the target surfaces are the same as the neutron group structure. No deuterons escape the target when it is bombarded with a proton beam, as shown in Fig. 8.3.

Neutron spectra escaping different targets from the Vinča analyses with 10^7 charged particles are shown in Fig 8.4 and 8.5. The corresponding results from IPEN analyses with 1 million charged particles are shown in Fig 8.6 and 8.7. The results of Fig 8.2–8.7 are obtained with the F2 tally of MCNPX per incident charged particle and the normalization factor of the uranium target results as explained above. The differences between Vinča and IPEN results are attributed to different MCNPX codes, cross-section libraries, and numbers of charged particles per simulation.

The neutron spectra obtained by Vinča and IPEN are compared in Fig 8.8–8.15 for different targets with deuteron and proton charged particles. These spectra were obtained by

the F2 Tally of MCNPX, and are normalized per lethargy units. The normalization is done in two steps. First the neutron spectrum is normalized to unity then each neutron group is divided by $\ln(E_{(g+1)}/E_g)$.

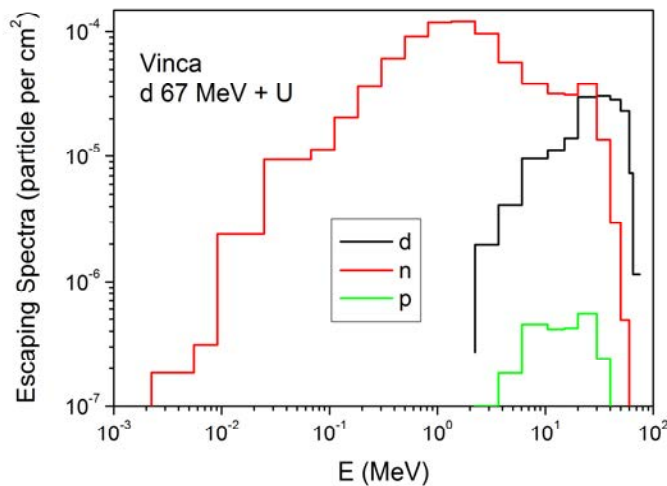


FIG. 8.2. Vinča particles spectra escaping a uranium target bombarded with a deuteron beam (Courtesy of the Vinča Institute of Nuclear Sciences, Belgrade, Serbia).

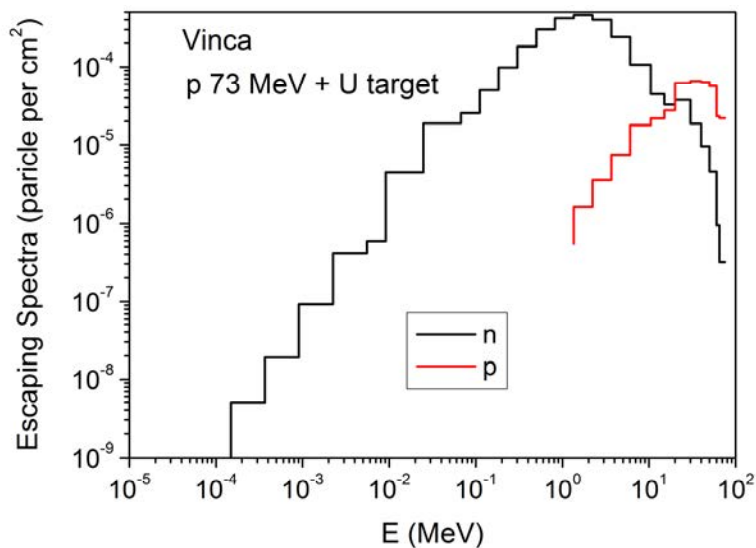


FIG. 8.3. Vinča particles spectra escaping a uranium target bombarded with a proton beam (Courtesy of the Vinča Institute of Nuclear Sciences, Belgrade, Serbia).

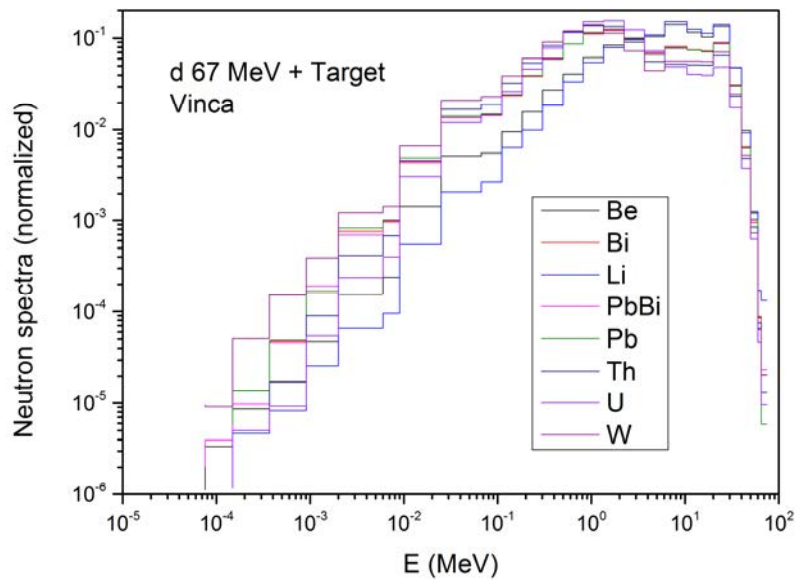


FIG. 8.4. Vinča neutron spectra escaping different target materials bombarded with a deuteron beam (Courtesy of the Vinča Institute of Nuclear Sciences, Belgrade, Serbia).

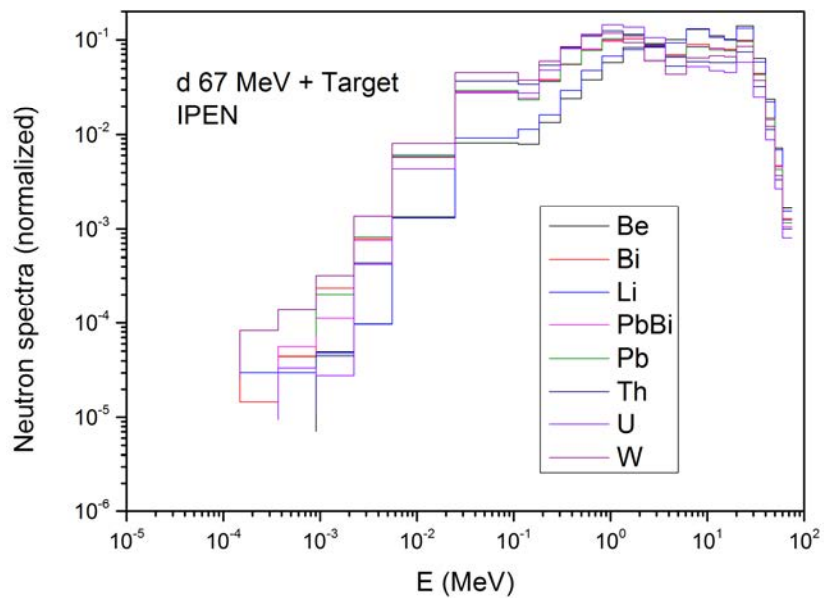


FIG. 8.5. Vinča neutron spectra escaping different target materials bombarded with a proton beam (Courtesy of the Vinča Institute of Nuclear Sciences, Belgrade, Serbia).

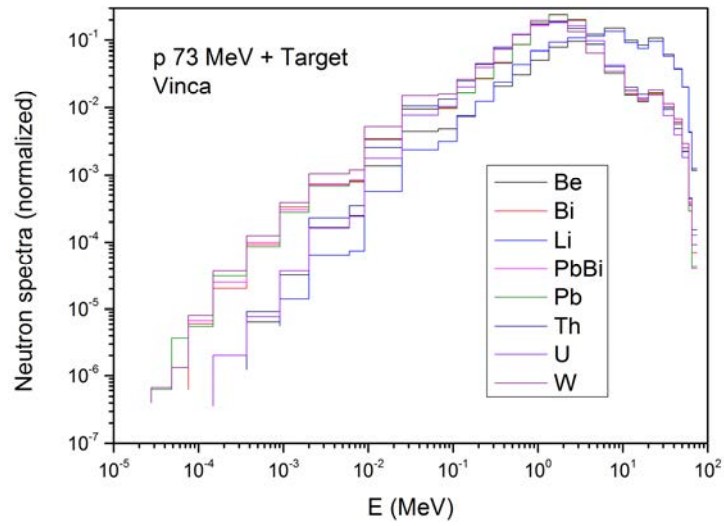


FIG. 8.6. IPEN neutron spectra escaping different target materials bombarded with a deuteron beam (Courtesy of the Vinca Institute of Nuclear Sciences, Belgrade, Serbia).

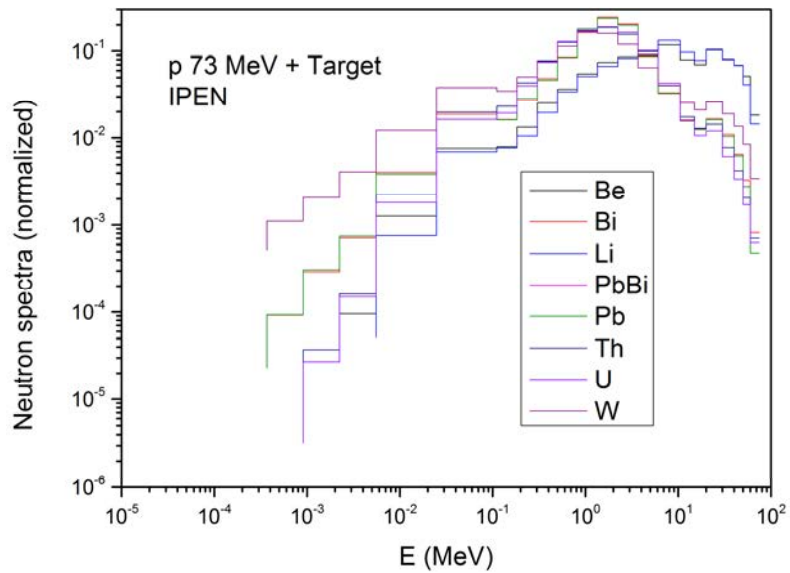


FIG. 8.7. IPEN neutron spectra escaping different target materials bombarded with a proton beam (Courtesy of the Vinca Institute of Nuclear Sciences, Belgrade, Serbia).

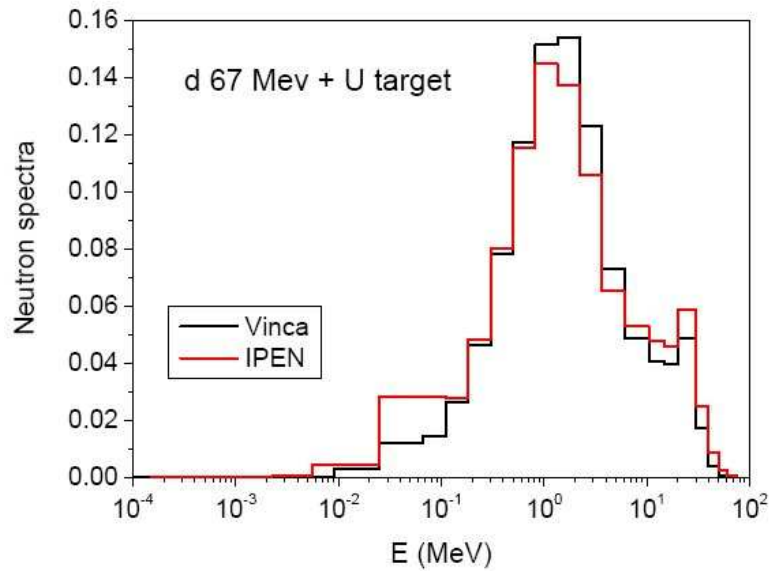


FIG. 8.8. Neutron spectrum escaping a uranium target bombarded with a deuteron beam (Courtesy of the Vinca Institute of Nuclear Sciences, Belgrade, Serbia).

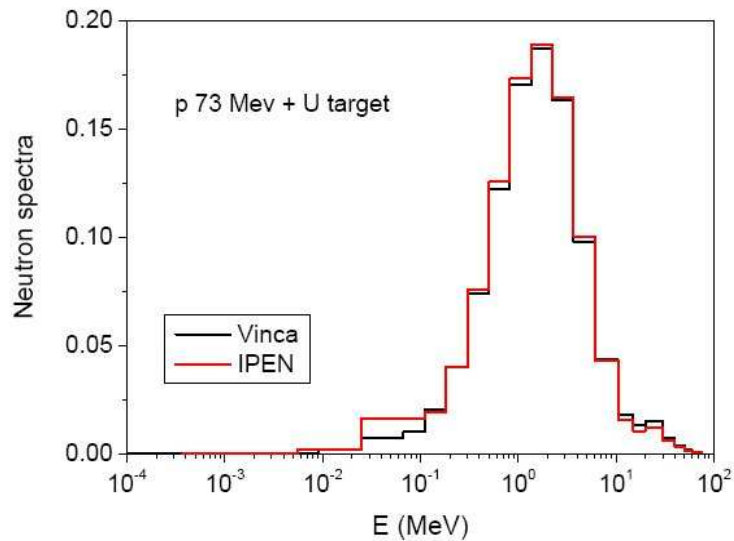


FIG. 8.9. Neutron spectrum escaping a uranium target bombarded with a proton beam (Courtesy of the Vinca Institute of Nuclear Sciences, Belgrade, Serbia).

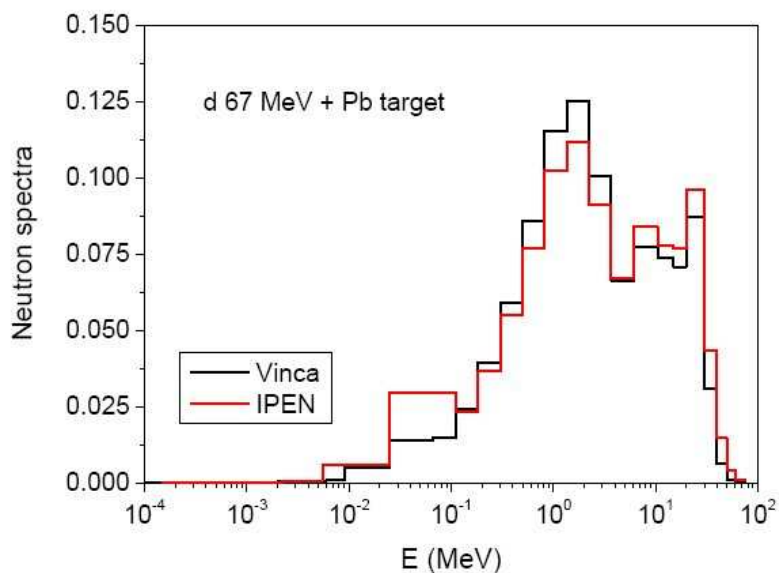


FIG. 8.10. Neutron spectrum escaping a lead target bombarded with a deuteron beam (Courtesy of the Vinca Institute of Nuclear Sciences, Belgrade, Serbia).

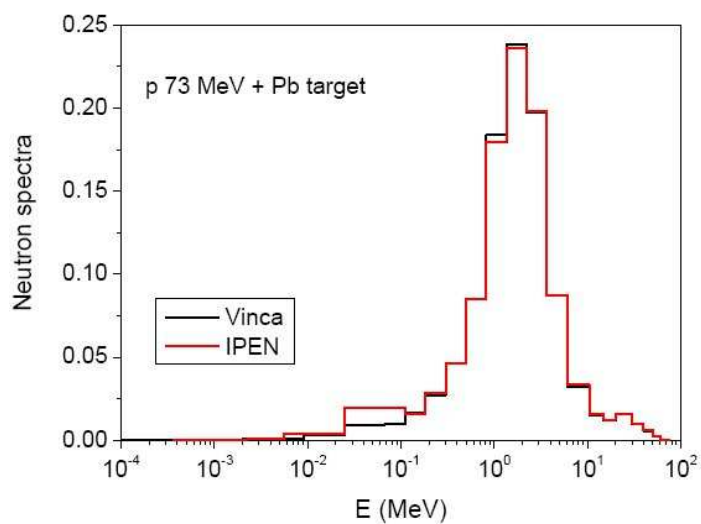


FIG. 8.11. Neutron spectrum escaping a lead target bombarded with a proton beam (Courtesy of the Vinca Institute of Nuclear Sciences, Belgrade, Serbia).

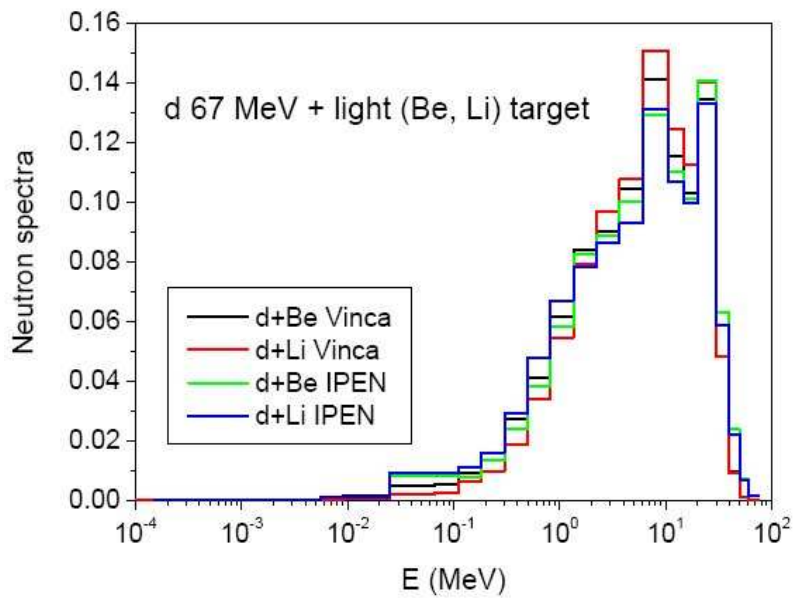


FIG. 8.12. Neutron spectra escaping beryllium and lithium targets bombarded with a deuteron beam (Courtesy of the Vinca Institute of Nuclear Sciences, Belgrade, Serbia).

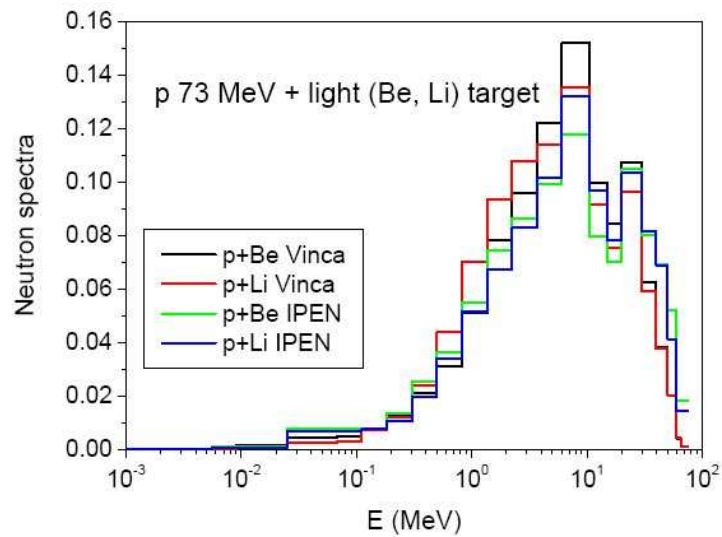


FIG. 8.13. Neutron spectra escaping beryllium and lithium targets bombarded with a proton beam (Courtesy of the Vinca Institute of Nuclear Sciences, Belgrade, Serbia).

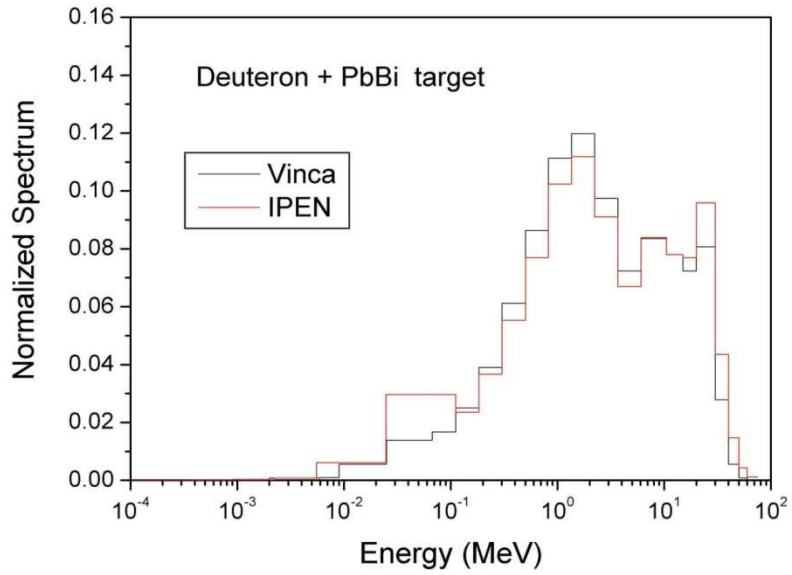


FIG. 8.14. Neutron spectrum escaping a Pb-Bi target bombarded with a deuteron beam (Courtesy of the Vinca Institute of Nuclear Sciences, Belgrade, Serbia).

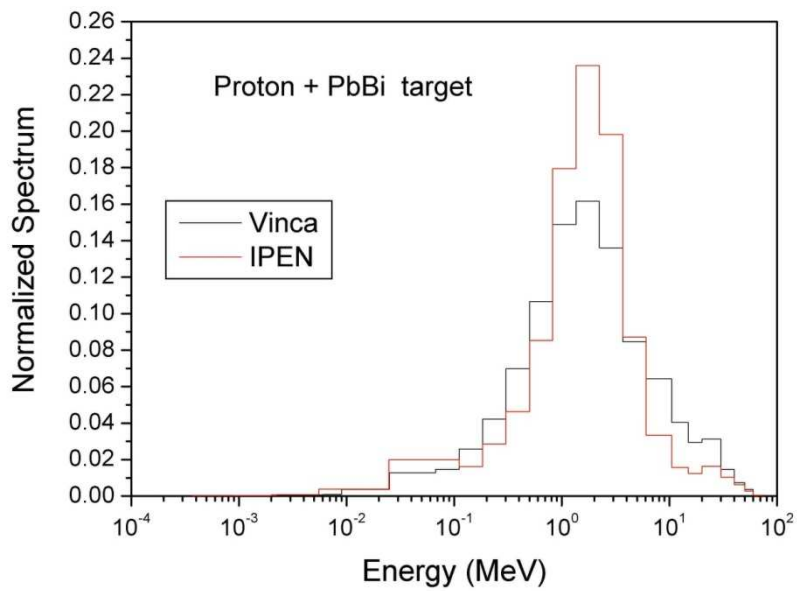


FIG. 8.15. Neutron spectrum escaping a Pb-Bi target bombarded with a proton beam (Courtesy of the Vinca Institute of Nuclear Sciences, Belgrade, Serbia).

TABLE 8.2. NEUTRON YIELDS FROM DIFFERENT TARGET MATERIALS BOMBARDED WITH PROTON AND DEUTERON BEAMS

Target material	Neutron yield per incident charged particle			
	Proton 73 MeV		Deuteron 67 MeV	
Laboratory	Vinca	IPEN	Vinca	IPEN
Computer Program	MCNPX2.4.0	MCNPX2.5.0	MCNPX2.4.0	MCNPX2.5.0
Nuclear Data	LA150	ENDF/B-VI	LA150	ENDF/B-VI
Library	Isabel	Bertini/Dresner	Isabel	Isabel/Dresner
MCNPX Model				
Lead, Pb	14.54	17.22	5.23	6.96
Uranium, U	27.33	30.89	8.83	10.51
Thorium, Th	22.97	26.72	7.08	8.80
Bismuth, Bi	15.45	16.33	4.95	6.79
Lithium, Li	12.72	16.56	8.43	7.80
Beryllium, Be	13.18	14.17	10.09	5.17
Tungsten, W	17.01	16.97	6.14	7.59
Pb-Bi alloy	15.51	17.26	5.20	7.13

TABLE 8.3. NEUTRON YIELD FROM DIFFERENT TARGET MATERIALS

(a) bombarded with deuteron beams (67 MeV deuteron energy, MCNPX-2.50,10,000,000 deuterons, ISABEL model)

Target Material	Nuclear Data Library	Neutron Yield	Neutron Production
Be	ENDF/B-VI.6	9.605 ± 0.044	10.16
Be	ENDF/B-VI.8	9.605 ± 0.044	10.16
Be	LA150	9.400 ± 0.043	10.09
Bi	LA150	5.015 ± 0.040	4.95
Li	ENDF/B-VI.6	8.598 ± 0.038	8.59
Li	ENDL92	8.501 ± 0.039	8.43
PbBi	LA150	5.266 ± 0.041	5.21
Pb	LA150	5.212 ± 0.041	5.16
Th	LA150	7.173 ± 0.060	7.10
U	LA150	8.824 ± 0.075	8.83
W	LA150	6.041 ± 0.047	6.10

(b) bombarded with a proton beam (73 MeV proton energy, MCNPX-2.50, 10,000,000 deuterons, ISABEL model)

Target material	Nuclear Data Library	Neutron Yield	Neutron Production
Be	LA150	12.486 ± 0.011	13.18
Bi	LA150	16.086 ± 0.081	15.49
Li	ENDL92	13.410 ± 0.044	12.67
PbBi	LA150	16.959 ± 0.008	16.34
Pb	LA150	16.990 ± 0.008	16.39
Th	LA150	23.757 ± 0.128	23.05
U	LA150	27.842 ± 0.147	27.44
W	LA150	15.757 ± 0.008	15.38

The neutron spectra peaks in the energy range of 0.2 MeV to 4 MeV for all the targets, except for the low Z targets (beryllium and lithium), for both charged particles. The corresponding peaks for the low Z targets are in the energy range of 1 MeV to 10 MeV. The neutron-spectrum yields below 1 keV are negligible, and no thermal neutrons were observed in the analyses. This is a consequence of the geometrical model simplifications used in the analyses.

8.3. SIMULATION OF THE NEUTRON FLUX IN THE SUBCRITICAL CORE

Vinča utilized MCNP5 for H5B ADSRF criticality calculations, in combination with the LA150 nuclear data library, for most of the nuclides. ENDL92 was used for the nuclides unavailable in the LA150 [8.4]. The LWTR.60 nuclear data library was used in the thermal scattering analyses for the water coolant/moderator. The ENDF-B/VI.8 nuclear data library was used for a few nuclides, mainly the impurities. IPEN used MCNPX2.5.0 with the ENDF/B-VI and LA150 cross-section libraries for performing their analyses.

The fuel elements in the H5B ADSRF design are of the TVR-S type, which were fabricated in the Russian Federation. Figure 8.16 shows the configuration of this fuel design and Fig 8.17–8.18 show the core model and the fuel loading pattern.

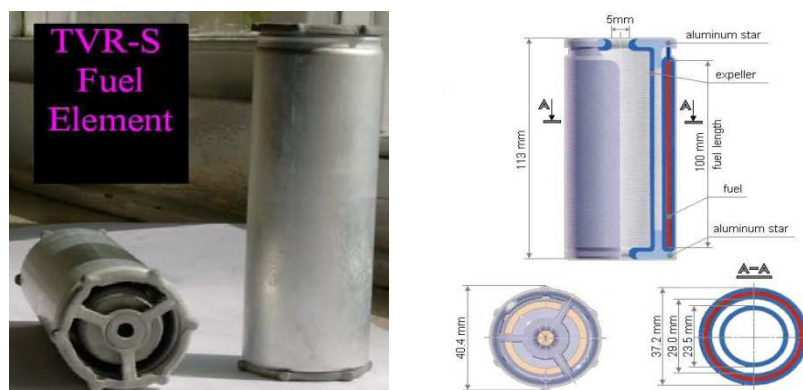


FIG. 8.16. Photograph and cross-sections of the TVR-S fuel element (Courtesy of the Vinca Institute of Nuclear Sciences, Belgrade, Serbia).

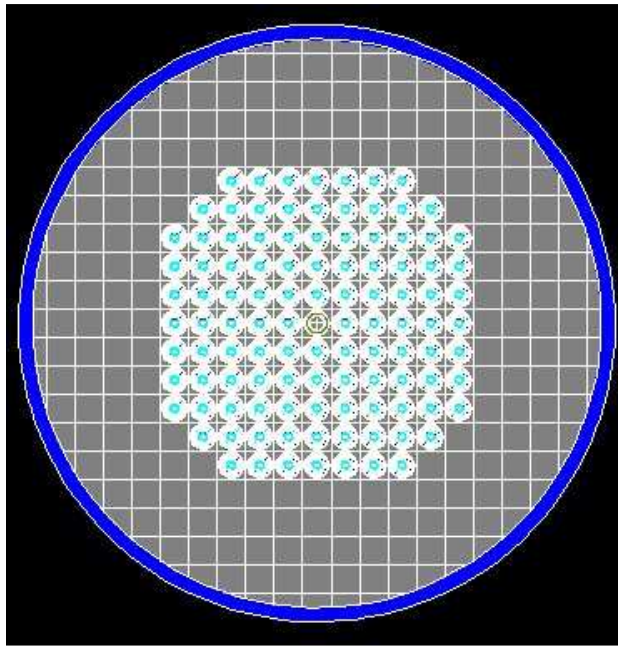


FIG. 8.17. Horizontal cross-section of the LEU H5B core model at the target level (H_2O within the fuel assembly light blue, Pb grey, SS-304 dark blue) (Courtesy of the Vinca Institute of Nuclear Sciences, Belgrade, Serbia).

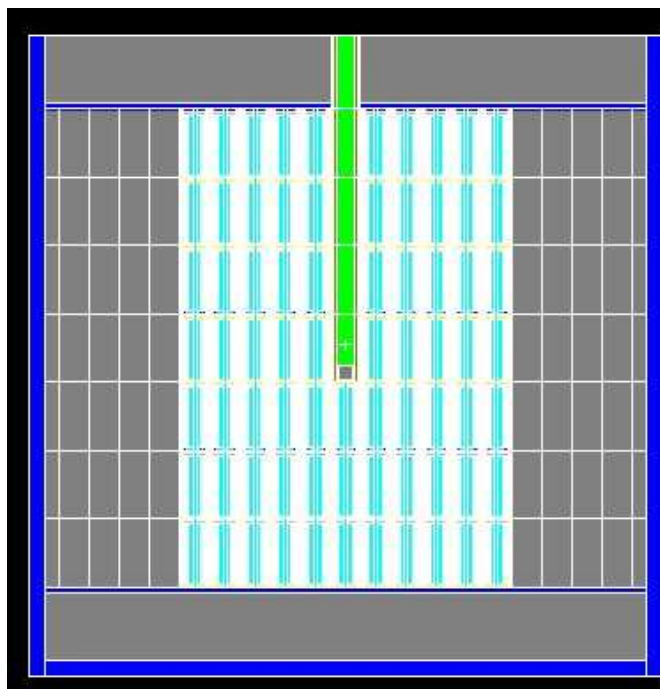


FIG. 8.18. Vertical cross-section of the LEU H5B core model (H_2O within the fuel assembly light blue, Pb grey, SS-304 dark blue, vacuum green) (Courtesy of the Vinca Institute of Nuclear Sciences, Belgrade, Serbia).

As mentioned earlier, the TVR-S fuel element design has uranium dioxide dispersed in an aluminium alloy matrix, and the ^{235}U enrichment is 19.7%. Seven TVR-S fuel elements are stacked vertically into one fuel assembly (FA) tube that is also filled with a water moderator. Demineralized water is used for the water moderator. The subcritical core is assembled inside

a cylindrical tank made of stainless steel (SS) with ID/OD equal to 1000/1050 mm. The tank bottom is a cylindrical plate with a thickness of 25 mm, and its height of 1037 mm matches exactly the total height of the core and both sections of the axial reflector. The core structure incorporates 109 fuel assemblies (FA's) arranged within an 11×11 rectangular matrix in the central part of the tank. The pitch of this square lattice is 50 mm. The central axis of the FA configuration coincides with the tank axis. The total number of LEU TVR-S fuel elements used for the core design is 759. Each one of the 109 FA's has 7 fuel elements, as described above, except for the central one. The central FA has only three fuel elements which are placed at the bottom of the beam tube and covered with demineralized water. This FA tube has a hole with diameter 30 mm that is located in the top plug to enable penetration of a SS beam guide tube. The target is placed in a high vacuum at the bottom of this beam guide tube. The core is moderated and reflected by lead material that, for the purpose of system modelling, matches exactly the inner wall of the core tank. A detailed core description and material specifications are provided in Ref. [8.2].

Neutrons escaping the target volume are represented in a multi-group format generated by the MCNPX2.5.0 code, and it used to define the neutron source for driving the subcritical core. In the Vinča calculations, MCNP5 is used with 2000 active neutron cycles; each cycle has 2500 neutrons following 200 initial ones. The neutron spectra of the various ADSRF cells were expressed in 58 energy groups. The energy boundaries of this neutron group structure are given in Ref. [8.2].

The Vinča results of the effective neutron multiplication factor k_{eff} and the prompt neutron lifetime l_p of the H5B ADSRF are given in Tables 8.4 and 8.5 along with statistical uncertainties corresponding to one standard deviation, σ . The IPEN results of the effective neutron multiplication factor k_{eff} and prompt neutron lifetime l_p for the H5B ADSRF are given in Table 8.6 along with statistical uncertainties that also correspond to a one standard deviation, σ .

TABLE 8.4. VINČA EFFECTIVE NEUTRON MULTIPLICATION FACTOR k_{eff}

Target Material	$k_{eff} \pm \sigma_k$	
	Proton Beam	Deuteron Beam
Lead	0.97444 ± 0.00032	0.97440 ± 0.00033
Uranium	0.97358 ± 0.00032	0.97374 ± 0.00032
Thorium	0.97384 ± 0.00033	0.97399 ± 0.00034
Bismuth	0.97432 ± 0.00033	0.97431 ± 0.00033
Lithium	0.96849 ± 0.00034	0.96910 ± 0.00033
Beryllium	0.97450 ± 0.00033	0.97447 ± 0.00034
Tungsten	0.97306 ± 0.00033	0.97309 ± 0.00033
Pb-Bi alloy	0.97440 ± 0.00033	0.97450 ± 0.00033

TABLE 8.5. VINČA PROMPT NEUTRON LIFETIME

Target Material	$l_p \pm \sigma_l$ [μs]	
	Proton beam	Deuteron beam
Lead	77.183 ± 0.045	77.306 ± 0.044
Uranium	77.180 ± 0.044	77.226 ± 0.047
Thorium	77.130 ± 0.045	77.187 ± 0.045
Bismuth	77.241 ± 0.045	77.222 ± 0.045
Lithium	76.847 ± 0.045	76.858 ± 0.046
Beryllium	77.305 ± 0.045	77.202 ± 0.045
Tungsten	77.065 ± 0.046	77.149 ± 0.046
Pb-Bi alloy	77.282 ± 0.0446	77.216 ± 0.046

TABLE 8.6. IPEN EFFECTIVE NEUTRON MULTIPLICATION FACTOR k_{eff} AND PROMPT NEUTRON LIFETIME l_p

Parameter	Value	statistical error
k_{eff}	0.98693	0.00002
l_p [μs]	85.07	0.08

The calculated effective neutron multiplication factor k_{eff} by Vinča is ~ 0.972 while the corresponding value by IPEN is ~ 0.987 . Further investigation is needed to better understand the difference between these results.

Neutron spectra were calculated in the H5B ADSRF at different positions for both types of charged particles (deuterons and protons) bombarding a uranium target. The following positions were considered:

- Below the target;
- Adjacent to the target in radial direction;
- Between the core edge and the reflector at the core height of the target;
- Between the reflector and the tank edge at the core height of the target.

These neutron spectra were calculated by Vinča and the results are shown in Figs 8.16 and 8.17. Comparisons of the neutron spectra per unit of lethargy in the H5B ADSRF, as obtained by Vinča and IPEN, are shown Figs 8.18–8.25. All the neutron-spectrum plots for the core have the same shape.

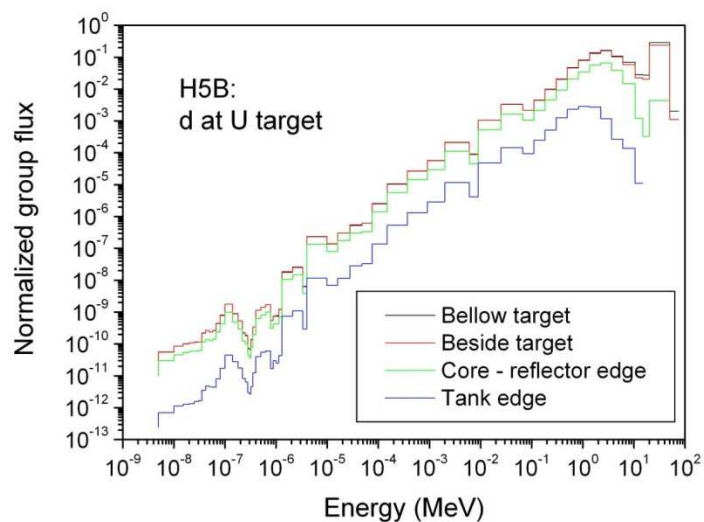


FIG. 8.19. Vinča neutron flux of the H5B ADSRF with a uranium target and a deuteron beam (Courtesy of the Vinča Institute of Nuclear Sciences, Belgrade, Serbia).

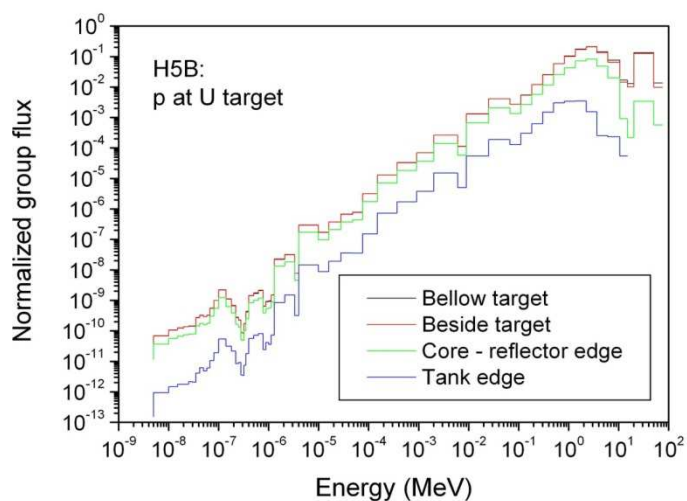


FIG. 8.20. Vinča neutron flux of the H5B ADSRF with a uranium target and a proton beam (Courtesy of the Vinča Institute of Nuclear Sciences, Belgrade, Serbia).

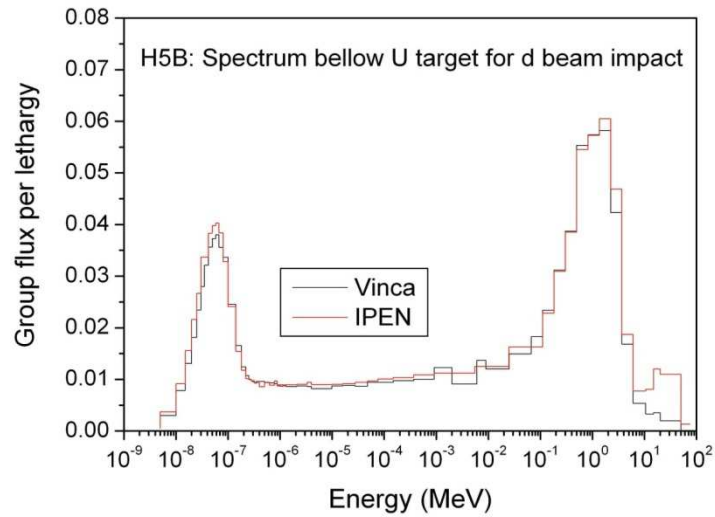


FIG. 8.21. Vinča and IPEN neutron flux of the H5B ADSRF below the uranium target with a deuteron beam (Courtesy of the Vinca Institute of Nuclear Sciences, Belgrade, Serbia).

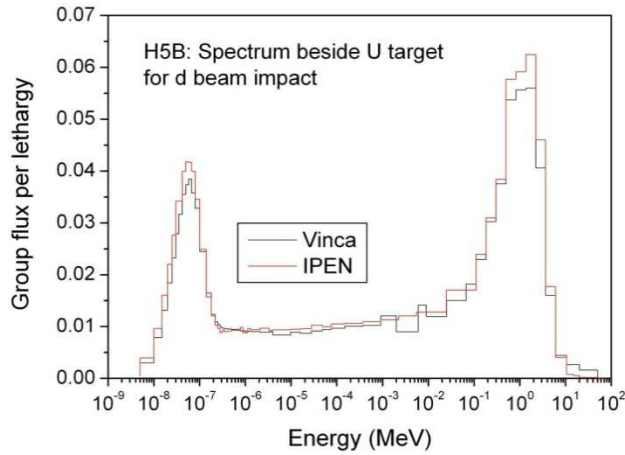


FIG. 8.22. Vinča and IPEN neutron flux of the H5B ADSRF adjacent to the uranium target with a deuteron beam (Courtesy of the Vinca Institute of Nuclear Sciences, Belgrade, Serbia).

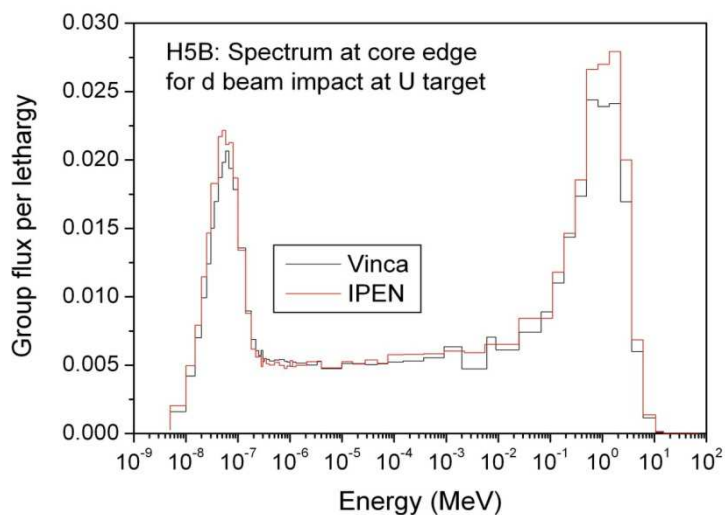


FIG. 8.23. Vinča and IPEN neutron flux of the H5B ADSRF at the core-reflector interface with a uranium target and a deuteron beam (Courtesy of the Vinča Institute of Nuclear Sciences, Belgrade, Serbia).

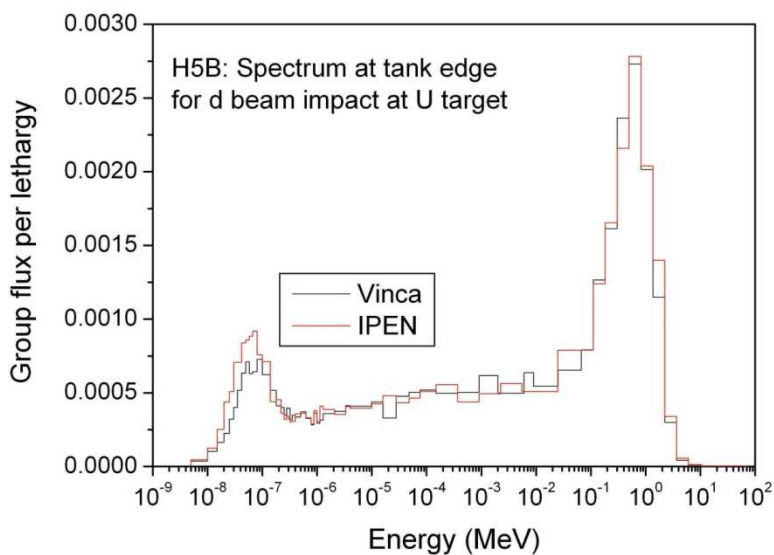


FIG. 8.24. Vinča and IPEN neutron flux of the H5B ADSRF at the tank edge over the uranium target length with a deuteron beam (Courtesy of the Vinča Institute of Nuclear Sciences, Belgrade, Serbia).

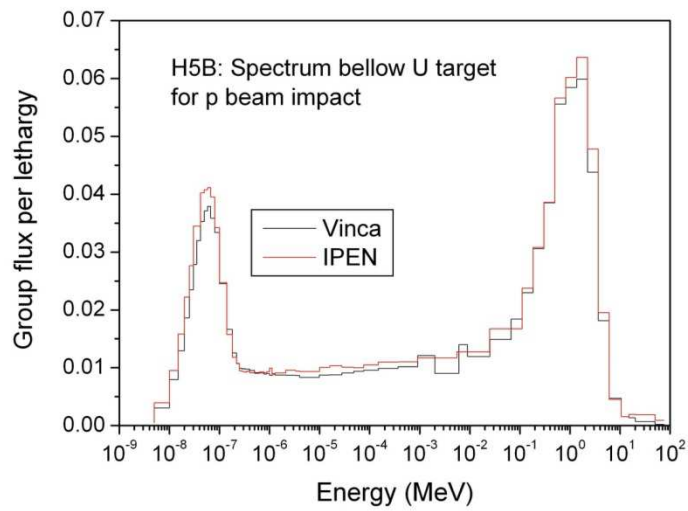


FIG. 8.25. Vinča and IPEN neutron flux of the H5B ADSRF below the uranium target with a proton beam (Courtesy of the Vinča Institute of Nuclear Sciences, Belgrade, Serbia).

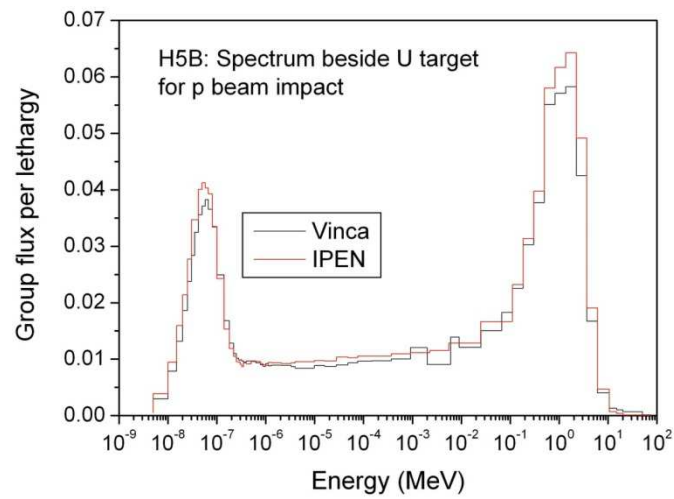


FIG. 8.26. Vinča and IPEN neutron flux of the H5B ADSRF adjacent to the uranium target with a proton beam (Courtesy of the Vinča Institute of Nuclear Sciences, Belgrade, Serbia).

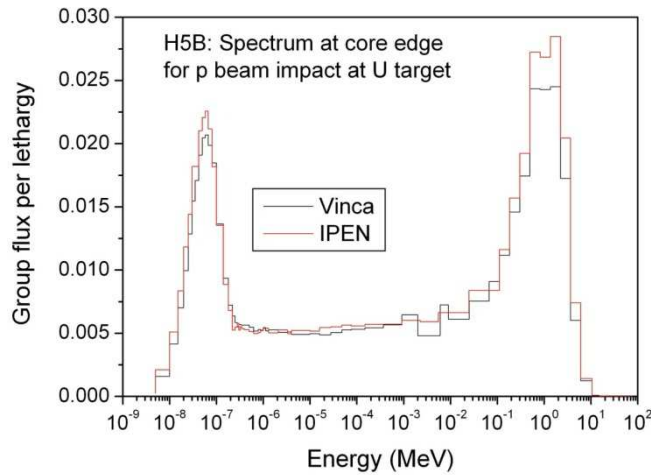


FIG. 8.27. Vinča and IPEN neutron flux of the H5B ADSRF at the core-reflector edge over the uranium target length with a proton beam (Courtesy of the Vinca Institute of Nuclear Sciences, Belgrade, Serbia).

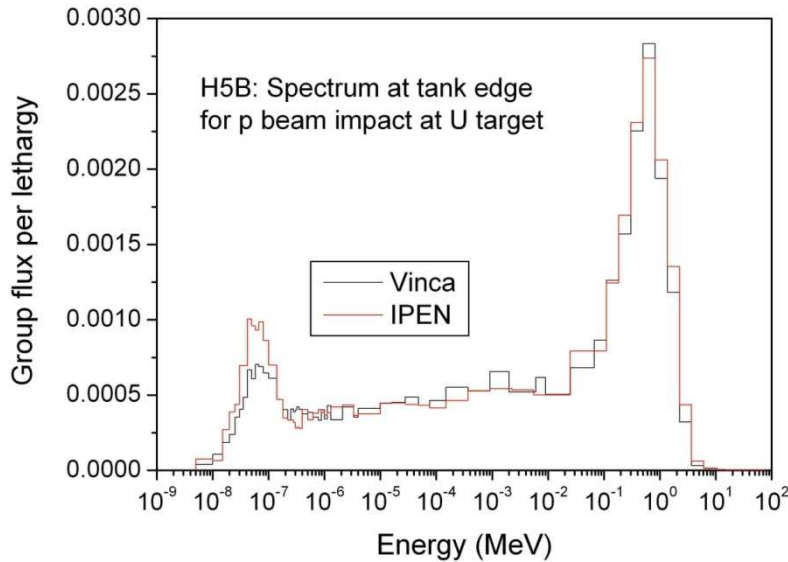


FIG. 8.28. Vinča and IPEN neutron flux of the H5B ADSRF at the tank edge over the uranium target length with a proton beam (Courtesy of the Vinca Institute of Nuclear Sciences, Belgrade, Serbia).

8.4. CONCLUSIONS

Benchmark simulation analyses of the accelerator driven system facility H5B with proton and deuteron beams were performed by the Vinča and IPEN institutes. In these simulations, the neutron yields and neutron emission spectra from different targets were generated using MCNPX Monte Carlo programs. The highest neutron flux values were obtained with a uranium target for both proton and deuteron charged particle beams. The highest neutron yield values were obtained from the uranium target with the proton beam and from the beryllium target with the deuteron beam. The neutron spectrum peaks in the energy range of 0.2 MeV to 4 MeV for all the targets except for the low-Z targets (beryllium and lithium) for both charged particles. The corresponding peaks for the low-Z targets are in the energy range of 1 MeV to 10 MeV. For low-Z targets the agreement between the obtained

neutron spectra from different laboratories is relatively poor, which suggests that further studies are required to determine the causes for these discrepancies.

The Vinča analyses used the MCNP5 Monte Carlo code for the criticality calculations of the subcritical benchmark core of the H5B ADSRF while IPEN used the MCNPX2.50 code. Neutron spectra for some representative cells of the H5B ADSRF core with the uranium target were calculated by both participants, and reasonable agreement was achieved. The calculated effective neutron multiplication factor of the H5B ADSRF by Vinča is 0.972 while the corresponding value by IPEN is 0.987. This latter value is noticeably higher than what is considered to be acceptable. The prompt neutron lifetime value of the H5B ADSRF calculated by Vinča is 77 μ s while the corresponding IPEN value is 85 μ s. The calculated neutron spectra in the core cells by both participants have the same shape.

The results from this collaborative research project suggest that further investigations are required to examine the obtained differences, with special attention paid to the system modelling, computer programs employed, and the cross-section nuclear data libraries used in the calculations. Special attention should also be given to verify the geometrical model and the input data.

REFERENCES TO SECTION 8

- [8.1] AVRAMOVIC, I., PESIC, M., Accelerator-driven sub-critical research facility with low-enriched fuel in lead matrix: Neutron flux calculation, Nuclear Technology and Radiation Protection, Vol. 22, Issue 2, (2007) 3-9.
- [8.2] PESIC, M., NESKOVIC, N. and PLECAS, I., "ADS Project in the Vinča Institute", Proc. Int. Mtg. Sub-Critical Accelerator Driven Systems, SSC RF ITEP, Oct. 11-15, Moscow, Russia, (1999) 27-33.
- [8.3] PESIC, M., AVRAMOVIC, I., BELICEV, P., NESKOVIC, N., H5B Accelerator Driven Sub-critical Research Facility with Low Enriched TVR-S Fuel in Lead Matrix – Basic Specification", Material Prepared for the IAEA Sub-Coordinated Research Project on 'Low Enriched Uranium (LEU) Fuel Utilization in Accelerator Driven Sub-Critical Assembly (ADS) Systems, Vinča-Centre NTI – 135/rev. 1, Vinča Institute, (2007).
- [8.4] MCNPX User's Manual, version 2.4.0. LANL, Los Alamos, Report LA-CP-02-408, 2002.

9. SUBCRITICAL FACILITY VENUS-1 OF THE CHINA INSTITUTE OF ATOMIC ENERGY

Contributed by

P. Xia, Y. Shi, H. Xia, Q. Zhu, T. Yu, X. Wu, W. Zhang, J. Cao, H. Luo, Y. Quan, H. Yinlu,
W. Haicheng
*China Institute of Atomic Energy, Beijing,
China*

9.1. INTRODUCTION

Analyses were performed for the experimental facility referred to as the China ADS Venus-1 subcritical facility (hereafter referred to as Venus-1 in this Section) of the China Institute of Atomic Energy (CIAE). This ADS is used for transmutation studies and operation in subcritical modes. These subcritical configurations are driven by an external neutron source, and they are used for measuring the neutronic parameters related to subcritical operating conditions. The obtained experimental data form a basis for the benchmarking of codes, models, and nuclear data usually employed for subcritical systems. In the current methodology, codes and data used for subcritical systems calculations were originally developed for critical systems analyses. This situation gives rise to the need for cross-checking analytical results and experimental data. The aim of the present project is to obtain standard static and kinetic parameters of the coupled system (subcritical core driven by a neutron source) to cross-check the computational results as well as the experimental data, if available. This approach should help in defining the accuracy that can be anticipated for subcritical core calculations, the needs for improvements in modelling the details, the identification of those parameters required to define the characteristics of subcritical systems, and in some cases, to refine the definition of these parameters. This last issue arises due to the fact that some of the standard parameters definitions for reactor systems have not been revised in order to account for the behaviour of source-driven subcritical systems. Analyses of the computed results and their comparisons to experimental data should provide insight regarding consistent criteria that are needed for characterizing LEU-ADS.

The present Section provides and discusses the results from calculations for Venus-1 that utilize four distinct nuclear data libraries, with a single Monte Carlo code (MCNP-5) used for these computations. The data libraries considered were ENDF/B-VI.6, ENDF/B-VII.0, CENDL 3.1, and the ADS 2.0 Library.

Note: When the label ‘ENDF/b7’ appears in certain plots of this TECDOC, it refers to as ENDF/B-VII.0. Similarly, ‘ENDF/b6’ refers to ENDF/B-VI.6. The obtained results pertain to k_{eff} , k_p , Λ , l_p , and β_{eff} for four fuel configurations (thermal-spectrum conditions), as well as the total neutron flux, the neutron flux distributions, and neutron spectra in the experimental channels for two fuel configurations (thermal-spectrum conditions) for the Venus-1 core when driven by an external neutron source (e.g. D-D or D-T reaction neutrons).

9.2. CHARACTERISTICS OF THE VENUS-1 ADS FACILITY

9.2.1. Structural Description of Venus-1

The Venus-1 core is comprised of fast-neutron and thermal-neutron spectrum zones in a coupled core design. It can be coupled in one direction or in both directions. The fast zone includes the external neutron source and is located in the core’s centre, surrounded by the thermal zone. The reflector, shielding, and a stainless steel shell (SS) surround both of these

zones. Figure 9.1 is a photograph showing one particular view of this arrangement (partially disassembled).



FIG. 9.1. Venus-1 ADS assembly (reproduced from Ref. [9.1] (Courtesy of China Institute of Atomic Energy, China).

The facility can be operated in two modes [9.1]:

“Venus-1 is driven by an external neutron source (e.g. ^{252}Cf , D-D reaction, or D-T reaction) to study the effect of external neutrons with various energies. It can also be driven in pulsed mode with a D-T pulsed-neutron source that is provided by the CPNG (CIAE Pulsed Neutron Generator) in order to investigate dynamic characteristics of the system.”

The facility is not equipped with safety or control rods. Sodium coolant in the fast zone was modelled by an aluminium structure and thermal zone moderator and coolant were modelled by polyethylene structure. Overall, the structure of the Venus-1 core is quite simple. Figure 9.2 is a photograph showing the arrangement for the neutron source and fast-neutron zones of this facility. Figure 9.3 is a comparable photograph showing the combined arrangement of the thermal- and fast-neutron zones.

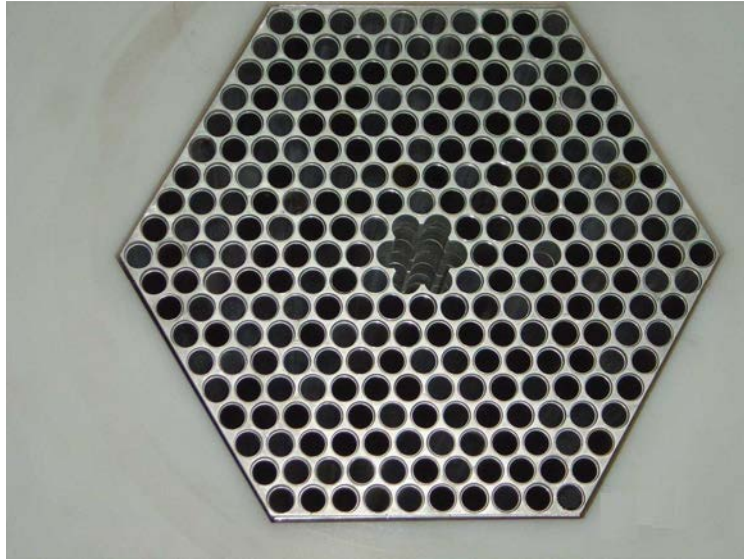


FIG. 9.2. Arrangement for the neutron-source and the fast-neutron zones (Courtesy of China Institute of Atomic Energy, China).

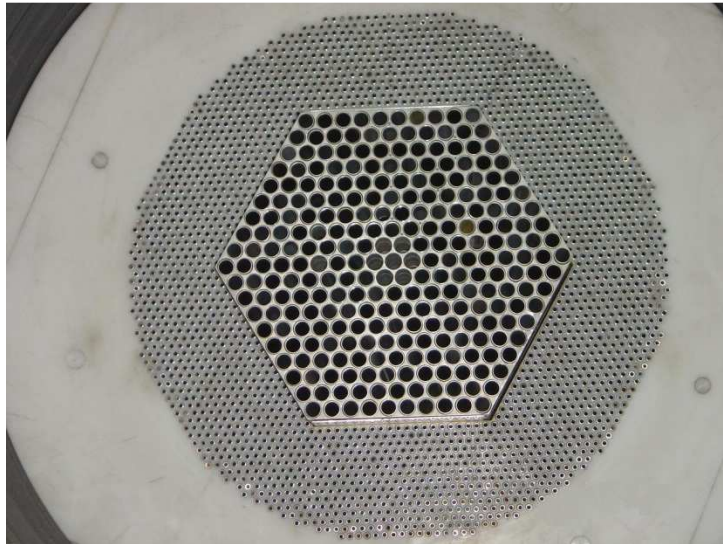


FIG. 9.3. Arrangement for the thermal- and fast-neutron zones (Courtesy of China Institute of Atomic Energy, China).

The Venus-1 design permits operation only in a subcritical state, with k_{eff} under 0.98. This value is less than the shutdown margin of a PWR, which eliminates the nuclear criticality concern for the Venus-1. Unlike critical reactors, which use safety and control rods for safe operation, the Venus-1 facility is controlled by the deuterium ion current and neutron source. Cutting off the current or removing the source shuts the reactor down.

The hexagonal aluminium structure forms the fast zone of the Venus-1 facility. Natural uranium fuel rods arranged with a 25 mm pitch produce an equilateral triangle. Fuel rods are loaded in layers, from layer number 3 to layer number 10 (see Fig. 9.2).

3%-enriched (^{235}U) fuel rods are inserted to form into the polyethylene structure forming the equilateral triangle pattern in the thermal zone of Venus-1 with the 12 mm fuel rod pitch surrounding the fast zone (see Fig. 9.3).

The overall dimensions of Venus-1 are as follows: diameter – 1600 mm, length – 1800 mm, and distance from the centre of the core to the floor surface – 1000 mm. Coupling with the CPNG is accomplished by mounting the subcritical assembly on a chassis that allows for horizontal and vertical adjustment (see Fig. 9.1).

9.2.2. Venus-1 Zone Description

In this section principal parameters of the Venus-1 facility are described.

9.2.2.1. Neutron-source Zone

The neutron source is inserted in the assembly's core through the central void, 50 mm in diameter, formed by the removal of seven central fuel rods from the fast zone. The neutron source tube length is only a half of the overall core length and another half is loaded with seven half-length fuel rods.

9.2.2.2. Fast-neutron Zone

As described in previous sections, the fast zone of the assembly is formed by natural uranium fuel rods, arranged in equilateral triangle form with 25 mm pitch within the hexagonal aluminium structure. Layers 1 and 2 are loaded with 7 half-length rods and layers from 3 to 10 are loaded with 264 full-length rods. Table 9.1 [9.2] represents the number of rods in each layer of the fast zone.

TABLE 9.1. NATURAL URANIUM FUEL RODS IN THE FAST ZONE

Layer No.	1	2	3	4	5	6	7	8	9	10
Fuel element	1	6	12	18	24	30	36	42	48	54

Source: Table 2 of Ref. [9.2].

9.2.2.3. Thermal-neutron Zone

The thermal zone is formed by 3% enriched UO₂ fuel rods. These rods arranged in equilateral triangle form with 12 mm pitch within the polyethylene structure. In the 15 layers there can be a total of 2268 fuel rods. Table 9.2 [9.2] represents the amount of rods in each layer of the thermal zone. Since the core assumed to have a cylindrical form, the amount of rods in three outer layers is reduced in comparison to the inner layers. The empty spaces of outer layers are loaded with polyethylene rods instead.

TABLE 9.2. FUEL ROD ARRANGEMENT IN THE THERMAL ZONE

Layer No.	1	2	3	4	5	6	7	8	9	10	11	12	13	14	15
Fuel elements	126	132	138	144	150	156	162	168	174	180	186	174	156	126	96

Source: Table 3 of Ref. [9.2].

9.2.2.4. Reflector Zone

A polyethylene structure of approximately 220 mm thick forms the cylindrical reflector zone of the core. The thickness of the reflector zone depends on the number of fuel rods loaded in the thermal zone.

9.2.2.5. Shield Zone and Stainless Steel Shell

The borated polyethylene cylindrical shield is 200 mm, surrounded by a 10 mm thick stainless steel (SS) outer shell.

Figure 9.4 shows the longitudinal sectional view of the Venus-1 assembly. The cross-sectional view of the Venus-1 assembly is shown in Fig. 9.5. The cross-sectional views of 3% enriched uranium fuel element and natural uranium fuel elements are shown in Figs 9.6 and 9.7 correspondingly.

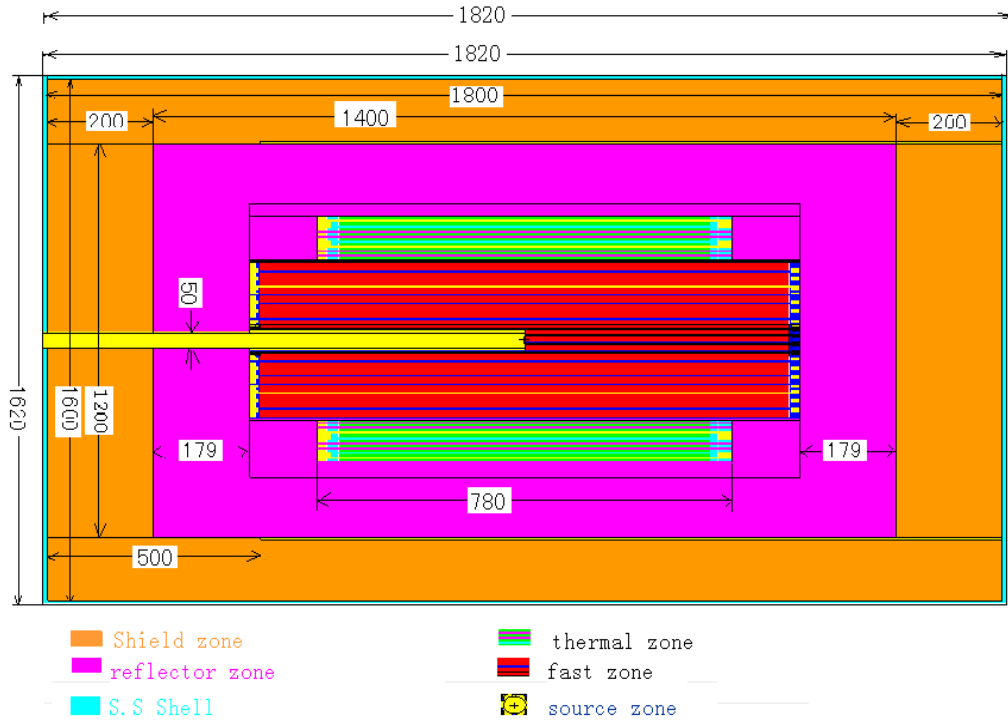


FIG. 9.4. Longitudinal sectional view of the Venus-1 assembly (Courtesy of China Institute of Atomic Energy, China).

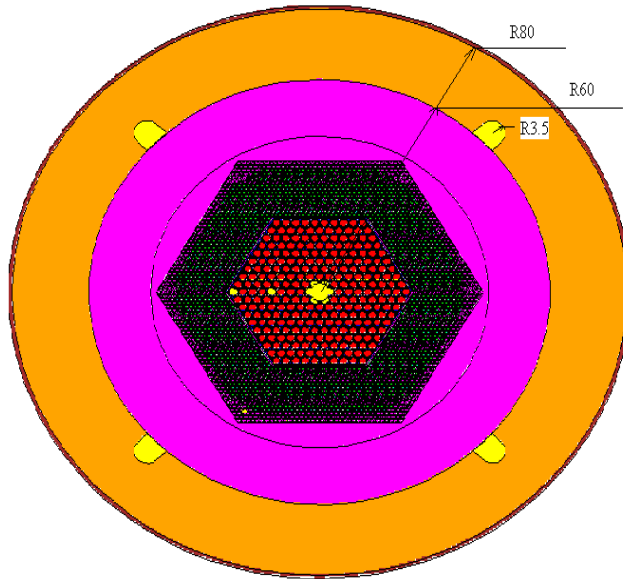


FIG. 9.5. Cross-sectional view of the Venus-1 assembly (Courtesy of China Institute of Atomic Energy, China).

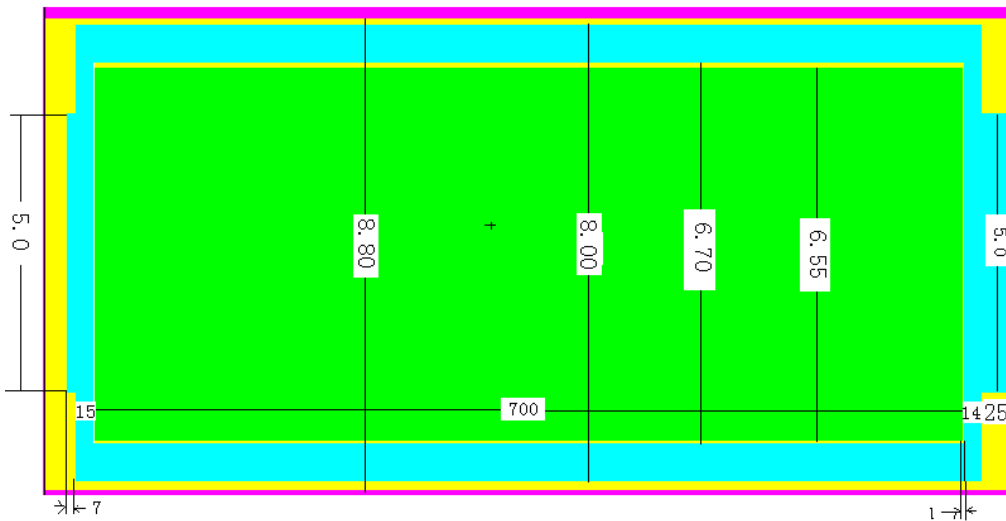


FIG. 9.6. Schematic diagram of a 3% ^{235}U enriched uranium fuel rod in the thermal zone (Courtesy of China Institute of Atomic Energy, China).

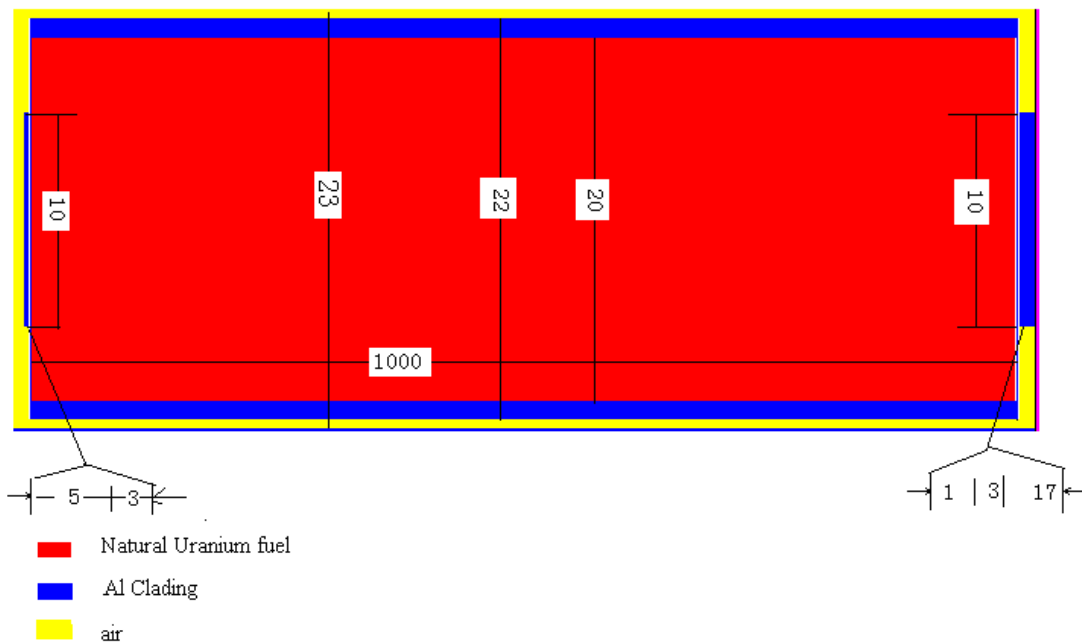


FIG. 9.7. Schematic diagram of a natural uranium fuel rod located in the fast zone (Courtesy of China Institute of Atomic Energy, China).

For the core arrangement just described, i.e. if aluminium is the material that occupies the gap between the fast zone and thermal zone, the neutrons in the Venus-1 assembly are coupled (bounded) in both directions. That is, both thermal and fast neutrons can travel between these two zones (two-way coupled).

However, if Cd or B absorber material is inserted into this gap, fast neutrons can travel between these two zones but the thermal neutrons that have been moderated by polyethylene in the thermal zone cannot travel to the fast zone. In this case, the neutrons in the assembly are coupled in one direction (one-way coupled). This enables the characteristics of a reactor core with one-way coupling of the neutrons to be investigated.

9.3. BENCHMARK DESCRIPTION

For the benchmarking effort, the calculated results of four subcritical configuration tests of Venus-1 were considered in order to compare with experimental results. The central void of the assembly core is considered as a half-empty space reserved for the neutron source, while another half consists of seven half-length natural uranium fuel rods, and the rest of the core is fuelled with full-length natural uranium fuel rods. The thermal zone is fuelled with 3% enriched uranium fuel rods and every time a rod is removed from the zone it is replaced with a polyethylene rod. This configuration is shown in Figs 9.8–9.11.

Two experimental channels, EC1 and EC2, were modelled by removing two fuel rods in layers number 6 and 10 to calculate the neutron flux and spectra in these channels. Locations of the channels are shown in Fig. 9.12.

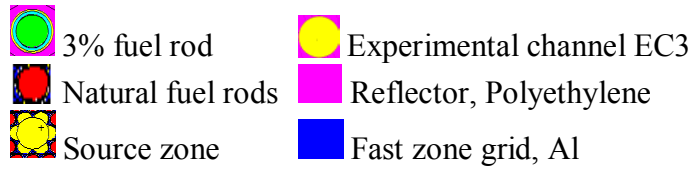
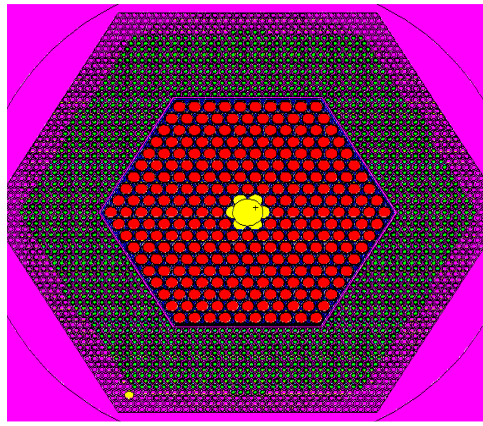


FIG. 9.8. Fuel loading of the Venus-1 configuration with 1,746 3% ^{235}U enriched fuel rods (Courtesy of China Institute of Atomic Energy, China).

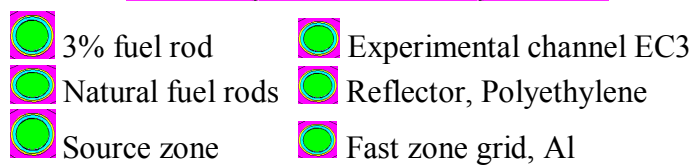
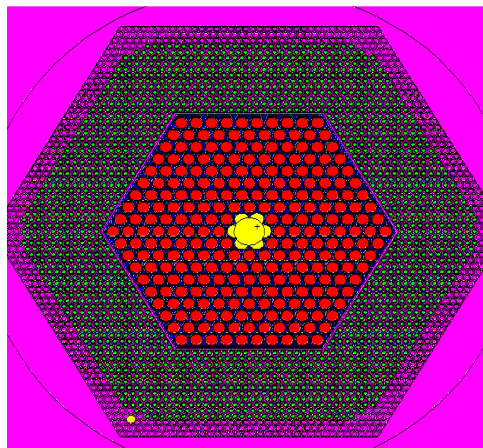


FIG. 9.9. Fuel loading of the Venus-1 configuration with 1,890 3% ^{235}U enriched fuel rods (Courtesy of China Institute of Atomic Energy, China).

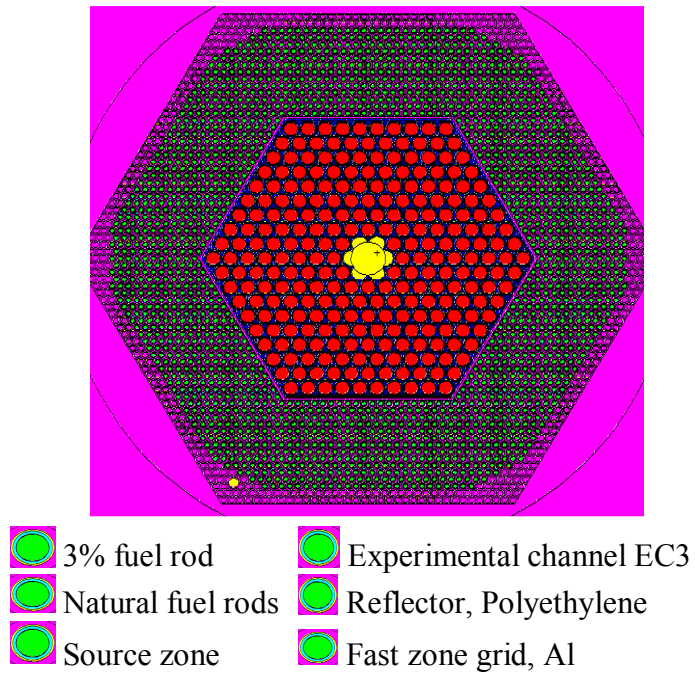


FIG. 9.10. Fuel loading of the Venus-I configuration with 2,046 3% ^{235}U enriched fuel rods (Courtesy of China Institute of Atomic Energy, China).

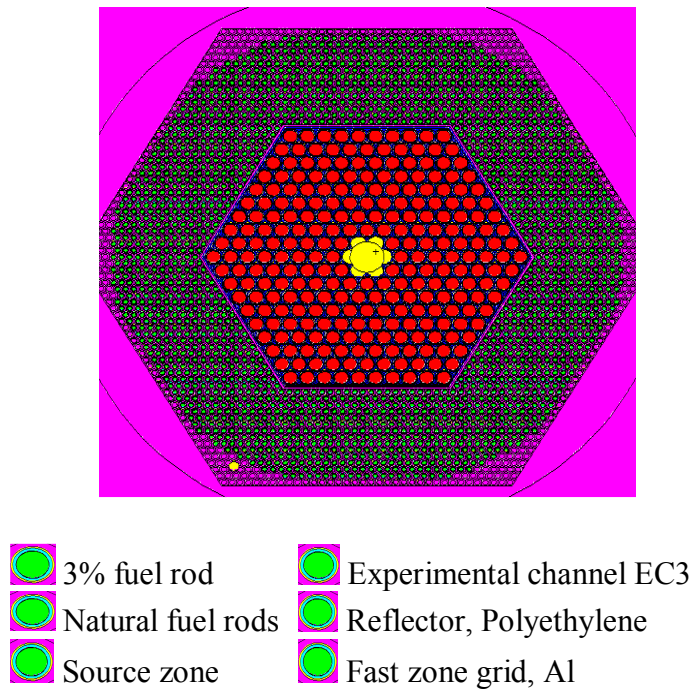


FIG. 9.11. Fuel loading of the Venus-I configuration with 2,172 3% ^{235}U enriched fuel rods (Courtesy of China Institute of Atomic Energy, China).

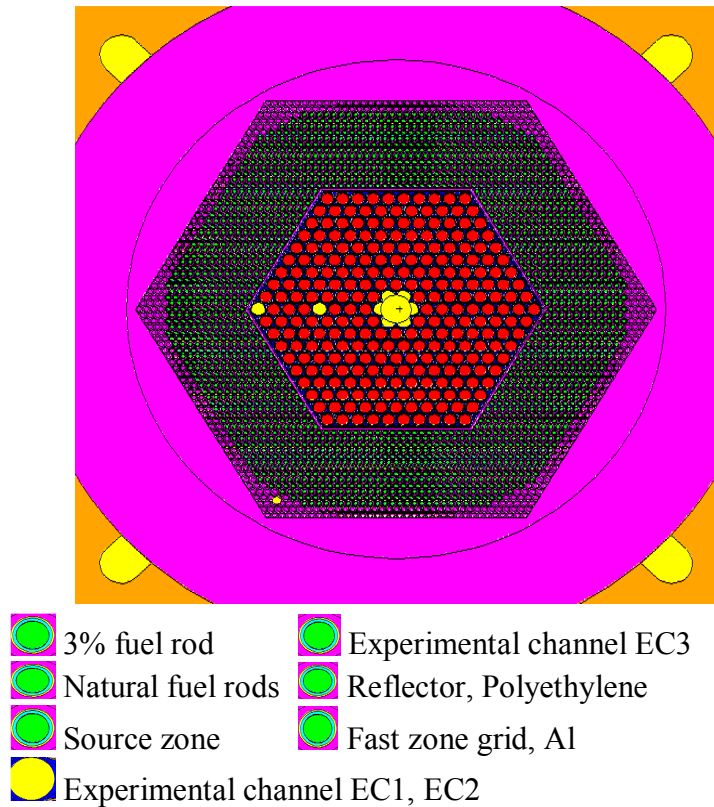


FIG. 9.12. Fuel loading of the Venus-1 configuration with 2,046 3% ^{235}U enriched fuel rods in the thermal zone and the experimental channels EC1 and EC2 in the fast zone (Courtesy of China Institute of Atomic Energy, China).

9.4. METHODOLOGY AND CALCULATIONS

9.4.1. Methodology

All the calculations were carried out with the use of the MCNP5 code to provide accurate analysis of the data obtained from different nuclear data libraries [9.1]:

“A continuous (point) cross-section data library from the ENDF/B-VI.6 nuclear data files corresponding to room temperature were used. Thermal neutrons were described using both the free gas and the $S(\alpha,\beta)$ models for the polyethylene and polyethylene with Boron materials. The computation time was variable depending on the case under consideration. Most of the calculations were done using 8 processors with a cpu-speed of 3400 MHz running MCNP-5 in a parallel mode”.

9.4.2. Computational Procedures

The various kinetic parameters were calculated using the following procedures:

9.4.2.1. Effective Multiplication Factor and Prompt Multiplication Factor

To determine k_{eff} and k_p values, the MCNP5 was used in the KCODE mode, together with the standard particle tracing procedures: 600 cycles with 100 000 particles for each cycle. The statistical error was less than 10^{-4} (10 pcm). The values of k_{eff} and k_p were obtained as a result of two runs of the KCODE: the first run with the use of delayed and prompt neutrons, and the second run was performed with only prompt neutrons.

9.4.2.2. Effective Delayed Neutron Fraction

The effective delayed neutron fraction was obtained from the following Eq. (9.1):

$$\beta_{eff} = 1 - \frac{k_p}{k_{eff}} \quad (9.1)$$

9.4.2.3. Mean Neutron Generation Time and Prompt Neutron Lifetime

The mean neutron generation time can be evaluated out of the prompt neutron lifetime obtained from MCNP5 KCODE calculations and Eq. (9.2):

$$\Lambda = \frac{l_p}{k_{eff}} \quad (9.2)$$

9.5. CALCULATED RESULTS

9.5.1. Effective Multiplication Factor and Effective Prompt Multiplication Factor

The results of calculations of the k_{eff} and k_p values using the KCODE card in MCNP5 are shown in Tables 9.3 and 9.4 [9.1]:

TABLE 9.3. EFFECTIVE MULTIPLICATION FACTOR COMPARISONS FOR DIFFERENT DATA LIBRARIES

Fuel loading	ENDF/B-VI.6		ENDF/B-VII.0		ADS 2.0		CENDL3.1	
	k_{eff}	σ	k_{eff}	σ	k_{eff}	σ	k_{eff}	σ
1,746	0.93195	0.00009	0.93496	0.00009	0.92743	0.00009	0.93439	0.00009
1,890	0.95044	0.00009	0.95359	0.00009	0.94612	0.00009	0.95289	0.00009
2,046	0.97007	0.00008	0.97343	0.00008	0.96570	0.00008	0.97270	0.00008
2,172	0.98483	0.00009	0.98852	0.00009	0.98054	0.00009	0.98722	0.00009

Source: Table 4 of Ref. [9.1].

TABLE 9.4. EFFECTIVE PROMPT MULTIPLICATION FACTOR COMPARISONS FOR DIFFERENT DATA LIBRARIES

Fuel loading	ENDF/B-VI.6		ENDF/B-VII.0		ADS 2.0		CENDL3.1	
	k_p	σ	k_p	σ	k_p	σ	k_p	σ
1,746	0.92444	0.00009	0.92809	0.00009	0.92032	0.00009	0.92668	0.00009
1,890	0.94281	0.00009	0.94664	0.00009	0.93900	0.00009	0.94511	0.00009
2,046	0.96237	0.00009	0.96629	0.00009	0.95852	0.00009	0.96475	0.00009
2,172	0.97718	0.00009	0.98135	0.00009	0.97307	0.00009	0.97954	0.00009

Source: Table 5 of Ref. [9.1].

The results in Tables 9.4 and 9.5 indicate that the ENDF/B-VII.0 gives the maximum values of k_{eff} and k_p , and the ADS 2.0 Library calculations give the minimum values. The relative statistical errors are about 0.81%.

9.5.2. Effective Delayed Neutron Fraction β_{eff}

The results of calculations of delayed neutron fraction β_{eff} using formula (9.1) above are shown in Table 9.5 [9.1]:

TABLE 9.5. β_{eff} COMPARISONS FOR DIFFERENT DATA LIBRARIES

Fuel loading	β_{eff} ENDF/B-VI.6	β_{eff} ENDF/B-VII.0	β_{eff} CENDL3.1	β_{eff} ADS 2.0
1,746	805.8	734.8	825.1	766.6
1,890	802.8	728.8	816.5	752.5
2,046	793.8	733.5	817.3	743.5
2,172	776.8	725.3	777.9	761.8

Source: Table 6 of Ref. [9.1].

9.5.3. Prompt Neutron Lifetime and Mean Neutron Generation Time

The results of calculations of the prompt neutron lifetime and the mean neutron generation time obtained from the formula (9.2) above are shown in Tables 9.6 and 9.7 [9.1]:

TABLE 9.6. PROMPT NEUTRON LIFETIME COMPARISONS FOR DIFFERENT DATA LIBRARIES

Fuel loading	ENDF/B-VI.6	
	l_p	σ
1.746	6.3011×10^{-5}	1.0427×10^{-8}
1.890	6.1235×10^{-5}	1.0030×10^{-8}
2.046	5.9414×10^{-5}	1.0122×10^{-8}
2.172	5.8024×10^{-5}	9.5888×10^{-9}
	ENDF/B-VII.0	
	l_p	σ
1.746	6.2897×10^{-5}	1.0548×10^{-8}
1.890	6.1165×10^{-5}	1.0459×10^{-8}
2.046	5.9316×10^{-5}	9.7178×10^{-9}
2.172	5.7947×10^{-5}	1.0017×10^{-8}
	CENDL3.1	
	l_p	σ
1.746	6.2548×10^{-5}	1.0114×10^{-8}
1.890	6.0819×10^{-5}	1.0128×10^{-8}
2.046	5.8965×10^{-5}	1.0475×10^{-8}
2.172	5.7634×10^{-5}	9.8621×10^{-9}
	ADS 2.0	
	l_p	σ
1.746	6.2636×10^{-5}	1.0006×10^{-8}
1.890	6.0912×10^{-5}	9.7730×10^{-9}
2.046	5.9099×10^{-5}	1.0594×10^{-8}
2.172	5.7715×10^{-5}	9.8646×10^{-9}

Source: Table 7 of Ref. [9.1].

TABLE 9.7. MEAN NEUTRON GENERATION TIME COMPARISONS FOR DIFFERENT DATA LIBRARIES

Fuel Loading	ENDF/B-VI.6	ENDF/B-VII.0	CENDL3.1	ADS 2.0
	Λ	Λ	Λ	Λ
1,746	6.7612×10^{-5}	6.7272×10^{-5}	6.6940×10^{-5}	6.7537×10^{-5}
1.890	6.4428×10^{-5}	6.4142×10^{-5}	6.3826×10^{-5}	6.4381×10^{-5}
2.046	6.1247×10^{-5}	6.0935×10^{-5}	6.0620×10^{-5}	6.1198×10^{-5}
2.172	5.8918×10^{-5}	5.8620×10^{-5}	5.8380×10^{-5}	5.8860×10^{-5}

Source: Table 8 of Ref. [9.1].

9.5.4. Total Flux in the Experimental Channel

Tables 9.8 and 9.9 [9.1] represent the calculation results of total neutron fluxes for two thermal configurations in EC1, EC2 and EC3 experimental channels of the Venus-1 facility, driven by either a D-D source or a D-T source.

TABLE 9.8. TOTAL NEUTRON FLUX IN THE EXPERIMENTAL CHANNELS OBTAINED USING DIFFERENT NUCLEAR DATA LIBRARIES AND A D-D SOURCE

Fuel loading		EC1	Σ	EC2	Σ	EC3	σ
2.046	ENDF/B-VI.6	3.8963×10^{-3}	6.7×10^{-3}	3.9152×10^{-3}	8.1×10^{-3}	2.9953×10^{-3}	1.09×10^{-2}
	ENDF/B-VII	4.1548×10^{-3}	7.2×10^{-3}	4.2700×10^{-3}	8.7×10^{-3}	3.3537×10^{-3}	1.14×10^{-2}
	CENDL 3.1	4.1086×10^{-3}	7.1×10^{-3}	4.2192×10^{-3}	8.5×10^{-3}	3.2815×10^{-3}	1.11×10^{-2}
	ADS 2.0	3.3179×10^{-3}	6.4×10^{-3}	3.2767×10^{-3}	7.9×10^{-3}	2.5068×10^{-3}	1.13×10^{-2}
2.172	ENDF/B-VI.6	6.7664×10^{-3}	9.7×10^{-3}	7.4084×10^{-3}	1.08×10^{-2}	6.2251×10^{-3}	1.23×10^{-2}
	ENDF/B-VII	8.1506×10^{-3}	1.12×10^{-2}	9.1269×10^{-3}	1.22×10^{-2}	7.8485×10^{-3}	1.34×10^{-2}
	CENDL 3.1	7.8370×10^{-3}	1.11×10^{-2}	8.7612×10^{-3}	1.22×10^{-2}	7.5584×10^{-3}	1.34×10^{-2}
	ADS 2.0	5.0767×10^{-3}	8.60×10^{-3}	5.4488×10^{-3}	1.00×10^{-2}	4.5634×10^{-3}	1.19×10^{-2}

Source: Table 9 of Ref. [9.1].

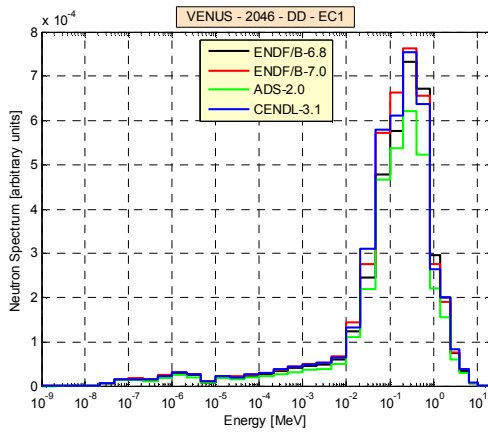
TABLE 9.9. COMPARISON OF TOTAL NEUTRON FLUX IN THE EXPERIMENTAL CHANNELS USING DIFFERENT DATA LIBRARIES AND A (D,T) SOURCE

Fuel loading		EC1	Σ	EC2	Σ	EC3	σ
2.046	ENDF/B-VI.6	8.6271×10^{-3}	4.6×10^{-3}	8.7620×10^{-3}	5.5×10^{-3}	6.8244×10^{-3}	7.4×10^{-3}
	ENDF/B-VII	9.2390×10^{-3}	4.9×10^{-3}	9.5843×10^{-3}	5.8×10^{-3}	7.4786×10^{-3}	7.6×10^{-3}
	CENDL3.1	9.0738×10^{-3}	4.9×10^{-3}	9.4194×10^{-3}	5.7×10^{-3}	7.3877×10^{-3}	7.5×10^{-3}
	ADS 2.0	7.3938×10^{-3}	3.4×10^{-3}	7.3817×10^{-3}	4.2×10^{-3}	5.6644×10^{-3}	5.9×10^{-3}
2.172	ENDF/B-VI.6	1.4900×10^{-2}	6.7×10^{-3}	1.6372×10^{-2}	7.4×10^{-3}	1.3798×10^{-2}	8.3×10^{-3}
	ENDF/B-VII	1.8409×10^{-2}	7.7×10^{-3}	2.0673×10^{-2}	8.4×10^{-3}	1.7714×10^{-2}	9.1×10^{-3}
	CENDL3.1	1.7146×10^{-2}	7.3×10^{-3}	1.9259×10^{-2}	7.9×10^{-3}	1.6476×10^{-2}	8.8×10^{-3}
	ADS 2.0	1.1387×10^{-2}	5.8×10^{-3}	1.2284×10^{-2}	6.7×10^{-3}	1.0225×10^{-2}	8.0×10^{-3}

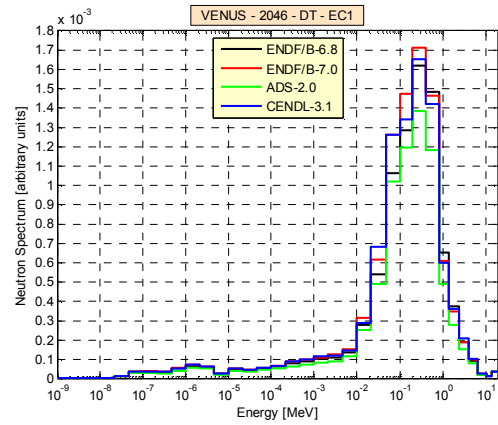
Source: Table 10 of Ref. [9.1].

9.5.5. Neutron Spectra

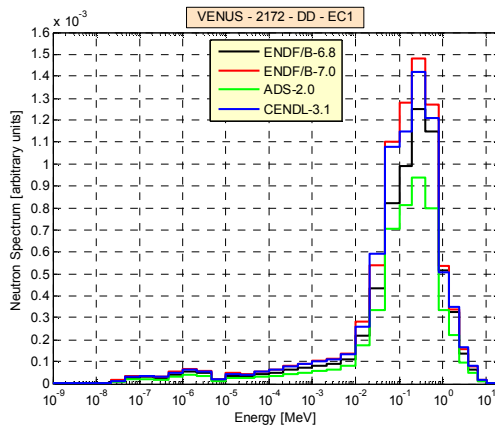
Plots 9.13 (a)–(l), with the master caption for all of the plots, show the calculation results of total neutron spectra for two thermal fuel configurations in EC1, EC2, and EC3 experimental channels of the Venus-1 facility, driven by either a D-D source or a D-T source.



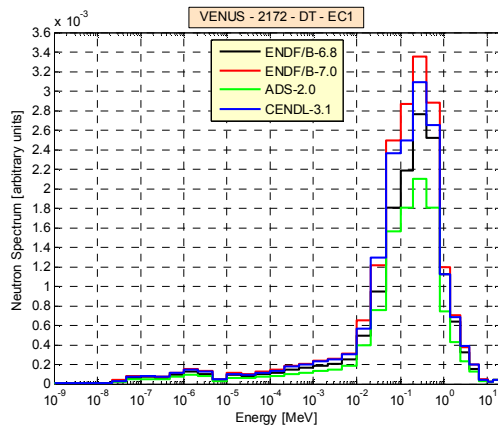
(a) EC1, 2,046 with D-D source



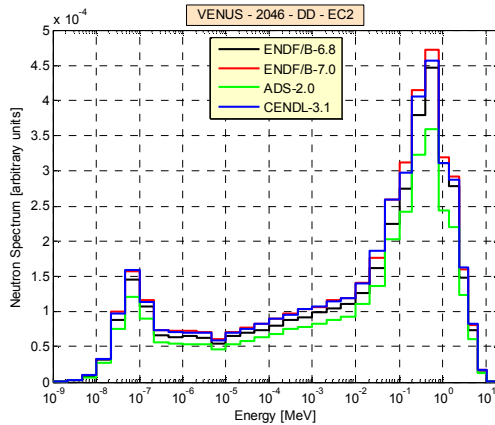
(b) EC1, 2046 with D-T source



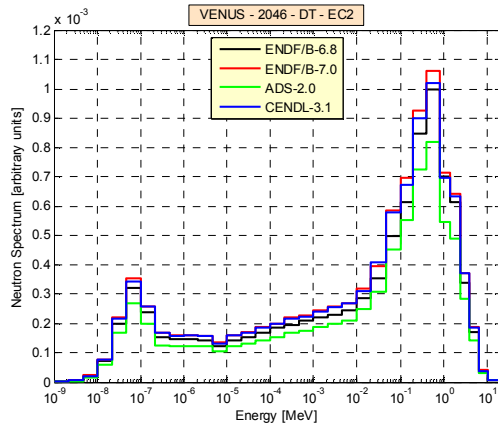
(c) EC1, 2172 with D-D source



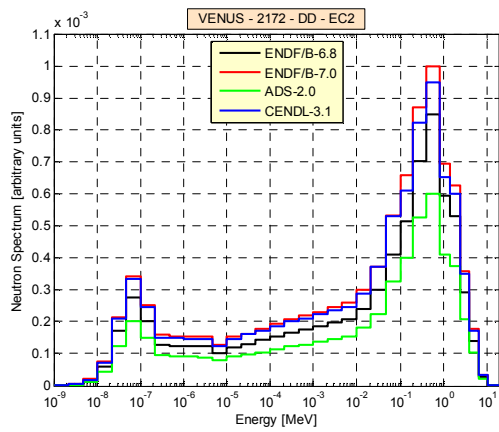
(d) EC1, 2172 with D-T source



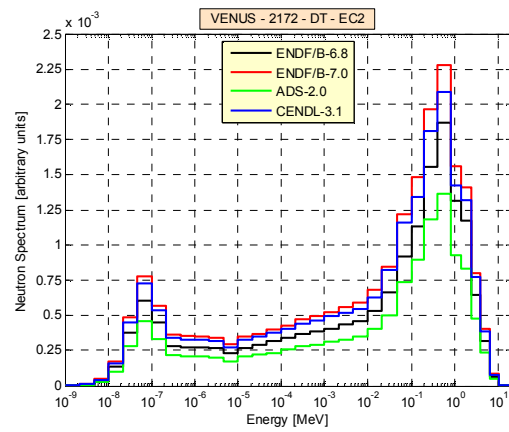
(e) EC2, 2046 with D-D source



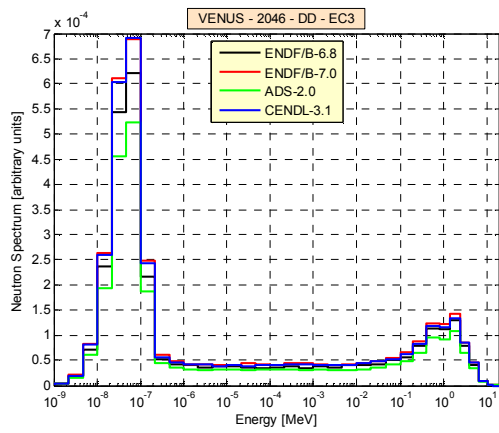
(f) EC2, 2,046 with D-T source



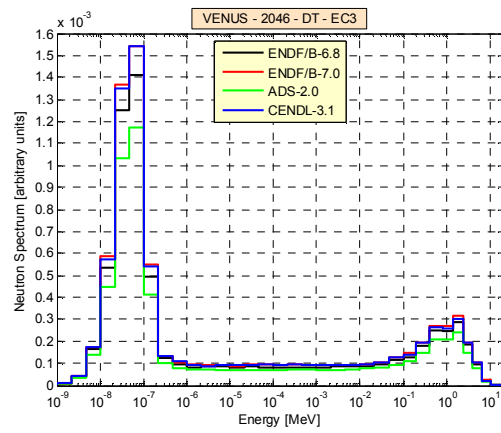
(g) EC2, 2172 with D-D source



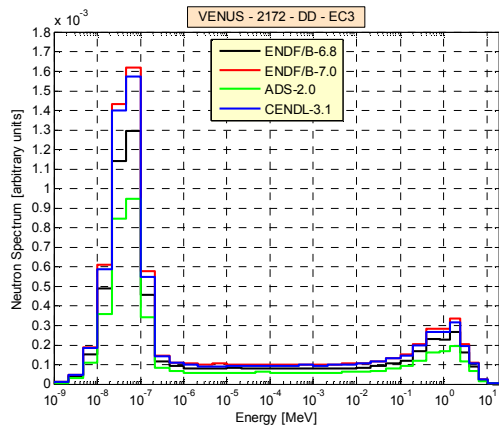
(h) EC2, 2172 with D-T source



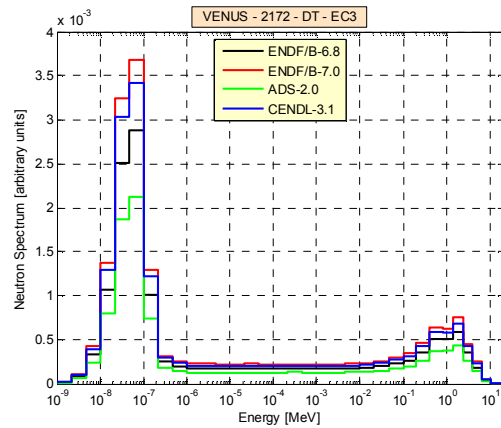
(i) EC3, 2046 with D-D source



(j) EC3, 2046 with D-T source



(k) EC3, 2172 with D-D source

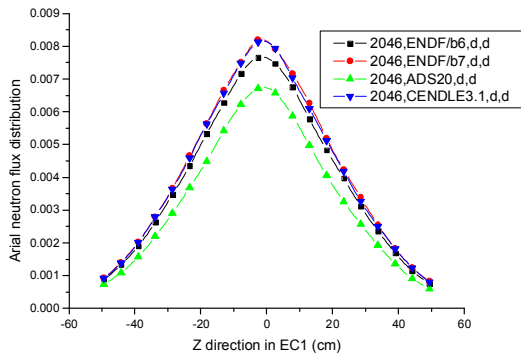


(l) EC3, 2172 with D-T source

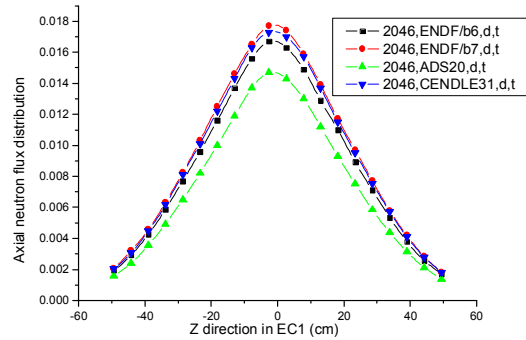
FIG. 9.13. Neutron spectra in experimental channels EC1, EC2, and EC3 with D-D and D-T neutron sources (Courtesy of China Institute of Atomic Energy, China).

9.5.6. Axial Distribution of the Total Neutron Flux

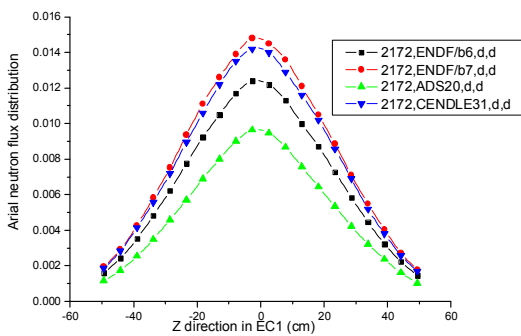
Plots 9.14 (a)–(l), with the common master caption for all of the plots, show the axial distributions of total neutron flux for two thermal configurations in EC1, EC2, and EC3 experimental channels of the Venus-1 facility, driven by either a D-D source or a D-T source.



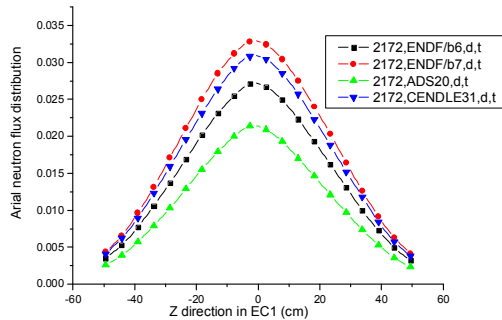
(a) EC1, 2046 with D-D source



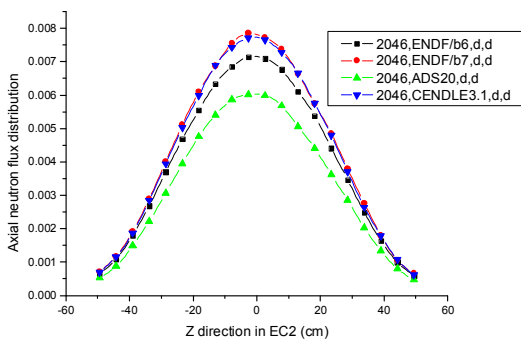
(b) EC1, 2046 with D-T source



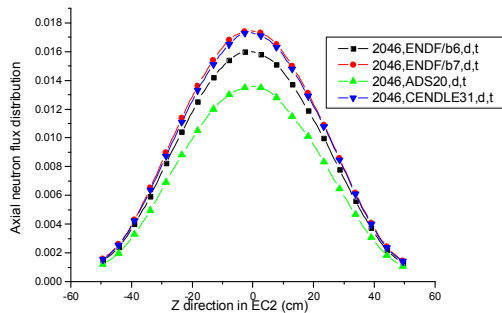
(c) EC1, 2172 with D-D source



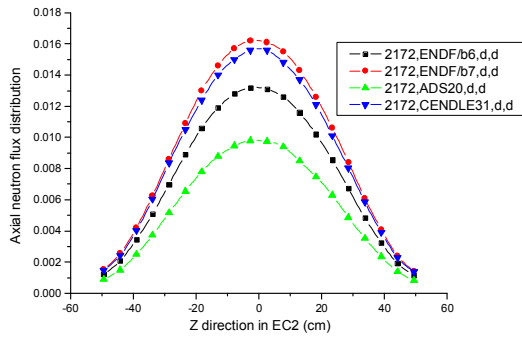
(d) EC1, 2172 with D-T source



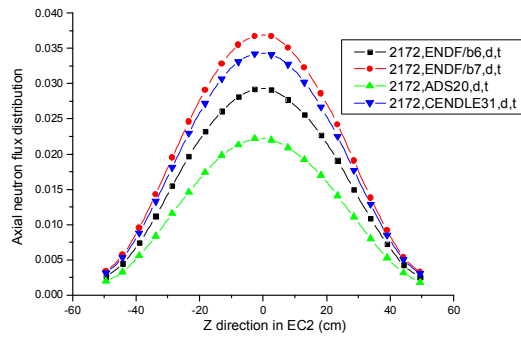
(e) EC2, 2046 with D-D source



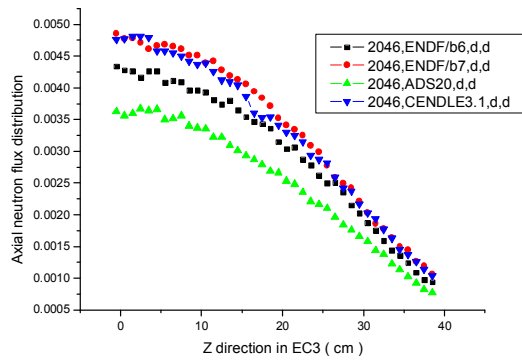
(f) EC2, 2046 with D-T source



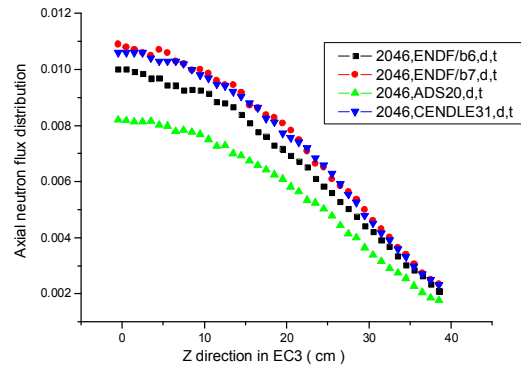
(g) EC2, 2172 with D-D source



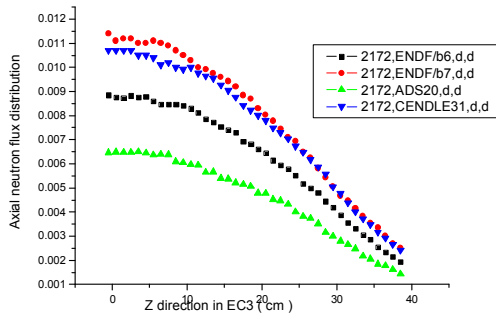
(h) EC2, 2172 with D-T source



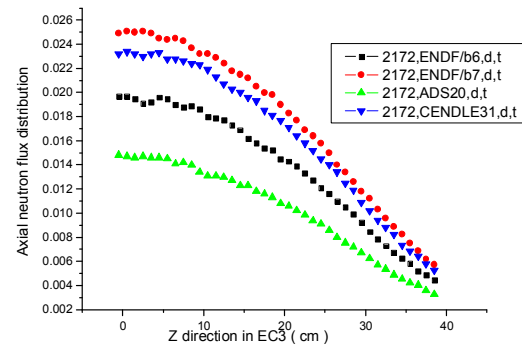
(i) EC3, 2046 with D-D source



(j) EC3, 2046 with D-T source



(k) EC3, 2172 with D-D source



(l) EC3, 2172 with D-T source

FIG. 9.14. Axial neutron flux distributions in experimental channels EC1, EC2 and EC3 with a D-D or D-T Source (Courtesy of China Institute of Atomic Energy, China).

9.6. SUMMARY AND CONCLUSIONS

The numerical simulations, along with static and dynamic parameters, for the Venus-1 facility were obtained with the use of MCNP5 along with the ENDF/B-VI.6, ENDF/B-VII.0, CENDL 3.1, and the ADS 2.0 data libraries.

The following summarizes the computational results and conclusions described in previous sections:

- The maximum values of k_{eff} and k_p were obtained with the use of ENDF/B-VII.0 data library, and the ADS 2.0 Library calculations result in the minimum values. The relative statistical errors are about 0.81%;
- The results of calculations of effective delayed neutron fractions showed that nuclear data libraries ENDF/B-VI.6 or CENDL 3.1 give larger values than either ENDF/B-VII.0 or ADS 2.0;
- The worths of prompt neutron lifetime and mean neutron generation time reduce with the increase of fuel loading. Use of different nuclear libraries results in negligible difference in the computational results;
- All nuclear data libraries show that a D-D neutron source produces the neutron flux in experimental channels 2.2 times denser than a D-T source. More specific, the ENDF/B-VII.0 gives the maximum value of the neutron flux, while the ADS 2.0 Library gives minimum;
- The simulations with ENDF/B-VII.0 tends to predict the maximum total neutron flux, while the ADS 2.0 Library predicts the minimum flux. A D-D neutron source gives the values of the neutron spectra and neutron flux distributions in experimental channels 2.2 times higher than a D-T source. These calculation results are substantially the same for all of the four nuclear data libraries used in this study.

REFERENCES TO SECTION 9

- [9.1] RESEARCH REACTOR INSTITUTE, Current Status on Research and Development of Accelerator-Driven System and Nuclear Transmutation Technology in Asian Countries, status report. Edited by Cheol Ho Pyeon, Research Reactor Institute, Kyoto University, ISSN 1349-7960, (2013) 50-70.
- [9.2] Utilisation and Reliability of High Power Proton Accelerators (HPPA5), Proceedings, Mol, Belgium, 6-9 May 2007, OECD 2008, NEA No. 6259

10. THE MARIA EXPERIMENT FOR USE OF LOW ENRICHED URANIUM (LEU) IN AN ACCELERATOR DRIVEN SUBCRITICAL ASSEMBLY (ADS)

Contributed by

S. Kilim, E. Strugalska-Gola, M. Szuta and A. A. Wojciechowski
*Institute of Atomic Energy, Otwock-Świerk,
Poland*

10.1. INTRODUCTION

A long range reactor research programme at the Institute of Atomic Energy, Otwock-Świerk, Poland, focuses on management of the spent fuel from nuclear power plants in the subcritical assembly of an accelerator driven system (ADS) from the perspective of long lived fission products (LLFP) transmutation and minor actinides (MA) utilization [10.1]. Reducing the radioactive waste (RW) quantities generated by nuclear power plants is an important aspect of the nuclear fuel cycle of these plants. The use of subcritical assemblies of ADS facilities is considered an attractive approach for this task. Analyses of possible ways to reduce radioactive waste by transmutation of radioactive long-lived fission products such as ^{99}Tc , ^{129}I , and ^{135}Cs , and by burning up of transuranic nuclides (MA) have been performed. The results suggest that the subcritical assemblies of accelerator-driven systems used for this purpose should have three distinct neutron-energy zones. This requirement of three neutron-energy zones emerges from the fact that various radioactive isotopes to be transmuted and MA to be utilized need to be located in different neutron-spectrum domains for optimal efficiency. These are: thermal-, epithermal-, and high-energy neutron zones. A very high-flux thermal neutron flux zone is expected to transmute most of the radioactive isotopes to stable or short-lived nuclides, and to increase the probability to fission actinide isotopes such as ^{237}Np and ^{238}Np .

In order to investigate this issue experimentally, it is proposed to employ a novel approach that involves using an intense thermal-neutron beam from the Institute of Atomic Energy research reactor MARIA and impinging it on a uranium converter that contains ^{235}U (EK-10 fuel rods). The thermal neutrons that impinge on the uranium converter produce fast neutrons by inducing fission reactions in ^{235}U . This approach is suggested as a possible alternative to producing fast neutrons from proton-induced neutron spallation sources. The latter are seen as potentially more expensive as well as more technologically complicated owing to the need for charged-particle accelerators in addition to subcritical reactor assemblies. As such, the facility proposed here would indeed be subcritical, but it would not be driven by an external accelerator neutron source. Thus, it would technically not be an ADS, but otherwise it resembles conventional ADS facilities. For this reason, the term 'ADS' is used freely in the ensuing discussion of the MARIA facility.

10.2. EXPERIMENTAL FACILITIES AND MEASUREMENTS

10.2.1. Transmutation of minor actinides and fission products

10.2.1.1. External Neutron Source

The MARIA reactor is, of course, a research critical reactor facility. However, the proposal is a type of subcritical system for the transmutation of nuclear waste which largely involves components that are external to the MARIA reactor core. Five uranium fuel rods are

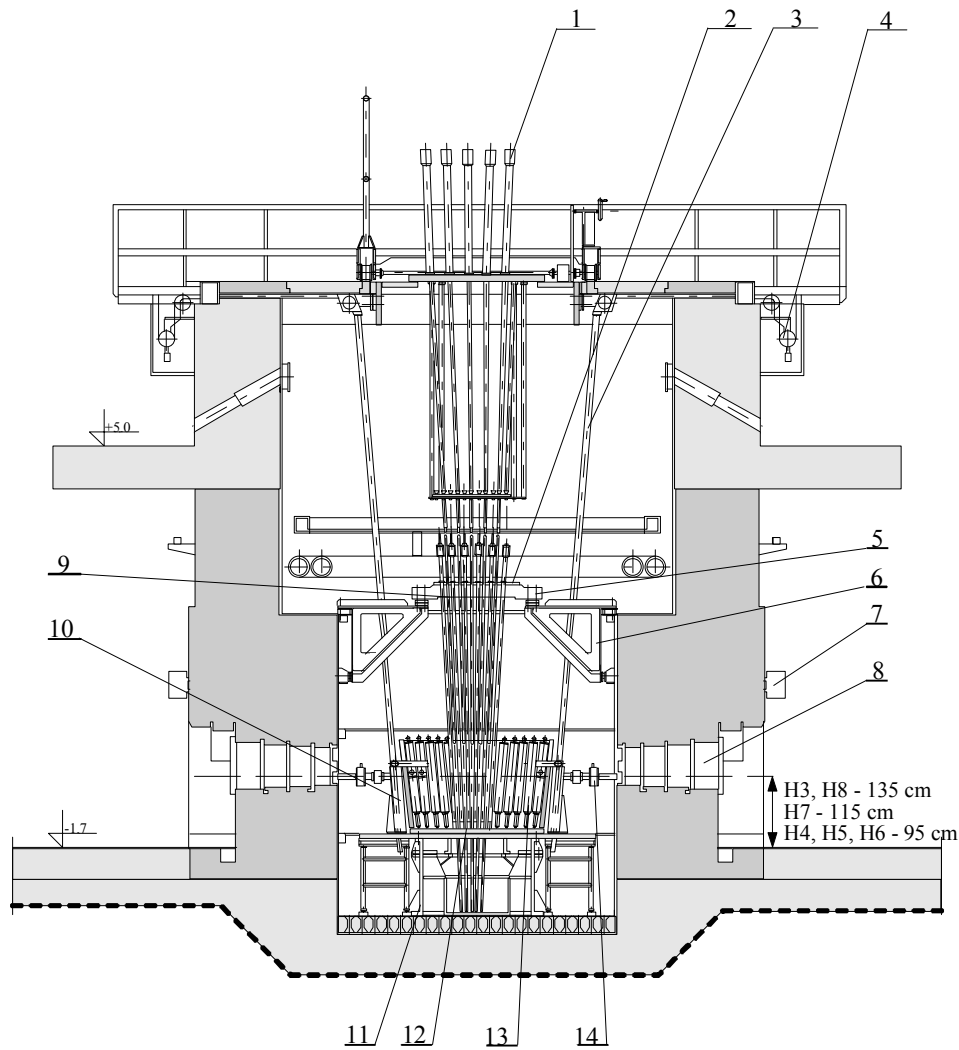
placed vertically with respect to a beam of thermal neutrons extracted from the reactor via a selected horizontal channel (neutron channel). They would be bombarded with thermal neutrons. This combination would therefore constitute a thermal-to-fast neutron converter. Preliminary calculations suggest that a fast neutron source intensity of approximately 2×10^{10} neutrons/s could be achieved using this arrangement. In such a system, the converter would be deeply subcritical.

A natural metallic uranium blanket with a moderator material would surround the fast neutron source provided by the converter arrangement described above. This would enable investigations of the transmutation of minor actinides (MA) and the long-lived fission products (LLFP) in a wide range of neutron-energy spectra. Implementation of this configuration requires building a stand at the horizontal channel of the MARIA research reactor to support the external apparatus. The essential components of a subcritical arrangement based on the MARIA reactor are described briefly below.

MARIA is a pool type reactor with 30 MW thermal power and 4×10^{14} thermal and 2×10^{14} n/cm²·s fast neutrons flux. It is moderated by water and beryllium blocks (70% and 30%, respectively). Water also serves as coolant. Graphite with aluminium cladding is used as reflector. Maria used HEU fuel (80% enrichment in ²³⁵U; 36% since 1999). Conversion of Maria to use low enriched uranium (LEU) began in 2004 and was completed in 2012. A vertical cross-section of the reactor pool is shown in Fig. 10.1.

MARIA is equipped with 8 horizontal channels (neutron beam ports). The location of the horizontal channels is shown in Fig. 10.2. One of these horizontal channels would be used for the proposed ADS project.

The measured total neutron flux density at the beginning of a horizontal channel is 8.4×10^{13} n/cm²·s (at the nominal operating power of the reactor), and the calculated flux density at the face of the channel is 1.1×10^{10} n/cm²·s. Thermal neutrons are the dominant component in the neutron spectrum of the neutrons extracted from a horizontal channel of MARIA. The contributions of epithermal and fast neutrons amount to 9.7 % and 4.2 % of the total flux density, respectively. The effective thermal-neutron flux output from a horizontal channel is $3\text{--}5 \times 10^9$ n/cm²·s. A schematic view of the horizontal channel is shown in Fig. 10.3.



- | | |
|---|--------------------------------------|
| 1. control rod drive mechanism | 8. beam tube shutter |
| 2. mounting plate | 9. fuel channel |
| 3. ionization chamber channel | 10. ionization chambers shield |
| 4. ionization chamber drive mechanism | 11. core and support structure |
| 5. fuel and loop channels support plate | 12. core and reflector support plate |
| 6. plate support console | 13. reflector blocks |
| 7. horizontal beam tube shutter drive mechanism | 14. beam tube compensator joint |

FIG. 10.1. Vertical cross-section view of the MARIA research reactor (Courtesy of the Institute of Atomic Energy, Otwock-Świerk, Poland).

The main characteristics and specifications of the MARIA reactor are as follows:

Nominal power:	30 MW(th)
Thermal neutron flux density:	4.0×10^{14} n/cm ² ·s
Moderator:	graphite
Fuel elements of the MARIA reactor:	
- Material	UO ₂ – Al alloy
- Uranium enrichment	36% in ²³⁵ U
- Cladding	aluminium
- Shape	six concentric tubes
- Active length	1000 mm

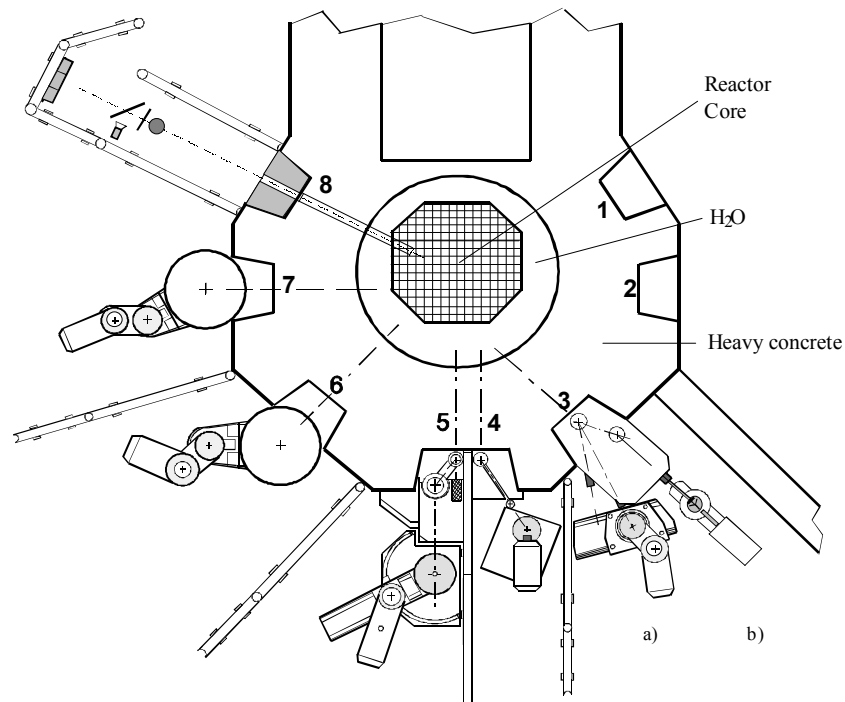


FIG. 10.2. Location of the horizontal channels of the MARIA reactor (Courtesy of the Institute of Atomic Energy, Otwock-Świerk, Poland).

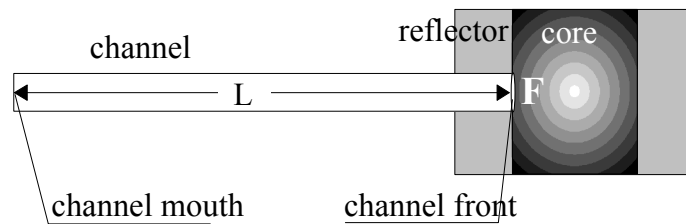


FIG. 10.3. Schematic view of a horizontal channel of the MARIA reactor (Courtesy of the Institute of Atomic Energy, Otwock-Świerk, Poland).

10.2.1.2. Neutron Energy Range of Interest for the Transmutation of LLFP and MA

The radiotoxicity of fission products can normally be neglected after about 250 years. However the radiotoxicity of actinides remains dangerously high after millions of years. This is clearly demonstrated in Fig. 10.4 from Ref. [10.1].

Since activity from two specific fission products, ^{99}Tc and ^{129}I , constitute 95% of the total activity of the long lived fission products, the microscopic cross-sections for the neutron reactions required to transmute them into short-lived radioactive isotopes, or into stable isotopes, are of great interest. This issue is especially important since the salts formed from these two elements are soluble in water, and their presence could contaminate the biosphere. These essential facts provide strong justifications for undertaking investigations aimed at developing methods for transmuting these isotopes.

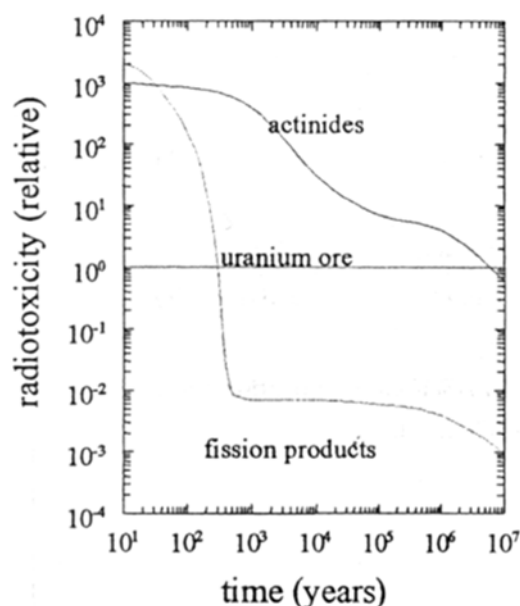


FIG. 10.4. Radiotoxicity of actinides and fission products as a function of decay time [10.1] (Courtesy of the Institute of Atomic Energy, Otwock-Świerk, Poland).

An intense thermal-neutron flux provides a rapid and efficient method for transmuting fission products. In the example shown in Fig. 10.5 from Ref. [10.2], ^{99}Tc captures a neutron to produce ^{100}Tc , which in turn decays after 16 s to the stable (non-radioactive) by-product ruthenium (^{100}Ru). Thus, the radiotoxicity of a single ^{99}Tc isotope can be eliminated by a single neutron capture reaction followed by the prompt decay of ^{100}Tc to the stable daughter nucleus ^{100}Ru . Furthermore, since ^{100}Ru has a small neutron capture cross-section, and both ^{101}Ru and ^{102}Ru are stable, essentially no new radioactive elements are produced by these sequential reactions. So, even if several successive neutron captures occur, the end result is the production of stable isotopes. Similar reaction chains can be observed for other major fission products of interest. A comparison of some reaction cross-sections for transmutation in the thermal- and fast-neutron energy regions is provided as part of Fig. 10.5. At thermal energies, fission-product transmutation cross-sections are uniformly about one order of magnitude larger than they are at fast-neutron energies.

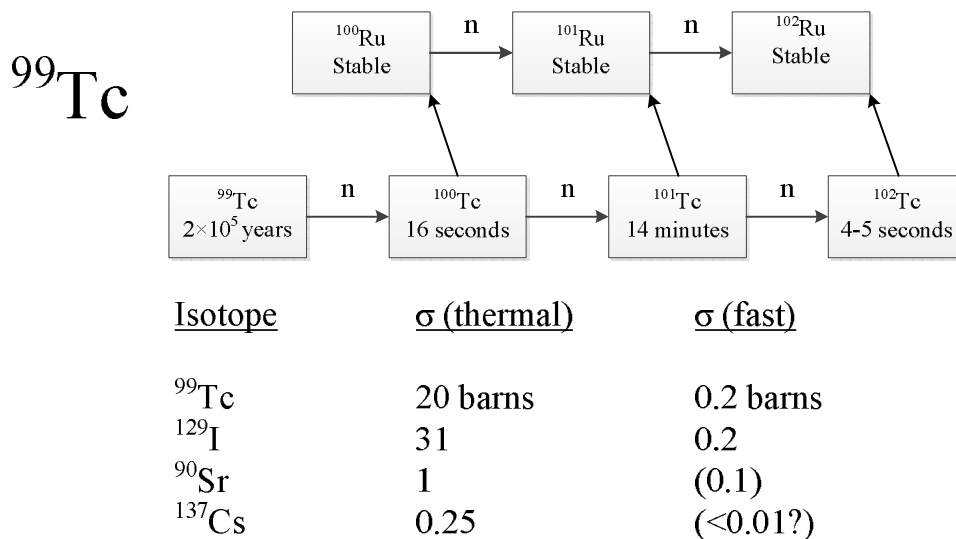
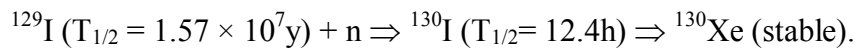


FIG. 10.5. The neutron capture chain of ^{99}Tc and thermal- and fast-neutron capture cross-sections for several fission products [10.2] (Courtesy of the Institute of Atomic Energy, Otwock-Świerk, Poland).

Long-lived radioactive iodine ^{129}I becomes ^{130}I following neutron capture. It in turn decays to stable ^{130}Xe according to the following reaction process [10.3]:



In fact, the neutron absorption cross-sections as functions of energy for the above mentioned fission products (^{99}Tc and ^{129}I) exhibit complex resonance structures. Clear evidence of pronounced resonance structure is seen in Figs 10.6 and 10.7. This supports the contention that the neutron energy range from 1 eV to 10 keV is a very important one for determining the effective transmutation rates of FP nuclei.

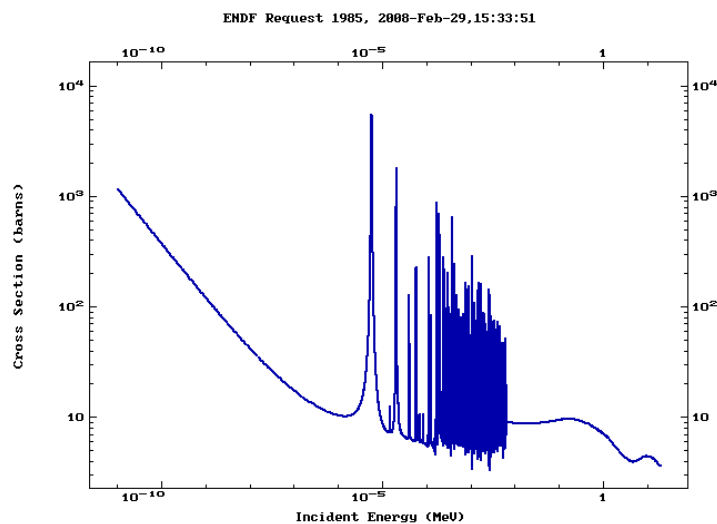


FIG. 10.6. ^{99}Tc neutron capture cross-section as a function of neutron energy (Courtesy of the Institute of Atomic Energy, Otwock-Świerk, Poland).

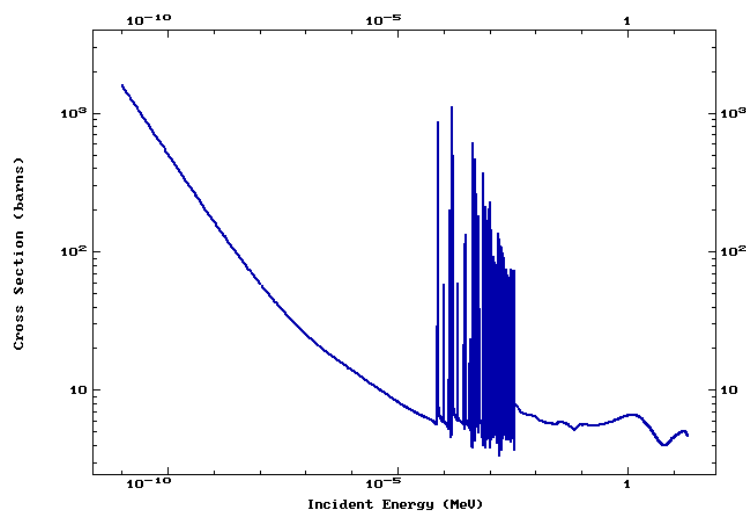


FIG. 10.7. ^{129}I neutron capture cross-section as a function of neutron energy (Courtesy of the Institute of Atomic Energy, Otwock-Świerk, Poland).

For example, ^{99}Tc has a strong neutron-capture resonance at 5.6 eV (4 000 barn). Its resonance integral is 310 barn. However, the cross-section at thermal/epithermal neutron energies ($E_n \leq 1\text{eV}$) is only about 20 barn.

Actinide isotopes, consist of neptunium and higher atomic number elements, are thought not to transmute very well in the thermal neutron fluxes (except plutonium) of typical commercial power reactors where the thermal neutron flux level is approximately $10^{14}\text{ n/cm}^2\cdot\text{s}$. Transmutation in this case implies destruction by fission (incineration) since there are no stable higher actinide nuclei. The concentrations of actinide isotopes ^{237}Np and ^{241}Am resulting from thermal fission are very small compared to their thermal capture cross-sections. Consequently, thermal neutrons are thought more likely to convert the material to heavier mass rather than to induce fission directly. The fission-to-capture ratios for the actinide isotopes are considered to be much more favourable in the higher neutron energy range.

For a sufficiently high neutron flux ($\geq 10^{14}\text{ n/cm}^2\cdot\text{s}$), two neutrons may be captured in succession by a target actinide nucleus before significant decay can occur in the targets. Fission then takes place, producing about 2.7 neutrons. Thus, the actinide isotopes can behave as net neutron producers. However, in a lower neutron flux environment, the actinide nucleus may capture just one neutron and experience a series of decay processes before finally undergoing fission. This requires, on average, about 4 neutrons input to obtain a release of about 2.9 neutrons from fission. So, in this situation the actinide nucleus will behave as a neutron absorber.

As an example, Fig. 10.8 shows the effective neptunium fission cross-section as a function of the intensity of the thermal-neutron flux. The effective cross-section has a monotonic behaviour. The high thermal neutron flux of $10^{16}\text{ n/cm}^2\cdot\text{s}$ provides a significant effective cross-section value. By comparison, the fission cross-section of ^{237}Np in the fast-neutron energy range is about 1.5–2 barn.

Since it is not possible to achieve such an intense thermal-neutron flux in a simple facility such as the converter described above, with a low actinide incineration rate due to the low-intensity thermal-neutron fluxes, attention is focused in the present research programme on the fast-neutron flux zone of this facility where the probability of fissions taking place is generally more favourable (see Figs 10.9, 10.10 and 10.11).

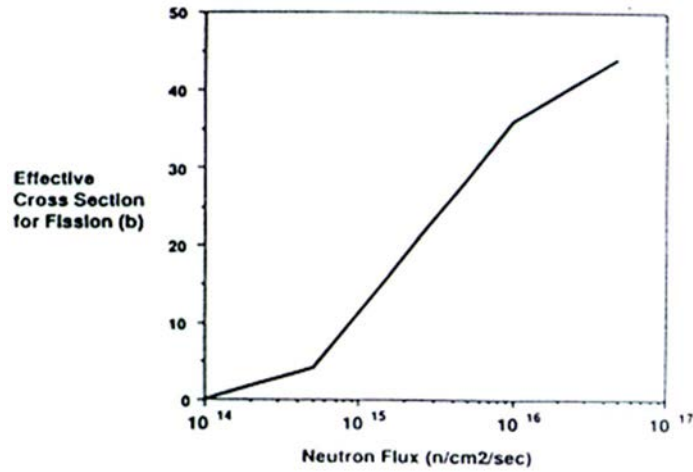


FIG. 10.8. Effective Neptunium fission cross-section in an intense thermal neutron flux (Reproduces from Ref. [10.2] with permission courtesy of the Institute of Atomic Energy, Otwock-Świerk, Poland).

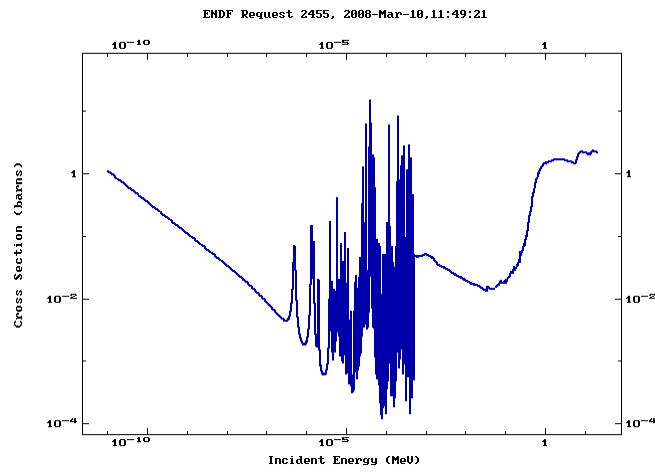


FIG. 10.9. ^{237}Np neutron fission cross-section as a function of neutron energy (Courtesy of the Institute of Atomic Energy, Otwock-Świerk, Poland).

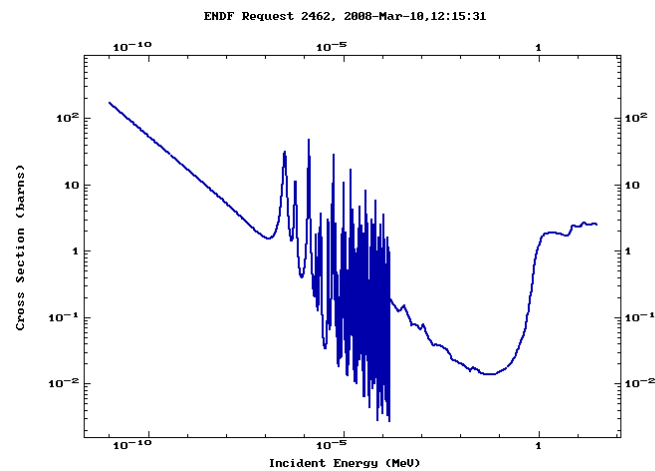


FIG. 10.10. ^{241}Am neutron fission cross-section as a function of neutron energy (Courtesy of the Institute of Atomic Energy, Otwock-Świerk, Poland).

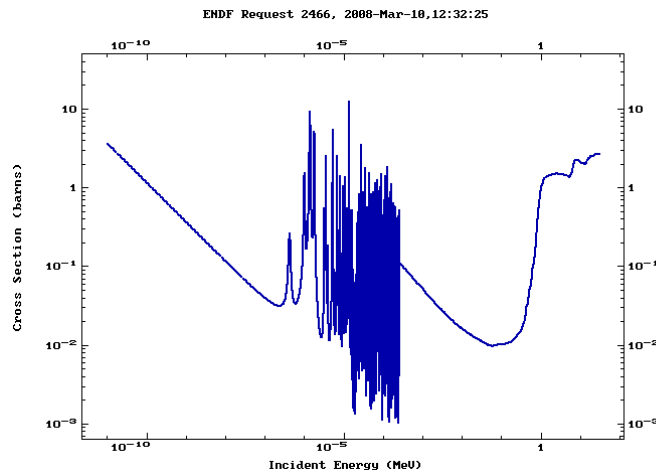


FIG. 10.11. ^{243}Am neutron fission cross-section as a function of neutron energy (Courtesy of the Institute of Atomic Energy, Otwock-Świerk, Poland).

10.2.1.3. Geometric Description of the Converter Stand

The simplified geometry used in the calculations to study the transmutation of fission products and minor actinides experimentally is described below. Two configurations (called setups) were analysed. The general view of the first setup is shown in Fig. 10.12 where the converter and the neutron island (lead or graphite block) for generating neutron flux for resonance transmutation are shown.

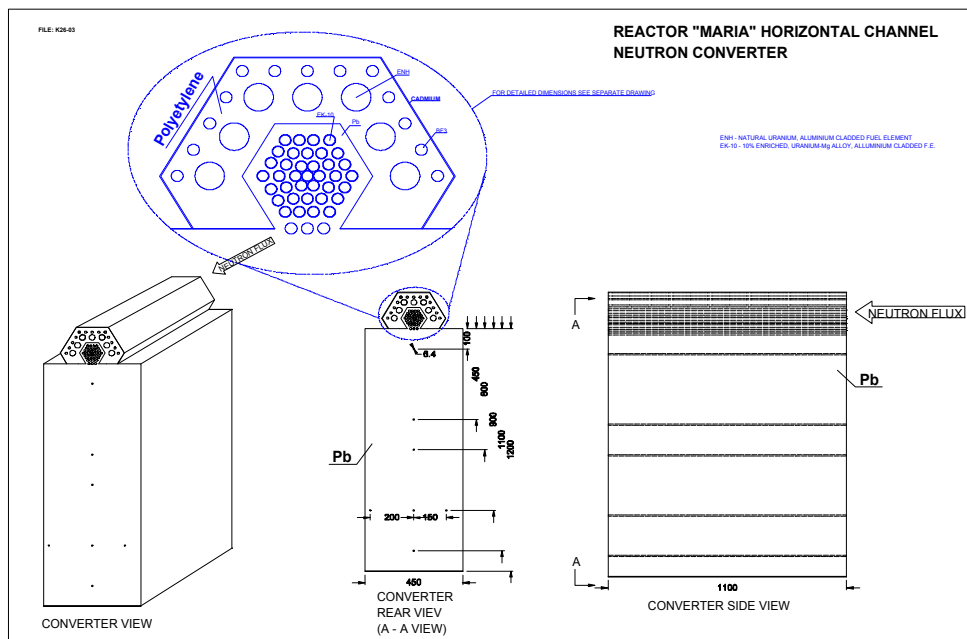


FIG. 10.12. Schematic view of the first setup for the converter and the neutron island (Courtesy of the Institute of Atomic Energy, Otwock-Świerk, Poland).

The main dimensions of the neutron island and the locations of the experimental channels in this island are shown in Fig. 10.12. The main components of the converter and the used materials are indicated in Fig. 10.13.

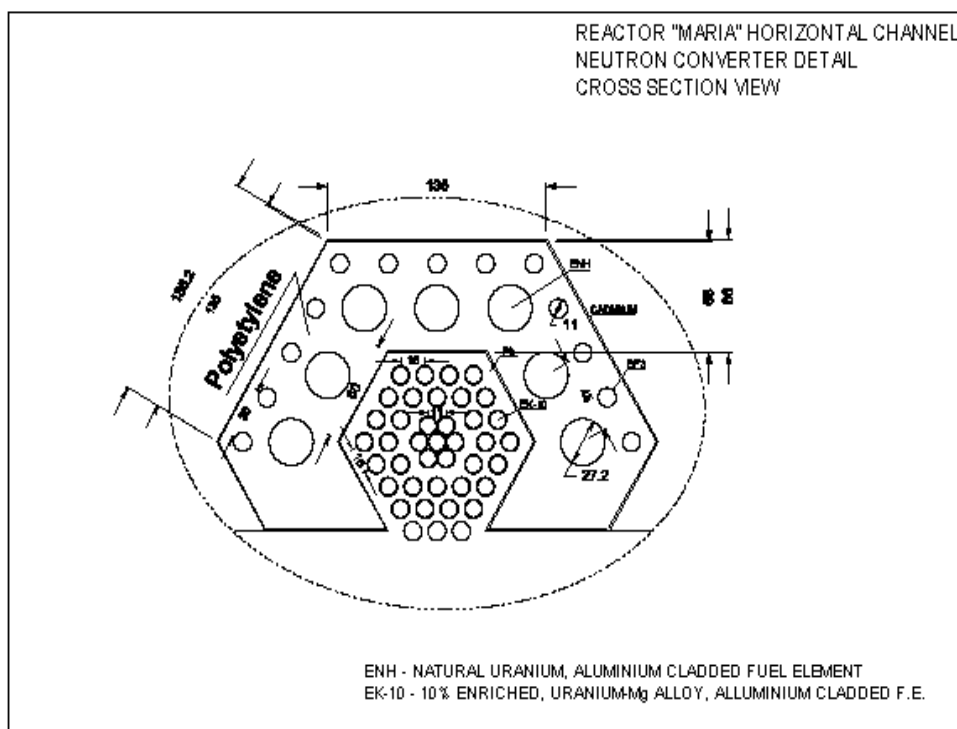
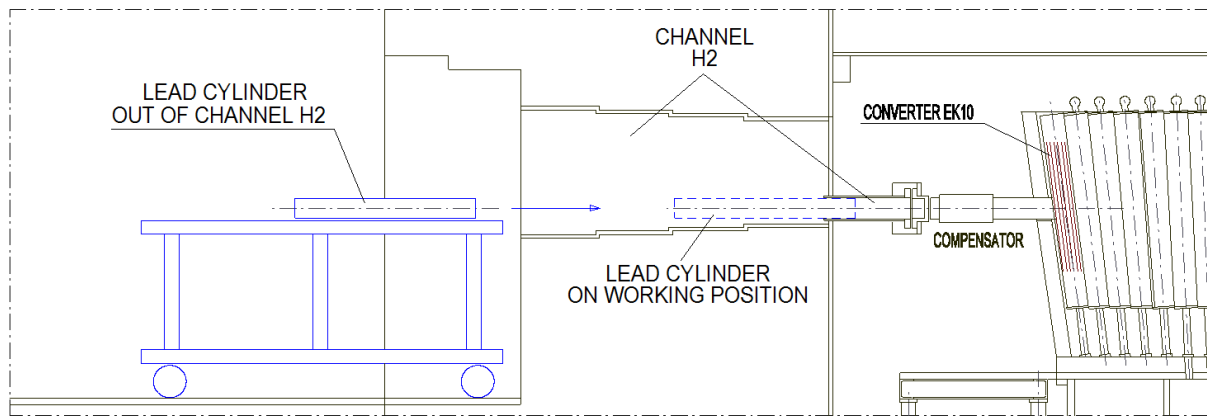
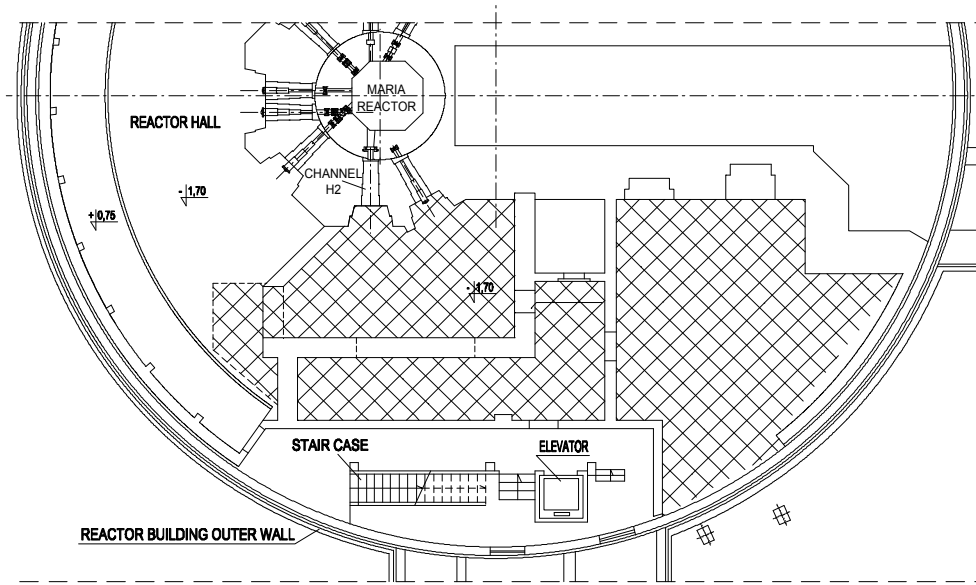


FIG. 10.13. The main components of the converter for the first configuration and the used materials are indicated. The fuel rods are EK-10 design using aluminium cladding and 10% enriched uranium (Courtesy of the Institute of Atomic Energy, Otwock-Świerk, Poland).

A general view of the second setup is shown in Fig. 10.14 (a) where the converter and the neutron island (lead or graphite block) for generating neutron flux for resonance transmutation are shown. Figure 10.14 (b) shows the location of the second stand configuration in the MARIA reactor using the horizontal channel H2.



(a) General View



(b) Horizontal View

FIG. 10.14. The second setup that displays the converter and the neutron island. The fuel rods are EK-10 design using aluminium cladding and 10% enriched uranium (Courtesy of the Institute of Atomic Energy, Otwock-Świerk, Poland).

The converter consisting of the EK-10 fuel rods is located in the reflector of the MARIA reactor core along the axis of the horizontal channel H2. This arrangement produces high-energy and epithermal neutron spectra. A lead cylinder consisting of several discs is placed in this channel during the experiments. Samples of fission products and minor actinides can then be placed between these discs. The neutron island uses lead or graphite to generate neutron fluxes for studying resonance transmutation rates.

A schematic drawing showing the MARIA reactor core and the location of the converter relative to this core is presented in Fig. 10.15. The triangular array of the EK-10 fuel rods is shown in Fig. 10.16. The research reactor MARIA is equipped with 8 horizontal channels. Six of these horizontal channels are already in use for other experiments. Two channels are currently available for installation of a stand for the transmutation research.

There are safety requirements which have to be considered. The experimental area has to have adequate biological shielding and safe access to the experimental stand for its

management. Fortunately, such requirements can be satisfied at the MARIA reactor. Therefore, there is no need to alter the existing biological shield or to construct a special building for this experiment. A similar stand was designed for the boron neutron-capture therapy (BNCT) project. The BNCT facility, and the proposed stand for the actinide and fission product transmutation studies, both utilize similar fission converters. Therefore, the two research activities could be carried out using the same neutron channel.

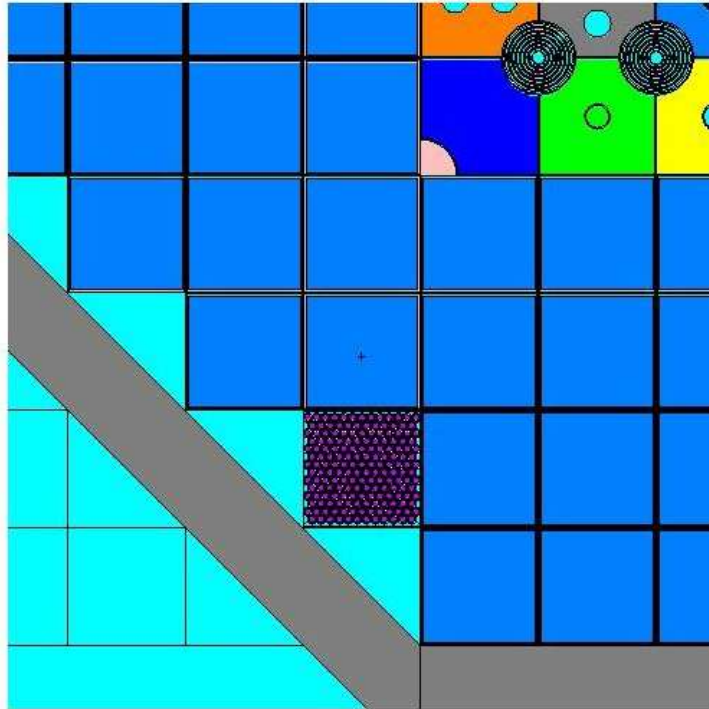


FIG. 10.15. Schematic drawing of the MARIA reactor core and proposed converter [10.4] (Courtesy of the Institute of Atomic Energy, Otwock-Świerk, Poland).

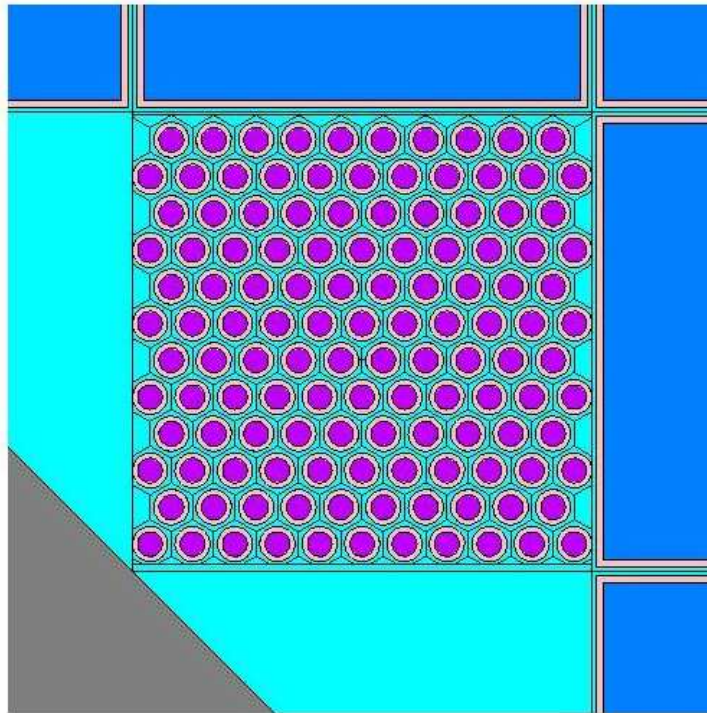


FIG. 10.16. Layout of the EK-10 fuel rods in a triangular array with a 12-mm pitch [10.4] (Courtesy of the Institute of Atomic Energy, Otwock-Świerk, Poland).

10.2.1.4. Specifications of the Components and Materials

Two converter options are considered and both involve using EK-10 fuel rods. Both converters are exposed directly to the thermal neutrons from the horizontal channel of the MARIA reactor core, as shown in Figs 10.12, 10.13, 10.14, 10.15, and 10.16. The EK-10 fuel rods are placed in a lead block to avoid slowing down the produced fission neutrons. The first converter option has a fast-neutron zone consisting of the EK-10 fuel rods placed in the lead block and a thermal-neutron zone consisting of metallic natural uranium rods placed in a polyethylene block, shown in Fig. 10.13. The natural uranium rods have 30 cm length, 2.72 cm diameter, and 2.8735 kg mass. They are hermetically sealed in aluminium cladding. The second converter option also consists of two zones, as shown Figs 10.14, 10.15, and 10.16. Both converter options have the same fast zone. However, the second converter option has a thermal zone consisting of polyethylene block without uranium material. Both the EK-10 fuel rods shown in Fig. 10.17 and the metallic natural uranium rods are available at the MARIA reactor facility for use in the proposed research.

The EK-10 fuel rods are characterized as follows:

— Material	mixture of UO_2 and Mg
— ^{235}U enrichment	10%
— Cladding	aluminium
— Active length	495 mm.
— Diameter of fuel sample	7 mm

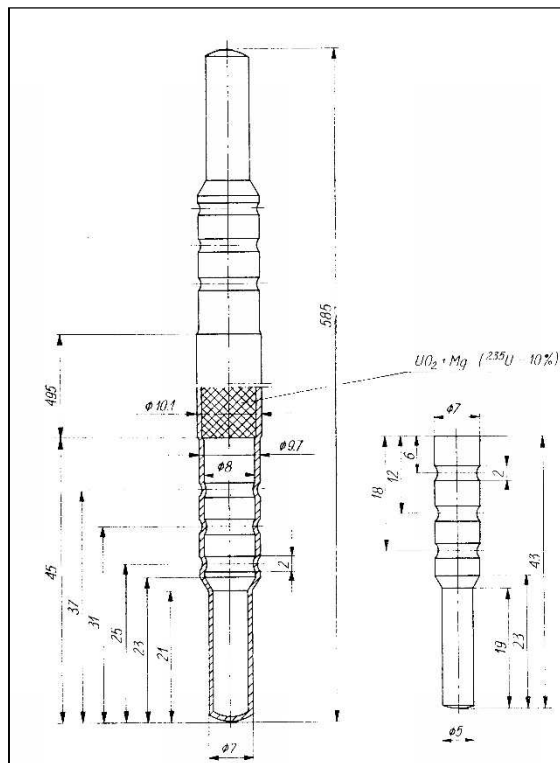


FIG. 10.17. EK-10 fuel rod design (Courtesy of the Institute of Atomic Energy, Otwock-Świerk, Poland).

A simplified model for the EK-10 fuel rod is shown in Fig. 10.18. The atom and mass fractions of the nuclides found in the EK-10 fuel are given in Table 10.1. These are used in performing Monte Carlo simulations for the present analyses.

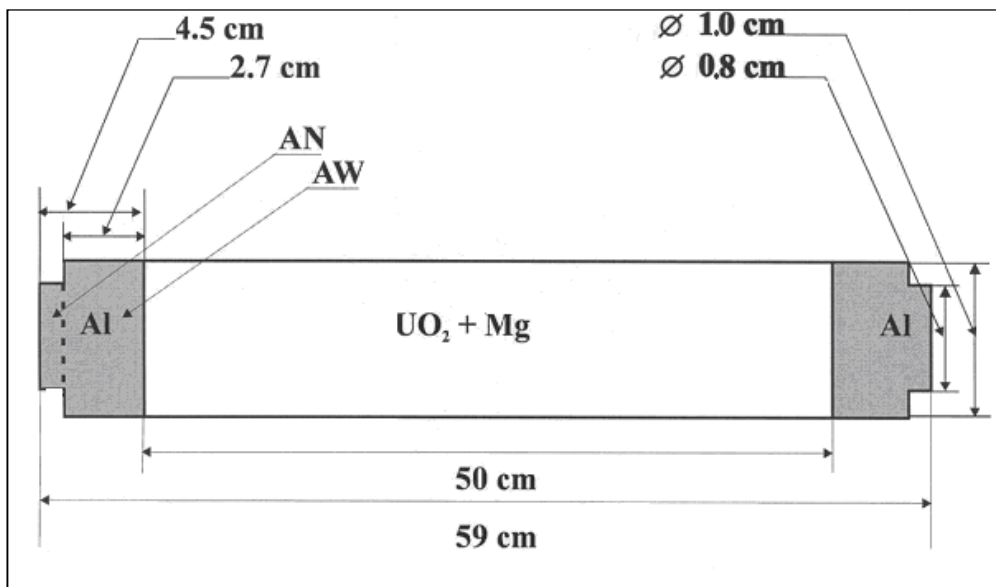


FIG. 10.18. EK-10 fuel rod model used in the Monte Carlo simulations (Courtesy of the Institute of Atomic Energy, Otwock-Świerk, Poland).

TABLE 10.1. ATOM AND MASS FRACTIONS OF NUCLIDES IN THE (UO₂ + MG) FUEL

Nuclide	²³⁵ U	²³⁸ U	¹⁶ O	Mg _{nat}
Atom fraction (%)	2.363	20.995	46.741	29.901
Mass fraction (%)	7.902	71.119	10.638	10.341

10.2.2. Pb-U-Blanket Target

10.2.2.1. Description of Pb-U-Blanket Target

The Pb-U-blanket target consists of a lead cylindrical core and natural uranium rods (see Ref. [10.5]). The lead cylinder has 48 cm length and 8.4 cm diameter. It is surrounded by four sections of a natural uranium blanket. Each section contains 30 uranium rods. These uranium rods have 10.4 cm length, 3.6 cm diameter, and 1.72 kg mass. The uranium rod has aluminium cladding. Each section contains 51.6 kg natural uranium, and the total uranium content of the four sections is 206.4 kg. Measurement foils are placed in the three gaps between the four sections, as well as at the front and back ends of the setup. This offers five possible locations for foil detectors along the axis. Two cross-section views of the Pb-U-blanket target are shown in Fig. 10.19.

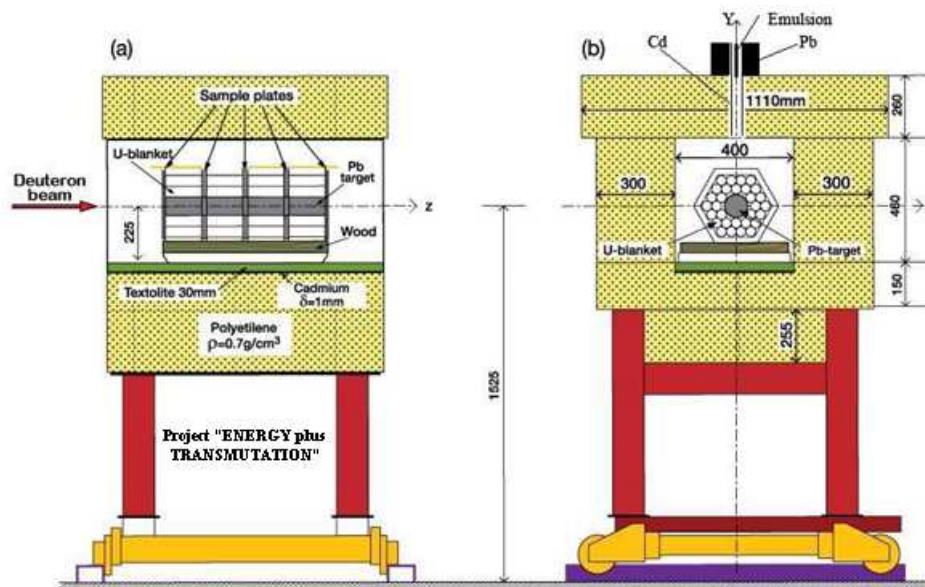


FIG. 10.19. Two cross-section views of the Pb-U-blanket target (Reproduced from Ref. [10.5 with permission courtesy of the Institute of Atomic Energy, Otwock-Świerk, Poland).

The Pb-U assembly is contained inside a massive shield, and it is mounted on a mobile platform which can be moved in front of the deuteron beam line. The left side of Fig. 10.19 shows a cut through the assembly along the beam line while the right side of the figure shows a cut through the assembly perpendicular to the beam line in the position between the first and the second sections of the Pb-U assembly. Nuclear emulsions are mounted over the hole on top of the shielding for the purpose of measuring the fast neutron spectrum. The neutron spatial distribution in the blanket target was obtained using sets of threshold activation detectors (Al, Y and Au) as well as solid-state nuclear track detectors (SSNTD).

The scientific group of the Institute of Atomic Energy – Swierk, Poland (IAE) has chosen to use Yttrium-89 (^{89}Y) activation detectors for neutron-spectrum metrology. These ^{89}Y activation detectors were placed at several radial positions on plastic foils located in the front of and the rear of the Pb-U assembly, as well as between the four sections. A plastic foil containing five yttrium samples, which is identified as Plane 0 in Fig. 10.20, was placed 30 cm in front of the experimental setup in order to detect any misalignment of the deuteron beam with respect to the lead target. The Pb-U assembly is also referred to as ‘Energy plus Transmutation.’ The arrangement of the ^{89}Y detectors on the plastic foils for the various planes in the experimental set-up ‘Energy plus Transmutation’ is shown in Fig. 10.20. This arrangement of the ^{89}Y detectors measured the axial and radial distributions of the generated isotopes (see Refs [10.6] and [10.7] for details). The activity in this research programme is divided into two parts: experimental and computational. The calculations were based on Monte Carlo method using the MCNPX program. A comparison was carried out of the acquired experimental data with the theoretical model calculations, and this yielded a satisfactory agreement.

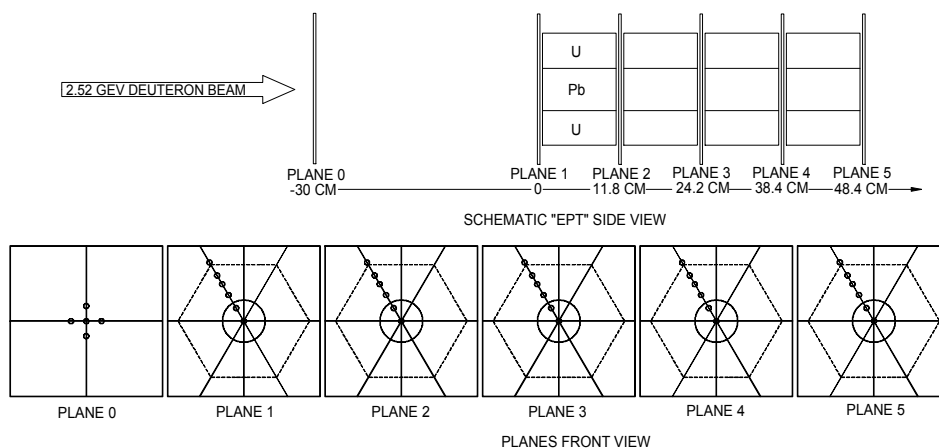
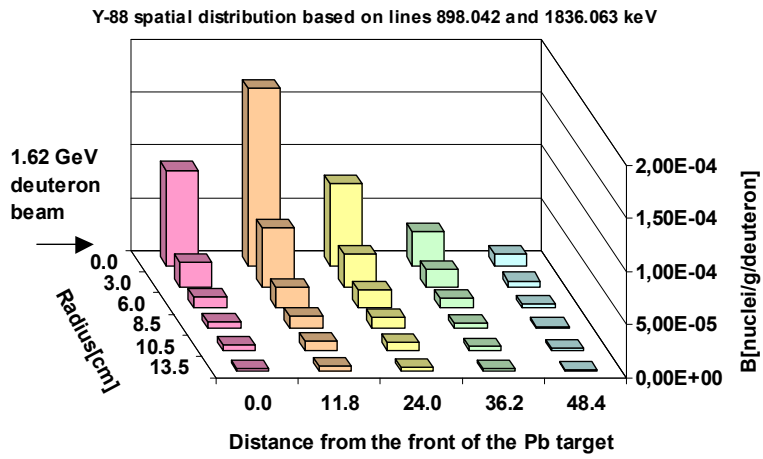


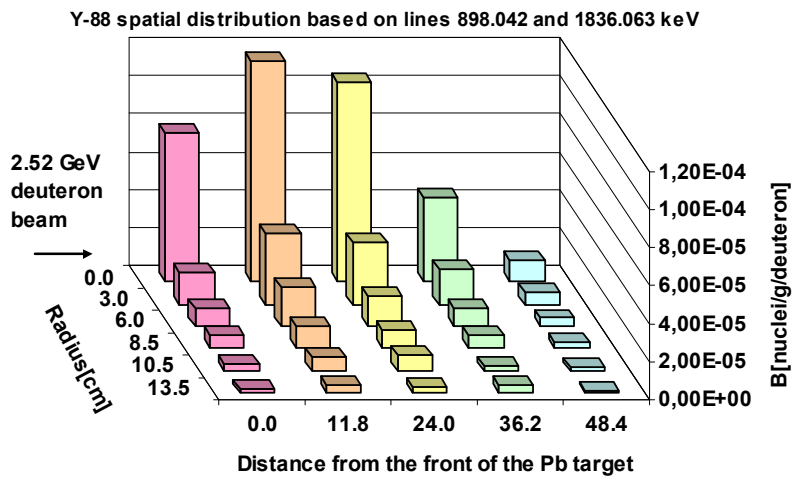
FIG. 10.20. Arrangement of the ^{89}Y detectors on the plastic foils for various planes in the Pb-U-Blanket target, Refs [10.6] and [10.7] (Courtesy of the Institute of Atomic Energy, Otwock-Świerk, Poland).

10.2.2.2. Experimental Spectroscopic Results for Pb-U-Blanket Target ($E_n > 10 \text{ MeV}$)

Measurements of the isotopes produced by neutrons generated in the Pb-U assembly from irradiations with deuteron beams of 1.62 GeV and 2.52 GeV yielded spatial distributions of ^{88}Y , ^{87}Y , and ^{86}Y isotope production in the assembly due to (n,xn) reactions. Numerical results are presented in Tables 10.2 (a) and 10.2 (b), as taken from Refs [10.6] and [10.7]. Spatial distributions of ^{88}Y , ^{87}Y , and ^{86}Y isotope production from (n,xn) reactions for $E_d = 1.62 \text{ GeV}$ are presented specifically in Table 10.2 (a) and Figs 10.21 (a), 10.22 (a) and 10.23 (a). The total number of incident 1.62 GeV deuterons is 2.08×10^{13} for an irradiation period of 24480 s. Spatial distributions of ^{88}Y , ^{87}Y , and ^{86}Y isotope production from (n,xn) reactions for $E_d = 2.52 \text{ GeV}$ are presented in Table 10.2 (b) and Figs 10.21 (b), 10.22 (b) and 10.23 (b). The total number of incident 2.52 GeV deuterons is 2.08×10^{13} for an irradiation period of 21 600 s.



a) 1.62 GeV deuteron beam



b) 2.52 GeV deuteron beam

FIG. 10.21. Spatial distribution (radial and axial) of ^{88}Y production (Courtesy of the Institute of Atomic Energy, Otwock-Świerk, Poland).

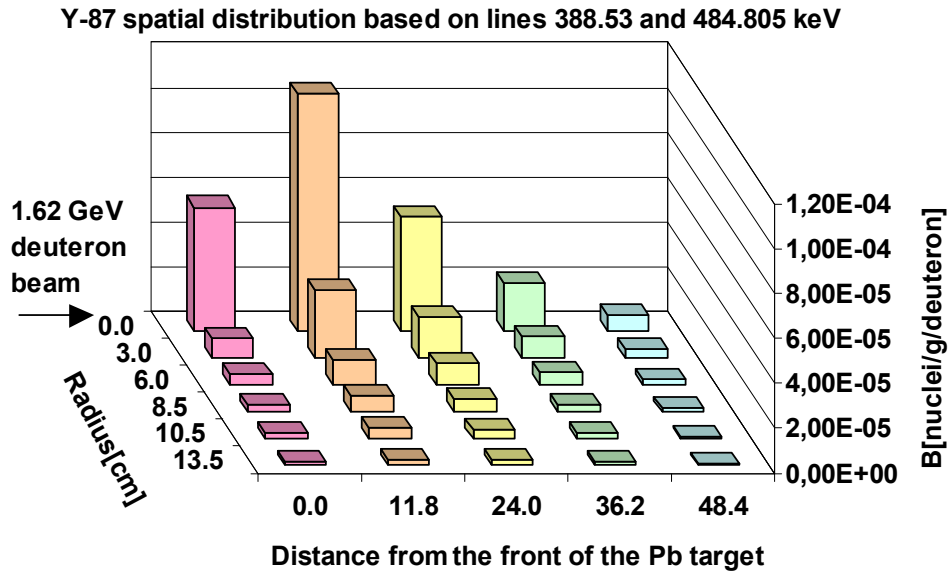
TABLE 10.2. SPATIAL DISTRIBUTIONS OF ^{88}Y , ^{87}Y AND ^{86}Y PRODUCED BY (N,XN)

 a) $E_d = 1.62 \text{ GeV}$

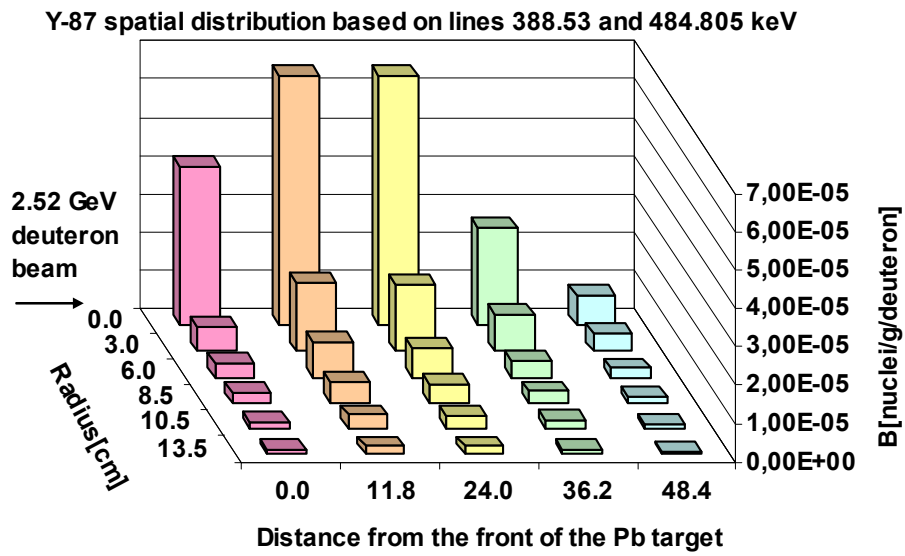
Residual nuclei, $T_{1/2}$, γ -lines used	Radius, (cm)	Axial position (cm)				
		0.0	11.8	24.0	36.2	48.4
^{88}Y $T_{1/2}=106.65 \text{ d}$, $E_\gamma=898.0$ and 1836.0 keV	0.0	9.00×10^{-5}	1.68×10^{-4}	7.80×10^{-5}	3.17×10^{-5}	1.07×10^{-5}
	3.0	2.30×10^{-5}	5.57×10^{-5}	3.15×10^{-5}	1.63×10^{-5}	5.55×10^{-6}
	6.0	1.09×10^{-5}	2.01×10^{-5}	1.65×10^{-5}	8.75×10^{-6}	3.95×10^{-6}
	8.5	7.00×10^{-6}	1.24×10^{-5}	1.04×10^{-5}	5.41×10^{-6}	2.35×10^{-6}
	10.5	4.67×10^{-6}	8.68×10^{-6}	7.06×10^{-6}	3.77×10^{-6}	1.79×10^{-6}
	13.5	2.61×10^{-6}	5.21×10^{-6}	3.70×10^{-6}	2.11×10^{-6}	1.11×10^{-6}
^{87}Y $T_{1/2}=3.32 \text{ d}$ $E_\gamma=388.5$ and 484.8 KeV	0.0	5.52×10^{-5}	1.05×10^{-4}	5.11×10^{-5}	2.15×10^{-5}	7.16×10^{-6}
	3.0	8.91×10^{-6}	3.05×10^{-5}	1.85×10^{-5}	9.78×10^{-6}	4.02×10^{-6}
	6.0	4.37×10^{-6}	1.08×10^{-5}	9.28×10^{-6}	5.24×10^{-6}	2.61×10^{-6}
	8.5	2.88×10^{-6}	6.75×10^{-6}	5.69×10^{-6}	3.08×10^{-6}	1.46×10^{-6}
	10.5	2.00×10^{-6}	4.52×10^{-6}	3.93×10^{-6}	2.14×10^{-6}	1.14×10^{-6}
	13.5	1.20×10^{-6}	2.62×10^{-6}	2.19×10^{-6}	1.27×10^{-6}	7.56×10^{-7}
^{86}Y $T_{1/2}=0.614 \text{ d}$ $E_\gamma=1076.0 \text{ keV}$	0.0	2.16×10^{-5}	3.89×10^{-5}	1.87×10^{-5}	8.18×10^{-6}	2.84×10^{-6}
	3.0	2.37×10^{-6}	1.03×10^{-5}	6.36×10^{-6}	3.72×10^{-6}	1.39×10^{-6}
	6.0	1.18×10^{-6}	3.43×10^{-6}	2.97×10^{-6}	1.77×10^{-6}	1.06×10^{-6}
	8.5	7.51×10^{-7}	2.05×10^{-6}	1.69×10^{-6}	1.15×10^{-6}	5.85×10^{-7}
	10.5	5.19×10^{-7}	1.29×10^{-6}	1.20×10^{-6}	7.15×10^{-7}	3.95×10^{-7}
	13.5	3.37×10^{-7}	7.53×10^{-7}	7.08×10^{-7}	4.32×10^{-7}	2.32×10^{-7}

 b) $E_d = 2.52 \text{ GeV}$

Residual nuclei, $T_{1/2}$, γ -lines used	Radius, radial distance (cm)	Axial position (cm)				
		0.0	11.8	24.0	36.2	48.4
^{88}Y $T_{1/2}=106.65 \text{ d}$ $E_\gamma=898.0$ and 1836.0 keV	0.0	7.83×10^{-5}	1.16×10^{-4}	1.05×10^{-4}	4.42×10^{-6}	1.15×10^{-5}
	3.0	1.63×10^{-5}	3.77×10^{-5}	3.26×10^{-5}	1.88×10^{-5}	6.45×10^{-6}
	6.0	9.66×10^{-6}	2.07×10^{-5}	1.57×10^{-5}	9.05×10^{-6}	4.20×10^{-6}
	8.5	7.29×10^{-6}	1.16×10^{-5}	9.91×10^{-6}	7.04×10^{-6}	3.41×10^{-6}
	10.5	3.85×10^{-6}	7.75×10^{-6}	8.30×10^{-6}	3.00×10^{-6}	1.37×10^{-6}
	13.5	2.33×10^{-6}	4.43×10^{-6}	3.14×10^{-6}	4.17×10^{-6}	1.19×10^{-6}
^{87}Y $T_{1/2}=3.32 \text{ d}$ $E_\gamma=388.5$ and 484.8 KeV	0.0	4.15×10^{-5}	6.56×10^{-5}	6.55×10^{-5}	2.55×10^{-5}	8.02×10^{-6}
	3.0	6.34×10^{-6}	1.82×10^{-5}	1.74×10^{-5}	9.58×10^{-6}	4.66×10^{-6}
	6.0	3.81×10^{-6}	9.38×10^{-6}	7.69×10^{-6}	4.44×10^{-6}	2.29×10^{-6}
	8.5	2.44×10^{-6}	5.58×10^{-6}	4.95×10^{-6}	2.95×10^{-6}	1.44×10^{-6}
	10.5	1.80×10^{-6}	3.51×10^{-6}	3.47×10^{-6}	2.11×10^{-6}	1.09×10^{-6}
	13.5	1.15×10^{-6}	1.97×10^{-6}	1.93×10^{-6}	1.31×10^{-6}	6.75×10^{-7}
^{86}Y $T_{1/2}=0.614 \text{ d}$ $E_\gamma=1076.0 \text{ keV}$	0.0	1.73×10^{-5}	2.44×10^{-5}	2.76×10^{-5}	1.15×10^{-5}	3.66×10^{-6}
	3.0	2.05×10^{-6}	5.20×10^{-6}	6.28×10^{-6}	3.21×10^{-6}	1.68×10^{-6}
	6.0	1.29×10^{-6}	2.78×10^{-6}	2.68×10^{-6}	1.69×10^{-6}	8.94×10^{-7}
	8.5	9.12×10^{-7}	1.59×10^{-6}	1.68×10^{-6}	1.15×10^{-6}	5.25×10^{-7}
	10.5	7.84×10^{-7}	9.07×10^{-7}	1.21×10^{-6}	7.80×10^{-7}	4.17×10^{-7}
	13.5	3.85×10^{-7}	5.52×10^{-7}	6.90×10^{-7}	5.51×10^{-7}	2.40×10^{-7}



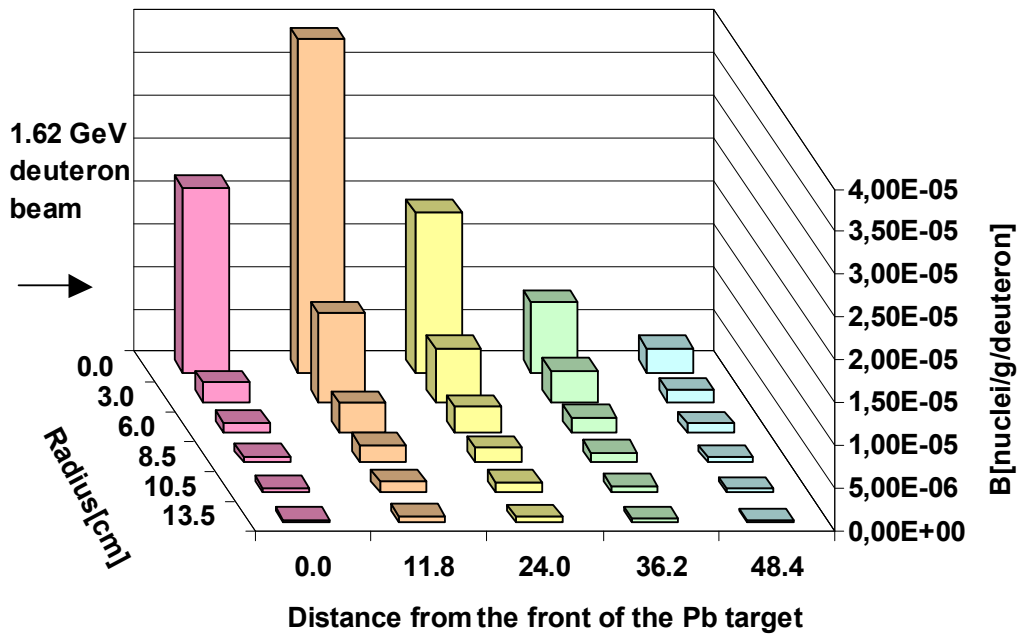
a) 1.62 GeV deuteron beam



b) 2.52 GeV deuteron beam

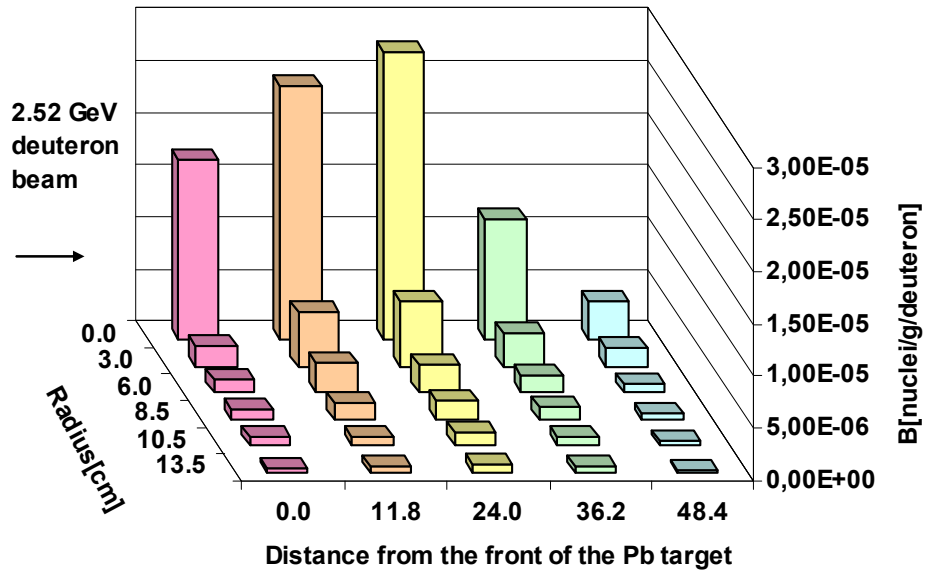
FIG. 10.22. Spatial distribution (radial and axial) of ^{87}Y production (Courtesy of the Institute of Atomic Energy, Otwock-Świerk, Poland).

Y-86 spatial distribution based on gamma line 1076.64 keV



a) 1.62 GeV deuteron beam

Y-86 spatial distribution based on gamma line 1076.64 keV



b) 2.52 GeV deuteron beam

FIG. 10.23. Spatial distribution (radial and axial) of ^{86}Y production (Courtesy of the Institute of Atomic Energy, Otwock-Świerk, Poland).

Figures 10.21 (b) – 10.23 (b) show that the axial isotope production distributions vary from one isotope to another. The ^{88}Y and ^{87}Y axial distributions exhibit maximum yields between the third foil (24.2 cm from the front side) and the second foil (11.8 cm), while the ^{86}Y isotope yields exhibit a maximum at the third foil (24.2 cm). On the other hand, the data from the experiment that corresponds to an irradiation of the Pb-U assembly with 1.65 GeV deuterons (Figs 10.21 (a) through 10.23 (a)) exhibit maxima in the axial distributions for the ^{88}Y , ^{87}Y and ^{86}Y isotopes at a position of about 12 cm from the target, Ref. [10.7].

Average high-energy neutron flux evaluation in the ^{89}Y detectors in the Pb-U assembly:

A precise characterization of the neutron fluxes at the yttrium detectors locations is not possible when the only experimental data available correspond to the production of ^{88}Y , ^{87}Y , and ^{86}Y isotopes by (n,xn) reactions. However, it is possible to make rough estimates of the average high-energy neutron flux values at each ^{89}Y detector location for three energy ranges by determining the production of ^{88}Y , ^{87}Y , and ^{86}Y isotopes per gram of sample and per incident deuteron at the specified positions allowed in the Pb-U assembly. The threshold energies, 11.5, 20.8 and 32.7 MeV, for the $^{89}\text{Y}(n,2n)^{88}\text{Y}$, $^{89}\text{Y}(n,3n)^{87}\text{Y}$ and $^{89}\text{Y}(n,4n)^{86}\text{Y}$ reactions, respectively, define the limits of the two lower energy ranges as well as the lower limit of the third range. Although the third energy range begins at 32.7 MeV, the upper end of that range is somewhat arbitrary. Effectively, it can be defined as that point in energy where the $^{89}\text{Y}(n,4n)^{86}\text{Y}$ cross-section value is small compared with the maximum cross-section value of this reaction. Based on this information, the average neutron fluxes $\overline{\phi}_1$ for the range 11.5–20.8 MeV, $\overline{\phi}_2$ for the range 20.8–32.7 MeV, and $\overline{\phi}_3$ for energies above 32.7 MeV can be estimated. Therefore, the ^{88}Y , ^{87}Y , and ^{86}Y production at the different locations provides spatial distributions for the three high-energy neutron flux ranges.

Yttrium (n,xn) cross-sections estimation:

In order to evaluate the high-energy neutron flux it is necessary to know the $^{89}\text{Y}(n,xn)$ cross-sections. The available experimental cross-section data for $^{89}\text{Y}(n,2n)^{88}\text{Y}$ and $^{89}\text{Y}(n,3n)^{87}\text{Y}$ reactions are shown in Figs 10.6 [10.4] and [10.5]. These are the only available experimental data for these two cross-sections, and it is clear that they are insufficient to adequately define the cross-sections over the entire energy range of interest.

Therefore, the TALYS code [10.6] and [10.7] has been used to calculate (n,xn) reactions cross-sections based on theoretical nuclear models. TALYS is a software system for the numerical simulation of nuclear reactions. Many state-of-the-art nuclear models are included to cover all the main reaction mechanisms encountered in light particle-induced nuclear reactions. TALYS generates fairly reliable nuclear data for applications in those situations where no experimental values exist. TALYS calculates total and partial cross-sections, energy spectra, angular distributions, double-differential spectra, residual nucleus production cross-sections, and light particle emission cross-sections.

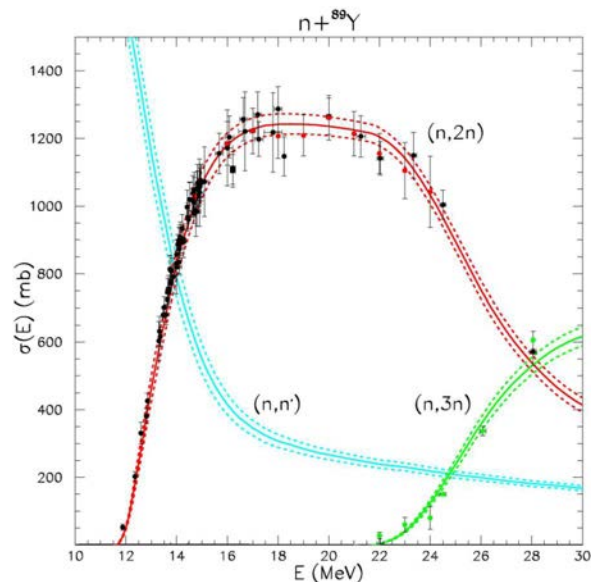


FIG. 10.24. Available $^{89}\text{Y}(n,2n)^{88}\text{Y}$ and $^{89}\text{Y}(n,3n)^{87}\text{Y}$ experimental data [10.8] and [10.9] (Courtesy of the Institute of Atomic Energy, Otwock-Świerk, Poland).

The TALYS code was used to generate cross-sections for several $^{89}\text{Y}(n,xn)$ reactions. The results are shown in Fig. 10.25. A comparison of experimental microscopic cross-sections for the reactions $^{89}\text{Y}(n,2n)^{88}\text{Y}$ and $^{89}\text{Y}(n,3n)^{87}\text{Y}$ with the generated microscopic cross-sections from TALYS for these two reactions shows very good agreement. This offered confidence that the results for the additional (n,xn) reactions associated with ^{89}Y are reasonably reliable, i.e. those for $^{89}\text{Y}(n,3n)^{87}\text{Y}$ and $^{89}\text{Y}(n,4n)^{86}\text{Y}$ for which measurements were also made in this work.

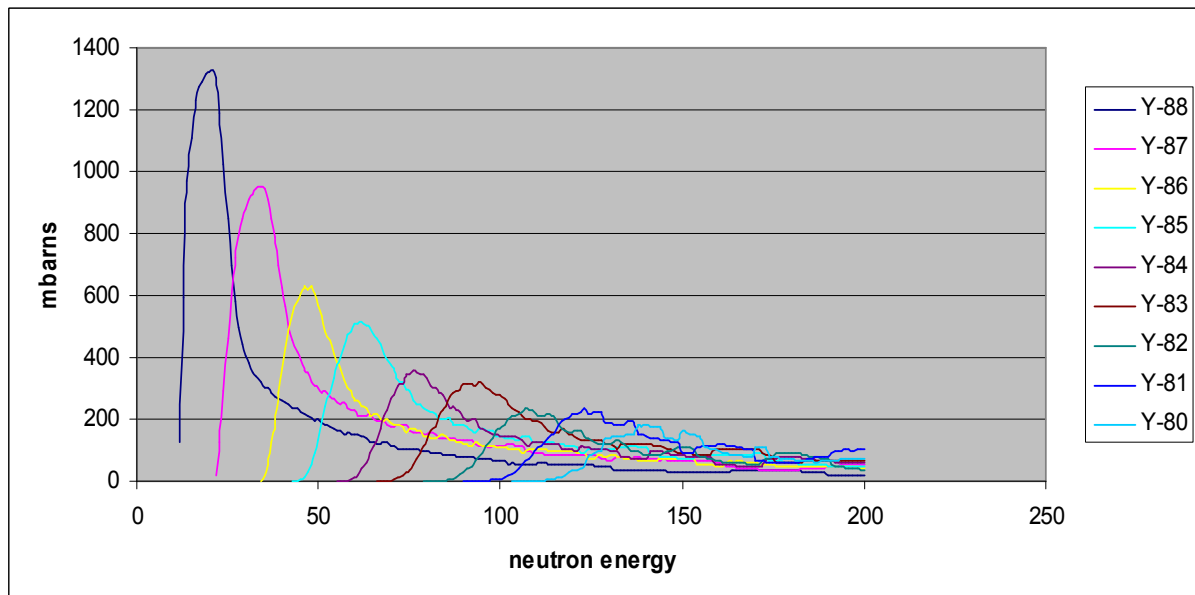


FIG. 10.25. $^{89}\text{Y}(n,xn)$ cross-sections from TALYS calculation (Courtesy of the Institute of Atomic Energy, Otwock-Świerk, Poland).

Derivation of the average neutron flux formula

In general, the number of yttrium isotopes (N_y) in the ^{89}Y detector of volume V_p in the chosen energy range can be expressed by the Eq. (10.1):

$$N_y = V_p \bar{\Phi} N \bar{\sigma} t \quad (10.1)$$

Where

$\bar{\Phi}$ is the average neutron flux in the chosen energy range [$\text{n/cm}^2 \cdot \text{s}$] $\bar{\Phi} = (E_2 - E_1) \bar{\Psi}$,

$$\bar{\Psi} = \frac{\int_{E_1}^{E_2} \Psi(E) dE}{E_2 - E_1};$$

$\Psi(E)$ is the neutron flux density [$\text{n/cm}^2 \cdot \text{s MeV}^{-1}$];

N is the number of ^{89}Y isotope atoms in volume unit [cm^{-3}];

$\bar{\sigma}$ is the average microscopic cross-section for the reaction (n, xn) in the energy range E_1 to E_2) [barns], $\bar{\sigma} = \frac{\int_{E_1}^{E_2} \sigma(E) dE}{E_2 - E_1}$;

σ is the microscopic cross-section for the reaction (n, xn);

t is the deuteron irradiation time.

Furthermore,

$$N = \frac{\rho_p}{G^{89}} A \quad (10.2)$$

Where

ρ_p is the specific weight of ^{89}Y ,

G^{89} is the gram-atom of ^{89}Y ,

A is the Avogadro's number.

It is assumed that the average neutron flux ($\bar{\Phi}$) in the chosen energy range is constant versus time during the deuteron irradiation. On the other hand, the number N_y of ^{88}Y , ^{87}Y , and ^{86}Y isotopes produced by (n, xn) reactions in the detector can be expressed as:

$$N_y = B^y W_p S \quad (10.3)$$

Where

B^y is the isotope production per one gram of sample and per one incident beam deuteron,

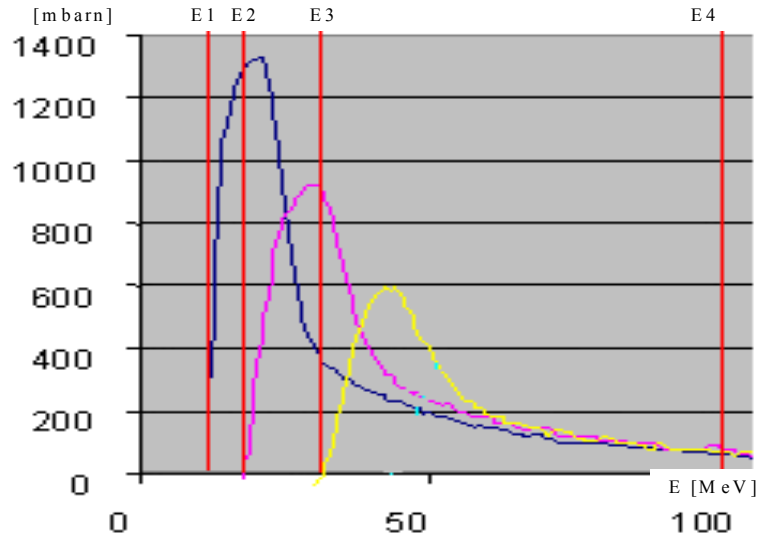
W_p is the weight of detector, $W_p = \rho_p V_p$;

S is the total number of deuterons.

Combining Eq. (10.1) with Eq. (10.3) yields the expression:

$$\bar{\phi} = \frac{B^y S G^{89}}{\bar{\sigma} A t} [\text{n/cm}^2 \cdot \text{s}]. \quad (10.4)$$

Eq. (10.4) pertains to only one assumed isotope. When three isotopes are considered it is necessary to solve three equations. First, the three energy ranges for the three average neutron fluxes which are of interest here have to be defined. Figure 10.26 illustrates the three energy ranges that pertain to the three average neutron fluxes which are of interest here.



FIG/ 10.26. Microscopic cross-sections for $^{89}\text{Y}(n,2n)^{88}\text{Y}$, $^{89}\text{Y}(n,3n)^{87}\text{Y}$, and $^{89}\text{Y}(n,4n)^{86}\text{Y}$ reactions generated by TALYS code are shown, and the three energy ranges for the three average neutron fluxes which are of interest are marked with vertical lines on the plot (Courtesy of the Institute of Atomic Energy, Otwock-Świerk, Poland).

The three average neutron fluxes, $\overline{\phi}_1, \overline{\phi}_2, \overline{\phi}_3$ which are of interest here are defined first by choosing the first three threshold energies $E_1=11.5$ MeV, $E_2=20.8$ MeV, and $E_3=32.7$ MeV for the reactions $^{89}\text{Y}(n, 2n)^{88}\text{Y}$, $^{89}\text{Y}(n, 3n)^{87}\text{Y}$ and $^{89}\text{Y}(n, 4n)^{86}\text{Y}$. Then, the fourth energy is chosen to be $E_4=100$ MeV since the microscopic cross-section at that energy is low when compared with the maximum cross-section for the $^{89}\text{Y}(n,4n)^{86}\text{Y}$ reaction. These assumptions enable the following three algebraic equations to be written:

$$B^{88}C = \overline{\phi}_1\overline{\sigma}_{11} + \overline{\phi}_2\overline{\sigma}_{12} + \overline{\phi}_3\overline{\sigma}_{13}, \quad (10.5)$$

$$B^{87}C = 0 + \overline{\phi}_2\overline{\sigma}_{22} + \overline{\phi}_3\overline{\sigma}_{23}, \quad (10.6)$$

$$B^{86}C = 0 + 0 + \overline{\phi}_3\overline{\sigma}_{33}. \quad (10.7)$$

Where

B^{88} , B^{87} , and B^{86} correspond to the measured yields of the isotopes ^{88}Y , ^{87}Y and ^{86}Y , respectively, per one gram of detector and per one incident beam deuteron;

$$C = \frac{SG^{89}}{At};$$

$\overline{\sigma}_{11} - \overline{\sigma}_{33}$ is the microscopic cross-section of the measured isotopes for the reaction (n,xn) in the three chosen energy ranges;

$\overline{\phi}_1, \overline{\phi}_2, \overline{\phi}_3$ is the unknown average neutron fluxes in the three chosen energy ranges.

Solution of the three equations above enables the average neutron fluxes in the three energy ranges to be evaluated. They are expressed in units $\text{n/cm}^2\cdot\text{s}$:

$$\overline{\phi}_1 = \frac{C}{\overline{\sigma}_{11}} \left[B^{88} - B^{87} \frac{\overline{\sigma}_{12}}{\overline{\sigma}_{22}} + B^{86} \left(\frac{\overline{\sigma}_{23} \overline{\sigma}_{12}}{\overline{\sigma}_{33} \overline{\sigma}_{22}} - \frac{\overline{\sigma}_{13}}{\overline{\sigma}_{33}} \right) \right], \quad (10.8)$$

$$\overline{\phi}_2 = \frac{C}{\overline{\sigma}_{22}} \left[B^{87} - B^{86} \frac{\overline{\sigma}_{23}}{\overline{\sigma}_{33}} \right], \quad (10.9)$$

$$\overline{\phi}_3 = \frac{C}{\overline{\sigma}_{33}} B^{86}. \quad (10.10)$$

The number of measured isotopes in the detector establishes the number of algebraic equations, and that determines the number of unknown neutron fluxes in the chosen neutron energy ranges which can be evaluated. More measured isotopes by the detector improves the evaluation of the high-energy neutron spectrum. For 'n' measured isotopes, this leads to the following set of equations:

$$\begin{bmatrix} B^1 \\ \vdots \\ B^i \\ \vdots \\ B^n \end{bmatrix} = \frac{1}{c} \begin{bmatrix} \overline{\sigma_{11}} & \cdots & \overline{\sigma_{1k}} & \cdots & \overline{\sigma_{1n}} \\ \vdots & & \vdots & & \vdots \\ \overline{\sigma_{i1}} & \cdots & \overline{\sigma_{ik}} & \cdots & \overline{\sigma_{in}} \\ \vdots & & \vdots & & \vdots \\ \overline{\sigma_{n1}} & \cdots & \overline{\sigma_{nk}} & \cdots & \overline{\sigma_{nn}} \end{bmatrix} \begin{bmatrix} \overline{\phi_1} \\ \vdots \\ \overline{\phi_i} \\ \vdots \\ \overline{\phi_n} \end{bmatrix} \quad (10.11)$$

Where

$B^1 \dots B^i \dots B^n$ are the measured isotopes per one gram of detector and per one beam deuteron;

$\overline{\sigma_{11}} \dots \overline{\sigma_{1k}} \dots \overline{\sigma_{1n}}$ is the average microscopic cross-section of the measured isotopes for the reaction (n, xn) in the chosen energy ranges,

$\overline{\phi_1} \dots \overline{\phi_i} \dots \overline{\phi_n}$ is the unknown average neutron fluxes in the chosen energy ranges.

High-energy neutron flux evaluation:

The average high-energy neutron flux in the ^{89}Y detectors location inside the Pb-U assembly for the three energy ranges 11.5–20.8 MeV, 20.8–32.7 MeV, and 32.7–100 MeV, were evaluated using the microscopic cross-sections for the reactions $^{89}\text{Y}(n,2n)^{88}\text{Y}$, $^{89}\text{Y}(n,3n)^{87}\text{Y}$, and $^{89}\text{Y}(n,4n)^{86}\text{Y}$ generated by the TALYS code and using the available experimental data. The spatial neutron flux distributions in the Pb-U assembly for the three energy ranges are presented in Tables 10.3 (a) and 10.3 (b), and Figs 10.27 (a) through 10.29 (a) and 10.27 (b) through 10.29 (b) (6 plots), for deuteron beam energies 1.62 GeV and 2.52 GeV, respectively

TABLE 10.3. EVALUATED NEUTRON-FLUX DISTRIBUTION IN THE PB-U ASSEMBLY FOR THREE ENERGY RANGES

(a) Deuteron beam energy of 1.62 GeV

Deuteron energy (1.62 GeV)	Radial position (cm)	Neutron flux from ⁸⁹ Y detectors Axial position (cm)				
		0.0	11.8	24.0	36.2	48.4
FLUX 1 From 11.5 MeV To 20.8 MeV (delta 9.3 MeV)	0.0	1.95×10^6	3.52×10^6	1.70×10^6	7.40×10^5	2.57×10^5
	3.0	2.14×10^5	9.36×10^5	5.75×10^5	3.37×10^5	1.26×10^5
	6.0	1.06×10^5	3.11×10^5	2.68×10^5	1.60×10^5	9.57×10^4
	8.5	6.80×10^4	1.85×10^5	1.53×10^5	1.04×10^5	5.29×10^4
	10.5	4.69×10^4	1.17×10^5	1.08×10^5	6.47×10^4	3.57×10^4
	13.5	3.05×10^4	6.81×10^4	6.40×10^4	3.91×10^4	2.09×10^4
FLUX 2 From 20.8 MeV to 32.7 MeV (delta 11.9 MeV)	0.0	6.06×10^6	1.21×10^7	5.89×10^6	2.41×10^6	7.75×10^5
	3.0	1.24×10^6	3.71×10^6	2.23×10^6	1.10×10^6	4.83×10^5
	6.0	6.03×10^5	1.37×10^6	1.17×10^6	6.38×10^5	2.78×10^5
	8.5	4.02×10^5	8.76×10^5	7.47×10^5	3.50×10^5	1.57×10^5
	10.5	2.80×10^5	6.07×10^5	5.09×10^5	2.63×10^5	1.37×10^5
	13.5	1.61×10^5	3.50×10^5	2.74×10^5	1.54×10^5	9.78×10^4
FLUX 3 From 32.7 MeV tot 100 MeV (delta 67.3 MeV)	0.0	1.07×10^7	1.93×10^7	9.27×10^6	4.04×10^6	1.40×10^6
	3.0	1.17×10^6	5.11×10^6	3.14×10^6	1.84×10^6	6.88×10^5
	6.0	5.81×10^5	1.70×10^6	1.47×10^6	8.77×10^5	5.23×10^5
	8.5	3.71×10^5	1.01×10^6	8.36×10^5	5.66×10^5	2.89×10^5
	10.5	2.56×10^5	6.38×10^5	5.91×10^5	3.53×10^5	1.95×10^5
	13.5	1.67×10^5	3.72×10^5	3.50×10^5	2.14×10^5	1.14×10^5

(b) Deuteron beam energy of 2.52 GeV.

Deuteron energy (2.52 GeV)	Radial position (cm)	Neutron flux from ⁸⁹ Y detectors Axial position (cm)				
		0.0	11.8	24.0	36.2	48.4
FLUX 1 from 11.5 MeV To 20.8 MeV (delta 9.3 MeV)	0.0	5.51×10^5	7.77×10^5	8.77×10^5	3.67×10^5	1.16×10^5
	3.0	6.53×10^4	1.65×10^5	2.00×10^5	1.02×10^5	5.35×10^4
	6.0	4.09×10^4	8.84×10^4	8.52×10^4	5.38×10^4	2.84×10^4
	8.5	2.90×10^4	5.06×10^4	5.35×10^4	3.66×10^4	1.67×10^4
	10.5	2.49×10^4	2.88×10^4	3.86×10^4	2.48×10^4	1.33×10^4
	13.5	1.22×10^4	1.75×10^4	2.20×10^4	1.75×10^4	7.64×10^3
FLUX 2 from 20.8 MeV to 32.7 MeV (delta 11.9 MeV)	0.0	1.51×10^6	2.63×10^6	2.36×10^6	8.53×10^5	2.66×10^5
	3.0	2.79×10^5	8.56×10^5	7.13×10^5	4.13×10^5	1.91×10^5
	6.0	1.63×10^5	4.34×10^5	3.23×10^5	1.74×10^5	8.82×10^4
	8.5	9.73×10^4	2.63×10^5	2.11×10^5	1.14×10^5	5.88×10^4
	10.5	6.30×10^4	1.73×10^5	1.45×10^5	8.46×10^4	4.30×10^4
	13.5	4.98×10^4	9.40×10^4	7.98×10^4	4.74×10^4	2.79×10^4
FLUX 3 from 32.7 MeV to 100 MeV (delta 67.3 MeV)	0.0	3.01×10^6	4.24×10^6	4.79×10^6	2.00×10^6	6.36×10^5
	3.0	3.57×10^5	9.03×10^5	1.09×10^6	5.57×10^5	2.92×10^5
	6.0	2.23×10^5	4.83×10^5	4.65×10^5	2.94×10^5	1.55×10^5
	8.5	1.58×10^5	2.76×10^5	2.93×10^5	2.00×10^5	9.12×10^4
	10.5	1.36×10^5	1.57×10^5	2.11×10^5	1.35×10^5	7.24×10^4
	13.5	6.69×10^4	9.59×10^4	1.20×10^5	9.57×10^4	4.17×10^4

The following average microscopic cross-sections for the reactions $^{89}\text{Y}(n,2n)^{88}\text{Y}$, $^{89}\text{Y}(n,3n)^{87}\text{Y}$, and $^{89}\text{Y}(n,4n)^{86}\text{Y}$, corresponding to the three chosen energy ranges, were used to generate the preceding two tables:

$$\overline{\sigma}_{11}=1.17 \times 10^{-24} \text{ cm}^2 \text{ for } ^{89}\text{Y}(n,2n)^{88}\text{Y} \text{ reaction in the energy range } 1.5 - 20.8 \text{ MeV};$$

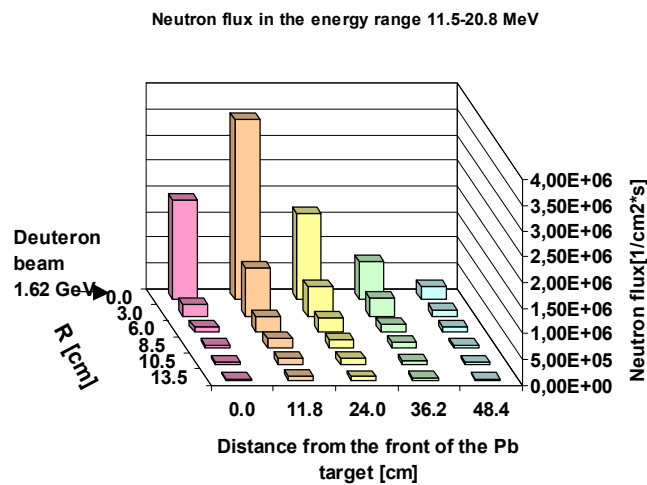
$$\overline{\sigma}_{12}=7.83 \times 10^{-25} \text{ cm}^2 \text{ for } ^{89}\text{Y}(n,2n)^{88}\text{Y} \text{ reaction in the energy range } 20.8 - 32.7 \text{ MeV};$$

$$\overline{\sigma}_{13}=1.53 \times 10^{-25} \text{ cm}^2 \text{ for } ^{89}\text{Y}(n,2n)^{88}\text{Y} \text{ reaction in the energy range } 32.7 - 100 \text{ MeV};$$

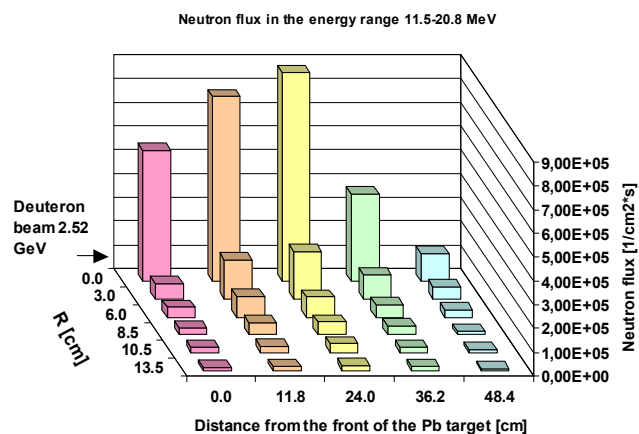
$$\overline{\sigma}_{22}=6.27 \times 10^{-25} \text{ cm}^2 \text{ for } ^{89}\text{Y}(n,3n)^{87}\text{Y} \text{ reaction in the energy range } 20.8 - 32.7 \text{ MeV};$$

$$\overline{\sigma}_{23}=2.94 \times 10^{-25} \text{ cm}^2 \text{ for } ^{89}\text{Y}(n,3n)^{87}\text{Y} \text{ reaction in the energy range } 32.7 - 100 \text{ MeV};$$

$$\overline{\sigma}_{33}=2.54 \times 10^{-25} \text{ cm}^2 \text{ for } ^{89}\text{Y}(n,4n)^{86}\text{Y} \text{ reaction in the energy range } 32.7 - 100 \text{ MeV}.$$

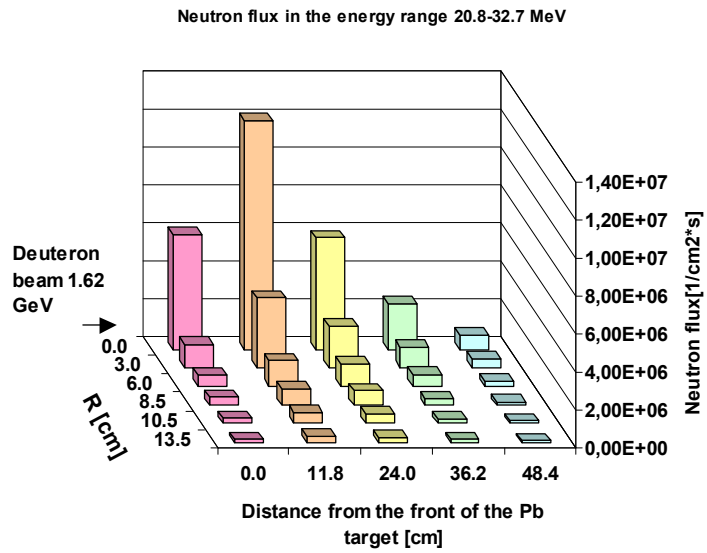


a) 1.62 GeV deuteron beam

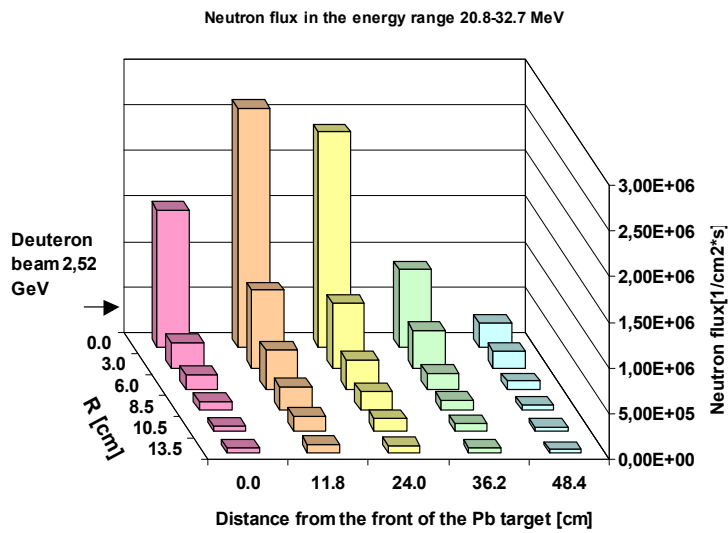


b) 2.52 GeV deuteron beam

FIG. 10.27 Spatial neutron-flux distribution in the Pb-U assembly for the neutron energy range 11.5–20.8 MeV with deuteron beam energy of 1.62 GeV (Courtesy of the Institute of Atomic Energy, Otwock-Świerk, Poland).



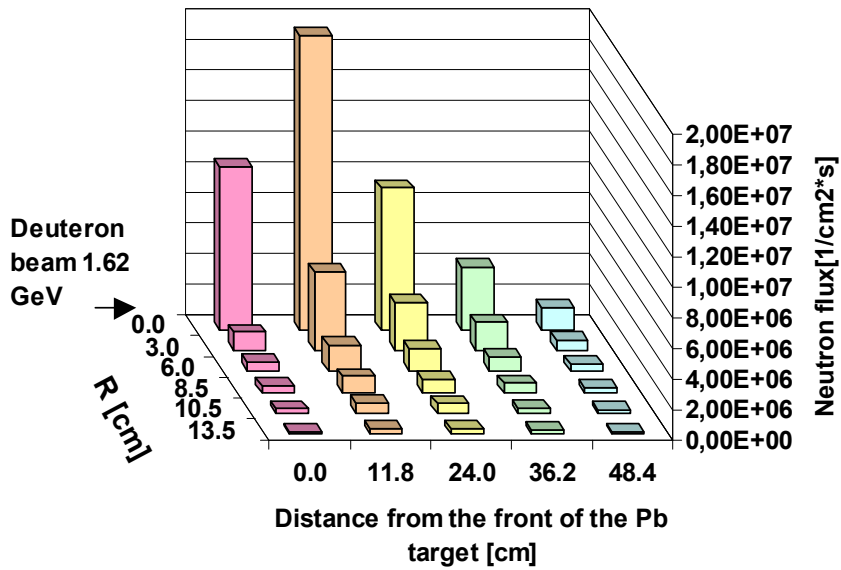
a) 1.62 GeV deuteron beam



b) 2.52 GeV deuteron beam

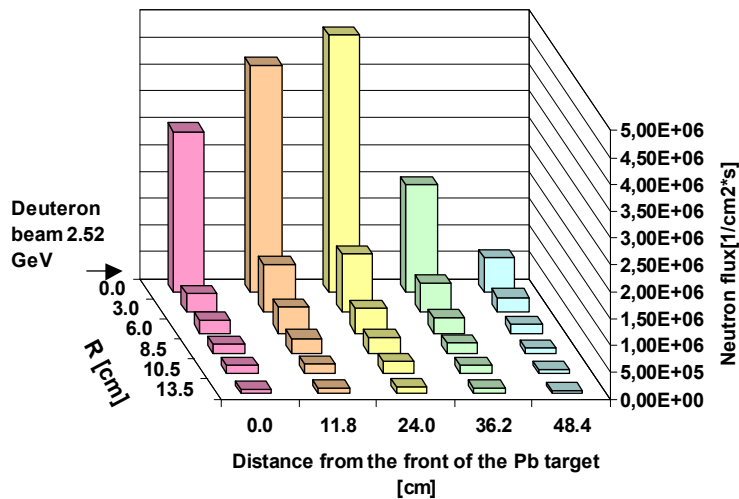
FIG. 10.28 Spatial neutron-flux distribution in the Pb-U assembly for the neutron energy range 20.8–32.7 MeV with deuteron beam energy of 1.62 GeV (Courtesy of the Institute of Atomic Energy, Otwock-Świerk, Poland).

Neutron flux in the energy range 32.7-100 MeV



a) 1.62 GeV deuteron beam

Neutron flux in the energy range 32.7-100 MeV



b) 2.52 GeV deuteron beam

FIG. 10.29. Spatial neutron-flux distribution in the Pb-U assembly for the neutron energy range 32.7–100 MeV with deuteron beam energy of 2.52 GeV (Courtesy of the Institute of Atomic Energy, Otwock-Świerk, Poland).

The shapes of the spatial distributions of ^{88}Y , ^{87}Y , and ^{86}Y isotopes generated in the ^{89}Y detectors positioned in the Pb-U assembly are similar to the shapes of the evaluated average high-energy neutron fluxes in the ^{89}Y detectors. The only exception is a small deviation that is observed in the case of the higher-energy 2.52 GeV deuterons.

10.3. NUMERICAL SIMULATIONS

10.3.1. Transmutation of minor actinides and fission products nuclei

10.3.1.1. Introduction

Subcritical calculations were performed using the Monte Carlo code MCNP4 for two configurations, referred to as setups. The stand was placed in front of the Horizontal Channel of the MARIA Research Reactor. The thermal neutron beam extracted from the MARIA research reactor was used to drive the subcritical assembly. The generated spatial neutron flux distributions were calculated. The total and resonance neutron fluxes were obtained from these calculations. The computational results were always normalized to one external source neutron.

10.3.1.2. Geometrical Model

Two geometrical models were developed for the Monte Carlo calculations using the MCNP4 code. The difference between the two geometrical models is the stand under the converter, either lead or graphite. Figures 10.30 and 10.31 are schematic diagrams of the converter geometry. For each stand, the central EK-10 type fuel rod was shifted so half of the fuel rod length is outside the converter as shown in Fig. 10.32. Therefore the calculations were performed for four configurations.

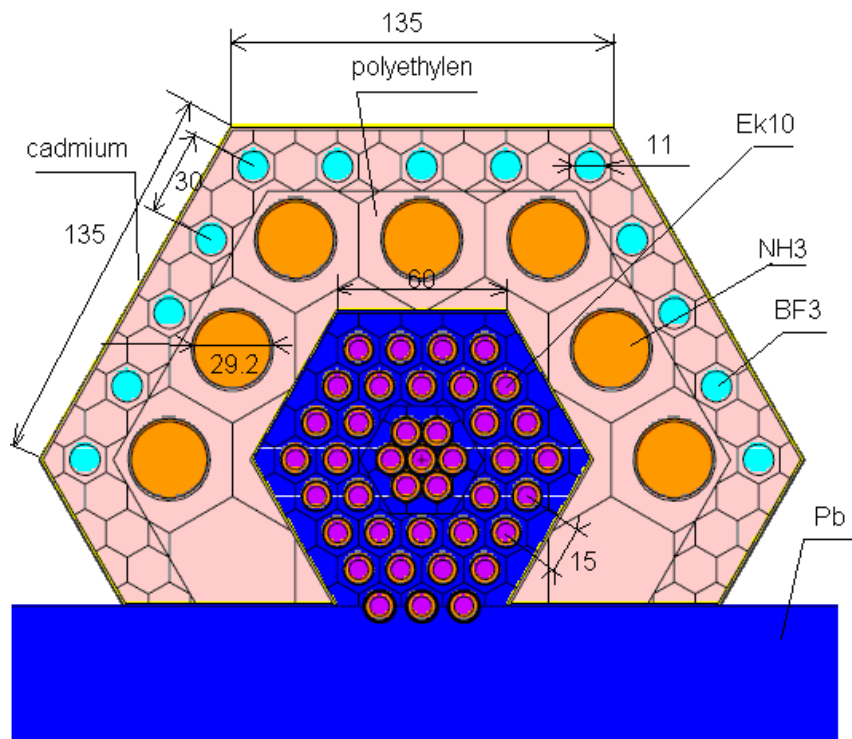


FIG. 10.30. Simplified geometrical model of the converter (Courtesy of the Institute of Atomic Energy, Otwock-Świerk, Poland).

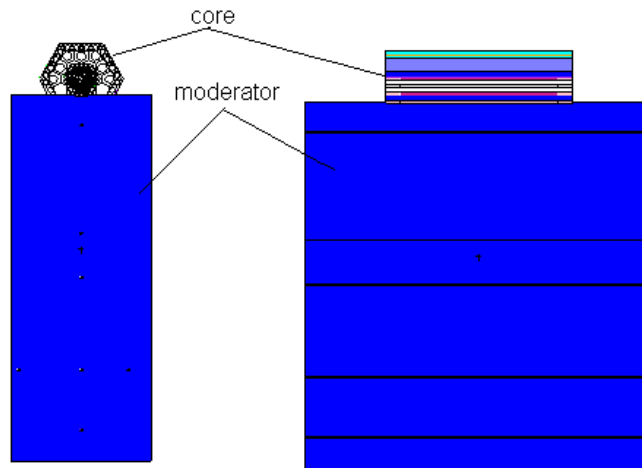


FIG. 10.31. Overall view of the stand and converter assembly where the moderator is lead or graphite material (Courtesy of the Institute of Atomic Energy, Otwock-Świerk, Poland).

The origin of the XYZ coordinate system for the neutron moderator in Fig. 10.31 was defined to be in the centre of the top surface of the block. The X and Y axes are perpendicular to the fuel elements, while the Z axis is parallel to the fuel elements. The calculated neutron flux spatial distributions are shown in Figs 10.33–10.41.

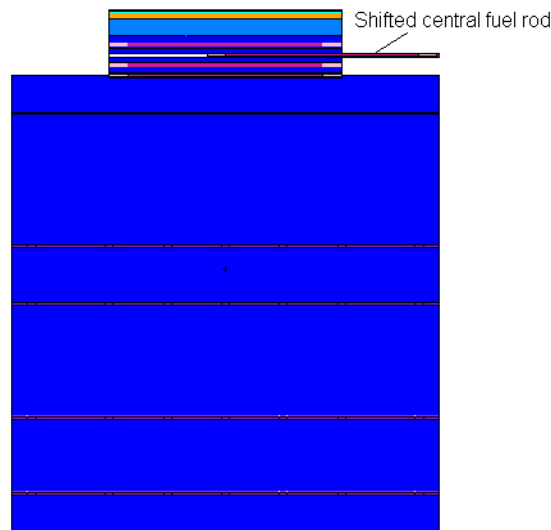


FIG. 10.32. Overall view of the stand and converter assembly with central fuel rod shifted where the moderator is lead or graphite material (Courtesy of the Institute of Atomic Energy, Otwock-Świerk, Poland).

10.3.1.3. Calculated neutron flux distributions for the lead and the graphite moderators

Converter with lead moderator:

For the converter with the lead moderator, the effective multiplication factor k_{eff} is 0.20196 with a standard deviation of 0.00131. The average number of neutrons per source particle is equal to 2.3489.

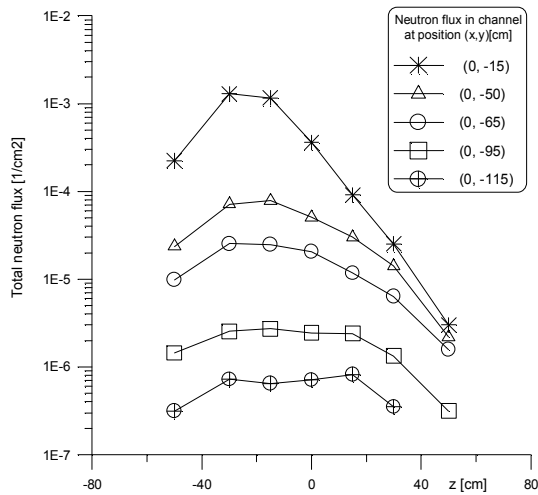


FIG. 10.33. Spatial distribution of the total neutron flux in the lead moderator, the total neutron flux is normalized per one external neutron (Courtesy of the Institute of Atomic Energy, Otwock-Świerk, Poland).

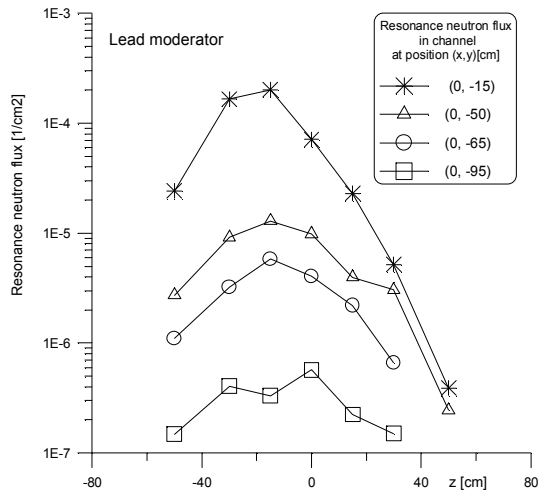


FIG. 10.34. Spatial distribution of the resonance neutron 1 eV–10 keV flux in the lead moderator, the resonance neutron flux is normalized per one external neutron (Courtesy of the Institute of Atomic Energy, Otwock-Świerk, Poland).

Converter with graphite moderator:

For the converter with the graphite moderator, the effective multiplication factor k_{eff} is 0.20566 with a standard deviation of 0.00040. The average number of neutrons per source particle is equal to 2.3538.

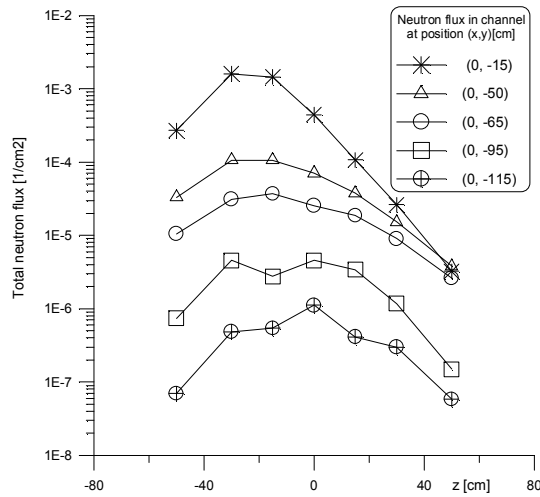


FIG. 10.35. Spatial distribution of the total neutron flux in the graphite moderator, the total neutron flux is normalized per one external neutron (Courtesy of the Institute of Atomic Energy, Otwock-Świerk, Poland).

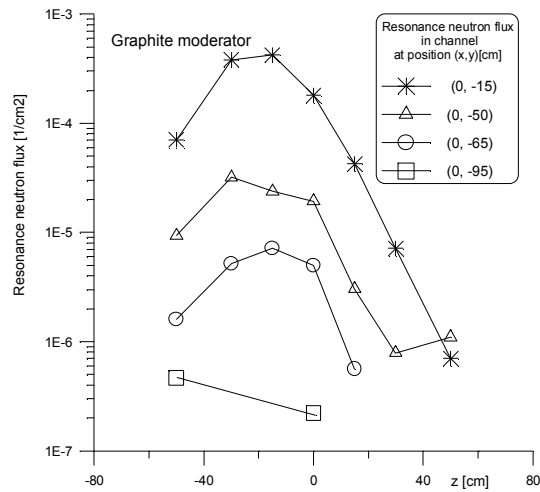


FIG. 10.36. Spatial distribution of the resonance neutron 1 eV–10 keV flux in the graphite moderator, the resonance neutron flux is normalized per one external neutron (Courtesy of the Institute of Atomic Energy, Otwock-Świerk, Poland).

Converter with lead moderator and shifted central fuel rod:

For the converter with the lead moderator and shifted central fuel rod, the average number of neutrons per source particle is equal to 2.9204.

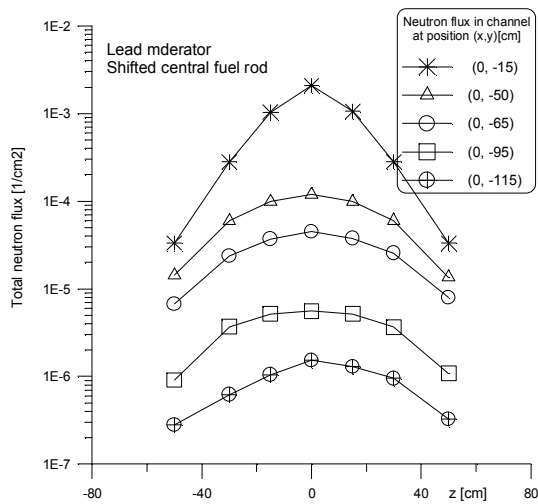


FIG. 10.37. Spatial distribution of the total neutron flux in the lead moderator, the total neutron flux is normalized per one external neutron (Courtesy of the Institute of Atomic Energy, Otwock-Świerk, Poland).

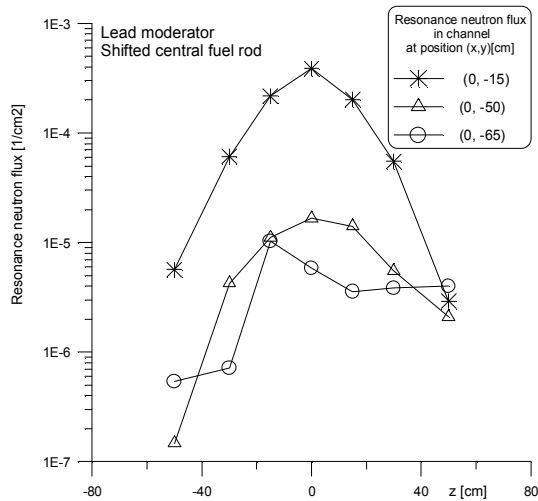


FIG. 10.38. Spatial distribution of the resonance neutron 1 eV–10 keV flux in the lead moderator, the resonance neutron flux is normalized per one external neutron (Courtesy of the Institute of Atomic Energy, Otwock-Świerk, Poland).

Converter with graphite moderator and shifted central fuel rod:

For the converter with the graphite moderator and shifted central fuel rod, the average number of neutrons per source particle is equal to 2.9322.

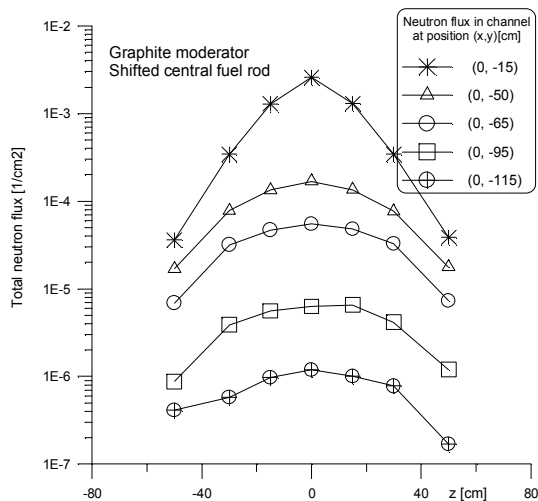


FIG. 10.39. Spatial distribution of the total neutron flux in the graphite moderator, the total neutron flux is normalized per one external neutron (Courtesy of the Institute of Atomic Energy, Otwock-Świerk, Poland).

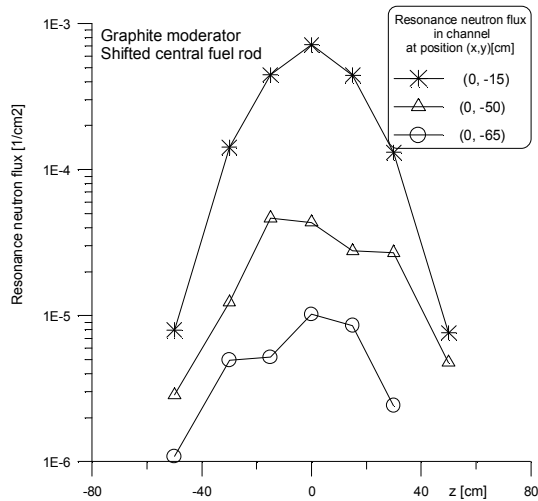


FIG. 10.40. Spatial distribution of the resonance neutron (1 eV-10 keV) flux in the graphite moderator, the resonance neutron flux is normalized per one external neutron (Courtesy of the Institute of Atomic Energy, Otwock-Świerk, Poland).

Comparison of resonance neutron-flux distributions at the (0,-15) position for the four configurations presented above:

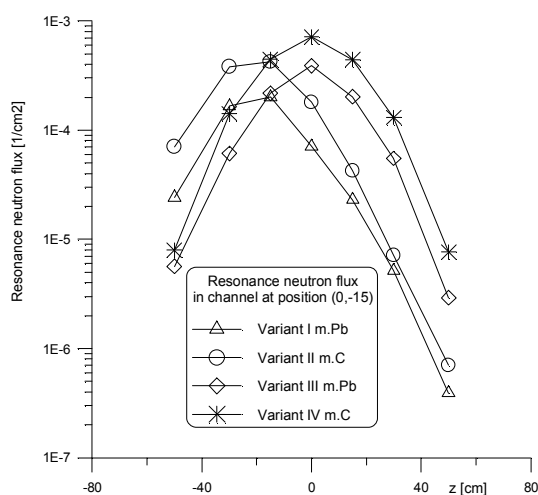


FIG. 10.41. Comparison of resonance neutron-flux distributions at (0,-15) position for the four different versions, the resonance neutron flux is normalized per one external neutron (Courtesy of the Institute of Atomic Energy, Otwock-Świerk, Poland).

10.4. CONCLUSIONS

The present calculations show that the interesting neutron energy range 1 eV–10 keV, where the neutron absorption and neutron fission cross-sections for several important LLFP and MA exhibit resonance structure, can be investigated in the proposed facility at the MARIA reactor. The installation of a fission converter in the reflector of the MARIA reactor core produces a reasonable neutron flux value in the energy range of 1 eV–10 keV.

The neutron flux spatial distributions obtained from neutrons produced by the interaction of deuterons with the Pb-U assembly depend on the deuteron energies. The spatial neutron-flux distribution exhibits a maximum on the third foil position (24.2 cm) and the second foil position (11.8 cm) for the deuteron beam energies of 2.52, and 1.62 GeV, respectively. In order to verify this observation, further measurements should be made at different energies.

The spatial distributions of ^{88}Y , ^{87}Y , and ^{86}Y radioactive isotopes produced in the Pb-U assembly from irradiating ^{89}Y due to the use of 1.62 GeV and 2.52 GeV deuterons are similar to the evaluated average high-energy neutron flux. However, a small deviation is observed for the 2.52 GeV deuterons.

In contrast to the experimental data, the Monte Carlo simulation calculations show the maximum neutron flux distributions for both deuteron energies (1.62 GeV and 2.52 GeV) at a distance of about 12 cm from the front surface of the lead target. Further investigations are warranted to resolve this discrepancy between the experimental and the calculated results.

REFERENCES TO SECTION 10

- [10.1] HAAS, D., “The Fuel Development Programme ADS at ITU”, R&D Activity in Support of ADS Development, Mol, Belgium, (2000).
- [10.2] JAMESON, R.A., LAWRENCE, G.P., BOWMAN, C.D., “Accelerator-Driven Transmutation Technology for Incinerating Radioactive Waste and for Advanced Application to Power Production”, Nucl. Instrum. Methods **B68**, (1992) 474.
- [10.3] WAN, J.S., et al., “Transmutation of ^{239}Pu with Spallation Neutrons”, J. Radioanalytical Nucl. Chemistry **247**, (2001) 151.

- [10.4] PYTEL, K., OWSIANKO, ANDRZEJEWSKI, I.K., Reconstruction of the BNCT (Boron neutron capture therapy) Channel in the MARIA Reactor, IAEA internal report (in Polish), (2008).
- [10.5] KRIVOPUSTOV, M., et al., "On a First Experiment on the Calorimetry of the Uranium Blanket Using the Model of the U/Pb Electro-Nuclear Assembly 'Energy plus Transmutation' on a 1.5 GeV Proton Beam of the Dubna Synchrophasotron, JINR Preprint P1-2000-168, Dubna, 2000", *Kerntechnik* **68**, (2003) 48-55.
- [10.6] KRIVOPUSTOV, M., et al., "First Results Studying the Transmutation of ^{129}I , ^{237}Np , ^{238}Pu and ^{239}Pu in the Irradiation of an Extended NatU/Pb-Assembly with 2.52 GeV Deuterons", *J. Radioanalytical Nucl. Chemistry* **279**, (2009) 567-584.
- [10.7] BIELEWICZ, M., KILIM, S., STRUGALSKA-GOLA, E., SZUTA, M., WOJCIECHOWSKI, A., KRIVOPUSTOV, M. I., PAVLIOUK, A.V., ADAM, I., KRASA, A., KUGLER, A., MAJERLE, M., WAGNER, V., "On Results of Y-89 Irradiation with Deuteron Beam on U/Pb-assembly 'Energy Plus Transmutation' using Nuclotron (JINR, Dubna)", *The XVIII Int. Baldin Seminar on High Energy Physics Problems, Dubna, Sep. 25 - 30, 2006*.
- [10.8] HILAIRE, S., *Statistical Nuclear Reaction Modeling, DIF/DPTA/SPN/LMED, Trieste, 2008*.
- [10.9] *Experimental Nuclear Reaction Data, EXFOR/CSISRS*.

RELATED IAEA PUBLICATIONS

IAEA-TECDOC-233, Research Reactor Core Conversion from the Use of Highly Enriched Uranium to the Use of Low Enriched Uranium Fuels Guidebook, 1980.

IAEA TECDOC-643, Research Reactor Core Conversion Guidebook, Volumes 1-5: Summary, Analysis, Analytical Verification, Fuels, and Operations, April 1992.

IAEA-TECDOC-1593, Return of Research Reactor Spent Fuel to the Country of Origin: Requirements for Technical and Administrative Preparations and National Experiences, Proceedings of a technical meeting held in Vienna, August 28-31, 2006, published in January 2009.

IAEA SAFETY STANDARDS SERIES No. NS-R-4, Safety Of Research Reactors, Safety Requirements. IAEA, Vienna, 2005.

IAEA SAFETY STANDARDS SERIES No. NS-G-2.12, Ageing Management For Nuclear Power Plants, Safety Guide. IAEA, Vienna, 2009.

IAEA SAFETY STANDARDS SERIES No. NS-G-27, Criticality Safety in the Handling of Fissile Material, IAEA, Vienna, 2014.

INTERNATIONAL ATOMIC ENERGY AGENCY, Nuclear Data Services,

<https://www-nds.iaea.org/>.

ADS CRP 1st phase TECDOC

CONTRIBUTORS TO DRAFTING AND REVIEW

Adelfang, P.	International Atomic Energy Agency
Aliberti, G.	Argonne National Laboratory, USA
Antunes, A.	Instituto de Pesquisas Energeticas e Nucleares- Universidade de Sao Paulo (IPEN-USP), Brazil
Avramović, I.	Vinca Institute of Nuclear Sciences, Serbia
Bajpai, A.	Bhabha Atomic Research Centre, India
Beličev, P.	Vinca Institute of Nuclear Sciences, Serbia
Bolshinsky, I.	National Nuclear Security Administration – Department of Energy, USA
Bournos, V.	Joint Institute for Power and Nuclear Research - Sosny, Belarus
Cao, J.	China Institute of Atomic Energy, China
Carta, M.	National agency for new technologies, energy and sustainable economic development (ENEA), Italy
Carluccio, T.	Instituto de Pesquisas Energeticas e Nucleares- Universidade de Sao Paulo (IPEN-USP), Brazil
Cintas, A.	Unidad de Energía Nuclear (CNEA) - Instituto Balseiro, Argentina
Degweker, S.B.	Bhabha Atomic Research Centre, India
Fokov, Y.	Joint Institute for Power and Nuclear Research - Sosny, Belarus
Gohar, Y.	Argonne National Laboratory, USA
Haicheng, W.	China Institute of Atomic Energy, China
Jammes, C.	The French Alternative Energies and Atomic Energy Commission (CEA), France
Karnaukhov, I.	National Science Centre Kharkov Institute of Science and Technology, Ukraine
Kilim, S.	Institute of Atomic Energy, Poland
Kim, C.H.	Seoul National University, Republic of Korea
Kiyavitskaya, H.	Joint Institute for Power and Nuclear Research – Sosny, Belarus
Kulkarni, K.	Bhabha Atomic Research Centre, India
Lee, S.M.	Instituto de Pesquisas Energeticas e Nucleares- Universidade de Sao Paulo (IPEN-USP), Brazil
Lopasso, E.M.	Unidad de Energía Nuclear (CNEA) - Instituto Balseiro, Argentina
Luo, H.	China Institute of Atomic Energy, China
Maiorino, J.R.	Instituto de Pesquisas Energeticas e Nucleares- Universidade de Sao Paulo (IPEN-USP), Brazil

Márquez Damián, J.I.	Unidad de Energía Nuclear (CNEA) - Instituto Balseiro, Argentina
Martina, M.	Politecnico di Torino, Italy
Masood, I.	Pakistan Institute of Nuclear Science and Technology (PINSTECH), Pakistan
Modak, R.S.	Bhabha Atomic Research Centre, India
Neklyudov, I.	National Science Centre Kharkov Institute of Science and Technology, Ukraine
Oliveira, F.L. de	Instituto de Pesquisas Energeticas e Nucleares- Universidade de Sao Paulo (IPEN-USP), Brazil
Park, H.J.	Seoul National University, Republic of Korea
Pešić, M.	Vinca Institute of Nuclear Sciences, Serbia
Pyeon, C.	Kyoto University, Japan
Quan, Y.	China Institute of Atomic Energy, China
Rossi, P.C.R.	Instituto de Pesquisas Energeticas e Nucleares- Universidade de Sao Paulo (IPEN-USP), Brazil
Routkovskaya, C.	Joint Institute for Power and Nuclear Research - Sosny, Belarus
Sadovich, S.	Joint Institute for Power and Nuclear Research - Sosny, Belarus
Sasa, T.	Japan Atomic Energy Agency (JAEA), Japan
Shi, Y.	China Institute of Atomic Energy, China
Shim, H.J.	Seoul National University, Republic of Korea
Smith, D.	Argonne National Laboratory, USA
Sugawara, T.	Japan Atomic Energy Agency (JAEA), Japan
Soares, A.J.	International Atomic Energy Agency
Sollychin, R.	International Atomic Energy Agency
Strugalska-Gola, E.	Institute of Atomic Energy, Poland
Szuta, M.	Institute of Atomic Energy, Poland
Talamo, A.	Argonne National Laboratory, USA
Ushakov, I.	National Science Centre Kharkov Institute of Science and Technology, Ukraine
Wojciechowski, A.	Institute of Atomic Energy, Poland
Wu, X.	China Institute of Atomic Energy, China
Xia, H.	China Institute of Atomic Energy, China
Xia, P.	China Institute of Atomic Energy, China
Yadav, R.D.S.	Bhabha Atomic Research Centre, India
Yinlu, H.	China Institute of Atomic Energy, China
Yu, T.	China Institute of Atomic Energy, China

Zelinsky, A. National Science Centre Kharkov Institute of Science and Technology,
Ukraine

Zhang, W. China Institute of Atomic Energy, China

Zhong, Z. Argonne National Laboratory, USA

Zhu, Q. China Institute of Atomic Energy, China



ORDERING LOCALLY

In the following countries, IAEA priced publications may be purchased from the sources listed below or from major local booksellers.

Orders for unpriced publications should be made directly to the IAEA. The contact details are given at the end of this list.

CANADA

Renouf Publishing Co. Ltd

22-1010 Polytek Street, Ottawa, ON K1J 9J1, CANADA

Telephone: +1 613 745 2665 • Fax: +1 643 745 7660

Email: order@renoufbooks.com • Web site: www.renoufbooks.com

Bernan / Rowman & Littlefield

15200 NBN Way, Blue Ridge Summit, PA 17214, USA

Tel: +1 800 462 6420 • Fax: +1 800 338 4550

Email: orders@rowman.com Web site: www.rowman.com/bernan

CZECH REPUBLIC

Suweco CZ, s.r.o.

Sestupná 153/11, 162 00 Prague 6, CZECH REPUBLIC

Telephone: +420 242 459 205 • Fax: +420 284 821 646

Email: nakup@suweco.cz • Web site: www.suweco.cz

FRANCE

Form-Edit

5 rue Janssen, PO Box 25, 75921 Paris CEDEX, FRANCE

Telephone: +33 1 42 01 49 49 • Fax: +33 1 42 01 90 90

Email: formedit@formedit.fr • Web site: www.form-edit.com

GERMANY

Goethe Buchhandlung Teubig GmbH

Schweitzer Fachinformationen

Willstätterstrasse 15, 40549 Düsseldorf, GERMANY

Telephone: +49 (0) 211 49 874 015 • Fax: +49 (0) 211 49 874 28

Email: kundenbetreuung.goethe@schweitzer-online.de • Web site: www.goethebuch.de

INDIA

Allied Publishers

1st Floor, Dubash House, 15, J.N. Heredi Marg, Ballard Estate, Mumbai 400001, INDIA

Telephone: +91 22 4212 6930/31/69 • Fax: +91 22 2261 7928

Email: alliedpl@vsnl.com • Web site: www.alliedpublishers.com

Bookwell

3/79 Nirankari, Delhi 110009, INDIA

Telephone: +91 11 2760 1283/4536

Email: bkwell@nde.vsnl.net.in • Web site: www.bookwellindia.com

ITALY

Libreria Scientifica "AEIOU"

Via Vincenzo Maria Coronelli 6, 20146 Milan, ITALY
Telephone: +39 02 48 95 45 52 • Fax: +39 02 48 95 45 48
Email: info@libreriaaeiou.eu • Web site: www.libreriaaeiou.eu

JAPAN

Maruzen-Yushodo Co., Ltd

10-10 Yotsuyasakamachi, Shinjuku-ku, Tokyo 160-0002, JAPAN
Telephone: +81 3 4335 9312 • Fax: +81 3 4335 9364
Email: bookimport@maruzen.co.jp • Web site: www.maruzen.co.jp

RUSSIAN FEDERATION

Scientific and Engineering Centre for Nuclear and Radiation Safety

107140, Moscow, Malaya Krasnoselskaya st. 2/8, bld. 5, RUSSIAN FEDERATION
Telephone: +7 499 264 00 03 • Fax: +7 499 264 28 59
Email: secnrs@secnrs.ru • Web site: www.secnrs.ru

UNITED STATES OF AMERICA

Bernan / Rowman & Littlefield

15200 NBN Way, Blue Ridge Summit, PA 17214, USA
Tel: +1 800 462 6420 • Fax: +1 800 338 4550
Email: orders@rowman.com • Web site: www.rowman.com/bernan

Renouf Publishing Co. Ltd

812 Proctor Avenue, Ogdensburg, NY 13669-2205, USA
Telephone: +1 888 551 7470 • Fax: +1 888 551 7471
Email: orders@renoufbooks.com • Web site: www.renoufbooks.com

Orders for both priced and unpriced publications may be addressed directly to:

Marketing and Sales Unit
International Atomic Energy Agency
Vienna International Centre, PO Box 100, 1400 Vienna, Austria
Telephone: +43 1 2600 22529 or 22530 • Fax: +43 1 2600 29302 or +43 1 26007 22529
Email: sales.publications@iaea.org • Web site: www.iaea.org/books

International Atomic Energy Agency
Vienna
ISBN 978-92-0-106217-8
ISSN 1011-4289

